

PROCEEDINGS OF SPIE



SPIE—The International Society for Optical Engineering

Light-Emitting Diodes: Research, Manufacturing, and Applications IV

H. Walter Yao
Ian T. Ferguson
E. Fred Schubert
Chairs/Editors

26-27 January 2000
San Jose, California

DISTRIBUTION STATEMENT A
Approved for Public Release
Distribution Unlimited

Sponsored by
U.S. Army Research Office
AIXTRON, Inc.
SPIE—The International Society for Optical Engineering



20001122 076

Volume 3938

DTIC QUALITY INSURED 4

REPORT DOCUMENTATION PAGEForm Approved
OMB NO. 0704-0188

Public Reporting burden for this collection of information is estimated to average 1 hour per response, including the time for reviewing instructions, searching existing data sources, gathering and maintaining the data needed, and completing and reviewing the collection of information. Send comment regarding this burden estimates or any other aspect of this collection of information, including suggestions for reducing this burden, to Washington Headquarters Services, Directorate for Information Operations and Reports, 1215 Jefferson Davis Highway, Suite 1204, Arlington, VA 22202-4302, and to the Office of Management and Budget, Paperwork Reduction Project (0704-0188,) Washington, DC 20503.

1. AGENCY USE ONLY (Leave Blank)		2. REPORT DATE September 2000		3. REPORT TYPE AND DATES COVERED Final report	
4. TITLE AND SUBTITLE I Light-Emitting Diodes: Research, Manufacturing, and Applications IV				5. FUNDING NUMBERS DAAD19-00-1-0025	
6. AUTHOR(S) Haude Walter Yao, Principal Investigator					
7. PERFORMING ORGANIZATION NAME(S) AND ADDRESS(ES) SPIE-International Society for Optical Engineering Bellingham, WA 98225				8. PERFORMING ORGANIZATION REPORT NUMBER	
9. SPONSORING / MONITORING AGENCY NAME(S) AND ADDRESS(ES) U. S. Army Research Office P.O. Box 12211 Research Triangle Park, NC 27709-2211				10. SPONSORING / MONITORING AGENCY REPORT NUMBER ARO 41034.1-EL-CF	
11. SUPPLEMENTARY NOTES The views, opinions and/or findings contained in this report are those of the author(s) and should not be construed as an official Department of the Army position, policy or decision, unless so designated by other documentation.					
12 a. DISTRIBUTION / AVAILABILITY STATEMENT Approved for public release; distribution unlimited.				12 b. DISTRIBUTION CODE	
13. ABSTRACT (Maximum 200 words) This book records the fourth conference dedicated to light-emitting diodes (LEDs), held during Photonics West in San Jose, California on 26-27 January 2000. The proceedings contain 30 invited and contributed papers arranged according to the 6 sessions of the conference. The papers cover LEDs emitting in the ultraviolet, visible, and infrared regions of the optical spectrum. LEDs are used for lighting, display, communication, and other applications. This book provides an overview of the current rapid progress in this field.					
14. SUBJECT TERMS				15. NUMBER OF PAGES	
				16. PRICE CODE	
17. SECURITY CLASSIFICATION OR REPORT UNCLASSIFIED	18. SECURITY CLASSIFICATION ON THIS PAGE UNCLASSIFIED	19. SECURITY CLASSIFICATION OF ABSTRACT UNCLASSIFIED	20. LIMITATION OF ABSTRACT UL		



PROCEEDINGS OF SPIE

SPIE—The International Society for Optical Engineering

Light-Emitting Diodes: Research, Manufacturing, and Applications IV

**H. Walter Yao
Ian T. Ferguson
E. Fred Schubert**
Chairs/Editors

**26–27 January 2000
San Jose, California**

Sponsored by
U.S. Army Research Office
AIXTRON, Inc.
SPIE—The International Society for Optical Engineering

Published by
SPIE—The International Society for Optical Engineering



Volume 3938

SPIE is an international technical society dedicated to advancing engineering and scientific applications of optical, photonic, imaging, electronic, and optoelectronic technologies.



The papers appearing in this book compose the proceedings of the technical conference cited on the cover and title page of this volume. They reflect the authors' opinions and are published as presented, in the interests of timely dissemination. Their inclusion in this publication does not necessarily constitute endorsement by the editors or by SPIE. Papers were selected by the conference program committee to be presented in oral or poster format, and were subject to review by volume editors or program committees.

Please use the following format to cite material from this book:

Author(s), "Title of paper," in *Light-Emitting Diodes: Research, Manufacturing, and Applications IV*, H. Walter Yao, Ian T. Ferguson, E. Fred Schubert, Editors, Proceedings of SPIE Vol. 3938, page numbers (2000).

ISSN 0277-786X
ISBN 0-8194-3555-4

Published by
SPIE—The International Society for Optical Engineering
P.O. Box 10, Bellingham, Washington 98227-0010 USA
Telephone 360/676-3290 (Pacific Time) • Fax 360/647-1445

Copyright ©2000, The Society of Photo-Optical Instrumentation Engineers.

Copying of material in this book for internal or personal use, or for the internal or personal use of specific clients, beyond the fair use provisions granted by the U.S. Copyright Law is authorized by SPIE subject to payment of copying fees. The Transactional Reporting Service base fee for this volume is \$15.00 per article (or portion thereof), which should be paid directly to the Copyright Clearance Center (CCC), 222 Rosewood Drive, Danvers, MA 01923. Payment may also be made electronically through CCC Online at <http://www.directory.net/copyright/>. Other copying for republication, resale, advertising or promotion, or any form of systematic or multiple reproduction of any material in this book is prohibited except with permission in writing from the publisher. The CCC fee code is 0277-786X/00/\$15.00.

Printed in the United States of America.

Contents

vii	Conference Committee
ix	Introduction

SESSION 1 III-NITRIDE LIGHT-EMITTING DIODES I

- 2 **High-brightness AlGaInN light-emitting diodes (Invited Paper) [3938-02]**
M. R. Krames, G. Christenson, D. Collins, L. W. Cook, M. G. Craford, A. Edwards,
R. M. Fletcher, N. F. Gardner, W. K. Goetz, W. R. Imler, E. Johnson, R. S. Kern, R. Khare,
F. A. Kish, C. Lowery, M. J. Ludowise, R. Mann, M. Maranowski, S. A. Maranowski,
P. S. Martin, J. O'Shea, S. L. Rudaz, D. A. Steigerwald, J. Thompson, J. J. Wierer, J. G. Yu,
LumiLeds Lighting; D. Basile, Y.-L. Chang, G. Hasnain, M. Heuschen, K. Killeen, C. P. Kocot,
S. Lester, J. N. Miller, G. O. Mueller, R. Mueller-Mach, S. J. Rosner, R. P. Schneider,
T. Takeuchi, T. S. Tan, Agilent Technologies

- 13 **Design and performance of nitride-based UV LEDs (Invited Paper) [3938-08]**
M. H. Crawford, J. Han, W. W. Chow, M. A. Banas, J. J. Figiel, L. Zhang, R. J. Shul, Sandia
National Labs.

- 24 **GaN-based MQW light-emitting devices (Invited Paper) [3938-05]**
M. Koike, S. Yamasaki, Y. Tezen, S. Nagai, S. Iwayama, A. Kojima, T. Uemura, A. Hirano,
H. Kato, Toyoda Gosei Co., Ltd. (Japan)

- 30 **White-light-emitting diodes for illumination [3938-06]**
R. Mueller-Mach, G. O. Mueller, Agilent Technologies

SESSION 2 III-NITRIDE LIGHT-EMITTING DIODES II

- 44 **InGaAlP and InGaN light-emitting diodes: high-power performance and reliability (Invited Paper) [3938-12]**
I. Eliashevich, J.-P. M. Debray, C. A. Tran, H. Venugopalan, R. F. Karliceck, Jr., GELcore
LLC/EMCORE Corp.

- 52 **Gain switching of GaInN MQW laser diodes [3938-14]**
C. Marinelli, I. Y. Khrushchev, J. M. Rorison, R. V. Penty, I. H. White, Univ. of Bristol (UK);
T. Takeuchi, H. Amano, I. Akasaki, Meijo Univ. (Japan); Y. Kaneko, S. W. Watanabe,
N. Yamada, Agilent Technologies (Japan); G. Hasnain, R. P. Schneider, S.-Y. Wang,
M. R. T. Tan, Agilent Technologies

- 60 **Photon recycling semiconductor light-emitting diode [3938-10]**
X. Guo, J. W. Graff, E. F. Schubert, Boston Univ.; R. F. Karliceck, Jr., GELcore LLC

SESSION 3 HIGH-EFFICIENCY LEDs

- 70 **Nonresonant-cavity light-emitting diodes (Invited Paper) [3938-03]**
R. Windisch, IMEC (Belgium); M. Kuijk, Vrije Univ. Brussels (Belgium); B. Dutta, IMEC (Belgium); A. Knobloch, P. Kiesel, G. H. Döhler, Friedrich-Alexander Univ. Erlangen-Nürnberg (Germany); G. Borghs, P. L. Heremans, IMEC (Belgium)
- 77 **High-power truncated-inverted-pyramid $(\text{Al}_x\text{Ga}_{1-x})_{0.5}\text{In}_{0.5}\text{P}$ light-emitting diodes [3938-09]**
M. O. Holcomb, M. R. Krames, G. E. Hofler, C. Carter-Coman, E. I. Chen, P. N. Grillo, K. Park, N. F. Gardner, J.-W. Huang, J. Posselt, D. Collins, S. A. Stockman, M. G. Craford, LumiLeds Lighting; F. A. Kish, I.-H. Tan, T. S. Tan, C. P. Kocot, M. Hueschen, Agilent Technologies
- 82 **Resonant-cavity LEDs at 655- and 880-nm wavelengths [3938-13]**
P. Sipilä, M. J. Saarinen, V. Vilokkinen, S. Orsila, P. Melanen, P. Savolainen, M. Toivonen, M. M. Dumitrescu, M. Pessa, Tampere Univ. of Technology (Finland)
- 90 **45% quantum-efficiency light-emitting diodes with radial outcoupling taper [3938-07]**
W. Schmid, F. Eberhard, R. Jäger, R. King, M. Miller, J. Joos, K. J. Ebeling, Univ. of Ulm (Germany)

SESSION 4 III-NITRIDES AND RELATED MATERIALS

- 100 **Highly efficient InGaN/GaN MQW for blue- and green-light-emitting structures grown in production MOVPE reactors [3938-16]**
M. D. Bremser, AIXTRON, Inc.; M. Luenenbuerger, H. Protzmann, M. Heuken, AIXTRON AG (Germany)
- 105 **Disorder in InGaN light-emitting diodes [3938-17]**
M. Pophristic, S. J. Lukacs, F. H. Long, Rutgers Univ.; C. A. Tran, I. T. Ferguson, EMCORE Corp.
- 113 **Optical properties of AlN/sapphire grown at high and low temperatures studied by variable angle spectroscopic ellipsometry and micro Raman scattering [3938-18]**
C. H. Yan, H. W. Yao, Univ. of Nebraska/Lincoln; A. C. Abare, S. P. DenBaars, Univ. of California/Santa Barbara; J. J. Klaassen, M. F. Rosamond, P. P. Chow, SVT Associates, Inc.; J. M. Zavada, U.S. Army European Research Office (UK)
- 124 **Novel processing for improving optical property of InGaN/GaN MQW light-emitting diode [3938-19]**
C. H. Hwang, K.-Y. Hsieh, National Sun Yat-sen Univ. (Taiwan); H. S. Huang, Military Academy/Kaohsiung (Taiwan); L.-W. Tu, National Sun Yat-sen Univ. (Taiwan)
- 131 **Optical properties of InN thin films [3938-20]**
V. Ya. Malakhov, Institute for Problems of Materials Science (Ukraine)
- 137 **Exciton localization and the Stokes' shift in undoped InGaN/GaN multiquantum wells (Invited Paper) [3938-21]**
Y. F. Chen, T. Y. Lin, H. C. Yang, National Taiwan Univ.

SESSION 5 III-As AND III-P LEDs

- 144 **Improved-efficiency positive and negative luminescent light-emitting devices for mid-infrared gas-sensing applications (Invited Paper) [3938-22]**
M. J. Pullin, X. Li, J. Heber, D. Gervaux, C. C. Phillips, Imperial College of Science, Technology and Medicine (UK)
- 154 **Native oxidized AlAs current blocking layer for AlGaInP high-brightness light-emitting diodes [3938-23]**
G. Wang, X. Ma, Y. Zhang, S. Wang, Y. Li, L. Chen, Institute of Semiconductors (China)

SESSION 6 NOVEL STRUCTURES AND MATERIALS

- 160 **Substrate-removed 850-nm RCLEDs and small core (63/125 μ m) plastic optical fibers for optical data communication (Invited Paper) [3938-25]**
T. Coosemans, R. Bockstaele, A. Van Hove, K. Naessens, J. Derluyn, L. Vanwassenhove, P. Van Daele, I. Moerman, R. G. Baets, IMEC (Belgium)
- 169 **Efficiency optimization in ionically self-assembled thin film polymer light-emitting diodes [3938-26]**
D. Marciu, M. Miller, A. L. Ritter, Luna Innovations, Inc.; M. A. Murray, P. J. Neyman, W. Graupner, J. R. Heflin, H. Wang, H. W. Gibson, R. M. Davis, Virginia Polytechnic Institute and State Univ.
- 180 **LED backlight: design, fabrication, and testing [3938-30]**
D. M. Brown, MEMS Optical, LLC; R. N. Dean, Auburn Univ.; J. D. Brown, MEMS Optical, LLC
- 188 **Multispectral reflectance-mode fiber optic deposition rate monitor [3938-31]**
J. T. Daly, J. A. Wollam, Ion Optics, Inc.; F. Luo, T. F. Morse, Boston Univ.; A. Kusmaul, D. Pulver, Lasertron, Inc.
- 196 **4-mW microcavity LED at 650 nm on germanium substrates [3938-41]**
M. D'Hondt, Union Minière (Belgium) and IMEC (Belgium); P. Modak, D. Delbeke, I. Moerman, P. Van Daele, R. G. Baets, P. M. Demeester, IMEC (Belgium); P. Mijlemans, Union Minière (Belgium)
- 205 **Long-wavelength shift of ZnSSe metal-semiconductor-metal light-emitting diodes with high injection currents [3938-33]**
Y. K. Su, W. R. Chen, S.-J. Chang, National Cheng Kung Univ. (Taiwan); F.-S. Juang, National Huwei Institute of Technology (Taiwan); W. H. Lan, A. C. H. Lin, H. Chang, Chung Shan Institute of Science and Technology (Taiwan)

POSTER SESSION

- 218 **Effects of buffer layer growth conditions on the GaN epilayer quality by MOCVD [3938-34]**
F.-S. Juang, National Huwei Institute of Technology (Taiwan); Y. K. Su, S.-J. Chang, T. K. Chu, C. S. Chen, National Cheng Kung Univ. (Taiwan); L. W. Chi, K. T. Lam, Kao Yuan Institute of Technology and Commercialism (Taiwan)

- 224 **Ohmic contacts to GaN with rapid thermal annealing [3938-35]**
L. W. Chi, K. T. Lam, Y. K. Kao, Kao Yuan Institute of Technology (Taiwan); F.-S. Juang,
Y. S. Tasi, National Huwei Institute of Technology (Taiwan); Y. K. Su, S.-J. Chang, C. C. Chen,
J. K. Sheu, National Cheng Kung Univ. (Taiwan)
- 234 **Optical properties of $\text{Fe}_{(1-x)}\text{Co}_x\text{Si}_2$ thin films [3938-38]**
Y.-J. Zhang, Y.-X. Zheng, R. J. Zhang, L.-Y. Chen, Fudan Univ. (China)
- 240 **Characterizing white LEDs for general illumination applications [3938-39]**
N. Narendran, N. Maliyagoda, A. Bierman, R. M. Pysar, M. Overington, Rensselaer
Polytechnic Institute
- 249 **High-performance epoxy casting resins for SMD-LED packaging [3938-40]**
G. Bogner, A. Debray, OSRAM Opto Semiconductor GmbH (Germany); K. Höhn, Siemens
AG (Germany)
- 263 *Addendum*
- 264 *Author Index*

Conference Committee

Conference Chairs

H. Walter Yao, University of Nebraska/Lincoln
Ian T. Ferguson, EMCORE Corporation
E. Fred Schubert, Boston University

Program Committee

Isamu Akasaki, Meijo University (Japan)
Hiroshi Amano, Meijo University (Japan)
Steven P. DenBaars, University of California/Santa Barbara
Kathy Doverspike, Cree Research, Inc.
Mitra Dutta, U.S. Army Research Office
Robert M. Fletcher, Hewlett-Packard Company
Paul L. Heremans, IMEC (Belgium)
Juergen Jahns, Fernuniversität Hagen (Germany)
Eric D. Jones, Sandia National Laboratories
Lionel C. Kimerling, Massachusetts Institute of Technology
Jeffrey N. Miller, Hewlett-Packard Laboratories
Shuji Nakamura, Nichia Chemical Industries, Ltd. (Japan)
Li Wei Tu, National Sun Yat-sen University (Taiwan)
Eli Yablonovitch, University of California/Los Angeles

Session Chairs

- 1 III-Nitride Light-Emitting Diodes I
 H. Walter Yao, University of Nebraska/Lincoln
 John M. Zavada, U.S. Army European Research Office (UK)
- 2 III-Nitride Light-Emitting Diodes II
 E. Fred Schubert, Boston University
- 3 High-Efficiency LEDs
 Steven P. DenBaars, University of California/Santa Barbara
- 4 III-Nitrides and Related Materials
 Eric D. Jones, Sandia National Laboratories
 Klaus H. Ploog, Paul-Drude-Institut für Festkörperelektronik (Germany)
- 5 III-As and III-P LEDs
 Paul L. Heremans, IMEC (Belgium)

- 6 Novel Structures and Materials
R. Scott Kern, LumiLeds Lighting
Masayoshi Koike, Toyoda Gosei Company, Ltd. (Japan)

Poster Session
Li Wei Tu, National Sun Yat-sen University (Taiwan)

Introduction

This book records the fourth conference dedicated to light-emitting diodes (LEDs), held during Photonics West in San Jose, California on 26–27 January 2000.

The proceedings contain 30 invited and contributed papers arranged according to the 6 sessions of the conference. The papers cover LEDs emitting in the ultraviolet, visible, and infrared regions of the optical spectrum. LEDs are used for lighting, display, communication, and other applications. This book provides an overview of the current rapid progress in this field.

We would like to thank the authors, program committee members, session chairs, and their affiliations for providing this valued and timely update on LED research, manufacturing, and applications.

**H. Walter Yao
Ian T. Ferguson
E. Fred Schubert**

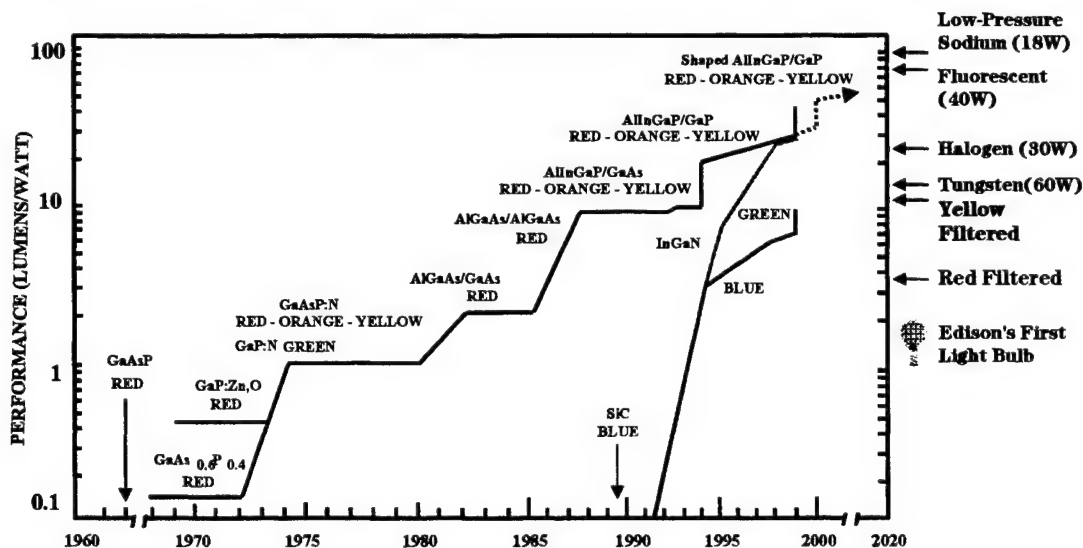
SESSION 1

III-Nitride Light-Emitting Diodes I

LumiLeds Lighting, 370 W. Trimble Rd., San Jose, CA. 95131

Agilent Laboratories, 3500 Deer Creek Road, Palo Alto, CA 94303

Keywords: LED, light-emitting diode, gallium nitride, high power LED, AlGaInN, InGaN



compound semiconductor alloys and the demonstration of the first practical LED (red-emitting GaAsP) in 1962 provided the foundation for the commercial development of the solid-state lamp.¹ The discovery of the isoelectronic trap, nitrogen, in GaAsP in 1971 extended the useful wavelength spectrum of light-emitting diodes (LEDs) to the yellow spectral region.² A significant increase in the efficiency of red emitters was achieved through the development of AlGaAs/GaAs LEDs employing a fully lattice-matched direct bandgap system and heterostructure active regions.^{3,4} In the 1970s the LED lamp exceeded the performance (luminous efficiency) of a red-filtered incandescent bulb. The performance of the AlGaAs LEDs was further improved by the development of transparent-substrate (TS) devices (AlGaAs/AlGaAs) which doubled the efficiency of these emitters compared to their absorbing-substrate (AS) counterparts.⁵ The emergence of AlGaInP/GaAs technology in the 1980s extended the useful wavelength range of high-brightness emitters into the orange and yellow spectral regions.⁶ The development of TS AlGaInP/GaP devices doubled the efficiency of these devices and demonstrated the commercial viability of direct compound semiconductor wafer bonding technology.⁷ Additional improvements to both the internal and external quantum efficiency of TS AlGaInP/GaP devices using multi-well active region structures have resulted in devices with efficiencies >70 lm/W at a peak wavelength (λ_p) of 615 nm and external quantum efficiencies >30% at $\lambda_p \sim 632$ nm.⁸ The utility of these devices as practical lighting sources has further been improved by the development of high-power, high-flux (10-20 lm) AlGaInP/GaP LED lamps.⁹ Most recently, the employment of chip shaping to AlGaInP/GaP LED technology has resulted in power LEDs with luminous efficiencies exceeding 100 lm/W in the orange spectral region ($\lambda_p \sim 610$ nm), and external quantum efficiencies exceeding 55% in the deep red spectral region ($\lambda_p \sim 650$ nm).¹⁰

Similar dramatic improvements in LED performance have been achieved in the blue and green spectra region through the development of the AlGaInN material system. Photoluminescence from polycrystalline GaN was observed in 1962¹¹, and the first GaN-based LEDs were fabricated by material grown by hydride-phased vapor epitaxy (HVPE)¹²⁻¹⁴. The first GaN LEDs grown by OMVPE employed sapphire substrates and were demonstrated in 1984¹⁵. Considerable improvement was realized after the development of low-temperature buffer layers for high-quality GaN films¹⁶ and the realization of p-type GaN:Mg using low-energy electron-beam ionization (LEEBI)¹⁷. In 1991, Nakamura and co-workers developed an annealing technique¹⁸ that provided similar activation of Mg and subsequently demonstrated violet LEDs employing an InGaN active region¹⁹. The brightest AlGaInN LEDs are achieved using quantum-well active regions wherein the mole fraction of InN in the wells determines the peak emission wavelength²⁰. Today, external quantum efficiencies of $\sim 21\%$ in the blue ($\lambda_p \sim 470$ nm) and $\sim 15\%$ in the green ($\lambda_p \sim 530$ nm) spectral regions have been observed. In photometric terms, these efficiencies correspond to ~ 10 lm/W and ~ 55 lm/W, respectively. The highest-reported luminous efficiencies of LEDs to date are shown in Fig. 2 and are dominated by the AlGaInN and AlGaInP material systems.

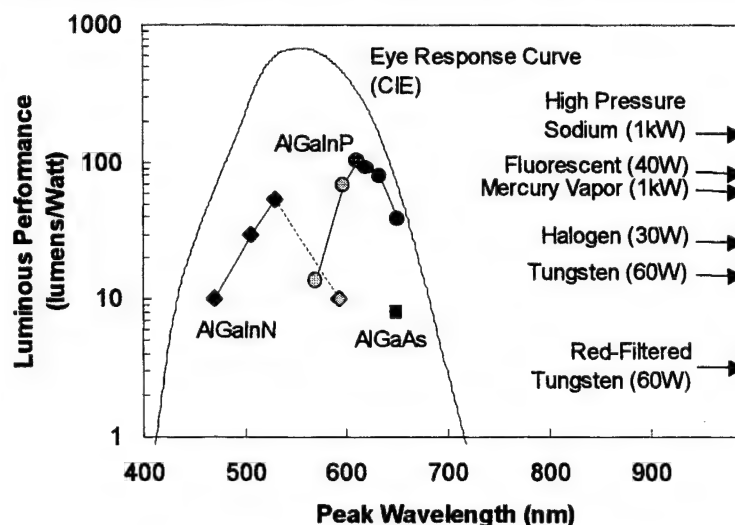


Fig. 2. Highest-reported LED luminous efficiencies.

2. STATUS OF III-NITRIDE LED TECHNOLOGY

The AlGaInN material system poses some unique challenges compared to conventional III-V material systems. Presently, the lack of a lattice-mismatched substrate results in very high defect densities, which, although not

strongly linked to poor quantum efficiency at the low current densities of LEDs, are nevertheless linked to reliability problems for AlGaInN laser diodes²¹. The two most common substrates used for OMVPE growth of AlGaInN are sapphire and SiC. Most commercial LED suppliers use sapphire substrates which are significantly less expensive than SiC. However, the use of sapphire as a growth substrate poses device design challenges. Sapphire is insulating and therefore both p and n Ohmic contacts must be formed on the top surface of the LED chip. This is performed by mesa etching the AlGaInN LED structure to

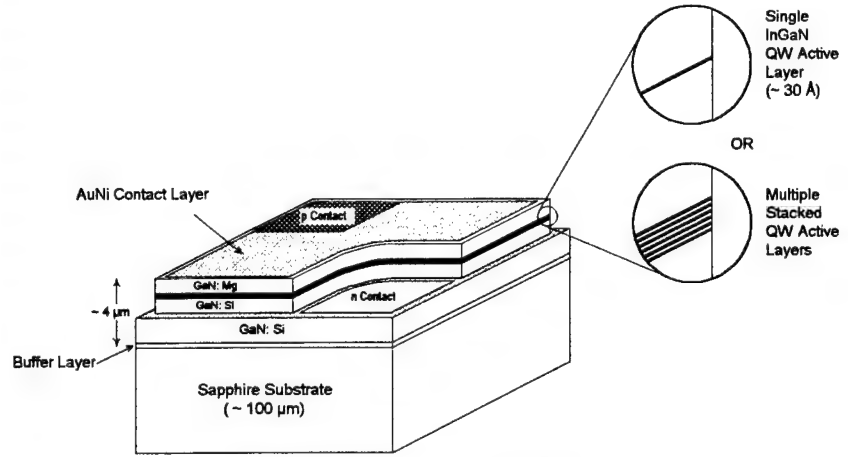


Fig. 3. Typical AlGaInN LED structure.

expose the n-type GaN layers beneath the active region. Ohmic n-contact metallization, typically Ti/Al, is applied to the n-type GaN. The p-type Ohmic contact is required to spread current from the p bond pad across the junction area because of the very low conductivity of GaN:Mg. This is typically done by depositing a semi-transparent Ni/Au Ohmic contact metallization across the GaN:Mg surface. Current from the n-type contact is required to spread through the GaN:Si layers beneath the active region. A typical device structure is shown in Fig. 3. In general, this type of structure results in an increased series resistance compared to LEDs based on other III-V material systems, and provides a challenge in terms of achieving the highest possible power conversion efficiencies.

Even accounting for the increased series resistance, AlGaInN LEDs presently exhibit higher forward voltages than LEDs in other III-V material systems. Figure 4 shows a plot of forward voltage (at 20 mA) vs. bandgap energy for LEDs based on several different material systems. It is notable that AlGaInN LEDs throughout the blue, green, and amber spectral regions exhibit forward voltages about 0.5-1.0 V higher than their bandgap voltages. A comparison of current-voltage characteristics of AlGaInP and AlGaInN LEDs, shown in Fig. 4b, show that this voltage increase is apparent at very low current levels. At 1 mA, the AlGaInP LED exhibits a forward voltage of 1.8 V, about 300 mV below the bandedge emission at 593 nm. At the same current, the AlGaInN LED exhibits a forward voltage of 2.4 V, which is only about 80 mV below the bandedge emission for 500 nm. The difference in series resistance between the two structures is, worst case, about 20 Ω . At 1 mA, the difference in series resistance can only account

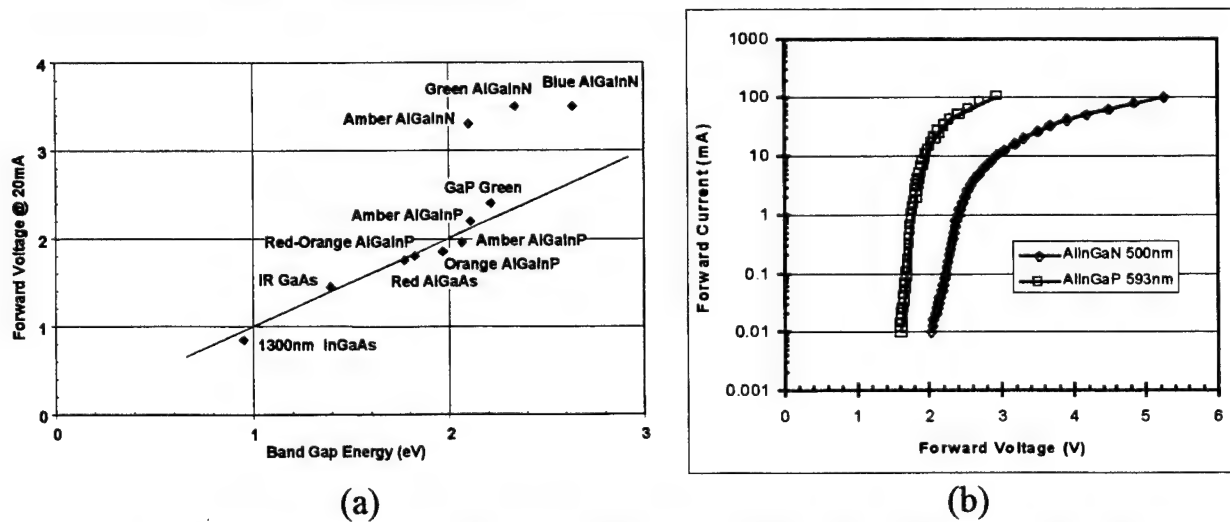


Fig. 4. (a) Comparison of forward voltage characteristics of AlGaInN LEDs compared to LEDs based on other III-V materials systems. (b) Comparison of current-voltage characteristics between an AlGaInP LED (593 nm) and a AlGaInN LED (500 nm).

for 20 mV of the difference in forward voltage. Thus, the AlGaInN LED has additional ~200 mV forward voltage increase at 1mA compared to the AlGaInP LED. At 20 mA, the same comparison yields ~400 mV of increased voltage (offset) for the AlGaInN LED. Presumably, the increased forward voltage for the AlGaInN LEDs are due to internal barriers to conduction through the p-n junction heterostructure. The heterostructure designs are typically comprised of InGaN quantum wells with GaN or InGaN barriers, surrounded by GaN confining layers. An AlGaIn "electron stopper" layer is usually provided on top of the active region to improve electron confinement. This type of design, coupled with piezoelectric effects and spontaneous polarization fields on the band structure, may be responsible for the increased forward voltages observed in today's AlGaInN LEDs.

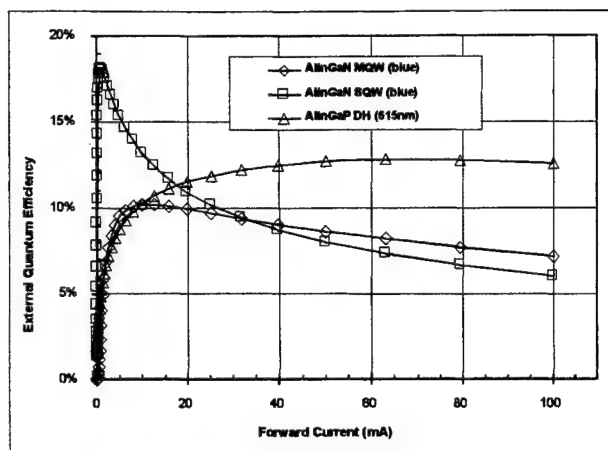


Fig. 5. External quantum efficiency of single- and multiple-quantum-well AlGaInN LEDs as function of current density, as compared to AlGaInP.

AlGaInN LEDs also differ from conventional III-V LEDs in terms of quantum efficiency as a function of current density. Figure 5 compares single- and multiple-quantum-well AlGaInN LED structures with a AlGaInP double-heterostructure LED. The AlGaInP LED exhibits increased quantum efficiency with increasing current density, until carrier leakage and thermal effects limit the maximum achievable efficiency. For the AlGaInN LEDs, the quantum efficiency peaks at low currents and decreases with increasing current density. This is especially apparent for the single-quantum-well structure, whose peak efficiency at ~1mA is 1.7x higher than that at 20 mA. For the multiple-quantum-well structure, the effect is less pronounced. Even so, the reduced quantum efficiency at higher current levels (e.g., 50 mA) for AlGaInN poses a challenge for realization of high-flux LEDs with high power-conversion efficiency. The details of the recombination physics in InGaIn-GaN-AlGaIn active regions needs to be better understood in order to provide a model for the decreased efficiency at high current levels and to provide hope for solving this problem.

Another issue with AlGaInN LEDs is obtaining a stable emission spectrum. Especially at long wavelengths, the electroluminescence peak shifts to shorter wavelengths with increasing current density. The effect is illustrated in Fig. 6. Blue AlGaInN LEDs at ~470 nm exhibit only a ~5 nm shift in going from 1 to 100 mA drive current. A "green" AlGaInN LED shifts from ~520 nm to ~505 nm over the same current range. Finally, an "amber" AlGaInN LED exhibits a very large FWHM, and shifts from ~595 nm to ~550 nm. Clearly the "amber" AlGaInN LED is no longer "amber" at the higher drive current. Even in going from 1 to 10 mA, the "amber" AlGaInN LED spectrum has shifted to the yellow spectral region. This problem makes the realization of long-wavelength AlGaInN LEDs difficult, since color control and stability provide enormous yield problems in high-volume manufacturing. Also, for AlGaInN emitters at wavelengths greater than $\lambda_p \sim 470$ nm, the quantum efficiency decreases significantly with increased In composition in the active region. Further development is necessary before AlGaInN LEDs can realistically compete

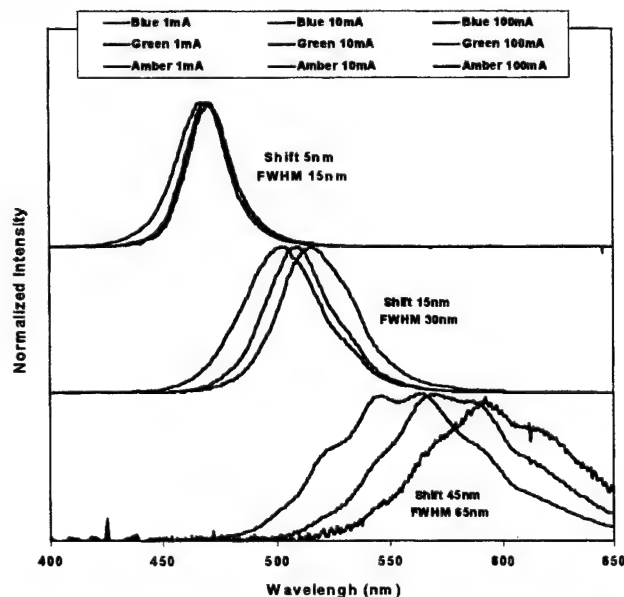


Fig. 6. Electroluminescence of blue, green, and "amber" AlGaInN LEDs at forward current levels of 1, 10 and 100 mA.

with AlGaInP LEDs in the yellow-amber wavelength regime.

Another serious issue for AlGaInN LED performance is reliability. Initial AlGaInN LED reliability was fairly poor, with a significant drop in light output observed under high-temperature operating lifetime tests beyond 500 hrs. Further investigation showed that the root cause of the degradation was due to the package, and not the LED chip²². By replacing the clear die-attach epoxy used to mount the LED chip to the lead-frame with a Ag-loaded die-attach epoxy, AlGaInN LED reliability was dramatically improved. Unfortunately, the switch to Ag-loaded die-attach epoxy resulted in a decrease in light output, presumably because of the poor reflectivity of this epoxy. By inserting a metal back-reflector on the sapphire substrate, the light output was recovered to result in a reliable AlGaInN LED with no penalty to light output. A summary of reliability characteristics of "first generation" and "improved" AlGaInN LEDs is shown in Fig. 7, along with a typical AlGaInP LED reliability characteristic for comparison. Presently, the best AlGaInN LED reliability performance begins to approach that of typical AlGaInP reliability at the same current density and junction temperature.

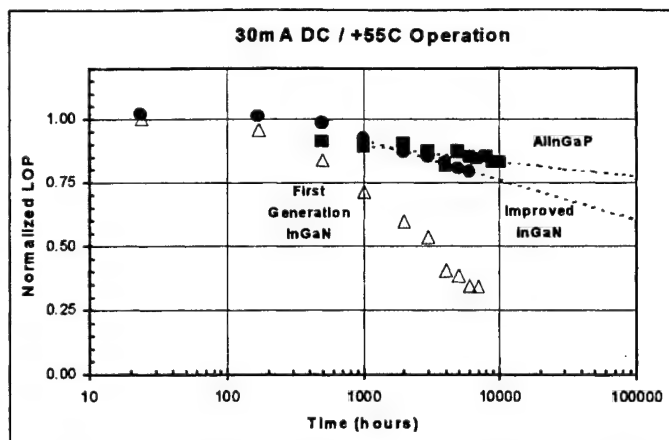


Fig. 7. Reliability performance of both "first-generation" and "improved" AlGaInN LEDs, as compared to AlGaInP.

3. HIGH-POWER III-NITRIDE LEDs

In order to compete effectively with conventional light sources, solid-state lamps based on LEDs must have comparable flux levels. Unfortunately, standard 5mm LED lamps driven at 20-30 mA only provide a few lumens of flux, in contrast to the many hundreds or thousands produced by conventional light sources. This disparity makes it difficult for LEDs to compete with conventional solutions in many applications. For example, in order to provide the same level of flux as a 60W incandescent light bulb, a solid-state light source would require several hundred LEDs. The required large number of packages increases assembly cost and real estate. Furthermore, the high thermal resistance of 5mm lamp packages limits the drive current and thus the total available flux that the LED chips can provide. By increasing the chip size and providing low-thermal-resistance power packages capable of dissipating several Watts, LEDs should be able to compete more favorably with conventional lighting technologies in many applications.

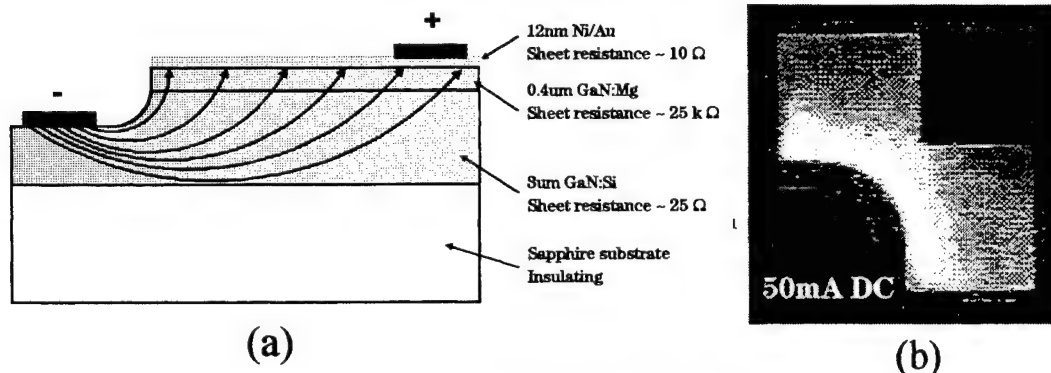


Fig. 8. (a) Sheet resistances in a typical AlGaInN LED structure. (b) Lit visual of AlGaInN LED at 50 mA, showing current crowding towards the n-type Ohmic contact.

In order to provide a power LED chip, the junction area must be increased to accommodate the larger input power. To spread current uniformly throughout the p-n junction for a large-area LED, the Ohmic contacts must be re-configured. The exact configuration will effect the series resistance of the device which is governed by the sheet resistances of the various layers of the AlGaInN LED structure. Typical values for these sheet resistances are shown in Fig. 8a. For a device with a typical Ni/Au p Ohmic contact ($\sim 10 \Omega$), the current spreading is limited not by this layer but by the GaN:Si layer instead ($\sim 25 \Omega$). This discrepancy suggests that it is current spreading from the n Ohmic contact that will be the dominant cause of current crowding at higher current densities. Indeed, this is observed in conventional device designs at high currents as illustrated in Fig. 8b, where light is generated at the n-contact due to crowding.

Clearly, a power AlGaInN LED requires an improved contact configuration in order to avoid the current crowding problem illustrated in Fig. 8b. Also, it is important that series resistance be kept to a minimum. A typical AlGaInN LED design like that shown in Fig. 8b has a series resistance of 20-30 Ω . Typical values for AlGaInP (vertical-injection) LEDs are 5-10 Ω . Improvement in an AlGaInN LED structure is evident in a new design, illustrated in

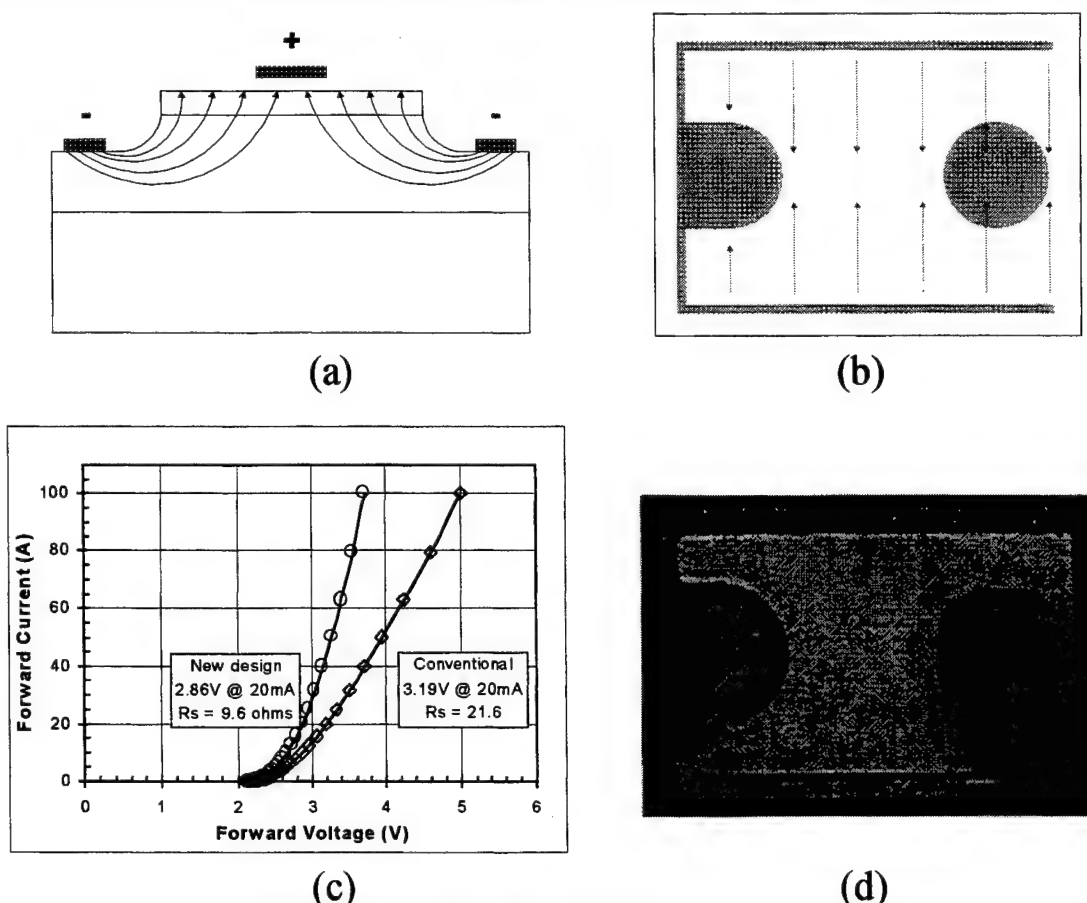


Fig. 9. (a) Cross-sectional and (b) plan views of improved AlGaInN LED structure. (c) Current-voltage characteristic of improved AlGaInN structure, as compared to the conventional device. (d) Lit visual of the improved structure at 50 mA.

Fig. 9. Figure 9a shows a schematic cross-section of an improved AlGaInN LED design, wherein the n Ohmic contact is brought along either side of the GaN:Mg mesa to reduce the spreading distance required by the current in the GaN:Si layers. A plan view of the device is shown in Fig. 9b. Such devices were fabricated and their current-voltage characteristics were measured and compared to those of standard AlGaInN LED structures from the same wafer. The results are shown in Fig. 9c. The improved design provides a series resistance of $\sim 9.6 \Omega$ at 20 mA, less than half that of the conventional design (21.6 Ω). The effect is dramatic at high currents: at 100 mA the improved

design exhibits a forward voltage of 3.6 V as compared to 5.0 V for the conventional structure. A lit visual of the improved LED at 50 mA is shown in Fig. 9d, which does not exhibit current crowding effects such as shown in Fig. 8b.

The above improved contact configuration can be extended to power AlGaInN LED design. This concept is illustrated in Fig. 10. By having interdigitated n and p Ohmic contacts, a large area LED may have excellent current spreading capability and low series resistance, both of which are very important for high-power operation. Figure 10a shows a plan view schematic of a $1 \times 1 \text{ mm}^2$ AlGaInN LED chip employing an interdigitated contact design. Figure 10b shows a schematic of the same structure in cross section. Each set of p Ohmic contacts is surrounded by two n Ohmic contact fingers, comprising a "cell" with a certain electrical resistance. By combining these cells as demonstrated in Fig. 10a and b, the total resistance of the device is the resistances of these cells in parallel. Therefore, the more cells in the design, the lower the series resistance.

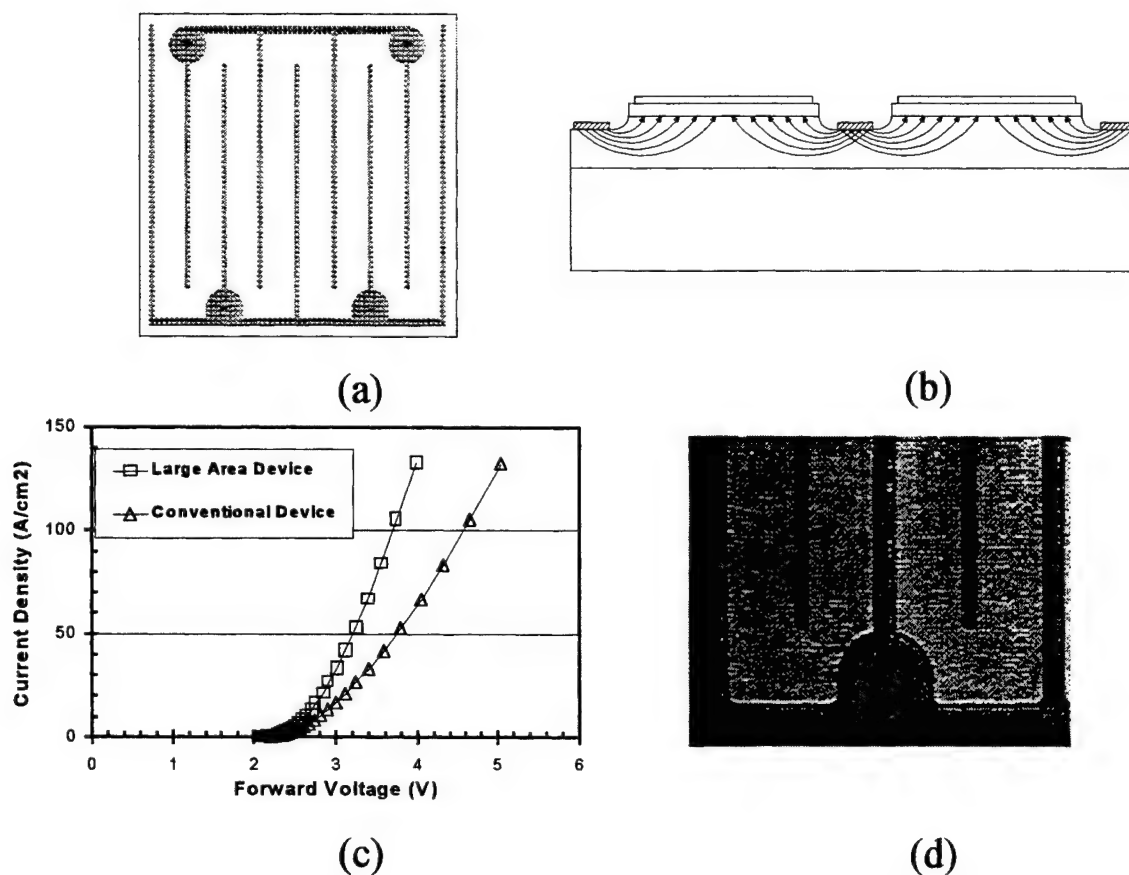
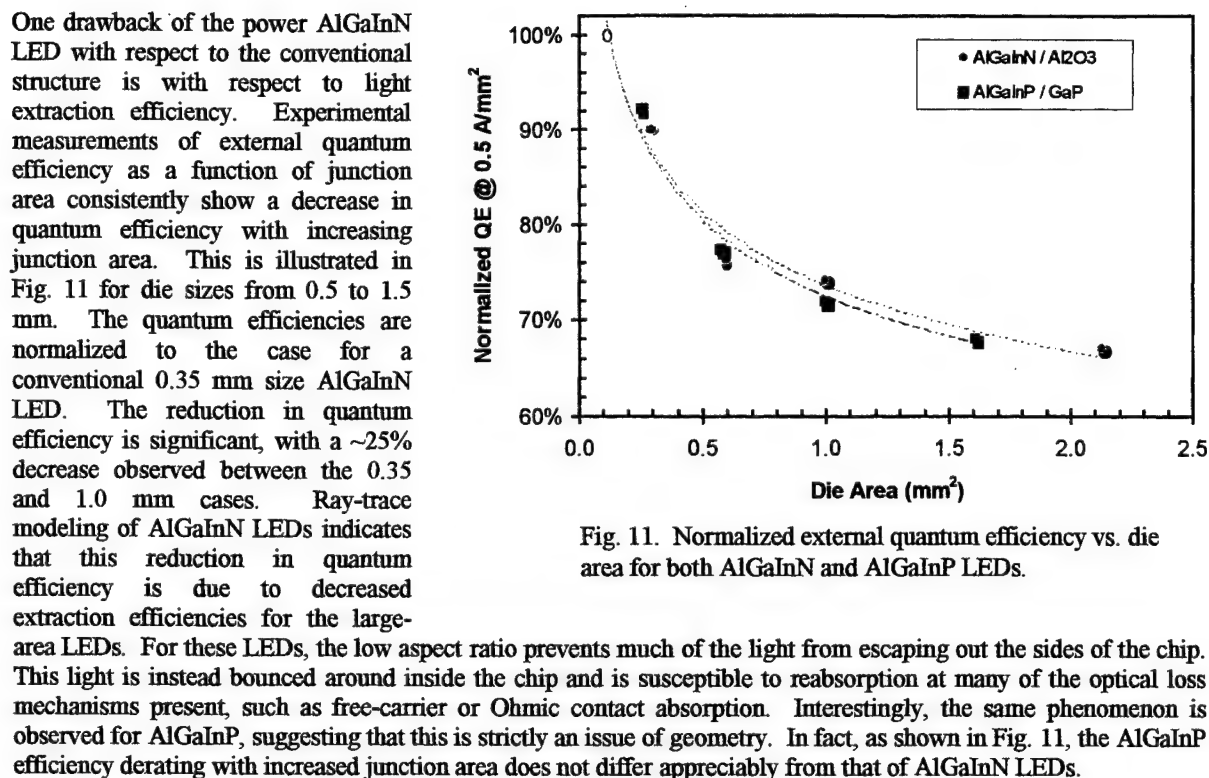


Fig. 10. (a) Cross-sectional and (b) plan views of a $1 \times 1 \text{ mm}^2$ power AlGaInN LED structure. (c) Voltage as a function of current density of the power AlGaInN LED, as compared to the conventional device ($\sim 0.35 \times 0.35 \text{ mm}^2$). (d) Lit visual of a portion of the power AlGaInN LED at 350 mA.

A simple calculation shows that the series resistance of the LED is proportional to N^{-2} , where N is the number of cells. Experimental optimization for the $1 \times 1 \text{ mm}^2$ device at 350 mA shows that four cells achieves the best performance in terms of power conversion efficiency. The forward voltage of such an LED is plotted in Fig. 10c as a function of current density, along with that of a conventional AlGaInN LED structure ($\sim 0.35 \times 0.35 \text{ mm}^2$). The power AlGaInN LED is shown to have an improved electrical performance even though it contains roughly ten times the junction area of the conventional device.



In order to derive full light-generating capability from the power AlGaInN LED chip, a high-power, low thermal resistance package is required. Recently, a power package for AlGaInP power LED chips has been demonstrated⁹. This package can dissipate several Watts of power and inserts a thermal resistance of only 2°C/W. The Cu body provides good heat-sinking while a two-part lens is comprised of a hard outer lens and a soft, low-stress inner encapsulant.

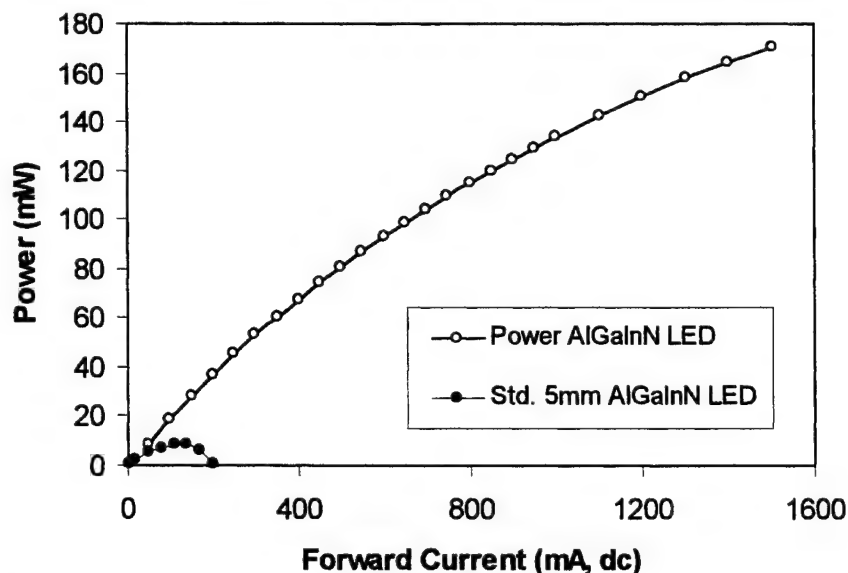


Fig. 12. Light output vs. current characteristic of a blue ($\lambda_p \sim 470$ nm), 1×1 mm² AlGaInN LED in a power package, compared to a conventional AlGaInN LED in a 5 mm lamp package.

The light output vs. current characteristic for a blue ($\lambda_p \sim 470$ nm), 1×1 mm² AlGaInN LED mounted in a power package is shown in Fig. 12. A power output of over 170 mW is obtained at a drive current of 1.5 A dc. The fact that the output power has not saturated at 1.5 A is a tribute to the excellent thermal characteristics of the power package and the low temperature dependence of quantum efficiency for the AlGaInN LED. For comparison, a conventional AlGaInN LED ($\sim 0.35 \times 0.35$ mm²) with similar quantum efficiency in a 5 mm lamp package exhibits a peak output power of less than 10 mW at 100 mA. A summary of the performance characteristics of a cyan ($\lambda_p \sim 505$ nm) power AlGaInN LED as compared to the conventional device are summarized in Table I for equivalent current densities (~ 45 A/cm²).

The heat dissipating capability of the power package, coupled with the low-stress inner encapsulant surrounding the chip, allow for excellent reliability performance of the high-power AlGaInN LED. Typical reliability performance for the high-power LEDs under high-temperature operating lifetime tests are shown in Fig. 13. At 350 mA (~ 1 W), the power AlGaInN LEDs exhibit excellent reliability performance, with projected degradation less than 20% out to 100,000 hrs. Referring to Fig. 7, the power LEDs exhibit improved performance compared to the case for conventional LEDs for the same current density (30 mA). Reasonable reliability performance is observed for the power LEDs at much higher current densities. At 1.0 A (~ 4 W) operation, the projected half-power lifetime is $\sim 100,000$ hrs. This performance is comparable to that for the conventional devices at 30 mA, but at more than 30 times the forward current!

4. APPLICATIONS

The high power AlGaInN LEDs enable applications wherein high flux density is important, and offer advantages over solutions employing conventional LEDs. An example of one application where high-flux LEDs offer unique advantages is traffic signaling. The advent of power LEDs has allowed the reduction in the number of LEDs required for a traffic ball from a few hundred down to just 12 to 18. This reduction in the required number of emitters is illustrated in Fig. 14. This allows the lighting engineer to treat the LEDs as a compact, high-flux light source in the design of the traffic ball. Through the use of secondary optics, the desired radiation pattern for the traffic signal application is achieved. Moreover, unlike for the case of conventional LEDs which can appear "spotty", the high-flux light engine mated with secondary optics results in an extremely uniform appearance of the radiance across the traffic ball.

Table I. Typical performance characteristics of high-power AlGaInN LEDs in power packages compared to conventional devices in 5 mm lamps ($\lambda_p \sim 505$ nm).

	Conventional LEDs	High-power LEDs
Drive Current	30 mA	350 mA
Forward Voltage	3.6 V	3.3 V
Input Power	0.1 W	1.1 W
Thermal resistance	~ 300 C/W	~ 12 C/W
Junction Temperature Rise	+ 30 C	+ 13 C
Flux	1-2 lm	10-15 lm

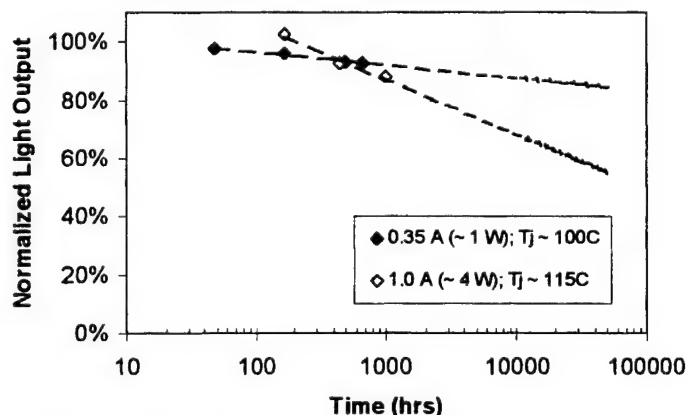


Fig. 13. High-temperature operating lifetime stress of power AlGaInN LEDs at forward currents of 0.35 and 1.0A.

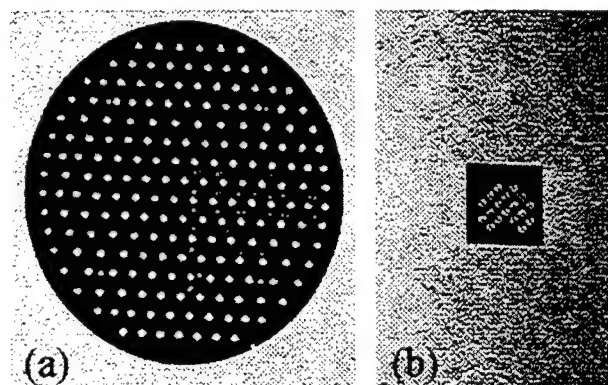


Fig. 14. High-flux LEDs has enabled light engines for traffic balls to reduce LED count from (a) a few hundred, to (b) eighteen.

One application that high-flux LEDs enable is lighting via fibres. The flux densities required for efficient lighting via fibres are not achievable using conventional LEDs. This is not the case for power LEDs, which offer more than ten times the flux in roughly the same area. A schematic cross-section of a power LED fibre light engine is shown in Fig. 15a along with a prototype module in Fig. 15b.

The possible applications for LED fibre light engines are many. Because they are solid state, the LED fibre engines are small, compact, and efficient, and do not require a cooling fan as is the case for fibre light engines using conventional light sources. Also, different color LEDs may be mixed in the light engine module to provide a wider variety of colors, even white. These colors may even be externally controlled to provide dynamic color changes for certain applications. Also, the LED fibre engine will benefit from the long-life of solid-state emitters. Finally, the system is actually cheaper to manufacture than its conventional counterpart.

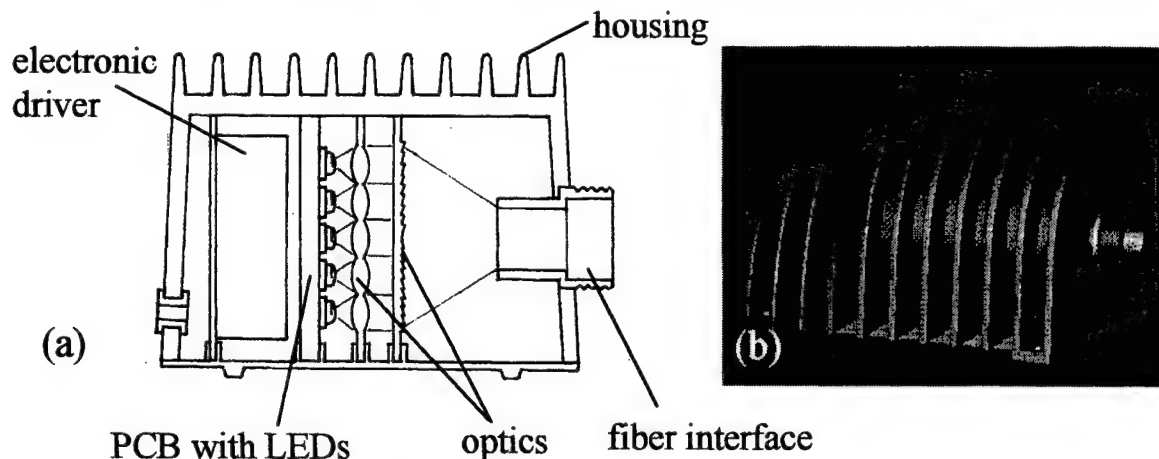


Fig. 15. Power LED fibre light engine: (a) schematic cross-section, and (b) photograph of prototype module.

5. CONCLUSIONS

There are of course many other applications suitable for the use of power AlGaInN LEDs. The conversion of blue light into white via phosphors enables power AlGaInN LEDs to produce several lumens of white light per emitter, such that one can envision a white flashlight which is comprised of only one LED and which draws less power than an incandescent bulb. As penetration into existing applications increases, and new applications emerge, solid-state light emitters will continue to increase their value proposition to the world, offering more lumens for reduced cost. Similarly, continued research and development of these material systems will yield more efficient and higher power LEDs, resulting in emitters with increased luminous output. This trend has been going on since the invention of the LED. Figure 16 illustrates this for red emitters, which have the longest history. The trend in cost reduction is dramatic, with ten-fold reduction in cost per lumen per decade. Similarly, the increase in lumens per emitter is

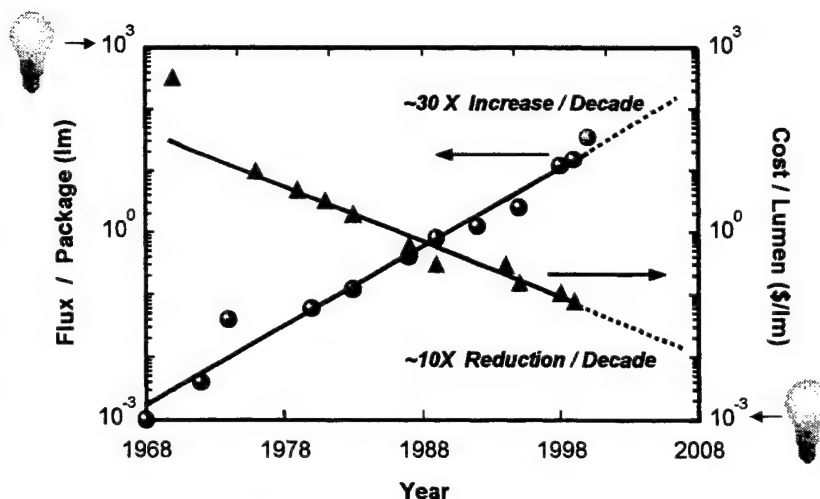


Fig. 16. The evolution of red LED technology in terms of cost and flux.

increasing at an incredible $\sim 30\times$ per decade. At these rates, the LED will catch up with the conventional light bulb in terms of cost and power in the early part of the 21st century, and penetrate the last vestiges of the lighting market now served by conventional lighting technologies.

ACKNOWLEDGEMENTS

The authors would like to acknowledge several people who contributed to this work, including: B. Kock and H. Konijn, at LumiLeds Lighting b.v. in Best, the Netherlands; A. Seppen-Saalberg, G. Harbers, and B. Hontele, at Philips Lighting in Eindhoven, the Netherlands; P. Arellano, C. Bautista, A. Davis, N. Felmoca, D. Patterakis, A. Rin, and J. Wood, at LumiLeds Lighting in San Jose, California.

REFERENCES

1. N. Holonyak, Jr. and S.F. Bevaqua, *Appl. Phys. Lett.*, **1**, 82-83 (1962).
2. W.O. Groves, A.H. Herzog and M.G. Craford, *Appl. Phys. Lett.*, **19**, 184 (1971).
3. H. Rupprecht, J.M. Woodall and G.D. Petit, *Appl. Phys. Lett.*, **11**, 81-83 (1967).
4. J. Nishizawa, K. Suto and T. Teshima, *J. Appl. Phys.*, **48**, 3484-3495 (1977).
5. H. Ishiguro, K. Sawa, S. Nagao, H. Yamanaka and S. Koike, *Appl. Phys. Lett.*, **43**, 1034-1036 (1983).
6. C.P. Kuo, R.M. Fletcher, T.D. Osentowski, M.C. Lardizabal, M.G. Craford and V.M. Robbins, *Appl. Phys. Lett.*, **57**, 2937-2939 (1990).
7. F.A. Kish, F.M. Steranka, D.C. DeFevere, D.A. Vanderwater, K.G. Park, C.P. Kuo, T.D. Osentowski, M.J. Peanasky, J.G. Yu, R.M. Fletcher, D.A. Steigerwald, M.G. Craford and V.M. Robbins, *Appl. Phys. Lett.*, **64**, 2839-2841 (1994).
8. N.F. Gardner, H.C. Chui, E.I. Chen, M.R. Krames, J.-W. Huang, F.A. Kish, S.A. Stockman, C.P. Kocot, T.S. Tan and N. Moll, *Appl. Phys. Lett.*, **74**, 2230-2232 (1999).
9. G.E. Hofler, C. Carter-Coman, M.R. Krames, N.F. Gardner, F.A. Kish, T.S. Tan, B. Loh, J. Posselt, D. Collins and G. Sasser, *Electron. Lett.*, **34**, 1781-1782 (1998).
10. M.R. Krames, M. Ochiai-Holcomb, G.E. Hofler, C. Carter-Coman, E.I. Chen, I.-H. Tan, P. Grillo, N.F. Gardner, H.C. Chui, J.-W. Huang, S.A. Stockman, F.A. Kish, M.G. Craford, T.S. Tan, C.P. Kocot, M. Hueschen, J. Posselt, B. Loh, G. Sasser, D. Collins, *Appl. Phys. Lett.*, **75**, pp. 2365-2367 (1999).
11. M.R. Lorenz and B.B. Binkowski, *J. Electrochem. Soc.*, **109**, 24 (1962).
12. H.P. Maruska and J.J. Tietjen, *Appl. Phys. Lett.*, **15**, 327 (1969).
13. J. I. Pankove, E.A. Miller, D. Richman, and J.E. Berkeyheiser, *J. Lumin.*, **4**, 63 (1971).
14. H.P. Maruska, W.C. Rhines, and D.A. Stevenson, *Mater. Res. Bull.*, **7**, 777 (1972).
15. T. Kawabata, T. Matsuda, and S. Koike, *J. Appl. Phys.*, **56**, 2367 (1984).
16. H. Amano, N. Sawaki, I. Akasaki, and Y. Toyoda, *Appl. Phys. Lett.*, **48**, 353 (1986).
17. H. Amano, M. Kito, K. Hiramatsu, N. Sawaki, and I. Akasaki, *Jpn. J. Appl. Phys.*, **28**, L2112 (1989).
18. S. Nakamura, M. Senoh, and T. Mukai, *Jpn. J. Appl. Phys.*, **30**, L1708 (1991).
19. S. Nakamura, T. Mukai, M. Senoh, S. Nagahama, and N. Iwasa, *J. Appl. Phys.*, **74**, 3911 (1993).
20. S. Nakamura, M. Senoh, N. Iwasa, and S. Nagahama, *Jpn. J. Appl. Phys.*, **34**, L797 (1995).
21. S.P. DenBaars, M.A. Hansen, H. Marchand, G. Parish, P. Fini, T. Katona, M. Craven, U.K. Mishra, to be published in *Proceedings of SPIE* Vol. 3938 (2000).
22. D. A. Steigerwald, *Proceedings of the 2nd International Conference on Nitride Semiconductors*, 514 (1997).

Design and Performance of Nitride-based UV LEDs

Mary H. Crawford, Jung Han, Weng W. Chow, Michael A. Banas, Jeffrey J. Figiel, Lei Zhang and
Randy J. Shul

Sandia National Laboratories, Albuquerque, NM 87185-0601

ABSTRACT

In this paper, we overview several of the critical materials growth, design and performance issues for nitride-based UV ($\lambda < 400$ nm) LEDs. The critical issue of optical efficiency is presented through temperature-dependent photoluminescence studies of various UV active regions. These studies demonstrate enhanced optical efficiencies for active regions with In-containing alloys (InGaN, AlInGaN). We discuss the trade-off between the challenging growth of high Al containing alloys (AlGaInN, AlGaInN), and the need for sufficient carrier confinement in UV heterostructures. Carrier leakage for various composition AlGaIn barriers is examined through a calculation of the total unconfined carrier density in the quantum well system. We compare the performance of two distinct UV LED structures: GaN/AlGaIn quantum well LEDs for $\lambda < 360$ nm emission, and InGaIn/AlGaIn quantum well LEDs for $370 \text{ nm} < \lambda < 390$ nm emission.

1. INTRODUCTION

While much of the research in the nitride field has focused on the development of blue and green LEDs and laser diodes, UV ($\lambda < 400$ nm) LEDs based on GaN, AlGaIn and/or AlGaInN active regions are also of great interest and are well suited to a number of applications. One of the most promising uses of a UV LED is as a high energy excitation source. In the biomedical and chemical sensing fields, UV LEDs can be used as compact and robust excitation sources of fluorescence. UV LEDs may also prove to be superior to blue LEDs in exciting phosphors for white lighting applications, due to improved color rendering. To date, there have been relatively few reports of UV LEDs based on the wide-bandgap nitride semiconductors. In particular, Akasaki et. al. [1] reported on a GaN/AlGaIn double heterostructure (DH) LED with emission at 370 nm and up to 1.5% external quantum efficiency. Mukai, et. al. [2] have achieved an impressive 5 mW output at 371 nm from an InGaIn/AlGaIn DH LED with very low levels of indium (In) in the active region. That LED was reported to have up to 7.5% external quantum efficiency but the efficiency dropped by more than an order of magnitude as the emission wavelength shifted to 368 nm with the total elimination of In from the active region. Shorter wavelengths have been achieved by Han, et. al. [3] through a GaN/AlGaIn multiquantum well (MQW) structure. These LEDs demonstrated a 354 nm emission peak with a narrow FWHM linewidth of 5.8 nm and relatively low output powers of 12 μ W at 20 mA. Thus, while one group has demonstrated high ($> 5\%$) efficiency LED performance for $\lambda > 370$ nm, many of the challenges inherent to the shorter wavelength emission regime still remain.

In this paper, we discuss a number of materials growth and design challenges for achieving high performance UV LEDs and present the performance of two distinct UV LED structures. In section 2, we describe the materials growth and the general heterostructure designs for the UV LEDs that we have developed. In section 3 we review critical materials and design issues such as optical efficiency of UV active regions, internal absorption effects, critical thickness limitations for AlGaIn layers and carrier leakage. We report on the performance of GaN/AlGaIn MQW LEDs with emission wavelengths < 360 nm as well as the performance of InGaIn/AlGaIn MQW LEDs for $370 \text{ nm} < \lambda < 390$ nm emission in sections 4 and 5, respectively.

2. MATERIALS GROWTH AND LED HETEROSTRUCTURE DESIGNS

The nitride materials described in this paper were grown in a high speed (~ 1200 rpm) rotating disk MOCVD reactor on two inch sapphire substrates. Different growth conditions were employed for non-indium containing alloys (GaN, AlGaIn) as compared to indium containing alloys (InGaIn, AlInGaIn). The GaN and AlGaIn growths [3] were typically carried out at $1000\text{--}1080^\circ\text{C}$ with hydrogen as the carrier gas. Ammonia (NH_3), Trimethylgallium (TMGa), Trimethylaluminum (TMAI) were used as the N, Ga, and Al precursors, respectively. The growth of InGaIn and AlInGaIn [4] was carried out at $750\text{--}800^\circ\text{C}$, with nitrogen as the carrier gas and Triethylaluminum (TEA) and Trimethylindium (TMI) as the Al and In sources,

respectively. A standard two-step growth (550 and 1050 °C for the low and high temperatures, respectively) with a GaN low-temperature buffer layer (~250 Å) was used in this work.

We will focus on two general heterostructures for UV LEDs. The overall layer sequence is quite similar for the two structures, and is shown in Figure 1. The first design is an MQW LED structure with GaN quantum wells and $\text{Al}_x\text{Ga}_{1-x}\text{N}$ barriers and emission in the $\lambda < 360$ nm region. The n-GaN buffer layer is typically 3 μm in thickness and Si-doped to a level of $2.5 \times 10^{18} \text{ cm}^{-3}$. The n-AlGaN cladding with $x=0.15-0.20$ is approximately 400 Å thick and doped to a similar level as the n-GaN layer. The multiquantum well region consists of 5 periods of 30 Å thick GaN quantum wells and 70 Å thick AlGaN ($x=0.15-0.2$) barriers. The p-AlGaN cladding is typically 400 Å thick and the contact layer is 0.05-0.1 μm thick p-GaN. The second type of UV LED structure utilizes InGaN QWs and AlInGaN barriers in the MQW active region. The MQW region consists of 47 Å thick $\text{In}_x\text{Ga}_{1-x}\text{N}$ quantum wells with $x=0.04$ and 48 Å thick $\text{Al}_y\text{In}_x\text{Ga}_{1-x-y}\text{N}$ barriers with $x=0.04$ and $y=0.14$. The p-GaN cap layer is thicker for these structures, due to the fact that the longer wavelengths emitted from the active regions are not as strongly absorbed by the p-GaN layer. Thicknesses of 0.1 μm to 0.25 μm have been used.

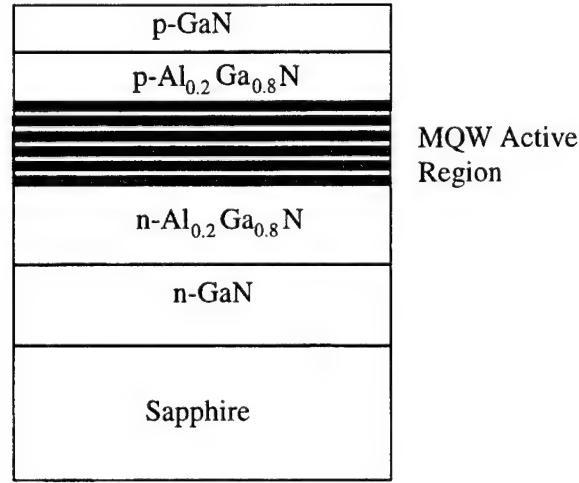


Figure 1: Schematic of UV LED MQW heterostructures

3. GROWTH AND DESIGN CHALLENGES FOR HIGH EFFICIENCY UV LEDs

The performance of nitride-based UV LEDs has yet to reach that of commercially available blue and green LEDs. Although relatively good performance has been reported in the near UV region of $\lambda > 370$ nm, there exist a number of distinct challenges for achieving high efficiency at the UV wavelengths, and these challenges become particularly difficult for wavelengths shorter than 370 nm. In this section, we review specific challenges that limit UV LED performance, including optical efficiency of the active regions, internal absorption effects, critical thickness limitations and carrier leakage.

3.1 Optical Efficiency of UV LEDs

One of the most intriguing issues in the nitride field concerns the high optical efficiency of nitride-based blue and green LEDs. Specifically, although a great deal of progress has been made in the development of InGaN-based light emitters, the role played by indium (In) in contributing to the optical efficiency is still quite controversial. A number of groups have proposed that the inhomogeneity of In incorporation results in carrier localization at In-rich regions and that this localization leads to enhanced optical efficiency [6-8]. Support of this hypothesis is found in cathodoluminescence experiments that demonstrate a variation of the PL emission energy on the microscale, suggesting that In composition variations on the order of several percent are possible [9]. Further insight is gained by the time-resolved spectroscopy experiments of InGaN quantum well structures performed by Narukawa, et. al. [10], which suggest that the density of non-radiative centers and possibly the non-radiative recombination mechanism itself is altered when In is included in the growth. A similar result was

obtained by Kumano, et. al. [11] who suggest that increased optical efficiency is due to reduced non-radiative recombination centers with In incorporation. Thus, it is clear that a strong consensus has not emerged as to how the presence of In in the QWs affects the optical efficiency and whether it is absolutely necessary for achieving high efficiency nitride LEDs.

This issue of whether In-containing QWs are needed for high efficiency is especially critical if we look at UV LED structures. Clearly the GaN MQW LEDs do not contain In in the active regions, and therefore would not benefit from the proposed improvements in optical efficiency seen in the blue and green LEDs. Furthermore, in order to achieve LED emission at $\lambda < 390$ nm from InGa_N MQW structures, the In composition must be reduced to relatively small values ($x < 0.06$). Thus even in the InGa_N/ AlInGa_N MQW structures described in this report, the role played by In could be significantly reduced from that of blue and green LED structures with higher In compositions in the InGa_N QWs.

In an effort to further elucidate these issues, we have performed a number of photoluminescence studies of InGa_N, GaN and AlGa_N MQW and bulk structures. In particular, we have performed temperature-dependent photoluminescence (PL) spectroscopy measurements on a number of MOVPE grown In_xGa_{1-x}N epilayers in the low In composition regime ($x < 0.10$) [12]. This composition regime was chosen to examine whether a clear trend in optical efficiency and temperature dependent quenching of PL intensity can be found with the addition of just small amounts of In. Our work has also intentionally focused on relatively thick (0.2 μ m) and doped bulk InGa_N epilayers so that the role of piezoelectric field effects would be minimized [13]. This work is therefore distinct from the majority of the previously reported work that has focused on InGa_N quantum wells with higher ($x \geq 0.1$) In composition.

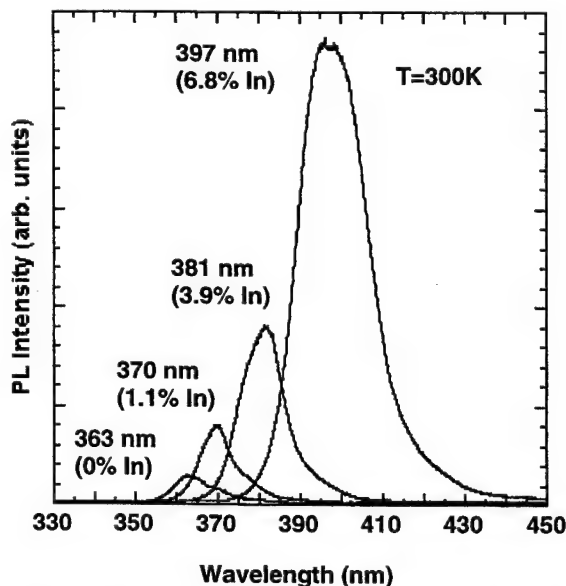


Figure 2a : Room temperature PL spectra of InGa_N bulk epilayers [12].

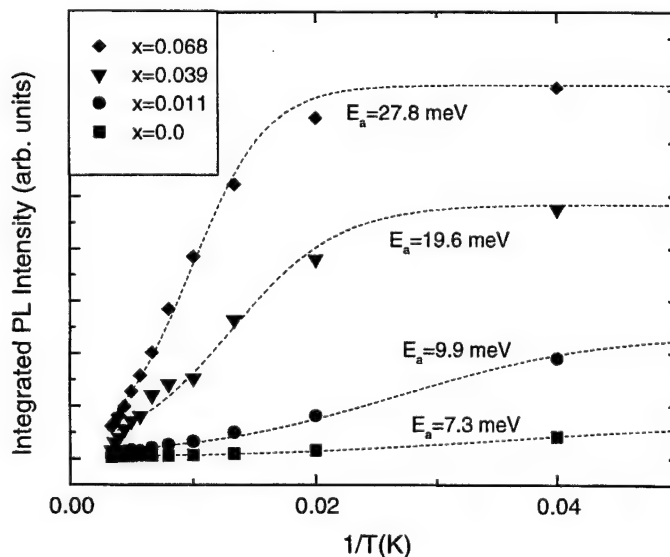


Figure 2b: Temperature dependent integrated PL intensity of InGa_N bulk epilayers with In composition x . The E_a values are derived from fitting the data to equation 1 [12].

The PL measurements were performed using a HeCd laser (325 nm) at a low power density of approximately 30 W/cm². A 0.3 meter spectrometer with an integrated UV enhanced CCD detector was used, with a spectral resolution of approximately 0.2 nm. The room temperature PL spectra for four InGa_N epilayer samples is shown in Figure 2b. A strong increase in the integrated PL intensity is seen as In composition is increased, with more than a 25X increase as the peak wavelength shifts from 363-397 nm. The data suggest that the optical efficiency is highly dependent on the In composition. The full temperature dependence of the integrated PL intensity is plotted in an Arrhenius plot in Figure 2b. The data is fit with the following formula [14]

$$I = I_0 / [1 + \alpha \exp(-E_a/kT)]. \quad (1)$$

Here the non-radiative decay is assumed to be thermally activated such that the non-radiative lifetime $\tau_{nr} = \tau_0 \exp(E_a/kT)$ and E_a is the activation energy for PL quenching. The parameter α is equal to τ_r/τ_0 where τ_r is the radiative lifetime. From the E_a values, we see a systematic increase in the activation energy as the indium composition is increased. The full temperature dependent data thus give further support of the hypothesis that increasing In composition improves the optical efficiency of the materials. Through the increasing E_a values with increasing In composition, we see that the In is reducing the effectiveness of non-radiative recombination mechanisms in quenching the PL intensity. Whether this effect is due to carrier localization or a modification of the nature of the non-radiative centers can not be determined from the data.

Additional temperature dependent PL measurements were performed on InGa_N, GaN and AlGa_N MQW structures. The InGa_N QW structures were supplied by Meijo University and have 10 periods of 23 Å thick In_{0.21}GaN_{0.79}N QWs with GaN barriers. The GaN MQW structure was grown at Sandia National Laboratories and consists of 4 periods of 30 Å thick GaN quantum wells with Al_{0.20}Ga_{0.80}N barriers. It should be noted that this GaN MQW structure was grown on an AlGa_N buffer so that the QW emission would not be confused with emission from a thick GaN buffer layer. The AlGa_N MQW structure was identical to the GaN MQW structure except that approximately 5% aluminum was added to the QWs. In Figure 3a, we show the low temperature (T=10K) photoluminescence spectra for the three MQW structures. In Figure 3b, we show the temperature dependence of the peak PL intensity for the three MQW structures. A strong distinction is seen in the total drop in peak PL intensity. In particular, the InGa_N MQW structure experiences a relatively small (4X) loss in peak PL intensity from 10-300K, while the peak PL drop is 60X and 1000X for the GaN MQW and AlGa_N MQW structure, respectively. In the quantitative comparison of the PL data for these three MQW structures, it is important to recognize that the growth conditions for the visible and UV MQW structures were quite different, and it is possible that further optimization of the growth conditions for the UV MQW structures would improve the performance. Nevertheless, this data is a good representation of the performance of our current GaN MQWs and high quality InGa_N MQWs. In this data, we see evidence

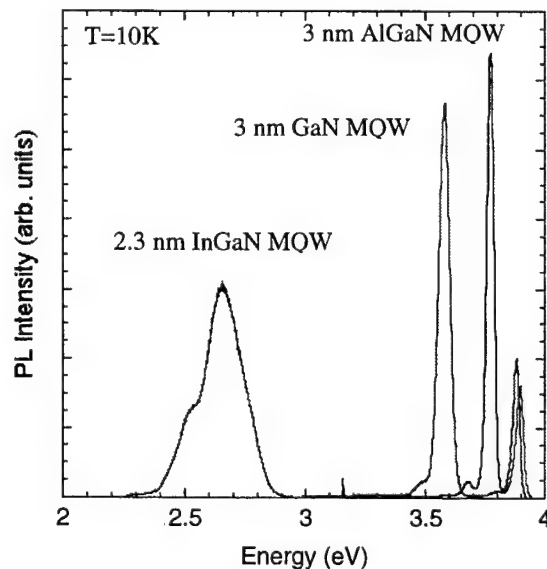


Figure 3a: T=10K PL of InGa_N, GaN and AlGa_N MQWs.

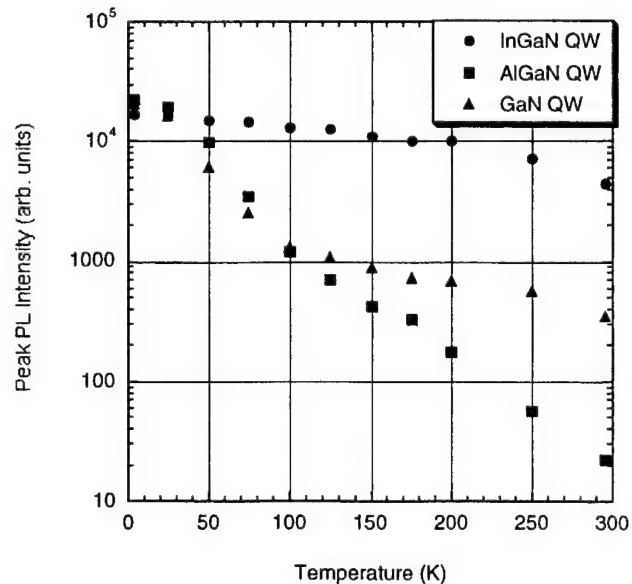


Figure 3b: Temperature dependence of peak PL intensity for InGa_N, GaN and AlGa_N MQWs.

that the discrepancy in the optical efficiency between the visible and UV MQW structures is highly temperature dependent. In particular, the UV MQW structures are more susceptible to non-radiative recombination processes which serve to quench the PL intensities at room temperature. Furthermore, the severe 1000X drop in intensity from 10-300K for the AlGa_N MQWs shows the increasing challenge of obtaining high optical efficiency at wavelengths in the 340 nm region and shorter.

As a final experiment, we performed temperature dependent PL studies of InGa_N MQW structures where the In composition was kept to a low value (~4%) to enable room temperature emission at 380 nm in the UV. These structures are similar to the

MQW region of the LED heterostructures described in section 2. The particular structures grown for PL studies consisted of 10 periods of 47 Å thick InGaN ($x=0.04$) QWs with AlInGaN barriers. A drop of $\sim 5X$ in the integrated PL intensity from 10-300K is seen [13], which is similar to the performance of the blue-emitting InGaN MQW structure described in Figure 3.

In summary, the spectroscopic studies that we have performed on InGaN bulk films and InGaN, GaN and AlGaIn MQWs have shown that samples with In-containing QWs can have significantly higher optical efficiency than samples with no In in the active region. This result might suggest that GaN/AlGaIn MQWs may not be intrinsically capable of performing to the level of InGaN near UV and visible MQWs. To improve the performance of GaN/AlGaIn MQWs, a further measure of growing the structures on epitaxially laterally overgrown GaN to significantly reduce dislocation densities may serve to largely improve the non-radiative recombination problem. Indeed, studies by Mukai et. al. have shown that GaN/AlGaIn DH LEDs had up to 2X increased output powers when this technique was employed [16].

3.2 Internal Absorption Effects for Shorter Wavelength ($\lambda < 370$ nm) UV LEDs

In consideration of the challenges in obtaining high efficiency UV LEDs, one must also seriously consider the detrimental role played by internal absorption for UV LEDs with $\lambda < 370$ nm. At the heart of this problem is the fact that most nitride-based LEDs rely on 3-4 μm thick n-GaN buffer layers and ~ 0.1 μm thick p-GaN capping layers for good current spreading and low contact resistance. While these GaN layers are rather transparent for blue LEDs operating at 450 nm, they become strongly absorptive as the QW emission wavelength reaches 370 nm and shorter wavelengths. This effect has been described by both Mayer et. al. [17] and Mukai et al. [18] as a significant contribution to the sudden loss of optical efficiency for $\lambda < 370$ nm.

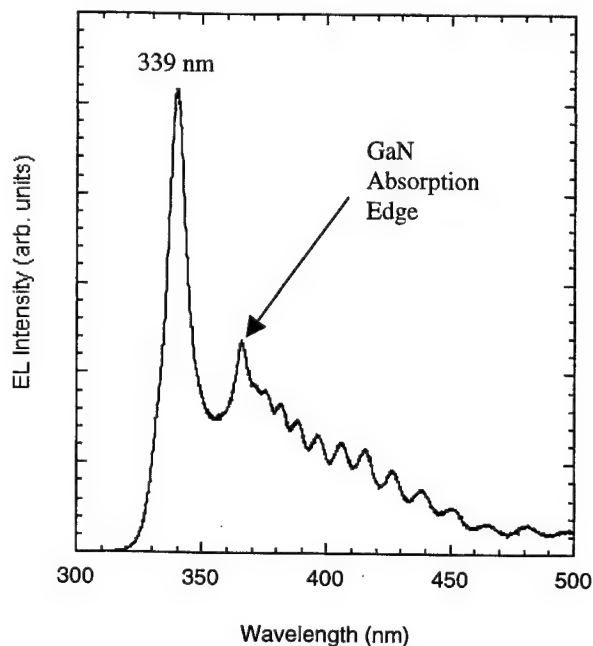


Figure 4: EL spectra for AlGaIn MQW LED at 80 mA.

We have most clearly seen this effect in the electroluminescence (EL) spectra of AlGaIn MQW LEDs operating at 340 nm. These LEDs have similar AlGaIn MQW active regions to those described in section 3.1. In Figure 4, we show the EL spectrum at 80 mA injected current. A clear delineation of the GaN absorption edge can be seen at approximately 365 nm. Fabry-Perot (F-P) oscillations exist in the spectrum for wavelengths below this absorption edge, signifying the transparency of the sample at those wavelengths. In contrast, the 340 nm peak from the AlGaIn QWs is significantly reduced in intensity compared to what one would expect from the tail emission and shows no F-P oscillations. Thus, it is clear that if one needs high efficiency at these shorter wavelengths, a more transparent buffer layer, such as one consisting of higher bandgap AlGaIn or AlInGaIn must be employed. Progress in AlGaIn buffer layers has been reported by Takeuchi et. al. [19], who have demonstrated growth of a blue laser structure on an $\text{Al}_{0.03}\text{Ga}_{0.97}\text{N}$ / $\text{Al}_{0.06}\text{Ga}_{0.94}\text{N}$ buffer layer.

3.3 AlGaIn Cladding Designs: Critical thickness Limitations and Carrier Leakage

Another challenge in the growth and design of nitride-based UV LEDs is the fact that one needs increasingly higher bandgap materials for the barrier and cladding layers. These high bandgap layers are needed to ensure sufficient carrier confinement in the quantum wells, as well as to reduce carrier leakage out of the active region. At present, $\text{Al}_x\text{Ga}_{1-x}\text{N}$ alloys with $x=0.10$ - 0.20 are most commonly used as cladding layers in InGaIn and GaN LEDs. Since AlGaIn is tensile strained when grown pseudomorphically on GaN buffer layers, there is a critical thickness before dislocations and/or cracking sets in. This requirement puts a strong limitation on the thickness and composition that one may use to reduce electron leakage in the

LEDs. In general, these thickness limitations are much more critical for laser diodes than for LEDs, since one needs a much thicker cladding layer to provide optical confinement. Nevertheless it is important to recognize that even for UV LEDs, one must make a compromise between the cladding composition and thickness and the optimal confinement. As will be discussed in section 5, this problem can be eliminated if one could grow high bandgap AlInGaN alloys lattice matched to GaN for cladding layers or grow structures on AlGaN buffer layers. In this section, however, we will focus on the issues of critical thickness and carrier leakage of UV LEDs with AlGaN claddings.

The critical thickness for stress relaxation in AlGaN/GaN heterostructures has been studied by Hearne, et al. [20] through in-situ stress measurements during MOVPE growth. This work determined that the observed critical thickness for cracking in AlGaN was consistent with the Griffith equation estimated critical thickness. Using the values from Ref. 20, the approximate critical thickness for an $\text{Al}_{0.3}\text{Ga}_{0.7}\text{N}$ epilayer on GaN is 700 Å, for an $\text{Al}_{0.2}\text{Ga}_{0.8}\text{N}$ epilayer on GaN is 0.15 μm, and for an $\text{Al}_{0.1}\text{Ga}_{0.9}\text{N}$ layer on GaN is 0.6 μm.

The effects of exceeding the critical thickness can be clearly seen in Figure 5, where we show a top-view photograph of a 100 μm diameter mesa-etched GaN MQW LED with $\text{Al}_{0.2}\text{Ga}_{0.8}\text{N}$ barrier and cladding layers. The total thickness of the AlGaN layers exceeds 0.2 μm. The cracking networks are especially visible in the etch-exposed n-GaN layer, where preferential etching in the cracks has made them more pronounced. I-V characterization of such LED structures yielded extremely poor reverse leakage characteristics, as shown for a number of cracked devices in Figure 5b.

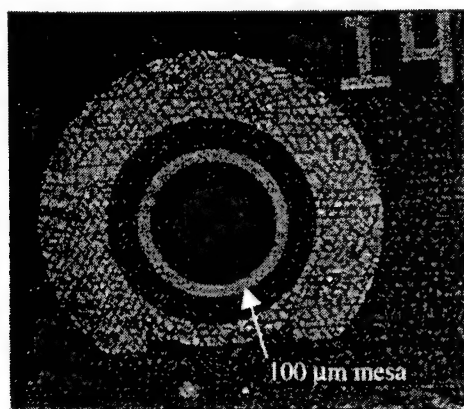


Figure 5a: Top view photograph of a GaN /AlGaN MQW LED with > 0.2 μm total thickness of $\text{Al}_{0.2}\text{Ga}_{0.8}\text{N}$ barrier.

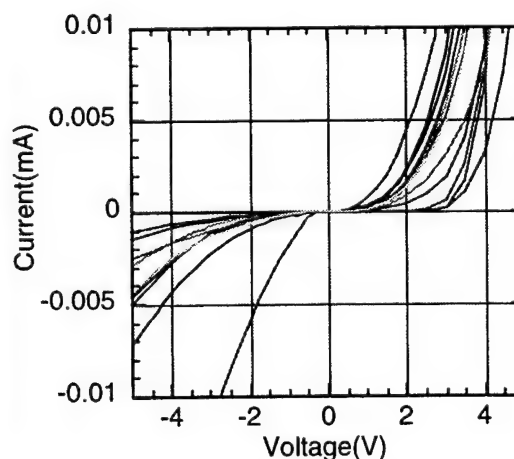


Figure 5b: I-V characteristics for several cracked GaN /AlGaN MQW LEDs

Given these limitations in Al composition and thickness, it is useful to evaluate the expected carrier leakage from GaN MQW structures with various composition AlGaN claddings. We have modeled the carrier leakage in a GaN/AlGaN single QW structure grown along the c-axis of the hexagonal wurtzite crystal structure. This particular structure assumes the AlGaN layers are relaxed and that the GaN QW is compressively strained. Such a structure is relevant for UV LED structures grown on transparent AlGaN buffer layers. The basic approach is detailed in Ref. 21. It involves calculating the bandstructure and carrier distribution in both the confined QW states and the unconfined barrier states as a function of injected carrier density. Piezo-electric and spontaneous polarization effects [22] are included in the calculation. Carrier leakage is determined by assuming that the unconfined states of the QW structure, which contribute to current leakage via carrier recombination, drift or diffusion, may be populated through thermalization with the population in the bound QW states. We determine the carrier leakage by the ratio of the unconfined carrier density to the confined carrier density. A schematic of the GaN SQW heterostructure and the processes described by the model are shown schematically in Figure 6. We use a 6 x 6 Luttinger-Kohn Hamiltonian and the envelope approximation [23] to compute the hole energy dispersions and the optical dipole matrix elements. Input parameters to the calculation are the bulk wurtzite materials parameters [24] for the binary alloys. A conduction band offset of 0.67 is assumed.

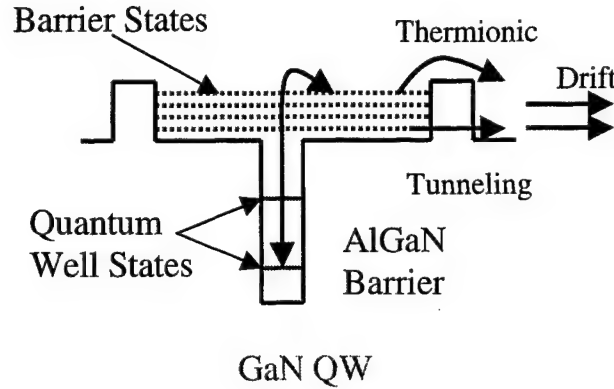


Figure 6: Schematic of the GaN SQW heterostructure and states involved in the carrier leakage model

We first explore the carrier leakage using a relatively low bandgap $\text{Al}_{0.1}\text{Ga}_{0.9}\text{N}$ barrier and plot the electron and hole densities in unconfined states versus total carrier population. In Figure 7 we show the results of our calculations for a 2 nm and a 4 nm thick GaN QW. The calculations assume $T=300\text{K}$.

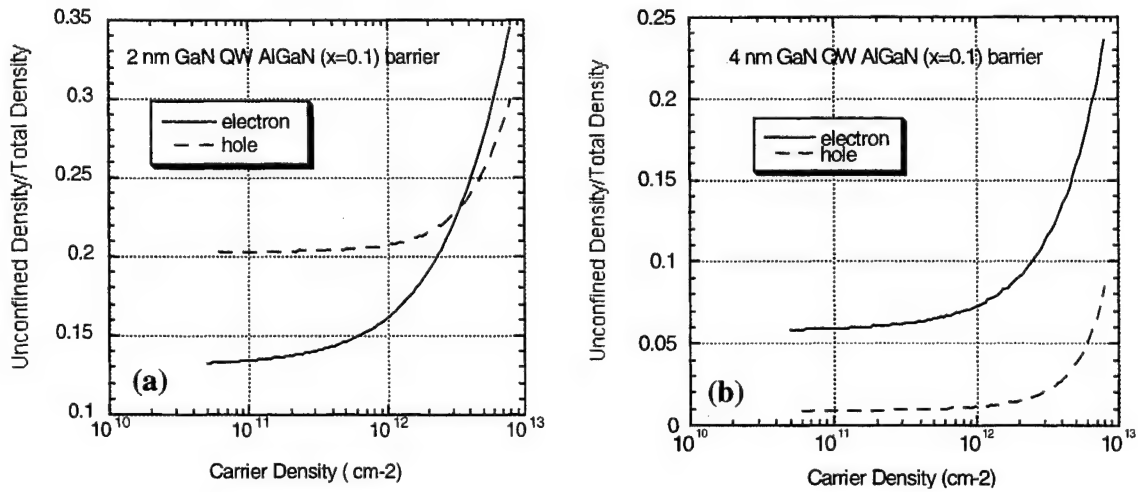


Figure 7: Electron (solid curve) and hole (dashed curve) densities in unconfined states versus total (confined and unconfined) carrier population at $T=300\text{K}$ for (a) 2 nm GaN QW/ $\text{Al}_{0.1}\text{Ga}_{0.9}\text{N}$ barrier structure and (b) 4 nm GaN QW/ $\text{Al}_{0.1}\text{Ga}_{0.9}\text{N}$ barrier structure.

For both the 2 nm QW and the 4 nm QW, we see that the unconfined carrier populations are relatively insensitive to the total carrier density until one reaches total densities of approximately $1 \times 10^{12} \text{ cm}^{-2}$. This density is higher than that typically used for LED operation, and thus the carrier leakage should be relatively insensitive to injected current for LED operation at modest injection levels. For UV laser diodes, however, where one would expect the threshold carrier densities to be as high as $1 \times 10^{13} \text{ cm}^{-2}$, our calculations predict a significant loss of 20-35% of the carriers due to leakage. For the narrower 2 nm QW in the low injection regime ($< 1 \times 10^{12} \text{ cm}^{-2}$), our analysis shows that hole leakage is dominant and can represent a carrier loss of up to 20%. In contrast, electron leakage dominates for the wider 4 nm well and is reduced to ~6% at these injection levels. The dominance of hole leakage for the 2 nm well can be explained by the fact that the valence band offset is significantly smaller than the conduction band offset ($\Delta E_c = 0.67 E_g$ is assumed) and the confined quantum well states are relatively close to the unconfined levels in this narrow well. In the thicker 4 nm well, the confined states have lower energy relative to the unconfined states and can provide sufficient confinement for the holes. In this case, the lighter electrons

experience more leakage. Although the 4 nm well is clearly superior in terms of reduced leakage, it is important to note that piezoelectric effects, which would significantly reduce electron-hole overlap, are more severe for the thicker wells.

We further explore the importance of higher Al composition claddings by calculating the carrier leakage for 2 nm GaN QWs with $\text{Al}_{0.1}\text{Ga}_{0.9}\text{N}$ barriers and $\text{Al}_{0.2}\text{Ga}_{0.8}\text{N}$ barriers. In Figure 8, we assume an injected carrier density of $1 \times 10^{11} \text{ cm}^{-2}$ and plot the unconfined carrier density as a function of LED temperature. From this calculation, we see that the benefit of the higher bandgap $\text{Al}_{0.2}\text{Ga}_{0.8}\text{N}$ barrier is quite significant, showing only a 0.5% electron leakage at 300K. The stronger confinement of this structure leads to electron leakage being dominant, as for the thicker QW case in Figure 7b. The electron and hole leakage levels increase strongly with temperature, resulting in up to 2.7% electron leakage at 100°C above room temperature.

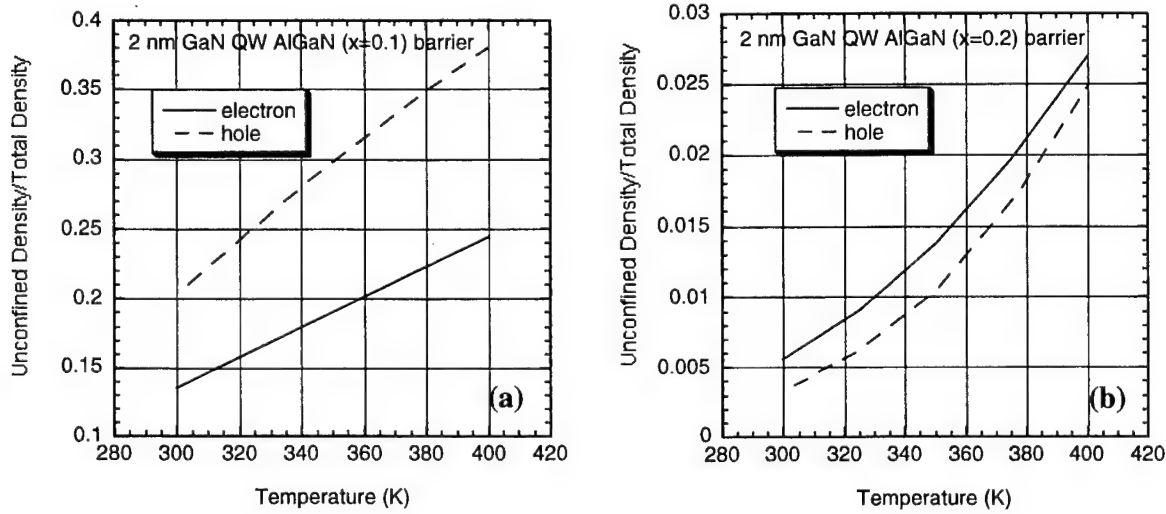


Figure 8: Electron (solid curve) and hole (dashed curve) densities in unconfined states versus total (confined and unconfined) carrier population as a function of temperature for (a) 2 nm GaN QW/ $\text{Al}_{0.1}\text{Ga}_{0.9}\text{N}$ barrier structure and (b) 2 nm GaN QW/ $\text{Al}_{0.2}\text{Ga}_{0.8}\text{N}$ barrier structure. A total carrier concentration of $1 \times 10^{11} \text{ cm}^{-2}$ was assumed.

In summary, we have shown that carrier leakage can significantly reduce the efficiency of GaN/AlGaIn MQW LEDs. A barrier Al composition of $x=0.2$ is sufficient to reduce carrier leakage to $< 1\%$ of the total carrier population for 2 nm thick GaN QWs at 300K. In-situ stress measurements suggest that up to $0.15 \mu\text{m}$ of $\text{Al}_{0.2}\text{Ga}_{0.8}\text{N}$ barrier and cladding layers can be employed before large scale cracking sets in. For shorter wavelength UV LEDs ($< 350 \text{ nm}$), such as those employing AlGaIn QWs, issues of carrier confinement and critical thickness are more critical.

4. PERFORMANCE OF GaN/AlGaIn MQW LEDs for $\lambda < 360 \text{ nm}$

We have fabricated GaN/AlGaIn MQW LEDs using the heterostructure design shown described in section 2. $100 \mu\text{m}$ - $250 \mu\text{m}$ mesas were defined by inductively coupled plasma (ICP) etching. Ti/Al/Ti/Au was used as the n-contact, and Ni/Au oxidized to form semi-transparent NiO [25] was used as the p-contact. Initial structures had a relatively narrow 30 \AA QW, and electroluminescence peaked at 354 nm [3], as shown in Figure 9a. The L-I-V data shown in Figure 9b was taken with a calibrated Si detector in close proximity to the sample, and demonstrates $12 \mu\text{W}$ of output power at a current of 20 mA ($\sim 180 \text{ A/cm}^2$ for these devices), and a turn-on voltage of approximately 4V . This performance results in an external quantum efficiency of below 0.1% , which is largely due to the internal absorption effects. The EL FWHM of 5.8 nm is significantly narrower than that reported for InGaIn blue and green LEDs; a feature which is often desirable for spectroscopic applications.

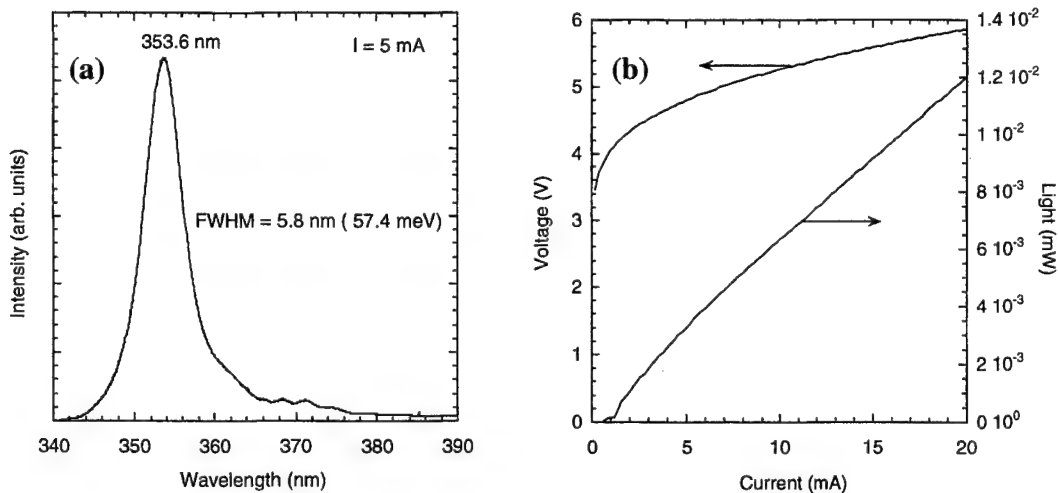


Figure 9: (a) Electroluminescence spectrum of 30 Å GaN/AlGaIn MQW LED at 5 mA. (b) Light output-current-voltage characteristic for this 120 μm diameter mesa-etched device. [3]

We have further optimized the growth of the GaN QW regions as well as explored QW structures emitting at slightly longer wavelengths where the internal absorption effects would be reduced. In Figure 10, we show the performance of a GaN/AlGaIn MQW LED with emission at 357.5 nm. From the EL spectrum, and one can see that the tail of the spectrum is enhanced due to the strongly reduced absorption of the GaN buffer layer at those wavelengths. The L-I data shown in Figure 10b was taken from LEDs bonded to TO-headers (no encapsulation or lens), and using an integrating sphere coupled to a calibrated Si detector. These LEDs showed > 100 μW output at currents up to 50 mA ($\sim 100 \text{ A/cm}^2$ for these larger devices). While these powers are at least an order of magnitude less than that measured from commercially available blue and green LEDs, such powers are already sufficient for a number of fluorescence-based sensing applications.

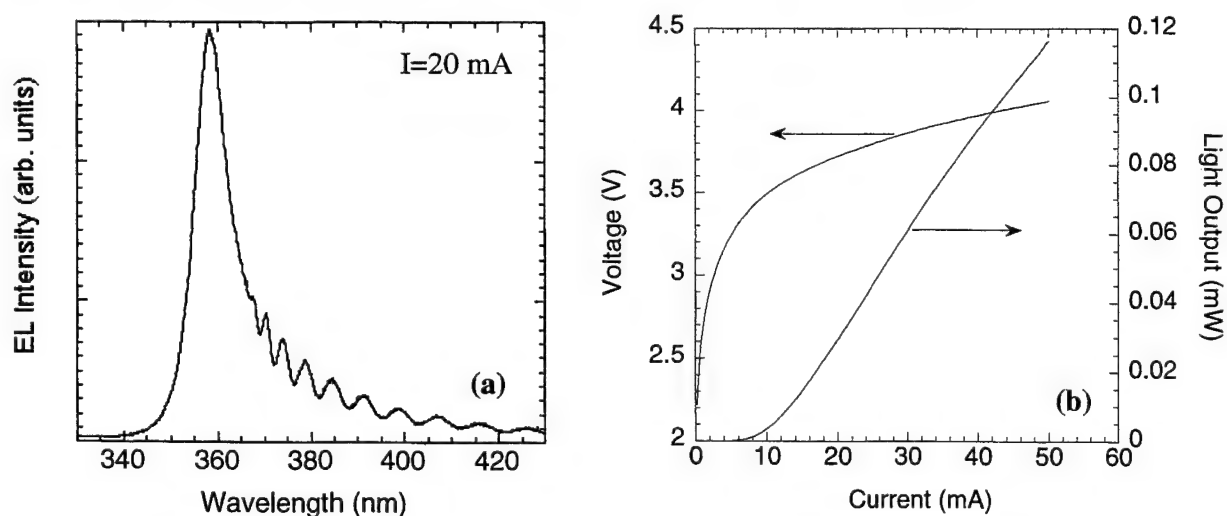


Figure 10: (a) Electroluminescence spectrum of a GaN/AlGaIn MQW LED at 20 mA. (b) Light output-current-voltage data for this larger device.

5. PERFORMANCE OF InGaN/AlInGaN LEDS FOR $370 \text{ nm} < \lambda < 390 \text{ nm}$

We have further explored UV LEDs employing AlInGaN quaternary alloys in the active region. These materials offer a great deal of flexibility in that they can be lattice matched to GaN and AlGaIn buffer layers and thus critical thickness and cracking issues may be eliminated. Despite the obvious benefits of these quaternary alloys, the materials growth is quite challenging due partly to very dissimilar optimal temperatures for Al and In incorporation. As a result, very few reports have been made on the growth and optical properties of these materials [26,27]. The buffer and cladding layer designs are similar to GaN/AlGaIn MQW structures, but the active region consists of 47 Å thick $\text{In}_x\text{Ga}_{1-x}\text{N}$ quantum wells with $x=0.04$ and 48 Å thick $\text{Al}_y\text{In}_x\text{Ga}_{1-x-y}\text{N}$ barriers with $x=0.04$ and $y=0.14$. This quaternary alloy composition has been found to have a room temperature PL peak at ~357 nm. As described in section 3.1, we have found that active regions consisting of this quantum well structure have very good optical efficiency.

In Figure 11, we show the electroluminescence spectrum and L-I-V data for a InGaN/AlInGaIn MQW LED. The EL spectrum, taken at 20 mA, shows a peak at approximately 386 nm and a FWHM of 10 nm (84 meV). The Fabry-Perot oscillations seen throughout the spectrum indicate that these longer wavelengths experience relatively little absorption from the GaN layers in the structure. The L-I-V data, taken on devices bonded to a TO-header and using an integrating sphere and calibrated Si detector, show 0.5 mW at 50 mA (~100 A/cm²) and greater than 1 mW powers at current levels of 100 mA (~200 A/cm²). The peak external quantum efficiency of these devices is approximately 0.3%. Work is in progress to optimize growth and design of these structures to achieve higher operating efficiencies.

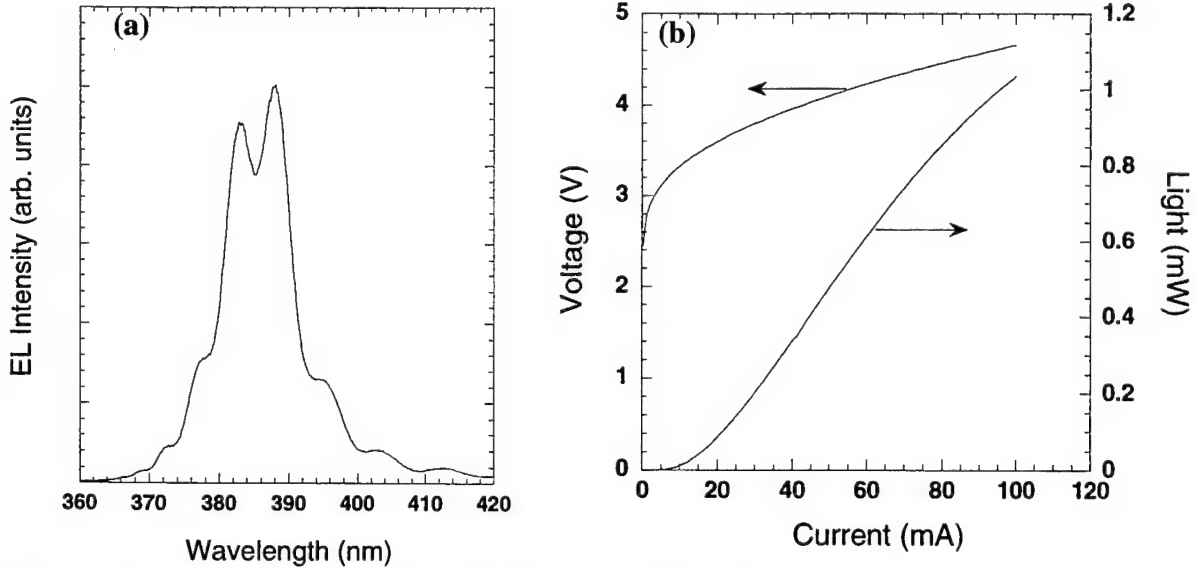


Figure 11: (a) Electroluminescence spectrum of InGaN/AlInGaIn MQW LED at 20 mA. (b) Light output-current-voltage data for this device.

6. SUMMARY

We have overviewed a number of critical issues that must be addressed to achieve high efficiency UV LEDs. The issue of optical efficiency of UV active regions was explored through photoluminescence studies of InGaIn, GaIn and AlGaIn bulk epilayers and MQW structures. Our results suggest that improved optical efficiency is achieved for active regions with In-containing alloys in the QWs. Through a carrier leakage model that determined the percentage of carriers in unconfined states of a GaIn SQW structure, we determined that $\text{Al}_{0.2}\text{Ga}_{0.8}\text{N}$ claddings provide relatively good carrier confinement for 2 nm GaIn QW structures. We presented performance data for GaIn/AlGaIn MQW LEDs with emission in the 354-358 nm region. Output powers > 100 μW have been achieved, which is sufficient for a number of fluorescence-based sensing applications. A new InGaIn/AlInGaIn MQW UV LED was described which demonstrated > 1 mW output powers at an emission wavelength of 386 nm. Further optimization of this structure may provide a high efficiency near-UV source suitable for phosphor excitation and white light generation.

ACKNOWLEDGEMENTS

The authors acknowledge stimulating technical discussions with S. R. Lee, S. J. Hearne, I. J. Fritz, T. M. Mayer, R. M. Biefeld, and H. Amano. InGaN MQW samples were provided by Prof. H. Amano at Meijo University. Technical contributions by A. V. Nurmikko, Y. K. Song, H. Zhou, N. A. Missert, G. A. Petersen and S. M. Myers are gratefully acknowledged. Sandia is a multiprogram laboratory, operated by Sandia Corporation, a Lockheed Martin company, for the U. S. Department of Energy, under Contract No. DE-AC04-94AL85000.

REFERENCES

- [1] I. Akasaki and H. Amano, *Jpn. J. Appl. Phys.*, **36**, 5395 (1997).
- [2] T. Mukai, D. Morita and S. Nakamura, *J. Cryst. Growth*, **189/190**, 778 (1998).
- [3] J. Han, M. H. Crawford, R. J. Shul, J. J. Figiel, M. Banas, L. Zhang, Y. K. Song, H. Zhou and A. V. Nurmikko *Appl. Phys. Lett.*, **73**, 1688 (1998).
- [4] J. Han, T. B.-Ng, R. M. Biefeld, M. H. Crawford, and D. M. Follstaedt, *Appl. Phys. Lett.* **71**, 3114 (1997)
- [5] J. Han, J. J. Figiel, G. A. Petersen, S. M. Myers, M. H. Crawford, and M. A. Banas, to appear in *Jpn. J. Appl. Phys.* (2000)
- [6] E. S. Jeon, V. Kozlov, Y.-K. Song, A. Vertikov, M. Kuball, A. V. Nurmikko, H. Liu, C. Chen, R. S. Kern, C. P. Kuo and M. G. Craford, *Appl. Phys. Lett.*, **69**, 4194 (1996).
- [7] S. Chichibu, T. Azuhata, T. Sota and S. Nakamura, *Appl. Phys. Lett.*, **70**, 2822 (1997).
- [8] T. Wang, D. Nakagawa, M. Lachab, T. Sugahara, S. Sakai, *Appl. Phys. Lett.*, **74**, 3128 (1999) and references therein.
- [9] S.F.Chichibu, A.Shikanai, T.Deguchi, A.Setoguchi, R.Nakai, H.Nakanishi, K.Wada, S.P.DenBaars, T.Sota, and S.Nakamura, *Jpn. J. Appl. Phys.* **39**, Part 1 (2000) (to be published)
- [10] Y. Narukawa, S. Saijou, Y. Kawakami, S. Fugita, t. Mukai, S. Nakamura, *Appl. Phys. Lett.*, **74**, 558 (1999).
- [11] H. Kumano, K. Hoshi, S. Tanaka, I. Suemune, X. Q. Shen, P. Riblet, P. Ramvall and Y. Aoyagi, *Appl. Phys. Lett.*, **75**, 2879 (1999).
- [12] M. H. Crawford, J. Han, M. A. Banas, S. M. Myers, G. A. Petersen and J. J. Figiel, to appear in *MRS Internet J. of Nit. Semicond. Research* (2000).
- [13] V. Fiorentini, F. Bernardini, *Phys. Rev. B*, **60**, 8849 (1999).
- [14] M. Leroux, N. Grandjean, B. Beaumont, G. Nataf, F. Semond, J. Massies, P. Gibart, *J. Appl. Phys.*, **86**, 3721 (1999).
- [15] M. H. Crawford, unpublished.
- [16] T. Mukai and S. Nakamura, *Jpn. J. Appl. Phys.*, **38**, 5735 (1999).
- [17] M. Mayer, A. Pelzmann, C. Kirchner, M. Schauler, F. Eberhard, M. Kamp, P. Unger and K. J. Ebeling, *J. Cryst. Growth*, **189/190**, 782 (1998).
- [18] T. Mukai, M. Yamada and S. Nakamura, *Jpn. J. Appl. Phys.*, **37**, L1358 (1998).
- [19] T. Takeuchi, T. Detchprohm, M. Iwaya, N. Hayashi, K. Isomura, K. Kimura, M. Yamaguchi, H. Amano, I. Akasaki, Yw. Keneko, R. Shioda, S. Watanabe, T. Hidaka, Y. Yamaoka, Ys. Kaneko and N. Yamada, *Appl. Phys. Lett.*, **75**, 2960 (1999).
- [20] S. J. Hearne, J. Han, S. R. Lee, J. A. Floro, D. M. Follstaedt, E. Chason and I. S. T. Tsong, *Appl. Phys. Lett.* (to be published)
- [21] W. W. Chow, M. Hagerott Crawford, A. Girndt and S. W. Koch, *IEEE J. Sel. Topics in Quant. Electron.*, **4**, 514 (1998).
- [22] O. Ambacher, J. Smart, J. R. Shealy, N. G. Weimann, K. Chu, M. Murphy, W. J. Schaff, L. F. Eastman, R. Dimitrov, L. Wittmer, M. Stutzmann, W. Rieger and J. Hilsenbeck, *J. Appl. Phys.*, **85**, 3222 (1999).
- [23] S. L. Chuang and C. S. Chang, *Phys. Rev. B*, **54**, 2491 (1996).
- [24] W. W. Chow and S. W. Koch, *Semiconductor-Laser Fundamentals*, Springer-Verlag, Berlin, 1999, p. 189.
- [25] Jin-Kuo Ho; Charng-Shyang Jong; Chiu, C.C.; Chao-Nien Huang; Kwang-Kuo Shih; Li-Chien Chen; Fu-Rong Chen; Ji-Jung Kai, *J. Appl. Phys.*, **86**, 4491 (1999).
- [26] M. E. Aurner, S. F. LeBoeuf, F. G. McIntosh and S. M. Bedair, *Appl. Phys. Lett.*, **75**, 3315 (1999).
- [27] J. Han, J. J. Figiel, G. A. Petersen, S. M. Myers, M. H. Crawford, M. A. Banas and S. J. Hearne, to appear in *MRS Internet J. Nitride Semicond. Research* (2000).

GaN-based MQW light emitting devices

M. Koike*, S. Yamasaki, Y. Tezen, S. Nagai, S. Iwayama,

A. Kojima, T. Uemura, A. Hirano and H. Kato

Optoelectronics, Toyoda Gosei Co., Ltd., Haruhi-cho, Nishikasugai-gun, Aichi 452-8564, Japan

ABSTRACT

The GaN-based MQW laser diodes have been improved excellently by introducing GaN/GaN optical-guiding. The continuous wave laser operation at room temperature has been achieved at the wavelength of 410 nm. The lifetime of room temperature continuous wave operation is longer than 60 minutes at around 1 mW output. The external efficiencies of GaInN/GaN MQW blue and green light emitting diodes (LEDs) have been increased by newly developed flip-chip (FC) type LED lamp structure. The luminous intensities of the FC-type blue and green LEDs were typically 6 cd and 14 cd at 20mA, respectively. The FC-type blue and green LEDs are the brightest levels in the world currently. The peak wavelengths and full widths at half maximums were typically 464 nm and 27 nm for the blue LEDs, and 515 nm and 32 nm for the green LEDs.

Keywords: GaInN/GaN MQW, LEDs, LDs, CW, MOVPE

1. INTRODUCTION

III-V nitride compound semiconductors are potential materials for high efficient optical devices in the ultraviolet to red spectral region. Excellent uniform epitaxial layers of GaN and nitride alloys were grown on sapphire substrates using an AlN buffer layer by metalorganic vapor phase epitaxy (MOVPE).¹ High-quality GaInN/GaN multiple quantum wells (MQWs) structure of GaN-based superlattices enhanced the optical efficiency by nearly two-orders of magnitude in comparison with bulk GaInN.² The high efficient GaInN/GaN MQW LEDs have been commercialized for UV, blue and green light sources. Akasaki, et al. reported for the first time the laser irradiation from GaInN laser diode by current injection at room temperature (RT) in 1996.³ Recently, III-V nitride semiconductor laser diodes (LDs) have been improved to the grade of a digital versatile disk (DVD) application. The MQW separated confinement hetero-structure (SCH) laser diodes have been realized with longer than 10,000 hours lifetime under continuous wave (CW) operations at RT.⁴

In this paper, we will report the improvements of the GaN-based LDs by applying GaInN/GaN optical guide. The RT CW operation also has been achieved in the range of hours in the lifetime at around 1 mW output. We will also report the higher efficient GaN-based LEDs improved by flip-chip (FC) type bonding structure.

2. EXPERIMENTS

The GaN-based epitaxial layers were basically grown by atmospheric metalorganic vapor phase epitaxy (MOVPE). The sources of Al, Ga, In, and N were the common gases such as trimethylaluminum (TMA), trimethylgallium (TMG), trimethylindium (TMI), and ammonia (NH₃), respectively. The Si and Mg dopants were incorporated using silane (SiH₄) and biscyclopentadienylmagnesium (bis-Cp₂Mg).

2.1 GaInN/GaN MQW SCH LDs

One of the schematic structures of GaInN/GaN MQW-SCH LDs is shown in Fig. 1. The LDs consisted of n-GaN contact layer, n-Al_{0.07}Ga_{0.93}N cladding layer, n-GaInN/GaN optical guide double layers, GaInN/GaN MQW active layer, p-GaInN/GaN optical guide double layers, p-Al_{0.07}Ga_{0.93}N cladding layer, and p-GaN contact layer which were grown on sapphire substrate with low temperature (LT) buffer layer. The number of MQWs was two to six. The conventional optical guide layers consisted of GaN. However, we applied GaInN/GaN optical guide layers, because an optical confinement factor of GaInN optical guide layer is superior to that of GaN. The LD

* Correspondence: Email: tg24053@toyoda-gosei.co.jp; Telephone: +81-52-400-5183; Fax: +81-52-400-1249

structures were mesa or ridge geometry. The widths mesa or ridge were 2 to 5 μm , the cavity lengths were 300 to 700 μm . The mirror facets were fabricated by reactive-ion-beam-etching (RIBE) and the high-reflection (HR) mirror coats were $\text{TiO}_2/\text{SiO}_2$ dielectric multi layers.

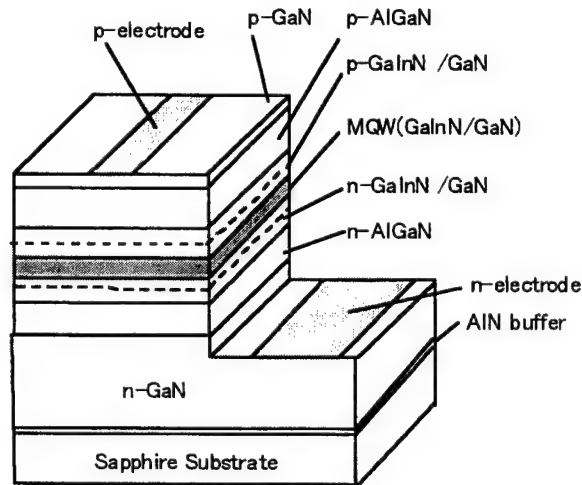


Fig. 1. Schematic layer structure of LEDs.

2.2 GaInN/GaN MQW LEDs

The blue and green MQW LEDs consisted of asymmetric double heterostructure p-n junction with GaInN/GaN MQW active layer. The MQW had two to five quantum wells. The layer structure of FC-type MQW LEDs is shown schematically in Fig. 2. The InN molar fraction of the GaInN quantum wells for the blue and green LEDs was approximately 0.2 to 0.4. Mg-doped AlGaIn layer was grown sequentially on the GaInN/GaN MQW layer. The p- and n-electrodes were partially etched by reactive-ion-etching (RIE) to form an ohmic contact onto the Si-doped n-GaN layer. The p- and n-electrodes were bonded onto sub-mounts and the emission irradiated upward through the sapphire substrates. The light transmission of a conventional electrode for p-type contact layer, which covered light emitting surface, was not always perfect. On the other hand, in the case of the FC-type LEDs, the p-electrode was not transparent, the light from MQW active layers emits directly through sapphire substrates to outside of LED chips without of any obstacles such as electrode metals.

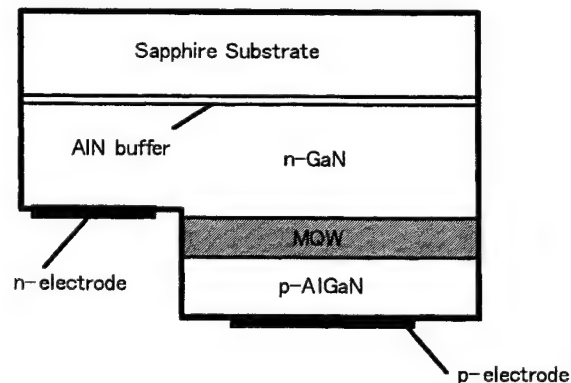


Fig. 2. Schematic layer structure of FC-type LEDs.

3. RESULTS AND DISCUSSION

3.1 GaInN/GaN MQW SCH LDs

The threshold current (I_{th}) of the double-guide-layer SCH LDs was 60-70 mA at RT-CW operation. The current-output-voltage (I-L-V) characteristics under the RT-CW operation are shown in Fig. 3. The operation voltage for the threshold current was approximately 8 V. The RT-CW emission spectrum is shown in Fig. 4. The laser wavelength was 408 nm and its full width at half maximum (FWHM) was 0.03 nm.

One of the preliminary lifetime evaluations is shown in Fig. 5. The CW laser operation at room temperature continued for one hour with around 1 mW output as shown in Fig. 5.

The longer lifetime is under investigation, which could be expected by reducing dislocation in LD epitaxial layers. The multi low-temperature (LT) buffer layers also could be effective for reducing dislocation. We applied the multi LT buffer layers to the laser diode for the first time. The density of etch pits in the epitaxial layers reduced from $1 \times 10^8 \text{ cm}^{-2}$ to $5 \times 10^6 \text{ cm}^{-2}$ using the multi LT buffer layers. Therefore, We have been optimizing the laser diode structure and investigating the lifetime.

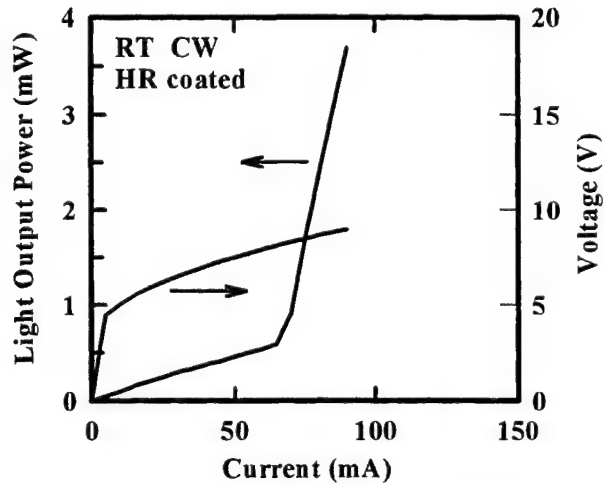
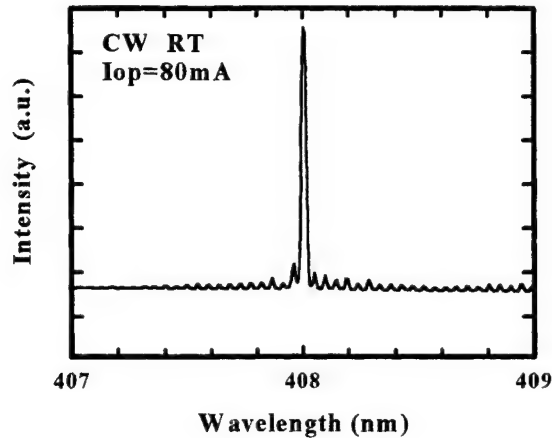


Fig. 3. I-L-V characteristics under RT-CW operation.



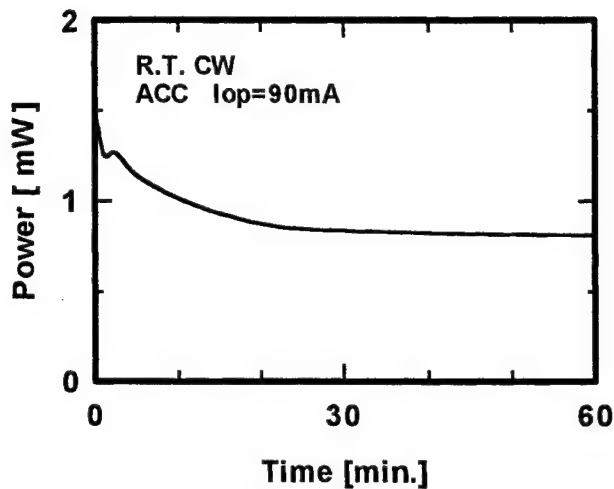


Fig. 5. Preliminary aging test at around 1 mW under RT-CW. operation

3.2 GaInN/GaN MQW LEDs

The external quantum efficiencies of GaInN/GaN MQW blue and green LEDs have been increased to almost double by newly developed flip-chip (FC) type LED lamp structure. The luminous intensities of the FC-type blue and green LEDs were typically 6 cd and 14 cd at 20mA, respectively. The brightness of FC-type blue and green LEDs are the highest levels in the world currently.

The output powers of the FC-type blue LEDs are much higher than that of the conventional face-up type blue LEDs. The output power of the FC-type LEDs was 14 mW at 20 mA, which was approximately two times higher than that of the conventional blue LEDs as shown in Fig. 6. The external quantum efficiency at 20 mW was as high as 20 %.

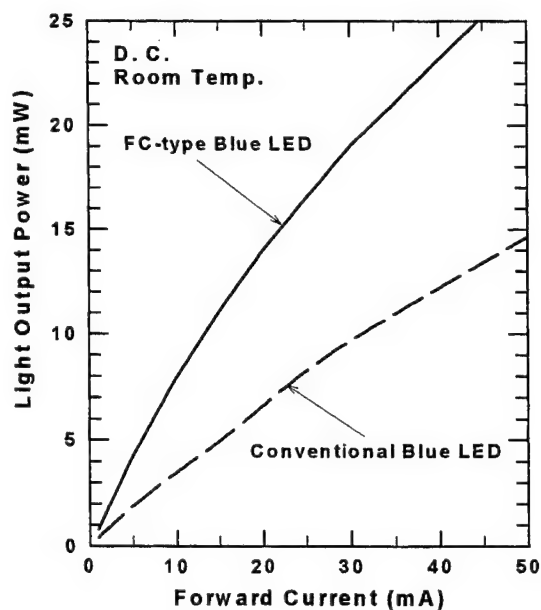


Fig. 6. Output power characteristics of FC-type and conventional blue LEDs as a function of forward current.

The FC-type LED lamp structure did not affect to the electroluminescence spectra. The peak wavelengths and full widths at half maximums were typically 464 nm and 27 nm for the blue LEDs, and 515 nm and 32 nm for the green LEDs as shown in Fig. 7.

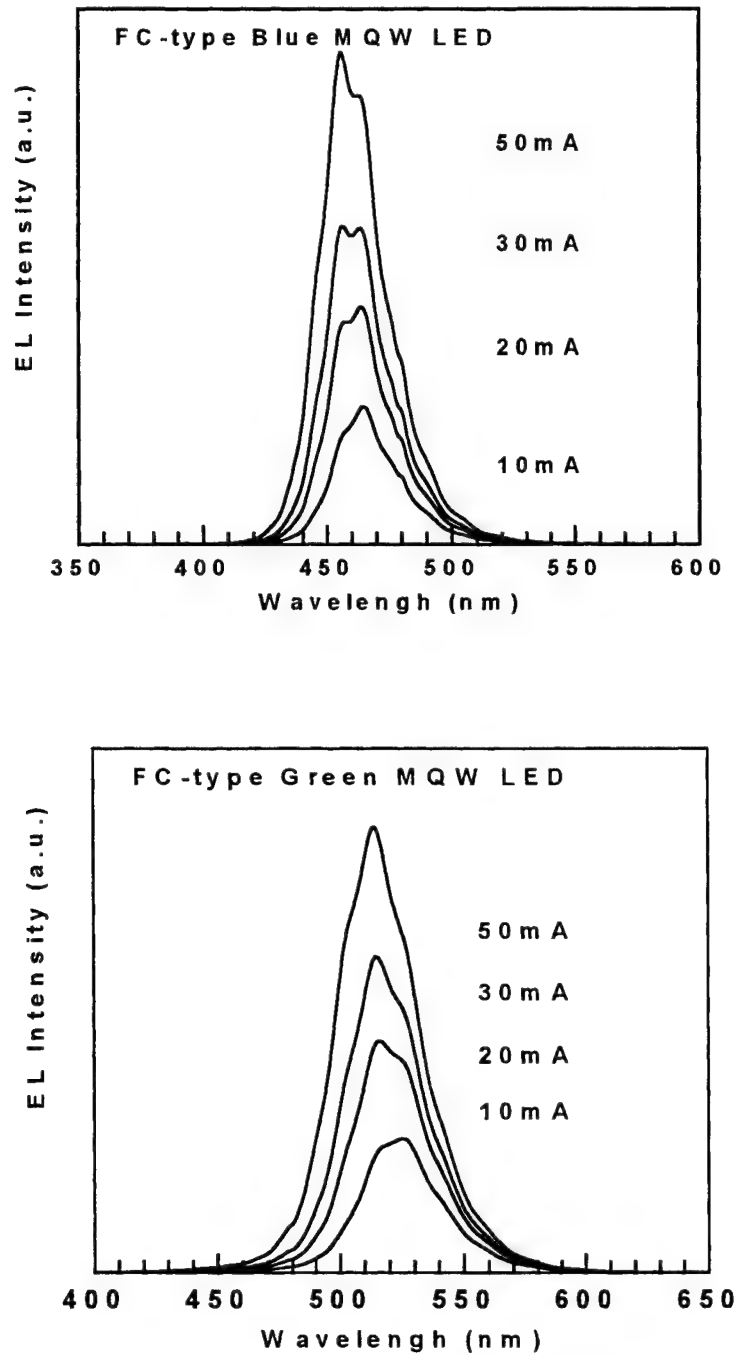


Fig. 7. EL spectra of FC-type blue and green LEDs.

4. CONCLUSION

We have succeeded in CW operation of GaInN/GaN MQW-SCH laser diodes at RT. The low threshold current of 60 mA (2.4 kA/cm²) was achieved by introducing the GaInN/GaN optical guide layer and the loss reduction. The lifetime of CW operation is longer than 60 minutes at around 1 mW output. The external efficiencies of GaInN/GaN MQW blue and green light emitting diodes (LEDs) have been increased by newly developed flip-chip (FC) type LED lamp structure. The luminous intensities of the FC-type blue and green LEDs were typically 6 cd and 14 cd at 20mA, respectively. The FC-type blue and green LEDs are the brightest levels in the world currently.

ACKNOWLEDGEMENTS

The authors would like to acknowledge Professors I. Akasaki and H. Amano of Meijo University for helpful suggestions and discussions.

REFERENCES

1. H. Amano, N. Sawaki, I. Akasaki and Y. Toyoda, *Appl. Phys. Lett.*, **48**, p.353, 1986.
2. M. Koike, N. Shibata, S. Yamasaki, S. Nagai, S. Asami, H. Kato, N. Koide, H. Amano, and I. Akasaki, *Mat. Res. Soc. Symp.* Vol. **395**, p.889, 1996.
3. I. Akasaki, S. Sota, H. Sakai, T. Tanaka, M. Koike and H. Amano, *Electron. Lett.*, **32**, p.1105, 1996.
4. S. Nakamura, M. Senoh, S. Nagahama, N. Iwasa, T. Matsushita and T. Mukai, *Proc. 2nd Intern. Symp. On Blue Laser and Light Emitting Diodes, Chiba, Japan*, p. 371, 1998 (Ohm-sha, Ltd. Tokyo, 1998).

White light emitting diodes for illumination

Regina Mueller-Mach and Gerd O. Mueller

Agilent Technologies
Agilent Laboratories, Communications and Optics Research Laboratory
Palo Alto, CA 94304, USA

ABSTRACT

White light for illumination can be produced from LEDs either by combining red, green and blue emitting chips in one lamp, or by using phosphors to down-convert the emission of short wavelength emitting InGaN LEDs. Both concepts will be critically reviewed, and simulations compared with experimental evaluations. As expected, each solution has advantages, but also drawbacks, which are weighted by the specifics of the applications. The overall picture strongly depends on the efficiencies of the single color chips, the temperature coefficients of all involved materials, and the wanted light output per lamp.

Keywords: Solid state lighting, LED, electroluminescence, phosphors, photoluminescence, GaN, color rendering

1. INTRODUCTION

Solid State Illumination (SSI) has long been dreamed about. The illumination market being some $\$10^{10}$ /year is of an attractive size even for large companies. Recently formed joint ventures of lighting companies with manufacturers of light emitting diodes (LED) indicate the direction of the development very clearly. In spite of the fact that the incandescent light bulb has moved down its cost development curve to a point where no newcomer can compete with it, a definite chance for penetration into certain application segments is obvious. "Cold Light" as opposed to light emitted as thermal radiation from hot enough filaments in incandescent bulbs, has been a dream since the discovery of electroluminescence in the '30s. The first successes in powder electroluminescence in the '50s sparked the vision of illuminating walls and ceilings, but reality ran short in efficiency and lifetime as well. The fluorescent lamp was the first realization of a cold light source, and turned out to be so successful, that all other attempts were deemed useless over the last decades. Lifetime was and is an as important issue. Especially in applications, in which maintenance is costly or inconvenient, a premium can be charged. Overall efficiency is an important factor, which determines cost of ownership to a large extent, and it is the last two points, which helped the LED to intrude for instance into the traffic light sector over the last years. Now that blue and green LED joined the red and amber LED, made in large numbers exclusively for signaling over many years, Solid State Lighting (SSL) becomes feasible. Very recently the efficiency values for the (In,Ga)N based blue and green LED approached the values common for high power (Al,Ga,In)P diodes, which go into the traffic lights and car lamps in ever growing quantities, and their power efficiency surpassed the value for the best incandescent lamps (**Fig. 1**). Very good pre-conditions are given right now to enter the era of 'cold', solid state light from sources with very high radiance (point sources) and virtually unlimited maintenance [1,2].

1.1 General Considerations

(In,Ga)N technology allows to manufacture diodes for any color between about 400 and 580 nm today, 590 to 670 nm is the realm of high power (Al,Ga,In)P. Typically the line width of the nitride-based LEDs varies between 20 and 35 nm (fwhm) and of the phosphide-based ones between 15 and 25 nm. As there is a quasi-continuum of peak wavelengths manufacturable, one could think of assembling many LEDs to compose a broad 'white' emission band – a near Planckian distribution. A much better, more efficient way to produce white light, however, is the mixing of relatively narrow lines of the basic colors – Red, Green, Blue – demonstrated and proven by the Philips 3-color fluorescent lamp. It showed that by choosing the right wavelengths and spectral widths it is possible to generate white light of any wanted

Correlated Color Temperature (CCT) and good Color Rendering Index (CRI). So, the first idea coming to mind in considering the new possibilities of LEDs, is to follow this example. Using 3 LEDs has even some advantages over the fluorescent case, as the broader emission bands, can give even better CRI. An example spectrum is given in Fig. 2.

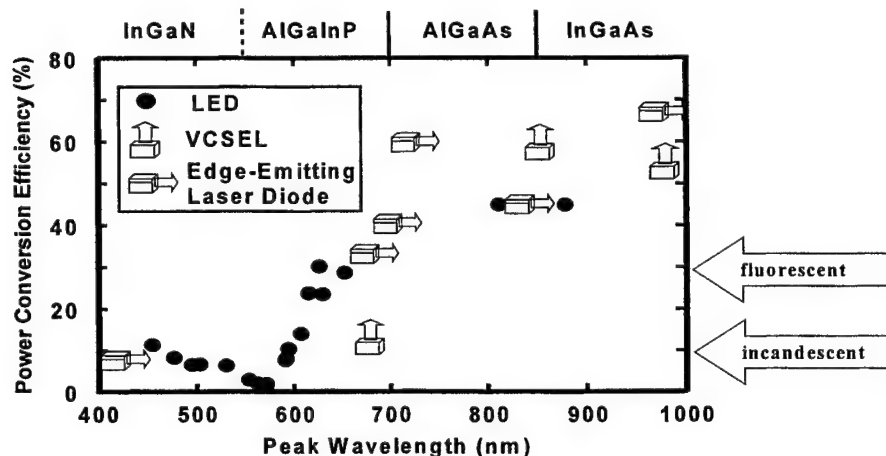


Fig.1: The power conversion efficiencies of LEDs and lasers approach 50 to 70% in the infrared with no obvious reason that the high values should be limited to this range, and not be reached in the InGaN range after further development; after Craford et al., p.35 in [2].

Before going into details, one might want to consider other examples given by previous developments. Mercury high pressure lamps have good radiometric efficiency but very poor color rendering as they are radiating besides UV only blue in any appreciable amount. One of the great ideas was the **color correction**, improvement of CRI, by adding a phosphor to the bulb, which converted part of the primary radiation into yellow. A reasonable 'white' resulted, and OSRAM products proved this, using a highly stable yellow phosphor - Ce^{3+} doped Yttrium-Aluminum-Garnet ($\text{Y}_3\text{Al}_5\text{O}_{12}$) [3]. It was an evident way to try, whether the same phosphor could be excited by the light of a blue LED, and at the same time mixed with a rest of the original blue. And it worked, as Nichia proved in their first white LED [4].

So, it has been proven, that there is an alternative way of producing white light by LEDs: mixing of blue from an LED and a complementary luminescence excited by the blue radiation in phosphor(s). The phosphor(s) have to meet a set of conditions to provide acceptable solutions of the problems involved. The conditions comprise: good light quality - CRI > 80 at a wanted CCT with very limited change over the range of operating temperatures; good mixing, angular or far-field, with the non-absorbed blue; good control of the absorbed fraction for all operating temperatures.

Following the show case of the fluorescent lamp, as a third possibility, one would have to use completely absorbed radiation from an LED, which excites phosphor(s), yielding blue, green and red, or blue and yellow, or any other combination, which mixes to white. The basic drawback of this 'UV LED' solution is the higher quantum deficit, which had to be compensated by other advantages over the 'blue LED' phosphor conversion. We are not going into details of the UV LED approach, which seems to be a favorite of GE [5].

The two different solutions, which we will term multi-chip LED lamps (mcLED), and phosphor-converted LED (pcLED) respectively, will be analyzed for their dis- and advantages [6,7]. The mcLED has the obvious advantage to provide no inherent loss mechanisms to the radiation from the primary sources, except for the absorption of the radiation of one LED by another in the process of color mixing.

Down conversion in a phosphor material, however, is an inherently lossy process, which for an ideal phosphor of quantum yield 100% has an upper bound, set by the quantum deficit. In all cases investigated, additional losses were encountered, and will be discussed with respect to their origin and estimated margins.

1.2 State of the Art

Nichia introduced mcLED to market some years ago, which had rather poor characteristics, and found not too broad an acceptance, and are not even advertised anymore. First commercially available 'white' pcLED, produced by Nichia and Hewlett Packard, in the form of 5 mm lamps, delivering some Lumens only (not meant for general lighting!), and so-called TopLED surface-mount lamps from Osram/Siemens

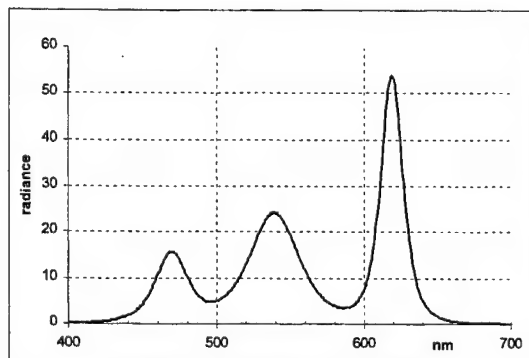


Fig.2: Combining a 470 nm, a 540 and a 620 nm chip into one LED lamp gives a white light source

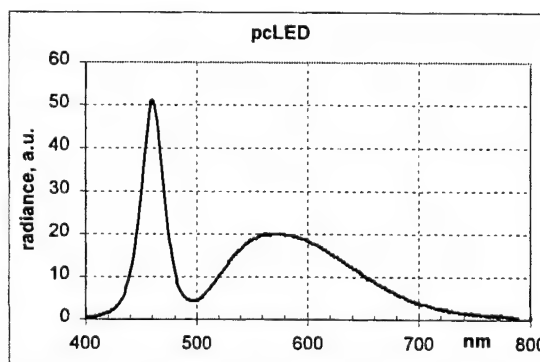


Fig.3: Emission spectrum of a state of the art white 5-mm LED lamp

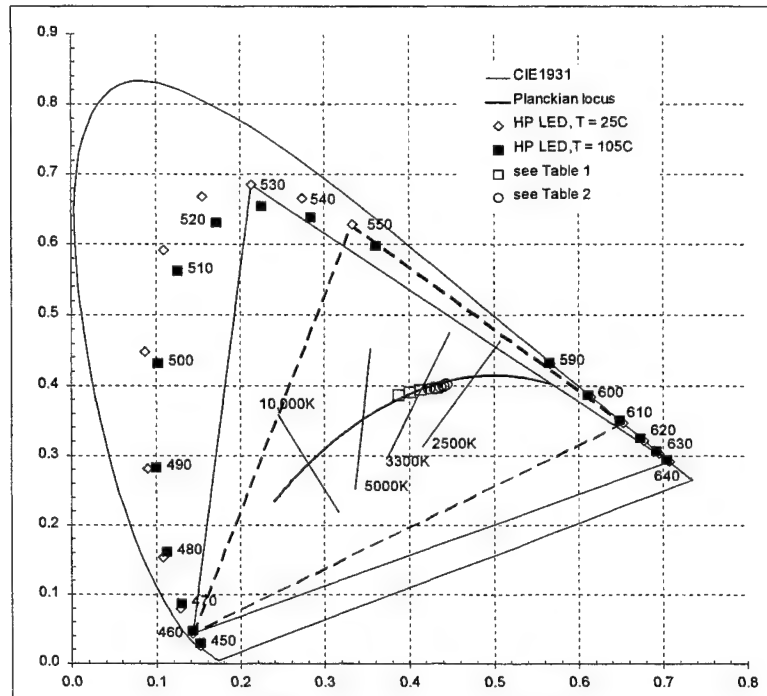
have found quite some market. However, in the context of SSI they can only be regarded as samples to study the problems. In all cases mentioned only one phosphor is used, which is excited by an LED at 460...470 nm (Fig. 3). In order to deliver a good CRI, the CCT has to be chosen in the 5000...8000 K range. This limitation will be analyzed as an example for more general design considerations under 'pcLED'. However one researcher [6] very recently claimed the high color temperature as a great achievement over 'warm' incandescent light, as it is more similar to day-light.

1.3 Scope of the Work

To get an oversight on the possibilities of generating white light for illumination, i.e. light which assures good color rendering, a simulation program was developed, which calculates color coordinates, CCT, CRI, Ra., luminous equivalent and distance from the Planckian locus in dependence on the power fractions of light from different LEDs, on conversion efficiencies of phosphor(s) and their respective temperature dependencies. LED spectra were assumed to be of (second order) Lorentzian shape, which is fairly good an approximation for the diodes used. First results obtained have been reported in [7,8]. This paper will for the first time report comparisons to experimental data. Furthermore it will point out the potential applications, in which special designs might be appropriate.

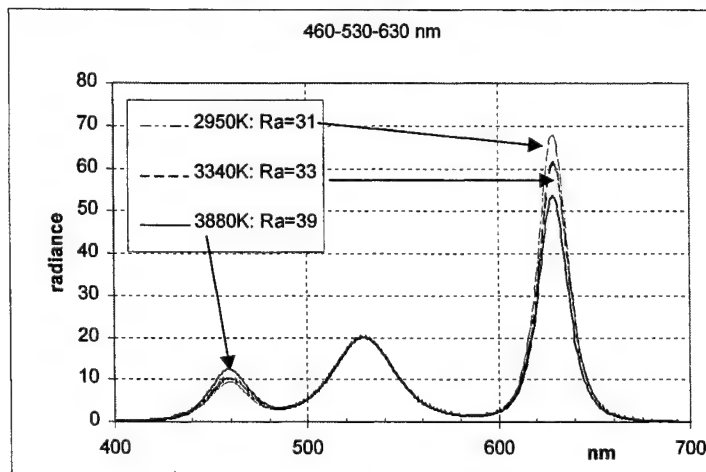
2. MULTICHIP LED

Any wavelength in the visible can be generated by either nitride or phosphide-based LEDs. The spectra of the LEDs are narrow enough to place their color coordinates near the border of the color space. As shown in the CIE-1931 color diagram of Fig.4, their chromaticity points move inwards with increasing junction temperature, equivalent to saying that their spectra become wider, color purity decreases. Color mixing in a color diagram can be described by drawing a line between the two color points, which correspond to the two colors to be mixed. All colors, which can be achieved by blending appropriate amounts of light of



those two end points, lie on this line. In the same way any chromaticity point within a triangle can be reached by mixing of the corner point colors. This is true even for strictly monochromatic radiation, which would correspond to points on the periphery of the color space. For display application, or any other (signaling) mode, in which direct view of the colors is aimed at, this description is perfect.

However, in illumination by no means: imagine monochromatic lines of blue, green and red to mix to a



perfect white – a point for a certain temperature on the Planckian locus. Objects illuminated by such a source will look very different from what they look under the black body radiation of that temperature. This failure to give a good rendition of certain colors is described by the Color Rendering Index (CRI), standardized by the CIE in 1974 [9]. The fictive source would give CRI values lying well below its maximum of 100. How subtle the differentiation of ‘display’ and illumination light quality can be, is demonstrated in **Fig.4** (showing the color points of some LEDs with the peak wavelengths indicated).

For display purposes the dashed triangle with the corners materialized by LEDs of 460, 530, 630 nm would generate delight by its large ‘color gamut’. However an attempt to compose a well rendering white of a CCT of 3000°K fails as exemplified by Fig.5 and Table 1. A comparison to experimental makes confirms the simulation results fully.

Table 1: mcLED from 460|530|630 nm LEDs (Fig5)

opt. power fraction, B G R	CCT, °K	Ra	LE, lm/W
14 38 48	3880	39	294
13 37 50	3590	36	294
12 36 52	3340	33	293
10 35 55	2950	31	290

Reducing the gamut to 460, 550, 610 nm LEDs, yields excellent CRI values, demonstrated in Fig.6 and Table2 with even the variation with junction temperature of the LEDs being acceptable. It is not well

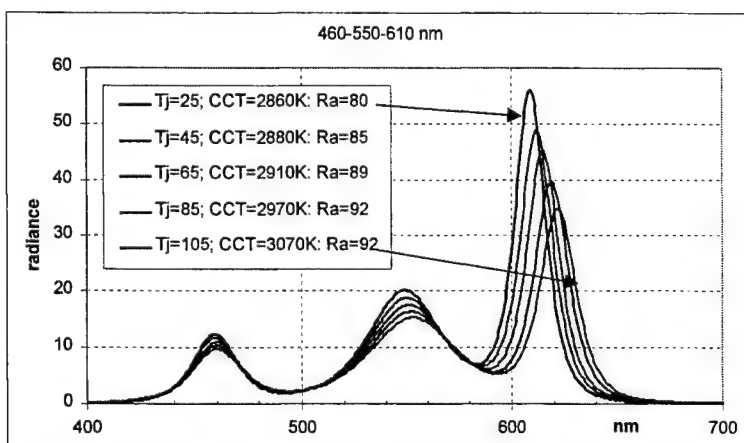


Fig.6: Composing LED spectra of peak wavelengths 460, 550, 610 nm, one can obtain good CRI values, but hardly acceptable shifts of CCT with junction temperature, Table 2.

predictable from first principles of color science how such changes of peak wavelengths affect CRIs, as they depend rather strongly on the detailed shape of the lines too (keeping in mind that there is no unique spectrum related to a chromaticity). Experimental spectra very closely correspond to those simulations.

A detailed analysis shows that good ‘illumination white’ of any color temperature between 3000 and 7000°K can be composed from LED spectra with peak wavelengths of 460, 550, 615 nm.

Table 2: mcLED from 460|550|610 nm LEDs (Fig.6)

Junction temperature Tj, °C	CCT, °K	Ra	lum. effi/ lum. effi.(25°C), %	LE, lm/W
25	2860	80	100	402
45	2880	85	92	391
65	2910	89	86	381
85	2970	92	79	368
105	3070	92	73	359

One important consideration has not been touched upon yet. Without going into cost deliberation in any numerical way, the most basic consideration leads to the conclusion that in an mcLED lamp the major cost items are the chips. As on the other hand the customer is interested in buying as much lumens per \$ as possible (in fact mostly lm*years/\$) the design has to aim at maximum lumen/chip area. This means

driving the chips at *maximum* current density. This maximum is set by temperature and reliability constraints. In general the efficiency, η , will decrease with increasing temperature. Besides the efficiency, peak wavelength and spectral width are T-dependent too. There are no good data in the sparse literature on these issues. We have included into Fig.4, what we believe are the best data, summoned into color coordinates. No major changes seemingly occur.

The conclusion to be drawn from these data is obvious: active color control is necessary, if the junction temperature is expected to change. As the efficiency cannot be increased at higher temperature, the active control will be limiting the efficiency at any lower temperature to just this value; the control has to burn off the efficiency surplus at the lower temperatures.

Going back to Fig.1 one could be inclined to do some projection of the power efficiency values just by comparison. External power efficiencies in the red spectral region based on phosphides, which are much longer under development, could be an indicator. A rather conservative assumption - in view of the roughly 30% in the deep red - for the blue spectral region would be 16% reached in 2 years from now. As green has been notoriously lower than blue, let us assume (without any proof of probability) a value of 10%, and for 610nm of 20%. Using these values, we come up with about 50 lm/W for the room temperature value in Table 2, which was used as a reference point. An assumed reduction of the efficiency by 10% for the nitrides, and for 610 nm one of 30% at $\Delta T=80^{\circ}\text{C}$ cuts it back to about 38 lm/W, as not only the radiometric efficiency drops, but also the luminous equivalent. However, this is in the range of compact fluorescence, and much beyond halogen lamps. It is hardly conceivable how to get a good color mixing in the lamp without additional losses, but no reliable estimates or even data are available at this time.

3. PHOSPHOR CONVERTED LED

As mentioned before, the basic concept of pcLEDs, as they are on the market now from Nichia, Agilent (Hewlett-Packard) and Osram/Siemens, is the old one of color correction as it was applied over years to high pressure Hg lamps.

The pcLED lamps are encapsulated in epoxy, which helps light extraction by its refractive index and by the lens shape. So the easiest way to

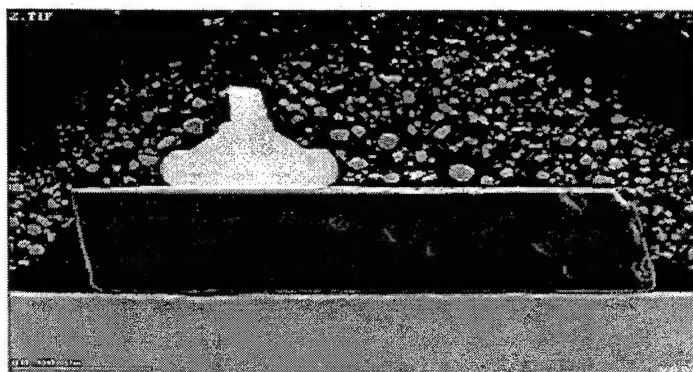


Fig.7: Micrograph of a pcLED lamp. Clearly visible the chip, the contact, and irregularly shaped phosphor particles in the epoxy encapsulant.

apply a phosphor is by suspending it in the epoxy before curing. The results is a rather uneven distribution of phosphor particles, somewhat sorted by size by gravity action, in a layer above the LED chip (Fig.7). A typical experimental spectrum has been shown in Fig.3. Clearly there is a remainder of the blue, emitted by the diode, sneaking through the space between phosphor particles or scattered by them. The broad yellow band is characteristic of the phosphor – YAG:Ce. To be more precise the phosphor in this case is an (Yttrium,Gadolinium)-Aluminum-Garnet doped with Ce^{3+} , and the Gadolinium has

the effect of changing the crystal field at the Ce^{3+} site, shifting the emission towards longer wavelengths. The precondition of working this way is a high enough absorption/excitation of the dopant at the diode emission wavelength. Fig.8 shows excitation and emission spectra for various Gd contents of the YAG:Ce³⁺.

Quite a variety of peak wavelengths of (In,Ga)N LEDs can obviously be used, judging from the excitability of the phosphors only. The additional selection criterion is the color temperature and the CRI one shoots for. In a 1931 color space the choices for the color coordinates look simple: Combining a given phosphor with some diodes of the peak wavelengths labeled allows for the straight lines in the left part of **Fig.9**. Combining a given diode (460 nm in this case) with phosphors of differing Gd content, allows for the lines in the right part. What point on the respective line is accomplished, depends on the amount of primary radiation from the diode converted into 'yellow', that means essentially on the phosphor amount admixed to the encapsulant. The color rendering is not as easy to describe. One has to go back to combined spectra, and run the routine devised by the CIE to determine the general color rendering index, Ra, or even all 14 special color rendering indices [9]. To avoid 'tint' (deviation from pure white), the color point should be very close to the Planckian locus. In an experimental make of pcLED with a wavelength variety of LEDs the heap of Ra versus CCT data of **Fig.9b** were obtained, while close control of the LED wavelength but

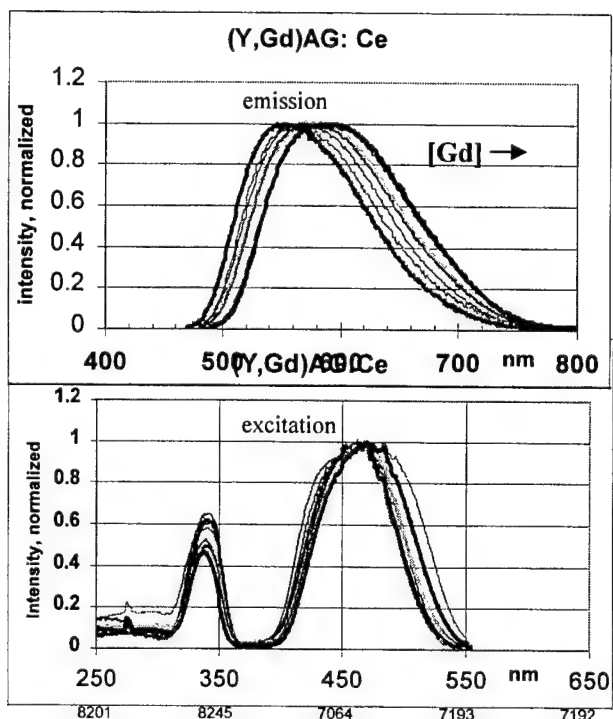


Fig.8: Emission (upper part) and excitation (lower part) spectra of YAG:Ce phosphors shift with increasing Gd content to the red.

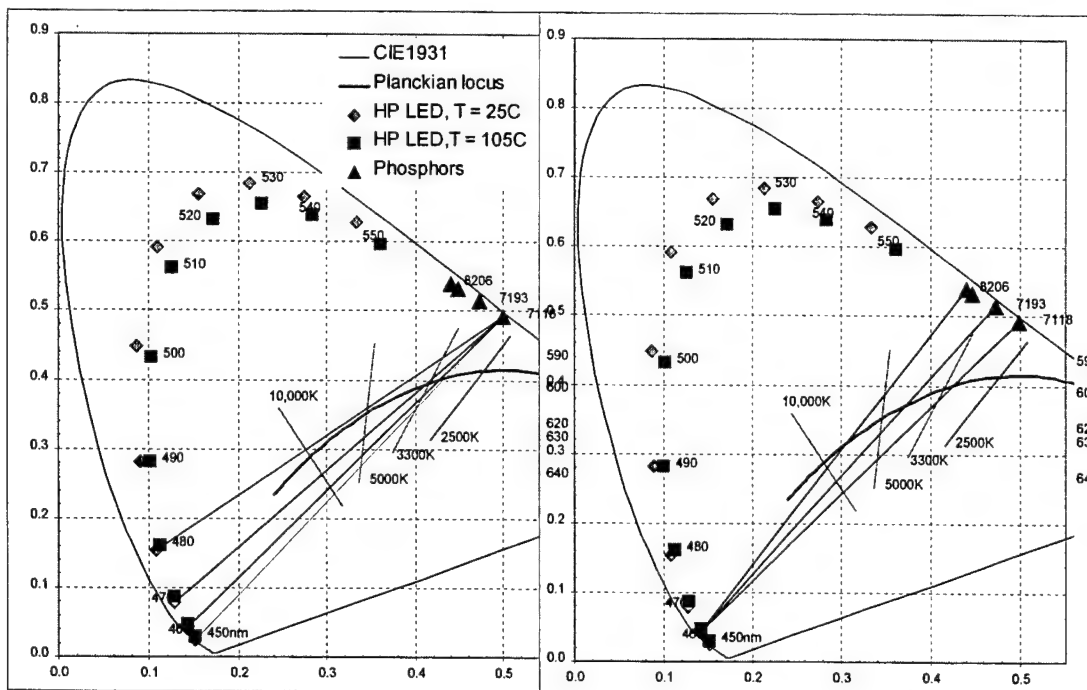


Fig.9: In a pcLED one has the choice of some LED wavelengths for each phosphor (left part) and for any LED wavelength several phosphors are possible (right part).

varying the phosphor amount yielded Fig.9c.

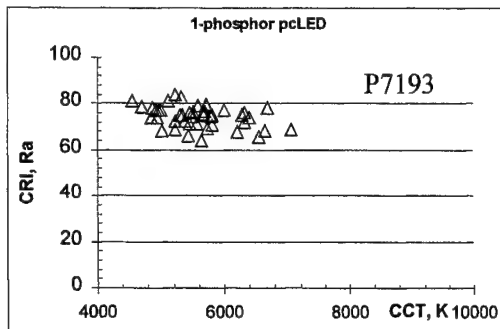


Fig. 9b: Experimental values from lamps made with one phosphor, and LEDs of various wavelengths.

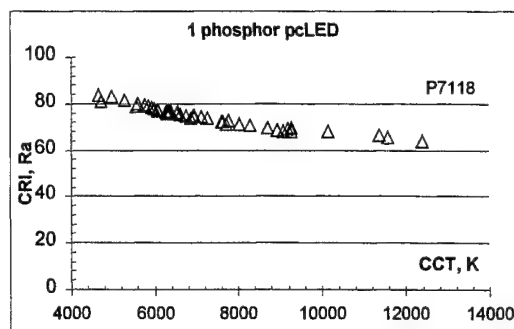


Fig.9c: Experimental values - varying the phosphor content

To convey some feeling for the matter to readers, who are not familiar with color science, Fig.10 shows some spectra, and Table 3 gives values of the respective CCT and Ra.. It is obvious, that it is difficult to reach good color rendering at low CCT. Customer satisfaction in Scandinavia, where CCT below 3000°K are most preferred will be difficult to reach, while in Japan with preferred values of 6000°K this solution will satisfy most wishes.

Table 3: pcLED from 460 nm LED + YAG:Ce (Fig.10)

opt. power fraction, LED phosphor	CCT, °K	Ra	LE, lm/W
12 88	3540	70	350
18 82	3860	73	330
22 78	4110	76	318
26 74	4490	79	304
31 69	5270	82	286

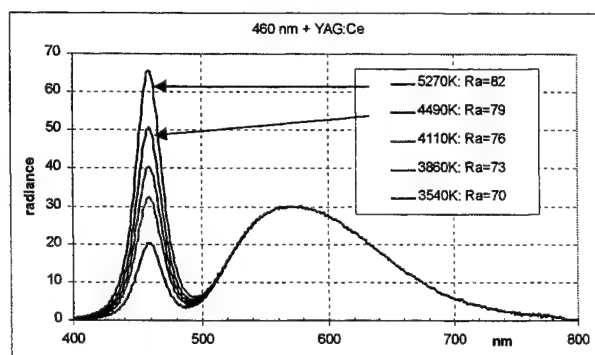


Fig.10: With YAG:Ce it is possible to achieve good CRI values ($R_a > 80$) at CCTs above 5000°K only; see Table 3 also.

Having highlighted the temperature dependence of color coordinates in mcLEDs Fig.11 presents similar data for the 1-phosphor converted LED (1-pcLED), which are supplemented by Table 4. Really the change with temperature is almost as pronounced as in mcLEDs, and by no means negligible. One might wonder whether customers will cope with it. Of course incandescent shows the same red shift with dimming, which one can achieve, if it is designed into the pcLED.

Of course certain assumptions had to be made about the temperature dependence of the LED and of the conversion efficiency of the phosphor. Both were based on measurements taken on the two components separately. The experimental spectra of the pcLED do not well compare to the simulations, as shown in Fig.11b. The question about the reason for the discrepancy can tentatively be answered by looking more closely into the shift and broadening of

the LED spectra with temperature and the decreasing overlap with the absorption spectrum of the phosphor. We will come back to this aspect.

Table 4: pcLED from 460 nm LED + YAG:Ce, varying junction temperature, T_j (Fig.11)

Junction temperature T_j , °C	CCT, °K	Ra	LE, lm/W
25	4490	79	304
45	4550	79	302
65	4610	80	301
85	4680	80	299
105	4750	81	298

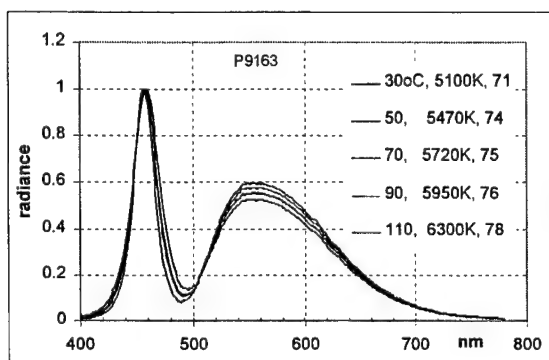


Fig.11: The temperature variation of the pcLED depends on the phosphor chosen; it is sensible in this case, but rendering improves with increasing temperature

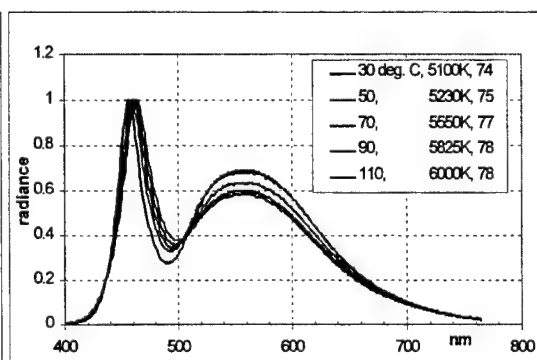


Fig 11b: Experimental values on 1-phosphor lamps in dependence on temperature, CCT and Ra given in the legend

As further improvements of color rendering are very possible, it seems a good idea to think about other phosphors. What the YAG:Ce does, as probably no other material, is to provide an extremely broad spectrum.. Ce^{3+} has the unique feature to combine the action of a dipole-allowed 5d-4f radiative transition, which is strongly lattice coupled (and therefore phonon-broadened) and crystal field dependent, with an additional ‘broadening’ by its spin-orbit split ground state. The two-peak structure is washed out by the other broadening influences. By this double action the emission band is much broader than the width, which for instance Eu^{2+} exhibits (another example of an allowed 5d-4f transitions). So, Ce^{3+} appears to be the ultimate choice for a 1-pcLED, and the host is right to shift excitation and emission into the right position.

Adding a second phosphor or a third color can vastly improve the color properties of the system. Very much alike the situation in the mcLED the blue from the diode can be complemented by a green from one phosphor and a red emission from a second phosphor. If the phosphors are ‘right’, this could be the ultimate choice. The problem

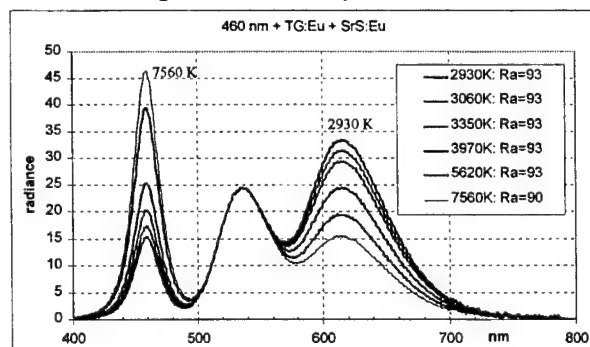


Fig.12: The spectra show the variety of CCTs, obtainable with excellent rendering by the combination of two highly balanced phosphors; see also Table 5.

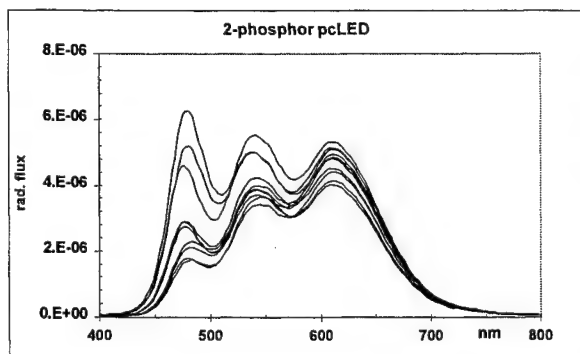


Fig. 12b: Experimental results on 2-phosphor pcLED exhibit $R_a > 85$ for all CCT obtained, 3200 - 4400 K in this case.

values at the respective CCTs. No doubt, *de-luxe* lighting can be achieved, based on this system.

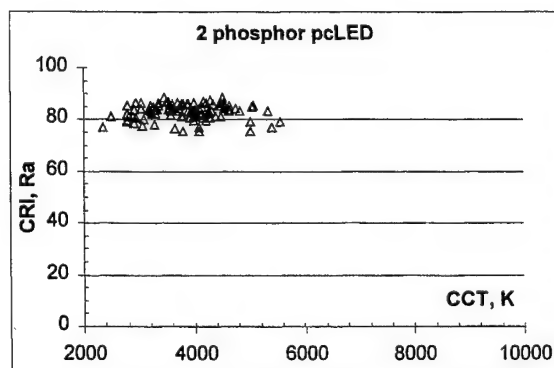


Fig. 12c: Experimental makes of 2-phosphor LEDs show the expected excellent rendering for all wanted color temperatures

lies in finding the right **combination**, which is excitable by the same blue diode emission. It is not evident, that a solution to this problem exists, which furthermore gives a good color rendering. But really there is a combination and it is Eu^{2+} in SrGa_2S_4 for green (TG:Eu) and the same dopant in SrS for red (SrS:Eu^{2+}). Their emission spectra are shown together with emission of a well exciting LED in Fig. 12. In the CIE1931 color space the combination looks as depicted in Fig. 13. It is obvious, that the corners of the triangle are not too far from the preferred mcLED combination of Fig. 5. No incident, as the spectral widths are also comparable. Table 5 shows some power fractions of the spectral components, which lead to the R_a

A reality check produced the experimental spectra shown in Fig. 12b, the variety of which is due to the varied amounts of each phosphor in the lamps.

Fig. 12c gives the (expected) good rendering behavior of the generated light for a whole bunch of wanted correlated color temperatures. This could have easily been extended to higher color temperatures but the present understanding is, that general indoor lighting will give a preference to the 'warm' whites. And as pointed out before, good rendering in the high CCT range can be achieved with one phosphor. The slight undershoot of the expectations, expressed in Table 5, which gives the simulated results of R_a lying above 90, has yet to be explained. As tentatively as the possible reason for the disagreement between Fig. 11 and 11b it could be the incomplete account taken of

the consequences of shift and broadening of the LED emission, which causes these differences.

Table 5: 2-pcLED from 460 nm LED + TG:Eu + SrS:Eu (Fig. 12, 13)

opt. power fraction, B G R	CCT, °K	R_a	LE, lm/W
10 32 58	2935	93	325
12 33 55	3062	93	325
14 34 52	3351	93	322
19 35 46	3973	93	320
29 36 35	5616	93	299
35 37 28	7561	90	290

An often-asked question is to the amount of efficiency one has to pay for the many advantages of pcLED. We know of no published systematic investigations of this problem. The major difficulty lies in the inevitable (at the present state of the art) variation of the output or efficiency of individual chips, even of one wafer. So, the only possibility, which we saw, was a statistical approach:

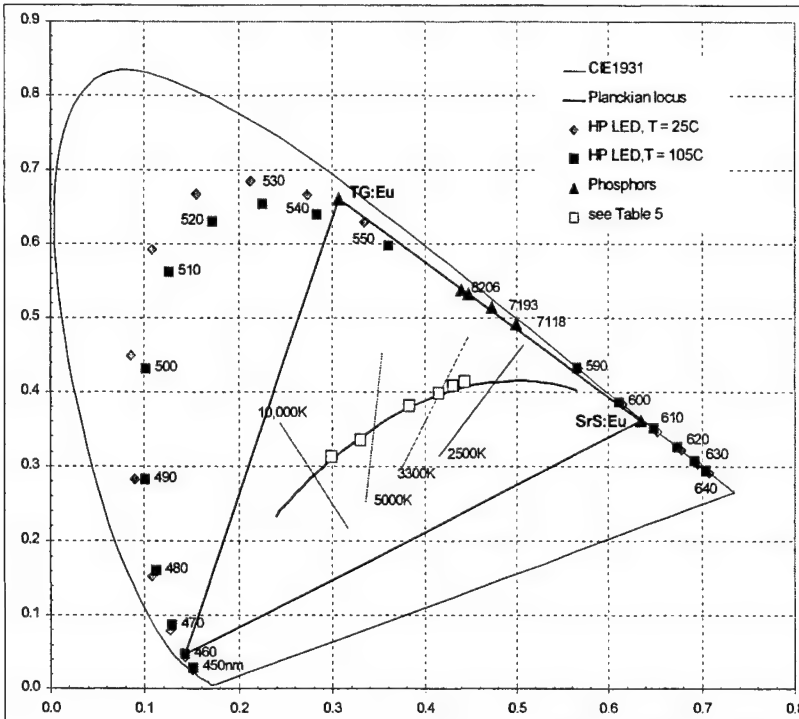


Fig.13: CIE diagram illustrating the two-phosphor de-luxe pcLED. All correlated color temperatures are possible with $R_a > 90$. The color points of Table 5 have evidently no tint.

efficiency is 84%. The quantum efficiency of YAG:Ce^{3+} , and of $\text{SrGa}_2\text{S}_4\text{:Eu}^{2+}$ has been reported to be $>95\%$. The product of these values yields an upper margin of 80%. So, evidently there is room for improvement. The losses presently encountered are not well investigated and will be the object of (many) further papers.

It is, however, tempting to try an estimate of the luminous efficiency on about as reliable a basis as the one used for the mcLED. The values are best guess values, extrapolated from much too few data, to be reliable. Nevertheless, they could provoke an exchange of data and predictions spurring further development. So, based on the same efficiency of the blue LEDs of 16%, used for mcLEDs, and on conversion efficiencies of 70% for the phosphors, we end up with values which are about 30% below the mcLED ones. (And of course the luminous efficiency increases dramatically.)

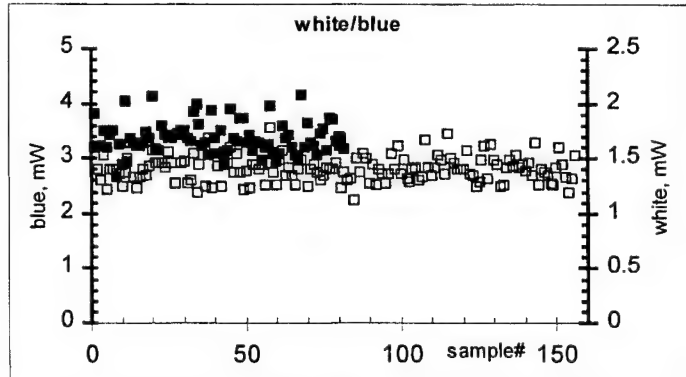


Fig.14: Statistical comparison of pcLED with blue LED from the same wafer, built in the same process, except for phosphor loading of part of the epoxy (full squares refer to white lamps and to the right scale).

4. FUTURE DEVELOPMENTS

In the discussion of white LEDs the kind of application, one aims at, is as important as the knowledge about the technological constraints. Landscape or parking lot illumination have completely different requirements from living room lighting. And may be a one-size-fits-all attitude would hinder the overall

manufacturing from the same wafer in the same way many pcLED and many reference blue LED. A comparison of the outputs of the two groups will yield the conversion efficiency. This was done some years ago with 5-mm lamps of conventional (HP) design. The result is summarized in Fig.14. Obviously the gross conversion efficiency is 58%. As the relative standard deviations in either of the groups are about 10%, this result can be well trusted.

Comparing the experimental values with principal margins, one has to state that there is a quantum deficit between the exciting photons and the emitted ones. As the emitted are a broad distribution it depends slightly on the CCT, but a conservative value for this factor in the energy

development of the field. We expect to see over the next years rather distinct product patterns to emerge, as the fundamental understanding of the constraints and great potentials grows.

In principle the concept of pcLED need not to be limited to the use of non-absorbed blue and a complementing phosphor spectrum. UV- emitting LED and phosphor emission covering the whole visible spectrum or phosphor mixtures emitting the basic color components are feasible. However, to offer advantages over the blue-retaining pcLED concept stringent conditions for the efficiency ratios of the involved LED and the phosphors must be met. Thinking medium-term towards Lasers instead of LEDs as primary light sources, this concept might gain momentum, as possibly the laser will be primarily developed for other purposes and eventually could have best properties, if operating near 400 nm. In this case, a three-phosphor variant appears appropriate.

In all phosphor-conversion light sources besides the right spectral position of the emission the spectral position of the absorption/excitation needs full attention - it has to coincide with the spectrum of the primary light source. So, the value of the Stoke's shift is an important selection criterion.

Two classes of phosphors come to mind under those considerations

absorption in the host's fundamental absorption, and recombination of generated electron-hole pairs in the wanted spectral position, almost inevitably 'on' dopants, or

absorption in the lines of a dopant at lower energy than the fundamental absorption of the host and emission in a dopant line (or in that of another dopant after transfer of the excitation).

Photoluminescence most often relies on the second class of phosphors, as seemingly it is easier to achieve very high efficiency of the internal transitions of ions (transition metals or rare earths) with unfilled inner shells. On the other hand the sulfides developed mainly for cathodoluminescence might catch up, if there is an incentive to optimize them for photoluminescence. However the rather complex temperature dependencies might limit usefulness in this application.

5. CONCLUSIONS

Solid State Lighting is on our doorsteps, may be even literally. The challenge is mainly on the LED side, as even 100 % efficiency of the phosphor and negligible quantum deficit cannot improve on it. However, phosphor development will greatly facilitate the introduction of a low(est) cost solution into many applications, where long life with no maintenance and/or small footprint are mandatory.

ACKNOWLEDGEMENT

Very helpful discussions with many colleagues from Agilent's Optoelectronic Division and LumiLeds especially Chris Lowery, Steve Paolini, Kee-Yean, George Craford, Fred Kish and Bob Taber are gratefully acknowledged, furthermore the support by John Wynbeek, Ron Moon and Waguih Ishak and the valuable assistance by Nora Chou, James Conway and Ellenora Mangisel.

REFERENCES

- [1] T.Mukai, M.Yamada, S. Nakamura, "InGaN-based UV/blue/green/amber LEDs", SPIE Vol. 3621, San Jose, Jan.99, p.2
- [2] see several contributions in "Semiconductors and Semimetals" (G.O. Mueller ed.), Vol.64, pp.1-196, Academic Press, San Diego 2000
- [3] G. Bogner, A. Debray, G. Heidel, K. Hoehn, U. Mueller, P. Schlotter, " White LED", SPIE Vol. 3621, San Jose, Jan.99, p.143
- [4] Web-page Nichia: www.nichia.com//led
- [5] W. Beers and A. Sivastava, "Phosphors for White Light LEDs", 196th Meeting of the Electrochemical Society, Hawai 1999, meeting Abstracts 1819
- [6] J.-Y. Duboz, "GaN as Seen by the Industry", phys.stat.sol.(a) 176, 5, 1999
- [7] G.O. Mueller and R. Mueller-Mach, "White Light from Light Emitting Diodes", 196th Meeting of the Electrochemical Society, Hawaii 1999, meeting Abstracts 1818, Proceedings, in press
- [8] G.O. Mueller and R. Mueller-Mach, "White Light from LEDs", Extended Abstracts 5th International Conference on the Science and Technology of Display Phosphors, p.271
- [9] CIE Technical Report 13.3-1995

SESSION 2

III-Nitride Light-Emitting Diodes II

InGaAlP and InGaN light-emitting diodes: high-power performance and reliability

Ivan Eliashevich*, Jean-Philippe Debray, Chuong A. Tran†, Hari Venugopalan, Robert F. Karlicek, Jr.
Emcore Corp./GELcore LLC, 394 Elizabeth Ave., Somerset NJ 08873

ABSTRACT

Increasing optical power and electrical-to-optical conversion efficiency enable visible light-emitting diodes to advance into new applications and wider markets. InGaAlP/GaAs and InGaN/sapphire material systems cover the whole visible spectrum of saturated colors used for display, signage, and automotive use. A combination of blue InGaN LEDs with phosphor delivers a “white” spectrum adequate for most lighting needs. Demand for high optical power requires larger chips suitable for high-current operation. Current crowding effects and their negative consequences for chip performance and reliability limit the performance of high-power chips based on both material systems. Despite the differences between InGaAlP/GaAs and InGaN/sapphire chip structures, a number of common design concepts leading to higher external efficiency and total luminous output have been proposed, including large chips operating at high drive currents. This paper highlights fundamental current spreading and reliability issues related to the chip size and operating current density, outlines a framework for quantitative analysis, proposes and compares a number of novel high-power chip designs.

Keywords: indium gallium aluminum phosphide, indium gallium nitride, light-emitting diode, reliability

1. INTRODUCTION

Recent successes in InGaAlP and InGaN-based LED development have enabled a commercialization of emitters covering the whole visible spectrum with external quantum efficiency in excess of 15%. Luminous efficiency of the best commercial LEDs has surpassed incandescent lamps and is approaching fluorescent sources. However, total optical power emitted from a single LED lamp is currently limited to less than 100mW. This limitation creates a major hurdle on the way to making LEDs viable for conventional lighting and other applications. Since the internal efficiency of the quantum well (QW) structures used for active regions of the LEDs already varies between 30% and 100%, further increase of the LED efficiency requires a better light extraction through innovative chip and package design. Still, a chip operating at high current remains an absolute requirement. A simple estimate shows that an ideal LED with 100% electrical-to-optical power conversion would only emit about 30 lumens at the standard operating current of 20 mA - a miniscule amount of light compared to the regular 1400 lumen (~100 W) incandescent bulb. While there is some room for an increase of operating current for standard 10-15 mil chips, current-dependent degradation mechanisms such as defect propagation and dopant diffusion apparently limit that value to 70 mA or less. Given a cost penalty inevitable for a module with a large number of small chips, the current tendency for increasing chip size and current density is likely to continue and accelerate¹.

Figures 1-3 illustrate the importance of the issues related to non-uniform current spreading in both InGaAlP and InGaN/sapphire-based LEDs which comprise the majority of devices designed for applications requiring high optical output and reliability. Similar effects of current crowding near a wire-bonding contact pad show up in a number of commercial LED designs at operating current levels exceeding the specified limit. Moreover, such effects appear after extended period of operation even at moderate current levels. Uniform current spreading is a common problem that spans the range of chip geometries and material systems. An aspect of the current crowding problem related to the conductivity of n-GaN layer in InGaN/sapphire LEDs was previously identified². A quantitative approach to LED structure design and specific n-GaN layer parameters were proposed to improve the chip reliability. We believe that an analysis built on the same assumptions may be applied to other elements of the nitride-based LEDs as well as InGaAlP-based LED structures. This paper discusses both the numerical model and some of the practical solutions for the optimum high-power chip design. Alternative designs are also presented in this volume¹.

*Correspondence: Email: ivan.eliashevich@gelcore.com; Telephone: 732 271 9090x4129; Fax: 732 560-5790

†New address: Semcolaser Technology, 18007 Cortney Court, City of Industry, CA 91748

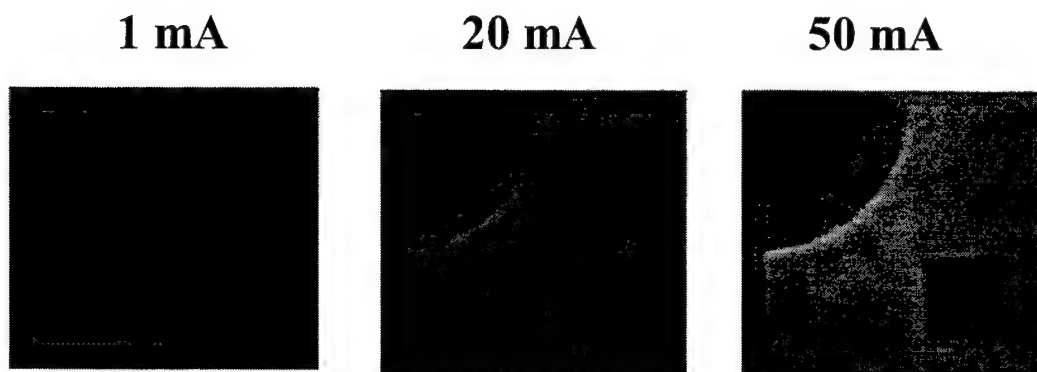


Figure 1. Current crowding in InGaN LEDs at high drive current.

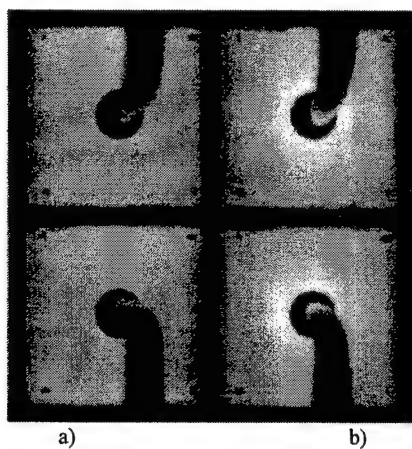


Figure 2. Current crowding in InGaAlP LEDs a) before and b) after 66 hours of aging at 30 mA, 55°C.

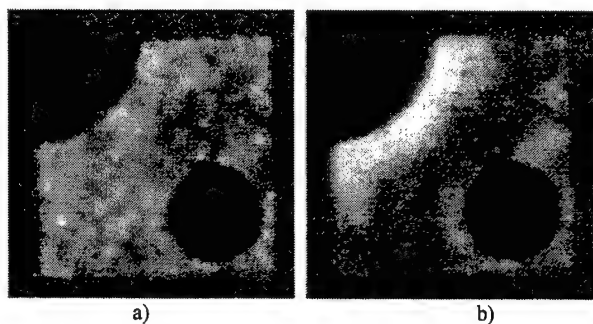


Figure 3. Current crowding in InGaN LEDs after aging.
Microphotographs of GaN LED with n-GaN doping $7 \times 10^{17} \text{ cm}^{-3}$ tested at 20 mA, RT:
a) before aging; b) after 1000 hours of aging at 30 mA, 55°C.

2. LIGHT-EMITTING DIODES WITH VERTICAL CURRENT PATH

Red, orange, yellow, and yellow-green InGaAlP LED structures are epitaxially grown on GaAs substrates, and may be subsequently transferred onto transparent GaP wafers in order to enhance the light extraction from the chip³. In either case, the substrate is electrically conductive, and p- and n-type metal contacts are applied to the opposing surfaces of the chip (see Fig. 4). The contacts are usually defined as “top” and “bottom”, and such configuration results in what may be called a vertical current path. The same contact geometry is used for InGaN LEDs grown on conductive SiC substrates using conductive buffer layers⁴, therefore the vertical current path model is applicable to those devices as well.

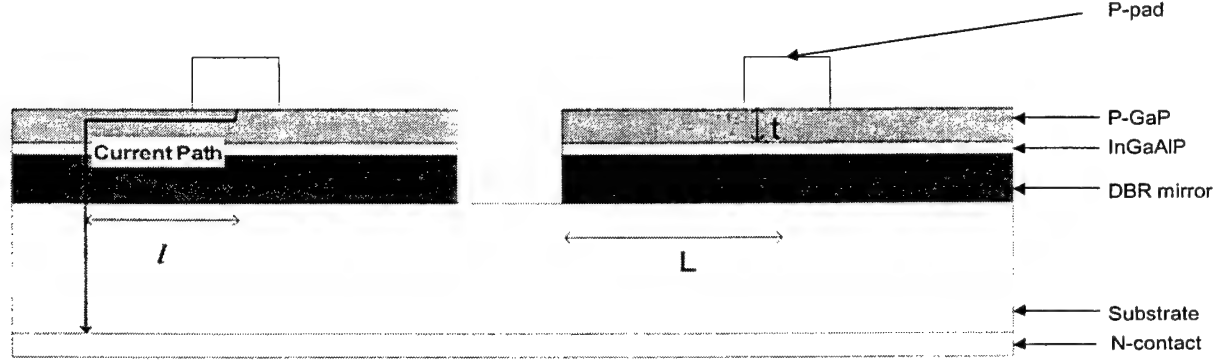


Figure 4. Current spreading in LEDs with a vertical current path.

In a typical InGaAlP LED, a current spreading p-type layer (GaP or AlGaAs) is grown on top of the active light-emitting part of the structure. In the case of absorbing GaAs substrates, a distributed Bragg reflector (DBR) stack is also grown under the active region. Possible current paths from top p-pad to bottom n-contact differ by the spreading distance l from the p-pad. Total voltage drop V_T along an arbitrary current path between the two contacts is given by the sum of voltage drops across the p-layers V_P , p-n junction V_J , and n-layers V_N as:

$$V_T = V_P + V_J + V_N = j(\rho_{p\text{-contact}}^s + \rho_{\text{GaP}} l + \rho_{\text{GaP}} t) + \frac{nkT}{e} \left(1 + \ln \frac{j}{j_0}\right) + j(\rho_{\text{DBR}}^s + \rho_{n\text{-contact}}^s) \quad (1),$$

where j is the current density, ρ_{GaP} and t are volume resistivity and thickness of p-type layers, n is the diode ideality factor, k is the Boltzmann constant, T is the junction temperature, e is the elementary charge, j_0 is the saturation current density; $\rho_{p\text{-contact}}$, $\rho_{n\text{-contact}}$, and ρ_{DBR} are resistivities of the contacts and DBR, respectively.

Assuming negligible ohmic contact resistances, the current spreading is uniform when total voltage drop is the same across any of the possible current paths, i.e. V_T is independent of l for $0 < l < L$:

$$\rho_{\text{GaP}}(L - t) \ll \frac{V_J}{j} \quad (2)$$

When this condition is not fulfilled, current is crowded through the paths with lower resistivity corresponding to shorter l , which leads to the increase of local carrier concentration in the area of the higher current density, further current crowding, and eventual collapse of the current under the p-pad. Similar feedback loops lead to current crowding developing during aging. In that case, a higher initial current density near the p-pad leads to a reduced V_J in that area of the device due to higher local rate of dopant diffusion (see Fig. 2).

Uniformity condition (2) is more stringent for higher current density and larger die size L . For high-power chip designs it is necessary to increase the thickness or conductivity of the current spreading layer. Alternatively, p-pad size may be increased in order to reduce the effective die size L . Such a design may be realized in a form of cross-shaped contact, as shown in Figure 5.

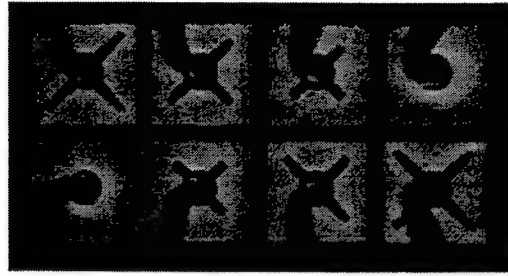


Figure 5. Current spreading improvement in LEDs with a vertical current path: cross-shaped contacts.

While solving the current spreading problem, such a design is detrimental to the light extraction efficiency due to the light absorption by the contact metal (contact shadowing). As shown in Figure 6, the decrease in light output is almost exactly proportional to the area of the chip covered by p-contact metallization.

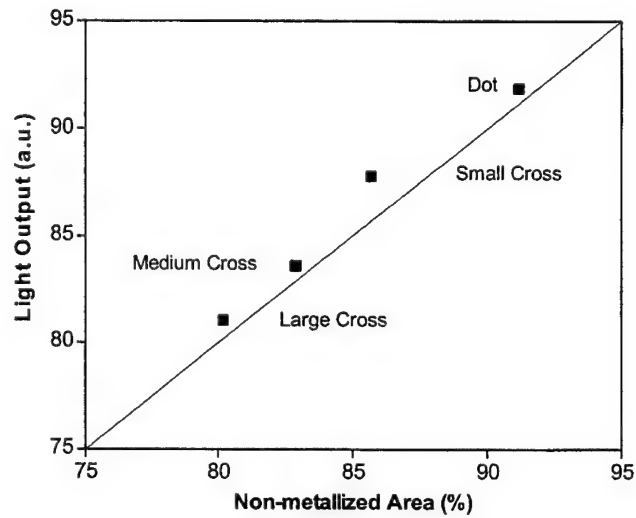


Figure 6. Contact shadowing penalty in LEDs with cross contacts.

A design that overcomes the shadowing the cross-shaped contacts is shown in Figure 7. A resistive or n-type current blocking layer grown under the p-pad by two-step epitaxial growth prevents the current collapse under the p-pad and eliminates the contact shadowing effect⁵.

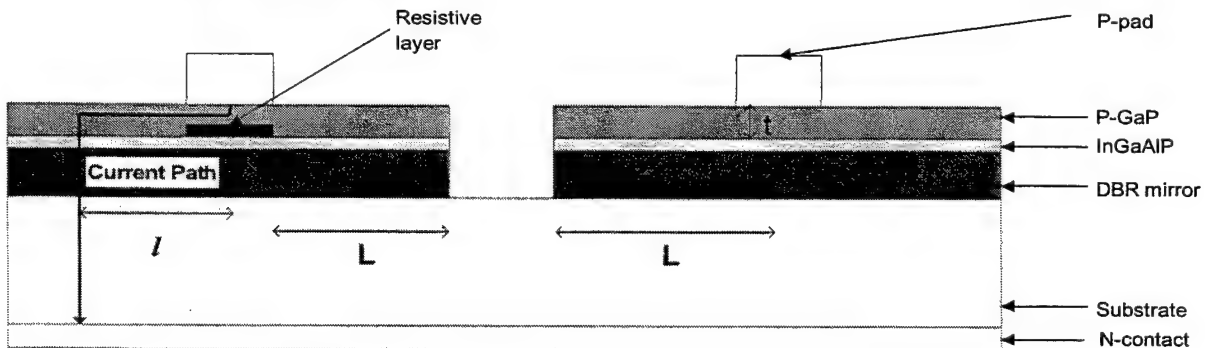


Figure 7. Current spreading improvement in LEDs with vertical current path: current blocking layer.

Indeed, a current blocking layer design proves to be the most effective for the chips operating at very high current densities as demonstrated in Figure 8.

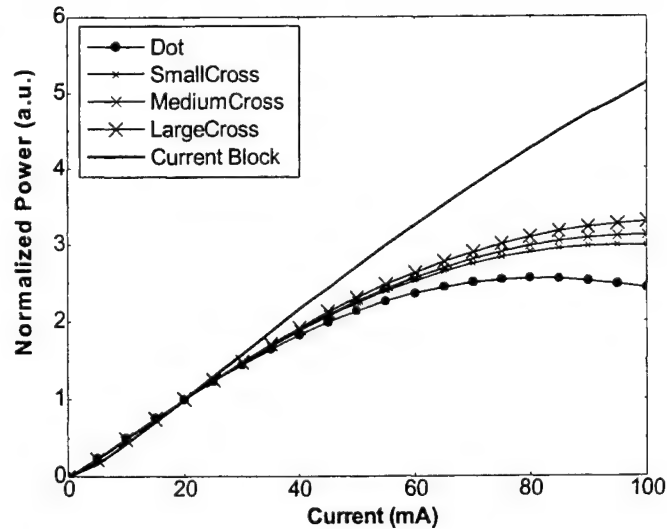


Figure 8. High-power performance of InGaAlP LEDs with improved current spreading.

3. LIGHT-EMITTING DIODES WITH LATERAL CURRENT PATH

InGaN LED structures grown on insulating sapphire substrates require both n-type and p-type ohmic contacts on the same side of the epitaxial wafer. Access to the bottom side of the p-n junction (usually, n-type) is provided by etching a mesa structure through the top p-type layers and p-n junction into the n-type material. N-type ohmic contacts may be subsequently formed to the exposed n-GaN surface while p-type contact is made to the mesa top surface. As a result of such a contact geometry, a structure with lateral current path is formed. A cross-section of the LED structure showing two adjacent devices on a wafer is shown in Figure 9.

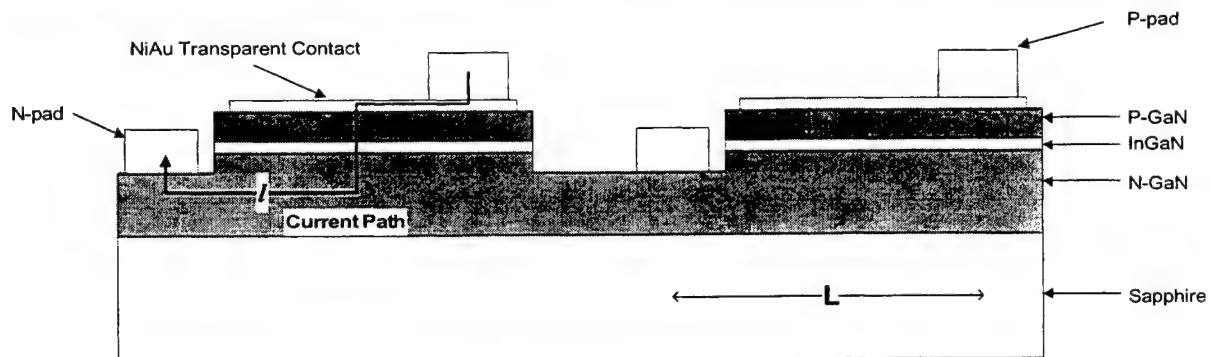


Figure 9. Current spreading in LEDs with a lateral current path.

Again, similar to the case of vertical current path structure, total voltage drop across the diode as function of current density j is given by:

$$V_T = V_P + V_J + V_N = j(\rho_{\text{Ni/Au}}(L-l) + \rho_{p\text{-contact}}^s + \rho_{p\text{-epi}}t) + \frac{nkT}{e}(1 + \ln \frac{j}{j_0}) + j(\rho_{n\text{-GaN}}l + \rho_{n\text{-contact}}^s) \quad (3),$$

where j is the current density, $\rho_{p\text{-epi}}$ and t are vertical resistivity and thickness of p-type layers, n is the diode ideality factor, k is the Boltzmann constant, T is the junction temperature, e is the elementary charge, j_0 is the saturation current density, $\rho_{n\text{-GaN}}$ and l are lateral resistivity of n-GaN and length of the lateral current path through the n-type layer, $\rho_{p\text{-contact}}$ and $\rho_{n\text{-contact}}$ are resistivities of the respective contacts.

We shall ignore the resistance of the ohmic contacts here for simplification. For the case when transparent Ni/Au metal layer may be considered a perfect current spreader with negligible contribution to the total resistance, and only the vertical component of the p-layers' resistance is significant, the condition of uniform current spreading becomes

$$\rho_{n\text{-GaN}}L \ll \frac{V_J}{j} \quad (4).$$

The form and physical meaning of the limitation (4) for LEDs with lateral current path is similar to the condition (2) for LEDs with vertical current path. Consequently, a current crowding near n-pad occurs in a structure with insufficient n-GaN conductivity as shown in Figures 1 and 3, and the effect is triggered or enhanced by higher current density, higher temperature, and larger chip size.

As reported earlier², the current crowding effect is eliminated for the standard operating conditions by increasing the doping level of the n-GaN layer to improve its conductivity (see Fig. 10).

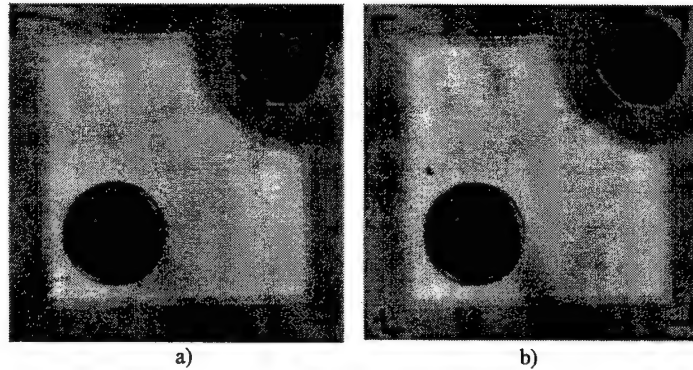


Figure 10. Microphotographs of GaN LED with n-GaN doping $1.5 \times 10^{18} \text{ cm}^{-3}$ tested at 20 mA, RT:
a) before aging; b) after 1000 hours of aging at 30 mA, 55°C.

The assumption of a perfect current spreading by Ni/Au metal layer is only valid for relatively high thickness and Au content of that layer. However, a thin layer with low Au concentration is preferable to achieve a better contact transparency and improve the light output. Simplifying equation (3) for the case when the transparent contact resistance is the limiting term gives the following limiting condition for Ni/Au layer resistivity:

$$\rho_{\text{Ni/Au}}L \ll \frac{V_J}{j} \quad (5).$$

In the case of insufficient transparent contact conductivity when condition (5) is not fulfilled, current crowding around the p-pad takes place similar to the InGaIP LED with low p-GaP conductivity in Figure 2. The chip design with ring n-contact and central p-pad placement in Figure 11b has the L effectively reduced by approximately a factor of 2 compared to the standard chip in Figure 11a, thus relaxing both condition (5) and condition (4). No current crowding around any of the pads has been observed up to 130 mA for the chips with the improved design even after the Ni/Au layer has been thinned down to have a sheet resistivity of $\sim 250 \Omega/\text{sq}$, up by a factor of 40 from the standard value.

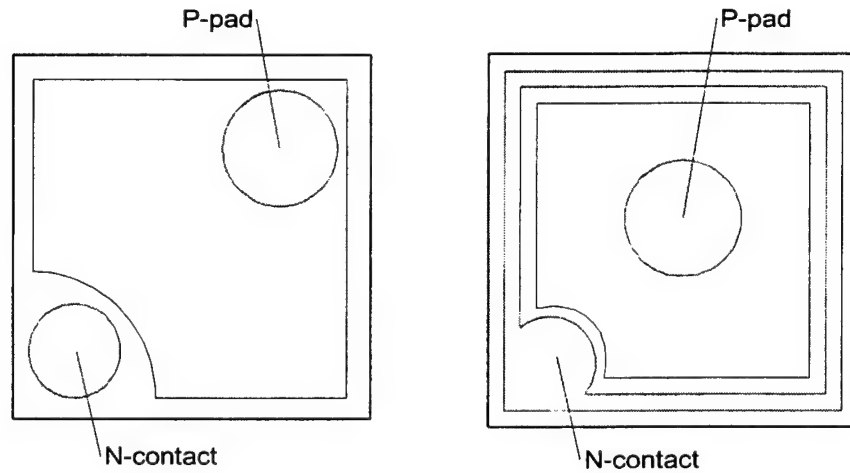


Figure 11. Current spreading improvement in LEDs with lateral current path: ring n-contact with reduced current path distance.

Aging tests were performed for LEDs with thin Ni/Au, ring n-contact and central p-pad at an ambient temperature of 55°C and injection current of 30 mA in constant current control mode (see Fig. 12). Bare chips without encapsulation were mounted on TO-46 headers and were taken out of the environmental chamber for periodic measurements of current-voltage characteristics and output power. Visual inspection was performed after 1000 hours of aging. For all the LEDs tested in this experiment, the power drop observed after 1000 hours of aging did not exceed 20% of the initial value, and no current crowding occurred during aging. The extrapolated aging rate was calculated to be ~9%/decade, indicating a lifetime to 50% degradation well in excess of 100,000 hours. For encapsulated chips tested at higher current or temperature conditions (40 mA and 75°C), the power drop after 1000 hours of aging still did not exceed 30% of the initial value, and no current crowding failures were observed.

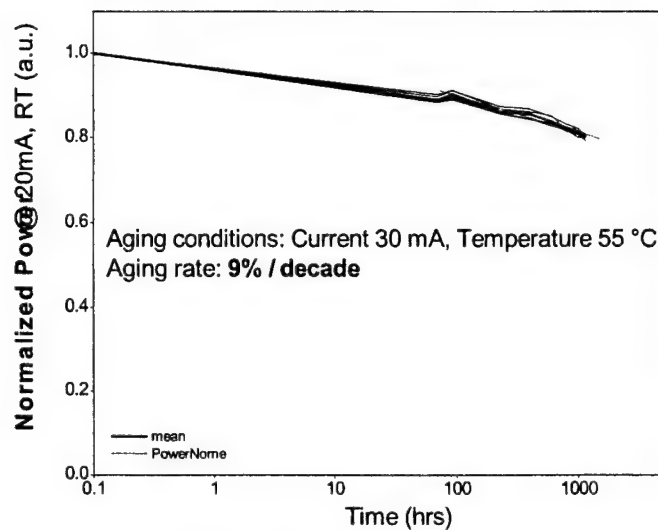


Figure 12. Reliability of Blue InGaN LEDs with ring n-contact.

The improved chip design with ring n-contact and central p-pad was also used to fabricate large size LEDs with side dimension up to 28 mil, i.e. 4 times the area of the standard chip. Such devices were operated at the drive current of 300 mA for as long as 200 hours without any current crowding effects.

4. CONCLUSIONS

In conclusion, a simple analytical approach is proposed to optimize the structure of both InGaAlP and InGaN LEDs with various current path geometries. An analysis is made of the contributions from different parts of the structure to the total voltage drop across the diode. Failure modes associated with current crowding are identified in LEDs based on InGaAlP and InGaN material systems. A number of improved chip designs is proposed and compared from the viewpoint of enabling high-current operation of larger than standard chip sizes. A possibility of reliable 300 mA operation is demonstrated for InGaN/sapphire blue LED chip four times larger than the industry standard.

ACKNOWLEDGEMENTS

The authors are indebted to Mr. Joseph Potopowicz for his help with device assembly and reliability testing, and to Mr. Paul Rotella, Jr. for the chip performance evaluation.

REFERENCES

1. M.R. Krames et al., "High-brightness AlGaInN light-emitting diodes," to be published in *Light-Emitting Diodes: Research, Manufacturing, and Applications*, E. Fred Schubert, Editor, Proc. SPIE, 2000.
2. I. Eliashevich et al., "InGaN blue light-emitting diodes with optimized n-GaN layer," in *Light-Emitting Diodes: Research, Manufacturing, and Applications*, E. Fred Schubert, Editor, Proc. SPIE, v. pp.28-36, 1999.
3. R. Scott Kern, "Progress and status of visible light-emitting diode technology", in *Light-Emitting Diodes: Research, Manufacturing, and Applications*, E. Fred Schubert, Editor, Proc. SPIE, v. pp.16-27, 1999.
4. C. Carter et al., "SiC-Based UV Photodiodes and Light-Emitting Diodes," in *Semiconductors and Semimetals, "SiC Materials and Devices,"* R. K. Willardson and E. R. Weber, Editors, v. 52, Academic Press, 1998.
5. F.A. Kish and R. M. Fletcher, "AlInGaP Light-Emitting Diodes," in *Semiconductors and Semimetals, "High Brightness Light Emitting Diodes,"* G. B. Stringfellow and M. G. Craford, Editors, v. 48, Academic Press, 1997.

Investigation on the gain-switching of GaInN MQW laser diodes.

Claudio Marinelli^{a*}, Igor Y. Khrushchev^a, Judy M. Rorison^a, Richard V. Penty^a and Ian H. White^a.
Tetsuya Takeuchi^b, Hiroshi Amano^b and Isamu Akasaki^b.
Yawara Kaneko^c, Satoshi Watanabe^c and Norihide Yamada^c.
Ghulam Hasnain^d, Rick Schneider^d, S.Y. Wang^d and Mike R. Tan^d.

^a Centre for Communication Research, University of Bristol, Bristol, BS8 1TR, UK

^b Department of Electrical and Electronic Engineering, High-Tech Research Center, Meijo University,
Nagoya, Japan

Agilent Laboratories, 3-2-2 Sakado, Takatsu-ku, Kawasaki, Kanagawa 213-0012, Japan

^d Agilent Laboratories, 3500 Deer Creek Road, Palo Alto, California 94303, US

ABSTRACT

A study of the gain-switching process in GaInN MQW laser diodes is reported. Single peak gain-switched optical pulses with pulse widths ≤ 40 ps and optical powers equal to 100mW are observed when electrical pulses with duration of 800ps are applied. Sub-nanosecond optical pulses with peak powers in excess of 450mW are also obtained and degradation mechanisms are analysed. The transient response characteristics of the laser diodes are studied in both the time and spectral domains.

Keywords: laser diode, gain-switching, GaInN, GaN, short pulses, relaxation oscillations

1. Introduction.

Picosecond optical pulses in the blue and ultraviolet (u.v.) wavelength range are widely used in scientific applications such as fluorescence spectroscopy, fluorescence lifetime measurements, gas analysis, interferometry and microscopy. Several of these applications would undoubtedly benefit from the realisation of cheaper and more compact sources of short optical pulses based on blue/u.v. emitting diode lasers. Recent developments in the technology for the growth and fabrication of diode lasers based on nitride compounds^{1,2} suggest that a gain-switched GaInN MQW laser could be a simple and viable solution for the realisation of such an optical pulse source. Gain-switching allows the direct generation of picosecond optical pulses on demand, allowing high peak power pulses to be generated at variable repetition rate.

In this paper we study the temporal structure and the spectral characteristics of optical pulses generated by gain-switched GaInN MQW laser diodes (LDs). The laser dynamics and the emission mechanisms in the short pulse regime are characterised. The analysis extends to the laser behaviour in the multi-peak regime, which is observed at higher levels of current injection. The laser performances and the degradation mechanisms are also studied under different driving conditions.

2. Laser structures and experimental set-up.

The investigation is performed on LDs consisting of a separate confinement multiple quantum well (QW) heterostructure. The epitaxial structures are designed and grown at the University of Meijo. The laser devices have been fabricated at the Agilent Laboratories in Japan. The structures are grown on a *c*-face sapphire substrate by low-pressure metalorganic vapour phase epitaxy. The stack of epitaxial layers comprises: a 30 nm thick AlN buffer layer, a 3 μ m *n*-Al_{0.03}Ga_{0.97}N contact layer, a 1 μ m *n*-Al_{0.06}Ga_{0.94}N lower cladding layer, a 0.1 μ m *n*-GaN guiding layer, 5 pairs of 2.5nm Ga_{0.9}In_{0.1}N QWs and 7.5nm Si-doped Ga_{0.98}In_{0.02}N barriers, a 15nm *n*-Al_{0.15}Ga_{0.85}N electron blocking layer, 0.1 μ m *p*-GaN guiding layer, a 0.5 μ m *p*-

* Electronic mail: claudio.marinelli@bristol.ac.uk

$\text{Al}_{0.06}\text{Ga}_{0.94}\text{N}$ upper cladding layer and a $0.1\mu\text{m}$ $p\text{-GaN}$ contact layer. The lasers have a $3\mu\text{m}$ wide ridge waveguide, $500\mu\text{m}$ long $p\text{-type}$ contacts and cleaved uncoated facets. Further details on the growth and design of the LDs structure are reported in reference ³.

The experimental set-up used for the generation and characterisation of short optical pulses is based on a Kentech Instruments APG-1 pulse generator. This produces 800ps long electrical pulses at a fixed repetition rate of 10kHz and is used to drive the LDs. A low reflected/transmitted voltage ratio for the electrical pulse ($<1/6$) indicates a good impedance match between the electrical signal generator and the LDs, and thereby the absence of significant distortions of the electrical pulse. The optical beam is collected from the laser facet by means of bulk lenses and focused onto the photodetector. This consists of a fast GaAs Schottky photodiode, which has an estimated bandwidth $\geq 15\text{GHz}$ ⁴. The electrical signal from the detector is analysed by a 34GHz Hewlett-Packard HP54120B/54124A oscilloscope. For the spectral characterisation of the laser emission the second order reflection from the grating of an Advantest Q8381 spectrometer is used. This allows spectral resolutions of 0.2-1nm. It should be stressed that all the experimental characterisations are carried out on uncooled devices, mounted p-side up on a copper and brass mount which provides a limited heat sink with a volume of about 2.5cm^3 .

3. Experimental Results and discussion.

The LDs tested can only be operated in pulsed mode at room temperature. Figure 3a shows an example of the light-versus-current (L-I) characteristic curve measured under quasi-CW conditions. The lasers are driven by 150ns square pulses at a repetition rate of 3kHz (duty cycle = 4.5×10^{-4}). Under these conditions the threshold current is normally observed in the 300-600mA range (see fig.1), corresponding to a threshold current density $\geq 19\text{kA/cm}^2$. The voltage at threshold is usually $\geq 15\text{V}$. The best devices exhibit a slope efficiency equal to ~ 0.37 A/W per facet, corresponding to a differential quantum efficiency of 12% per facet. The laser emission wavelength can vary between 405nm and 410nm, depending on the device. Optical output powers of the order of 5-10mW are measured for a driving current equal to $1.05I_{\text{th}}$. As illustrated in fig.1, a significant power roll-off due to saturation effects is observed in the quasi-CW L-I characteristics of uncooled devices. The power roll-off is probably caused by junction heating.

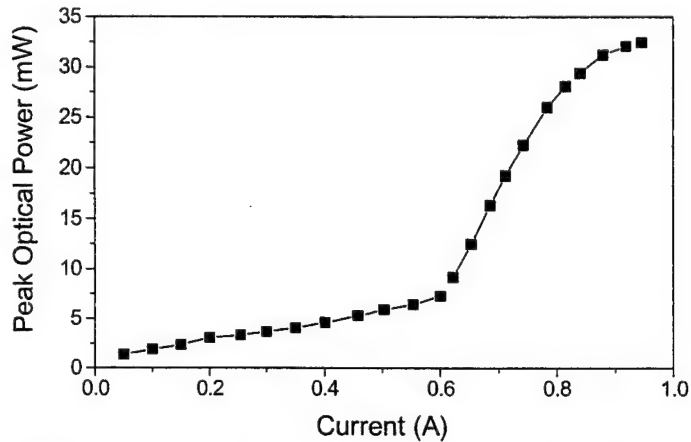


Figure 1. Quasi-CW L-I characteristics curve. The device is driven by 150ns square signals at a repetition rate of 3kHz.

Short pulse generation is obtained driving the LDs by means of 800ps electrical signals at a repetition rate of 10kHz (duty cycle $\cong 1 \times 10^{-5}$). Fig.2 shows a typical L-I curve measured under these driving conditions. The peak optical powers are calculated assuming a fixed optical pulse width of 800ps (i.e., equal to the electrical pulse width), and dividing the measured average powers by the duty cycle. This method underestimates the peak optical power, particularly for the lower

current values, and causes the superlinearity of the curve in fig. 2. However, it can be safely concluded that sub-nanosecond optical pulses with peak optical powers in excess of 450mW and pulse energies higher than 350pJ can be obtained for a peak driving current equal to 6.7A ($\approx 13I_{th}$). These are the highest peak power and pulse energy values measured on sub-nanosecond optical pulses generated by nitride based LDs. It is also worth stressing that, as a consequence of the reduced duty cycle, the L-I characteristics in Fig.2 shows no sign of power saturation effects.

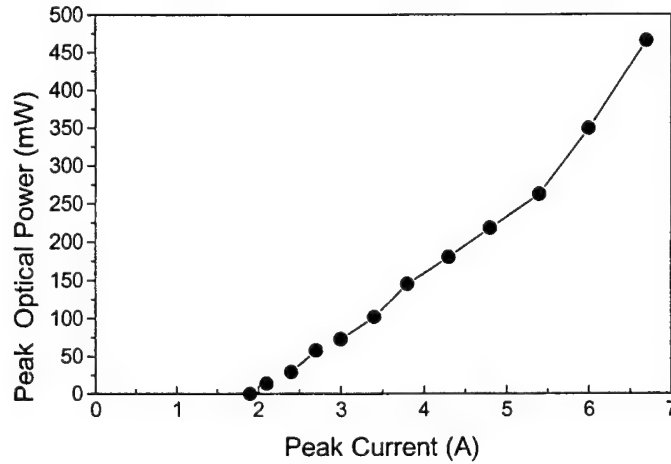


Figure 2. L-I characteristics curve measured on a device driven by 800ps long electrical pulses with a repetition rate of 10kHz. The values reported for the optical power are obtained from the measured average power, assuming a fixed duty cycle.

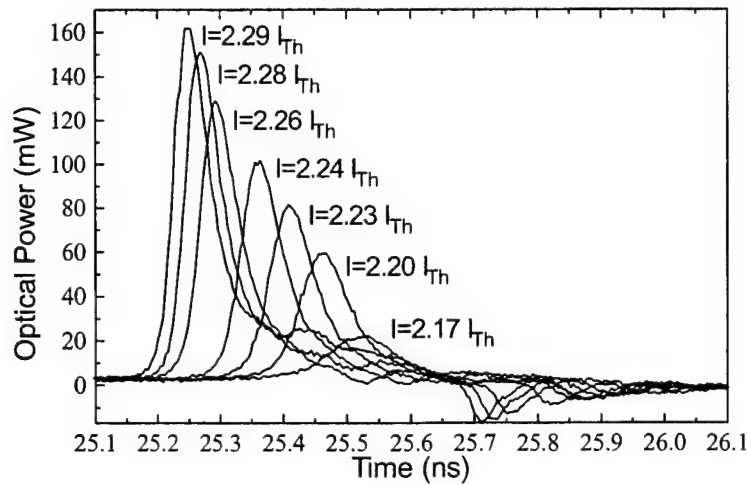


Figure 3. Dynamical characterisation of the gain-switched laser emission for different peak driving currents. The graph refers to a GaInN MQW LD driven by 800ps electrical pulses at a repetition rate of 10kHz

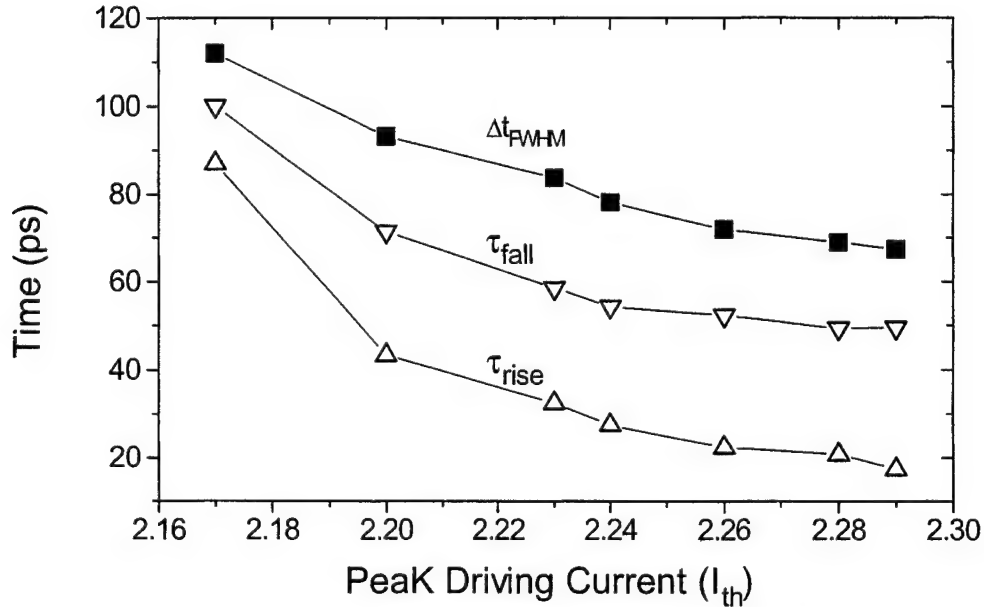


Figure 4. Optical pulse width (Δt_{FWHM}) and time constants for the rising (τ_{rise}) and falling edge (τ_{fall}) of the pulse trace in fig.3. All the values refer to non deconvolved measurements. The values for τ_{rise} and τ_{fall} are obtained by means of exponential fits to the pulse edges.

Short pulse generation is observed for peak driving currents $\geq 2I_{th}$. First, the emission dynamics of nitride lasers in the proper single peak gain-switching regime is studied. For the LD shown in figures 3 and 4, gain-switching operation is obtained for peak driving current in the $2.19I_{th} - 2.31I_{th}$ range, with $I_{th} = 0.29A$. The results in fig. 3 indicate that within such a current range there is an increase in the optical peak power of more than 120mW and, correspondingly, a decrease in the laser turn-on delay of more than 220ps. Further characterisations of the temporal structure of these pulses are presented in fig.4. Here, we plot the optical pulse width Δt_{FWHM} , and the time constants τ_{rise} and τ_{fall} for the rising and trailing edges of the optical pulses, as a function of the peak driving current. The profiles of the rising and trailing edges can be accurately fitted by the functions $exp(t/\tau_{rise})$ and $exp(-t/\tau_{fall})$, respectively. The τ_{rise}/τ_{fall} ratio varies within 1.15-2.85, whereas the sum $\tau_{rise} + \tau_{fall}$ approximates the pulse width value Δt_{FWHM} with good agreement for peak a driving current $\geq 2.24I_{th}$. A comparison between figures 3 and 4 indicates that the increase in peak optical power is accompanied by a decrease in the optical pulse width Δt_{FWHM} of more than 45ps. The temporal characterisations presented thus far allow us to conclude that gain-switched AlGaIn/GaN/GaInN LDs exhibit the same dynamical behaviour as other material systems^{5,6}.

An example of optimum single pulse generation is presented in figure 5. Here, a driving current equal to $2.7I_{th}$ produces high quality single peak gain-switched pulses with no relaxation tails. The peak optical power is as high as 100mW and the optical pulse width is about 60ps. Since the overall time response of our detecting system is estimated to be $\geq 45ps$, the deconvolved pulse width therefore is $\leq 40ps$.

Fig. 6 illustrates, for the same device, the changes in the optical pulse induced by increased levels of current injection. The gain-switched pulse of fig. 5 is shown in the curve (a) of the graph. The pulse curve (b) indicates the onset of relaxation oscillations for the peak currents above $2.8I_{th}$. The effect of a further increase in the peak driving current is illustrated by the bottommost pulse trace (c). Curve (c) is measured for a driving current higher than $3.2I_{th}$. This allows an increased number of relaxation oscillation cycles, producing an overall optical pulse width $> 400ps$.

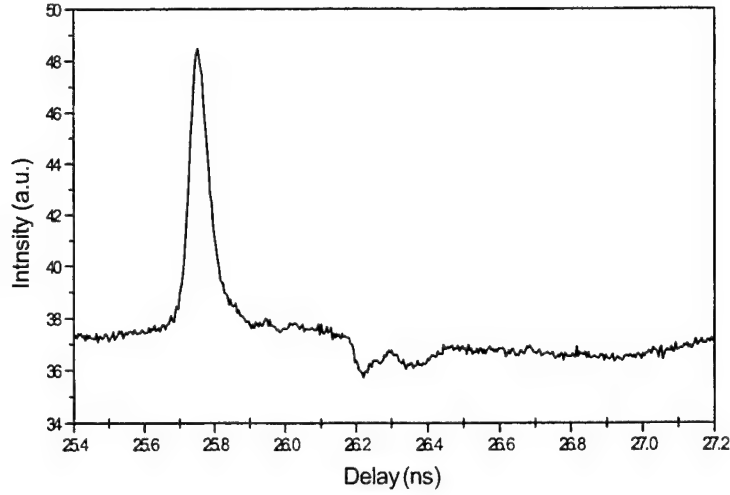


Figure 5. Example of optimum single peak pulse generation under gain-switching conditions. The peak driving current is equal to $2.7I_{th}$.

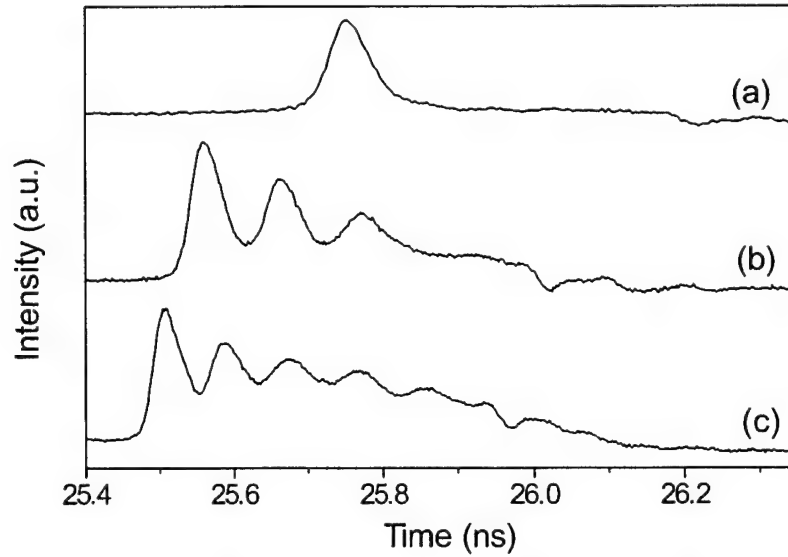


Figure 6. The plot shows the onset of relaxation oscillations for increased driving currents. Trace (a) reproduces the pulse of fig. 5. Trace (b) refers to a peak driving current $>2.8I_{th}$. Trace (c) corresponds to a driving current above $3.2I_{th}$.

A further characterisation of the relaxation oscillation cycles is presented in fig.7. Here we show the measured dependence of the relaxation oscillation frequency (considered as the inverse of the relaxation oscillation period) on the peak driving current. The trend appears to be almost linear. The relaxation frequency values are high (see for instance the value reported in reference ⁷). We speculate that this may be a consequence of a low photon lifetime.

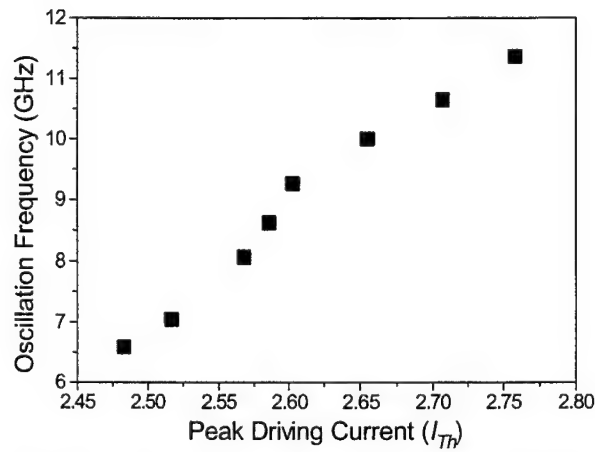


Figure 7. Relaxation oscillation frequency as function of the peak driving current expressed in unit of I_{th} . The trend is approximately linear.

To gain a deeper physical insight in the short pulse generation mechanism of GaInN MQW LDs, the spectral characteristics of the optical pulses presented in fig.6 are investigated. The topmost curve in fig. 8 refers to the laser spectrum measured under quasi-CW conditions. This is centred at 408.1nm. The spectrum (a) corresponds to the single peak gain-switched pulse (a) of fig.6. The spectrum, centred at 404.8nm, exhibits a pronounced blue-shift with respect to the quasi-CW peak and, in the limit of the our experimental resolution, appears also significantly broader. The spectra (b) and (c) in fig. 8 correspond to the pulse traces (b) and (c) of fig. 6. Both suggest that a gradual red-shift towards the wavelength of the quasi-CW peak occurs as the laser undergoes an increased number of relaxation oscillation cycles. Again, all these characteristics are typical of the gain-switching emission and the relaxation process ⁶. We can therefore conclude that also from a spectral point of view the gain-switched operation of nitride lasers is similar to other material systems.

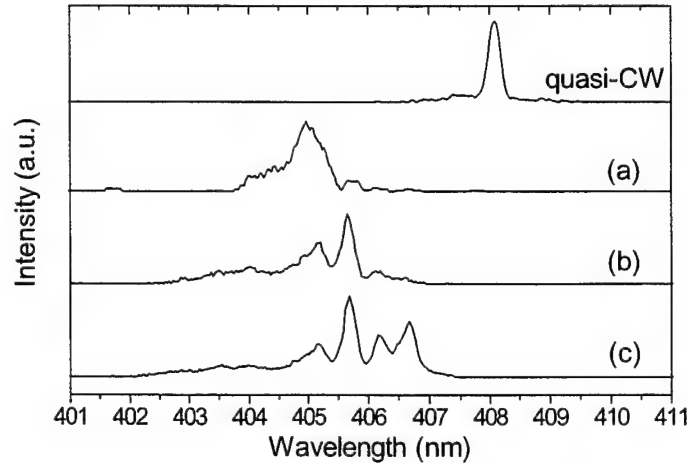


Figure 8. The emission spectrum measured under quasi-CW operation (topmost) is compared with the spectra of the short pulses shown in fig.6.

Another parameter which is known to influence the laser emission under gain-switching conditions is the presence of an additional DC bias ⁶. In the case of the LDs examined in this paper, only a quasi-DC bias can be applied. To study its effect on the optical pulses we combine the usual 800ps electrical pulses with 200ns long square signals with a repetition rate of 10kHz. Fig. 9 shows the optical pulses obtained for increased levels of quasi-DC bias but maintaining a fixed peak driving current. The increase in the quasi-DC bias is found to induce a decrease in the laser turn-on delay and in the optical pulse width. These effects are accompanied by an increase in peak power. Almost negligible variations are observed in the trailing edge of the optical pulse. Given that the time constant τ_{fall} of the trailing edge reflects how far below threshold the carrier density is pulled during the pulse emission ⁶, the negligible changes in the pulse tails of fig. 9 may reflect the fact that the minimum carrier density reaches a similar values for the different pulses. This could be related to the presence of the additional quasi-DC bias and the additional carrier supply thus provided. The trends for the optical pulse width and the peak power are presented in fig. 10. Here, the threshold current is also indicated to highlight the fact that a slight increase in pulse width occurs when the quasi-DC bias crosses the threshold level.

Finally, we examine the degradation of the laser. We observe that by applying driving current below $3I_{\text{th}}$, one can produce peak optical powers in excess of 150mW for more than two hours without significant device degradation. It is worth stressing that even for peak currents as high as $11I_{\text{th}}$, and peak optical powers of the order of 350mW sudden failures are not observed. The gradual nature of the device degradation suggests that, up to this current and power levels, catastrophic optical damage of the laser facets does not occur.

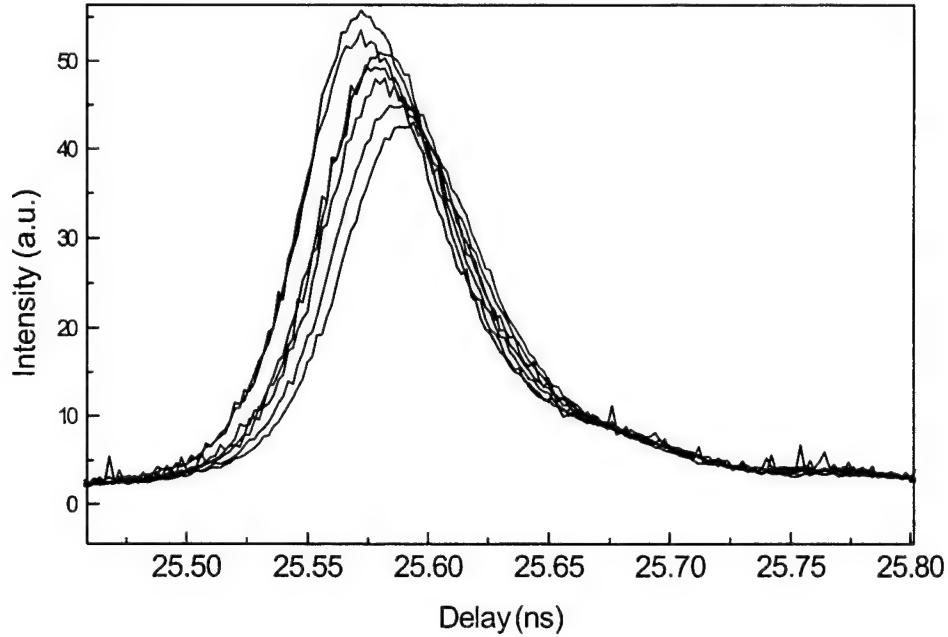


Figure 9. Pulse traces measured for different quasi-DC levels and for a fixed value of a pulse current. The short current pulses consist of 800ps long electrical signals with a repetition rate of 10kHz. The quasi-Dc bias is applied in the form of 200ns long square pulses with a repetition rate of 10kHz. The values for the quasi-DC bias are: 403, 336, 268, 201, 134, and 67 mA.

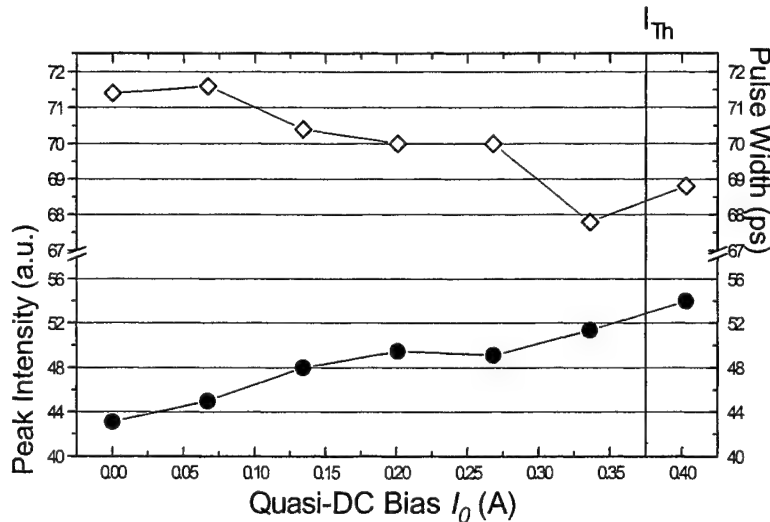


Figure 10. Optical pulse width (topmost part of the plot) and peak intensity (bottommost part of the plot) as function of the quasi-DC level. The data refers to the optical traces in fig.8.

3. Conclusions.

The generation of short optical pulses from AlGaIn/GaN/GaInN lasers is investigated in both the time and spectral domain by means of 800ps driving electrical pulses. Our study shows that the dynamic behaviour of gain-switched nitride lasers is generally similar to those observed on other material systems. We demonstrate that LDs which can only perform room temperature pulsed operation can be safely gain-switched to provide a source of optical pulses shorter than 50ps with peak powers of ~100mW. Optical power roll-off due to saturation effects is not observed on the L-I characteristics of devices driven by 800ps pulses at a repetition rate of 10kHz. Sub-nanosecond optical pulses with peak powers exceeding 450mW and pulse energies higher than 350pJ can therefore be obtained. Our investigations also indicate that facet damage is not responsible for the device degradation up to peak powers of the order of 350mW.

Acknowledgement.

EPSRC is acknowledged for financial support of the work carried out at the University of Bristol.

The work at Meijo University was partly supported by JSPS Research for the Future Program in the Area of Atomic Scale Surface and Interface Dynamics, under the project of Dynamic Process and Control of the Buffer Layer at the Interface in a Highly-Mismatched System.

References.

1. Nakamura, M. senoh, S. Nagahama, N. Iwasa, T. Yamada, T. Matsushita, H. Kyoku, Y. Sugimoto, T. Kozaki, U. Umemoto, M. Sano and K. Chocho, "Present status of InGaIn/GaN/AlGaIn-based laser diodes", *Proc. Int. Conf. Nitride semiconductors (ICNS-97)*, pp.444-445, 1997
2. Nakamura "Present status of InGaIn-based LEDs and laser diodes", *Proc. Third Int. Conf. Nitride semiconductors (ICNS-3)*, pp.8-9, 1999
3. T.Takeuchi, T.Detchprohm, M Iwaya, N. Hayashi, K.Isomura, K. Kimura, and M. Yamaguchi, H. Amano and I. Akasaki, Yw. Kaneko, R. shioda, S. Watanabe, Y. Yamaoka, Ys. Kaneko "Improvement of far-field pattern in nitride laser diodes", *Appl. Phys. Lett.* **75**, pp. 2960-2962, 1999.
4. Wang, D.M. Bloom, and D.M. Collins, "20-GHz bandwidth GaAs photodiode", *Appl. Phys. Lett.* **42**, pp. 190-192, 1983
5. C. Lin, J.E. Bowers, "Measurement of 1.3 and 1.5 mm gain-switched semiconductor laser pulses with a picosecond IR streak camera and a high speed InGaAs PIN photodiode", *Electr. Lett.* **21**, pp. 1200-1202, 1985
6. P. Vasil'ev, *Ultrafast diode lasers. Fundamentals and applications*, pp. 55-62 and references therein, Artech House Publishers, Boston-London, 1985
7. Nakamura, M. senoh, S. Nagahama, N. Iwasa, T. Yamada, T. Matsushita, Y. Sugimoto, and H. Kyoku, "Longitudinal mode spectra and ultrashort pulse generation of InGaIn multiquantum well structure laser diodes", *Appl. Phys. Lett.* **70**, pp. 616-618, 1997

Photon Recycling Semiconductor Light Emitting Diode

Xiaoyun Guo, John W. Graff, E. Fred Schubert

Department of Electrical and Computer Engineering, Boston University
8 Saint Mary's St., Boston, MA 02215, Boston, MA 02215

and

Robert F. Karlicek, Jr.

GELcore Corporation
394 Elisabeth Ave., Somerset NJ 08873

Abstract

A new white light emitting diode, the photon recycling semiconductor light emitting diode (PRS-LED) is demonstrated. The device consists of a GaInN/GaN LED emitting in the blue spectral range and an AlGaInP photon recycling semiconductor emitting at the complementary color. Thus the PRS-LED has two emission peaks, one in the blue and one in the amber wavelength range. The theoretical luminous performance of the PRS-LED exceeds 300 lm/W, higher than the performance of phosphor-based white LEDs.

1. Introduction

Currently, white-light LEDs are based on photo-excitation of phosphors by a GaInN/GaN LED emitting in the blue or ultraviolet (UV) range of the spectrum. The quantum efficiencies of both, optically excited high-quality semiconductors and photoluminescent phosphors, can be close to 100 %^{1,2,3}. YAG-based phosphors are known to have broad emission spectra, while the emission spectra of semiconductors are much narrower. A typical phosphor-based white LED has a broad emission spectrum⁴ ranging from 425 to 700 nm.

Due to the fact that the human eye sensitivity decreases rapidly when approaching IR and UV wavelengths, white light emission based on the emission of a *broad* spectrum does not have the maximum possible luminous efficacy. Since there are only three types of color-sensitive receptors or *cones* in the human eye, one can generate white light by the generation of light with two or three distinct colors. One can show that the most efficient white light source consists of two monochromatic sources emitting at complementary wavelengths. The maximum theoretical luminous efficacy to produce white light is 400 lumens per Watt of optical power^{1,5} with two 100 % efficient monochromatic sources emitting at 448 nm and 569 nm^{3,5}.

In this publication, we report on a dichromatic semiconductor light source emitting two complementary colors. The higher-energy light is emitted by a current-injection blue LED. An electrically passive semiconductor, optically excited by the blue LED, re-emits light at lower energy. The wavelengths of the two sources are chosen in such a way that they are complementary wavelengths, as shown in Fig. 1. The combination of the two complementary colors yields white light with a location on the chromaticity diagram identical to the standardized *Illuminant C*.

The schematic structure of the PRS-LED is shown in Fig. 2. The figure indicates that a fraction of the light emitted by the blue LED is absorbed by the AlGaInP active region and re-emitted ("recycled") as lower energy photons. In order to obtain white light, the intensity of the two light sources must have a certain power ratio that will be calculated below. The power budget of the device is shown in Fig 3. It is assumed that the electrical input power is P_0 , and the

Keywords: LED, white LED, photon recycling, efficiency.

output powers in the blue and amber spectral range are P_1 and P_2 , respectively. The efficiency of the blue LED and the photon-recycling semiconductor are assumed to be r_1 and r_2 , respectively. A detailed calculation of efficiency and luminous performance of the device will be performed in a subsequent section of this publication.

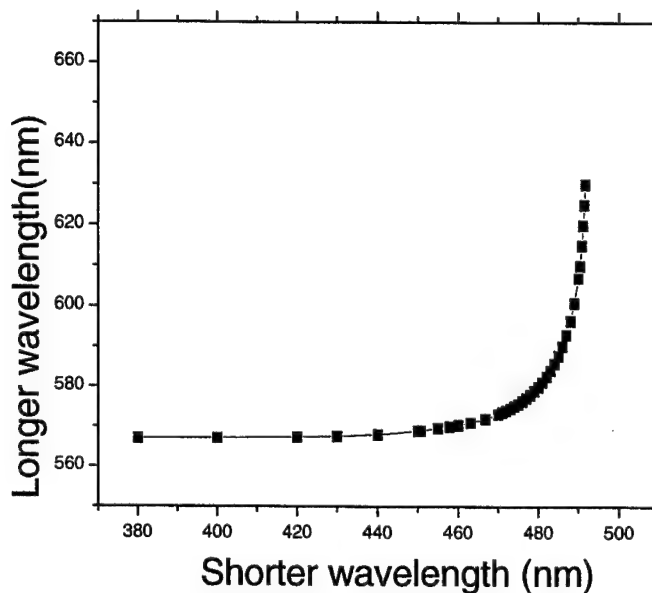


Fig. 1. Complementary wavelengths yielding the color of the standard white Illuminant C.

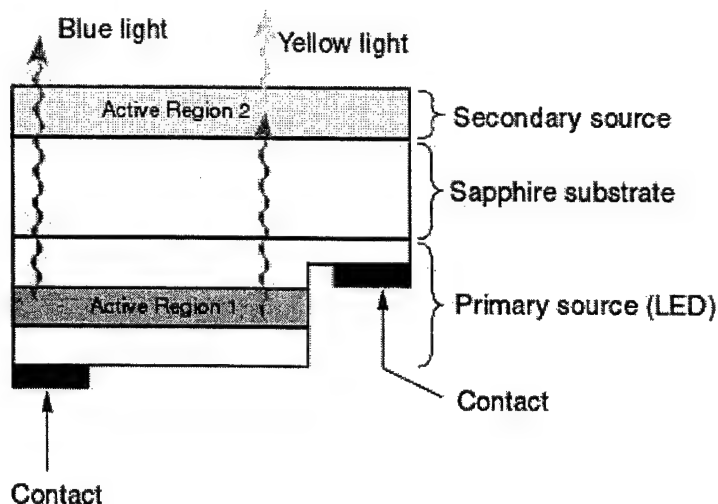


Fig. 2. Schematic structure of the photon-recycling semiconductor LED (PRS-LED)

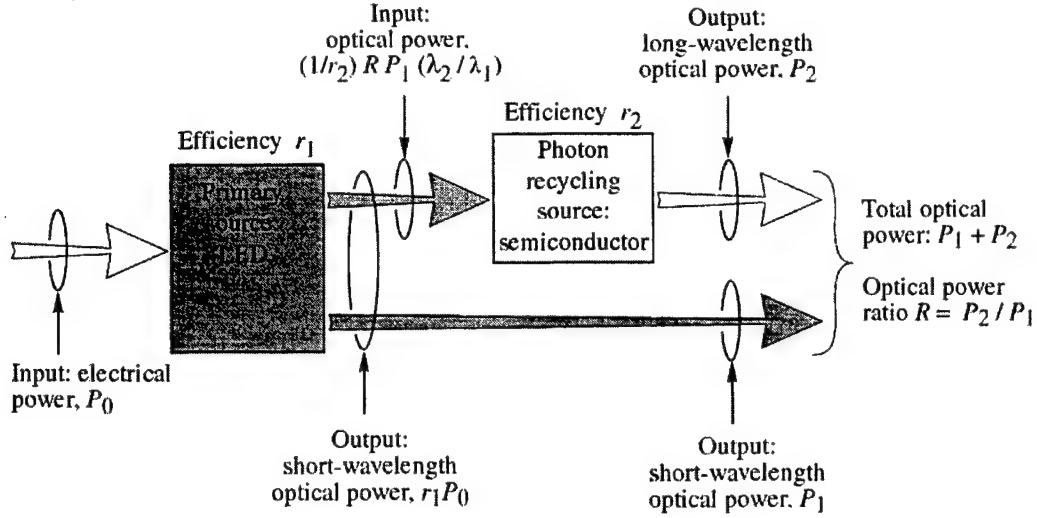


Fig. 3. Power budget of the PRS-LED

The energy loss occurring in the photon recycling process must be taken into account when determining the optimum choice of wavelengths for highest efficiency. Note that energy is lost even if the recycling process occurs with unity quantum efficiency. To calculate the optimum wavelength of operation, we represent white light by the *Illuminant C* standard, whose chromaticity coordinates are $x_c = 0.3101$, $y_c = 0.3163$, $z_c = 0.3736$. Using these chromaticity coordinates, the optimum pair of complementary wavelengths, as shown in Fig. 1, can be determined⁵.

2. Calculation of Power Ratio

Next, we calculate the light power ratio between two sources and the luminous performance of the photon-recycling semiconductor LED. We refer to λ_1 and λ_2 as the primary (short) and secondary (long) wavelength, respectively, and assume that $\lambda_1 < \lambda_2$. For white light, λ_1 and λ_2 are pairs of complementary wavelengths. We define the color masses of the two light sources as

$$m_1 = x_1^* + y_1^* + z_1^* \quad \text{and} \quad m_2 = x_2^* + y_2^* + z_2^* \quad (1)$$

where x_1^* , y_1^* , z_1^* , x_2^* , y_2^* , z_2^* are color matching functions of two light sources^{6,7,8,9}. We define the power ratio of the two light sources as

$$R = P_2 / P_1 \quad (2)$$

where P_1 and P_2 are the optical powers of short wavelength source (λ_1) and long wavelength source (λ_2), respectively. The chromaticity coordinates of the newly generated color are then given by:

$$y_c = \frac{P_1 y_1^* + P_2 y_2^*}{P_1 m_1 + P_2 m_2} = \frac{(y_1^* + R y_2^*) P_1}{(m_1 + m_2 R) P_1} = \frac{y_1^* + R y_2^*}{m_1 + m_2 R} \quad (3)$$

$$x_c = \frac{x_1^* + R x_2^*}{m_1 + m_2 R} \quad (4)$$

For a white light emitter, x_c and y_c are chromaticity coordinates of the *Illuminant C* standard^{10,11}. Solving Eq. (4) for the power ratio R yields:

$$R = \frac{y_1^* - y_c m_1}{y_c m_2 - y_2^*} \quad (5)$$

The power ratio as calculated from Eq. (5) is shown in Fig. 4.

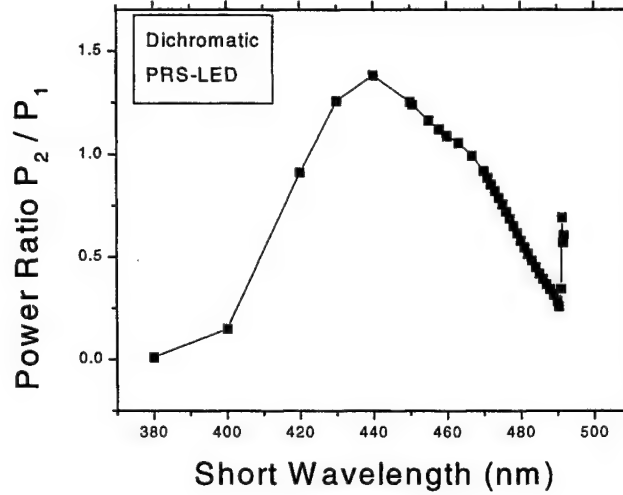


Fig. 4. Power ratio of two monochromatic light sources $P(\lambda_2)/P(\lambda_1)$, with $\lambda_2 > \lambda_1$, required to produce white light.

3. Calculation of Luminous Performance

To produce the optical power P_2 at the wavelength of λ_2 through the recycling of photons from the primary source with wavelength λ_1 , the optical power required from the primary source is given by:

$$\frac{P_2}{r_2} \frac{\lambda_2}{hc} \frac{hc}{\lambda_1} = \frac{P_2 \lambda_2}{r_2 \lambda_1} \quad (6)$$

where r_2 is the optical-to-optical conversion efficiency of the photon recycling light source. If P_0 is the electrical input power, then optical power emitted by the primary LED source is $r_1 P_0$, where r_1 is the electrical-to-optical power conversion efficiency of the primary LED. Thus the optical power emitted by the primary LED is given by

$$P_1 + \frac{P_2 \lambda_2}{r_2 \lambda_1} = r_1 P_0 \quad (7)$$

Solving the equation for the electrical input power yields

$$P_0 = \frac{P_1}{r_1} + \frac{R P_1 \lambda_2}{r_1 r_2 \lambda_1} = P_1 \left(\frac{1}{r_1} + \frac{R \lambda_2}{r_1 r_2 \lambda_1} \right) \quad (8)$$

The total optical output power of the PRS-LED is given by

$$P_{\text{out}} = P_2 + P_1 = (1+R) P_1 \quad (9)$$

so the total efficiency of the photon-recycling dichromatic light source is given by

$$\eta = \frac{P_{out}}{P_0} = \frac{P_1(1+R)}{P_1 \left(\frac{1}{r_1} + \frac{R \lambda_2}{r_1 r_2 \lambda_1} \right)} = \frac{(1+R)}{\left(\frac{1}{r_1} + \frac{R \lambda_2}{r_1 r_2 \lambda_1} \right)}. \quad (10)$$

In the following calculation, X_c , Y_c , Z_c are the tristimulus values of the white light emitted by the PRS-LED^{10,11}. The tristimulus value Y_c , *i. e.* the luminosity function¹¹ of the new color, is given by

$$Y_c = y_1^* P_1 + y_2^* P_2 = y_1^* P_1 + y_2^* R P_1 = (y_1^* + y_2^* R) P_1. \quad (11)$$

Then the luminous efficacy (measured in lumens per optical Watt) of the photon-recycling semiconductor LED is given by

$$\frac{Y_c}{P_{out}} = \frac{y_1^* + y_2^* R}{1 + R}. \quad (12)$$

Thus, the luminous performance (measured in lumens per electrical Watt) of the PRS-LED is given by

$$\frac{Y_c}{P_0} = \frac{Y_c}{P_{out} / \eta} = \eta \frac{Y_c}{P_{out}}. \quad (13)$$

Using this formula, we calculate the luminous performance as a function of the primary wavelength. The result of the calculation is shown in Fig. 5 for ideal monochromatic sources, *i. e.* for $r_1 = r_2 = 100\%$.

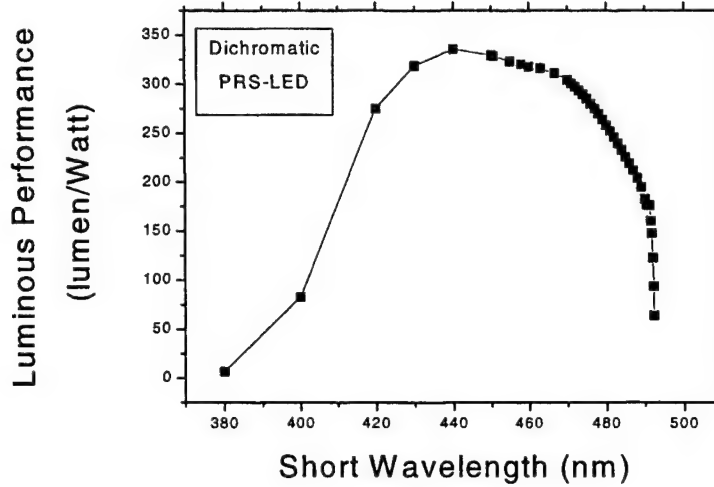


Fig. 5. Luminous performance as a function of the primary source wavelength for an ideal photon-recycling semiconductor LED.

Inspection of Fig. 5 reveals that the maximum efficiency occurs when the primary source emits at 440 nm and the secondary wavelength is 568 nm. A theoretical luminous performance of 336 lm/W is obtained for this wavelength. Note that we assume in the calculation that both light sources emit monochromatic light. However, the spontaneous emission from semiconductors has a 1.8 kT spectral width. Taking into account a 5 nm linewidth, the expected luminous performance would be slightly lower, approximately 326 lm/W.

4. Device Fabrication

The PRS-LEDs are fabricated according to the following 3 processing steps.

- *Blue LED processing.* This includes oxide mask deposition, reactive ion etching, Ni p-type contact deposition (500 Å), and Al n-type contact deposition (500 Å).
- *Photon recycling wafer (AlInGaP Wafer) processing.* This includes the substrate removal by (1) chemical assistant polishing and (2) selective etching.
- *Wafer fusion.* This includes a silicone-based bonding of the primary LED wafer to the recycling wafer.

The process described above yields an LED emitting in the blue spectral range. The AlGaInP/GaAs recycling wafer is processed by first removing the GaAs substrate. The AlGaInP/GaAs photon recycling wafer is mounted epi-side down on a glass slide. Then, the GaAs substrate is removed by polishing and selective wet chemical etching. Subsequently, the primary LED and the photon-recycling semiconductor are brought into close contact by a silicone based adhesion process.

Figure 6 shows a top view of a processed and wire-bonded blue LED. The n-type contact is 500 Å Al and p-type contact is 500 Å Ni. The mesa etching depth is 1.5 μm. The size of the device is 600 × 600 μm. The recycling wafer is located on the backside of the transparent sapphire substrate. The emission efficiency of the recycling wafer can be further optimized, for example by surface texturing, deposition of an index matching layer for the blue LED, and other steps.

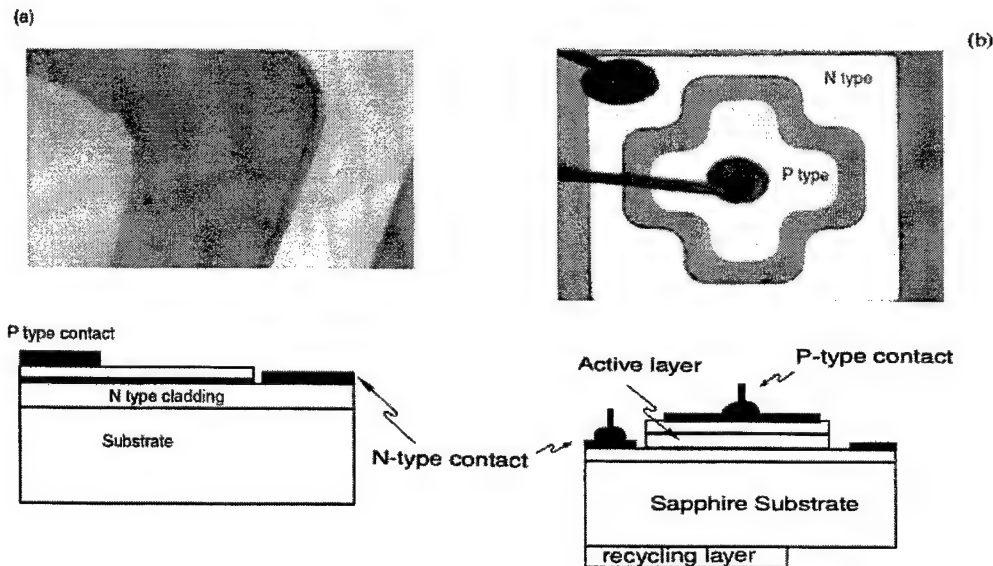


Fig. 6. LED device structure (a) mesa etching and its cross session (b) bonded device structure

5. Experimental Results and Discussions

A prototype PRS-LED has been demonstrated using a GaInN/GaN LED emitting in the blue and an electrically passive AlGaInP photon recycling semiconductor emitting in the red part of the

spectrum. The emission spectrum of the device is shown in Fig. 7. It shows the primary LED emission at 470 nm and a second emission line at 630 nm due to absorption of 470 nm light in the AlGaInP layer and re-emission of light at 630 nm.

To avoid absorption of light in the GaAs substrate, the GaAs substrate of the AlGaInP epitaxial layer was removed. The experimental results indicate that the LED light is sufficiently intense for optical pumping and also indicates very good quantum efficiency of the recycling semiconductor. The recycling semiconductor used in this experiment is a AlGaInP/GaAs double heterostructure. At the present time, the photon-recycling semiconductor is planar LED structure wafer and no surface texturing has been performed. The color is controlled by the size of the recycling wafer. In later research this can be done by other mechanisms, such as by the thickness of the active region.

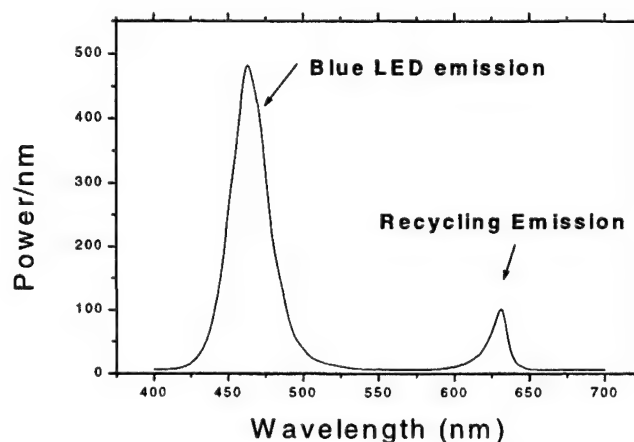


Fig. 7. Room temperature luminescence spectrum of a photon-recycling semiconductor LED showing the blue GaInN/GaN LED emission and the red AlGaInP emission due to photon recycling.

A program was developed to calculate the general color rendering index and luminous performance of the different emitters. The results are shown in Table 1. Note that a dichromatic light source has a lower color-rendering index as compared to a spectrally broad emitter. It can be shown that there is a fundamental trade off between color rendering and luminous performance of light-emitting devices¹². Inspection of Table 1 indeed reveals that an increased luminous performance can be attained at the expense of the color rendering capability of the light source. The color rendering capability is estimated by the general color-rendering index (CRI). In order to improve the general CRI of the dichromatic PRS LED, we consider two possibilities. First, the emission lines can be intentionally broadened, *e. g.* by compositional grading of the semiconductor active region. Second, a second photon-recycling semiconductor can be added thus creating a tri-chromatic PRS-LED. Such a trichromatic semiconductor white LED has a color-rendering index of 60. Also note that the overall efficiency of our device is currently limited by the quantum efficiency of the primary blue LED.

Type of LED	FWHM (nm)	Luminous performance (lumens/Watt)	Chromaticity coordinates (x, y)	General CRI
Dichromatic LED	5	326	0.31, 0.32	10
Broadened Dichromatic LED	20	306	0.31, 0.32	26
Trichromatic LED	5	283	0.31, 0.32	60
Phosphor-based LED	100	280	0.31, 0.32	57

Table 1. Calculated efficiency and general color rendering index (CRI) of different white LEDs for a given FWHM of the emission peaks. For the phosphorous-based white LED, the CRI value is based on the spectrum provided by the vendor.

6. Conclusions

In conclusion, we have analyzed a white-light emitting photon-recycling semiconductor LED. And a prototype photon-recycling semiconductor LED has been demonstrated. The device consists of a primary current-injection LED and a photon-recycling semiconductor that is optically excited by the primary LED. Based on our calculation, luminous performance exceeding 300 lm/W can be expected for an ideal device with unity quantum efficiency. Due to the narrow emission spectra of the two light sources, the PRS-LED has a higher luminous performance than phosphor-based white LEDs. A PRS-LED is demonstrated by using a GaInN/GaN LED emitting in the blue and an AlGaInP/GaAs photon recycling semiconductor emitting in the red-to-amber part of the spectrum.

Acknowledgements. The authors gratefully acknowledge useful discussions with Dr. R. Fletcher of the HP Corp.

References

1. Ivey H. F., *J. Opt. Soc. Am.* **53**, 1185 (1963)
2. Schnitzer I., Yablonoitch E., Caneau C. and Gmitter T. J., *Appl. Phys. Lett.* **62**, 131 (1993)
3. Schnitzer I., Yablonoitch E., Caneau C., Gmitter T. J. and Scherer A., *Appl. Phys. Lett.* **63**, 2174 (1993)
4. Shuji Nakamura and Gerhard Fasol, "The Blue Laser Diode" (Springer, New York, 1997)
5. Wyszecki G. and Stiles W.S., *Color Science* (2nd ed.) (Wiley, New York 1982).
6. Judd, D. B. *Report of U.S. Secretariat Committee on Colorimetry and Artificial Daylight. In Proceedings of the Twelfth Session of the CIE, Stockholm (Vol. 1, p. 11).* Paris: Bureau Central de la CIE (1951)
7. Vos, J.J. Colorimetric and photometric properties of a 2-degree fundamental observer. *Color Research and Application*, **3**, 125-128 (1978)
8. MacAdam D. L., *J. Opt. Soc. Am.* **40**, 120 (1950)
9. Macadam "Color Measurement" (Springer-Verlag, New York 1985)
10. CIE *Commission Internationale de l'Eclairage Proceedings, 1931* (Cambridge University Press, Cambridge, 1932)
11. Judd, D.B. *Report of US Secretariat Committee on Colorimetry and Artificial Daylight. In Proceedings of the Twelfth Session of the CIE, Stockholm (Vol. 1, P. 11).* Paris: Bureau central de la CIE (1951).
12. W. Walter, *Applied Optics*, Vol.10, No.5, May (1971)

SESSION 3

High-Efficiency LEDs

Non-Resonant Cavity Light-Emitting Diodes

R. Windisch^a, M. Kuijk^b, B. Dutta^a, A. Knobloch^c, P. Kiesel^c, G. H. Döhler^c,
G. Borghs^a, and P. Heremans^a

^aIMEC, Kapeldreef 75, B-3001 Leuven, Belgium

^bVrije Universiteit Brussel, Dept. ETRO-LAMI, Pleinlaan 2,
B-1050 Brussels, Belgium

^cUniversität Erlangen-Nürnberg, Institut für Technische Physik I, Erwin-Rommel-Str. 1
D-91058 Erlangen, Germany

— Invited Paper —

ABSTRACT

The external efficiency of conventional light-emitting diodes (LED's) is limited by total internal reflection at the semiconductor-air interface. For conventional GaAs-based LED's, this results in an extraction efficiency of 2%. In non-resonant cavity (NRC) LED's, this problem is overcome by a combination of internal scattering at a textured top surface and reflection on a back mirror, which increases the probability of escape. Using this approach, we demonstrate external quantum efficiencies of up to 40% without encapsulation of the LED. To gain a more detailed understanding of the out-coupling mechanisms in NRC-LED's, the scattering properties of the textured surface are investigated experimentally. The optimum surface texture is found to randomize the direction of the internally reflected light almost perfectly. In addition, NRC-LED's also enables the enhancement of the external quantum efficiency for small and fast LED's. With efficiencies of about 15%, we demonstrate bitrates of more than 1.3 GBit/s. In order to modify the lambertian output characteristics, we have successfully applied microlenses, allowing 50% coupling efficiency into optical fibers with NA=0.5.

Keywords: Light-emitting diodes, optical scattering, micro-lenses

1. INTRODUCTION

In most semiconductor light-emitting diodes (LED's), internal quantum efficiencies close to 100% can be achieved.¹ The external efficiency is thus limited by the extraction efficiency. For conventional LED's, only $\approx 2\%$ of the generated light can be extracted from the semiconductor material, due to total internal reflection at the semiconductor-air interface. Several approaches have been reported to circumvent this problem. The highest external quantum efficiency reported so far has been obtained with transparent-substrate LED's with an inverted-truncated-pyramid geometry.² In this way, 55% external quantum efficiency has been obtained with fully packaged LED lamps, and 32.6% with unpackaged devices. As the light extraction relies on the geometry of the complete LED chip, this method does not allow the fabrication of high density arrays of LED's, as required for parallel optical communication systems. Alternative approaches available for the fabrication of LED arrays are the resonant-cavity (RC) LED³ and the surface-textured thin-film LED.⁴ The highest efficiencies reported for RC-LED's are 22% external quantum efficiency⁵ and 27% slope efficiency.⁶ For optical communication purposes, an RC-LED with a quasi-static external quantum efficiency of 11.8% was demonstrated at 1 Gb/s.⁷

In surface-textured LED's, the light is coupled out of the semiconductor by a combination of surface scattering and reflection on a back mirror. Light, which is internally reflected at the semiconductor-air interface, changes its direction of propagation due to internal scattering at the textured front surface. After reflection on a rear reflector, it gets additional chances to escape from the LED medium.⁴ In other words, the surface scattering leads to an effective perturbation of resonances associated with internal waveguiding within the cavity formed between the front surface and the back mirror. The perturbation of such waveguide modes, in which a large fraction of the emitted light is trapped for untextured thin-film LED's, is essential for the efficient out-coupling of light.^{8,9} Emphasizing this aspect of the light out-coupling, surface-textured thin-film LED's can also be called non-resonant cavity (NRC) LED's. Using this concept, we have previously reported a maximum external quantum efficiency of 31%.⁸ For communication LED's, a bitrate of 622 Mbit/s has been achieved with 17% external quantum efficiency.¹⁰ In this paper, we present a further improvement in the performance of NRC-LED's, and we introduce a method to investigate the internal scattering at the textured surface.

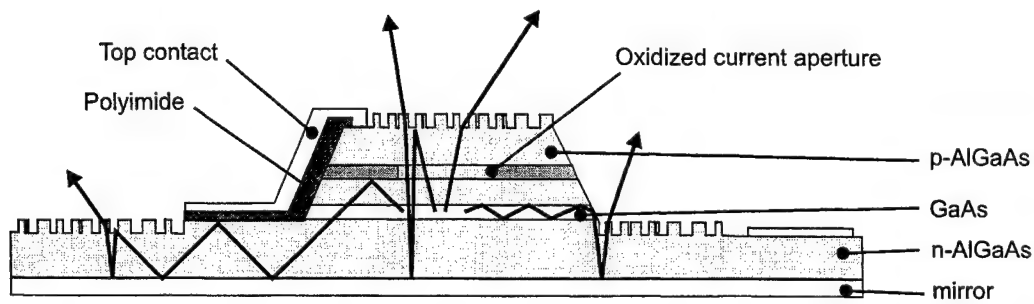


Figure 1. Schematic structure of our NRC-LED. Typical photon trajectories are also shown.

2. DEVICE FABRICATION

The structure of our NRC-LED's is shown schematically in Fig. 1. The GaAs/AlGaAs LED structure is grown by MBE on a GaAs substrate. The processing, which is described in more detail elsewhere,^{8,9} includes wet thermal oxidation of an $\text{Al}_{0.98}\text{Ga}_{0.02}\text{As}$ layer located above the active GaAs layer. The current aperture fabricated in this way prevents the generation of light underneath the top contact, which is placed above the oxidized $\text{Al}_{0.98}\text{Ga}_{0.02}\text{As}$. The back mirror is fabricated via substrate removal, which is performed by epitaxial lift-off, and consecutive Van der Waals bonding onto a polyimide/gold mirror. The surface is textured using natural lithography, where a monolayer of randomly positioned polystyrene spheres acts as a mask for dry etching. This process creates randomly distributed pillars on the LED surface. In order to create a reproducible spacing in between the spheres, their size is reduced in an oxygen plasma before dry etching. Our optimized texturing conditions^{11,10} employ spheres 400 nm in diameter, which are reduced to ≈ 300 nm and etched to a depth of 180 nm.

In contrast to our previously reported devices, the device mesa is etched through the active GaAs layer, as shown in Fig. 1. As a significant fraction of the generated light is waveguided within the active GaAs layer, this light can be coupled out very efficiently at the tilted mesa edge, in a manner similar to the out-coupling in tapered LED's.¹²

3. EXTERNAL QUANTUM EFFICIENCY

The altered device geometry leads to a significant improvement in the external quantum efficiency from 31% to 40%, both obtained for identical LED layers with a 120 nm thick active GaAs layer. Figure 2 shows the total output power

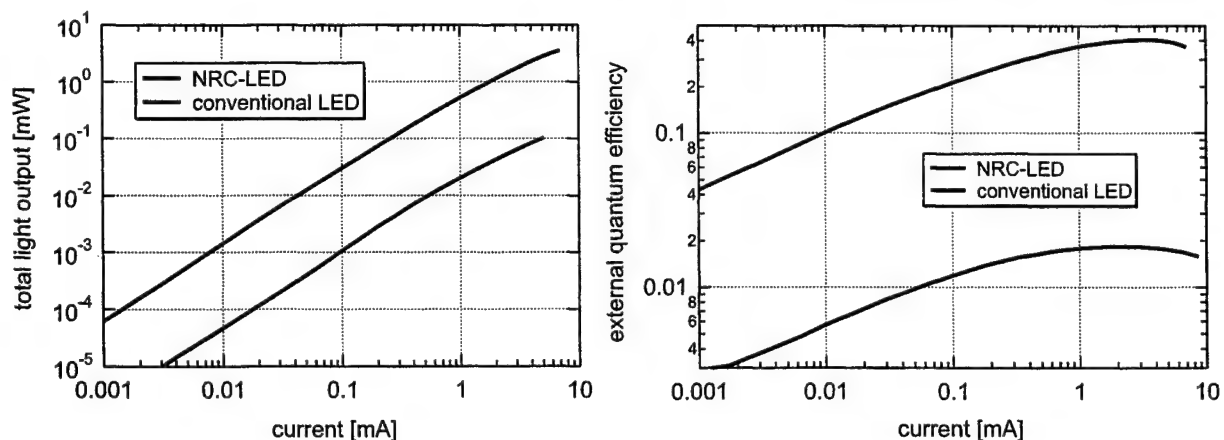


Figure 2. Total output power (a) and external quantum efficiency (b) of our NRC-LED's compared to a conventional LED, i.e. an LED with a flat top surface and no rear reflector.

and the external quantum efficiency of unpackaged NRC-LED's versus the injection current, and compares their performance to that of conventional reference LED's. The mesa diameter of the LED's is $45\text{ }\mu\text{m}$, and the diameter of the current aperture is $29\text{ }\mu\text{m}$. The emission wavelength is 870 nm with a FWHM of $\approx 30\text{ nm}$.

4. SURFACE SCATTERING

For a better understanding of the light extraction mechanism in NRC-LED's we have investigated the internal scattering of light at the textured surface. As we know of no theory which can describe the scattering at surfaces roughened by natural lithography with the structure sizes employed for NRC-LED's, we have introduced a novel technique to experimentally determine the directionality of internal scattering. This directionality cannot be measured with an external detector, as the light scattered into angles larger than the angle of total internal reflection will not be coupled out of the semiconductor and will thus not reach an externally positioned detector. Thus, we have integrated an InGaAs detector onto the bottom side of the GaAs substrate in order to detect the light scattered at the textured top surface (see Fig. 3). Previously, we have demonstrated that this method allows the reliable measurement of the angular distribution of light transmitted from air through the textured surface into the GaAs.¹³

Figure 3(a) shows the measurement technique. The textured top surface is illuminated from the bottom by light from an optical fiber. Due to the large index of refraction of the GaAs substrate, the beam divergence from the optical fiber does not influence the direction of propagation inside the GaAs significantly, as the light is refracted towards angles $< 16^\circ$. Thus, the light is incident almost vertically onto the textured surface. A part of the light is transmitted, the rest of the light is scattered during its reflection at the rough surface. The InGaAs detector detects the light which is scattered into a spherical angle which is determined by the horizontal distance between the fiber spot and the location of the detector. The angular spectrum can be measured by moving the optical fiber as shown in Fig. 3(a). Only angles larger than 20° are accessible, as the external illumination cannot occur through the detector.

Figure 3(b) shows the measured dependence of the detected light on the fiber position. As the observed spherical angle decreases with increasing distance between the fiber spot and the detector, the amount of detected light is also decreasing with the distance. The influence of the spherical observation angle can be calculated for a complete randomization of the scattered light. The result is represented by the dashed line in Fig. 3(b). The excellent agreement between the measurement and this calculated curve shows that the directionality of the internally scattered light is almost perfectly randomized. The total amount of scattered light can be obtained by an integration of the measured curve from Fig. 3(b). Comparing the obtained optical power to the incident optical power and the transmitted optical

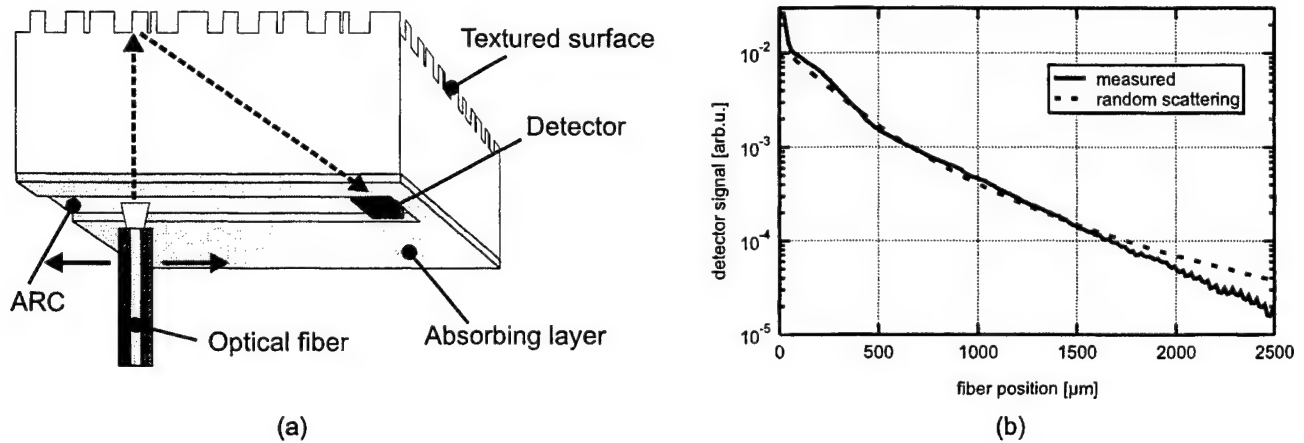


Figure 3. Measurement of internal scattering at a textured surface. (a) Principle of the employed method. (b) Measured detector signal versus distance between the fiber spot and the edge of the $200\text{ }\mu\text{m}$ large detector. $120\text{ }\mu\text{m}$ distance corresponds to an observation angle of 30° , $350\text{ }\mu\text{m}$, $950\text{ }\mu\text{m}$ and $2050\text{ }\mu\text{m}$ correspond to 50° , 70° , and 80° , respectively. The peak at the position of the detector edge is due to direct illumination of the detector. The surface has been textured using 400 nm spheres and an etch depth of 180 nm , without the size reduction step.

power, which have been measured separately, allows the calculation of the scattering efficiency. We have obtained a scattering efficiency close to 100%, i.e. almost all the light which is reflected at the textured surface is scattered and specular reflection is almost negligible.

5. APPLICATIONS IN OPTICAL COMMUNICATION

5.1. Introduction

Highly efficient LED's are attractive candidates for application in optical communication. Low-power light sources, which are manufacturable in large two-dimensional arrays, are especially applicable for inter-chip communication. Here, LED's are a promising alternative to VCSEL's, as they have no threshold and are thus more efficient at low current levels. In addition, LED's exhibit an excellent temperature stability,¹⁰ which is required for direct integration onto CMOS chips.

The major problems in such applications is the integration of LED's to CMOS and the light coupling into optical fibers. Recently, we have described a possible solution to these problems. We have fabricated arrays of NRC-LED's on a fiber optic face plate¹⁴ as a host substrate, which can be flip-chip bonded onto CMOS. A face plate is a slice of a bundle of glass fibers, thus the light does not diverge as it would in a simple transparent substrate. Hence, the transmitted light from the LED through the face plate forms a sharp image of an LED array with negligible cross-talk between adjacent LED's. Further, we proposed to transport the emitted light through an image fiber bundle attached on top of the face plate to an array of integrated CMOS detectors.¹⁵

An alternative to the above approach for low density parallel optical links is the direct coupling of LED light to an optical fiber with a large numerical aperture (NA). To enable the efficient coupling of the emitted light from NRC-LED's to high-NA fibers, we have integrated microlenses on top of the LED's. This is particularly necessary, since the emission pattern of unpackaged NRC-LED's is Lambertian.

5.2. Directionality

In order to obtain a high directionality, a micro-lens should ideally be positioned at the focal length f from the emitter. As a glass sphere of radius r is a lens with $f = 1.5r$, a glass sphere integrated on the LED surface is very close to an ideal micro-lens. Figure 4(a) shows an SEM photo of such a micro-lens. As shown in Fig. 4(b), the micro-lensed NRC-LED exhibits excellent directionality. Calculations show that 50% of the light is emitted within an angle of 30° , which is the acceptance angle of an optical fiber with a numerical aperture of 0.5.

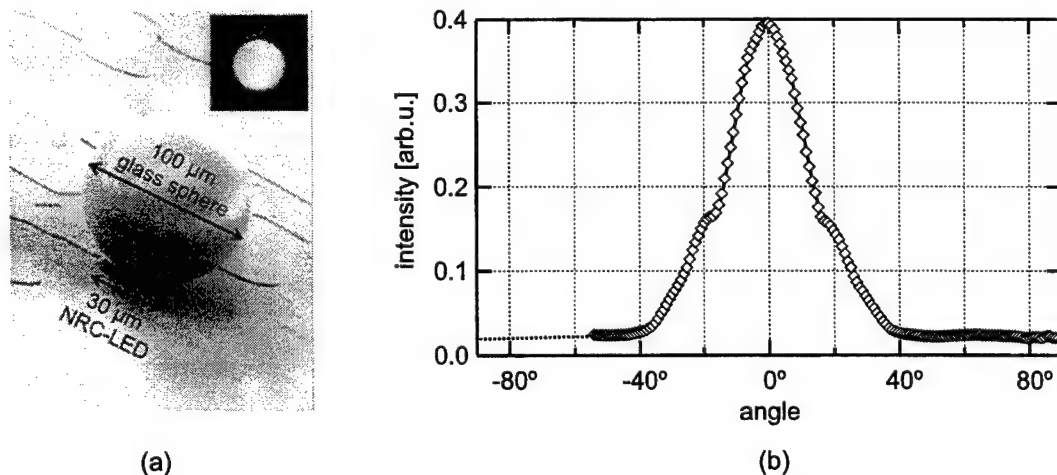


Figure 4. Micro-lensed NRC-LED's. (a) SEM photograph of an NRC-LED with a glass microlens. The inset shows the top-view of the LED under operation. The light is emitted almost uniformly from the area of the sphere. (b) Measured angular light distribution of an NRC-LED with a glass microlens. Due to the probe needles, the regime between -90 and -54 could not be measured.

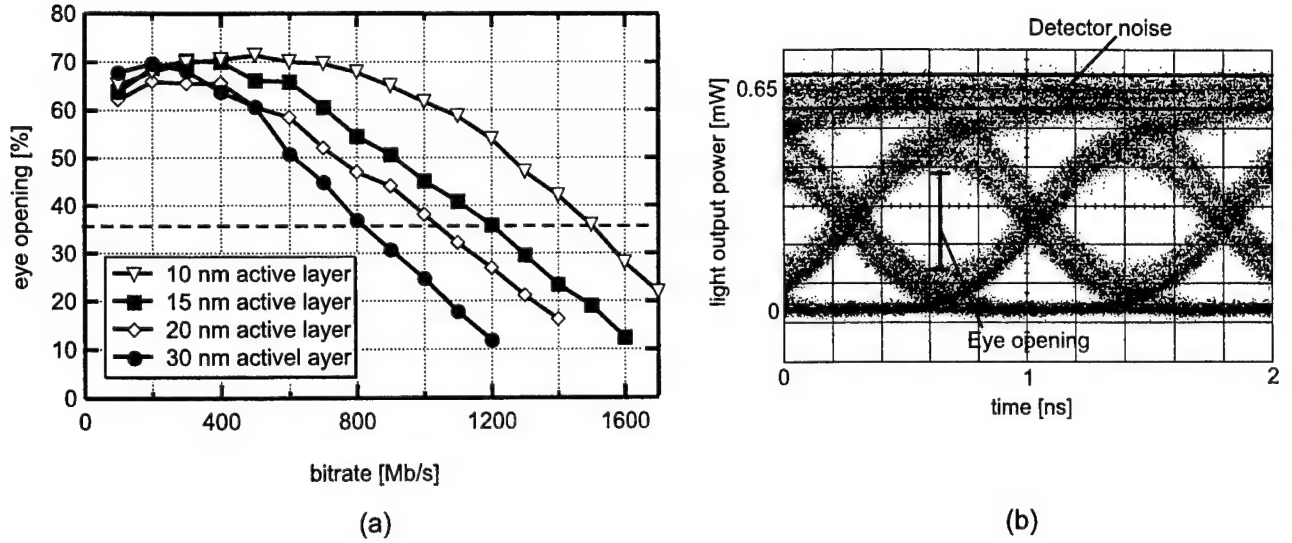


Figure 5. Dynamic performance of QW-NRC-LED's. (a) Eye opening of the various NRC-LED's vs. bitrate. The dashed line shows the approximate limit for optical communication. (b) Eye diagram obtained at 1.3 Gbit/s for the 10-nm QW NRC-LED with a glass microlens. The opening of the eye is 40% of the total amplitude. This total amplitude includes the detector noise.

5.3. Dynamic performance

The dynamic behaviour is a key issue for LED's in optical communication. The fastest LED's have been realized using extremely highly ($> 10^{19} \text{ cm}^{-3}$) *p*-doped active layers.¹⁶ However, to date there has been no demonstration that this approach can be combined with any of the existing approaches which enable high external efficiencies. In order to reduce re-absorption within the LED structure, highly efficient LED's usually employ thin active layers, i.e. an active layer thickness below 200 nm. In contrast, high internal quantum efficiencies for highly doped active layers have only been obtained for active layers of about $0.5 \mu\text{m}$ thickness.

An alternative method to improve the frequency response of LED's is to use very thin active layers and relatively high current densities,¹⁷ as this results in large injected carrier concentrations and reduces the radiative recombination lifetime in the LED, thus reducing the time constant.¹⁸ We have fabricated quantum-well (QW) NRC-LED's with QW thicknesses of 30, 20, 15 and 10 nm. The mesa diameter of the QW-NRC-LED's is $30 \mu\text{m}$ and the diameter of the current aperture is $12 \mu\text{m}$. We have measured optical eye diagrams with a NRZ random bitstream of $2^{23} - 1$ bits with an on-state voltage of 3 V, corresponding to $\approx 3 \text{ mA}$ device current and a current density of about 3500 A/cm^2 . The off-state voltage was set to 1 V. Figure 5(a) shows the obtained eye openings for the four QW-NRC-LED's versus bitrate, Fig. 5(b) shows an eye diagram for the 10-nm QW-NRC-LED at 1.3 Gbit/s. In order to compare the behaviour of various LED's we have defined an acceptable bitrate limit at the bitrate where the eye diagram is half as open as in the case of low-frequency modulation, which is close to the situation shown in Fig. 5(b). This limit is indicated by the dashed line in Fig. 5(a).

5.4. Efficiency and bitrate

The external quantum efficiency and the achievable bit rate obtained for the QW-NRC-LED's are shown in Fig. 6. The thicker the active layer, the higher the efficiency and the lower the achievable bitrate. The figure shows the maximum external quantum efficiency of the respective devices, which is obtained at currents of around 1 mA, and the quantum efficiency measured under realistic conditions for data transfer, i.e. at 3 V corresponding to $\approx 3 \text{ mA}$ device current, and an average duty cycle of 50%. The decrease of the efficiency for thinner active layers is due to carrier spill-over to the current-confining AlGaAs layers, which is caused by bandfilling in the quantum well. The application of a glass microlens only results in a small further increase of the external efficiency, as the lens geometry

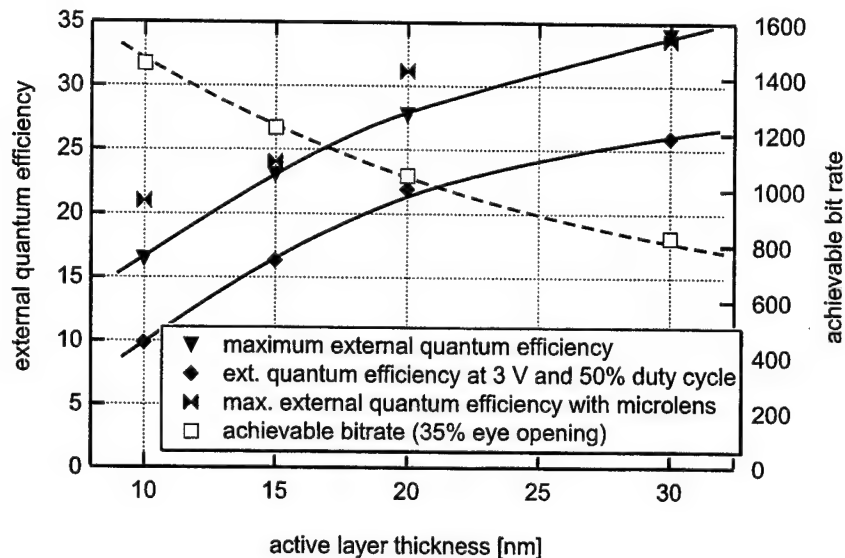


Figure 6. Comparison of the external quantum efficiency and the achievable bit rate of the four NRC-LED's investigated.

is not optimized for optimum light out-coupling, but for directionality. The dynamic behaviour of the NRC-LED's also remains unaffected by the microlens.

With the micro-lensed 20-nm-QW NRC-LED, an external quantum efficiency above 30% is obtained, and the device reaches a bit rate of 1 Gbit/s. This efficiency-bitrate product is exceeding all previously reported LED's.

6. CONCLUSIONS

Employing the concept of the non-resonant cavity LED, we have demonstrated the highest reported external quantum efficiency of 40% from unpackaged LED's. The use of thin active layers allows the simultaneous achievement of high bitrates as required for communication LED's. For this purpose, we have improved the angular output pattern by applying spherical micro-lenses on top of the LED surface.

ACKNOWLEDGMENTS

The authors acknowledge W. van de Graaf for the MBE-growth of the samples and S. Peeters for his help in processing. This work was in part supported by the EC under contract No. 22641 (OIIC).

REFERENCES

1. I. Schnitzer, E. Yablonovitch, C. Caneau, and T. J. Gmitter, *Ultra-high spontaneous emission quantum efficiency, 99.7% internally and 72% externally, from AlGaAs/GaAs/AlGaAs double heterostructures*, Appl. Phys. Lett. **62**, 131 (1993)
2. M. R. Krames, M. Ochiai-Holcomb, G. E. Höfler, C. Carter-Coman, E. I. Chen, I.-H. Tan, P. Grillot, N. F. Gardner, H. C. Chui, J.-W. Huang, S. A. Stockman, F. A. Kish, M. G. Crawford, T. S. Tan, C. P. Kocot, M. Hueschen, J. Posselt, B. Loh, G. Sasser, and D. Collins, *High-power truncated-inverted-pyramid $(Al_xGa_{1-x})_{0.5}In_{0.5}P/GaP$ light-emitting diodes exhibiting > 50% external quantum efficiency*, Appl. Phys. Lett. **75**, 2365 (1999)
3. E. F. Schubert, Y.-H. Wang, A. Y. Cho, L.-W. Tu, and G. J. Zydzik, *Resonant cavity light-emitting diode*, Appl. Phys. Lett. **60**, 921 (1992)
4. I. Schnitzer, E. Yablonovitch, C. Caneau, T. J. Gmitter, and A. Scherer, *30% external quantum efficiency from surface-textured, thin-film light-emitting diodes*, Appl. Phys. Lett. **63**, 2174 (1993)

5. H. De Neve, J. Blondelle, P. Van Daele, P. Demeester, R. Baets, and G. Borghs, *Recycling of guided mode light emission in planar microcavity light-emitting diodes*, Appl. Phys. Lett. **70**, 799 (1997)
6. J. J. Wierer, D. A. Kellog, and N. Holonyak, Jr., *Tunnel contact junction native-oxide aperture and mirror vertical-cavity surface-emitting lasers and resonant-cavity light-emitting diodes*, Appl. Phys. Lett. **74**, 926 (1999)
7. R. Bockstaele, T. Coosemans, C. Sys, L. Vanwassenhove, A. Van Hove, B. Dhoedt, I. Moerman, P. Van Daele, R. G. Baets, R. Annen, H. Melchior, J. Hall, P. L. Heremans, M. Brunfaut, and J. Van Campenhout, *Realization and characterization of 8×8 resonant cavity LED arrays mounted onto CMOS drivers for POF-based interchip interconnections*, IEEE J. Sel. Top. Quantum Electron. **5**, 224 (1999)
8. R. Windisch, P. Heremans, A. Knobloch, P. Kiesel, G.H. Döhler, B. Dutta, G. Borghs, *Light-emitting diodes with 31% external quantum efficiency by outcoupling of lateral waveguide modes*, Appl. Phys. Lett. **74**, pp. 2256-2258 (1999)
9. R. Windisch, P. Heremans, B. Dutta, S. Nemeth, A. Knobloch, G.H. Döhler, G. Borghs, *Size dependence of record-efficiency non-resonant cavity light-emitting diodes*, Proc. SPIE **3621**, pp. 213-220 (1999)
10. R. Windisch, A. Knobloch, J. Potemans, B. Dutta, G.H. Döhler, G. Borghs, P. Heremans, *Non-resonant cavity light-emitting diodes with 17% external quantum efficiency at 622 Mbit/s*, IEEE J. Sel. Top. Quantum Electron. **5**, 166 (1999)
11. R. Windisch, P. Heremans, B. Dutta, S. Schoberth, J. Genoe, M. Kuijk, P. Kiesel, G. H. Döhler, and G. Borghs, *Systematic photoluminescence and electroluminescence study of high-efficiency surface-textured thin-film light-emitting structures*, Proc. SPIE **3279**, 94 (1998)
12. W. Schmid, F. Eberhard, M. Schauler, M. Grabherr, R. King, M. Miller, E. Deichsel, S. Stareev, U. Martin, R. Jaeger, J. Joos, R. Michalzik, and K. J. Ebeling, *Infrared light-emitting diodes with lateral outcoupling taper for high extraction efficiency*, Proc. SPIE **3621**, 198 (1999)
13. R. Windisch, S. Schoberth, S. Meinlschmidt, P. Kiesel, A. Knobloch, P. Heremans, B. Dutta, G. Borghs, G.H. Döhler, *Light Propagation through Textured Surfaces*, J. Opt. A: Pure Appl. Opt. **1**, 512 (1999)
14. P. Heremans, M. Kuijk, S. Peeters, R. Windisch, D. Filkins, and G. Borghs, *Thin-film 850-nm light-emitters on fiber optic face plate*, ECOC'99, 26-30 Sept 1999, Nice, France, proceedings p. II-304 (1999)
15. R. Vounckx, P. Heremans, D. Coppée, R. Windisch, G. Borghs, and M. Kuijk, *Optical chips interconnects: economically viable*, Proc. SPIE **3491**, 294 (1998)
16. C. H. Chen, M. Hargis, J. M. Woodall, M. R. Melloch, J. S. Reynolds, E. Yablonovitch, and W. Wang, *GHz bandwidth GaAs light-emitting diodes*, Appl. Phys. Lett. **74**, 3140 (1999)
17. P. Heremans, R. Windisch, A. Knobloch, J. Potemans, B. Dutta, G. H. Döhler, G. Borghs, *Frequency limits of high-efficiency non-resonant cavity light-emitting diodes*, Proc. SPIE **3621**, 206 (1999)
18. K. Ikeda, S. Horiuchi, T. Tanaka, and W. Susaki, *Design parameters of frequency response of GaAs-(Ga,Al)As double heterostructure LED's for optical communications*, IEEE Trans. Electron Dev. **ED-24**, 1001 (1977)

High power Truncated-Inverted-Pyramid ($\text{Al}_x\text{Ga}_{1-x}$) $_{0.5}\text{In}_{0.5}\text{P}$ Light-Emitting Diodes

Mari O. Holcomb^a, Michael R. Krames^a, Gloria E. Hofler^a, Carrie Carter-Coman^a, Eugene Chen^a,
Patrick Grillot^a, Kwang Park^a, Nate.F.Gardner^a, Jen-Wu.Huang^a, Jason Posselt^a, David Collins^a,
Steve.A.Stockman^a, George M. Craford^a, F.A.Kish^b, I-H.Tan^b, T.S.Tan^c, Chris.P.Kocot^c,
Mark.Hueschen^c

^a LumiLeds, San Jose, CA

^b Agilent Technologies, San Jose, CA

^c Agilent Laboratories, Palo Alto, CA

ABSTRACT

High power light emitting diodes (LEDs) are of interest for many lighting applications. Flux improvements can be achieved by scaling conventional chips to larger dimensions. However this scaling results in a decrease in extraction efficiency. These penalties can be offset by modifying the chip geometry such that the number of internal reflections is reduced, thereby increasing the probability of photon escape. LEDs with a truncated-inverted-pyramid (TIP) geometry have been fabricated and packaged. Peak efficiencies exceeding 100 lm/W have been measured (100 mA dc, 300 K) for orange ($\lambda_p \sim 610$ nm) devices. In the red wavelength regime ($\lambda_p \sim 650$ nm), peak external quantum efficiencies of 55% (100 mA dc, 300 K) have been achieved. Flux exceeding 65 lumens from a single 594 nm device has also been demonstrated. These characteristics match and/or exceed the performance of many conventional lighting sources.

1. INTRODUCTION

An increasing number of commercial solid state lighting applications is driving the development of high power light emitting diodes (LEDs) in the visible regime. Application examples include automobile lighting, traffic signaling, neon replacement for commercial signs, and area lighting. LEDs offer the advantage of lower drive power and long lifetime over conventional lighting sources.

LEDs based in the ($\text{Al}_x\text{Ga}_{1-x}$) $_{0.5}\text{In}_{0.5}\text{P}$ material system provide emission in the 570-650 nm wavelength regime. Early ($\text{Al}_x\text{Ga}_{1-x}$) $_{0.5}\text{In}_{0.5}\text{P}$ LEDs exhibited external quantum efficiencies of 11 lm/W.¹ Subsequent improvements to efficiency were achieved by incorporation of a hydride VPE grown GaP top layer which serves as both a current spreading and window layer.² The efficiency of these devices was doubled by wafer bonding to transparent GaP substrates.³

Recently, additional efficiency improvements have been achieved by reducing the active layer thickness.⁴ The reduction in active layer thickness has the primary benefit of increasing the extraction efficiency, η_{ext} . However if the active layer is too thin, the LED internal quantum efficiency, η_i , decreases due to carrier leakage. Devices with the active layer thickness optimized for maximum external quantum efficiency, η_{eq} , ($\eta_{\text{eq}} = \eta_i * \eta_{\text{ext}}$) have exhibited efficiencies of 74 lm/W. The active area of these devices are comprised of several thin layers. The total thickness of the layers is typically ~ 2000 Å.

2. HIGH POWER CHIP DESIGN

The most direct method of achieving more power per LED is by increasing the active area.⁵ For example, a five fold increase in LED flux was achieved by increasing the area of a standard $0.22 \times 0.22 \text{ mm}^2$ chip by five times, and by proper thermal management. Lamp packaging is discussed in Section 4.

Scaling to larger chip sizes, however, results in a decrease in extraction efficiency, as the aspect ratio (chip width to height) increases. Internally reflected light must travel farther before escape, however may be absorbed before entering

an escape cone. This has the net effect of reducing the side escape cone volume. Experimentally, extraction efficiency penalties of 20% are typically observed, when comparing lamps made from $0.5 \times 0.5 \text{ mm}^2$ square chips to standard $0.22 \times 0.22 \text{ mm}^2$ chips.

This scaling extraction efficiency penalty can be offset by modifying the chip geometry such that the number of internal reflections is reduced, thereby increasing the probability of photon escape before being absorbed during multiple passes through the chip. Examples include hemispherical, conical, and cylinder shaped devices.^{6, 7} A truncated inverted pyramid (TIP) geometry was chosen for this work.⁸

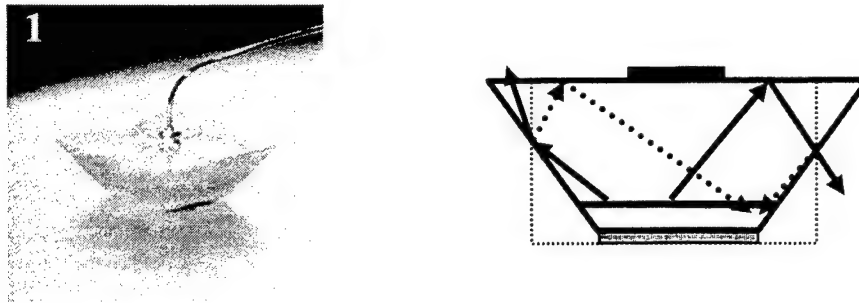


Figure 1

A photograph and schematic of a TIP LED device is shown in Fig. 1. Increased flux comes from light initially internally reflected from the beveled side wall which subsequently escapes from the top surface. Additional flux contributions come from light which is initially internally reflected from the top surface which then escapes from the bevel side wall. For both cases, the dashed line shows the photon path for vertical side walls, indicating additional internal reflection and subsequent absorption by the active layer.

TIP LED devices were fabricated from wafers with device structures similar to that discussed in the previous section. Bevel sawing is used to obtain the truncated inverted pyramid chip geometry.

3. TIP LED EFFICIENCY CHARACTERISTICS

The power efficiency characteristics of the TIP LEDs are summarized in Figure 2 for encapsulated chips, driven at 100mA DC at 300K. The solid squares data points are measured external quantum efficiencies, indicated on the right axis. The efficiency of $(\text{Al}_x\text{Ga}_{1-x})_{0.5}\text{In}_{0.5}\text{P}$ LEDs increase with increasing wavelength, due primarily to higher carrier confinement in the conduction band. A maximum external quantum efficiency of 55% is observed at a peak wavelength of 652 nm. This corresponds to a wall plug efficiency of 45%. Under pulsed operations, (not shown) external quantum efficiencies as high as 60% has been observed. This 60% represents the minimum extraction efficiency of these TIP LED devices.

The external quantum efficiency of the TIP LEDs is among the highest reported. The external quantum efficiency of the 652 nm TIP LED chip described above measured in air without encapsulation is 33%. This is comparable to the 40% efficiency achieved from 870 nm non resonant cavity LED structures with textured surfaces.⁹ 27% efficiencies have been observed from 980 nm resonant LEDs employing oxide mirrors.¹⁰

The measured luminous efficiency for the TIP LEDs is shown as open data points in Figure 2, corresponding to the left axis. $(\text{Al}_x\text{Ga}_{1-x})_{0.5}\text{In}_{0.5}\text{P}$ LEDs devices have a peak luminous efficiency near 610 nm, due to increasing eye sensitivity with decreasing wavelength. Luminous efficiencies as high as 233 lm/A at this wavelength has been observed. This corresponds to a power efficiency of over 100 lm/W. These efficiencies exceed the performance of most fluorescent lamps.

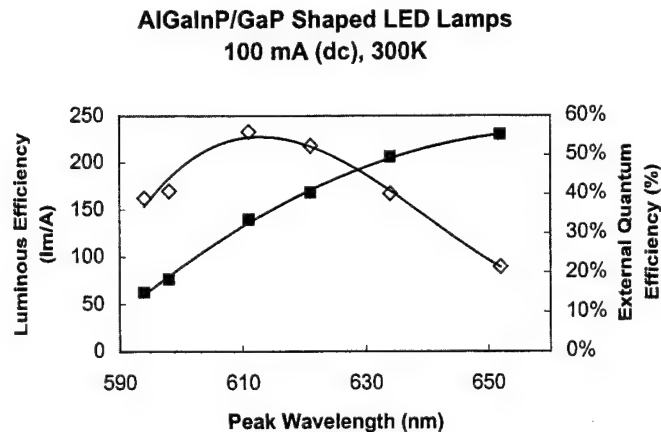


Figure 2

In the amber wavelength regime (peak wavelength ~ 594 nm) where commercial LEDs are prevalent, TIP LEDs have luminous and power efficiencies of 162 lm/A and 67 lm/W, respectively. These efficiencies are typically 50% higher compared to lamps made from conventional large square chips of the same 0.25mm^2 active area. In addition, they are 20% more efficient compared to lamps made from the much smaller $0.22 \times 0.22\text{mm}^2$ chips. Finally, $(\text{Al}_x\text{Ga}_{1-x})_{0.5}\text{In}_{0.5}\text{P}$ TIP LEDs efficiencies are also higher than the 10 lm/W efficiencies observed to date for amber LEDs grown in the InGaP material system.¹¹

4. TIP LED HIGH POWER OPERATION

For high power operation, the TIP LED devices are typically driven at current densities between $110\text{--}215\text{ A/cm}^2$, which corresponds to a power consumption of 0.8 - 2W per LED. Both the chip and package design incorporate features to accommodate these drive powers. For example, the chip is fabricated n-side up, such that the active layer is closer to the heat sink. In addition, an In solder layer is used which is deposited on the wafer bottom surface before dicing. This provides a controllable uniform thin layer which enables automated die attach.

The chip lamp housing is also custom designed for high power operation. An automated die attach process is used to mount the die to a heated sub-mount, with a matching coefficient of thermal expansion. This sub-mount is surrounded by a copper heat sink body. The lens is comprised of a hard plastic shell into which a soft encapsulating gel is injected. This soft gel reduces the stress on the chip edges compared to conventional encapsulating epoxy. Typical junction to pin thermal resistances of TIP LED devices are $10\text{--}20^\circ\text{C/W}$.

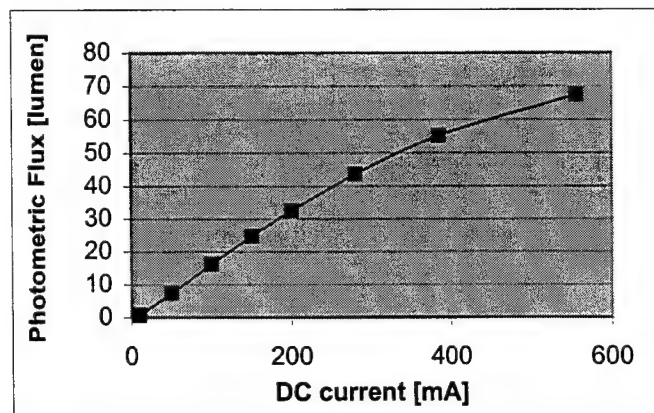


Figure 3

The DC room temperature luminous flux is shown in Figure 3, as a function of drive current, for a lamp with a peak wavelength of 594 nm. No saturation in output power is observed for drive currents over 0.5A. The maximum power

measured for this single device is 67 lumens at 560mA. This is ~ 15 times the flux typically observed in conventional lamps with a smaller $0.22 \times 0.22 \text{ mm}^2$ chip. The typical amber flux gain is 50% over large square chips with the same 0.25 mm^2 active area.

The TIP LED devices are both mechanically robust and reliable under high power operating conditions. Shown in Fig. 4 are results of accelerated operating life tests. Each line represents the average degradation of 20 lamps from a single wafer. The lamps were operated at a drive current density of 150 A/cm^2 , at a board temperature of 85°C . Flux degradation of less than 10% is observed out to at least 500 hours. This reliability is comparable to traditional square chips of the same area. Similarly, in low temperature operating life tests, where lamps were driven at a board temperature of -40°C at 110 A/cm^2 (data not shown), average flux degradation of less than 15% was observed out to 1000 hours.

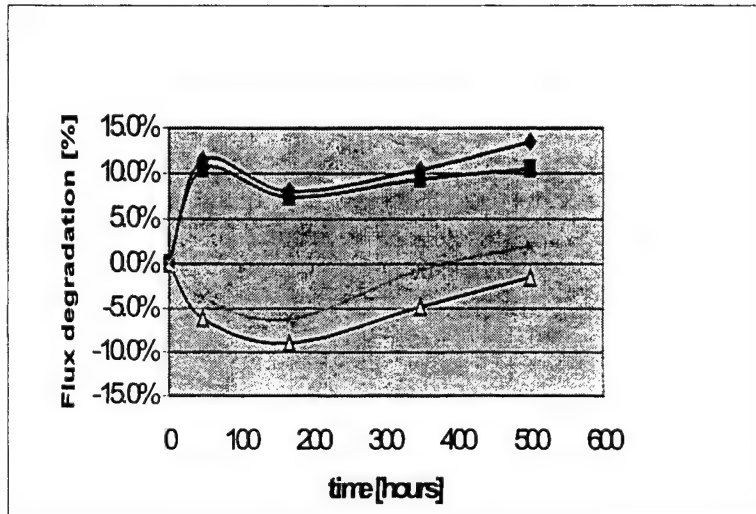


Figure 4

5. SUMMARY

Chip shaping has been demonstrated to increase the extraction efficiency of $(\text{Al}_x\text{Ga}_{1-x})_{0.5}\text{In}_{0.5}\text{P}$ LED devices by 50% over conventional large area square chips. LEDs with a truncated inverted geometry have luminous efficiencies exceeding 60 lm/W over the 595 - 625 nm visible wavelength regime. Over 100 lm/W for 610 nm orange devices and 55% external quantum efficiencies for 652 nm devices have been achieved. Flux exceeding 65 lumens from a single 594 nm device has also been demonstrated. The TIP LED devices are both mechanically robust and reliable under high power operating conditions, making them suitable for many lighting applications.

¹ R.M. Fletcher, C.P. Kuo, T.D. Osentowski, K.H. Huang, M.G. Craford, V.M. Robbins, *J. Electron. Matr.*, **20**, 1125 (1991).

² K.H. Huang, J.G. Yu, C.P. Kuo, R.M. Fletcher, T.D. Osentowski, L.J. Stinson, M.G. Craford, A.S.H. Liao, *Appl. Phys. Lett.* **61**, 1045 (1992).

³ F.A. Kish, F.M. Steranka, D.C. DeFevere, D.A. Vanderwater, K.G. Park, C.P. Kuo, T.D. Osentowski, M.J. Peanasky, J.G. Yu, R.M. Fletcher, D.A. Steigerwald, M.G. Craford and V.M. Robbins, *Appl. Phys. Lett.* **64**, 2839-2841 (1994).

⁴ N.F. Gardner, H.C. Chui, E.I. Chen, M.R. Krames, J.-W. Huang, F.A. Kish, S.A. Stockman, C.P. Kocot, T.S. Tan and N. Moll, *Appl. Phys. Lett.* **74**, 2230-2232 (1999).

⁵ G.E. Hofler, C. Carter-Coman, M.R. Krames, N.F. Gardner, F.A. Kish, T.S. Tan, B. Loh, J. Posselt, D. Collins and G. Sasser, *Electron. Lett.* **34**, 1781-1782 (1998).

⁶ A.R. Franklin, R. Newman, *J. Appl. Phys.*, **35**, 1153, 1964.

⁷ Dierschke, *IEEE Trans. Elect. Dev.*, **8**, 1210, 1979.

-
- ⁸ M.R.Krames, M.Ochiai-Holcomb, G.E.Hofler, Carter-Coman, E.I.Chen, I-H.Tan, P.Grillot, N.F.Gardner, H.C.Chui, J-W.Huang, S.A.Stockman, F.A.Kish, M.G.Craford, T..S.Tan, C.P.Kocot, M.Hueschen, J. Posselt, B.Loh, G.Sasser, D.Collins, , Appl. Phys. Lett. **75** (1999).
- ⁹ C R. Windisch, B. Dutta, M. Kuijk, A. KnoblochA. Knobloch, S. Meinlschmidt, Schoberth, P. Kiesel, G. Borghs, G.H. Dohler, P. Heremans, to be published
- ¹⁰ J.J. Wierer, D.A. Kellogg, and N. Holonyak, Jr., Appl. Phys. Lett. **75** (1999).
- ¹¹ T. Mukai, H. Narimatsu, S. Nakamura, Jpn. J. Appl. Phys. **37**, 480, 1998.

Resonant cavity LEDs at 655 and 880 nm wavelengths

Pekko Sipilä*, Mika Saarinen, Ville Vilokkinen, Seppo Orsila, Petri Melanen,
Pekka Savolainen, Mika Toivonen, Mihail Dumitrescu, Markus Pessa

Tampere University of Technology, Optoelectronics Research Centre,
P. O. Box 692, 33101 Tampere, Finland

ABSTRACT

Monolithic top-emitting resonant cavity light-emitting diodes (RCLEDs) have been fabricated by solid-source MBE. The RCLEDs in the 650-nm range, with modulation bandwidths exceeding 180 MHz, are possible low-cost transmitter candidates for systems using plastic optical fibers (POFs), such as IEEE-1394 at 100 Mb/s and 200 Mb/s and ATM at 155 Mb/s. Modulation bandwidth of >120 MHz and light power of 2 mW (cw) have been achieved for $\varnothing 84\text{-}\mu\text{m}$ devices driven at a 40 mA current. Accelerated ageing tests for 27,500 device-hours indicate no degradation in output power. A variation in device temperature significantly modifies the far-field pattern and thus the fibre coupling efficiency, due to a cavity detuning effect. The effects of detuning and the temperature and bias dependencies of the devices are investigated. The 880-nm RCLEDs have a maximum output power of 25 mW. Applications include open-air optical communication systems, collision avoidance and measurement systems.

Keywords: Light-emitting diodes, RCLED, MBE, quantum well devices, plastic optical fibers

1. INTRODUCTION

Resonant cavity enhanced light-emitting diodes (RCLEDs) have several interesting properties that make them suitable for various applications, where the usage of conventional LEDs is limited by their poor performance or where edge-emitting laser diodes would be too expensive. RCLEDs present several advantages compared to conventional LEDs such as narrow spectral linewidth, better beam directionality and increased efficiency¹, and higher modulation speed². The enhancements result from the modification of the spontaneous emission by an optical microcavity. Edge-emitting laser diodes require chip-level testing, facet coatings, and precise alignment to an optical fiber, which make them too expensive for many low-level applications. RCLEDs and vertical cavity lasers (VCLs) benefit from their surface-emitting structure which enables wafer-level testing, thus reducing the device fabrication cost in a noticeable degree. Moreover, the circular output beam improves the fiber coupling efficiency.

The RCLED has an optically active region, which consists of quantum wells (QWs) located at antinodes of a standing wave Fabry-Perot cavity mode. The cavity is sandwiched between two distributed Bragg reflectors (DBRs) or between a high-reflectivity metal layer and a DBR mirror. Emission properties of the RCLED can be significantly modified by cavity detuning. Detuning is defined as a difference between the Fabry-Perot mode λ_{FP} and the quantum well emission λ_{qw} ; i.e., $\Delta\lambda_d = \lambda_{FP} - \lambda_{qw}$. A positive detuning increases the extraction efficiency (η_e) and output power (P_{out}), and broadens the far-field (FF) distribution³. When compared to a VCL, the RCLED has favorable structural features: the top DBR needs not be of very high reflectivity ($80 < R_t < 90\%$ is adequate), and the window area may be large to yield a good extraction efficiency. Therefore, medium-speed high-brightness RCLEDs can be designed for a wide spectral range, including visible light where lasing action of vertically emitting devices is difficult to be achieved^{4,5,6}.

A driving force of our RCLED studies is the market introduction of polymethyl methacrylate (PMMA) polymer optical fibers (POFs). PMMA-POF, exhibiting a data transmission window at $\lambda \approx 650\text{ nm}$, is suitable for low-cost short-haul communications systems⁷. Due to its large core diameter ($0.1 \leq \varnothing \leq 3.0\text{ mm}$), POF can easily be aligned and terminated. However, light propagation losses are high, typically 0.15 - 0.20 dB/m at the optimal wavelength. Another drawback of the POF technology is the absence of a low-cost, high performance light source. In principle, an LED could be used as a transmitter but it would produce a narrow modulation bandwidth (f_m), typically $20 < f_m < 30\text{ MHz}$, and broad emission of 20 to 30 nm in terms of full width at half maximum (FWHM). An edge-emitting laser, in turn, would allow for large f_m , but

* Correspondence: Email: pekko.sipila@orc.tut.fi; Telephone: +358 3 365 2552; Fax: +358 3 365 3400

would be expensive and its high-temperature behaviour — a key issue particularly in automotive applications — is not well known. Bearing these difficulties in mind, a cost-effective medium-speed RCLED may be a viable device for POF-based communication systems.

In this paper, we will describe our work on RCLEDs at 650-655 nm and 880 nm wavelengths. Design issues, experimental procedures and device performance will be discussed. Because of their more obvious applications, the main focus here will be on the red RCLEDs.

2. DESIGN ISSUES

We have studied several kinds of RCLED structures in order to optimize the device performance. The basic structure consisted of a cosine-type $1\text{-}\lambda$ -thick cavity delimited by AlGaAs DBR mirrors and having an active region (with 3 to 5 QWs) centred at the cavity antinode. The cavity thickness was designed to be $L_c = m_c \lambda_{FP} / 2n$, where λ_{FP} is the wavelength in the outside medium, n is the refractive index of the cavity material, and m_c is the cavity order ($m_c = 2$ for a $1\text{-}\lambda$ cavity). Top emission was considered because of the GaAs substrate absorption in the working spectral ranges and monolithic structures were chosen since they enable integration and have reduced fabrication complexity.

Transfer matrix based modeling together with a self-consistent model were used to optimise the devices' performance. The design of the layer structure (DBRs, microcavity, QWs, barriers, current spreading and cap layers) and doping profile was assisted by computer simulations that enabled many device improvements.

In a first modeling and simulation step the QW composition and thickness together with the barrier thickness were chosen, using a self-consistent model, so that the resulted spontaneous emission spectrum is peaked at the desired wavelength. The self-consistent model uses interband transition; strained QWs are treated using the $k\text{-}p$ theory and valence band mixing effects are included. It has to be mentioned that since the spontaneous emission spectrum depends strongly upon bias and temperature while the active region temperature and the relation between injected current and QW carrier densities (used in the model) are highly uncertain, the calculated spontaneous emission spectrum must be fitted to measurements.

Once the cavity was defined, the bottom and top DBRs were designed. Besides a desired large refractive index contrast Δn , one should achieve low photon absorption and small potential barriers between individual layers. Unfortunately, high contrast in AlGaAs layers is limited in the red range by significant absorption at reduced aluminum content.

Since the devices' electrical characteristics are as much important as the optical ones an electrical analysis was performed in conjunction with the optical analysis. The absorption edge's (bandgap) and potential barriers' variation with layer composition, layer thickness and bias were analyzed at this stage with the aid of the self-consistent model. In order to alleviate the adverse effects of the DBR potential barriers, intermediate-composition barrier reduction layers were used before each high bandgap material layer (in the direction of majority carrier flow). The composition and thickness of the intermediate DBR layers were adjusted by analyzing the band profile calculated with the self-consistent model. The resulted optimum composition was roughly in the middle of the composition gap between low and high bandgap layers. In order to keep the optical properties of the mirrors unaffected the intermediate composition layer thickness was kept much smaller than the emission wavelength. The thickness of the high bandgap layer was adjusted so that the optical thickness of the combined intermediate composition and high bandgap layer is $\lambda_0/4$.

Also in order to improve the electrical device characteristics of the 650-nm RCLEDs the bottom DBR was made of N instead of the typical $N\text{+}1/2$ periods, starting with low bandgap (high refraction index) layer on the substrate side. This was done since the GaAs to low-bandgap material interface produces a favorable barrier reduction step for electrons. The number of periods in the bottom mirror was high enough, so that the contrast at the interface with the GaAs substrate is not important from the optical point of view. In a similar attempt to introduce a barrier reduction step at the first potential barrier for holes the current spreading layer was made of low bandgap (high refraction index) material.

The reflection coefficients of the DBRs were calculated using a transfer-matrix-based program⁸. The optical analysis of the RCLED layer structure is very much based on the determination of the reflectivity dependence upon wavelength, incidence angle, polarization, layer contrast, layer thickness, and the number of DBR periods. Once the DBR layer composition, order and thickness are established the remaining variable to adjust the DBR mirror reflectivities is the number of periods. For top-emitting structures, the bottom DBR should have a reflectivity close to unity. We chose a 20-period

$\text{Al}_{0.9}\text{Ga}_{0.1}\text{As}/\text{Al}_{0.2}\text{Ga}_{0.8}\text{As}$ bottom DBR for the 880-nm RCLEDs and a 32-period $\text{AlAs}/\text{Al}_{0.5}\text{Ga}_{0.5}\text{As}$ bottom DBR with $\text{Al}_{0.75}\text{Ga}_{0.25}\text{As}$ intermediate composition layers for the 650-nm RCLEDs, giving calculated reflectivities of 98 and 99 % at normal incidence, respectively. The top mirror reflectivity must be adjusted to significantly lower values – so that the cavity modes over the whole emission spectrum occupy as much as possible of the escape window. For lateral current confinement, an $\text{Al}_{0.98}\text{Ga}_{0.02}\text{As}$ wet thermal oxidation layer was placed in the top DBR, one period away from the cavity in order to avoid oxide modes and strain propagation into the cavity. Ion implantation could also be used for current confinement, with the advantage of maintaining planar device structure. However, ion implantation used in VCL fabrication has been reported to deteriorate device reliability by introducing crystalline defects that propagate into the device's active region⁹.

In order to optimize the extraction efficiency the DBR mirrors and the cavity must be detuned with respect to the emission spectrum peak. Unfortunately, a trade-off must be made between extraction efficiency and directionality. The extraction efficiency is at maximum when the cavity mode is centered in the middle of the escape window, corresponding to an double-lobed FF with maxima at an angle of $\theta \approx 45^\circ$ off the surface³. On the other hand, such a large θ is not desired for optical fiber coupling experiments. Detuning allows the FF to be optimized according to the application. The effect of detuning on the FF can be seen in figure 1, which shows the measured far-fields for three 650-range RCLEDs with different detunings.

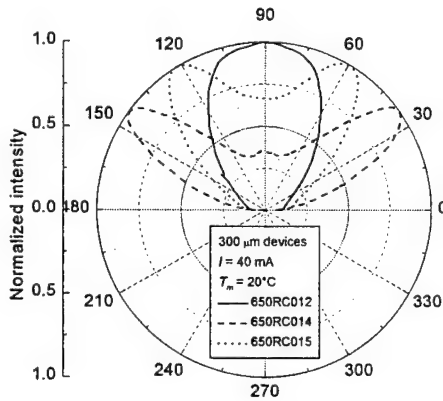


Figure 1 Measured far-field patterns for three RCLEDs in the 650-nm range with different nominal detunings: $\Delta\lambda_d(650\text{RC012}) \approx 0\text{nm}$, $\Delta\lambda_d(650\text{RC015}) \approx 6\text{nm}$, $\Delta\lambda_d(650\text{RC014}) \approx 14\text{nm}$

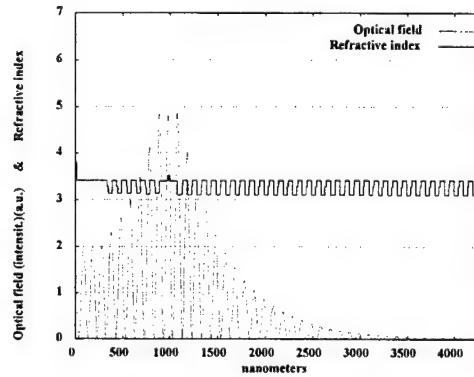


Figure 2 Refractive index and optical field intensity profiles along a $1-\lambda$ cosine cavity RCLED.

Based on the transfer matrix formalism the study of optical field longitudinal distribution enabled us to analyse the QW placement and evaluate doping profiles to reduce the free carrier absorption. Figure 2 shows the refractive index and the optical field profile for a $1-\lambda$ cosine-cavity 650-nm RCLED. Only one of the QWs can be placed at the single antinode available; the additional QWs being less effectively coupled with the cavity mode. The optimum number of QWs is odd – to have one QW placed exactly at the antinode – and in the range of 3 to 7 depending on the QW and barrier thickness. Higher number of QWs induces reduced and non-uniform carrier injection into the QWs besides bad coupling to the cavity mode for the QWs farther from the antinode.

3. GROWTH AND DEVICE PROCESSING

All our RCLED structures were grown on 2" GaAs wafers by solid-source MBE¹⁰ using valved cracker cells for arsenic and phosphorous. Silicon and beryllium were used as n - and p -type dopants, respectively. Prior to the growth of the device structures, test samples were grown to adjust the stop-band of the DBRs, and for photoluminescence (PL) studies.

The 650-nm RCLED structure consisted of a 32 period n -doped $\text{Al}_{0.5}\text{Ga}_{0.5}\text{As}/\text{AlAs}$ bottom DBR mirror (with $\text{Al}_{0.75}\text{Ga}_{0.25}\text{As}$ intermediate composition layers), a $1-\lambda$ cosine cavity with 3 to 5 $\text{In}_{0.55}\text{Ga}_{0.45}\text{P}$ QWs and $(\text{Al}_{0.5}\text{Ga}_{0.5})_{0.51}\text{In}_{0.49}\text{P}$ barriers and

semicavities, a 5 to 12 period p -doped $\text{Al}_{0.95}\text{Ga}_{0.05}\text{As}/\text{Al}_{0.5}\text{Ga}_{0.5}\text{As}$ top DBR mirror (also with $\text{Al}_{0.75}\text{Ga}_{0.25}\text{As}$ intermediate composition layers) having an $\text{Al}_{0.98}\text{Ga}_{0.02}\text{As}$ wet thermal oxidation layer in the second period from the cavity and an $\text{Al}_{0.5}\text{Ga}_{0.5}\text{As}$ current spreading layer with a thin p^{++} GaAs contact layer on top.

The 880-nm RCLED structure consisted of a 20 period n -doped $\text{Al}_{0.2}\text{Ga}_{0.8}\text{As}/\text{Al}_{0.9}\text{Ga}_{0.1}\text{As}$ bottom DBR mirror, a $1\text{-}\lambda$ cosine cavity with three $\text{In}_{0.04}\text{Ga}_{0.96}\text{As}$ QWs, $\text{Al}_{0.2}\text{Ga}_{0.8}\text{As}$ barriers and semicavities and a 5 to 7 period p -doped $\text{Al}_{0.9}\text{Ga}_{0.1}\text{As}/\text{Al}_{0.2}\text{Ga}_{0.8}\text{As}$ top DBR mirror with an $\text{Al}_{0.97}\text{Ga}_{0.03}\text{As}$ wet thermal oxidation layer. On top a thick $\text{Al}_{0.2}\text{Ga}_{0.8}\text{As}$ current spreading layer with a p^{++} GaAs contact layer was grown. No barrier reduction layers were used in the 880-nm RCLEDs.

The samples were processed into circular top-emitting mesas with emission window diameters of $40 \leq \varnothing \leq 500 \mu\text{m}$. To enhance the current distribution over the window area, 3-10 μm wide contact stripes crossed the circular emission window. The oxide aperture for lateral current confinement was formed by a wet thermal oxidation step at 375-400 $^{\circ}\text{C}$. The p -type metal contact, Ti/Pt/Au, was made on the mesas by e-beam evaporation and standard lift-off. The n -type contact, Ni/Au/Ge/Au, was evaporated on the backside of a thinned (100 μm) substrate. Finally, the GaAs contact layer was removed from the window area by wet selective etching to avoid light absorption. The devices were bonded on TO-46 cans with silver filled epoxy. Some of the devices were encapsulated in transparent epoxy to enhance light extraction through decreased refractive index contrast at the semiconductor/air interface.

4. RESULTS AND DISCUSSION

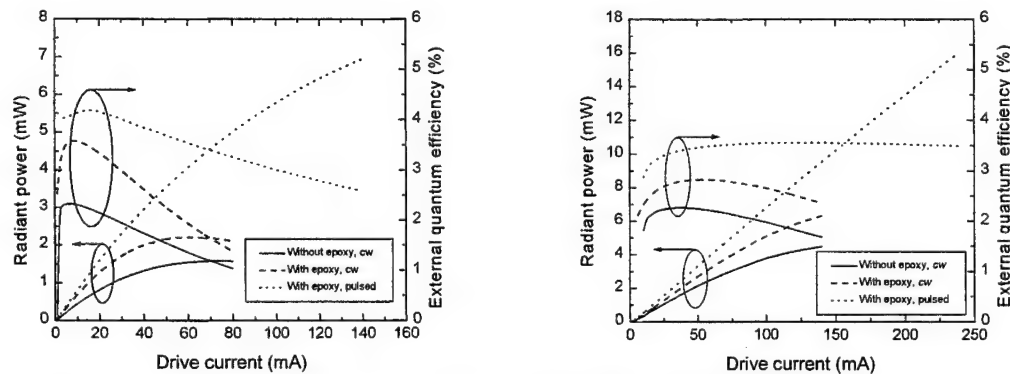


Figure 3 Radiant power and external quantum efficiency for a 650-nm RCLED having an $\varnothing 84\text{-}\mu\text{m}$ (left) and a $\varnothing 300\text{-}\mu\text{m}$ (right) emission window without an epoxy cap in cw mode, and with an epoxy cap in cw mode and in pulsed mode.

Figure 3 shows light-current-external quantum efficiency (I - η) curves for 650-nm RCLEDs having an $\varnothing 84\text{-}\mu\text{m}$ and a $\varnothing 300\text{-}\mu\text{m}$ emission window with and without transparent epoxy caps. The curves were measured at the device temperature (T_m) of 20 $^{\circ}\text{C}$, defined as a temperature of the TO-46 mount, using an integrating sphere and a calibrated optical spectrometer. The $\varnothing 84\text{-}\mu\text{m}$ devices turned on at bias voltage $1.7 \leq V_b \leq 1.8 \text{ V}$ and had a differential series resistance of 3 Ω at drive current $I_{dr} = 50 \text{ mA}$. According to figure 3, P_{out} saturated at about 1.6 mW (cw) for a chip with no epoxy cap, due to internal heating, and at 2.2 mW (cw) for a chip with the cap. Maximum η of about 2.3 % and 3.6 % for the device without and with the epoxy cap, respectively, was achieved at $I_{dr} \approx 8 \text{ mA}$. The power values are somewhat smaller than reported by Streubel *et al.* for MOCVD-grown devices of the same size that had a hydrogen ion implanted current confinement structure⁶. However, our devices with the barrier reduction layers in the DBRs have a slightly smaller forward voltage and a lower differential series resistance. Since detrimental effects of heating on P_{out} (cw) were remarkable, we measured P_{out} in pulsed mode as well (pulse width = 2 μs , duty cycle = 2.5 %), as shown in figure 3. We obtained $P_{out} \approx 7 \text{ mW}$ at $I_{dr} = 140 \text{ mA}$ with no remarkable indication of thermal saturation. For the $\varnothing 300\text{-}\mu\text{m}$ devices, the external quantum efficiency remains smaller, the maximum being 2.8 % for the epoxy-capped component in cw mode. Due to the larger contact area, the differential series resistance for the larger device size is smaller, only 1.2 Ω .

The performance curves in cw mode for 880-nm RCLEDs having $\varnothing 80\text{-}\mu\text{m}$ and $\varnothing 500\text{-}\mu\text{m}$ emission windows and an epoxy cap are shown in figure 4. The maximum external quantum efficiencies are $>16\%$ and 14% , respectively. These values are similar to the efficiencies reported by other groups for near-IR RCLEDs, such as 14.8% by Dill *et al.*¹¹ for a 960-nm RCLED (pulsed measurement), and 19.8% for a $\varnothing 1.5\text{ mm}$ and 16.8% for an $\varnothing 85\text{-}\mu\text{m}$ RCLED by De Neve *et al.* at 980 nm ¹². The voltage and the series resistance are significantly higher than for the red RCLEDs with the barrier reduction layers.

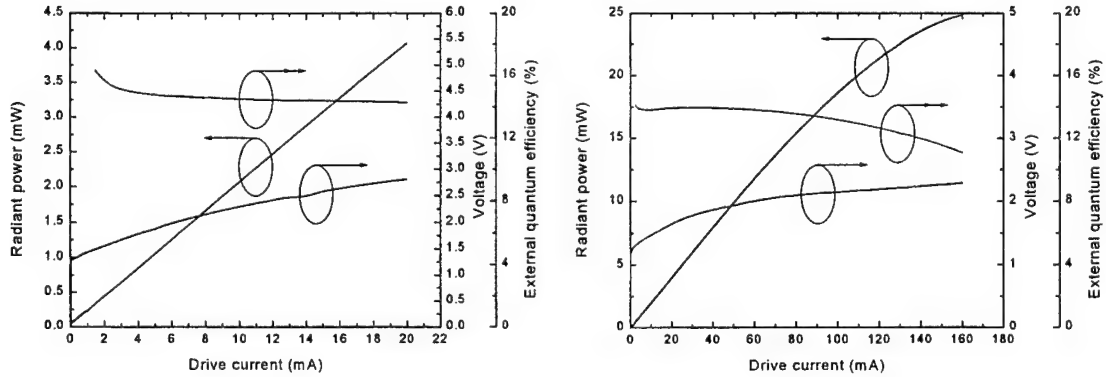


Figure 4 Radiant power, forward voltage and external quantum efficiency in cw mode for 880-nm RCLED having an $\varnothing 84\text{-}\mu\text{m}$ (left) and a $\varnothing 500\text{-}\mu\text{m}$ (right) emission window.

The spectrum for an 880-nm RCLED together with a commercial reference LED is shown in figure 5. When talking about the spectral properties of an RCLED, one should note that in contrast to conventional LEDs, the RCLEDs show angular wavelength dispersion caused by the resonant cavity³. Consequently, the peak wavelength and the *FWHM* depend both on θ and on the solid angle inside which the light is collected. The spectra in figure 4 are measured using an integrating sphere, thus collecting all the light emitted by the devices. If a fiber with a small numerical aperture would be used instead, a much smaller *FWHM* would be measured for the RCLED.

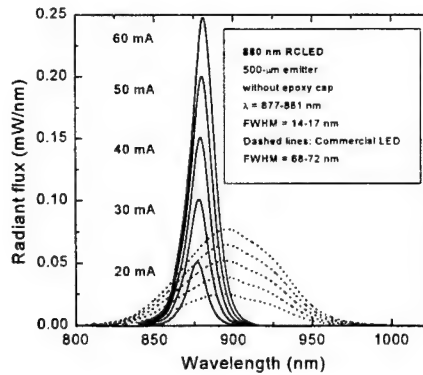


Figure 5 Electroluminescence spectra for an 880-nm RCLED and a commercial LED.

An increase in T_m caused a line shift ($\Delta\lambda$) in λ_{qw} and λ_c towards longer wavelengths. This red-shift was due to thermal expansion of the crystal lattice and a concomitant decrease in band gap, which lowered the energy states of the quantum well and broadened the cavity. The quantum well emission was shifted more than the cavity mode, forcing $\Delta\lambda_d \rightarrow 0\text{ nm}$ and leading to single-lobed emission normal to the exit window.

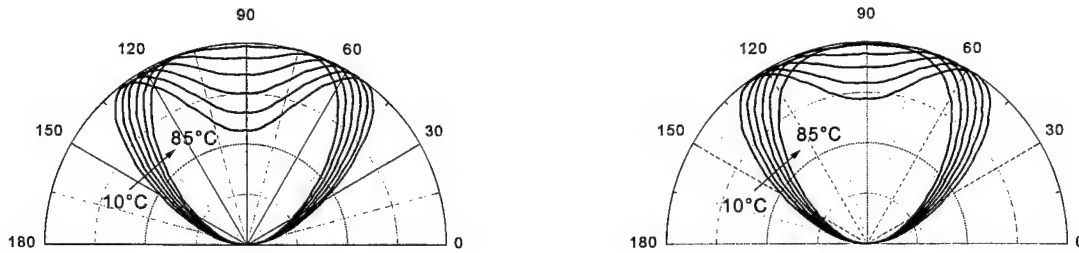


Figure 6 Far-field pattern of an 650-nm RCLED at $I_{dr} = 10$ mA (left) and $I_{dr} = 40$ mA (right) as a function of device temperature ($10 \leq T_m \leq 85$ °C, 15 °C step). The emission cone becomes remarkably narrower, as temperature is increased, improving the coupling of light into an optical fibre.

Figure 6 shows the evolution of FF for a 650-nm RCLED with an $\varnothing 84$ - μ m window in the temperature interval $10 \leq T_m \leq 85$ °C when $I_{dr} = 10$ and 40 mA, respectively. For low $T_m = 10$ °C, where $\Delta\lambda_d \gg 0$ nm, emission takes place preferably at the angle of $\pm 32^\circ$ for $I_{dr} = 10$ mA and $\pm 37^\circ$ for $I_{dr} = 40$ mA, while for $T_m = 85$ °C the angle of the lobe is zero for both drive currents. The narrower angle at higher current is a consequence of internal heating. The exact resonance at normal emission reduces η_e , which is not desired for high- T_m applications, as noted previously. Nevertheless, the fact that FF is a function of T_m and can vary tens of degrees is very useful. This is because the narrowing of FF at high T_m improves the fibre coupling efficiency and offsets, in part, a decrease in P_{out} .

This is shown in figure 7, where the output power and coupling efficiency determined for emission from the end of a fibre (1 m long 0.98 / 1.00 mm PMMA-POF, $NA = 0.5$) at $I_{dr} = 10$ –40 mA is presented. To couple the light into the fibre, a $\varnothing 84$ - μ m device having neither epoxy nor a collimating lens was placed on the optical axis of the fibre, with an air gap of ~ 1 mm between the fibre and the device. The temperature coefficient (TC) describing a change in P_{out} varies from -0.72 for $I_{dr} = 10$ mA to -0.89 %/°C for $I_{dr} = 40$ mA in the range $10 < T_m < 85$ °C. Our devices having wider far-fields ($\theta \sim 50^\circ$) exhibited somewhat smaller TC , -0.50 and -0.83 %/°C at the aforementioned currents, respectively, but due to the wider FF the coupling efficiency was poorer. All these TC s are probably too large for cost-effective POF-based data transmission systems. Therefore, a new cavity design is needed; otherwise, the system would require a receiver with a large dynamic range or a transmitter with a Peltier cooler, both solutions being expensive.

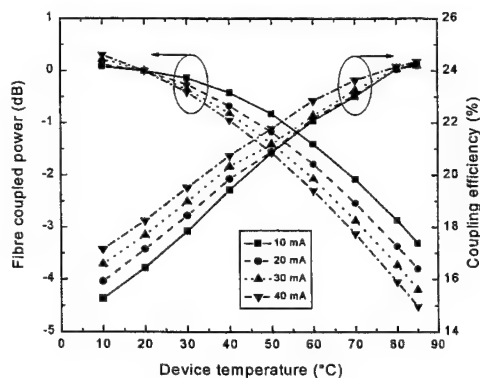


Figure 7 Fibre-coupled power (with respect to the power at 20 °C) and coupling efficiency at four different drive currents as a function of device temperature. Fibre: 0.98/1.00 mm PMMA step-index POF, $NA = 0.5$.

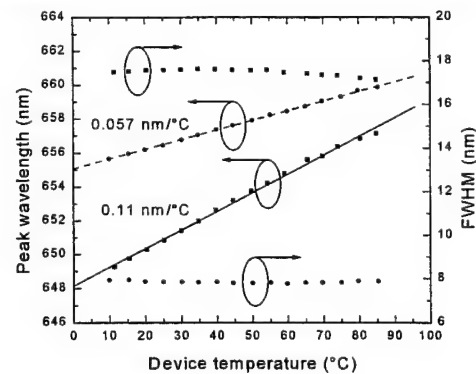


Figure 8 Peak wavelength and $FWHM$ for emission into free space (■) and for emission from the end of a POF (●).

Figure 8 displays λ and $FWHM$ plotted against T_m for emission into free space and for emission from the exit of a 1-m long fibre. The fibre-coupled spectrum exhibits longer λ . This is because of the resonant $\theta - \lambda$ dispersion relation, and because emission normal to the surface (with the longest λ) is best coupled into the fibre. The temperature gradient is reasonable, only $+0.11 \text{ nm/}^\circ\text{C}$ and $+0.057 \text{ nm/}^\circ\text{C}$ for the two cases, respectively. The $FWHM$ shows very stable temperature behavior in both cases.

Dynamic properties were studied using a network analyser, a 3 GHz bias-tee, and a Si detector equipped with a low-noise amplifier and free-space collimation optics. The detector had a modulation bandwidth of 1 GHz. To avoid the signal saturation at low bias, we used a rf modulation signal power of -15 dBm at $I_{dr} < 20 \text{ mA}$. At higher currents, a rf power of -5 dBm was applied.

Figure 9 shows room-temperature $f_{i,-3dB}$ as a function of I_{dr} . The bandwidth increased almost linearly with I_{dr} , being about 85 - 100 MHz at 15 - 20 mA and 180 MHz at 80 mA. This dependence of $f_i = f_i(I_{dr})$ can be accounted for by two major effects. Namely, it is known that the input impedance decreases, as I_{dr} is increased (this effect is important at low bias) and, secondly, the carrier lifetime decreases as the current density increases¹⁴. Adding an epoxy cap improved f_i by about 10 %, this improvement being due to enhanced heat conduction.

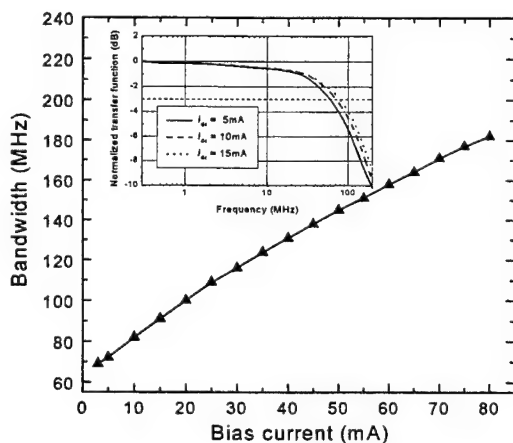


Figure 9 Modulation bandwidth of an $84\text{-}\mu\text{m}$ RCLED as a function of dc bias current. Inset shows transfer functions at three different bias currents.

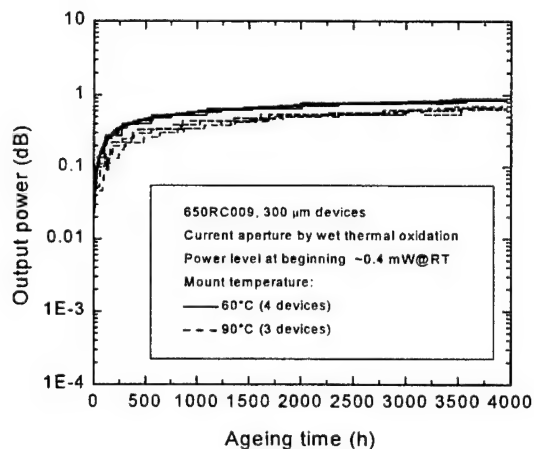


Figure 10 Accelerated ageing tests for nine $300\text{-}\mu\text{m}$ devices in a constant current mode. Neither a sudden failure nor any degradation has taken place during 27,500 device-hours on test.

Finally, we present reliability features of RCLEDs as deduced from preliminary experiments. Accelerated ageing tests on nine $300\text{-}\mu\text{m}$ devices were carried out in a constant current mode at 60°C and 90°C at initial $P_{out}(20^\circ\text{C}) \approx 0.4 \text{ mW}$. The results are shown in figure 10. No sudden unexpected failure has occurred during 27,500 device hours on test. In fact, the devices still exhibit a slight improvement in output power, likely due to a residual burn-in effect with a related reduction in non-radiative carrier traps in the quantum wells.

5. SUMMARY

We have fabricated MBE-grown, monolithical RCLEDs emitting in the 650-nm range and at 880 nm. The 650-nm RCLEDs, with measured modulation bandwidth of 180 MHz, are possible low-cost transmitter candidates for systems using plastic optical fibers (POF), such as IEEE-1394 at 100 Mb/s and 200 Mb/s and ATM at 155 Mb/s. For these devices, good beam directionality ensures efficient fiber coupling. A small temperature dependence of peak wavelength, $0.057 \text{ nm/}^\circ\text{C}$, and a nearly temperature independent $FWHM$ of $\sim 8 \text{ nm}$ were observed for POF-coupled emission. The 880-nm RCLEDs had a maximum output power of 25 mW (cw). Applications include open-air optical communication systems, collision avoidance and measurement systems. The effects of detuning on beam directionality and coupling efficiency were demonstrated. Also, the temperature and bias dependences of the devices were investigated. It was shown that increase in device temperature

significantly improves the coupling efficiency into an optical fiber. Preliminary ageing tests show very good reliability for the devices with an oxidized current aperture.

ACKNOWLEDGMENTS

This work was supported, in part, by a European Union research project (SMILED) and a Finnish national research project (SUPREME).

REFERENCES

1. E. F. Schubert, Y.-H. Wang, A. Y. Cho, L.-W. Tu, and G. J. Zyzdzik, "Resonant cavity light-emitting diode," *Appl. Phys. Lett.*, **60**, pp. 921-923, 1992.
2. E. F. Schubert, N. E. J. Hunt, R. J. Malik, M. Micovic, and D. L. Miller, "Temperature and modulation characteristics of resonant-cavity light-emitting diodes," *J. Lightwave Technol.*, **14**, pp. 1721-1729, 1996.
3. H. Benisty, H. De Neve, and C. Weisbuch, "Impact of planar microcavity effects on light extraction – Part I: Basic concepts and analytical trends," *IEEE J. Quantum Electron.*, **34**, pp. 1612-1631, 1998.
4. J. A. Lott, R. P. Schneider, Jr., J. C. Zolper, K. J. Malloy, "AlGaInP visible resonant cavity light-emitting diodes," *IEEE Photon. Technol. Lett.*, **5**, pp. 631-633, 1993.
5. M. Jalonen, J. Köngäs, M. Toivonen, P. Savolainen, A. Salokatve, and M. Pessa, "Monolithic super-bright red resonant cavity light-emitting diode grown by solid source molecular beam epitaxy," *IEEE Photon. Technol. Lett.*, **10**, pp. 923-925, 1998.
6. K. Streubel, U. Helin, V. Oskarsson, E. Bäcklin, and Å. Johansson, "High brightness visible (660 nm) resonant-cavity light-emitting diode," *IEEE Photon. Technol. Lett.*, **10**, pp. 1685-1687, 1998.
7. T. Ishigure, M. Satoh, O. Takanashi, E. Nihei, T. Nyu, S. Yamazaki, and Y. Koike, "Formation of the refractive index profile in the graded index polymer optical fiber for gigabit data transmission," *J. Lightwave Technol.*, **15**, pp. 2095-2100, 1997.
8. M. Dumitrescu, P. Sipilä, V. Vilokinen, L. Toikkanen, P. Melanen, M. Saarinen, S. Orsila, P. Savolainen, M. Toivonen, and M. Pessa, "Resonant cavity light-emitting diodes: modeling, design and optimization", SIOEL'99, SPIE 6th Symp. on Optoelectronics, Bucharest, Romania, 22-24 Sept. 1999.
9. W. Jiang, C. Gaw, P. Kiely, B. Lawrence, M. Leiby, and P. R. Claisse, "Effect of proton implantation on the degradation of GaAs/AlGaAs vertical cavity surface emitting lasers", *Electronics Letters*, **33**, pp. 137-139, 1997.
10. M. Pessa, M. Toivonen, M. Jalonen, P. Savolainen, and A. Salokatve, "All-solid-source molecular beam epitaxy for growth of III-V compound semiconductors," *Thin Solid Films*, **306**, pp. 237-243, 1997.
11. C. Dill, R. P. Stanley, U. Oesterle, D. Ochoa, and M. Ilegems, "Effect of detuning on the angular emission pattern of high-efficiency microcavity light-emitting diodes", *Appl. Phys. Lett.*, **73**, pp. 3812-3814, 1998.
12. H. De Neve, J. Blondelle, P. Van Daele, P. Demeester, R. Baets, and G. Borghs, "Recycling of guided mode light emission in planar microcavity light emitting diodes", *Appl. Phys. Lett.*, **70**, pp. 799-801, 1997.
13. G. E. Shtengel, D. A. Ackerman, and P. A. Morton, "True carrier lifetime measurements of semiconductor lasers," *Electron. Lett.*, **31**, pp. 1747-1748, 1995.

45% Quantum Efficiency Light-Emitting Diodes with Radial Outcoupling Taper

W. Schmid, F. Eberhard, R. Jäger, R. King, M. Miller, J. Joos, and K.J. Ebeling

Department of Optoelectronics, University of Ulm, D-89069 Ulm, Germany

ABSTRACT

We have investigated efficient light outcoupling from light-emitting diodes (LEDs) by introducing lateral tapers. The concept is based on light generation in the very central area of a circularly symmetric structure. After propagating between two highly reflecting mirrors light is outcoupled in a tapered mesa region. By proper processing we achieve quantum and wallplug efficiencies of almost 30% for outcoupling via a planar surface or, respectively, 45% and 44% for encapsulated devices.

Keywords: Light-emitting diodes, high-efficiency, thin-film, outcoupling taper

1. INTRODUCTION

One of the cardinal problems limiting the performance of light emitting diodes (LEDs) is their low external efficiency caused by total internal reflection of light in semiconductor material. Various approaches already exist to overcome this problem. Among those are resonant cavity LEDs with their modified internal direction of spontaneous emission,^{1,2} surface textured devices with a back side mirror where photons repeatedly try to escape,^{3,4} or the use of transparent substrates.^{5,6} We introduced a new method of efficient light outcoupling from light-emitting diodes by introducing lateral tapers.⁷ The concept is based on light generation in the very central area of a circularly symmetric structure. After propagating between two highly reflecting mirrors light is outcoupled in a tapered mesa region. In this paper we present a systematic improvement of our devices leading to record high 45% and 44% quantum and wallplug efficiencies, respectively. Devices studied use InGaAs active quantum wells and GaAs cladding layers. Emission occurs at 980 nm wavelength.

2. PRINCIPLE OF OPERATION

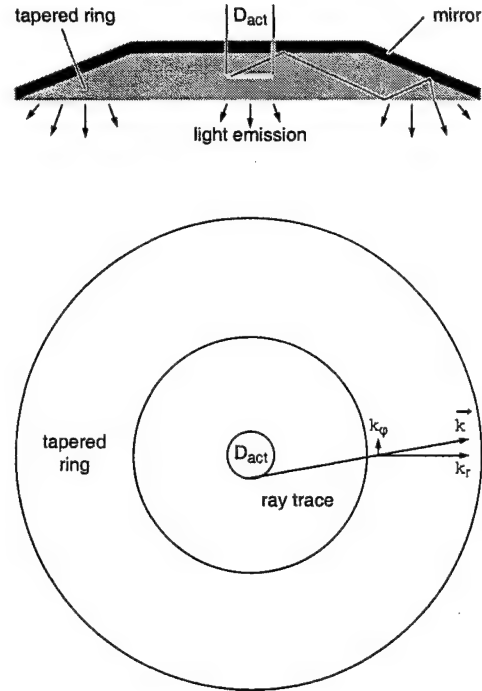
Fig. 1 shows the general structure of the devices studied. The active area is restricted to the center of a circularly symmetrical structure and surrounded by a tapered ring. The generated light is intended to couple out at the lower semiconductor surface.

Light can only escape the semiconductor for a small incident angle to the surface. In terms of wave vector \vec{k} the in-plane part has to be small, i.e.

$$\sqrt{k_{\varphi,\text{in}}^2 + k_{r,\text{in}}^2} \leq |\vec{k}_{\text{out}}| ,$$

where $k_{\varphi,\text{in}}$ and $k_{r,\text{in}}$ are the azimuthal and radial component inside the semiconductor, respectively, and \vec{k}_{out} is the wave vector outside. Since outcoupling requires both components to be small only a negligible part of light is emitted directly below the active area. The major part of the generated light undergoes total internal reflection and is guided to the taper using an effective back-side reflector. Since the azimuthal component is inversely proportional to the distance from the center it is kept small simply by restricting the active area. The radial component is reduced by successive reflections at the taper surface. Therefore, each initial elementary ray can contribute to the optical output power. A more detailed description is presented in⁷ where rough design rules are given.

Figure 1. The upper part indicates the simplified cross-sectional structure of the circularly symmetrical device investigated. The semiconductor has a shape of an extremely flat truncated cone, which is covered by a mirror. The light is guided radially towards a taper where it is redirected. Outcoupling is only effective when light hits the taper surface with small azimuthal wave vector component k_ϕ . The lower sketch indicates that this condition is simply met by restricting the cross section of the active area.



3. DEVICE PROCESSING

Fig. 2 shows the processing route to form the tapered structure. After MBE growth a few hundred nm thick pedestal with the outer diameter corresponding to the intended device is wet chemically etched. Photoresist is deposited and circularly structured with a slightly smaller size. In a reactor with a well defined temperature and organic solvent concentration the photoresist reflows to the edge of the pedestal and takes a lens shaped form due to surface tension.⁸ Using ion beam etching with low selectivity the structure is partially transferred into the semiconductor. The remaining photoresist is removed leading to a flat top surface surrounded by a tapered ring as shown in the SEM picture in Fig 3.

For further processing we refer to Fig. 4. A GeNiAu metallization is deposited on the outer n-type part of the taper serving as n-contact. Since the reflectivity of the contact metallization is low only a small fraction, more precisely a quarter of the ring is covered by the metal. The p-type contact is realized as a small circle on the center of the top surface. Moderate p-doping and high n-doping levels of the cladding layers prevent current spreading in

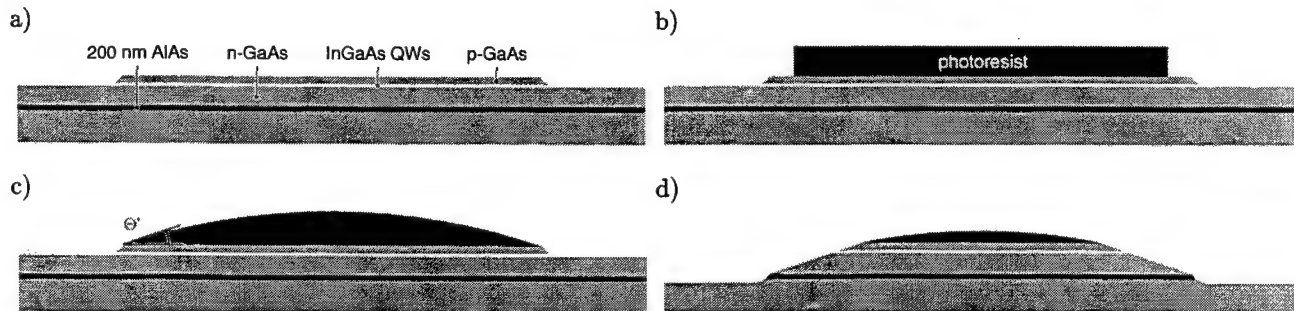


Figure 2. Processing steps to achieve a tapered structure. After wet-etching of a 300 nm pedestal in the upper p-type GaAs cladding layer (a) a structured photoresist (b) becomes lens-shaped after treatment in a solvent atmosphere (c). Using chemical-assisted ion-beam etching (CAIBE) the structure is partly transferred into the semiconductor.

the active layer. Light generation occurs in an area just slightly larger than the p-contact size.

For passivation of the pn-junction at the taper surface we use polyimide layers which are opened at the central p-contact area. As shown later, outcoupling is improved by thin polyimide layers. However, the typical thickness of 400 nm is not sufficient to passivate the n-contact. Therefore, we have to avoid lateral overlap of the following mirror metallization with the n-contact, as indicated in Fig. 4b. Fig. 4c illustrates that a second thicker passivation layer is used to cover the n-metallization. The thickness of a top metallization is galvanically increased to form a quasi substrate. After gluing the wafer upside down on a glass carrier, the substrate is chemo-mechanically thinned down to 50 μm . Finally the substrate is selectively etched with an $\text{H}_2\text{O}_2:\text{NH}_4\text{OH}$ solution where the pH is adjusted to 8.1.⁹ In this way the n-contact appears at the surface and can be used for independent addressing current supply.

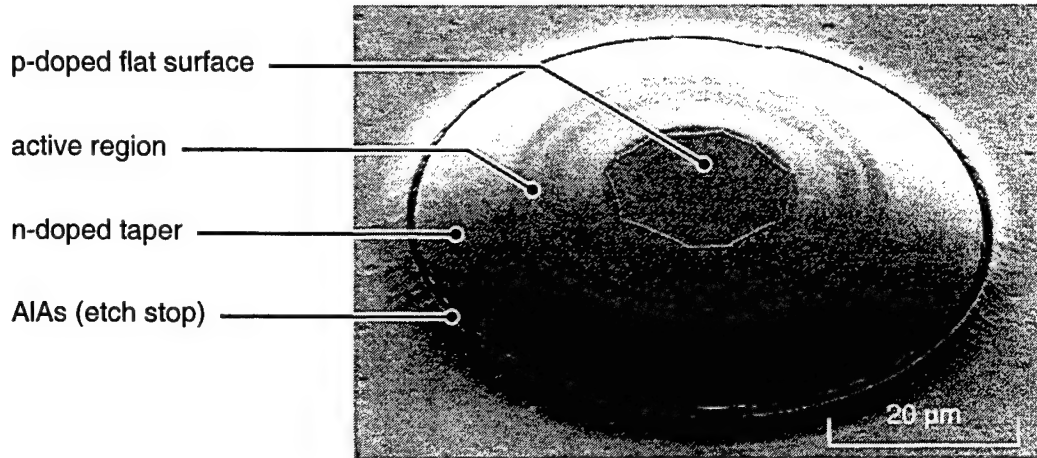


Figure 3. SEM picture of a structured semiconductor.

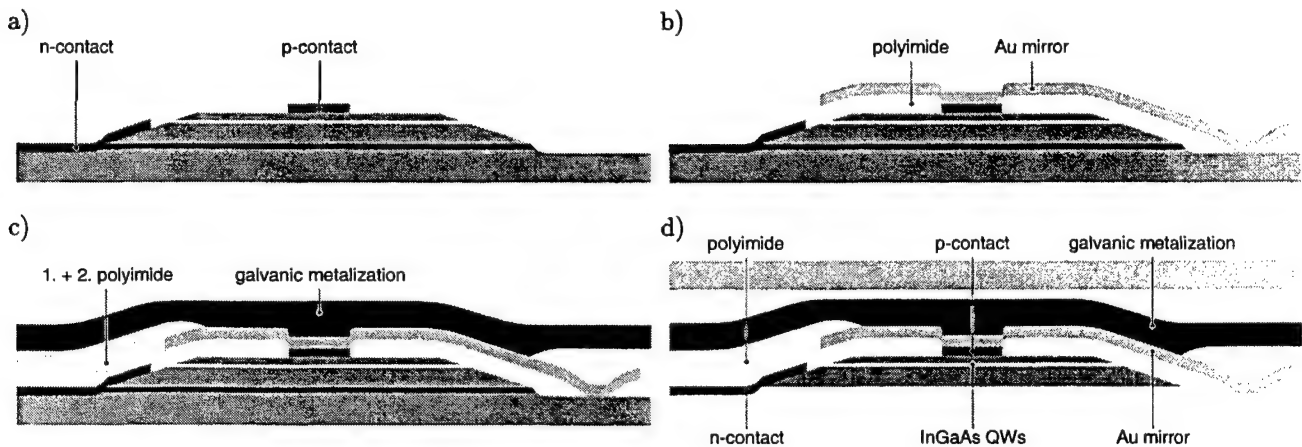


Figure 4. Remaining processing steps: (a) n- and p-contact are deposited, (b) an Au mirror is deposited onto a first passivation layer, (c) a homogeneous metallization is deposited onto a second passivation layer and galvanically enhanced, (d) substrate and etch stop layer are removed.

4. OPTIMIZATION OF EFFICIENCY

Early devices based on lateral taper outcoupling have shown quantum and wallplug efficiencies of about 15%.⁷ Here we want to show our systematic improvement of the device characteristics. We consider p-type contact, advanced passivation technique, lateral device size, and number of active quantum wells.

For measurement of the optical output power we use an integrating sphere. The spectrum is recorded with a conventional spectrum analyzer. For simple calibration we take the sensitivity of the photodiode-sphere system at the peak wavelength. Since the spectrum has a large short wavelength tail this method is not very precise. The calculated efficiencies are therefore not very accurate but nevertheless should give a good indication of the relative influences of various processing methods.

For comparison a state-of-the-art device was analyzed at OSRAM, Regensburg, using a calibrated power meter which takes the shape of the spectrum into account. As shown in Section 5 this analysis leads to optical output powers being about 10% larger than in preliminary measurements. The efficiencies given in this section may therefore be only 90% of calibrated figures.

4.1. P-type contact

Since lateral current confinement is realized by suitable doping of n- and p-layers, the p-contact has to be close to the active area. The usual Ti/Pt/Au contact metallization shows low reflectivity, i.e. 40% for a Ti thickness of 10 nm¹⁰ or 17% for a thickness of 15 nm (own measurements). Therefore we expect considerable re-absorption of light lowering the efficiency.

In order to estimate the influence, a sample was partially covered during Ti/Pt/Au p-contact deposition. Subsequently we deposited pure Au onto the primarily unmetallized structures. In this way same processing of the remaining steps is ensured. Fig. 5 compares output characteristics of both kinds of devices. The influence on the IV-characteristics is negligible. While the Ti/Pt/Au-contacted devices have maximum quantum efficiencies η_q of 15% the high reflectivity of Au raises quantum efficiencies up to 18%. It is to be mentioned that Au can diffuse in GaAs and therefore reduce long term stability. A better choice might be a highly reflective non-diffusing material with good adhesion.

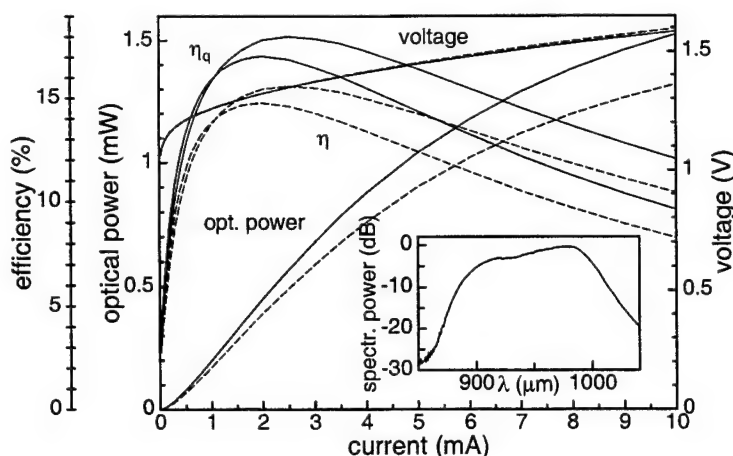


Figure 5. Comparison of 100 μm devices with conventional Ti/Pt/Au-p-contact (dashed line) and Au-p-contact (solid line). The increased efficiency of the latter device clearly shows the improvement of using highly reflecting p-metallization.

4.2. Passivation

The upper left sketch in Fig. 6 illustrates strong parasitic waveguiding of polyimide passivation. This undesired effect is additionally enhanced since planarising polyimide increases its thickness especially in the critical area at the tip of the outcoupling taper. The guided light is absorbed in the adjacent Au mirror and therefore can no longer contribute to the optical output power.

In order to reduce waveguide absorption two modifications were introduced. First, polyimide of very low viscosity was used to obtain thin passivation layer as indicated in the lower left part of Fig. 6. * Second, finite lateral extent of the passivation layer results in additional light ejection by endfire-like radiation. The CCD picture in Fig. 6 of a device under operation therefore shows a second luminous ring. The efficiency is improved to nearly 22% for a 100 μm diameter device.

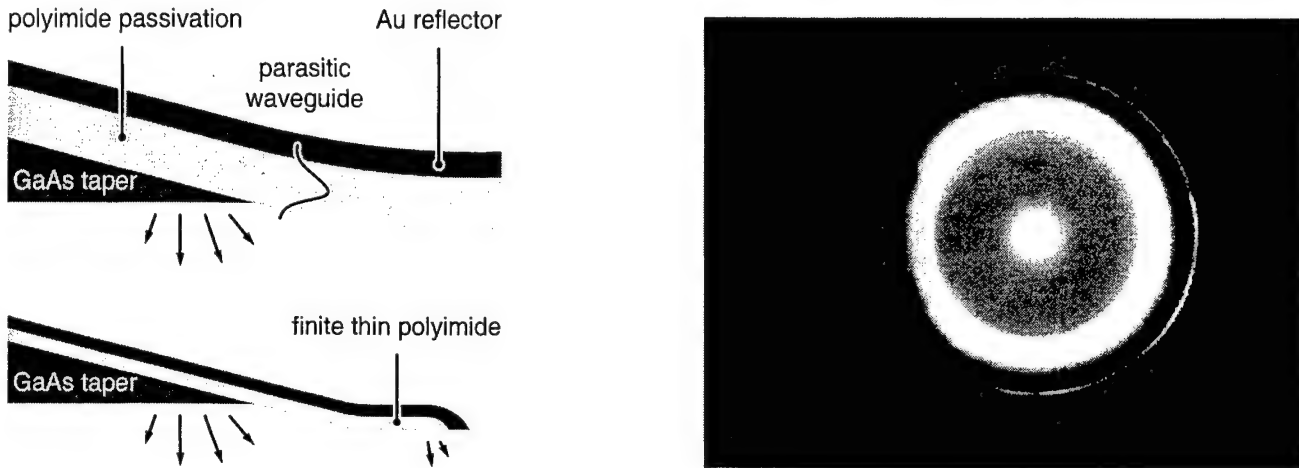


Figure 6. The upper left hand picture illustrates parasitic waveguiding in the polyimide passivation layer. The influence of waveguide absorption is reduced when polyimide is of finite lateral extent and has a smaller thickness as indicated in the lower left part. In the CCD scan in the right hand part a second illuminating ring appears due to the finite polyimide diameter. The darker area in the left part of the ring results from the lower reflectivity of the n-contact.

4.3. Lateral size of devices

As shown in section 2, efficient outcoupling requires a small azimuthal component of the wave vector, to be realized by a small ratio of active to overall diameter. In our devices we use p-contacts with 20 μm diameter to restrict the active area. Further lowering of the contact area is not suitable since current spreading would avoid effective reduction of active area but series resistances would increase. A better way is to enlarge the overall lateral size.

In earlier studies⁷ we already presented output characteristics in dependence on up to 100 μm device diameter. Since we did not observe saturation of the maximum efficiencies versus diameter up to these sizes, larger devices were fabricated. Fig. 7 shows output characteristics for devices of 100 to 140 μm diameter. As expected, for the largest devices the highest quantum and wallplug efficiencies are achieved with values of 26% and 25%, respectively. Measurements show that the increase of efficiency starts to saturate for devices in the 140 μm range. In the future, new masks have to be designed to study size dependence in even more detail.

An obvious advantage of larger devices is the reduced saturation of output power for higher currents. This behavior can be explained by different effects. Thermal conductivity to the homogeneous top metallization increases with overall lateral size. Lower temperature means lower leakage current over non-perfect heterobarriers and therefore larger internal efficiencies. Also the extraction efficiency of a large device is less sensitive to the slight increase of the effective active diameter occurring for increased currents.

* Spinning with 8000 rpm of modified polyimide on planar GaAs leads to a residual thickness of 400 nm after curing.

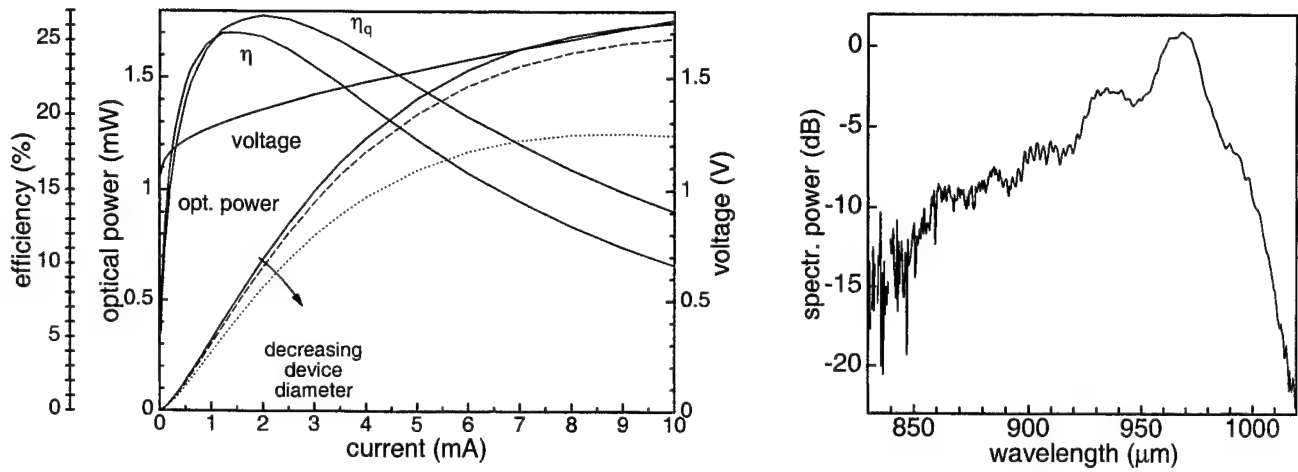


Figure 7. The left hand part shows output characteristics for devices of 100 (dotted), 120 (slashed) and 140 μm diameter (solid). The emission spectrum at 4 mA for the 140 μm device is shown in the right hand part.

4.4. Number of quantum-wells

Fig. 8 shows a comparison of light-emitting diodes with one or two quantum wells (QW), respectively. The wafers were grown in two subsequent runs to minimize variations in the MBE system. Both kinds of devices were processed simultaneously to minimize variations in thickness for the contacts or mirrors, and so on. The current-voltage-characteristics of both devices are very much the same that we can also assume similar heating for the structures.

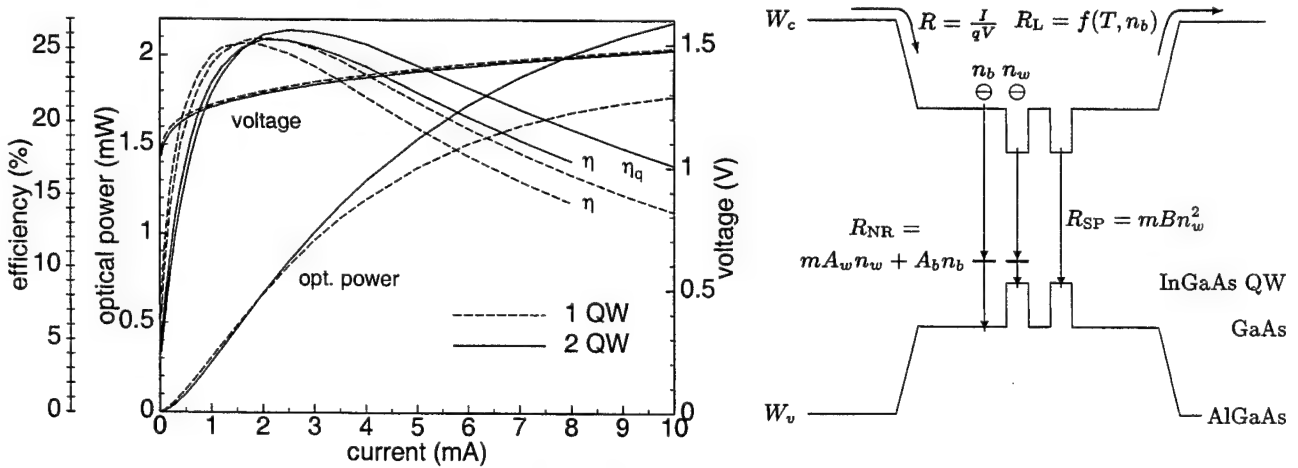


Figure 8. Output characteristics for a single (dashed) and double (solid) quantum well light-emitting diode. The different behavior is explained by the simple band diagram model shown on the right side.

While the maximum efficiency of both devices is almost the same, the 2-QW device has its optimum at larger currents and therefore for higher output power. This behavior can be explained by a simple model for internal efficiencies η_i depending on different recombination mechanisms as shown in the right hand part of Fig. 8. The overall recombination rate R of carriers per unit volume V can be divided into three terms

$$R = R_{nr} + R_{sp} + R_t = \frac{I}{qV} \quad (1)$$

where I is the injection current and q is the electron charge. The non-radiative recombination R_{nr} occurs in the

quantum wells or in the barrier region and is assumed to be proportional to the carrier densities n_w or n_b , for the well or barrier region, respectively. Therefore $R_{nr} = m(A_w n_w) + A_b n_b$ where m is the number of QWs and A_w and A_b are non-radiative recombination coefficients. The leakage current over a non-perfect heterobarrier can be commonly described as a function of temperature and carrier density $R_l = f(T, n_b)$. The spontaneous emission is governed by bimolecular recombination resulting in $R_{sp} = mBn_w^2$. The internal efficiency is the ratio of radiative to overall recombination and therefore can be written as

$$\eta_i = \frac{mBn_w^2}{mA_w n_w + A_b n_b + mBn_w^2 + f(T, n_b)} \quad (2)$$

For low injection current we can neglect the leakage current and the bimolecular recombination in the denominator of eqn. (2). In this case the internal efficiency η_i can be expressed as

$$\eta_i = \frac{I}{qV} \frac{mB}{(mA_w + A_b \frac{n_b}{n_w})^2} \quad (3)$$

For non-radiative recombination taking place mainly in the QWs we have $A_b n_b \ll A_w n_w$ and $\eta_i \sim I/m$. Doubling the number of QWs leads to half the slope of efficiency for low currents to be seen in Fig. 8 for currents smaller than 1 mA.

For larger currents non-radiative recombination can be neglected. Increasing the number of QWs m the spontaneous recombination rate mBn_w^2 increases independent of the functional form of $f(T, n_b)$ and therefore the internal efficiency increases. Summarizing, larger numbers of QWs need not necessarily lead to higher efficiencies but to a shift of the optimum operation condition to higher currents and therefore higher output power.

It should be noted that this simple model neglects effects from differing injections into several QWs. To calculate external efficiencies one additionally has to consider the dependence of reabsorption on the number of QWs.

5. ENCAPSULATION

Commercial LEDs of planar geometry rely upon their efficiency from encapsulation in material with high refractive index to provide reasonably high external efficiencies. To apply encapsulation to our substratless devices minor changes in the final processing route are required. To this end the galvanic metallization is deposited with small ditches allowing separation of individual devices after removing of the substrate. The devices are mounted upside down on a TO-46 socket using silver glue or Pb/Sn solder. The n-contact is bonded to a pin. For casting we use UV sensitive glue of 1.48 refractive index. A drop of glue is simply put on the sample and hardened with UV light. Compared to epoxy casting this technique has the disadvantage of giving a not perfect hemispherical shape but handling is much easier.

Fig. 9 compares output characteristics before and after casting. Casting raises the output power by a factor of about 1.5. leading to quantum and wallplug efficiencies of about 40% applying our simple measurement method. As mentioned at the beginning of section 4 we performed calibrated optical power measurements at OSRAM which are assumed to be more accurate. These measurements result in quantum and wallplug efficiencies of 45 and 44%, respectively, which are the highest reported so far in the 980 nm emission wavelength regime. Assuming the same inaccuracy in the measurements of non-encapsulated devices quantum and wallplug efficiencies in this case should be close to 30%.

6. CONCLUSION

We have presented a detailed processing route for fabricating efficient tapered LEDs. By systematic changes of processing we have achieved quantum and wallplug efficiencies near 30% for outcoupling via planar surface. Encapsulation in a medium with a refractive index of 1.48 raises quantum and wallplug efficiencies up to 45% and 44%, respectively.

ACKNOWLEDGMENT

The authors like to thank Dr. C. Jung and M. Scheubeck at OSRAM, Regensburg, for calibrated measurements. This work is supported by the "Deutsche Forschungsgemeinschaft" under contract No. EB 83/10-1.

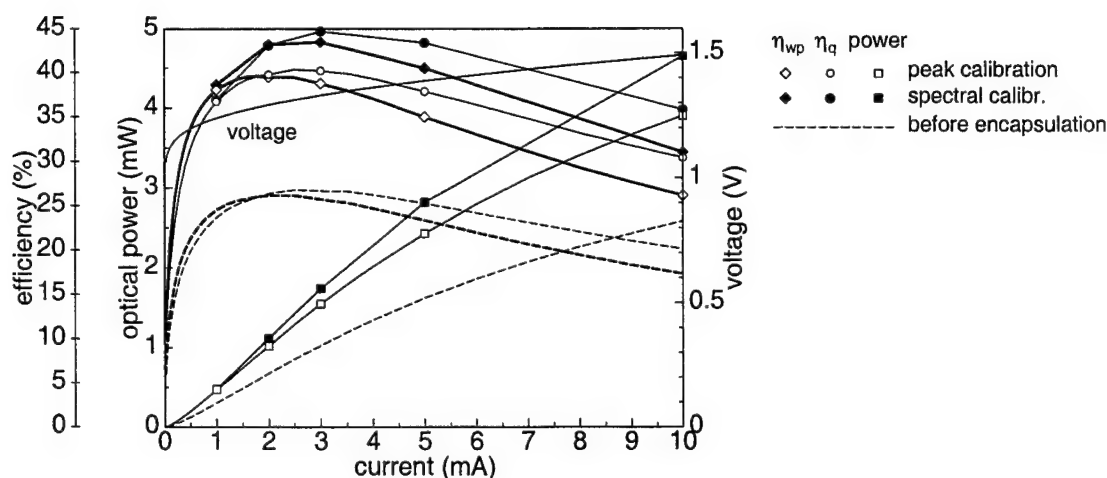


Figure 9. Device characteristics of a 140 μm diameter device encapsulated in a medium with a refractive index of 1.48. Dashed (solid) lines are characteristics before (after) encapsulation. Open symbols represent own measurements calibrated on the peak wavelength of the emission spectrum while filled symbols are more exact measurements performed at OSRAM taking the whole emission spectrum into account for calibration.

REFERENCES

1. E. F. Schubert, N. E. J. Hunt, M. Micovic, R. J. Malik, D. L. Sivco, A. Y. Cho, and G. J. Zydzik, "Highly efficient light-emitting diodes with microcavities," *Science* **265**, pp. 943-945, 1994.
2. H. D. Neve, J. Blondelle, P. van Daele, P. Demeester, and R. Baets, "Recycling of guided mode light emission in planar microcavity light emitting diodes," *Appl. Phys. Lett.* **70**, pp. 799-801, 1997.
3. I. Schnitzer, C. Caneau, T. J. Gmitter, A. Scherer, and E. Yablonovitch, "30 % external quantum efficiency from surface textured, thin-film light-emitting diodes," *Appl. Phys. Lett.* **63**, pp. 2174-2176, 1993.
4. R. Windisch, P. Heremans, G. H. Döhler, and G. Borghs, "Light-emitting diodes with 36 % external quantum efficiency operating at 600 Mbit/s," *ECOC'99 II*, pp. 306-307, 1999.
5. D. A. Vanderwater, I.-H. Tan, G. E. Höfler, D. C. Defever, and F. A. Kish, "High-brightness AlGaInP light emitting diodes," *Proc. IEEE* **85**, pp. 1752-1763, 1997.
6. M. R. Krames, M. Ochiai-Holcomb, G. E. Höfler, C. Carter-Coman, E. I. Chen, I.-H. Tan, P. Grillot, N. F. Gardner, H. C. Chui, J.-W. Huang, S. A. Stockman, F. A. Kish, and M. G. Craford, "High-power truncated-inverted-pyramid $(\text{Al}_x\text{Ga}_{1-x})_{0.5}\text{In}_{0.5}\text{P}/\text{GaP}$ light-emitting diodes exhibiting >50% external quantum efficiency," *Appl. Phys. Lett.* **75**, pp. 2365-2367, Oct. 1999.
7. W. Schmid, F. Eberhard, M. Schauler, M. Grabherr, R. King, M. Miller, E. Deichsel, G. Stareev, U. Martin, R. Jäger, J. Joos, R. Michalzick, and K. J. Ebeling, "Infrared light-emitting diodes with lateral outcoupling taper for high extraction efficiency," in *Light-Emitting Diodes: Research, Manufacturing, and Applications III*, SPIE **99 3621**, pp. 198-205, SPIE, 1999.
8. L. Erdmann and D. Efferenn, "Technique for monolithic fabrication of silicon microlenses with selectable rim angles," *Opt. Eng.* **36**, pp. 1094-1098, 1997.
9. J. LePore, "An improved technique for selective etching of GaAs and $\text{Ga}_{1-x}\text{Al}_x\text{As}$," *J. Appl. Phys.* **51**, pp. 6441-6442, 1980.
10. C.-L. Ho, W.-J. Ho, M.-C. Wu, and J.-W. Liaw, "Comparison of ingaas pin photodiodes with ti/pt/au and au reflectors," *Electron. Lett.* **35**, pp. 1767-1768, 1999.

SESSION 4

III-Nitrides and Related Materials

Highly efficient InGaN/GaN MQW for blue and green light emitting structures grown in production MOVPE reactors

Michael Bremser^{*b}, Markus Luenenbuerger^{*a}, Harry Protzmann^{*a}, Michael Heuken^{*a}

^aAIXTRON AG, Kackertstr. 15 - 17, D-52072 Aachen, Germany

^bAIXTRON Inc., 1785 Locust Street, Suite 11, Pasadena, CA 91106, USA

ABSTRACT

Normal incidence reflectivity measurements were carried out in an AIX 2000G3HT Multiwafer Planetary Reactor[®] MOVPE system, a large scale production tool for GaN-based devices, and in the single wafer AIX 200 RF system. In situ monitoring was used to investigate nucleation behaviour, temperature dependence of GaN growth, and the deposition of GaN/InGaN multi-quantum wells, especially the quality of interfaces. The obtained results were compared with RT photoluminescence, and high resolution X-ray measurements. The optimised SQW and MQW structures were embedded in Si and Mg doped cladding layers. Contacting the layers with simple metal electrodes without any contact processing results in an intense green electroluminescence. Electroluminescence test structures emitting at 540nm show minimum forward voltages around 4V with a current of 20 mA. Since no contact technology is applied this is a proof of high p-type doping and excellent structural properties of the InGaN. We found a standard deviation of the wavelength at about 533nm of less than 1% across the wafer. Since these results were reproducibly obtained for structures emitting in the blue or green the basic demands of a reliable production equipment are fulfilled:

- a) high precursor yield (typical 20% for the Ga source)
- b) uniformity of electrical and optical performance
- c) demonstration of electroluminescence with high efficiency.

Keywords: MOVPE, GaN, InGaN, Planetary Reactor, Uniformity, Multiwafer, blue LED, green LED

1. Introduction

Due to the increasing interest in group-III-nitride based devices on the optoelectronic market we have investigated the structural and optical properties of InGaN/GaN-SQW and MQW structures. As these structures are the active layers of most optoelectronic applications like light emitting diodes and lasers [1,2], we have to focus on quantum efficiency of these layers with respect to radiative QW-emission and reduction of non radiative recombination paths. Hence, we have investigated the temperature regime as well as the interface treatment for bright and long wavelength emission. An extended structural investigation as well as in-situ monitoring was helpful to understand the growth mechanisms.

2. Experimental

All layer growth was performed on 2" sapphire substrates of c-plane orientation. Before growth of the low temperature GaN nucleation layer with a thickness of about 20 nm the wafers were pre-treated by a desorption step at high temperatures under H₂ as carrier gas. For this study we were using an AIX 2000G3 system in 6x2" configuration which provides unique uniformity capabilities due to the two fold rotation of the substrates. Using an RF-heating principle in combination with a very low thermal mass we are able to use heating rate of 3°C/s which allow growth interruption

Correspondence:

^aTel: +49(241)8909-0, Fax: +49(241) 8909-40, E-Mail: heu@aixtron.com

^bTel: +1(626)577-8618, Fax: +1(626) 577-8217, E-Mail: mb@aixtron.com

times in the QW-structure of less than 150 seconds, while the corresponding cooling time is below 120s. Pre-reactions are neglected by using an injection cone which separates the NH_3 from the metalorganics until they are introduced into the reactor. Further details of the principle of the reactor are published elsewhere [3]. Epitaxial growth has been monitored by in-situ reflectance using a reflectometry system. Details of the principle are published separately [4]. The InGaN-wells were grown at 750°C at 200 mbar under N_2 as carrier gas using a total flow of 16slm. For the growth of the GaN-barriers we used temperatures in the range of 750°C to 950°C at 200 mbar and 14 slm total flow using H_2 as carrier gas. The metalorganics we used in this study were TMGa and TMIIn. n-doping of the GaN buffer was performed by using 2% SiH_4 in H_2 . Layer quality was measured by room and low temperature photoluminescence as well as by high resolution X-ray diffraction measurements [5]. RT-PL has been completely screened by full wafer mapping to get wafer uniformity information.

3. Results and Discussion

From high resolution x-ray measurements ($\omega/2\theta$) and texture analysis we know that all GaN buffer layers are of hexagonal wurtzite type. The orientation is (0001) plane parallel to the sapphire substrates. Full width at half maximum of the rocking curves of the GaN buffers are ranging around 400arcsec. Within the resolution of measurements all GaN buffer layers are fully relaxed. Typical background doping level of undoped GaN layers is $1 \times 10^{16} \text{ cm}^{-3}$ with corresponding mobility of about $250 \text{ cm}^2/\text{Vs}$. Using a growth rate of about $2 \mu\text{m/h}$ the Ga-efficiency results in about 15%. In low temperature PL we observe up to three free exciton transitions as well as sharp donor bound excitons with full widths at half maximum of about 3meV. These values are comparable to reported ones in literature [6]. Yellow luminescence emission at about 550nm which is due to deep level radiation can be suppressed by fine tuning the critical parameters such as growth temperature and V/III-ratio as well as a proper growth of the nucleation layer. The blue to yellow ratio amounts to several orders of magnitude for constant optical excitation conditions.

Having in mind that the buffer conditions are good and reproducible we have grown a series of MQW structures with different interface treatments. Reference sample was a structure using comparable conditions for the growth of GaN and InGaN. This layer was deposited without growth interruptions using 750°C at 200mbar under N_2 atmosphere. To investigate the influence of growth interruption we grew a series of samples. Starting from a sample grown with a growth interruption at the interface between GaN buffer and MQW stack we also introduced growth interruptions at all interfaces in the MQW stack. Using the in-situ growth control we were able to prove etching during growth interruption while stabilising the crystal with NH_3 [3]. This etching is a function of temperature and NH_3 flow rate. We are able to find process conditions to minimize the etching rate. The emission intensity was drastically enhanced by introduction of growth interruptions. Further enhancement of intensity could be achieved by growth of a MQW instead of a SQW. Figure 1 shows the comparison of a SQW- and a ten stacks MQW structure grown using growth interruptions at all interfaces at the MQW-stack under comparable growth conditions. The peak wavelength is constant within a accuracy of about 0.5%. The peak width at half maximum is shifting from 21.9nm (SQW) to 31.7nm (MQW). Peak intensity could be enhanced by a factor of about 20 when a MQW was grown instead of a SQW, while an enhancement of intensity by a factor of about 100 was achieved by using growth interruptions during QW growth. This demonstrates the enormous impact on reduction of non radiative centers at the interfaces when using growth interruptions. Both spectra are modulated by thin film interference signals due to mirror like surfaces. In figure 2 the high resolution x-ray spectrum of the MQW structure is depicted. One can identify the zero order peak which is due to the average In-content, as well as several satellite peaks. The number and shape of the satellite peaks is reflecting the quality of the superlattice. In the depicted spectrum we observe three satellites on each side of the zero order peak demonstrating the excellent quality of the superlattice. From the distance of the zero order peak to the GaN peak we can calculate the period D of each stack to be $D = d_{\text{GaN}} + d_{\text{InGaN}} = 11.5\text{nm}$. This is exactly the value we observed by in-situ growth control, as the total thickness of the 10x MQW stack was monitored to be about 120 nm. The strain status of the MQW systems was evaluated by reciprocal space maps around the symmetric (0002) and asymmetric (10-15) Bragg reflections. Hence, we know the discussed superlattice to be fully strained. The mean In-concentration in the whole MQW-stack is calculated to be 4.2%. From simulations we can calculate the individual thickness of well and barrier to be $d_{\text{GaN}} = 7.6\text{nm}$ and $d_{\text{InGaN}} = 3.9 \text{ nm}$. The In-concentration in the InGaN well is in this sample series about 10%. Using these deep structural investigations we can estimate an interface roughness of about 0.7nm. These extended structural investigations demonstrate the high structural quality of the MQW-structures.

The influence of barrier growth temperature on the emission wavelength was studied by a series of layers grown with different barrier temperatures in the range of 950°C to 850°C. We found an increase in emission wavelength with decreasing growth temperature of the GaN barriers. Simultaneously we found an enhancement in growth rate with lower temperatures. The wavelengths were shifted from 440 nm to 490 nm while the growth rate was enhanced by a factor of two. The increase of growth rate could be found as a consequence of reduced etching rate during growth at lower temperatures. Hence, we have a

double well width resulting in a lower quantization with corresponding red shift. This is also observed by in-situ control and proven by HRXRD measurements where we found the total stack thickness to be about 240nm. In figure 3 a full wafer PL map of a MQW structure is depicted. The average emission wavelength is 463nm with a standard deviation of 1.94nm (0.4%). By adjusting the well widths of the quantum wells we tuned the emission wavelength of the structures in the range of 420nm to 530nm. As an example for high wavelength uniformity in figure 4 a comparison of the PL-mappings of six wafers grown in the same run are depicted. The mean emission wavelength is about 500 nm. The std. dev. on a single wafer amounts to 5nm while the wafer to wafer std. dev. is around 3nm using 2mm rim exclusion, which is comparable to the run to run uniformity. For wavelengths from 500nm to 530nm the on wafer uniformity is about 8nm and the wafer to wafer uniformity is in the range of 5nm and has to be further optimised.

4. Conclusion

In summary we have investigated the influence of growth interruptions at the GaN/InGaN/GaN interfaces of SQW and MQW structures. We also studied the wavelength and intensity of the QW emission as function of barrier growth temperature. We noticed a drastic improvement of structural and optical layer quality when using growth interruptions in combination with a proper thermal management of the reactor. We were able to demonstrate 3nm std. dev. in wavelength on a single wafer and about 5nm wafer to wafer uniformity for emission wavelengths around 500 nm.

References

- [1] S. Nakamura, T. Mukai, M. Senoh, *Appl. Phys. Lett.* Vol.64, 1994
- [2] R. Beccard, O. Schön, B. Schineller, D. Schmitz, M. Heuken and H. Jürgensen *Proc. of MRS Fall Meeting*, Boston, Massachusetts, USA, Dec. 1-5, 1997
- [3] D. Schmitz, R. Beccard, O. Schön, R. Niebuhr, B. Wachtendorf, Holger Jürgensen, *MRS Internet Journal of Nitride Semiconductor Research*, Vol. 2, Article 9, 33-41, 1997
- [4] M. Lünenbürger, H. Protzmann, M. Heuken, H. Jürgensen, to be published in *Proceedings of 8th European Workshop on MOVPE and Related Growth Techniques*, Prague, June 8-11, 1999
- [5] A. Krost, J. Bläsing, M. Lünenbürger, H. Protzmann, M. Heuken, to be published in *Appl. Phys. Lett.*, 1999
- [6] S.N. Mohammed, A.A. Salvador and H. Morkoc, *Proc. of the IEEE*, Vol. 83, Mo 10, 1995

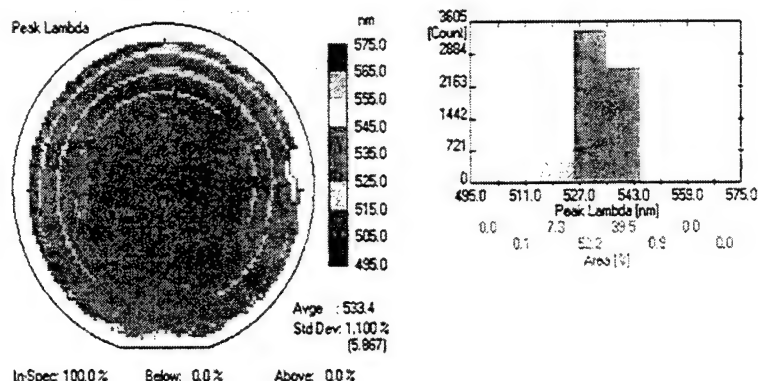


Fig. 1: GaInN MQW Structure – Peak Wavelength Mapping

Average Wavelength: 533.0 nm
Standard Deviation: 5.9 nm (1.1%)

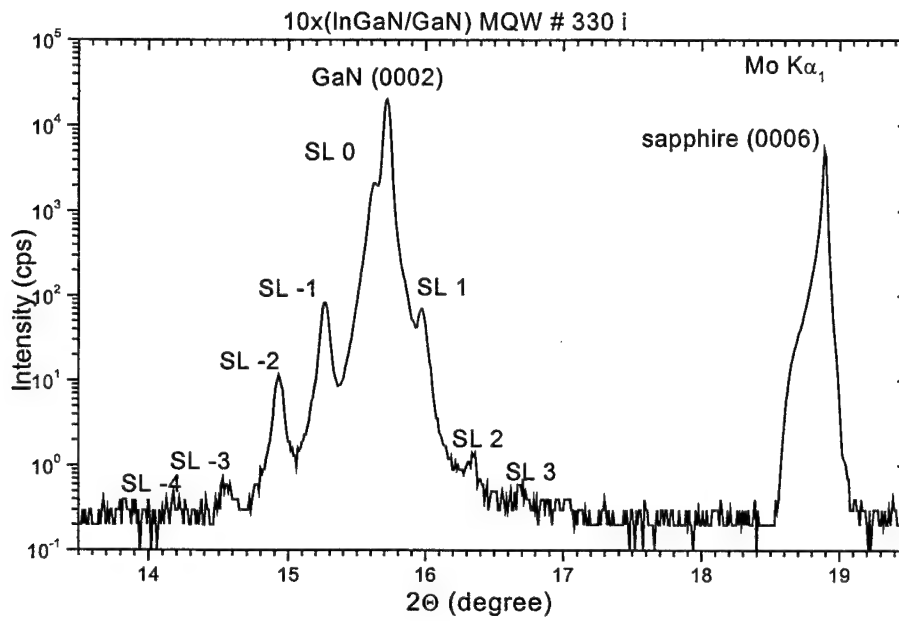


Fig. 2: $\Theta/2\Theta$ -scan of (0002) reflection of 10x(InGaN/GaN) MQW

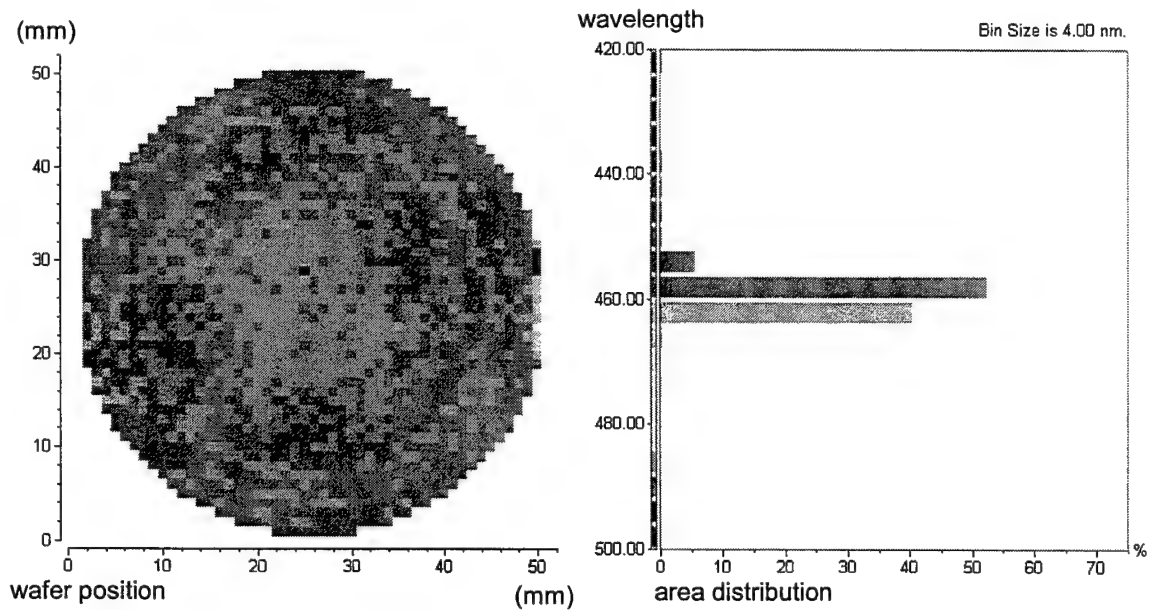


Fig. 3: mapping of the peak wavelength across a full 2" wafer of a 10 period MQW structure the average peak wavelength is 462.7 nm with a standard deviation of 1.94 nm (0.4%)

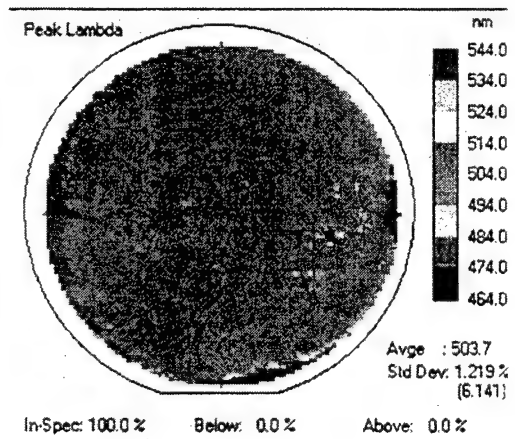
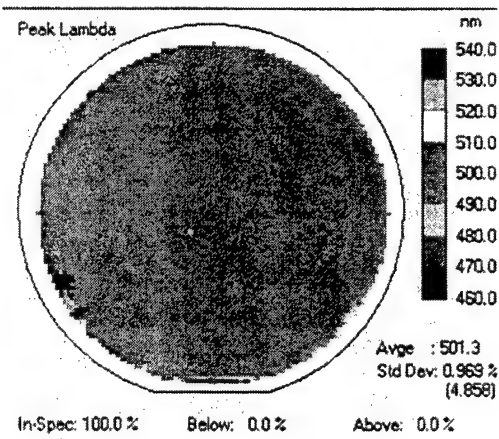
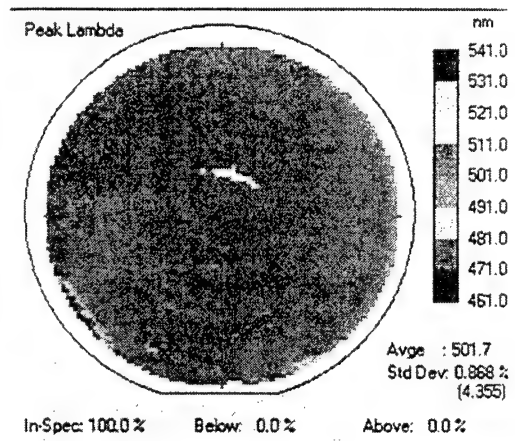
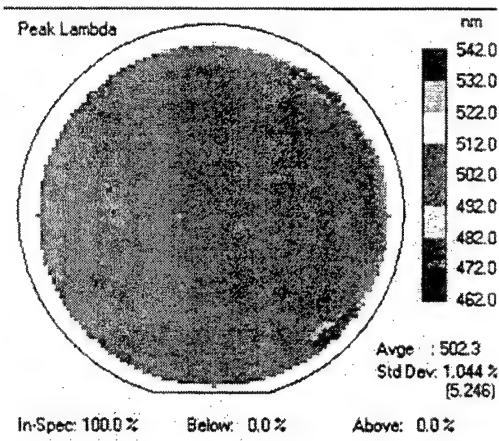
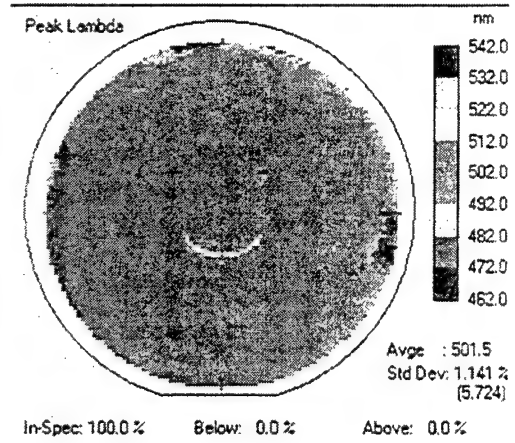
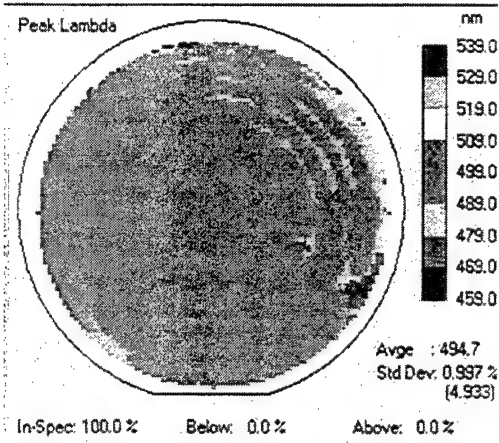


Fig. 4: 300 K PL spectra of a full loaded run of a MQW structure with mean emission wavelength of about 500 nm. std. dev. on a single wafer is about 5nm and wafer to wafer std. dev. of 3 nm.

Investigations of disorder in InGaN light-emitting diodes

Milan Pophristic^a, Stephan J. Lukacs^a, Frederick H. Long^{*a}, Chuong Tran^b, Ian T. Ferguson^b

^aDepartment of Chemistry, Rutgers University, Piscataway, NJ 08854

^bEMCORE Corporation, Somerset, NJ 08873

ABSTRACT

We have used time-resolved photoluminescence (PL), with 400 nm (3.1 eV) excitation, to examine $\text{In}_x\text{Ga}_{1-x}\text{N}/\text{GaN}$ light-emitting diodes (LEDs) before the final stages of processing at room temperature. We have found dramatic differences in the time-resolved kinetics between dim, bright and super bright LED devices. The lifetime of the emission for dim LEDs is quite short, 110 ± 20 ps at photoluminescence (PL) maximum, and the kinetics are not dependent upon wavelength. This lifetime is short compared to bright and super bright LEDs, which we have examined under similar conditions. The kinetics of bright and super bright LEDs are clearly wavelength dependent, highly non-exponential, and are on the nanosecond time scale (lifetimes are in order of 1 ns for bright and 10 ns for super bright LED at the PL max). The non-exponential PL kinetics can be described by a stretched exponential function, indicating significant disorder in the material. Stretched exponential lifetimes are consistent with a distribution of lifetimes. Typical values for β , the stretching coefficient, are 0.45 – 0.6 for bright LEDs, at the PL maxima at room temperature. We attribute this disorder to indium alloy fluctuations. From analysis of the stretched exponential kinetics we estimate the potential fluctuations to be approximately 75 meV in the super bright LED. Assuming a tunneling based hopping mechanism, the average distance between indium quantum dots in the super bright LED is estimated to be 20 Å.

Keywords: InGaN, photoluminescence, disorder, indium alloy fluctuations, stretched exponential kinetics

1. INTRODUCTION

Recently there has been world-wide interest in the use of nitride semiconductors (e.g., GaN, InN, and AlN) for opto-electronic devices such as lasers and light-emitting diodes. The large changes in physical properties such as band gap, crystal structure, phonon energy, and electronegativity difference between GaN and GaAs, demonstrate that nitride semiconductors are fundamentally distinct from traditional III-V semiconductors. In spite of the impressive progress made in recent years in the development of LEDs and lasers¹, significant work needs to be done in terms of the optimization of device performance. In order to achieve this goal, the physics underlying the operation of these devices must be better understood. Furthermore, new diagnostic techniques for the characterization of materials and devices will greatly aid in the long-term commercialization of this technology.

It has been recognized that under typical growth conditions there is a positive enthalpy for indium mixing in GaN². Electron microscopy and cathodoluminescence of InGaN has demonstrated the existence of nanometer and micron scale regions of high indium concentration³. It has been hypothesized that the nanoscale regions of high indium concentration are critical to LED operation¹. We have previously used time-resolved photoluminescence (TRPL) to investigate indium concentration fluctuations, in InGaN/GaN multiple quantum wells and LEDs^{4,5}. In

* Correspondence: Email flong@littonairtron.com, telephone 973-539-5500

this paper we discuss the result of time-resolved photoluminescence obtained from a set of LEDs with different quantum efficiencies.

2. EXPERIMENT

The light emitting diodes were grown by metal organic chemical vapor deposition at EMCORE Corp. The average indium mole fraction was about 11 %. LEDs consist of ten layers of $\text{In}_{0.11}\text{Ga}_{0.89}\text{N}$, each 35 Å thick, and nine layers of GaN, each 45 Å thick. The whole structure was on c-plane sapphire with 3 microns of unintentionally doped (n-type $5 \times 10^{16}/\text{cm}^3$) GaN as a substrate. The LEDs studied in this work were grown under slightly different conditions, leading to large changes in brightness. After final processing, the electroluminescence from samples was in order of 100 μW , 400 μW and $\geq 2 \text{ mW}$. Based on the electroluminescence efficiency we divide samples in three groups: dim, bright, and super bright LEDs.

An amplified and doubled Ti-sapphire laser from Coherent Corporation operating at 250 kHz was used. TRPL measurements were performed with a Hamamatsu streak camera (model C5680). The frequency doubling was done using a beta-barium borate (BBO) crystal. The excitation pulse was at 400 nm (3.10 eV) for time-resolved PL. Calibrated neutral density filters adjusted the excitation power used in the experiments. The typical response time was 60 ps and was determined by electrical jitter in the triggering electronics. The laser power used was 1.6 mW, $2.56 \mu\text{J}/\text{cm}^2$. The experimental setup is illustrated in Fig. 1.

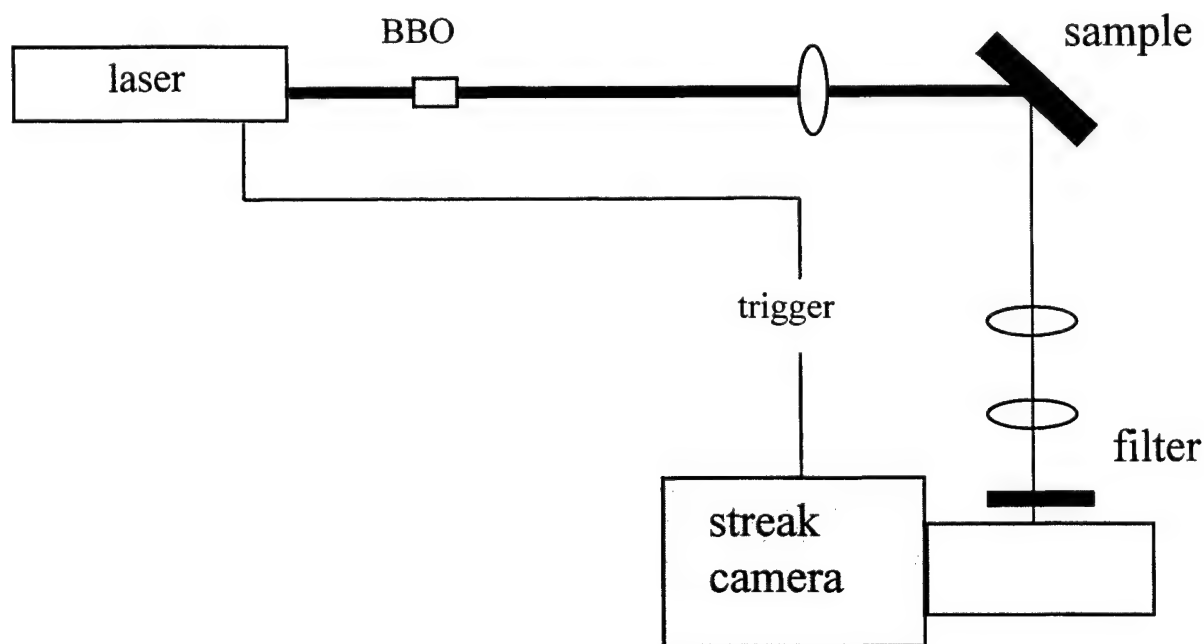


Figure 1. Experimental apparatus

The choice of using 400 nm (3.10 eV) excitation was deliberate. At this wavelength, there is not sufficient energy to excite the GaN barrier layers or the p-type and n-type layers on both sides of the multiple quantum well. By selective excitation of the InGaN active layer, we can neglect the important effects of carrier diffusion on the time-resolved photoluminescence. We have discussed some of these effects elsewhere⁶.

3. RESULTS AND DISCUSSION

3.1. Lifetime measurements

Time-resolved PL data for dim, bright and super bright LED are shown in Fig.1. The lifetime of the emission for dim LED is quite short, 110 ± 20 ps at PL maximum, and the kinetics are not dependent upon wavelength. The short lifetime and low PL intensity of dim LED are due to fast non-radiative recombination processes, which are dominant in this case. This lifetime is short compared to bright and super bright LEDs, which we have examined under similar conditions. The kinetics of bright and super bright LEDs are clearly wavelength dependent, highly non-exponential, and are on the nanosecond time scale. The lifetimes are on the order of 1 ns for bright and 10 ns for super bright LED at the PL max. Such long times are consistent with carrier localization in regions of high indium concentration.

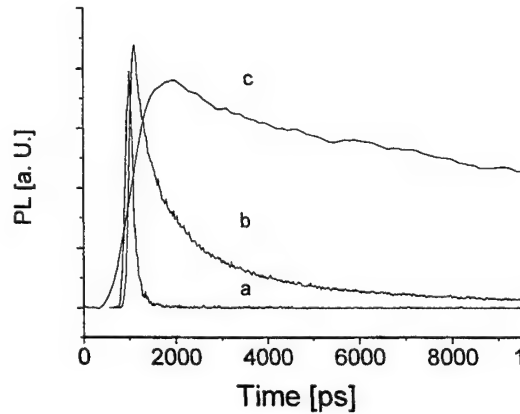


Figure 2. TRPL from a) dim, b) bright and c) super bright LED.

3.2. Stretched exponential decays

The non-exponential PL kinetics of bright and super bright LEDs, can be described by a stretched exponential function, equation 1, where β is between 0 and 1 and $I(t)$ is the PL intensity as a function of time. τ is the stretched exponential lifetime and β is the stretching coefficient.

$$I(t) = I_0 \exp\left(-\left(\frac{t}{\tau}\right)^\beta\right) \quad (1)$$

Stretched exponential decays are consistent with disorder and have been observed in wide variety of physical systems^{7,8}. There is growing evidence from our group LEDs^{4,5} and others^{9,10} that stretched exponential decays correctly describe the PL decays from InGaN under a variety of conditions. In the case of InGaN, the dominant source of disorder is alloy disorder. Results of fitting the time-resolved PL from a super bright LED to equation one are shown in Figs. 3 and 4. Both the stretched exponential lifetime and stretching parameter are dependent upon the emission wavelength. The existence of stretched exponential decays is consistent with a broad distribution of lifetimes, which must be included in the theoretical modeling of LEDs. The trends observed in Figures 3 and 4 are typical of a series of InGaN LEDs examined. The wavelength dependence of β , the stretching parameter for the super bright LED is shown in Fig. 3. We note that β is maximum at the PL maximum and

decreases at both higher and lower emission energies. Similar observations have been made by us in a series of multiple quantum wells⁵.

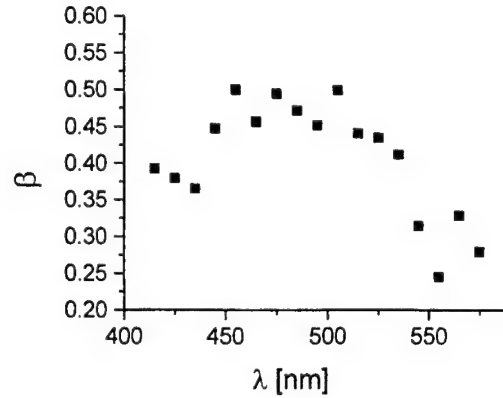


Figure 3. Analysis of the time-resolved PL from super bright LED. The stretching parameter β is clearly wavelength dependent. The stretching parameter is largest at the PL maximum of 480 nm and decreases on both the high and low energy sides of the spectra.

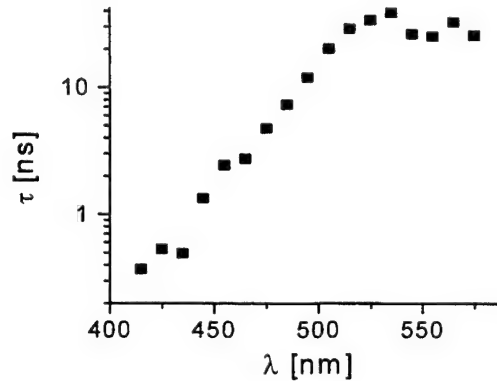


Figure 4. Analysis of the time-resolved PL from super bright LED. The stretched exponential lifetime is observed to dramatically increase as the emission wavelength is varied from 420 to 500 nm. The PL maximum is at 480 nm. Note that the vertical axis is a log scale.

By analogy with previous simulations of localized excited states in other disordered semiconductors, the wavelength dependence of β and τ , Figs. 3 and 4, imply that excited state migration is important in InGaN LEDs. The same simulations have demonstrated that, without excited state migration, β would be expected to be wavelength independent¹¹.

3.3. Distribution of lifetimes

The occurrence of stretched exponential decays is consistent with a distribution of lifetimes. Mathematically, a distribution of single exponential lifetimes is written as a convolution integral, where $\rho(\tau)$ represents the distribution of lifetimes.

$$I(t) = \int_0^{\infty} d\tau e^{-t/\tau} \rho(\tau) \quad (2)$$

This integral is mathematically equivalent to a Laplace transform. In the case of stretched exponential kinetics the equation is written

$$\exp\left(-\left(\frac{t}{\tau_S}\right)^\beta\right) = \int_0^\infty d\tau e^{-t/\tau} \rho(\tau) \quad (3)$$

Therefore by using an inverse Laplace transform, one calculates the distribution of lifetimes for stretched exponential kinetics. This calculation can be done numerically, and is shown in Figs. 5 and 6. When β , the stretching parameter is one, the lifetime distribution is a delta function. As β becomes smaller, the distribution becomes broader. Note that the probability density, $\tau\rho(\tau)$, for the lifetime distribution is plotted on the vertical axis.

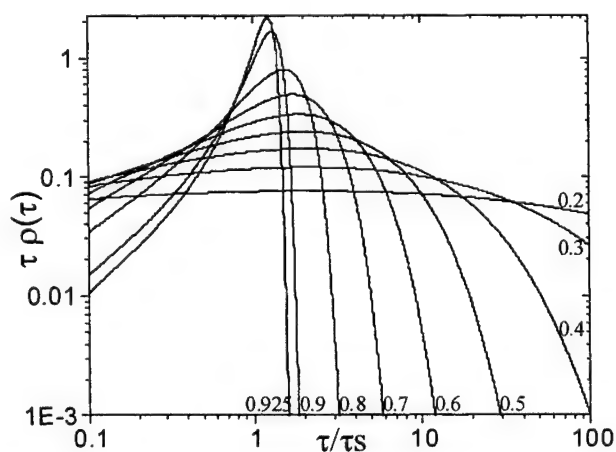


Figure 5. Distribution of lifetimes for a series of different stretching parameters, β .

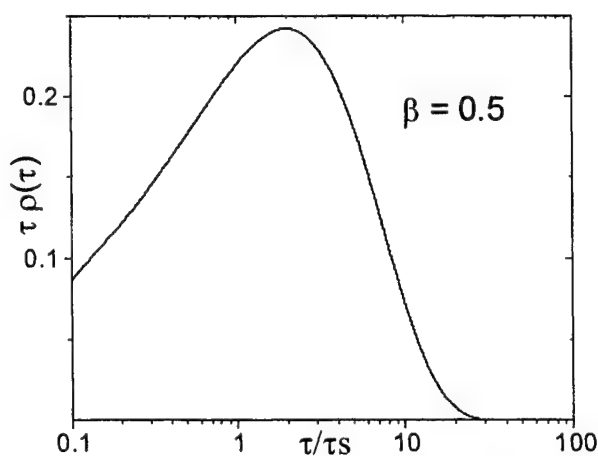


Figure 6. Distribution of lifetimes for $\beta = 0.5$, note linear vertical scale. This distribution is consistent with the room temperature operation of the InGaN superbright LEDs.

3.4. Estimate of distance between InGaN quantum dots

Fig. 3 clearly demonstrates that the stretched exponential lifetime is strongly dependent upon wavelength or emission energy. The data can be successfully fit to an exponential dependence of τ on emission energy, where ω is the emission frequency and E_0 is a parameter that depends upon the potential fluctuations associated with the disorder¹².

$$\tau(\hbar\omega) \approx \exp\left(-\frac{\hbar\omega}{E_0}\right) \quad (4)$$

For the super bright LED, E_0 was found to be 570 meV, which is much greater than the thermal energy. Similar results were obtained for several bright and super bright LEDs. It can be shown that equation 4 is consistent with a tunneling mechanism¹². We conclude that the carriers produced in the TRPL experiments migrate between different indium quantum dots by a tunneling mechanism. We can relate E_0 , an experimental parameter, to the average quantum dot size using a simple model. This can be estimated by equation 5

$$a = \frac{3\hbar}{E_0} ((E_b) / m_e)^{1/2} \quad (5)$$

where E_b is the potential difference between the InGaN quantum dot energy and the InGaN conduction band, and m_e is the electron effective mass. By using equation 5, the average tunneling distance can be estimated to be approximately 20 Å¹². Therefore the TRPL data confirms the existence and importance of nanometer scale indium alloy fluctuations on the operation of super bright LEDs. Similar results have been obtained for a series of LEDs.

3.5. Temperature dependence

Often the temperature dependence of a decay rate is given by an $\exp(-\Delta E/k_b T)$, where ΔE is the barrier height. If the material is disordered, one would expect a distribution of barrier heights. If the distribution of barrier heights is sufficiently large, one would expect to observe stretched exponential decays. This can be shown to be correct by considering a distribution of barrier heights, which is larger than kT , the thermal energy. In this case, it can be shown that stretched exponential decays occur, with β equal to

$$\beta = T/T_0 \quad (6)$$

where T_0 is the width of the barrier distribution in units of temperature⁸. Therefore temperature dependent measurements of β , the stretching parameter, allow for the direct determination of the width of the potential fluctuations associated with indium alloy disorder. Temperature dependent measurements of β shown in Fig. 7 suggest that the potential fluctuations associated with the disorder are approximately 75 meV, which is much bigger than thermal energy at room temperature (25 meV). This result implies that the excited states are heavily localized in the LED. Furthermore, the magnitude of the potential fluctuations in the super bright LED are much larger than the previously examined 300 Å InGaN film, 25 meV⁶.

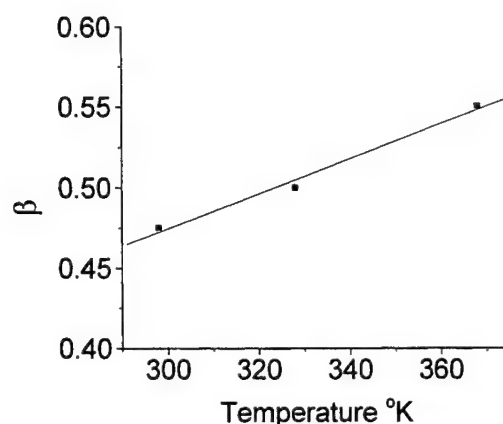


Figure 7. The temperature dependence of β at the PL maximum for the super bright LED

3.6. Importance of piezoelectric fields

It is well known that piezoelectric fields are large in nitride semiconductors and can influence optical properties. In a previous study, we examined a series of MQWs with the same physical structure but very different PL spectra and dynamics⁵. Because the piezoelectric fields are determined by physical structure, the changes in PL spectra were attributed to the dominance of indium alloy fluctuations in our samples. Theoretical calculations suggest that the piezoelectric fields are too small to cause the large PL linewidths in our experiments¹³. Furthermore, the large PL linewidths in the InGaN LEDs are hard to explain with piezoelectric fields, especially when compared to GaN, where similar piezoelectric fields are expected. In addition we mention that nanometer scale fluctuations in local indium concentration would be expected to produce variations in the local strain, thereby producing random local piezoelectric fields that would be another source of disorder.

4. CONCLUSIONS

In summary, we have used TRPL to examine wafers of InGaN LEDs before the final stages of processing. We have found that in the bright and super-bright LED examined, PL lifetimes at room temperature were on the nanosecond timescale. The PL kinetics were strongly dependent upon the emission wavelength and were well described by a stretched exponential. Both observations are strong experimental evidence for the importance of disorder in actual light emitting diodes. An analysis of the data based on this hypothesis confirms the existence and importance of nanometer scale indium alloy fluctuations on the operation of super bright LEDs.

ACKNOWLEDGEMENTS

We would like to thank EMCORE Corporation for partial support of this work.

REFERENCES

1. S. Nakamura and G. Fasol, *The Blue Laser Diode*, Springer, New York, 1997.
2. I.-H. Ho and G. B. Stringfellow, "Solid Phase immiscibility in GaInN," *Appl. Phys. Lett.* **69**, pp.2701-2703, 1996.
3. M. D. McCluskey, L.T. Romano, B. T. Krusor, D.P. Bour, N.M. Johnson, and S. Brennan, "Phase separation in InGaN/GaN multiple quantum wells," *Appl. Phys. Lett.* **72**, pp. 1730-1732, 1998.
4. M. Pophristic, F. H. Long, C. Tran, I. T. Ferguson, and R. F. Karliceck, Jr., "Time-resolved photoluminescence measurements of InGaN light-emitting diodes," *Appl. Phys. Lett.* **73**, pp.3550-3552, 1998.
5. M. Pophristic, F. H. Long, C. Tran, I. T. Ferguson, and R. F. Karliceck, Jr., "Time-resolved photoluminescence measurements of quantum dots in InGaN multiple quantum wells and light-emitting diodes," *J. Appl. Phys.* **86**, pp.1114-1181, 1999.
6. M. Pophristic, F. H. Long, C. Tran, I. T. Ferguson, and R. F. Karliceck, Jr., "Time-resolved photoluminescence measurements of InGaN light-emitting diodes, films and multiple quantum wells," *Proceedings of SPIE* **3621**, pp.64-72, 1999.
7. M. F. Shlesinger, "Fractal Time in Condensed Matter," *Ann. Rev. Phys. Chem.* **39**, 269-290, 1988.
8. H. Scher, M. F. Shlesinger, and J. T. Bendler, "Time-scale invariance in transport and relaxation," *Phys. Today* **44**, pp.26-34, 1991.
9. A. Vertikov, I. Ozden, and A. V. Nurmikko, "Diffusion and relaxation of excess carriers in InGaN quantum wells in localized versus extended states," *J. Appl. Phys.* **86**, 4697-4699, 1999.
10. T. Y. Lin, J. C. Fan, and Y. F. Chen, "Effects of alloy potential fluctuations in InGaN epitaxial films," *Semiconductor Science & Technology* **14**, pp.406-411, 1999.
11. S. Sawada, N. Hamada, and N. Ookubo, "Mechanisms of visible photoluminescence in porous silicon," *Phys. Rev. B* **49**, pp. 5239-5245, 1994.
12. J. C. Vial, A. Bsiesy, F. Gaspard, R. Herino, M. Ligeon, F. Muller, R. Romestain, and R. M. Macfarlane, "Mechanisms of visible-light emission from electro-oxidated porous silicon," *Phys. Rev. B* **45**, pp.14171-14176, 1992.
13. A. N. Cartwright, *private communication*.

Optical properties of AlN/sapphire grown at high and low temperatures studied by variable angle spectroscopic ellipsometry and micro Raman scattering

C. H. Yan^a, H. Yao^{*a}, A. C. Abare^b, S. P. Denbaars^b, J. J. Klaassen^c, M. F. Rosamond^c,
P. P. Chow^c, J. M. Zavada^d

^aUniversity of Nebraska, Center for Microelectronic and Optical Material Research,
and Department of Electrical Engineering, Lincoln, NE 68588

^bUniversity of California at Santa Barbara, CA

^cSVT Associates, Eden Prairie, MN

^dUS Army European Research Office, London, UK

ABSTRACT

Variable angle spectroscopic ellipsometry (VASE) and micro Raman scattering have been employed to study the optical anisotropy and optical constants of AlN films grown at high and low temperatures (HT and LT). The AlN films were grown by metalorganic vapor phase epitaxy (MOVPE) and molecular beam epitaxy (MBE) on c-plane sapphire (α -Al₂O₃) substrates, respectively. Anisotropic optical phonon spectra of AlN have been measured along two directions so that the optical axis $\langle c \rangle$ of AlN is either perpendicular or parallel to the polarization of the incident beam. Nonzero off-diagonal elements A_{ps} and A_{sp} of Jones matrix in the reflection VASE (RVASE) measurements indicate that the $\langle c \rangle$ of AlN is slightly away from surface normal due to substrate miscut. The ordinary optical constants of both HT AlN have been determined spectroscopic ellipsometry at small angles of incidence so that the extraordinary response is greatly reduced. The film thickness along with the surface overlayer was determined via the VASE data analysis as well.

Keywords: AlN, sapphire, Raman scattering, spectroscopic ellipsometry, optical anisotropy, optical constants.

1. INTRODUCTION

The wide band gap AlN along with GaN and InN, are the important building blocks for both high temperature electronic devices and short wave-length optical emitters.^{1,2} AlN films grown on c-plane sapphire usually have wurtzite crystal structure (α -AlN), which is anisotropic (uniaxial). There are some valuable optical property studies have been carried out on textured³ and single crystal^{4,5} AlN films by various kinds of techniques. For instance, prism-coupling^{3,4} can give very accurate values of reflective index at several discrete wavelengths but lacks spectroscopic information. Transmittance and reflectance⁵ can obtain spectroscopic data but do not have enough sensitivity on surface overlayer since it does not contain the phase information. Ellipsometry, on the other hand, is an ideal choice for measuring the spectroscopic optical constants and structural parameters of thin films, especially when the films have interface or surface roughness. In this work, the ordinary optical constants of both HT and LT AlN thin films were accurately determined by transmission variable angle spectroscopic ellipsometry (TVASE) and reflection VASE (RVASE). The extraordinary optical response from the uniaxial AlN films was greatly reduced by using small angle of incidence. Small angle of incidence is also good for minimizing the error caused by the substrate miscut that can result in non-zero off-diagonal elements of Jones matrix. Surface and interface roughness were carefully considered in the VASE model analysis using the effective medium approximation (EMA).⁶

* Correspondence: Email: hyao@unl.edu; Telephone: 402-472-5914; Fax: 402-472-4732

2. Theory

2.1 Raman Scattering

The irreducible representation of Wurtzite AlN optical phonons is:⁷

$$\Gamma = A_1(z) + 2B_1 + E_1(x, y) + 2E_2, \quad (1)$$

for phonon propagating along or perpendicular to the optical axis $\langle c \rangle$. Where x, y, z in parentheses represents the directions of phonon polarization. A_1 and E_1 modes are polar modes and each split into a propagation-parallel longitudinal optical (LO) and a propagation-perpendicular transverse optical (TO) mode. The A_1 and E_1 modes are both Raman and infrared active, two E_2 modes are only Raman active, and B_1 modes are both Raman and IR silent. Therefore, there are total six active Raman phonon modes in the AlN crystal.

2.2 Generalized Ellipsometry

The variable angle spectroscopic ellipsometry is designed to accurately determine the values of two standard ellipsometry parameters ψ and Δ , which are related to the complex ratio of reflection (or transmission) coefficients for light polarized parallel (p) and perpendicular (s) to the plane of incidence.⁸ For isotropic material systems,

$$\rho = \frac{R_p}{R_s} = \tan(\psi)e^{i\Delta}. \quad (2)$$

The electric-field reflection coefficient at an incident angle of ϕ is defined as r_p (r_s) for p (s)- polarized light. They are the diagonal elements of Jones matrix.

$$[J]_{sample} = \begin{bmatrix} r_p & 0 \\ 0 & r_s \end{bmatrix} \quad (3)$$

The ψ and Δ are not only dependent on dielectric functions, also on the surface condition, sample structure, and other properties such as the optical anisotropy.

Generalized ellipsometry was first introduced by Azzam and Bashara.⁹ The recent developments makes this technique more complete and powerful.^{10,11} In a word, the Generalized ellipsometry is a technique which can be used to determined all the elements of Jones matrix of arbitrarily anisotropic and homogeneous layered systems with nonscalar dielectric susceptibilities.

For the anisotropic material system, the non-diagonal elements of Jones matrix are not necessary to be zero. In the reflection VASE configuration,

$$[J]_{sample} = \begin{bmatrix} r_{pp} & r_{sp} \\ r_{ps} & r_{ss} \end{bmatrix} \quad (4)$$

By using the same approach with considerably more algebra involved, we can still predict the ψ and Δ values, but the Fourier coefficients related to ψ and Δ become more complicated.¹² The generalized ellipsometric parameters are defined as below.

$$A_{nE} = \frac{r_{pp}}{r_{ss}} = \tan \psi_{nE} e^{i\Delta_{nE}} \quad (5)$$

$$A_{ps} = \frac{r_{ps}}{r_{pp}} = \tan \psi_{ps} e^{i\Delta_{ps}} \quad (6)$$

$$A_{sp} = \frac{r_{sp}}{r_{ss}} = \tan \psi_{sp} e^{i\Delta_{sp}} \quad (7)$$

where the A_{ps} and A_{sp} describe how much amount p- or s-polarized light becomes s- or p-polarized light after the reflection, respectively. If the optical axis is strictly perpendicular (perfect c-plane situation) to the electric field of the incident beam, the Jones matrix is strictly diagonal. While it may not true for real AlN films grown on nominal c-plane sapphire substrates since the substrates are usually miscut within 1° . The off-diagonal elements A_{ps} and A_{sp} are dependent on sample positions, angles of incidence.

3. Experiments

The Raman spectra were taken at room temperature with a SPEX 1877E triple spectrometer equipped with a liquid-nitrogen cooled CCD camera. The excitation light source was the Coherent Innova 300 Ar+ laser operating at 488 nm with the output power kept at 150 mW. A back scattering geometry was employed for all the Raman measurements.

Two identical thin AlN films (about 130 nm thick) were grown at high temperature (1070°C) side by side by MOVPE on two c-plane sapphire substrates with polished and unpolished backsides to serve the transmission type and reflection type VASE measurements. About 20 nm thick LT (525°C) GaN nucleation layers were deposited before the HT AlN growth. Another two films were grown by MBE at high (800°C) and low (400°C) temperatures with different thickness, respectively. The very thin (~36 nm) LT AlN film was grown on a one-side polished c-plane sapphire. The thickness of the MBE grown HT AlN film is about 1 μm. Both isotropic and anisotropic mode VASE measurements were performed in the energy range of 0.75 eV to 6.5 eV with a 0.02 eV increment at room temperature. The range of angle of incidence is from 20° to 80° for reflection VASE, and 0° to 30° for transmission VASE.

4. Results and discussion

4.1. Optical phonons of AlN films

Raman scattering is a nondestructive technique used to detect the lattice vibration modes related with crystal orientation and symmetry. A series of Raman scattering measurements have been carried out on various kinds of AlN samples. The optical phonon spectra of a 1 μm thick AlN film grown on c-plane sapphire at back-scattering geometry $Z(Y, Y+X)\bar{Z}$ are shown in Fig. 1(a). The solid line was obtained from the front surface, in which the optical axis $\langle c \rangle$ of AlN (and sapphire substrate) is perpendicular to the incident polarization (Y). Three AlN related optical phonon were observed under such condition including 656 cm^{-1} E_2 (high), 888 cm^{-1} A_1 (LO), and a 246 cm^{-1} E_2 (low) which is not shown in this figure. The other two phonons of 577 cm^{-1} E_g (LO) and 750 cm^{-1} E_g (LO) are due to the sapphire substrate. The dash line in Fig. 1(a) was obtained from the side cross-section surface in which the AlN optical axis $\langle c \rangle$ is parallel to the polarization of the incident laser beam. There are three new phonons appeared, 612 cm^{-1} A_1 (TO), 670 cm^{-1} E_1 (TO), and 909 cm^{-1} E_1 (LO). All the above six optical phonons measured from AlN film are in good agreement with the theoretical calculation based on the rigid-ion model.¹³ The comparison is listed in Table 1. Fig. 1 (b) is a phonon line-width comparison of HT and LT AlN films. The solid line represents the thin LT AlN (36 nm) grown by MBE; the dash line represents the thin HT AlN (130 nm) grown by MOVPE. The broadening of AlN E_2 (high) may be due to the high-density structural defects (such as group III vacancies) in LT material and the misfit dislocations due to the large lattice mismatch. It is observable that the AlN E_2 (high) in both thinner films moves to lower frequency comparing with the AlN E_2 (high) in Fig. 1 (a). This may be caused by the partial strain relaxation in stead of full relaxation in a thin lattice-mismatched film even for a thickness of 130 nm.

Table 1. Zone-center optical phonons in wurtzite AlN, in cm^{-1} .

Mode	A_1 (LO)	A_1 (TO)	E_1 (LO)	E_1 (TO)	E_2 (low)	E_2 (high)
Theory ¹²	885	614	923	668	252	660
This work	888	612	909	670	246	656

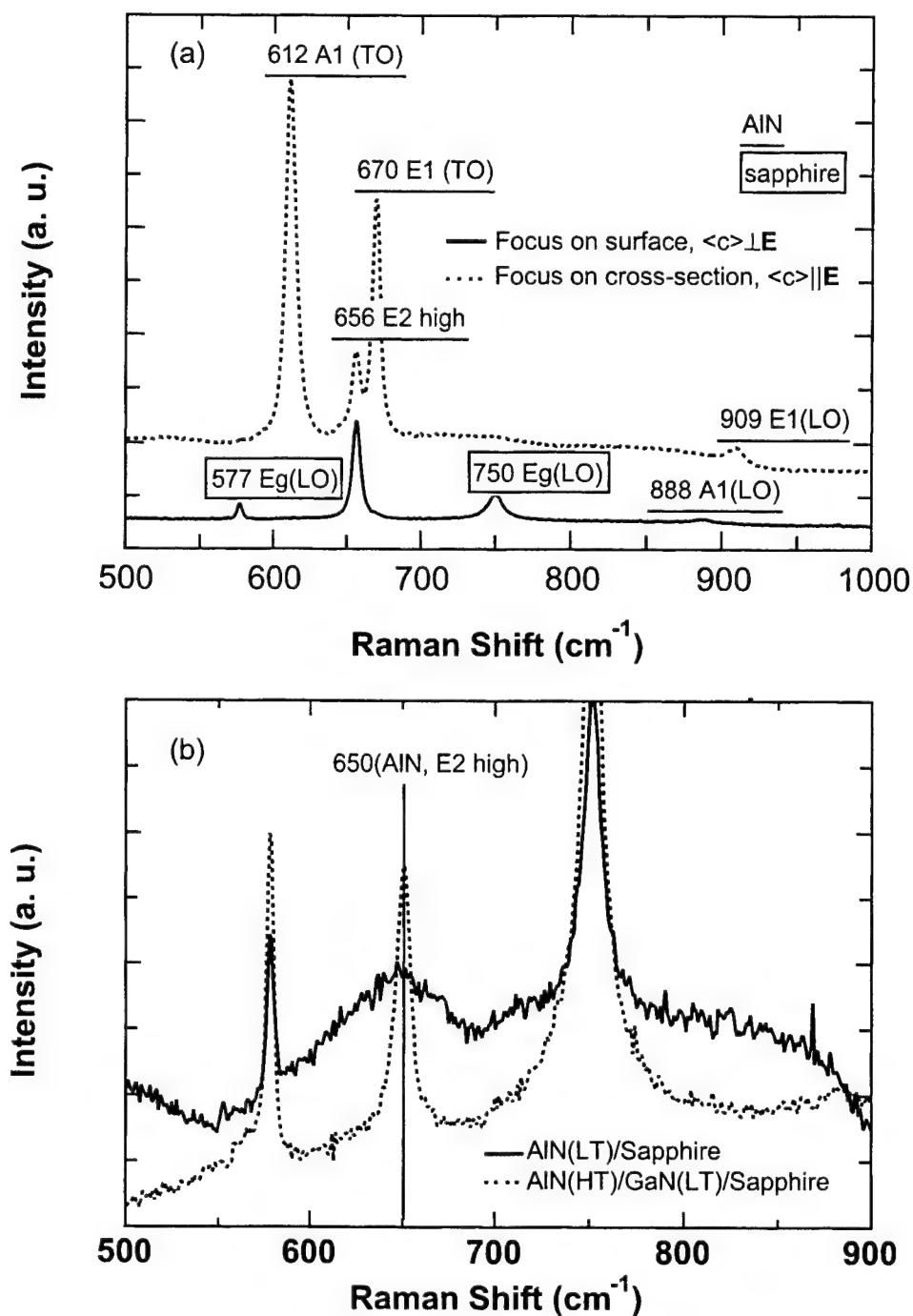


Fig. 1. Optical phonons of HT and LT AlN films. (a) 1 μm thick MBE grown HT AlN film on c-plane sapphire substrate. Solid line and dash line represent that $\langle c \rangle$ is perpendicular and parallel to the incident polarization E , respectively. (b) HT and LT thin MOVPE grown AlN films on c-plane sapphire substrates. Solid line represents 36 nm thick LT AlN film; dash line represents 130 nm thick HT AlN film.

4.2. VASE data analysis

For ideal c-plane samples, its off-diagonal element of Jones matrix must be zero as we pointed out in the theory part. But for real nominal c-plane samples, since there is a small miscut (usually within 1°) on the substrate, the off-diagonal elements

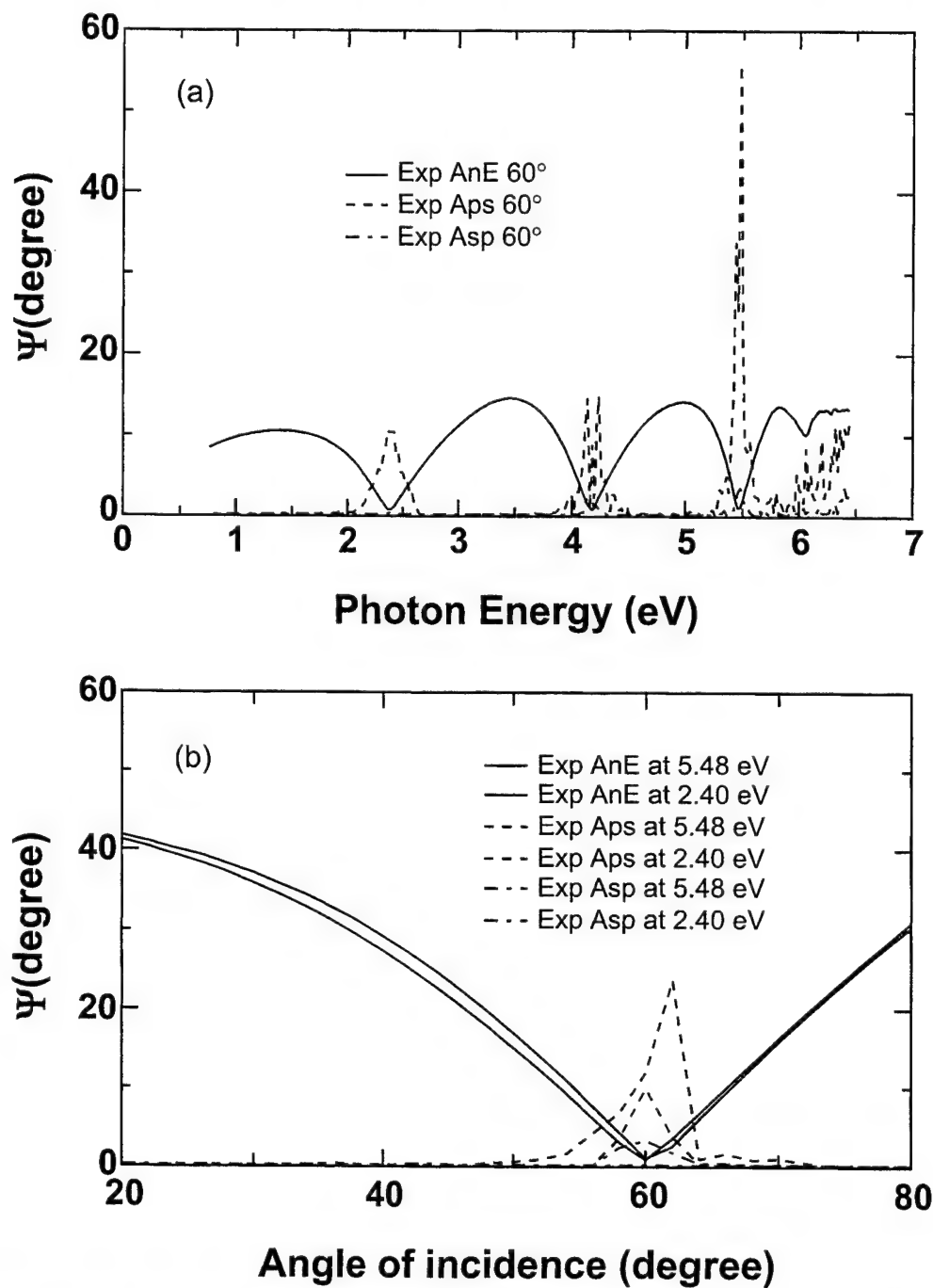


Fig. 3. Anisotropic mode RVASE data of HT AlN/c-sapphire grown by MOVPE. (a) Ψ as a function of photon energy at 60° angle of incidence; (b) Ψ as a function of incident angle at 2.40 and 5.48 eV.

may not vanish completely, as shown in Fig. 2. Fig. 2 (a) is an anisotropic mode RVASE data obtained from a 130 nm MOVPE grown AlN/c-sapphire sample. It was taken at 60° angle of incidence, which is near the pseudo Brewster angle. It can be seen clearly that the off-diagonal elements A_{ps} and A_{sp} are not negligible. The incident angular dependent measurements were made at certain wavelengths (1.4 and 5.48 eV), as shown in Fig. 1 (b). The angular increment was 1°. The off-diagonal elements are detectable in the angle range of 50° to 70°, but they are negligible at the angle of incidence below 40° or above 80°. Therefore, small angle of incidence (<40°) can be used to reduce the cross-conversion of p- to s- or s- to p- polarization caused by the <c> axis offset.

Small angle of incidence is not only good for overcoming the miscut error, but also can greatly reduce the anisotropic effect on the diagonal elements as shown in our previous GaN study.¹⁴ By using small angles of incidence, the ordinary dielectric functions of anisotropic AlN can be determined from the diagonal Jones matrix element without losing the accuracy. Thus standard ellipsometry will be suffice to determine the ordinary dielectric functions and other structural parameters.

Fig. 3 shows the nominal sample structures and the corresponding VASE analysis models. Fig 3 (a) is the structure for the two 130 nm AlN/c-sapphire structures on one-side and double-side polished substrates grown by MOVPE. The nominal thickness of the HT AlN and LT GaN nucleation layers are 130 nm and 20 nm, respectively. Fig. 3 (b) is the VASE model representing the structure in Fig. 3 (a). At the small incident angle condition, all the layers in the structure are simulated as

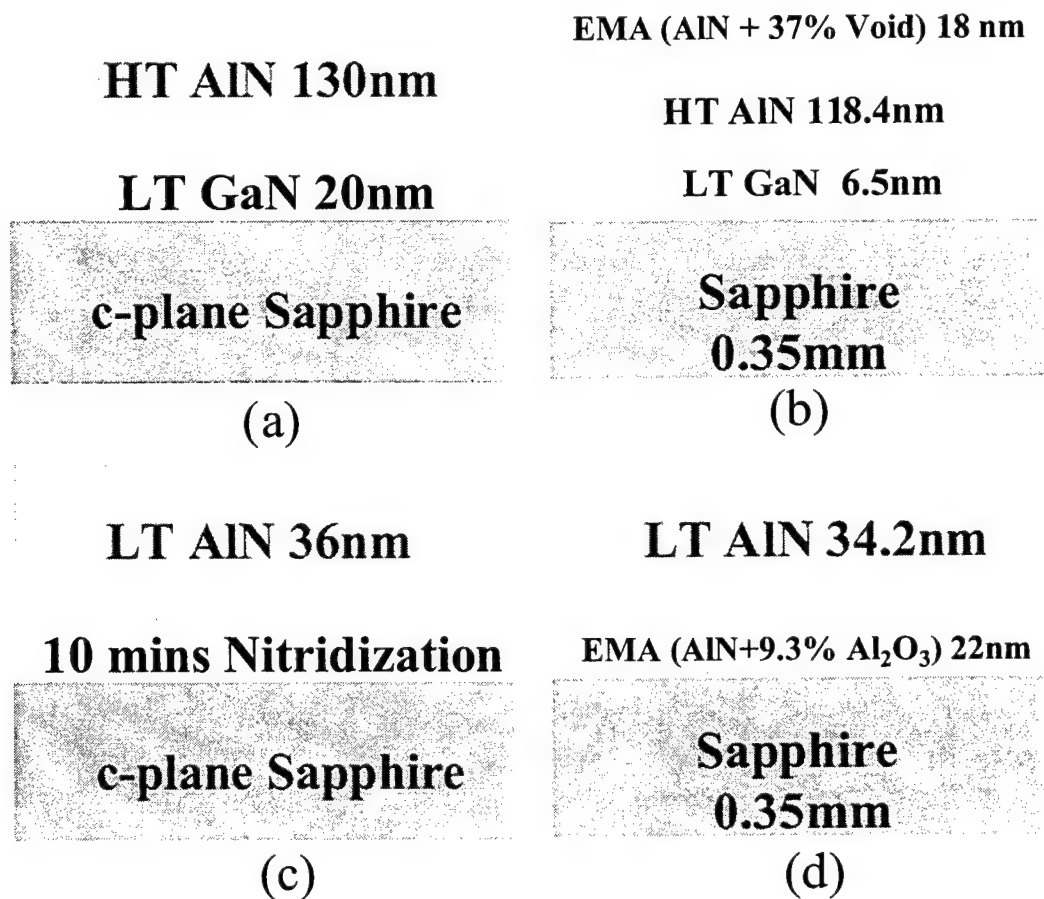


Fig. 3. AlN sample nominal structures and their corresponding VASE model. (a) Sample structure of 130 nm thick HT AlN/c-sapphire grown by MOVPE. (b) VASE model of the HT AlN/c-sapphire. (c) Sample structure of 36 nm thick LT AlN/c-sapphire grown by MBE. (d) VASE model of the LT AlN/c-sapphire.

isotropic material. The surface overlayer was modeled by an EMA layer to account for the surface oxide and roughness. The optical constants of LT GaN and sapphire used in the analysis are from our previous study. Fig. 3 (c) is the nominal structure for 36 nm LT AlN grown by MBE. Notice that there is a 10 minutes nitrogenation process before grow the LT AlN, and it was represents by a EMA layer as shown in Fig. 3 (d). The optical constants of HT and LT AlN in the model were represented by two parametric semiconductor models, which are constructed based on their critical point structures. The details about the parametric model is described in reference. 15. The thickness and EMA composition listed in the model are the best values from VASE data fitting.

The VASE data and best fit of HT AlN/c-sapphire are shown in Fig. 4. Fig. 4 (a) and (b) are ψ and Δ of TVASE at four angles of incidence (0° , 10° , 20° , and 30°). Fig. 4 (c) and (d) are the ψ and Δ of RVASE at three small angles of incidence (20° , 30° , and 40°). The two sets of ellipsometric data were coupled together during the data fitting to further reduce the correlation between the fitting parameters. The resulted AlN layer thickness is 118.4 nm with 18 nm surface overlayer. The thickness of overlayer is consistent with previous thermal stability study.¹⁶ Fig. 5 (a) and (b) show the RVASE data and

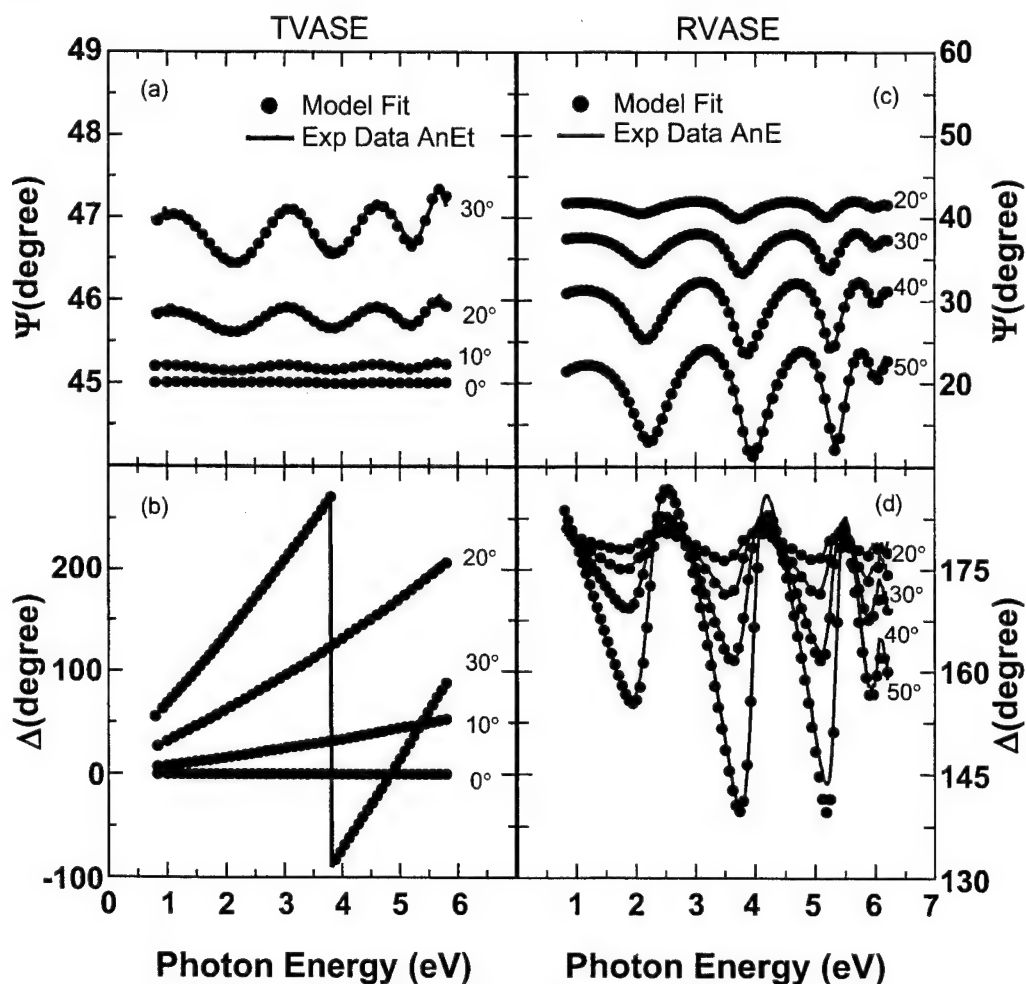


Fig. 4. VASE data and best fit of two HT AlN/c-sapphire samples. (a) ψ data and best fit of TVASE; (b) Δ data and best fit of TVASE; (c) ψ data and best fit of RVASE; (d) Δ data and best fit of RVASE. Solid lines represent experimental data. Dash lines represent the best model fit.

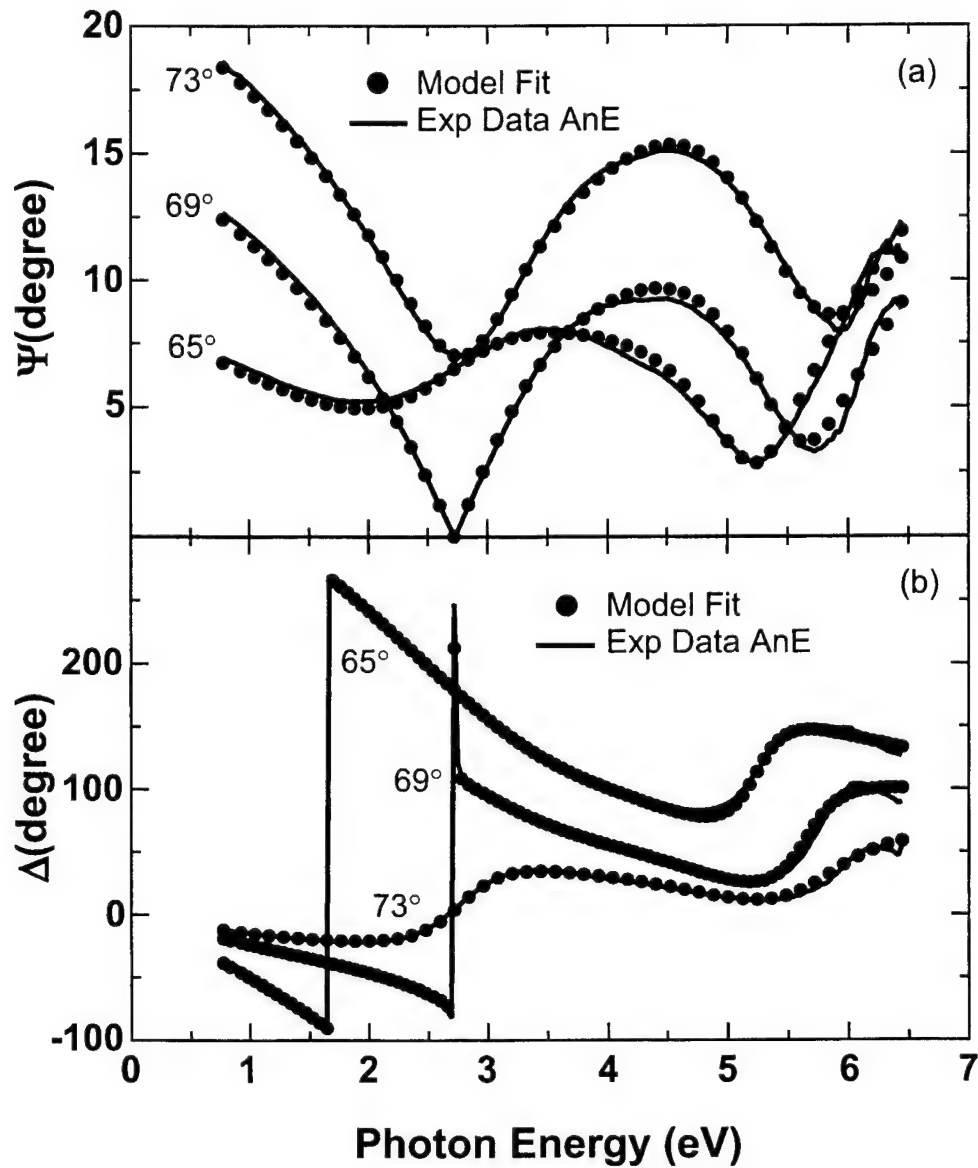


Fig. 5. RVASE data and best fit of LT AlN/c-sapphire. (a) Ψ data and best fit; (b) Δ data and best fit. Solid lines represent experimental data. Dash lines represent best model fit.

best fit of the LT AlN/c-sapphire. The resulted film thickness of LT AlN is 34.2 nm which is very close to the nominal value 36 nm. A 22 nm interfacial layer was formed due to the 10 minutes nitrogenation. No surface overlayer is needed in the LT AlN VASE data analysis. High incident angles used for the LT AlN sample is because the anisotropy of such a LT material is not an issue in the material quality study.

The optical constants HT and LT AlN films obtained from VASE data analysis are shown in Fig. 6. The HT AlN is fully transparent below 5 eV, but the absorption of LT AlN starts from below 3 eV. This long absorption tail below the fundamental band gap (~ 6.2 eV) of AlN may be due to the high-density structure defects caused by both low temperature growth and large lattice-mismatch between AlN and sapphire substrate, the same reason caused the E_2 phonon broadening.

The parametric semiconductor model is Kramer-Kronig (K-K) consistent, the K-K fitting is shown in Fig. 7. The solid lines are the best ϵ_1 result from the VASE data analysis, and the dots represent the calculated ϵ_1 from the known ϵ_2 values using the K-K relation. Fig. 7 (a) and (b) are for HT and LT AlN, respectively. The final results of all fitting parameters are given in Table 2. The K-K relation used in the calculation is¹⁷

$$\epsilon_1^{kk}(E) = \epsilon_1^{offset} + \sum_{i=1}^2 \frac{A_i}{E_i^2 - (E)^2} + \frac{2}{\pi} P \int_{0.75\text{eV}}^{6.5\text{eV}} \frac{E' \epsilon_2^{meas}(E')}{E'^2 - (E)^2} dE' \quad (8)$$

For a specified material, the K-K integral is numerically evaluated to calculate ϵ_1 values from ϵ_2 . The model then adds the contribution from two non-broadening oscillators and a fixed offset to account for contribution outside the experimental measuring range. E_i is the energy location of a non-broadening oscillator that is added to simulate contribution outside the integration range; A_i is the magnitude of the oscillator located at E_i position. In our calculation one oscillators were used outside the measured region.

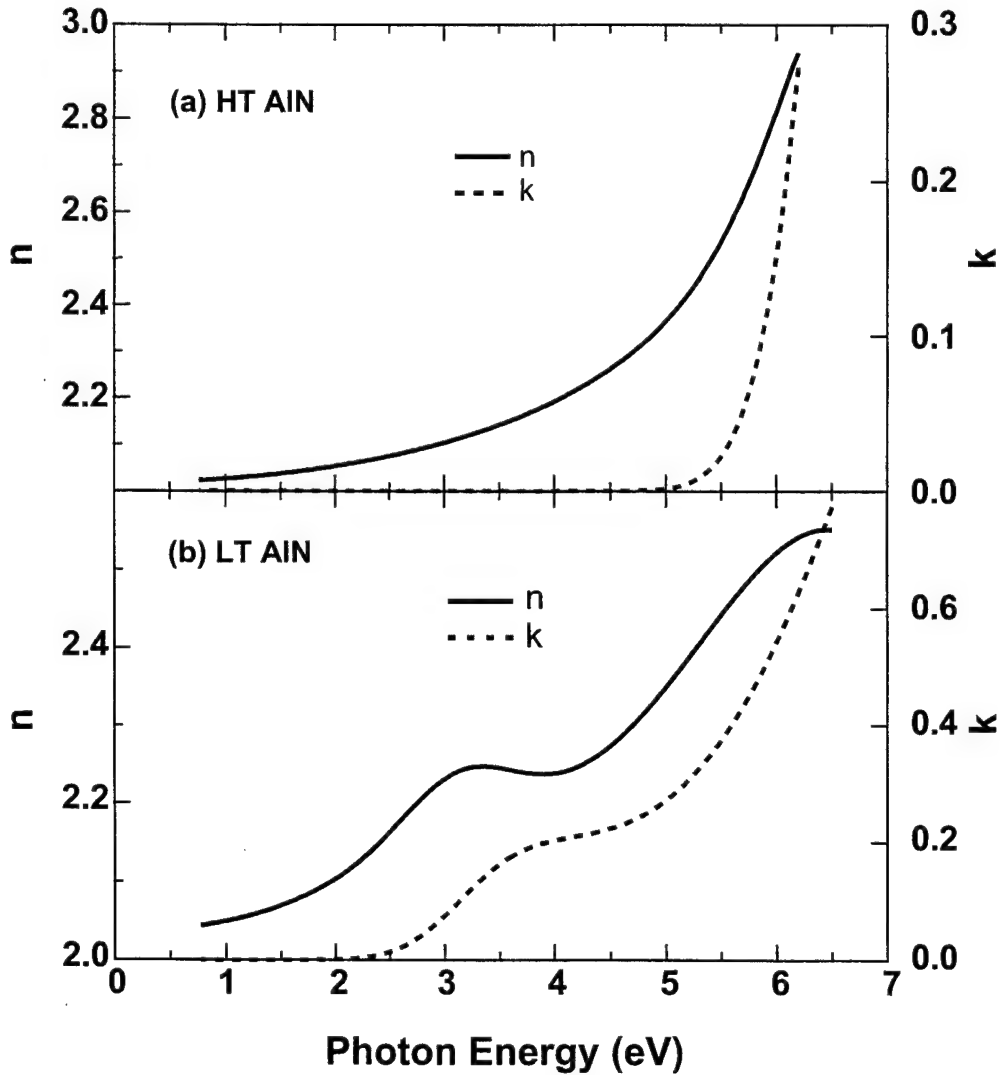


Fig. 6. Optical constants of (a) HT AlN, and (b) LT AlN.

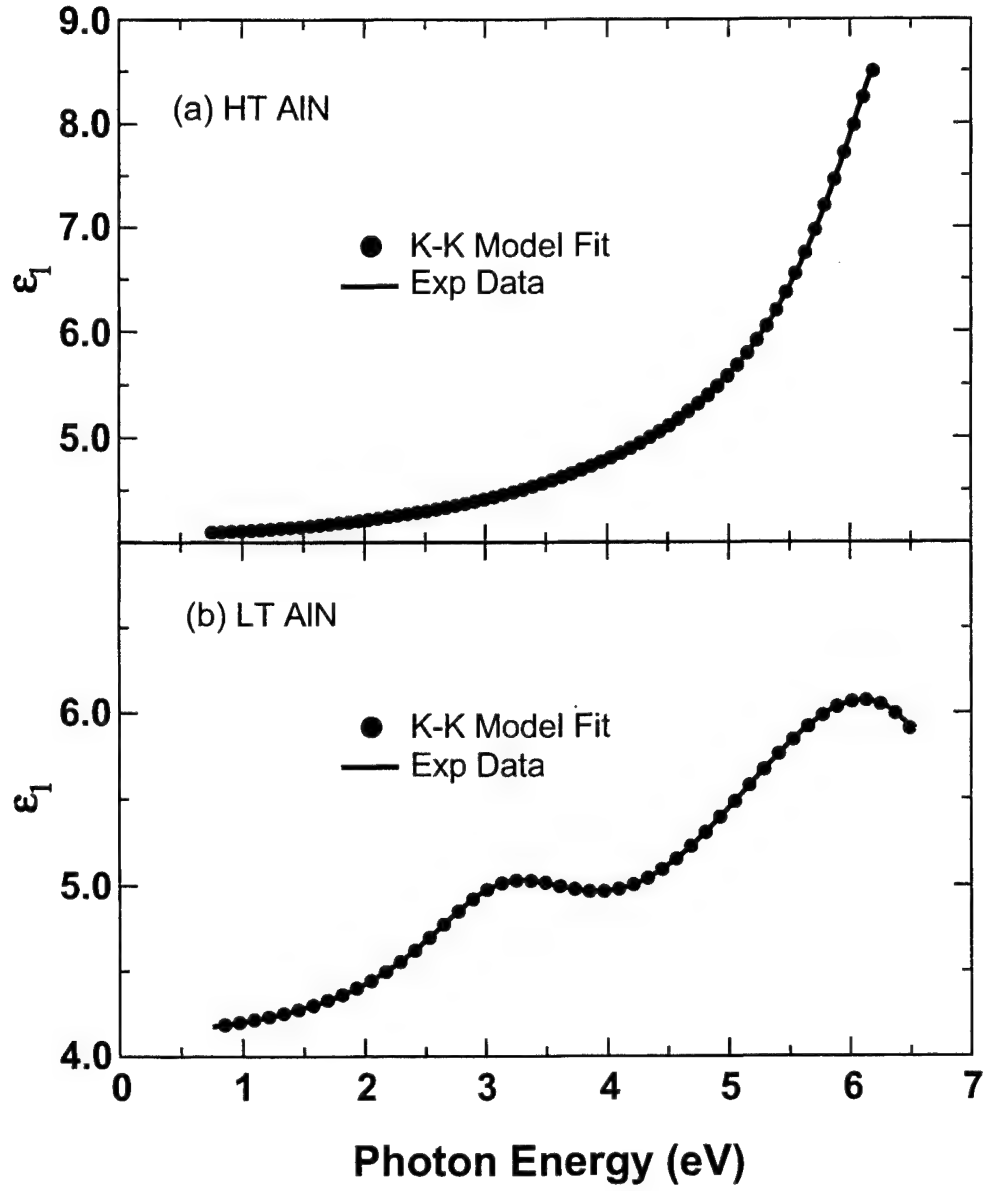


Fig. 7. Kramers-Kronig consistency check AlN dielectric functions. (a) HT AlN; (b) LT AlN.

Table 2. K-K fitting parameters for HT and LT AlN dielectric functions.

Fitting Parameters	E_i	A_i	$\epsilon_1^{\text{offset}}$
Pole (HT AlN)	7.87 eV	17.27	2.29
Pole (LT AlN)	7.76 eV	13.23	2.17

5. Summary

The optical anisotropy nature of AlN films grown on c-plane sapphire substrates was revealed by Raman scattering and generalized variable angle spectroscopic ellipsometry. Optical phonons measured from a 1 μm thick HT AlN agrees very well with the theoretical prediction. Optical constants of HT and LT AlN are determined by TVASE and RVASE along with the structure parameters. The broadening in E_2 phonon and long absorption tail indicate that LT AlN has very high defect density due to low temperature growth and large lattice-mismatch.

Acknowledgments

This work was supported by US Army Research Office under contract No. DAAG55-98-1-0462.

References

1. H. Morkoc, S. Strite, G. B. Gao, M. E. Lin, B. Sverdlov, and M. Burns, "Large-band-gap SiC, III-V nitride, and II-VI ZnSe-based semiconductor device technologies," *J. Appl. Phys.* **76**, pp. 1363-1398, 1994.
2. S. Nakamura, T. Mukai, and M. Senoh, "Candela-class high-brightness InGaN/AlGaIn double-heterostructure blue-light-emitting diodes," *Appl. Phys. Lett.* **64**, pp. 1687-1679, 1994.
3. E. Dogheche, D. Remiens, A. Boudrioua, and J. C. Loulergue, "Growth and optical characterization of aluminum nitride thin films deposited on silicon by radio-frequency sputtering," *Appl. Phys. Lett.* **74**, pp. 1209-1211, 1999.
4. X. Tang, Y. Yuan, K. Wongchotigul, and M. G. Spencer, "Dispersion properties of aluminum nitride as measured by an optical waveguide technique," *Appl. Phys. Lett.* **70**, pp. 3206-3208, 1997.
5. J. F. Muth, J. D. Brown, M. A. L. Johnson, Z. Yu, R. M. Kolbas, J. W. Cook Jr., and J. F. Schetzina, "Absorption coefficient and reflective index of GaN, AlN, and AlGaIn alloys," *MRS Internet J. Nitride Semicond. Res.*, **4S1**, G5.2 1999.
6. D. E. Aspnes, J. B. Theeten, and F. Hottier, "Investigation of effective-medium models of microscopic surface roughness by spectroscopic ellipsometry," *Phys. Rev. B* **20**, 3292, 1979.
7. T. Azuhata, T. Sota, K. Suzuki and S. Nakamura, "Polarized Raman spectra in GaN," *J. Phys.: Condens. Matter* **7**, pp. L129-L133, 1995.
8. R. M. A. Azzam and N. M. Bashara, *Ellipsometry and Polarized Light*, North-Holland, Amsterdam, 1977.
9. R. M. A. Azzam, and N. M. Bashara, "Generalized ellipsometry for surface with directional preference: application to diffraction gratings," *J. Opt. Soc. Am.* **62**, pp. 1521-1523, 1972.
10. D. W. Berreman, "Optics in stratified and anisotropic media: 4x4 matrix formulation," *J. Opt. Soc. Am.* **62**, pp. 502-510, 1972.
11. M. Schubert, "Polarization dependent parameters of arbitrarily anisotropic homogeneous layered systems," *Phys. Rev. B*, **53**, pp. 4265-4274, 1996.
12. M. Schubert, B. Rheinlander, J. A. Woollam, B. Johs, and C. M. Herzinger, "Extension of rotating analyzer ellipsometry to generalized ellipsometry: determination of the dielectric function tensor from uniaxial TiO_2 ," *J. Opt. Soc. Am.* **A13**, pp. 875-883, 1996.
13. G. H. Wei, J. Zi, K. M. Zhang, X. D. Xie, "Zone-center optical phonons in wurtzite GaN and AlN," *J. Appl. Phys.* **82**, pp. 4693-4695, 1997.
14. C. H. Yan, H. Yao, J. M. Van Hove, A. M. Wowchak, P. P. Chow, and J. M. Zavada, "Ordinary Optical Dielectric Functions of Anisotropic Hexagonal GaN Film Determined by Variable Angle Spectroscopic Ellipsometry," to be published.
15. C. M. Herzinger, B. Johs, U.S. Patent 5,796,983, issued Aug 18, 1998.
16. G. A. Slack and T. F. McNELLY, "Growth of high purity AlN crystals," *J. Cryst. Growth*, **34**, pp. 263-279, 1976.
17. H. Yao, B. Johs, and R. B. James, "Optical anisotropic-dielectric response of mercuric iodide," *Phys. Rev. B*, **56**, 9414 9421, 1997.

The Novel Processing for Improving Optical Property of InGaN/GaN MQW Light Emitting Diode

C. H. Huang^a, K. Y. Hsieh^a, H. S. Hwung^b, L. W. Tu^c

^aInstitute of Materials Science and Engineering, National Sun Yat-sen University, Kaohsiung, Taiwan

^bMilitary Academy, Kaohsiung, Taiwan

^cDept. Of Physics, National Sun Yat-sen University, Kaohsiung, Taiwan

ABSTRACT

The optical property and microstructure of InGaN/GaN MQW before and after annealed has been investigated by using photoluminescence (PL) and Transmission Electron Microscope (TEM) technique. The photoluminescence intensity of InGaN/GaN MQW LED annealed within AlN powder can be enhanced by 5 times compared with the as-grown one. The diffused Al converted the InGaN/GaN into AlGaIn/InGaIn. Less dislocation density in the annealed film and more carrier collection ability due to the band gap difference between InGaIn/GaN and InGaIn/AlGaIn can be applied to explain the astonished result. This simple process can improve the optical property of GaN/InGaIn QW LED without spending heavy cost in thin film growth.

Keywords: GaN, InGaIn, quantum well, photoluminescence, diffusion, annealing

1. INTRODUCTION

Recently, group-III nitride compound semiconductors have attracted much attention due to its large direct band gap range from 1.9eV(InN)¹ to 6.2eV(AlN)². The emitted luminescence wavelength for these compound semiconductor is between red to violet spectral region. Thus this unique physical property has provided a widely application in optical and electrical devices such as full-color LED displays or high power, high temperature transistor. In 1994 Nakamura announced the first high brightness blue GaN based LED³, since then the enormous fund and colossal research activity are tracked and move forward very fast. Since the LED has a longer lifetime, high efficiency, less energy needed. It is expected that the daylight lamp will be replaced by LED in the near future.

In the early research, it is difficult to find out a suitable substrate to grow GaN. Sapphire (Al₂O₃) is the most common substrate. It have 16% lattice constant mismatch with GaN⁴. Such a large mismatch causes the stresses existed in the interface layer resulted in a high density dislocation in GaN layer. Several researchers try to grow buffer layer with AlN⁵ and GaN⁶ on sapphire in order to reduce the density of the dislocation, however the high density dislocation still can not avoid. Kato et al. developed using ELOG method to limit the dislocation in some area and get better quality in selective area⁷. It is reported that the intensity of the blue LED is not directly related with the density dislocation, but the life time of the LED will be affected with the dislocation density⁸. In this paper, we report a simple process to enhance the optical property of InGaIn/GaN LED without spending too much effort on sample growth. Even the low quality of the GaN films

Email: kyhsieh@www.ora.nsysu.edu.tw; Telephone: 886-7-525-2000 ext 4066; Fax: 886-7-525-4099

still can be improved after post annealed. The experiment results show that the optical property can be improved 5 times compared with the sample without annealed process.

2. EXPERIMENT

The sample used in this study was grown on a (0001) oriented sapphire (Al_2O_3) substrate by metalorganic chemical vapor deposition (MOCVD) technique. The structure of these samples consist of 4 μm thick GaN buffer layer, 5 pairs of InGaN/GaN MQW and a 0.5 μm GaN cap layer. Two different In content were choosen. One is around 17% the other is 30%. The thermal process was performed in cleaned and etched quartz ampoules (approximately 3.5-4 cm^3), evacuated to 10^{-6} Torr, under different ambients (Ga, AlN, or no-overpressure), where sufficient gallium(5mg) or AlN(5mg) was included to provide an excess overpressure of Column III or column V atoms. The annealing temperatures ranged from 750-950°C and the annealing time was fixed at four hours.

Spontaneous emission under various excitation energy densities were measured at 300K under the excitation of a continuous wave He-Cd laser (325nm). In order to compare the relative intensity of each set experiment, the as-grown sample is measured first and then the system operating parameters will be maintained to continue the following measurement.

The specimen for cross-sectional microanalysis was prepared by mechanical thinning and ion milling with Ar^+ at 77K. Bright field images were observed using a TEM (Jeol 200CX) operated at 200Kev. EDX measurements were performed with high resolution TEM (Jeol 3010) operated at 300KeV.

3. RESULTS AND DISCUSS

Figure 1 shows a PL spectra(300K) form a InGaN/GaN MQW before and after thermal annealing with different annealing temperature in a no overpressure environment. The oscillation interference of the photoluminescence curves is due to the roughness of the sample surface. The main PL peak of the as-grown sample is located at 475nm. It was found that the peak was shifted to 460 nm (blue shift) after 750 C annealed process. The higher temperature annealed the more shift of the main peak. The intensity of the PL was reduced with increasing annealing temperature. The blue shift of the PL can be explained with the interdiffusion of group III (Ga and In) took place after thermal annealed in the quantum well region. The lower In content in the well, the shorter photoluminescence wavelength was emitted. The degraded intensity of the PL spectrum is due to the degraded crystal quality which was damage without any cap layer protection during thermal process. The column V atoms can easily leave away the surface and create more nonradiation recombination center. Figure 2 shows another PL spectra from the same InGaN/GaN sample with different annealing temperature. However, this time the annealing environment was changed in a gallium over pressure condition. The blue shift was occurred again. The intensity of the PL spectrum was also reduced with increasing annealing temperature. Compared with figure1 and figure 2, it was found that the displacement of the PL peak energy was retarded when the annealing environment was in the gallium overpressure. The similar results have been reported in GaAs/AlGaAs system⁹. The Column III vacancies played a important role. The concentration of the column III vacancy affected the interdiffusion coefficient of the column III atom in the well. The more column III vacancies generated from the surface the quick interdiffusion of the column III occurred¹⁰. In a gallium overpressure condition, the concentration of the column III vacancy is less than that with no over pressure

condition. Therefore, it can be expected that the blue shift of the PL peak will have less extent when the annealing process was performed in a gallium overpressure condition.

Figure 3 displays a stack PL spectrum that emitted from a InGaN/GaN MQW after in a AlN annealing environment for different annealing temperature. This figure shows the total different result compared with the previous figures. Firstly, the main peak of each PL spectra did stay in the same position. Secondly, the intensity of PL for high temperature annealing at 850°C was increased 5 times compared with the as grown one. The annealing process enhanced the optical property dramatically. In order to reveal this unusual result, the structure analysis and the EDX measurement were performed by cross-sectional TEM. Figure 4 and figure 5 show the 0002 bright field images of the LD structure which were a as-grown one and a thermal annealing under AlN condition respectively. Both of these micrograph were taken from the $[0\bar{1}10]$ crystal axis. Apparently, the density of dislocation shown in the figure 4 is higher than those in the figure 5. It indicated that the number of the dislocation can be reduced after the thermal process applied. The dislocation in the sample that annealed with AlN power became to merge together. It is well known that the dislocation is one kind of defects. It can play as a nonradiation center. The less dislocation existed, the more carriers can be applied in a radiation process. The decrease of the number of the dislocation would be one of the reasons to explain why the intensity of the PL emitted from the InGaN/GaN MQW can be improved after high temperature annealed with a AlN powder. The other reason for explaining the enhancement of the PL intensity is that the AlN molecular was broken into Al and N atoms due to the thermal energy and then the Al atom diffused into the quantum well. This action converted the InGaN/GaN into InGaN/AlGaN. According to the previous report, the energy band gap of the InGaN and AlGaIn can be written as^{11,12}

$$E_{g,In_xGa_{1-x}N}(x) = xE_{g,InN} + (1-x)E_{g,GaN} - bx(1-x)$$

$$E_{g,Al_xGa_{1-x}N}(y) = yE_{g,AlN} + (1-y)E_{g,GaN} - by(1-y)$$

The band gap discontinuities of the InGaN/GaN and the InGaN/AlGaIn is quite different. Before the thermal process, the band gap difference was decided by GaN and InGaIn. Once the Al diffused through the interface of the InGaN/GaN. The GaN could be added some Al and changed into AlGaIn. Small amount of Al can cause the band gap difference have a big change. It is noted that the LED structure consisted of 5 pairs InGaN/GaN MQW sandwiched by two GaN layers. These two GaN layers have the functions of the optical confinement and the carrier collection. The larger band gap difference between the well and the barrier existed, the more superior optical property appeared. In this case, the original barrier layer of this LED structure is GaN. After the annealing, the barrier is changed into AlGaIn. The increase of the band gap discontinuities enhanced the ability of the optical property of this LED. In order to identify the Al atom was indeed diffused into the LED layers. EDX measurement for Al atomic percentage was applied. Seven points have been measured. There were two points located in the cap layer region, three points were probed in the multiple quantum well region and the other two points were shot in the GaN buffer layer. The result was shown in the Table 1. From the Table 1, it was found that the aluminum atom distributed uniformly all over the layer and the atomic percentage is around 12. The In atom was not detected in the buffer layer. Most of the In atoms stayed inside the quantum well. This indicated that the In had not out diffusion at all. It is very common that there will be a impurity concentration gradient existed if any impurity diffusion process is applied. However, in this experiment the aluminum distribution is very uniform. There is no concentration difference. The aluminum diffused

into the sample through the dislocation will be the better explanation for the results.

In order to make sure that the experiment of the enhancement of the PL intensity emitted from InGaN/GaN MQW under AlN powder annealed can be repeated. Another LED sample that has the same structure but with different In content (30%) in the well was employed. The result is shown in the figure 6. The optimum annealing temperature for this sample was at 900°C. The intensity of the PL peak is twice larger than that as-grown sample. Although the factor of intensity increase is not as large as the previous result, the behavior of PL intensity enhancement is very consistent. When the annealing temperature reached at 950°C, the PL intensity decreased. It is due to the degraded crystal after thermal process.

4. CONCLUSION

The optical property and microstructure of InGaN/GaN MQW before and after annealed has been investigated by using photoluminescence (PL) and Transmission Electron Microscope (TEM) technique. The photoluminescence intensity of InGaN/GaN MQW LED annealed within AlN powder can be enhanced by 5 times compared with the as-grown one. The diffused Al converted the InGaN/GaN into AlGaIn/GaN. Less dislocation density in the annealed film and more carrier collection ability due to the band gap difference between InGaN/GaN and InGaIn/GaN can be applied to explain the astonished result. This simple process can improve the optical property of GaN/InGaIn QW LED without spending heavy cost in thin film growth.

REFERENCE

1. Yuichi Sato, and Susumu Sato, "Growth and some properties of $\text{In}_x\text{Ga}_{1-x}\text{N}$ thin films by reactive evaporation," *Thin Solid Films* **261**, pp. 87-89, 1995.
2. J. Siwiec, A. Sokolowska, A. Olszyna, R. Dwilinski, M. Kaminska and, J. Konwerska-Hrabowska, "Photoluminescence properties of nanocrystalline, wide band gap nitrides (C_3N_4 , BN, AlN, GaN)," *NanoStructured Materials* **10**, pp. 625-634, 1998.
3. Shuji Nakamura, Takashi Mukai, and Masayuki Senoh, "Candela-class high-brightness InGaIn/AlGaIn double-heterostructure blue-light-emitting diodes," *Applied Physics Letters* **64**, pp. 1687-1689, 1994.
4. William A. Melton and, Jacques I. Pankove, "GaN growth on sapphire," *J. Crystal Growth* **178**, pp. 168-173, 1997.
5. H. Amano, N. Sawaki, and I. Akasaki, "Metalorganic vapor phase epitaxial growth of a high quality GaN film using an AlN buffer layer," *Applied Physics Letters* **48**, pp. 353-355, 1986.
6. S. Nakamura, Y. Harada, and M. Senoh, "Novel metalorganic chemical vapor deposition system for GaN growth," *Applied Physics Letters* **58**, pp. 2021-2023, 1991.
7. Y. Kato, S. Kitamura, K. Hiramoto, and N. Sawaki, "Selective growth of wurzite GaN and $\text{Al}_x\text{Ga}_{1-x}\text{N}$ on GaN/sapphire substrates by metalorganic vapor phase epitaxy," *J. Crystal Growth* **144**, pp. 133-140, 1994.
8. P. Kozodoy, J. P. Ibbetson, H. Marchang, P. T. Fini, S. Keller, J. S. Speck, S. P. DenBaars, and U. K. Mishra, "Electrical characterization of GaN p-n junctions with and without threading dislocations," *Applied Physics Letters* **73**, pp. 975-977, 1998.

9. R. M. Kolbas, Y. L. Hwang, T. Zhang, M. Prairie, K. Y. Hsieh. And U. K. Mishra, "Enhanced suppressed interdiffusion of lattice-matched and pseudomorphic III-V heterostructures by controlling Ga vacancies," *Optical and Quantum Electronics* **23**, pp. s805-s812, 1991.
10. Michael C. Y. Chan, Elaine M. T. Cheung, and E. Herbert. Li, "A tunable blue light emission of InGaN/GaN quantum well through thermal interdiffusion," *Material Science and Engineering* **B59**, pp. 283-287, 1999.
11. Shuji Nakamura, "III-V nitride-based light-emitting diodes," *Diamond and Related Materials* **5**, pp. 496-500, 1996.
12. H. Wang, G. A. Farias, and V. N. Freire, "Graded interface effects on the carriers confinement in single GaN/Al_xGa_{1-x}N wurtzite quantum wells," *Solid State Communications* **110**, pp. 587-592, 1999.

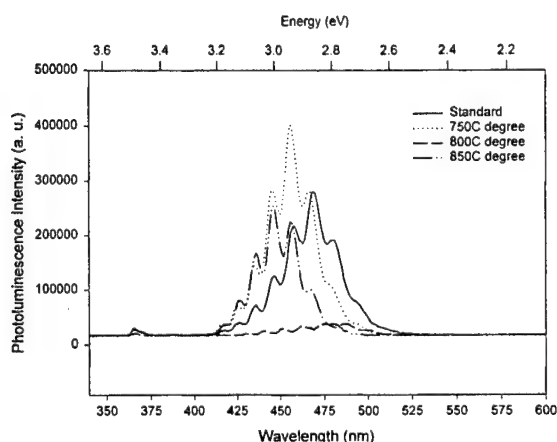


Figure 1 Photoluminescence spectra (300K) from an InGaN/GaN multiple quantum well before and after thermal annealing at different annealing temperature (750, 800, 850°C) for 4 hours in a no overpressure environment.

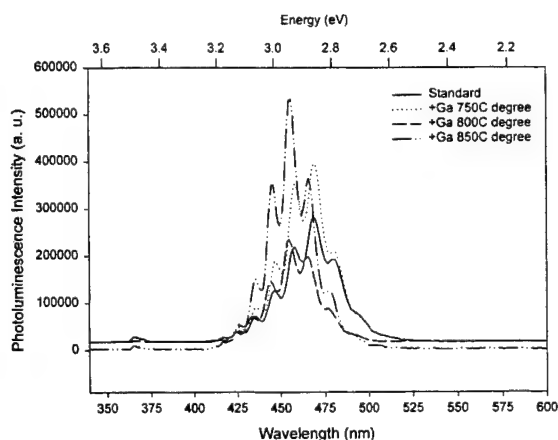


Figure 2. Photoluminescence spectra (300K) from an InGaN/GaN multiple quantum well before and after thermal annealing at different annealing temperature (750, 800, 850°C) for 4 hours in a gallium overpressure environment.

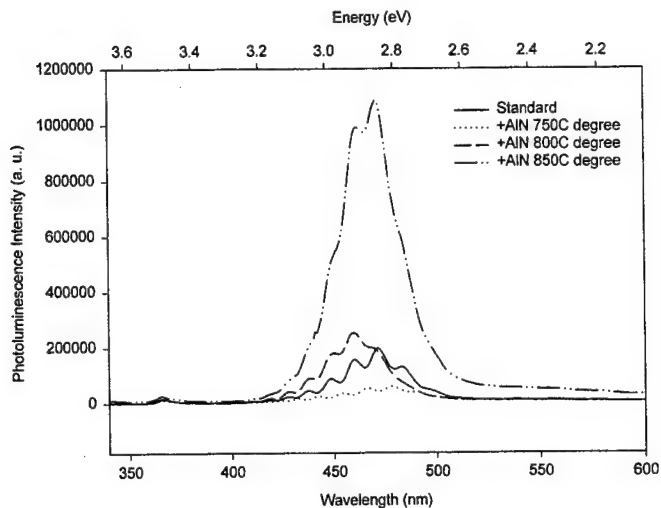


Figure 3 Photoluminescence spectra (300K) from an InGaN/GaN multiple quantum wells before and after thermal annealing at different annealing temperature (750, 800, 850°C) for 4 hours in a Al and N atom rich environment. It is noted that the PL intensity increased 5 times for annealing at 850°C compared with that the as grown one sample.

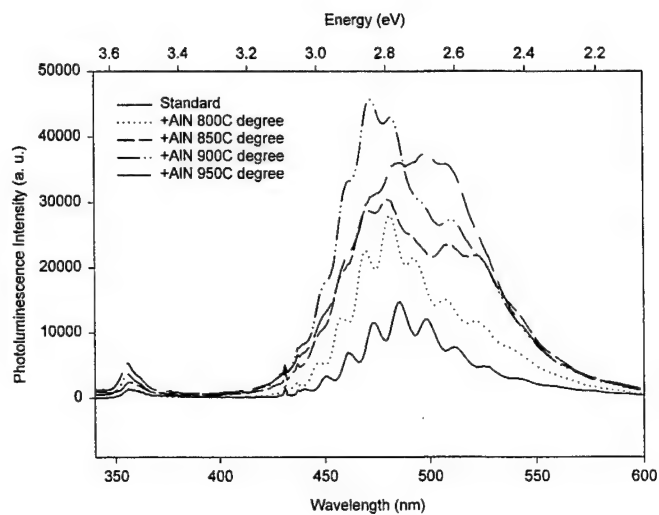


Figure 6 Photoluminescence spectra (300K) from an InGaN/GaN multiple quantum wells before and after thermal annealing at different annealing temperature (750, 800, 850°C) for 4 hours in AlN annealing environment. The In content in this sample is larger than the previous sample.

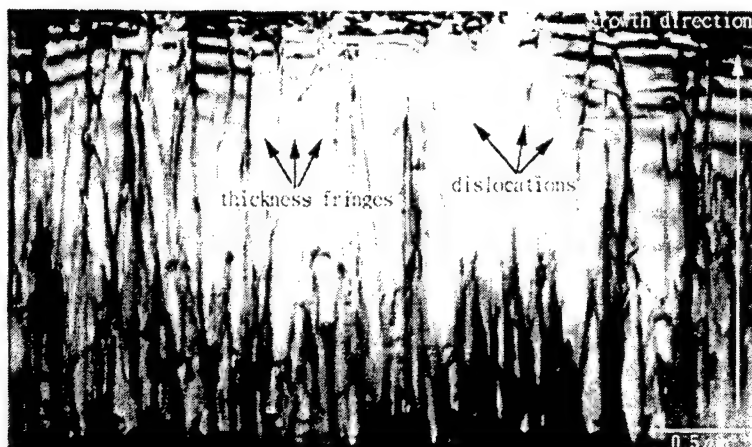


Figure 4 Cross-sectional TEM micrograph of a GaN-capped InGaN/GaN MQW. High density of the dislocation was observed.



Figure 5. Cross-sectional TEM micrograph of InGaN/GaN MQW annealed with AlN powder at 850°C. The number of dislocation has been reduced. Several dislocations merged together and became a thick dislocation line.

Table 1 The compositional variation of the InGaN/GaN MQW after 850°C annealed in a AlN rich environment. The aluminum content is uniformly distributed.

EDX point location	Al atom. %	Ga atom. %	In atom. %
Point1 (cap layer)	12.08	88.22	-0.30
Point2 (cap layer)	12.31	87.55	0.14
Point3 (MQW)	12.02	87.84	0.15
Point4 (MQW)	11.85	87.59	0.55
Point5 (MQW)	11.92	87.21	0.87
Point6 (GaN buffer)	12.27	87.92	-0.19
Point7 (GaN buffer)	12.49	87.56	0.05

Optical Properties of InN Thin Films

Vladislav Ya. Malakhov

Dept. of Functional Electronics Materials, Institute for Problems of Materials Science, 03142 Kiev

ABSTRACT

The basic optical properties of low temperature plasma enhanced chemical reactionary sputtered (PECRS) InN thin films are presented. Optical absorption and reflectance spectra of InN polycrystalline films at room temperature in visible and near infrared (NIR) regions were taken to determine direct band gap energy (2.03 eV), electron plasma resonances energy (0.6 eV), damping constant (0.18 eV), and optical effective mass of electrons (0.11). In addition the UV and visible reflectance spectra have been used to reproduce accurately dielectric function of wurtzite InN for assignments of the peak structures to interband transitions (1.5-12.0 eV) as well as to determine dielectric constant (9.3) and refractive index (>3.0). The revealed reflectance peaks at 485 and 590 cm^{-1} respectively in IR spectra are connected with TO and LO optical vibration modes of InN films. Some TO (485 cm^{-1}) and LO (585 cm^{-1}) phonon features of indium nitride polycrystalline films on ceramics were observed in Raman spectra and also discussed. The excellent possibilities of InN polycrystalline layers for potential application in optoelectronic devices such as LEDs based InGaAlN and high efficiency solar cells are confirmed.

Keywords: InN polycrystalline films, optical properties, solar cells

1. INTRODUCTION

Escalating interest in recent 10 years to III group nitride semiconductors with direct band gaps ($> 6.0 - 2.0$ eV) reflects their potential application in photonic devices such as LEDs, lasers, full colour displays, and high efficiency solar cells¹⁻⁶. The extensive utilization of InGaAlN film compositions as active layers in high performance photonic devices has facilitated these accomplishment due to its tunability of the energy band gap covering the visible to near UV light spectrum. Optical properties of InN thin films obtained by different methods have been studied in numerous works^{8, 10-23} including ones of the author. However some optical and electric parameters such as dielectric and optical constants, energy gap, effective mass of carriers as well as phonon wavenumbers await for further more accurate definition. A lack of single crystalline, stoichiometric samples explains the situation around mentioned above data. Any structural and thermal properties of InN have not been studied for epitaxial films on lattice-matched substrates. The development of advanced growth techniques (e.g. MOCVD, PIMBE or PLD)^{1, 6, 16} have resulted in promising improvements in the structural, electrical and optical properties. For this reason presented paper demonstrates some original optical data obtained for InN thin polycrystalline films synthesized earlier and nowadays by low temperature plasma enhanced chemical reactionary synthesis (PECRS) technique.

2. EXPERIMENTAL DETAILS

Since a dissociation temperature of InN is about 650 $^{\circ}\text{C}$ ⁷ therefore a low temperature growth technique is required. In our case the PECRS system to synthesize InN thin films was used⁸. Intensive Ti-wire evaporation used as getter was carried out during all the time of deposition process to reduce oxygen contamination inside of reactor as well as in growing films. High quality smooth surfaces of Si, quartz, fluorite and compound ceramics were used as substrates. In the time of films growth substrates temperature was about 320 $^{\circ}\text{C}$ due to intensive ion bombardment of a top electrode (anode) during sputtering process. The surface morphology including a microstructure of cross-section of the films were investigated by Philips SEM5V scanning electron microscope and by AFM as well. The film thickness was changing in the range 100-1600 nm and was measured by means of optical microscope-interferometer as well as by estimation of fractured edge dimension in SEM cross-section image. Auger spectrometer JAMP-10 was used to determine chemical composition of sputtered InN films. The crystalline structure parameters of obtained films were determined using of X-ray diffractometer

DRON-3 employing $\text{Cu(K}\alpha\text{)}$ radiation and also by means of standard electronograph EG-100a. The reflectance and transmittance measurements in visible and near infrared (NIR) regions ($25000\text{--}200\text{ cm}^{-1}$) have been carried out with help of Bruker IFS66 Fourier transform spectrometer (FTIR) and Carl Zeiss M40 grating spectrometer respectively. The Raman spectrometer Dilor XY equipped with microscope (Olympus BH-6) was used for study of phonon spectra of nitride films. A horizontal and vertical polarisation configuration of the incident and scattered Kr^+ laser light (647.1 nm) with power of 20 mW entering the sample surface were used there.

3. RESULTS AND DISCUSSION

X-ray diffraction pattern of InN layer deposited on ceramic substrate demonstrates that several intensive peaks appear there including free In peak and also ones connected with ceramic but most strong diffraction peak corresponding to the InN (002) plane suggests some textured crystalline structure of the films where the c axis is perpendicular to the plane of substrate. Fig. 1 displays of the RHEED investigation of natural surfaces of InN layers deposited on ceramics versus defferent deposition time.

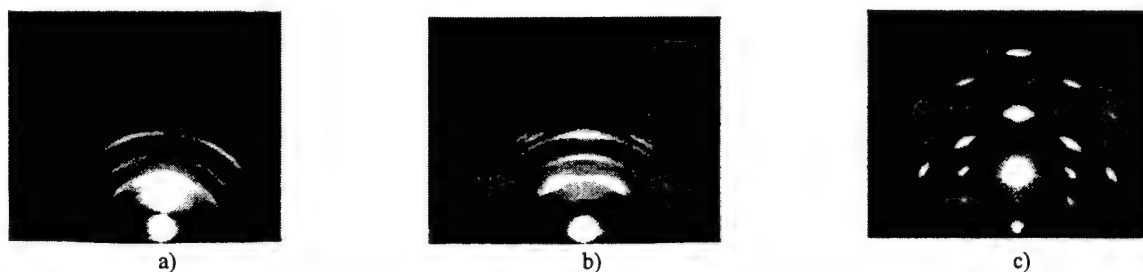


Figure 1: RHEED patterns from wurtzite InN film surfaces synthesized at different deposition time: a) 5 min., b) 8 min., c) 15 min.

Some textured structure appears soon there (Fig. 1c) and characterizes a structural quality of sputtered InN films. These results testify that any outsider phases except of InN and In ones were found inside films. Therefore most likely explanation of high oxygen concentration presented there is such when some quantity of chemically unactive oxygen molecules incorporate to voids between graines as shown in⁹ and other part of oxygen is probably binded in amorphous indium oxide.

The AFM images of natural surface morphology of InN film on ceramics are shown in Fig. 2.

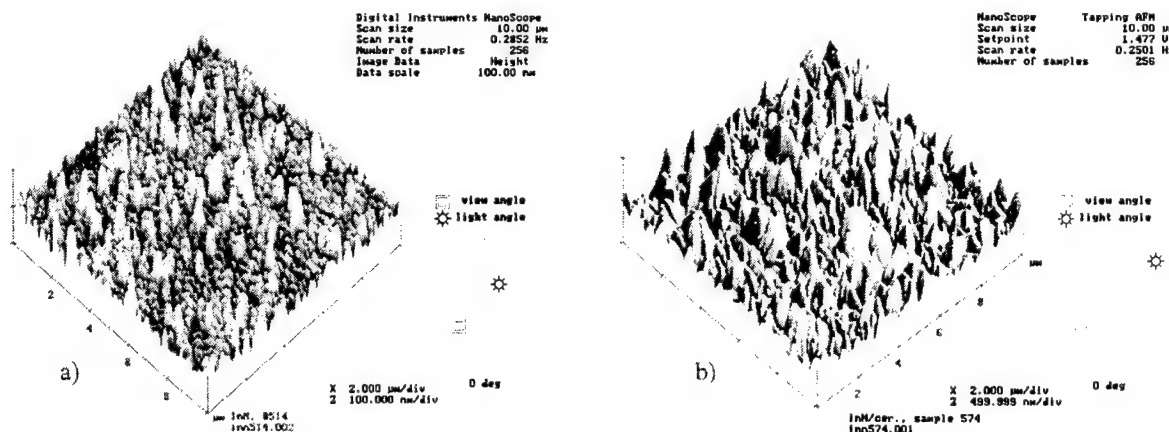


Figure 2: AFM images of natural surface of InN films synthesized on ceramic substrates at different deposition time : a) 5 min.; b) 10 min.

It is clear a surface texture with a pyramidal form of grains which are of dimensions about 400 nm across and 1600 nm in vertical direction respectively.

The transmittance spectra in visible spectral range are used to determine the band gap energy of InN thin films on CaF₂ (fluorite) substrates. In this procedure the band gap energy can be derived from absorption coefficient α of InN by:

$$\alpha(E) = \alpha_0 \cdot (E - E_g), \quad E > E_g \quad (1)$$

It is clear that the absorption coefficient or the product $\alpha \cdot d$ should be measured or derived most accurately. For a thin film on a substrate this is not as stright forward as it is for a free standing film. In our case we have a highly transparent substrate (fluorite - s) and a highly absorbing layer (InN - l) for the situation of our samples at photon energies larger than the gap energy. Thus an assumption that multireflections will only occur in the substrate holds and the transmittance may be written as the sum of the contributions of this multireflections:

$$\begin{aligned} T &= \sum T_{s,i} \\ &= (1-R_l) \cdot \Phi_l \cdot (1-R_{ls}) \cdot \Phi_s \cdot (1-R_s) \\ &\quad + (1-R_l) \cdot \Phi_l \cdot (1-R_{ls}) \cdot \Phi_s^{2n+1} \cdot R_s^n \cdot R_{ls}^n \cdot (1-R_s) \end{aligned} \quad (2)$$

where $\Phi_{l,s} = \exp[\omega d/c (iN_{l,s} - K_{l,s})]$. As this is a geometric series eqv. 3 may be written as:

$$T = (1-R_l) \cdot \Phi_l \cdot (1-R_{ls}) \cdot (1-R_s) \cdot \Phi_s / 1 - R_{ls} \cdot R_s \cdot \Phi_s^2 \quad (3)$$

The transmittance of the bare substrate can easily be derived in the same way ending at the well known correlation:

$$T_s = (1-R_s)^2 \cdot \Phi_s / 1 - R_{ls} \cdot R_s \cdot \Phi_s^2 \quad (4)$$

As the reflectance measurement of the bare substrate yields R_s , if the sample apperture is small enough, the reflectance and transmittance measurements of the substrate finally give R_s and Φ_s . The later has to calculated from eqv. 3 which has to be solved for Φ_s :

$$\Phi_s = - (1-R_s)^2 / 2T_s \cdot R_s^2 + \{ [(1-R_s)^2 / 2T_s \cdot R_s^2]^2 + 1/R_s^2 \}^{1/2} \quad (5)$$

The derivation of R_l can not be processed such easily, as reflectance measurements of layered samples still include substrate contributions at photon energies near the energy gap of InN, where the thin film still shows some transmittance, while at energies above the gap region, knowing that the error introduced by this procedure is small compared to the error introduced by just assigning the reflectance of the substrate is low (R_{ls} may well be approximated as R_l). The result of this procedure is shown in Fig. 3. Here the square of $\alpha \cdot d$ is plotted together with an extrapolation of the data near the energy gap ($E_g \approx 2.03$ eV). Fig. 4 reconstructs the absorption spectrum of InN film deposited on quartz substrate (it was measured at room temperature earlier⁸).

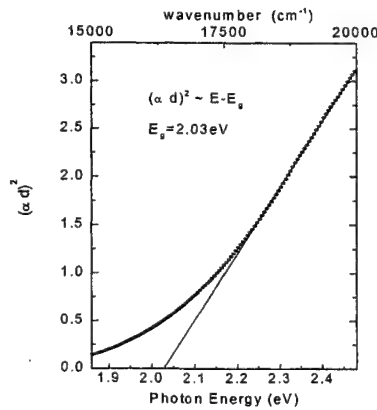


Figure 3: Square of $\alpha \cdot d$ vs $(h\nu)$ for InN layer deposited on fluorite.

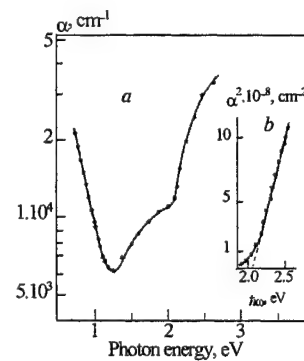


Figure 4: Absorption spectrum of InN film on quartz⁸.

In addition the UV and visible reflectance spectra (Fig 5, 6) have been used to reproduce accurately dielectric function of wurtzite InN for assignments of the peak structures to interband transitions (1.5-12.0 eV) as well as to determine dielectric constant (9.3), refractive index (>3.0). Also the electron plasma resonances energy (0.6 eV), damping constant (0.18 eV), optical effective mass of electrons (0.11) were calculated from visible reflectance spectra (Fig. 7).

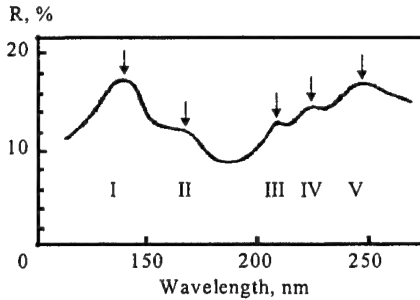


Fig. 5: UV reflectance spectra of InN film¹⁰.

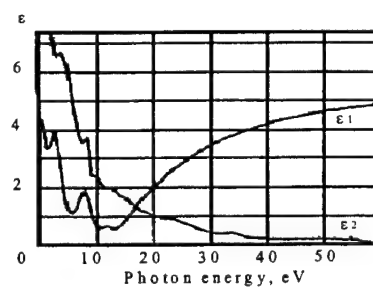


Fig. 6: Dielectric function of InN layer¹¹.

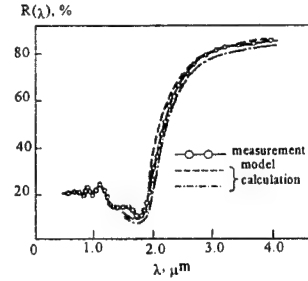


Fig. 7: EPR edge spectra of InN⁸.

Von-Hove point energies which assign the peaks in Fig. 5 as: I (8.8 eV) for $\Gamma_6 - \Gamma_1$, II (7.3 eV) for $M_{2,4} - M_{1,3}$ and $K_3 - K_2$, III (5.8 eV) for $U_4 - U_3$, IV,V (5.5 - 5.0 eV) for $\Gamma_5 - \Gamma_3$ interband transitions respectively were used earlier to calculate zone band structure of InN¹² (Fig. 8).

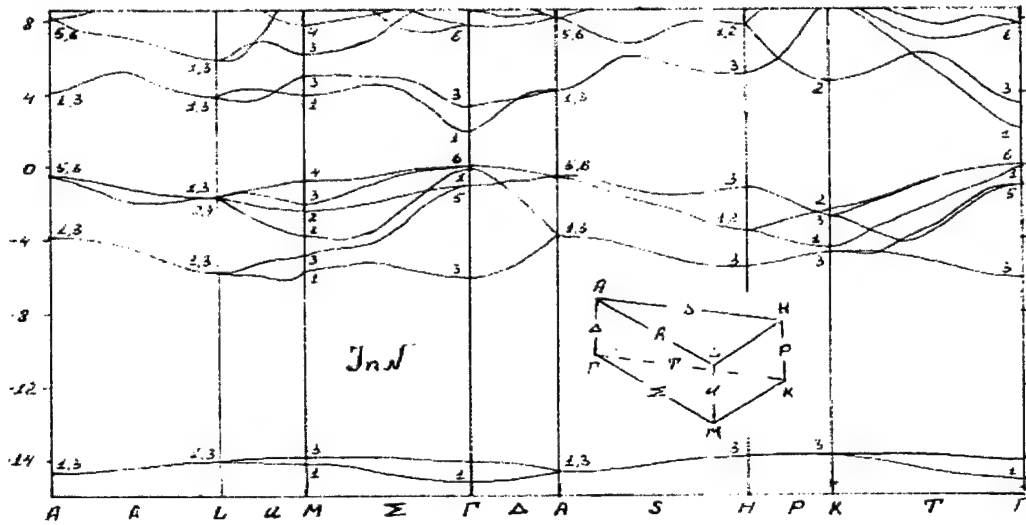


Fig. 8: The band structure of InN computed with the ab initio pseudofunction method¹².

In order to obtain a necessary information about phonon features of InN films as well as to determine precisely some optical parameters the Drude-Lorentz formalism was used for dielectric function modeling procedure by use reflectance spectra from both InN films surface and bare fluorite substrate. Fig. 9 shows a good agreement between experimental data and calculated curve. In addition as shown there the reflectance peaks at 485 and at 590 cm^{-1} respectively by our opinion are connected with TO and LO mode vibration of indium nitride^{9,13-14}. Moreover calculated here dielectric function of InN film was close to ones obtained earlier¹¹ as well as the value of electrons effective mass 0.11 determined from plasma resonance minimum peak⁸. The Raman spectra of InN films >1000 nm of thickness on ceramics in spectral region 400-700 cm^{-1} using polarised light were observed at the room temperature. The broadening peak at 485 cm^{-1} in Raman spectra of nitride film on ceramic (Fig. 10) is close to one observed in the reflectance spectra. Accordingly to⁴ indium nitride has 12 phonon modes at Γ -point of Brillouin zone (3-acoustic and 9-optical). But IR active modes are $E_1(\text{LO})$, $E_1(\text{TO})$, $A_1(\text{LO})$ and $A_1(\text{TO})$. Therefore because of imperfect crystalline structure of used samples we observe only two optical phonon modes: $E_1(\text{TO})$ and $A_1(\text{LO})$. An absence of $E_2(2)$ phonon peak revealed in¹⁵ is probably to be masking by films imperfection or substrate influence in our case. For this reason it was difficult to observe here also the main LO phonon

mode at 694 cm^{-1} as was predicted earlier by Osamura et al.¹³.

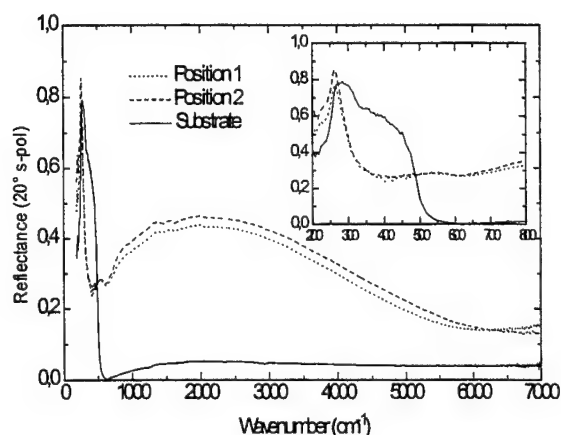


Figure 9: NIR reflectance spectra of InN film on fluorite (dotted curve is model calculation).

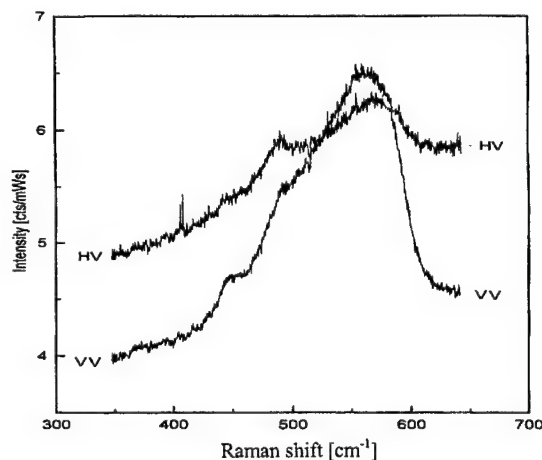


Figure 10: Typical Raman spectra of InN film deposited on ceramics.

Besides that there are two peaks near 445 and 585 cm^{-1} appear respectively. The first peak belongs to ceramic substrate and second one is close to LO phonon mode A_1 of InN^{15} .

4. CONCLUSIONS

InN thin films synthesized by low temperature PECRS are textured and also demonstrate of preferred $\langle 002 \rangle$ orientation with c axis perpendicular to substrate plane. Off-stoichiometric In/N ratio with In abundance inside nitride films is caused by nitrogen vacancies. A perceptible oxygen concentration has been revealed in the films probably leads to amorphous indium oxide forming partially (binded oxygen). Moreover other part of unactive oxygen molecules incorporate to voids between InN grains or are on a surface of films. It was confirmed of direct energy gap 2.03 eV of InN polycrystalline films as well as value of electron effective mass 0.11 which were obtained by one of the authors earlier from identical InN film samples. Moreover the TO (485 cm^{-1}) and LO (585 cm^{-1}) phonon features observed from Raman and NIR reflectance spectra are in good agreement with those obtained by other authors. The comparison of these data obtained now with those obtained 20 years ago for identical samples shows no differences are existed and thus demonstrating nowadays a high long term stability of this compound as to optical characteristics. Therefore some promising possibilities of InN stable polycrystalline layers for potential application in photonic devices including high efficiency solar cells are confirmed. Adequate excellent results will appear with progress in growth techniques for monocrystalline, stoichiometric InN samples.

ACKNOWLEDGEMENTS

We are grateful for the help of R. Zeugfang and G. Beketov for providing SEM and AFM measurements on our samples, S. Morley, A. Schneider for NIR and Raman investigations, O. Malakhova and V. Bekenev for technical assistance. The author has benefited from discussions with numerous colleagues but would like to thank in particular R. Beyer, G. Proesch, S. Morley, D. Zahn, V. Kulikovskiy and L. Shaginyan. The work is supported by NASU.

REFERENCES

1. O. Ambacher, "Growth and applications of group III-nitrides", *J. Phys. D: Appl. Phys.*, **31**, pp. 2653-2710, 1998.
2. H. Morkoc, "Potential applications of III-V nitride semiconductors", *Mater. Sci. and Engineering*, **B43**, pp. 137-146, 1997.

3. S. Strite and Morkoc, "Growth and properties of group III nitrides", J. Vac. Sci. Technol. **B10**, pp.1237-1240, 1992.
4. Properties of Group III Nitrides, Ed.: J.H. Edgar, INSPEC, Chapter 1.5, London, pp. 1-290, 1994.
5. O. Madelung. Semiconductors-Basic Data, Ed.: Springer, 2nd rev., Chapter 2.12, pp. 122-124, 1996.
6. A. Yamamoto, M. Tsujino, M. Ohkubo and A. Hashimoto, "Metalorganic chemical vapor deposition growth of InN for InN/Si tandem solar cell", Sol. Energy Mater. and Sol. Cells, **35**, pp. 53-60, 1994.
7. S. P. Gordienko, B. V. Fenochka, "Thermodynamic properties of group III nitrides", Zh. Fiz. Khim. (USSR), **5**, pp. 530-535, 1977.
8. V. A. Tyagai, A. M. Evstigneev, A. N. Krasiko, A. F. Andreeva, V. Ya. Malakhov, "Optical properties of indium nitride films", J. Sov. Phys. Semicond., **11**, pp. 1257-62, 1977.
9. S. Kumar, Li Mo. Motlan, T. L. Tansley, "Elemental composition of reactively sputtered indium nitride thin films", Jpn. J. Appl. Phys, **35**, pp. 937-940, 1996.
10. V.V. Sobolev, S.G. Kroitoru, A.F. Andreeva, V.Ya. Malakhov, "Reflectance spectra of indium nitride", Sov.Phys.-Semicond., (USA), **13**, pp. 485-486, 1979.
11. A. F. Andreeva, V. Ya. Malakhov, E. G. Ostroumova, "Study of the features of electron structure of InN by characteristical losses of electrons energy spectrum", Naukova Dumka, Kiev, pp. 136-139, 1980.
12. S.N. Grinyeav, V.Ya. Malakhov, V.A.Chaldyshev, "Calculation of zone structure of GaN and InN by pseudopotential model technique", Sov.Phys. J. (USA), **29**, pp. 311-316, 1986.
13. K. Osamura, S. Naka, Y. Murakami, "Preparation and optical properties of $Ga_{1-x}In_xN$ thin films", J. Appl. Phys., **46**, pp. 3432-3440, 1975.
14. T. L. Tansley, R. J. Egan, "Properties of sputtered nitride semiconductors", Thin Solid Films., **164**, pp. 441-445, 1988.
15. H-J. Kwon, Y-H. Lee, "Raman spectra of indium nitride thin films grown by microwave-excited metalorganic vapor phase epitaxy on (0001) sapphire substrates", Appl. Phys. Lett., **69**, pp. 937-942, 1996.
16. D. Feiler, R. Williams, A. Talin, H. Yoon, M. Goorsky, "Pulsed laser deposition of epitaxial AlN, GaN, and InN films on sapphire (0001)", J. Crystal Growth, **171**, pp. 12-20, 1997.
17. T. L. Tansley, R. J. Egan, "Properties of sputtered nitride semiconductors", Thin Solid Films., **164**, pp. 441-445, 1988.
18. T. L. Tansley, C. P. Foley, "Optical band gap of indium nitride", J. Appl. Phys., **59**, pp. 3241-3250, 1986.
19. T. L. Tansley, C. P. Foley, "Infrared absorption in indium nitride", J. Appl. Phys., **60**, pp. 2092-2100, 1986.
20. K. L. Westra, M. J. Brett, "Near IR optical properties of sputtered InN films", Thin Solid Films, **192**, pp. 227-230, 1990.
21. Q. Guo, O. Kato, M. Fujisawa, A. Yoshida, "Optical constants of indium nitride", Solid State Commun., **83**, pp. 721-723, 1992.
22. V. Ya. Malakhov, " Low temperature synthesis of the III-a sub-group metal nitrides. Properties and their novel applications in the opto- and acoustoelectronics", Proc. of the 6th Euro Conf. DF-95, Barcelona, pp. 11-12, 1995.
23. V. Ya. Malakhov, T. L. Brysina, " Optical properties and electronic structure of InN thin films", Proc. of the 6th Int. Symp. TFE-95, Lazurnoye, pp. 161-162, 1995.

Exciton localization and the Stokes' shift in undoped InGaN/GaN multiquantum wells

Y. F. Chen, T. Y. Lin and H. C. Yang

Department of Physics, National Taiwan University, Taipei, Taiwan, Republic of China

ABSTRACT

Optical properties of undoped InGaN/GaN multiquantum wells(MQWs) have been investigated by photoconductivity, photoluminescence, and photoluminescence excitation measurements. We report the first observation of persistent photoconductivity (PPC) in InGaN/GaN MQWs and show that the PPC effect arises from In composition fluctuations in the InGaN well layer. From the analysis of the decay kinetics, the localization depth caused by composition fluctuations has been determined. Compared with the results of complementary absorption and photoluminescence measurements, it is found that the quantum-confined Stark effect due to piezoelectric field and composition fluctuations both exist in the InGaN/GaN MQWs. These two effects are responsible for the photoluminescence Stokes' shift in the InGaN well layers. Here, we provide an unique way to distinguish the individual contribution to the Stokes' shift for the piezoelectric field and composition fluctuations.

Keywords: InGaN quantum wells, localization, Stokes' shift

1. INTRODUCTION

The InGaN-based materials have been attracting much interest because of their importance in both scientific and technological aspects¹⁻³. Many studies on the characteristics of the InGaN-based quantum wells(QWs) have recently been reported. One of the important issues in InGaN material is its phase-separating nature due to a mismatch of thermodynamical and chemical stabilities between the InN and the GaN, strain in InGaN caused by lattice mismatch to the underlying GaN layer, or threading dislocation(TD) or defect-related driving forces⁴. Remarkable compositional separation and inhomogenities are reported both in bulk epilayers and QWs. The performance of many conventional optoelectronic devices has been limited by the ability to control both point defects and structural defects in these materials. However, recent reports suggest that InGaN-based emitting devices are less sensitive to TD(1×10^8 to $1 \times 10^{12} \text{ cm}^{-2}$) than conventional III-V compound semiconductor-based devices⁵. Thus, it is interesting to clarify the emission mechanism of InGaN-based QWs and double-hetero(DH) structures for further improvement of device performance.

It is known that group III nitrides have very large piezoelectric constants. Therefore if nitride layers are under biaxial strain, large piezoelectric fields can be generated and the quantum confined Stark effect(QCSE) caused by this field can strongly effect on the optical properties of the materials. Recently, several experiments have observed the large piezoelectric fields⁶, redshift in the photoluminescence(PL) peak energy⁶ and blueshift in electroluminescence(EL) peak energy with

increasing driving current or excitation intensity⁷ of the InGaN QWs. These results suggest the existence of a piezoelectric field in the strained InGaN layers.

On the other hand, the importance of localized states caused by potential fluctuations of InGaN alloys in QWs and even in bulk has been pointed out by several groups^{4,8-11}. In particular, the observation of higher efficiency of the LEDs, with increasing strain in the single quantum well(SQW) upon an increase in the In content in the InGaN well layers, cannot be explained only by the QCSE induced by the piezoelectric fields^{8,9}. It is suggested that the localization effects induced by compositional fluctuations must overcome these intrinsic limitations due to the piezoelectric field. Thus, the actual electronic states in InGaN QWs may be determined by competition between the QCSE and the influence of the potential fluctuations of InGaN alloys. Because both QCSE and potential fluctuations contribute to the Stokes' shift, it is very difficult to determine the individual contribution. However, in order to completely understand the properties of InGaN-based devices, the determination is desirable.

It has been demonstrated that the localization depth from the flat band edge of localized states due to potential fluctuations of alloy system, including InGaN epilayer¹¹ can be determined by probing the decay kinetics of the persistent photoconductivity(PPC) phenomenon. In this letter, we report the observation of the PPC effect in the undoped InGaN/GaN multi-quantum wells(MQWs) for the first time. In order to obtain the depth of potential fluctuations, the observed PPC effect was investigated with focus on its decay kinetics. Together with the studies on the complementary absorption and PL spectra, we are able to separate the effect of the strain and the influence of potential fluctuations on the Stokes' shift in InGaN QWs.

2. SAMPLES AND EXPERIMENTS

The samples were prepared by metalorganic chemical vapor deposition. A series of MQWs with 10 periods of 4-nm-thick $\text{In}_{0.11}\text{Ga}_{0.89}\text{N}$ wells and 8-nm-thick GaN barriers capped by 20-nm-thick GaN were grown on 2.2- μm -thick GaN on (0001) sapphire. All the grown layers were intentionally undoped. Since the critical thickness of $\text{In}_x\text{Ga}_{1-x}\text{N}/\text{GaN}$ ($0 < x < 0.2$) samples are reported to be greater than 40 nm¹², we assume the coherent growth of InGaN layers in the MQWs. For PL measurements under low excitation conditions (less than $1\text{W}/\text{cm}^2$), we used photons with energy about 3.8eV from a Xe lamp, which were dispersed by a 0.27m monochromator. Emitted light was dispersed by a 0.85m focal length grating monochromator and detected phase sensitively by a photomultiplier tube. Similar arrangements were used for the photoluminescence excitation(PLE) measurements except the dispersed light from the Xe lamp was used as the continuous radiation. For the photoconductivity(PC) measurements, ohmic contacts were formed by depositing indium drops to the four corners of the sample and annealing the sample at 400°C for 10s. A constant direct voltage was applied and the conductivity was measured by Keithley 236 source measure unit. Details of PPC measurement procedure were similar those described previously¹³. All the data obtained under different conditions were taken in such a way that the system was always allowed to relax to equilibrium. The measurements were carried out between 10K and room temperature(RT).

3. RESULTS AND DISSCUSION

Figure 1 shows the photocurrent as a function of time and illumination in an undoped $\text{In}_{0.11}\text{Ga}_{0.89}\text{N}/\text{GaN}$ MQWs with monochromatic radiation at a photon energy of 3.31eV taken at 10K. A persistent photoconductivity effect is clearly observed, and similar transient behavior was seen when other monochromatic light with photon energy up to 3.81eV was used as the illumination source. This behavior clearly indicates that the PPC effect is caused by the carrier generation in the InGaN layer. A similar PPC effect has been observed in $\text{In}_{0.3}\text{Ga}_{0.7}\text{N}$ epilayer as shown in our previous report¹¹. This observed PPC effect can be easily understood in terms of the alloy potential fluctuations(APF) in the InGaN alloy. At low temperature, the photoexcited electrons and holes are trapped and spatially separated by local potential fluctuations, the recombination of electron-hole pairs is inhibited, and hence PPC occurs.

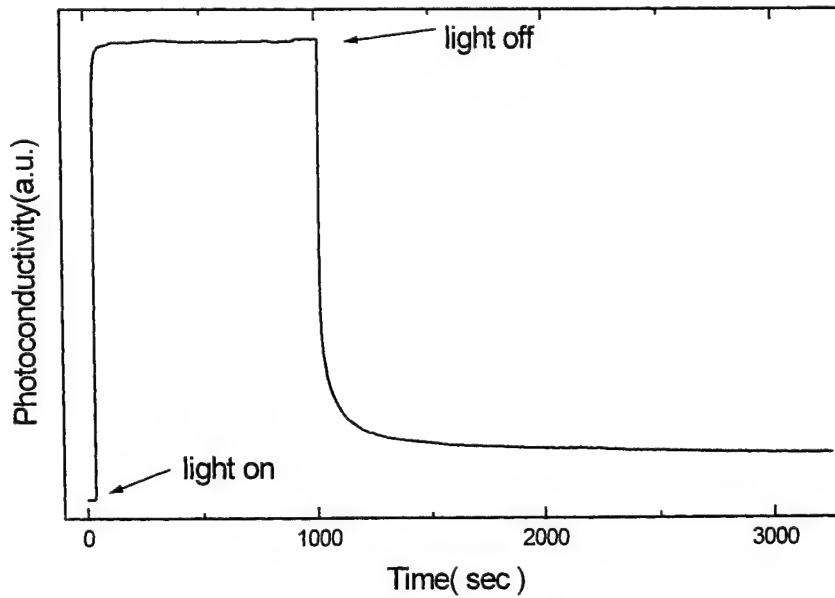


Fig. 1 Typical buildup and decay behavior of PPC in the undoped $\text{In}_{0.11}\text{Ga}_{0.89}\text{N}/\text{GaN}$ MQWs at 10K.

The decay kinetics in photocurrent after turning off the illumination shows a stretched-exponential behavior that can be expressed as

$$I_{\text{ppc}}(t) = I_{\text{ppc}}(0) \exp[-(t/\tau)^\beta], \quad (0 < \beta < 1) \quad (1)$$

where $I_{\text{ppc}}(0)$ is the PPC buildup level at the mount of light excitation being removed, τ is the PPC decay time constant and β is the decay exponent. Figure 2 shows a representative plot of $\ln[\ln(I_{\text{ppc}}(0)) - \ln(I_{\text{ppc}}(t))]$ versus $\ln(t)$. The good linear behavior of the plot demonstrates that the PPC decay is well described by equation (1). A least-squares fit to the experimental data results in a time constant $\tau \sim 400\text{s}$, which is much shorter than the previous value for an undoped $\text{In}_{0.3}\text{Ga}_{0.7}\text{N}$ epilayer. This shorter time constant can be easily understood by the fact that the In content in the InGaN/GaN

MQWs sample is less than that in the $\text{In}_{0.3}\text{Ga}_{0.7}\text{N}$ layer, because the depth of potential fluctuations increases with increasing In content. The PPC effect can be observed up to RT characterized by a decay time constant in several seconds. To obtain the average depth of potential fluctuations, we perform the temperature evolution of the PPC effect. The carrier capture barrier ΔE , which characterizes the energy difference between the localized states and the flat band edge, can be estimated from the temperature of the time constant, τ :

$$\tau = \tau_0 \exp(\Delta E / \kappa T) \quad (2)$$

It was found that ΔE is about 50 meV as shown in the inset of Fig. 2. Thus, a Stokes' shift of 50 meV in magnitude with respect to the flat band edge of InGaN/GaN MQWs sample can be expected if only the potential fluctuations is taken into account.

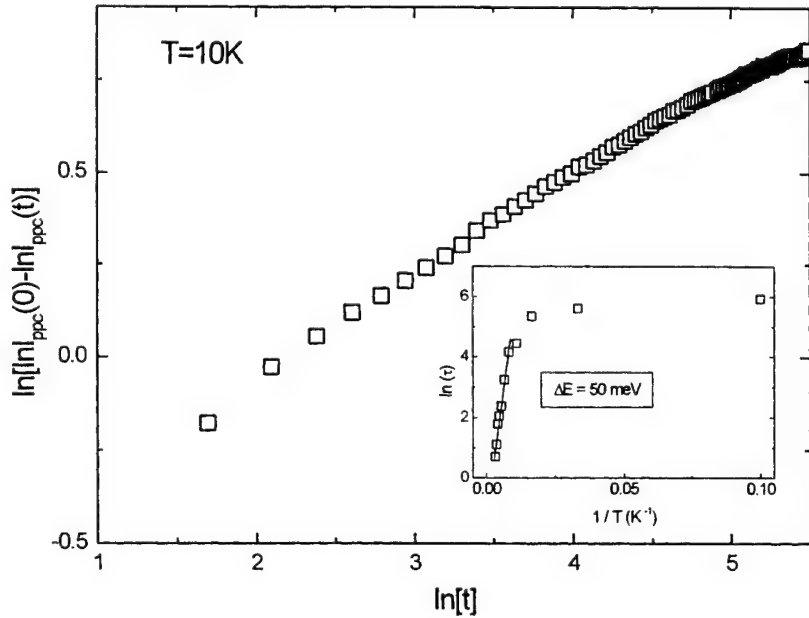


Fig 2 Plot of $\ln[\ln(I_{ppc}(0)-I_{ppc}(t))]$ versus $\ln(t)$ for the undoped $\text{In}_{0.11}\text{Ga}_{0.89}\text{N}/\text{GaN}$ MQWs at 10K. The linear curve indicates that the PPC decays according to the stretched-exponential function $I_{ppc}(t)=I_{ppc}(0)\exp[-(t/\tau)^\beta]$. The inset shows the capture barrier ΔE obtained according to $\tau = \tau_0 \exp(\Delta E / \kappa T)$.

In order to further investigate the emission properties of the InGaN/GaN MQWs sample, we performed the PL, PLE and PC measurements respectively. Figure 3 summarizes the PL, PLE and PC spectra taken at 10K. The PL spectrum is dominated by a single emission band with peak energy centered at 3.21eV and there is no observable deep level emission. The full width at half maximum is about 65meV. The PLE measurements for the InGaN-related main PL emission were monitored at 3.00, 3.10, 3.15, 3.22, and 3.28 eV, respectively. We only show the PLE spectrum taken at the PL emission edge(3.10eV). Similar behaviors were observed for the different detection energies. The absorption of InGaN wells

increases monotonically, reaching a maximum at 3.35 eV, and remains almost constant until absorption by the GaN barrier occurs at about 3.44 eV. The PC spectrum also indicates the absorption edge of InGaN layer at around 3.35 eV which is consistent with the PLE results. Thus, the emission of the InGaN layer shows a large Stokes' shift of 140 meV in magnitude with respect to the absorption edge as determined by PLE or PC spectra. The fact that the Stokes' shift is larger in value than that of the localization depth determined independently by PPC decay kinetics indicates that additional effects on the emission properties of the InGaN/GaN MQWs sample should be taken into account.

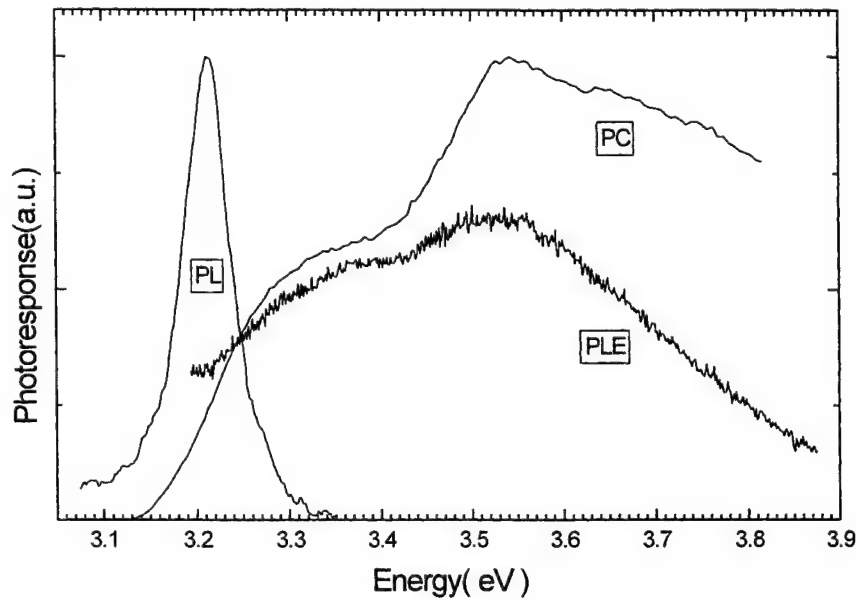


Fig 3 PL, PLE and PC spectra of the undoped $\text{In}_{0.11}\text{Ga}_{0.89}\text{N}/\text{GaN}$ MQWs sample taken at 10K.

The discrepancy in value between the localization depth and the Stokes' shift found in this InGaN/GaN MQWs can be understood by further considering the strain effect in the InGaN alloy layers. Recently, T. Takeuchi et al.⁶ have shown that the PL peak energy of strained $\text{In}_{0.13}\text{Ga}_{0.87}\text{N}$ MQWs was redshifted with respect to that of thick single $\text{In}_{0.13}\text{Ga}_{0.87}\text{N}$ layers. This phenomenon is attributed to the influence of the QCSE induced by the piezoelectric field, taking into account that the quantum size effect cannot cause the PL peak energy of QWs to shift to lower energy than that of thick strained single layer. It has been pointed out that to evaluate the redshift strictly, important factors, such as detailed material parameters of InN, the amount of screening by photo-generated carriers and the influence of local fluctuations of alloy composition at the InGaN layer should be incorporated. Since the MQWs used in this work contain only nominally undoped layers, screening of the piezoelectric field in the InGaN wells should be limited and can be ignored under low excitation conditions. Our investigations on the PPC effect and the Stokes' shift therefore lead to the fact that the QCSE caused by piezoelectric field dominates the emission mechanism of the undoped InGaN/GaN MQWs and contributes a redshift of 90 meV to the total

Stoke-like shift, while the contribution of alloy potential fluctuations is only 50 meV.

4. CONCLUSION

In summary, we observed the existence of persistent photoconductivity(PPC) effect in the undoped InGaN/GaN MQWs for the first time. The decay kinetics of PPC effect is investigated and a localization depth of the localized energy states caused by In composition fluctuations in the InGaN well layers is determined. Compared with the results of complementary absorption and PL measurements, it is found that the QCSE and alloy potential fluctuations(APF) both exist in the $\text{In}_{0.11}\text{Ga}_{0.89}\text{N}/\text{GaN}$ MQWs and the QCSE may dominate the emission mechanism. We point out that the piezoelectric field and APF can significantly influence the optical properties of the InGaN-based materials and should be taken into account for the design and fabrication of group-III nitride based heterointerface devices.

ACKNOWLEDGEMENTS

This work was partially supported by the National Science Council of the Republic of China.

REFERENCES

1. S. N. Mohammad, A. A. Salvador and H. Morkoc, Proceedings of IEEE, **83**, 1306(1995)
2. "GaN and Related Materials", S. J. Pearton ed., Gordon and Breach Science Publishers, (1997)
3. S. Nakamura, M. Senoh, S. Nagahama, N. Iwasa, T. Yamada, T. Matsushita, H. Kiyoku, Y. Sugimoto, T. Kozaki, H. Umemoto, M. Sano and K. Chocho, Appl. Phys. Lett. **72**, 211(1998), *ibid* **72**, 2014(1998)
4. For a review, see S. ChiChibu, T. Soda, K. Wada and S. Nakamura, J. Vac. Sci. Technol. B **16**, 2204(1998)
5. S. Nakamura, Science, **281**, 956(1998)
6. T. Takeuchi, S. Sota, M. Katsuragawa, M. Komori, H. Takeuchi, H. Amono. and I. Akasaki, Jpn. J. Appl. Phys. **36**, Pt.2, L382(1997)
7. T. Mukai, M. Yamada and S. Nakamura, Jpn J. Appl. Phys. **37**, Pt.2, L1358(1998)
8. S. Nakamura, M. Senoh, N. Iwasa, S. Nagahama, T. Yamada and T. Mukai, Jpn. J. Appl. Phys. **34**, Pt.2, L1332(1995)
9. T. Mukai, D. Morita and S. Makamura, J. Cryst. Growth. **189/190**, 778(1998)
10. M. S. Minsky, S. B. Fleischer, A. C. Abare, J. E. Bowers, E. L. Hu, S. Keller and S. P. Denbaars, Appl. Phys. Lett. **72**, 1066(1998)
11. T. Y. Lin, J. C. Fan and Y. F. Chen, Semicond. Sci. Technol. **14**, 406(1999)
12. T. Takeuchi, H. Takeuchi, S. Sota, H. Sakai, H. Amono. and I. Akasaki, Jpn. J. Appl. Phys. **36**, Pt.2, L177(1997)
13. L. H. Chu, Y. F. Chen, D. C. Chang and C. Y. Chang, J. Phys.: Condens. Matter, **7**, 4525(1995)

SESSION 5

III-As and III-P LEDs

Improved efficiency positive and negative luminescent light emitting devices for mid-infrared gas sensing applications

Mark Pullin^{*}, Xiaobing Li, Jörg Heber, David Gevaux and Chris Phillips

Solid State Group, Physics Department, Imperial College, London UK, SW7 2BW

ABSTRACT

InAs / InAsSb SQW LED's incorporating $\text{AlAs}_{0.02}\text{Sb}_{0.98}$ or $\text{In}_{0.83}\text{Al}_{0.17}\text{As}$ electron confining barrier layers are reported. Devices emitting 108 μW and 84 μW at 300 K with QW emission at $\lambda = 4.1 \mu\text{m}$ and $\lambda = 4.7 \mu\text{m}$ exhibit quantum efficiencies that are improved by factors of 7 and 3.4 respectively over control samples without the barrier. The operating wavelength of negative luminescent (NL) devices with InAs / In(As,Sb) strained-layer-superlattice (SLS) active regions has been extended to $\lambda = 6.8 \mu\text{m}$. NL performance is limited by leakage currents that originate in the n^+ contact layer.

Keywords: mid-IR, LED, In(As,Sb), negative luminescence

1. INTRODUCTION

There is great demand for improved gas sensing and measurement systems for many common gases (CO_2 , CO, NO_2 , SO_2 , NH_3 , O_3 , CH_4) in areas such as pollution monitoring, horticulture, biomedical and petrochemical industries. Improved systems could offer superior sensitivity and selectivity, increased portability and reduced maintenance/calibration all at a lower overall cost. Spectroscopic methods are particularly effective in the mid-infrared (mid-IR) range (3-10 μm) since the strongest absorption bands of many gases occur in this region.

For ultimate sensitivity (ppb and less), selectivity and portability, tuneable laser diode based sources will be used and much progress has been made recently in interband and intraband, cascaded and non-cascaded mid-IR laser diodes.^{1,2,3,4} In this method the laser wavelength is swept through individual vibration-rotation lines within an absorption band. The cost of such systems is high due to the requirements of stringent laser diode output specification and sophisticated line stabilisation techniques. For many applications the typical gas concentrations to be detected are much higher (100 ppm to 100 %) and overall system purchase and ownership cost become the critical factor. Here broadband sources are utilised and the integrated absorption over an entire manifold of gas absorption lines used to determine gas concentration.⁵

Mid-IR light emitting diodes (LED's) have been considered as alternatives to currently employed incandescent sources because they offer increased efficiency, reliability, are more robust and intrinsically safe, can be modulated at high frequencies, offer longer lifetimes and may not require "burn-in" before operation. Significant advances have recently been made with device output powers up to 1 mW^{6,7} at shorter wavelengths ($\lambda = 4.2\text{--}4.6 \mu\text{m}$). Longer wavelength ($\lambda \sim 5.5 \mu\text{m}$) InSb p-i-n LED's have also been demonstrated with internal quantum efficiencies (η_{int}) of 5.5 % at room temperature,⁸ and these have been incorporated into prototype NO_2 gas detection systems.⁹

Our previous studies of single quantum well (SQW) LED's that comprise a strained InAsSb QW active region embedded in an InAs cladding layer have demonstrated promising results at $\lambda \sim 5 \mu\text{m}$ and $\lambda \sim 8 \mu\text{m}$ with room temperature $\eta_{\text{int}} = 1.3 \%$ and 0.83 % respectively.¹⁰ The type-II band offset¹¹ found in InAs / InAsSb heterostructures results in an effective bandgap smaller than the bulk alloy and facilitates the design of longer wavelength emitters without exceeding the 'strain budget' for pseudomorphic growth.

We have also investigated the use of strain relaxed type-II InAs / InAsSb strained-layer-superlattice (SLS) active regions grown on InAs substrates.¹² By incorporating an electron confining AlSb barrier layer into this $\lambda \sim 4.2 \mu\text{m}$ emitter the 300 K η_{int} was increased by a factor of 4 to 2.8 %. In this paper we study the effect of incorporating electron confining barriers into our pseudomorphic SQW LED designs.

^{*} Electronic mail: m.pullin@ic.ac.uk

Auger recombination (AR) is a major obstacle to efficient device operation at longer wavelengths. Electron-hole pairs recombine non-radiatively in an AR event with the surplus energy transferred to a third carrier which is excited to a higher energy state. As such it is an intrinsic process that will occur in bulk material regardless of its quality. AR rates increase with carrier concentration, temperature or as the bandgap is reduced and are thought to currently limit both mid-IR LED and interband laser diode performance. Bandstructure engineering in semiconductor heterostructures has been proposed as a means to reduce AR rates and both theoretical and experimental results support this.^{13,14,15}

A novel route to sources in the mid-IR that avoids some of the above problems associated with AR in high J emitters is so called "negative luminescence" (NL). In essence this process involves suppressing a portion of the thermally generated radiation an object emits as a consequence of its finite temperature. In a narrow gap semiconductor the physical origin of this radiation is the recombination of thermally-generated electron-hole pairs. Carriers are extracted from the active (near intrinsic) region of p-i-n structures by a reverse bias, and their reduced concentrations ($np \ll n_0p_0$) result in the net absorption of ambient blackbody radiation. The "extraction" process may be limited by leakage currents originating in the contacting layers that tend to restore the active region np product to its thermal equilibrium level n_0p_0 , but these can be blocked using additional excluding barriers. NL has been demonstrated in InAs,¹⁶ InSb and CdHgTe bulk materials systems¹⁷ and from type II InAs/GaSb¹⁸ and InAs/InAsSb superlattice diodes¹⁹ utilising carrier exclusion and extraction. The NL spectrum is characterised by the product of the emissivity of the material and the Planck blackbody function. For gas sensing purposes a NL device is in principle just as useful as a more conventional forward biased LED, since the ability to modulate a body's thermally generated radiation in effect allows it to be used as an emission source.

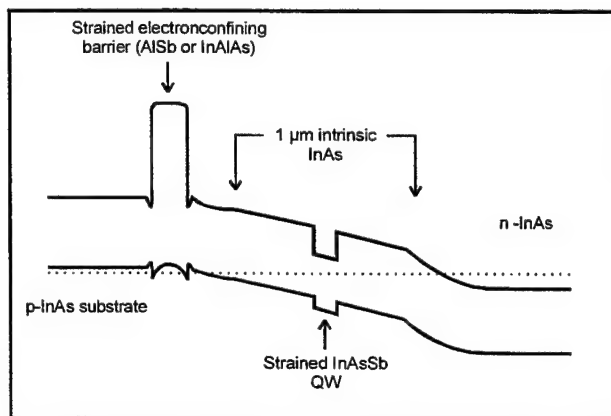


Figure 1. Schematic band diagram of pseudomorphic SQW LED with electron confining barrier layer.

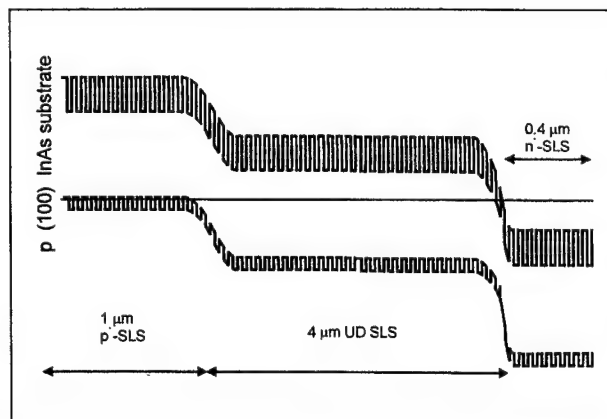


Figure 2. Schematic band diagram of SLS NL device.

2. EXPERIMENTAL DETAILS

2.1. Sample design and growth

All samples were grown by MBE in a VG Semicon V80H MBE system equipped with uncracked As_4 and Sb_4 sources and using Si and Be as the n- and p-type dopants respectively. Five SQW wafers (3 with an electron confining barrier layer and 2 control samples with no barrier) and one sample designed for negative luminescent operation are studied here.

We investigated the use of AlSb and InAlAs electron confining barriers in the SQW LED's. AlSb possess the larger band gap ($E_g^{300K}(AlSb)=1.6$ eV) but the additional compressive strain and change of group V species may pose growth problems. As an alternative we also considered $In_{1-x}Al_xAs$ barrier layers with $x \sim 17\%$ ($E_g^{300K}(InAl_{0.17}As)=0.72$ eV). As in previous structures, hole confinement is accomplished via a valence band step at the interface of the intrinsic and n+ doped layers (Fig. 1 and 2).

All InAs and QW layers were grown at substrate temperatures $T_{sub}=470$ °C using As/In flux ratios of 3-4. A 5 s pause was employed at each interface during which the surface was exposed to only the group V fluxes for the subsequent layer

growth. The AlSb and InAlAs barrier layers were grown at a higher substrate temperature of $T_{\text{sub}} = 500$ °C and this necessitated a longer pause while the substrate temperature stabilised. For the AlSb layer the interfaces were grown to be "Sb-like".

All SQW samples possessed a mirror-like surface. The SLS sample surface was also shiny although a faint cross-hatch pattern could be observed when viewed under a microscope. This is consistent with the expected relaxation of the SLS with respect to the InAs substrate.

2.2. Structural Characterisation

As-grown wafers were analysed by HRXRD before processing in order to determine QW and barrier layer parameters. HRXRD rocking curves of all six samples are shown in Fig. 3, along with numerical simulations for the pseudomorphic SQW samples. Sample parameters thus determined are detailed in Table 1.

Layer	SQW Samples					SLS NL sample
	IC653 Al(As,Sb) "BARRIER"	IC675 "CONTROL"	IC692 "CONTROL"	IC693 (In,Al)As "BARRIER"	IC694 (In,Al)As "BARRIER"	IC720 SLS: 105 Å InAs / 105 Å InAs _{0.83} Sb _{0.97}
n+ InAs	1 µm	1 µm	1 µm	1.1 µm	1 µm	0.5 µm n+ SLS
UD InAs	0.5 µm	0.5 µm	0.5 µm	0.9 µm	0.5 µm	
UD QW	240 Å	150 Å	180 Å	180 Å	180 Å	4 µm UD SLS
	InAs _{0.86} Sb _{0.14}	InAs _{0.87} Sb _{0.13}	InAs _{0.9} Sb _{0.1}	InAs _{0.9} Sb _{0.1}	InAs _{0.91} Sb _{0.09}	
UD InAs	0.52 µm	0.5 µm	0.5 µm	0.11 µm	0.5 µm	1 µm p+ SLS
Barrier"	250 Å UD- AlAs _{0.02} Sb _{0.98}	-----	-----	220 Å p- In _{0.83} Al _{0.17} As	220 Å p- In _{0.83} Al _{0.17} As	
p+ InAs	0.86 µm	1 µm	0.2 µm	0.2 µm	0.2 µm	0.25 µm p InAs
p+ InAs substrate	$2 \times 10^{18} \text{ cm}^{-3}$					

Table 1. SQW and SLS NL device parameters as determined by HRXRD analysis.

Consistent with the mirror like surfaces, the SQW rocking curves all reveal interference artifacts that confirm growth was indeed pseudomorphic for these samples, as intended. For the SQW samples IC693 and IC694 incorporating a compressively strained In(As,Sb) QW with an (In,Al)As barrier under tensile strain, the corresponding Bragg peaks in the XRD spectra occur on opposite sides of the substrate diffraction peak, making numerical simulation straightforward and accurate. This is not the case for the SQW LED IC653 with the Al(As,Sb) barrier under similar compressive strain to the In(As,Sb) QW ($dA/A = 0.022$ and 0.019 respectively) and their Bragg angles are also similar. It was found to be impossible to get a good numerical fit to the experimental data unless a small amount of As is incorporated into the AlSb layer[†]. This is not unrealistic given that some As will remain in the growth chamber when the As shutter is closed following the growth of the preceding InAs layer, even after the "Sb soak" procedure described above.

IC653, with 4 adjustable parameters for the QW and barrier layers all contributing to what is effectively a single resolved layer peak, means there actually exists a region of parameter space all yielding similar numerical simulations. That the barrier layer does actually exist however, is confirmed by the rapid oscillations superimposed on top of the main layer peaks (shown in inset, Fig. 3) and is consistent with a QW-barrier layer separation of $0.52 \mu\text{m}$, close to the nominal value of $0.5 \mu\text{m}$, and demonstrates good group III flux calibration in our system. Oscillations of the same origin are more readily apparent in the XRD spectra of IC693 where the QW-barrier spacing is approximately a factor of 5 lower. In both cases the existence of these Fabry-Perot oscillations demonstrate good planarity of the QW and barrier layers over the $\sim 3\text{mm}^2$ X-ray probe beam area.

[†] A satisfactory fit could be obtained by employing an AlSb layer thickness < 50 Å, but this is unrealistic given the nominal growth thickness of 200 Å for a layer whose growth is determined by the Al flux

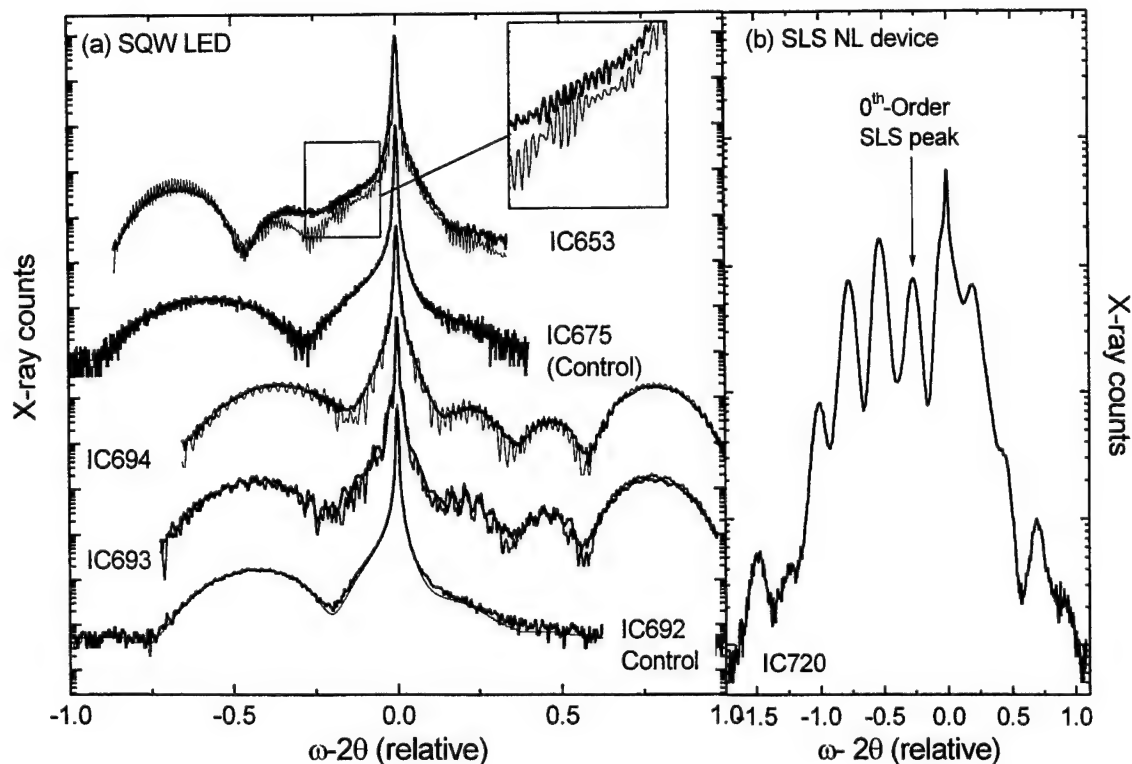


Figure 3. HRXRD (004) rocking curves and numerical simulations of SQW and SLS NL device wafers.

The SLS sample IC720 is relaxed with respect to the InAs substrate and this precludes a simulation using dynamic diffraction theory. However the observations of 5 orders of satellite diffraction peaks attest the good structural quality of the SLS away from the InAs-SLS interface (where the misfit dislocation density is expected to be high). In conjunction with asymmetric (115) reflections the SLS parameters are determined to be 105 \AA InAs / 105 \AA $\text{InAs}_{0.83}\text{Sb}_{0.17}$, somewhat less than the target alloy composition of $\text{InAs}_{0.75}\text{Sb}_{0.25}$, and the emission will occur at wavelengths shorter than the 300K design wavelength of $\sim 8 \text{ \mu m}$. The SLS is determined to be 70 % relaxed with respect to the InAs substrate.

2.3. Electroluminescence measurements

For forward bias electroluminescence measurements 600 \mu m diameter mesa etched LED's were fabricated using conventional wet-etch photolithography and a Cr/Au annular contact evaporated on the top of each device. The etch was stopped after the QW layer but before the barrier layer in order to protect these Al-containing layers from oxidation. Later experiments indicated that device performance was not sensitive to the etch depth, although no long term trials have been performed to date.

Larger area devices were required for negative luminescence measurements on the SLS sample IC720, and this was achieved by cleaving $2 \times 2 \text{ mm}$ squares from the wafer after contact evaporation had been performed. The resulting 9×9 array of annular contacts that formed the top contact probably does not represent the optimal geometry for this large area device. No passivation layers or AR coatings were applied to any of the devices studied.

Packaged devices were attached to the cold finger of a cryostat for measurements in the range 10-325 K. Current pulses up to 1.5 A, duration 6 \mu s and PRF 20 kHz were used to drive the devices. Luminescence was passed through a BOMEM DA3.02 spectrometer fitted with CaF_2 windows and reflecting optics onto either a 77 K CMT ($\lambda_{\text{cutoff}} = 12 \text{ \mu m}$) photoconductive or 77 K InSb ($\lambda_{\text{cutoff}} = 5.5 \text{ \mu m}$) photovoltaic detector, depending on the device emission wavelength.

Absolute device output powers were determined at room temperature using only the detector (calibrated to a blackbody standard) and no other optics in order to avoid spectrometer losses. Emission was spatially and spectrally integrated and this reference datum used to scale the cryostat spectra.

3. DEVICE RESULTS

3.1. "Barrier"- SQW devices

Electroluminescence spectra at 10 K from the SQW devices under low forward bias are shown in Fig. 4. The spectra are dominated by two distinct emission peaks, the lower energy feature we attribute to recombination in the QW and the higher feature at 400-425 meV to recombination in the surrounding InAs region. The lower QW emission energies from the sample IC653 and its control sample IC675 are consistent with greater Sb content in the QW. QW emission from the control sample IC692 (IC675) occurs at an energy some 37 (45) meV lower than the "barrier" sample IC693 (IC653) despite their similar QW parameters. The FWHM of the control samples (IC675, IC692) QW peaks are also much narrower than those observed in the corresponding "barrier" samples (IC653, IC693, IC694), and the overall intensities are over an order of magnitude lower so that broad impurity related luminescence is visible. The above is all consistent with a lower injected electron density in the QW of the control samples compared to the "barrier" samples, indicating that the barrier is effective in confining carriers at these temperatures.

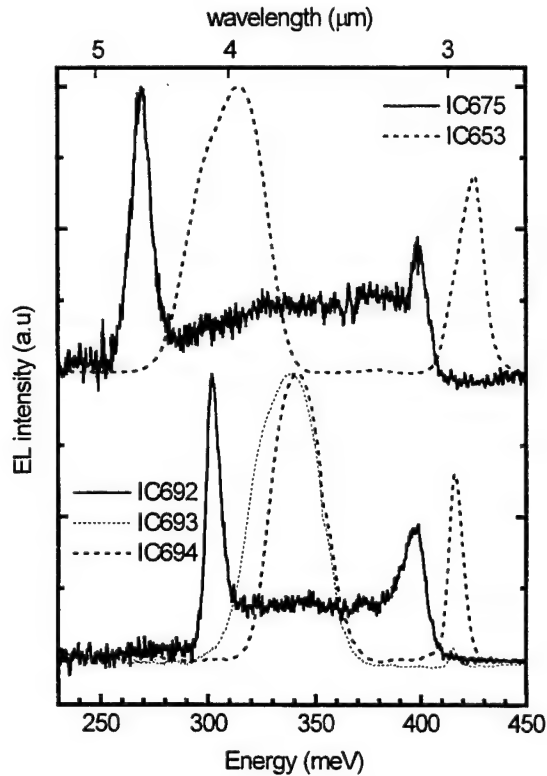


Figure 4. Normalised 10 K low injection spectra for the SQW LED's with $I_0=100$ mA.

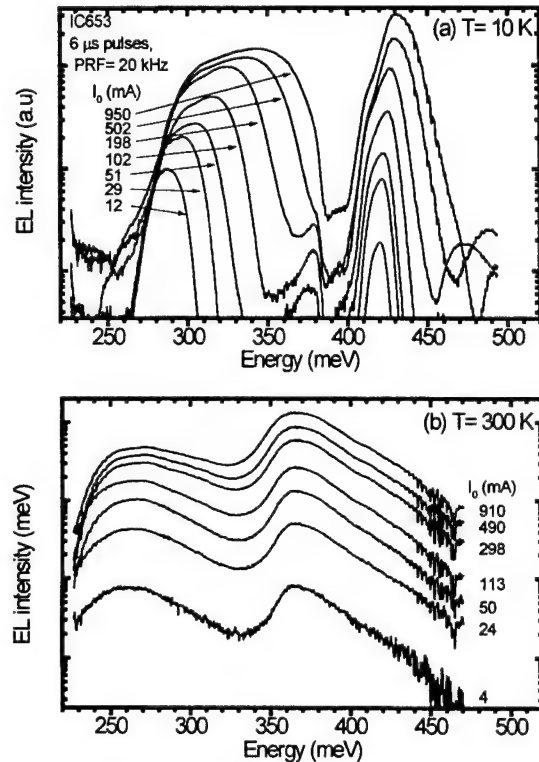


Figure 5. Electroluminescence spectra (plotted on a semi-logarithmic scale) of SQW + AlAsSb "barrier" LED IC653 as a function of injection current at (a) 10 K and (b) 300 K.

As the bias current density is increased the "barrier" samples exhibit further pronounced blue shift and broadening due to band filling in the QW. Fig. 5(a) showing 10 K spectra of IC653 under increasing bias current, demonstrates that this blue shift may be as large as 56 meV (corresponding increase in FWHM from 22 to 70 meV) and shows the QW spectral profile becoming more asymmetric. Near the electron subband edge, the QW joint density-of-states is determined by random local variations in the QW width and/or alloy composition and this yields symmetric spectral profiles. At higher bias currents the

electron quasi-Fermi level moves higher into the electron subband and these band edge states no longer dominate the QW spectral profile which becomes more asymmetric as a result.

The temperature evolution of the device spectra are studied under high pulsed injection currents ($I_0=600$ mA) found under typical operating conditions, and these are shown in Fig. 6 (a)-(d). The y-axis scaling is identical for each graph so relative emission intensities may be compared. Several initial observations can be made;

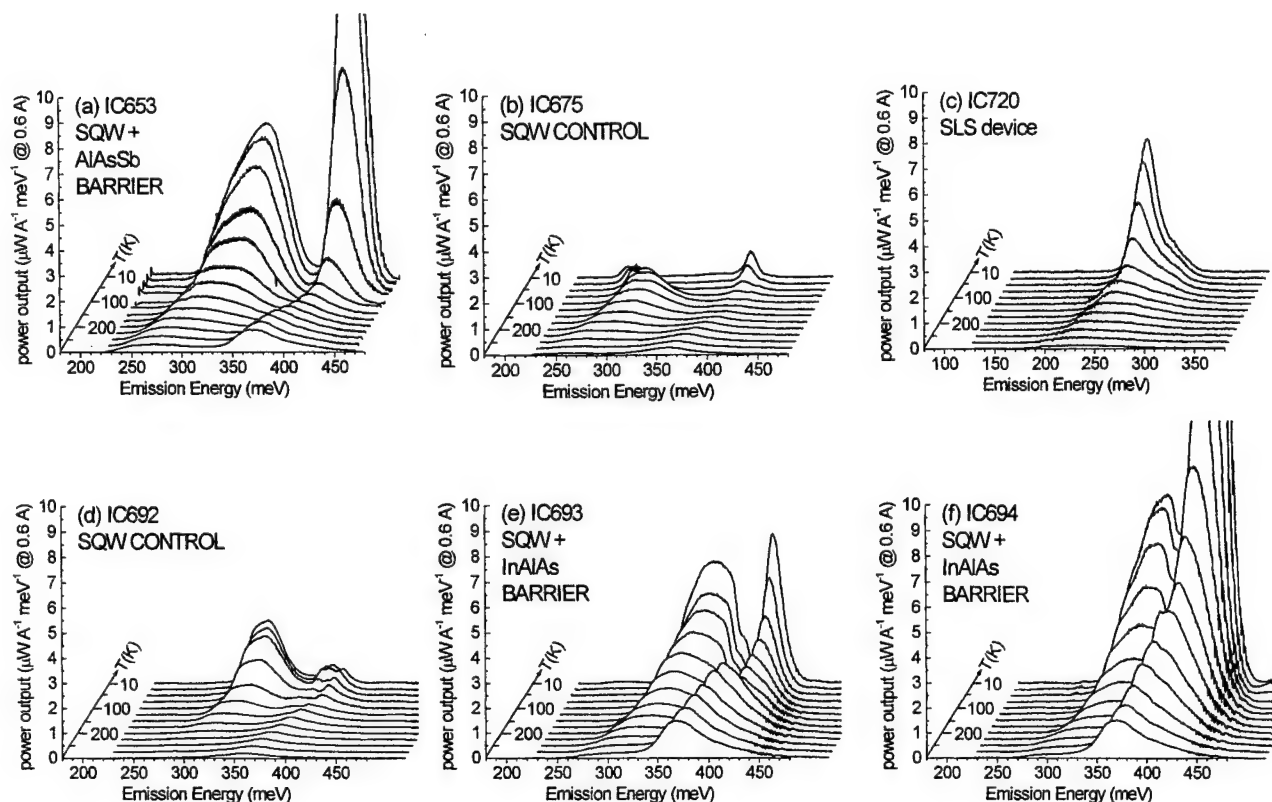


Figure 6 (a) -(e). Luminescence spectra from SQW and SLS NL devices as a function of temperature (10-300 K).

(a) In all cases electroluminescence (both QW and InAs related) from the "barrier" SQW samples (IC653, IC693 and IC694) is much greater than that from the control samples (IC675, IC692).

(b) QW electroluminescence intensity from the "barrier" samples is comparable at all temperatures. Whilst the InAs electroluminescence intensity is also similar for the "barrier" samples near room temperature, at low temperatures IC693 (asymmetric 0.1 μm /0.9 μm InAs cladding layers) emits significantly less InAs-related luminescence than the other two "barrier" samples (both symmetric 0.5 μm /0.5 μm InAs cladding layers).

(c) For many of the samples the InAs related recombination exhibits a complex temperature dependence typically characterised by a rapid fall as the temperature is initially increased followed by a recovery at higher intermediate temperatures.

(d) It is worth noting that electroluminescence from the lattice mismatched SLS device IC720 exhibits only a single peak characteristic of the SLS, and that its intensity is of the same order of magnitude as the QW peaks of the "barrier" devices. It suggests good optical quality in the active region and hence that the p-SLS layer is effective in blocking the propagation of misfit dislocations from the SLS-InAs interface to the undoped SLS active region. The SLS feature has lower FWHM~ 23 meV ($T=10$ K) compared to the "barrier" samples, consistent with an absence of band filling in the 4 μm -thick undoped active region.

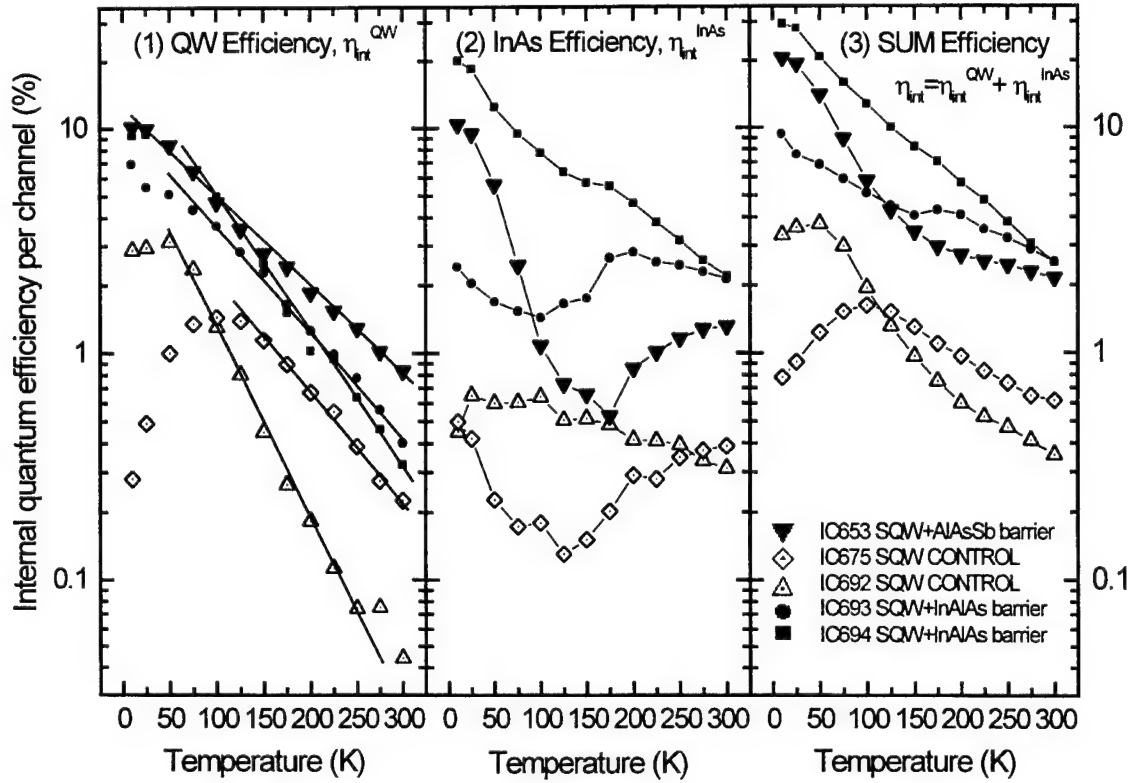


Figure 7. Internal quantum efficiencies per channel (QW and InAs related luminescence) for the SQW LED's as a function of temperature.

In order to more fully analyse the interdependence between the 2 principle radiative channels in the SQW devices the internal quantum efficiency (assumed proportional to the carrier recombination rate in each channel) is calculated for each channel. This procedure removes the effect of different photon energies for the 2 emission peaks and peak broadening effects as the temperature is increased. Output power is corrected for the 18 % contact obscuration and we assume an internal to external efficiency ratio of $1/n(n+1)^2 \approx 72$, and neglect free carrier re-absorption effects in the top $n+$ contact layer. A curve fitting procedure is used to separate QW from InAs peaks where they are not separately resolved (typically near room temperature) and the quantum efficiency for each channel (η_{int}^{QW} and η_{int}^{InAs}) obtained by integrating over these peaks after dividing by photon energy. Results for η_{int}^{QW} and η_{int}^{InAs} and the total (summed) efficiency are shown in Fig. 7.

η_{int}^{QW} for the "barrier" samples IC653, IC693 and IC694 all decrease exponentially with increasing temperature, this behaviour may be somewhat empirically represented by a parameter T_0 (where $\eta(T) = \eta(0)\exp(-T/T_0)$) and we have $T_0(653) = 110$ K, $T_0(693) = 93$ K and $T_0(694) = 72$ K. Initially η_{int}^{QW} for the control samples IC675 and IC692 *increases* with T , probably as the result of increasing diffusion lengths and thus increasing carrier concentration in the QW (supported by a rapid broadening in the QW emission profile that is characteristic of band filling effects described earlier). Thereafter the control samples η_{int}^{QW} both fall exponentially and are described by $T_0(675) = 89$ K and $T_0(692) = 52$ K.

The higher T_0 of the "barrier" SQW devices compared to their respective control samples demonstrates a clear improvement in device performance. The η_{int}^{QW} for the "barrier" samples are always greater than those for the control samples at a given T . The T_0 values themselves are the result of a complex interdependence of processes determined by diffusion lengths, thermal escape rates from the QW and non-radiative (Auger and Shockley-Read) recombination rates in the quantum well and surrounding InAs. That the T_0 values for the shorter wavelength (and thus shallower well) control sample $T_0(IC692) = 52$ K is less than that for the longer wavelength (deeper well) QW $T_0(IC675) = 89$ K; that this trend is also mirrored by the

"barrier" devices (irrespective of the actual barrier material), and that similar wavelength samples possess similar T_0 's suggest that thermal escape from the QW rather than Auger recombination is the limiting factor for efficient high temperature operation at the operating wavelengths considered here.

Sample	IC653 (BARRIER)	IC675 (CONTROL)	IC692 (CONTROL)	IC693 (BARRIER)	IC694 (BARRIER)	IC720 (BARRIER)
T_0 (K)	110	89	52	93	72	127

Table 2. T_0 parameters determined from exponential decay of QW electroluminescence as a function of temperature.

Further evidence for thermal escape of carriers from the QW as the temperature is increased is evident from $\eta_{\text{int}}^{\text{InAs}}$. The mid-T range increase in $\eta_{\text{int}}^{\text{InAs}}$ is believed to be attributable to carriers having sufficient thermal energy to escape from the QW and recombine in the surrounding InAs region. For the deeper well (longer wavelength) samples IC653 and IC675 (control) this transfer of carriers out of the well begins at higher temperatures (125-175 K) than for the shallower well (shorter wavelength) devices IC693 and IC694 (in the range 100-150 K)

For the shorter wavelength ($\lambda \sim 4.1 \mu\text{m}$) "barrier" samples IC693 / IC694 studied here the total 300 K power output is 108 μW , corresponding to $\eta_{\text{int}} = 2.5 \%$ and a factor of 7 greater than the $\lambda \sim 4.1 \mu\text{m}$ control sample IC692 with $\eta_{\text{int}} = 0.4 \%$. Of the total EL output 11-14 μW (12-13 % of the total emission) originates from the QW compared to 1.5 μW for the control, a factor of 7 improvement.

Overall 300 K power output from the longer wavelength ($\lambda \sim 4.7 \mu\text{m}$) "barrier" sample IC653 is slightly less than the shorter wavelength "barrier" samples (84 μW against 108 μW) but the fraction of electroluminescence originating from the QW is actually increased at 27 μW (32 % of the total emission). This reflects the beneficial effect of deeper quantum wells in reducing thermal escape. For the corresponding $\lambda \sim 4.7 \mu\text{m}$ control sample IC675 the total power output is 7.6 μW with a similar fraction originating from the QW. The $\eta_{\text{int}} = 2.1 \%$ for the longer wavelength "barrier" sample IC653 is a factor 3.4 greater than that found in the control.

3.2. Negative luminescence (NL) devices

We have previously reported initial NL results from devices containing an InAs / InAsSb SLS active region that emitted at 4.2 μm .¹⁹ These initial devices had relatively short operating wavelengths, thin (1 μm) active regions and NL efficiencies $\eta_{\text{NL}} < 20 \%$ (where η_{NL} is defined at a given temperature by the ratio of maximum NL power (Fig. 9) to that of a BB at the same temperature). Here we extend the operating wavelength and investigate the feasibility of growing thicker ($\sim 4 \mu\text{m}$) SLS active regions in order to offset the reduced absorption co-efficient at longer wavelengths. With the SLS composition of IC720 yielding an effective 300 K bandgap at $\sim 6.8 \mu\text{m}$ the available blackbody emittance is 3.4 mWcm^{-2} .

Room temperature (FB) positive and (RB) negative luminescence spectra from a 4 mm^2 device are shown in Fig. 8 at a bias current $I_0 = 1 \text{ A}$. A contact obscuration factor of 11.5 % has been taken into account, although the non-optimal top contact geometry may result in current crowding beneath the contacts that would cause a deterioration from the true spectral emittance values shown. The theoretical limit corresponding to a 300 K blackbody has been included for reference. The negative luminescence operating wavelength has been extended to $\lambda = 6 \mu\text{m}$.

A useful feature of negative luminescence operation, namely the increase in output power with temperature, is evident in Fig. 9. This contrasts conventional FB operation where the output is seen to decrease with increasing temperature in the range 270-300 K (reducing slope of positive luminescence branch of Fig. 9). Temperature dependent variations of output power currently constitute a major obstacle to the successful implementation of LED's into low cost gas sensing systems where expensive temperature stabilisation hardware must be avoided. AC bias schemes utilising both positive and negative luminescent device operation may eventually prove useful in this respect.

The peak spectral emittance in RB (at $\lambda = 6 \mu\text{m}$) is $-0.5 \mu\text{W/cm}^2 \text{ meV}$, about the same as the earlier $\lambda = 4.2 \mu\text{m}$ NL device ($-0.45 \mu\text{W/cm}^2 \text{ meV}$).¹⁹ The present device is operating at longer wavelengths where more of the 300 K blackbody spectrum is available and so there is a consequent reduction in η_{NL} (1.1 % at the peak of the NL spectrum, climbing to $\sim 5\%$ at shorter wavelengths) compared to the earlier $\lambda = 4.2 \mu\text{m}$ device. However, that the emittance has not decreased despite a substantial increase in the operating wavelength highlights the potential of this operating mode.

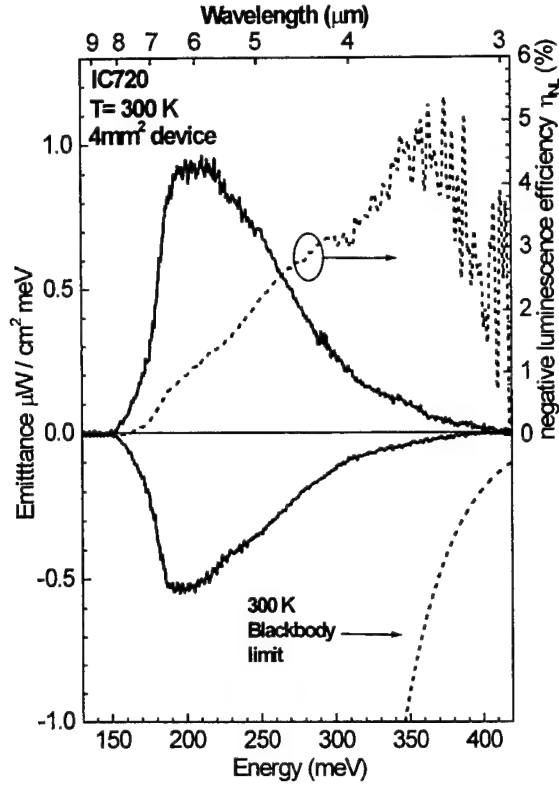


Figure 8. Positive and negative luminescence from SLS NL device IC720 at 300K, and negative luminescence efficiency.

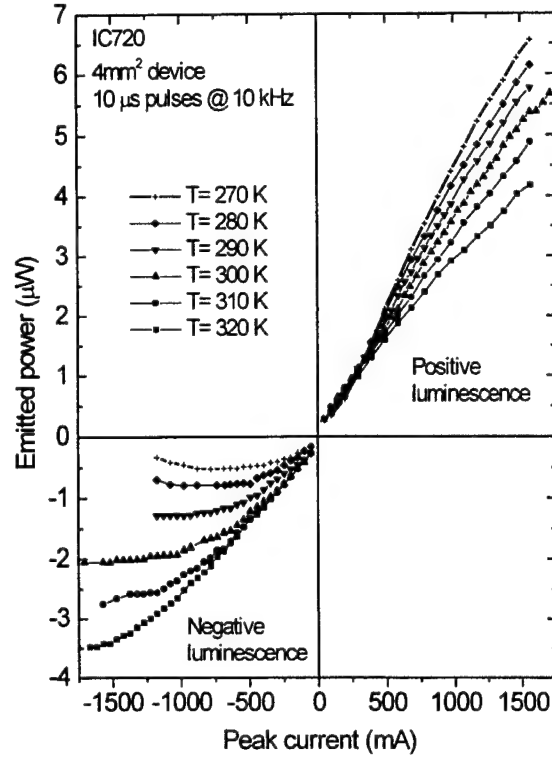


Figure 9. FB and RB L-I curves for SLS NL device IC720 in the temperature range 270-320 K. FB power output decreases while RB power increases as the temperature is increased.

The reduction in η_{NL} occurs despite the present device incorporating a thicker active region to offset the reduction in absorption co-efficient as the active region wavelength is increased. This suggests that the present device η_{NL} is being limited by leakage currents that act to reduce the extraction process and limit the reduction in np product in the active region. We believe that the dominant mechanism negating the extraction process in RB may be the generation of minority holes, possibly by a CHHL Auger process, in the top n⁺ SLS layer. Suitable wide bandgap n-doped layers, such as short period n-InAs / AlSb superlattices, may prove beneficial in reducing this leakage current and improving device performance.

4. CONCLUDING REMARKS

Further improvements in SQW LED device performance have been realised by incorporating electron confining barrier layers. Both compressively strained $\text{AlAs}_{0.02}\text{Sb}_{0.98}$ and $\text{In}_{0.83}\text{Al}_{0.17}\text{As}$ barriers under tensile strain have been successfully grown into SQW devices whilst maintaining pseudomorphic growth to the available InAs substrates. Room temperature quantum efficiencies have been improved by factors by up to 7.

Negative luminescence operation has been extended to $\lambda=6 \mu\text{m}$ in the InAs / InAsSb SLS system without any reduction in emittance compared to earlier $\lambda=4.2 \mu\text{m}$ devices. NL device performance appears to be limited by leakage currents originating in the top n⁺ contact layer that act to limit the extraction process. The use of wide gap n-doped contact layers may bring significant improvements in this respect.

ACKNOWLEDGMENTS

Financial support from the UK Engineering and Physical Sciences Research Council and a European Community Marie Curie Fellowship (JH) are gratefully acknowledged.

REFERENCES

1. A. Müller, M. Beck, J. Faist, U. Oesterle, M. Illegems, "Electrically tunable, room-temperature quantum-cascade lasers" *Appl. Phys. Lett.* **75** (11), pp 1509-1511, 1999
2. G. Strasser, S. Gianordoli, L. Hvozda, W. Schrenk, K. Unterrainer, E. Gornik, "GaAs/AlGaAs superlattice quantum cascade lasers at $\lambda \approx 13 \mu\text{m}$ ", *Appl. Phys. Lett.* **75** (10), pp 1345-1347, 1999
3. J.L. Bradshaw, R.Q. Yang, J.D. Bruno, J.T. Pham, D.E. Wortman, "High-efficiency interband cascade lasers with peak power exceeding 4 W/facet", *Appl. Phys. Lett.* **75** (10), pp 2362-2364, 1999
4. C.L. Felix, W.W. Bewley, I. Vurgaftman, L.J. Olafsen, D.W. Stokes, J.R. Meyer, M.J. Yang, "High-efficiency midinfrared "W" laser with optical pumping injection cavity", *Appl. Phys. Lett.* **75** (19), pp 2876-2878, 1999
5. S.D. Smith, A. Vass, P. Bramley, J.G. Crowder, C.H. Wang, "Comparison of IR LED gas sensors with thermal source products.", *IEE Proc.-Optoelectron.* **144** (5), pp 266-270, 1997
6. A.A. Popov, V.V. Sherstnev, Y.P. Baranov, C. Alibert, "Powerful mid-infrared light emitting diodes for pollution monitoring" *Electron. Lett.* **33** (1), pp. 86-88, 1997
7. A. Krier, H. Gao, V. Sherstnev, Y. Yakovlev, "High power 4.6 μm LED's for CO detection", *Electron. Lett.* **35** (19), pp. 1665-1667, 1997
8. T. Ashley, "Electronic and optoelectronic devices in narrow-gap semiconductors", *Inst. Phys. Conf. Ser. No. 144*, pp 345-352, 1995
9. C.H. Wang, J.O. Crowder, V. Mannheim, T. Ashley, D.T. Dutton, A.D. Johnson, G.J. Pryce and S.D. Smith, "Detection of NO_2 using a room temperature operation mid-infrared InSb light emitting diode", *Electron. Lett.* **34** (3), pp 300-301, 1998
10. P.J.P. Tang, H. Hardaway, J. Heber, C.C. Phillips, M.J. Pullin, R.A. Stradling and W.T. Yuen, "Efficient 300 K light-emitting diodes at $\lambda \sim 5$ and $\sim 8 \mu\text{m}$ from InAs / $\text{In}(\text{As}_{1-x}\text{Sb}_x)$ single quantum wells", *Appl. Phys. Lett.* **72** (26), pp 3473-3475, 1998
11. Y. B. Li, D. J. Bain, L. Hart, M. Livingstone, C. M. Ciesla, M. J. Pullin, P. J. P. Tang, W. T. Yuen, I. Galbraith, C. C. Phillips, C. R. Pidgeon and R. A. Stradling, "Band Alignments and offsets in $\text{In}(\text{As}, \text{Sb})/\text{InAs}$ Superlattices". *Phys. Rev. B* **55** (7), pp. 4589-4595, 1997.
12. M.J. Pullin, H.R. Hardaway, J.D. Heber, C.C. Phillips, W.T. Yuen, P. Möck, "Room-temperature InAsSb strained-layer superlattice light-emitting diodes at $\lambda = 4.2 \mu\text{m}$ with AlSb barriers for improved carrier confinement", *Appl. Phys. Lett.* **74** (16), pp 2384-2386, 1999
13. C.R. Pidgeon, C.M. Ciesla, B.N. Murdin, "Suppression of non-radiative processes in semiconductor mid- infrared emitters and detectors", *Prog. Quantum. Electron.* **21** (5), pp 361-419, 1997
14. M.E. Flatté, C.H. Grein, T.C. Hasenberg, S.A. Anson, D.-J. Jang, J.T. Olesberg, T.F. Boggess, "Carrier recombination rates in narrow-gap $\text{InAs}/\text{Ga}_{1-x}\text{In}_x\text{Sb}$ -based superlattices" *Phys. Rev. B* **59** (8), pp 5745-5749, 1999
15. W.W. Bewley, C.L. Felix, E.H. Aifer, I. Vurgaftman, L.J. Olafsen, J.R. Meyer, H. Lee, R.U. Martinelli, J.C. Connolly, A.R. Sugg, G.H. Olsen, M.J. Yang, B.R. Bennett, B.V. Shanabrook, "Above-room-temperature optically pumped midinfrared W lasers", *Appl. Phys. Lett.* **73** (26), pp 3833-3855, 1998
16. S.S. Bologov, V.K. Malyutenko, A.P. Savchenko, "Charge-carrier exclusion in InAs", *Semiconductors* **31** (5), pp 444-445, 1997
17. T. Ashley, C.T. Elliot, N.T. Gordon, R.S. Hall, A.D. Johnson, G.J. Pryce, "Negative luminescence from $\text{In}_{1-x}\text{Al}_x\text{Sb}$ and $\text{Cd}_x\text{Hg}_{1-x}\text{Te}$ diodes", *Infrared Phys.* **36**, pp 1037-1044, 1995
18. L.J. Olafsen, I. Vurgaftman, W.W. Bewley, C.L. Felix, E.H. Aifer, J.R. Meyer, J.R. Waterman, W. Mason, "Negative luminescence from type-II InAs/GaSb suprlattice photodiodes", *Appl. Phys. Lett.* **74** (18), pp 812-814, 1999
19. M. J. Pullin, H.R. Hardaway, J.D. Heber, C.C. Phillips, "Type-II InAs / InAsSb strained-layer-superlattice negative luminescence devices", *Appl. Phys. Lett.* **75** (22), pp 3437-3439, 1999

Native oxidized AlAs current blocking layer for AlGaInP high brightness light emitting diodes

WANG Guohong*, MA Xiaoyu, ZHANG Yufang,
WANG Shutang, LI Yuzhang, CHEN Lianghui
National Engineering Research Center for Optoelectronics Devices
Institute of Semiconductors, Chinese Academy of Sciences

ABSTRACT

Native Oxide AlAs layer were employed to block the current injection from the top anode. The luminous intensity exceeded 75mcd of the LED chip with native oxide AlAs layer sandwiched 5 μ m AlGaAs current spreading layer under 20mA current injection. Electrical and optical properties the LED chip and plastically sealed lamp were measured. Aging of the LED chip and lamp were performed under 70°C and room temperature, Experiment results shown that there is no apparent effect of the native oxidized AlAs layer and the process on the reliability of the LED devices.

Keywords: Native Oxided AlAs, Current blocking layer, AlGaInP,
High Brightness Light Emitting Diodes.

1.INTRODUCTION

High-brightness visible light-emitting diodes(LEDs) are becoming increasingly important and have numerous potential applications, such as in the field of optical display system, traffic signal and automobile lamp. The quaternary AlGaInP alloy, which can be precisely lattice matched to GaAs substrate, have a direct bandgap ranged from 1.88 to 2.30eV^[1], with different aluminum composition, Mass production of AlGaInP high-brightness LEDs has been realized by using multi-wafers metal organic chemical vapor deposition (MOCVD) system recently. One of the problem in the InGaAlP LEDs was a restriction of light extraction efficiency caused by light absorption of top anode, Because the current injection concentrate under the anode. Thick current spreading layer, transparent anode^[2] and reverse biased pn junction current blocking layer^[3] were considered to reduce the current injection under anode. But these measurements whether lead to large cost or make fabrication process difficulty. In this article native oxide AlAs layer sandwiched 5 μ m AlGaAs were employed to block the current injection from the top anode, The fabrication process is simple and cost less.

2.STRUCTURE OF THE DEVICE

The Schematic cross sectional structure of the device was shown in fig.1, The epilayers were grown by LP-MOCVD on GaAs substrate, In sequence the device consist of 0.2 μ m GaAs buffer layer, 10 pairs AlAs(525nm)/GaAs(500nm) DBR for reflection of light toward absorptive GaAs substrate, DH structure active region with 1 μ m n-(Al_{0.7}Ga_{0.3})_{0.5}In_{0.5}P lower confinement layer,

* Emailaddress:ghwang@red.semi.ac.cn

This work is supported by "High Technology 863 Plan".

0.5 μm $i\text{-(Al}_x\text{Ga}_{1-x})_{0.5}\text{In}_{0.5}\text{P}$ and 1 μm $p\text{-(Al}_{0.7}\text{Ga}_{0.3})_{0.5}\text{In}_{0.5}\text{P}$ upper confinement layer. For current spreading and the blocking of the current injection under the top anode 0.1 μm AlAs sandwiched in 5 μm $\text{Al}_{0.8}\text{Ga}_{0.2}\text{As}$. Contact layer was 0.1 μm $p^+\text{-GaAs}$ doped $1 \times 10^{19}\text{cm}^{-3}$. In the center of the top anode 100 μm^2 square oxidation window were etched. Selective oxidized AlAs region is larger than the top anode to block current injection shown as the dashed arrow.

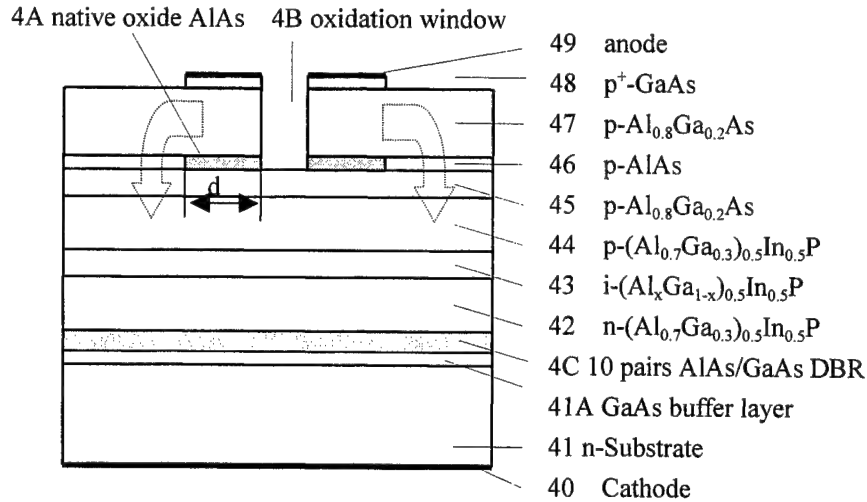


Fig. 1 Schematic cross sectional structure of the device

3.MATERIAL GROWTH AND DEVICE FABRICATION

AlGaAs/AlGaInP material were grown on GaAs substrate with orientation (001) off (111)A 6° by AXITRON AIX 200 MOCVD system, TMGa,TMAI,TMIn were used as group III elements precursors, PH3 and AsH3 were used as group V element precursors. For AlGaInP material growth the V/III ratio was 100. DEZn and SiH4 were used as p-typed and n-typed dopants respectively. The growth temperature was 700°C-750°C, The total hydrogen flow was 7l. The oxidation window was formed by lithograph after top anode deposition, Then $\text{Al}_{0.8}\text{Ga}_{0.2}\text{As}$ current spreading layer was etched with $\text{H}_2\text{SO}_4\text{:H}_2\text{O}_2\text{:H}_2\text{O}=3\text{:}1\text{:}1$ solution at room teperature., This solution only etch AlGaAs and stop at the surface of AlGaInP.

Au/Zn/Au was used as p-type , $\phi 100\mu\text{m}$ circle top anode was formed by lithography.

AlAs Oxidation process were performed after anode pattern lithograph. High purity N_2 through 80°C deionized water bath were used as oxidation gas, The oxidation were processed under 500°C with different time to check the current blocking effect variation.

AuGeNi was used as n-type contacts, The wafer was sawn to 300 \times 300 μm^2 square dice bounded on copper heat sink for measurement.

4.DEVICE PROPERTIES AND DISCUSSION

The device optoelectronic properties are strongly depend on the oxidation time, The oxidation speed is slowed down with oxidation time increase (shown in fig.2), The oxidation pattern is square when the oxidation time is less than 30 minutes, but when the oxidation time increased the oxidation pattern is rounded at the corner of the square because of the oxidation

speed is slowed down.

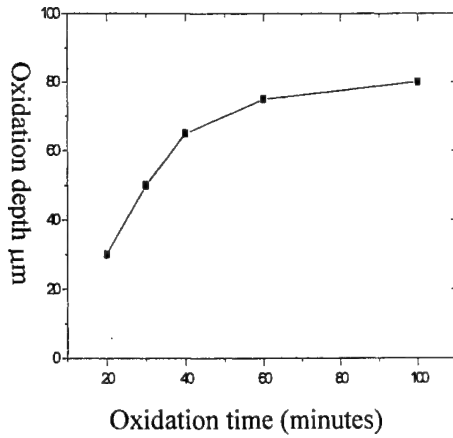


Fig.2 Oxidation depth d variation with oxidation time

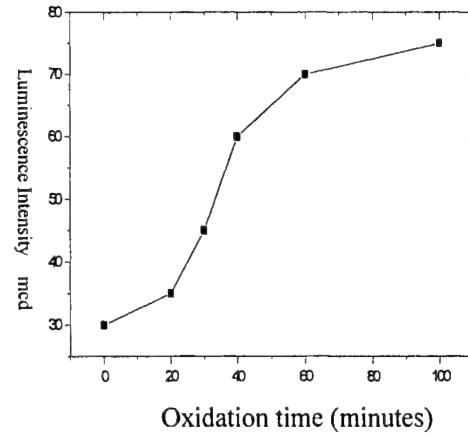


Fig.3 Luminescence Intensity (20mA) variation with oxidation time

Fig.3 shows the device luminescence intensity variation versus oxidation time, We found that the luminescence intensity increases slow at first 20 minutes and tends to saturation when the oxidation time is longer than 60 minutes. When the oxidation time is less than 20 minutes the oxidation depth is less than $30\mu\text{m}$, so the blocking layer is still under the top anode. When the oxidation is longer than 60 minutes, the oxidation blocking layer is larger than the top anode, so the current injection region is far away from the top anode, Light from active region almost cant reach the top anode.

As the oxidation depth increase the hole injection from anode need longer path to reach active layer combine with electron, so the series resistance increases, This caused the device operation voltage increasing with the oxidation time increase.

Fig.4 shows the operation voltage under 20mA versus oxidation. Compare with Fig.3, we think the optimized oxidation time is around 60 minutes, under this condition the light extraction is tend saturation and the operation voltage is acceptable.

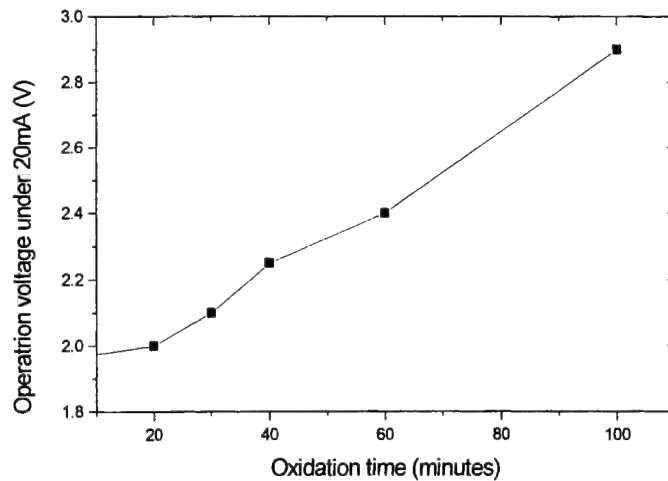


Fig.4. Device operation voltage under 20mA versus oxidation time

Fig.5 compared the reliability for different oxidation time under 70°C 20mA, Experiment results shows no apparent decreasing after oxidation process.

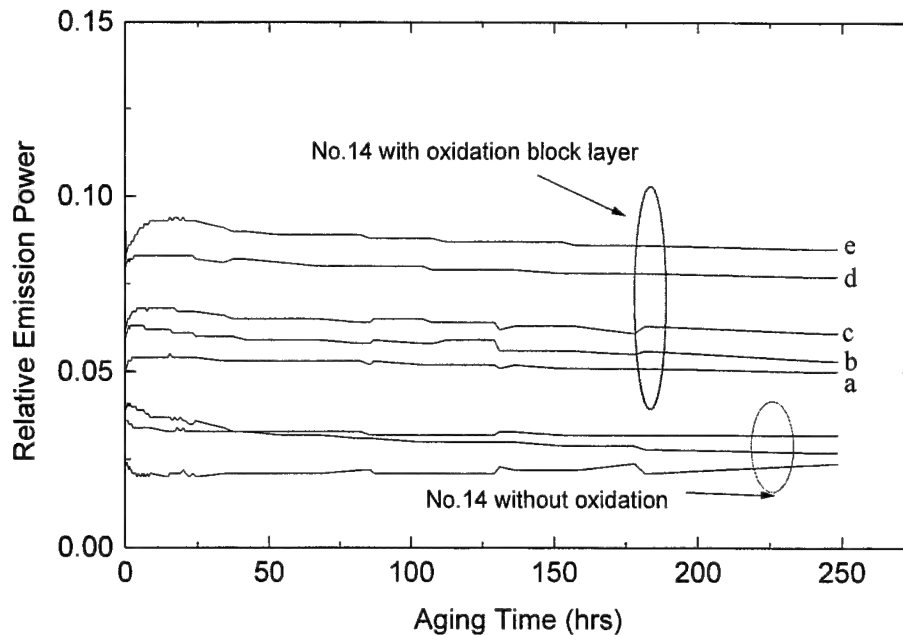


Fig.5 Device reliability for different oxidation time under 70°C 20mA
a:20, b:30, c:40, d:60, e:100 (minutes)

SUMMARY

Native Oxide AlAs layer was successfully employed to block the current injection from the top anode. The luminous intensity exceeded 75mcd of the LED chip with native oxide AlAs layer sandwiched 5 μ m AlGaAs current spreading layer under 20mA current injection. This result can be compared with LEDs which have thick GaP current spreading layer grown by VPE^[4]. Electrical and optical properties of the LEDs, The results show that oxidized AlAs depth must be well controlled to optimum the operation voltage and light emitting efficiency. Aging properties of the LED shown that there is no apparent effect of the native oxidized AlAs layer and the process on the reliability of the LED devices.

REFERENCES:

- [1] G.C.Chi, Y.K.Su, M.J.Jou, W.C.Hung "Window Layer for Current Spreading in InGaAlP Light-Emitting diode" J.Appl.Phys. 76(5) 1. 1994.
- [2] J.F.Lin M.C.Wu M.J.Jou et.al. "Highly reliable operation of Indium tin oxide AlGaInP orange light-emitting diodes" Electronics Letters. Vol.30 No.21 p.1793 .994.
- [3] Hideto Sugawara, Kazahiko Itaya and Genichi Hatakoshi, "Hybrid-Type InGaAlP/GaAs Distributed Bragg Reflectors for InGaAlP Light-Emitting Diodes", Jpn.J.Appl.Phys. Vol.33 (1994) p.6195-6198.
- [4] K.H.Huang J.G.Yu. J.G.Yu et.al. "Twofold efficiency improvement in high performance AlGaInP light-emitting diodes in the 555-620nm spectral region using a thick GaP window layer" Appl.Phys.Lett.61(9) 31 1992,p.1045.

SESSION 6

Novel Structures and Materials

Substrate Removed 850nm RCLED's and Small Core (63/125 μ m) Plastic Optical Fibers for Optical Data Communication.

Thierry Coosemans[#], Ronny Bockstaele, An Van Hove, Kris Naessens, Joff Derluyn,
Luc Vanwassenhove, Peter Van Daele, Ingrid Moerman, Roel Baets

University of Gent-IMEC, Department of Information Technology, Gent, Belgium, B-9000

ABSTRACT

Current developments in computer technology give rise to increasing data communication over relatively short distances at backplane- and inter MCM interconnect level. It is foreseen that electrical interconnect will not be able to accommodate the necessary data traffic in advanced data processing systems in the future and hence a bottleneck will be created. A potential remedy for this interconnect problem is the use of parallel optical datalinks. In this paper we propose small diameter step index plastic optical fiber ribbons in combination with high efficient resonant cavity LED's as a cheap and feasible option for these optical links. A design for such an optical link is presented with special attention for the optical pathway. Experimental results on the optical properties of the used POF are shown. We describe the development of RCLED's at 850nm specially designed for efficient coupling into POF. We measured a RCLED to POF coupling efficiency up to 40%. Additionally we report on the technologies used for the fabrication and assembly of the optical pathways and finally some experiments were carried out on the first realized assemblies.

Keywords: Resonant Cavity LED's, Plastic Optical Fiber, Parallel Optical Datalink,

1. INTRODUCTION.

Increasing component density, chip size and clock frequencies may create a bottleneck in electrical interconnections of data processing systems over a few years. Parallel optical interconnect with direct access to any location within a CMOS chip, has been proposed as a solution to the problems inherent to the electrical interconnect¹. Resonant Cavity LED's are suitable light sources for that kind of interconnect systems since they can be integrated into large 2D arrays. Moreover, they have a high efficiency at low current (no threshold), a low thermal and electrical resistance and they emit light vertically. In addition they are reliable, eye-safe, and relatively cheap. The cost of the optical link is indeed a dominating factor in realization of such optical interconnect systems. Therefore the use of polymer optical fibers (POF's) is extremely attractive: it is a very cheap product and moreover a quick end facet termination technique has been developed: the POF's are simply cut with a hot knife. In this way time the time consuming (and hence expensive) process of polishing the end facet, necessary in the case of glass fibers is avoided. In addition POF's exhibit smaller bending losses due to their large numerical aperture. Consequently compact optical links are possible. Moreover the large numerical aperture allows to capture a relative large part of the emitted light of the RCLED. Nowadays POF's with a diameter of 125 μ m are available what permits us to use the standard channel pitch of 250 μ m. Compact optical connections using a 4 X4 POF array bent over 90° have been reported^{2,3}. The fact that POF has a higher loss than glass fiber is of little importance since we consider interconnect distances that vary between a few centimeter and 1 meter. In this paper we propose the use of 850nm substrate removed RCLED's in combination with small diameter (63/125 μ m) step index POF for parallel optical links on backplane- and inter MCM interconnect level. We illustrate the optical properties of POF with some experimental results. We describe the development of these RCLED's specially designed for a maximal power coupling into the POF. In addition the power coupling between RCLED's and POF is studied with special attention for the alignment tolerances. Further on the realization of the optical pathways in the optical links is discussed. The design of these optical pathways is based on plates with grooves in which the POF's are fixed. These grooves are made with laser ablation in polymethyl metacrylate (PMMA) plates. After fixing the POF's in the grooves, the plates are aligned and stacked in order to create a 2-dimensional POF array. We developed a

versatile and flexible alignment method we called “virtual” alignment. First experimental results on the assembly are shown and discussed. Large part of the work has been done in the framework of the European Community ESPRIT-OIIC project ^{4,5}. The aim of this project is to realize several demonstrators in which parallel optical links interconnect FPGAs (Field Programmable Gate Arrays). In this way a 3D stack of interconnected gates with low latency and large programmability flexibility is realized.

2. 63/125 μm STEP INDEX PLASTIC OPTICAL FIBERS.

Since step index POF has been reported for the first time in 1968 by Dupont it has been evolving rapidly ⁶. Nowadays low loss graded index fibers are introduced in WDM systems ⁷, home networks ⁸ and automotive systems ⁹. Most of the available POF has a large core ($>300\mu\text{m}$) what results in low loss (and hence cheap) connectors. However for compact parallel chip-to-chip interconnect links a standard pitch of $250\mu\text{m}$ is adequate. Hence a POF with a core diameter of $63\mu\text{m}$ and an overall diameter of $125\mu\text{m}$ is a compatible choice. Moreover, reducing the core diameter allows the use of smaller detector diameters what increases the data transmission speed. For that purpose PMMA POF has been purchased at ASAHI chemical and the geometrical and optical properties were studied. In addition extensive work was done on the end facet termination of POF ¹⁰. Several techniques were studied and evaluated. All the samples used for the experimental work reported in this paper are terminated with “hot knife cutting”: a 110°C warm knife edge is used to cut the POF's.

2.1. Geometrical properties.

The POF's have been measured on their core and cladding diameter: we found an average core diameter of $63\mu\text{m}$ with standard deviation of $2.36\mu\text{m}$. This variation on the core diameter can cause some limited losses on the transmission efficiency while coupling a POF to a RCLED/detector or to another POF. For example, even in the case of perfect alignment two butt-coupled POF's will still suffer an average transmission loss of 0.18dB caused by difference in core diameter. For the overall diameter a value of $122.6\mu\text{m}$ was found, with a standard deviation of $5.8\mu\text{m}$. How this will influence the coupling efficiency has not been investigated yet, but it will depend on the shape of the grooves in which the POF's are fixed. Also the core-cladding concentricity will influence the coupling efficiency, but it has not been investigated neither.

2.2. Absorption losses.

Absorption losses are one of the main drawbacks of the use of POF. As opposed to glass fiber having losses of few dB per

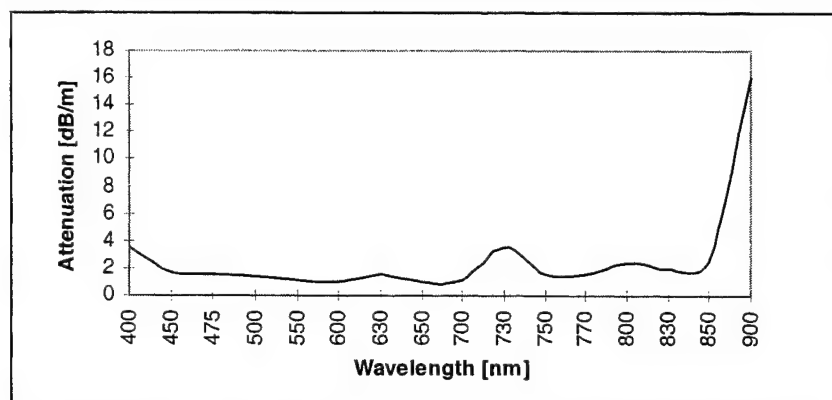


Fig. 1: Absorption spectrum for a PMMA step index fiber.

kilometer, POF's have losses in the order of few dB per meter. (fig 1). Moreover the low loss wavelength domain is situated between 400 and 850nm. This is one of the reasons why we chose 850nm as the emitter wavelength. However, for optical links of maximal 1 meter the absorption losses are acceptable. The absorption loss at 850nm has been measured with a cut back method: a value of 2.8dB/meter was found.

2.3. Numerical aperture and bending losses.

The numerical aperture of the POF is specified at 0.5. This has been verified experimentally: the numerical aperture was

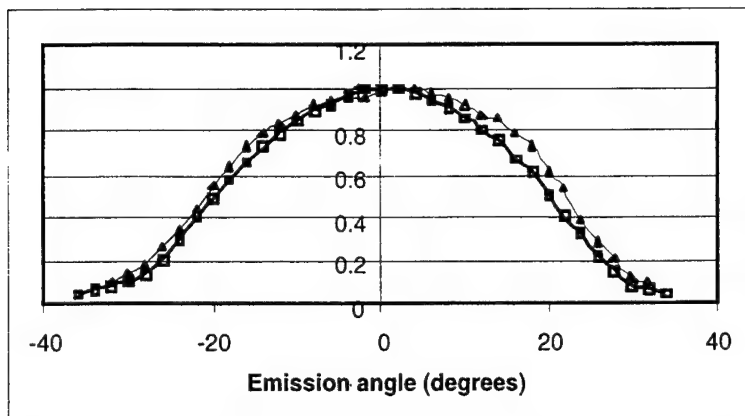


Fig 2: Far field emission pattern of a 50cm long POF. The curve with the squares gives the field without a bend, the curve with the triangles gives the field after a 360 degrees bend.

calculated from a far field emission pattern of a 1 meter long POF. A value of 0.5 was found indeed. A high numerical aperture decreases the bandwidth of the link. But here again for small distances this is irrelevant. On the other hand this relatively high NA permits low bending losses. In order to verify this, POF's were bent and the transmission losses were measured. Bending radii down to 2 millimeter did not cause any losses. Moreover we looked at the influence of bends on the mode distribution in the POF. Therefore a 360° bend (radius 2mm) was introduced in a 50cm long POF. As can be seen from figure 2 the far field emission pattern is only slightly disturbed. This implies that the efficiency of the POF to detector coupling at the end of the optical link is independent of any bends in the POF. Neither is there any risk of crosstalk at detector level induced by bends.

3. 850nm SUBSTRATE REMOVED RESONANT CAVITY LED'S.

Standard planar LED's have a low efficiency due to the total internal reflection at the semiconductor-air interface. However, if the active layer is sandwiched between 2 mirrors, the resonant cavity effect alters the radiation pattern, resulting in a more directed beam and smaller emission spectra¹¹⁻¹³. These devices are called RCLED's. Compared to standard LED's, more power is emitted within the solid angle of escape, resulting in increased extraction efficiency. This effect has been used to increase the total extraction efficiency, up to values of 22 % for 980 nm RCLED's¹⁴. Other techniques for increasing the efficiency of LED's include the use of surface roughening as in the case of the non resonant cavity LED. Over 17% overall efficiency at high speed has been reported¹⁵. For the considered POF based optical link, RCLED's at 850nm were developed. This emission wavelength has the advantage of allowing the detection by integrated Si detectors. However, the GaAs substrate of the through-substrate emitting devices has to be removed completely, as it is highly absorbing. This substrate removal is achieved by a combination of a mechanical polish and a wet chemical etching technique. The RCLED is designed in such a way that a maximum amount of power is launched into the numerical aperture of POF, at the lowest possible drive current.

3.1. Structure and performance of the RCLED's.

The RCLED structure is shown in fig 3. The active layer (3 GaAs quantum wells embedded in Al₂₀Ga₈₀As barriers) is

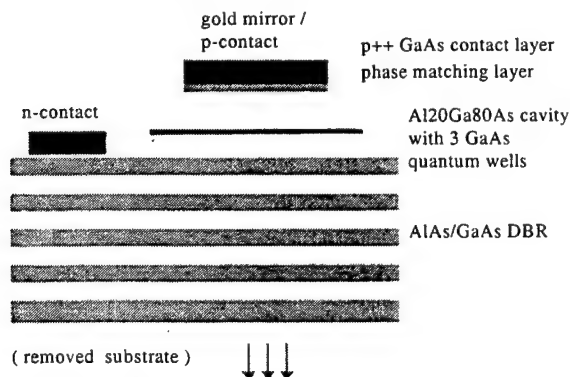


Fig3: The bottom emitting 850nm RCLED.

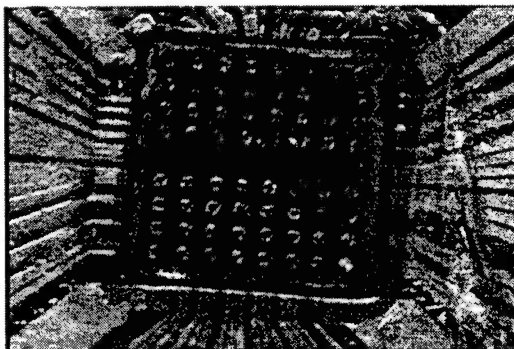


Fig 4: Flip-chipped 8X8 RCLED array.

sandwiched in between a metal (gold) top mirror and DBR outcoupling mirror. The cavity thickness is chosen to match the cavity resonance wavelength with the intrinsic spontaneous emission wavelength. The active layer is placed at the anti node position of the internal standing wave profile. Simulations were done to optimize the layer structure of the RCLED for coupling to POF and to determine the optimal cavity detuning and number of DBR pairs.

In a first run, a AlAs/GaAs DBR was chosen, to minimize the penetration depth of the outcoupling mirror and thus maximize the extraction efficiency. The devices were realized in 8x8 array and flip-chipped on glass and semiconductor carriers (fig4), then they were characterized. The overall extraction efficiency was rather poor: only 5 % was achieved. This was contributed to the absorption losses in the GaAs-layers of the DBR. The bandgap energy of GaAs is about 870nm, and the emitted 850nm light is absorbed very fast. Therefore, a new experiment was started, with a $\text{Al}_{1.5}\text{Ga}_{0.5}\text{As}/\text{AlAs}$ DBR. The layer structure was again optimized for maximal coupling to POF. The design also includes a high Al content layer, to be oxidized selectively to form a current window. Figures 5 and 6 show the measured optical power and voltage drop as function of the current, for 50 μm diameter RCLED's (70 μm mesa diameter). The 8x8 array was highly non-uniform. This is contributed to a non-optimized substrate removal process. However, some important conclusions can be made. The best overall quantum efficiency was about 9 %. Only one device did not work at all, but only 33 % of the devices had the large efficiency. Three devices have a very small saturation current (max efficiency at 2mA), and also a larger voltage drop. This can be explained by cracks in the RCLED-film. The voltage drop over the LED's after the substrate removal process increases, for example from 1.8 to 3.1 V at 2mA drive current. This is contributed to an increased lateral resistance, because of the absence of the substrate. A 2 μm $\text{Al}_{1.5}\text{Ga}_{0.5}\text{As}$ layer under the etch stop layer can enhance the mechanical stability (cracks) and the current spreading. Currently we are investigating this solution as well as an improved etching mechanism.

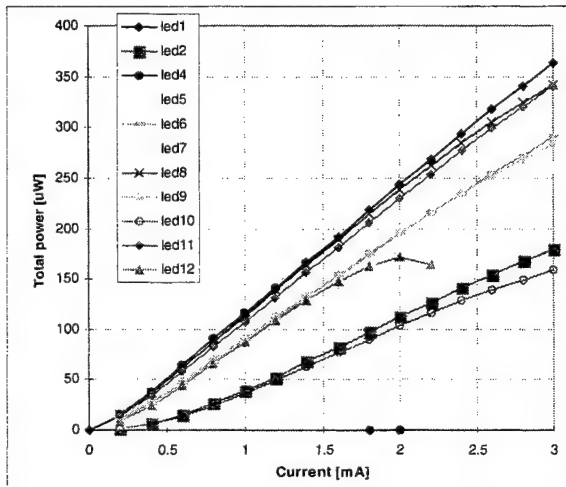


Figure 5 : Measured (P,I) curves of 50 μm RCLED (70 μm mesa).

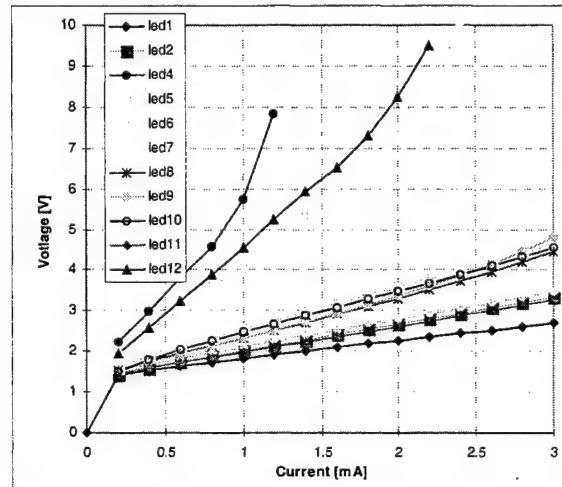


Figure 6 : Measured (V,I) curves of 50 μm RCLED (70 μm mesa).

3.2. Coupling efficiency and alignment tolerances.

The coupling efficiency of RCLED's to POF was experimentally tested. RCLED's with a mesa of 70 μm were butt coupled with the 63/125 μm POF. Up to 40% of the emitted power is coupled into POF. This can be explained by the fact that since the substrate is removed, the end facet of the POF is very close to the emitting area of the RCLED. Hence almost all the light emitted by the RCLED falls on the end facet, and all the light within the NA of the POF is captured. A maximal ratio coupled power in POF/drive current of 16 $\mu\text{Watt}/\text{mA}$ was found (at 1.8mA drive current)

Another key element in the design of an optical link is the alignment tolerance of the RCLED to POF coupling. Therefore a RCLED with a mesa of 52 μm was butt coupled with the 63/125 μm POF and a lateral offset was introduced (fig 7). As can be seen from figure 8, a misalignment of $\pm 15\mu\text{m}$ is allowed with negligible penalty. For higher offsets the efficiency decreases dramatically.

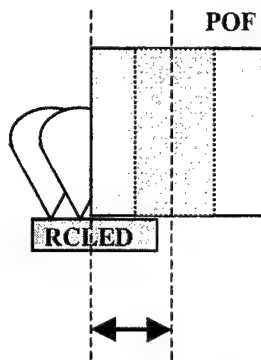


Fig 7: Lateral offset of a RCLED to POF coupling.

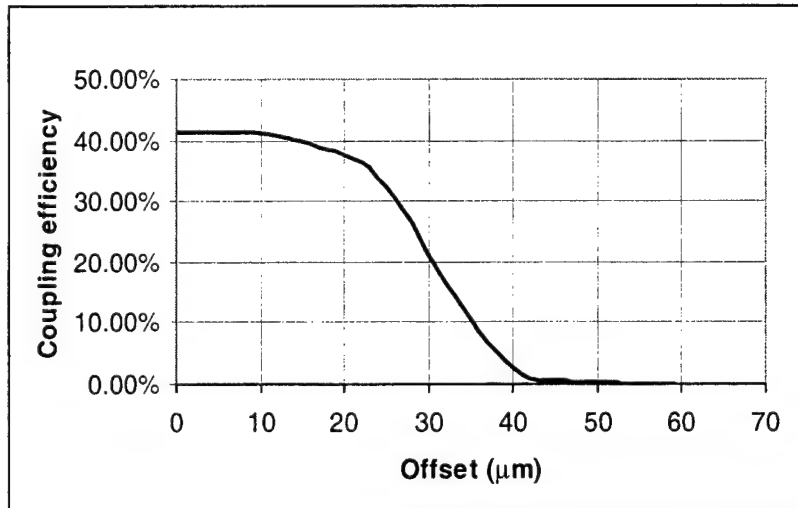


Fig 8: Coupling efficiency for a butt coupled POF and RCLED (mesa 52μm).

4. OPTICAL PATHWAYS.

Besides the development of RCLED's a lot of our research work has been focused on the development of the optical pathways for the parallel link. 2D-arrays of POF's need to be assembled in order to interconnect 2D arrays of RCLED's and detectors. Alignment structures need to be developed for efficient coupling of these POF arrays to the RCLED/detector arrays. The construction of these structures is based on PMMA plates with grooves at a pitch of 250μm in which the POF's are fixed (fig 9,10) By stacking the plates at a pitch of 250μm a 2D POF array is created (fig 11). These grooves are made with laser ablation (ArF excimer laser, 193nm). During the stacking the plates are aligned with a method we called "virtual" alignment. No master tool is needed and hence the method is versatile and can be used to align devices with different shapes without having to adapt the alignment setup. In a first step we develop a 4X8 POF patchcord (fig 12). In a further step we will develop more complicated structures containing a router function.

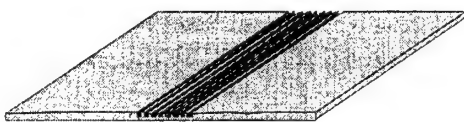


Fig 9: PMMA plate with grooves at 250μm.

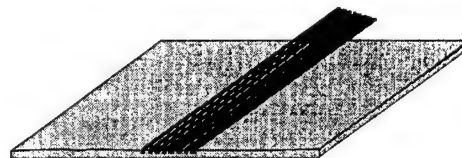


Fig 10: POF's are fixed in grooves.

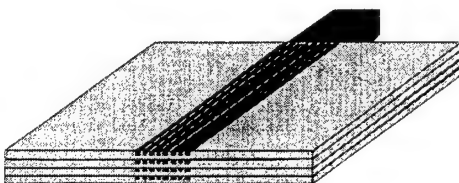


Fig 11: Plates are stacked at 250μm.

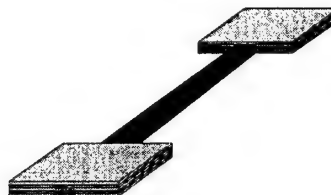


Fig 12: A 4X8 POF patchcord.

4.1. PMMA plates with POF's.

4.1.1. Laser ablation.

Laser ablation can be defined as controlled local removal of material through laser pulse - substrate interaction. A substrate is irradiated with a high power ($0.07 - 4 \text{ J/cm}^2$) laser beam. The light interacts with the material and particles are ejected

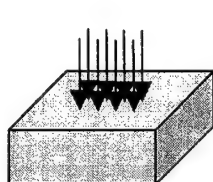


Fig 13a: Material is irradiated.

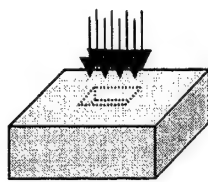


Fig13b: Light is absorbed locally.

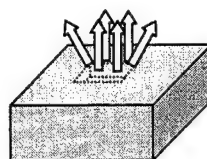


Fig13c: Particles are ejected.

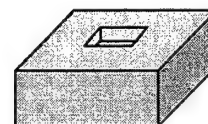


Fig13d: Microhole is realized.

(fig13). In this way a microhole is created. This technique has several advantages: it is a non-resist technique, it does not require severe conditions, nor on the ablation environment and neither on the substrate. However the material should be highly UV absorbing. Finally, it is a very versatile and fast prototyping technique. Different materials were irradiated with two different excimer lasers (193nm (ArF), 248nm (KrF)). PMMA plates irradiated at 193nm generated the best results. Very steep sidewalls (78°) and low RMS roughness ($0.33\mu\text{m}$) at the bottom of the grooves were obtained (fig 14). The grooves are ablated with mask method; the laser light passes a mask containing the pattern of four grooves. While the laser is irradiating the material with consecutive pulses (frequency 10Hz), the sample is translated. Since a large area is irradiated and since 4 grooves are ablated simultaneously the whole procedure takes only about 15minutes for a plate with 8 grooves of 1cm long.

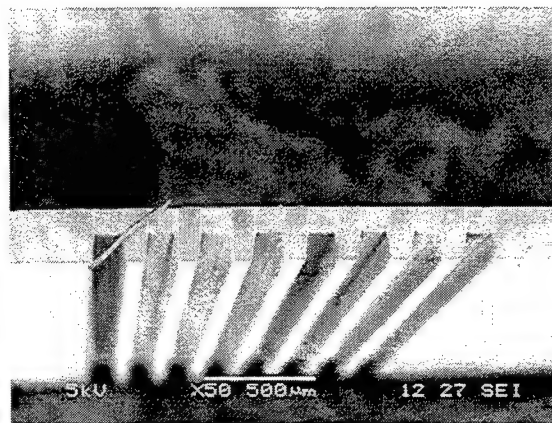


Fig 14: Laser ablated grooves in a PMMA plate.

4.1.2. POF's in grooves.

In a second step the POF's need to be fixed in the grooves. Therefore a special setup has been build (fig 15). A 1X8 array POF's is tended at pitch of $250\mu\text{m}$ by two MT ferrules. These are standard commercially available ferrules for 1X8 glass fiber arrays. Two plates are positioned on a translation table. The table is moved upwards and the POF's are pushed into the

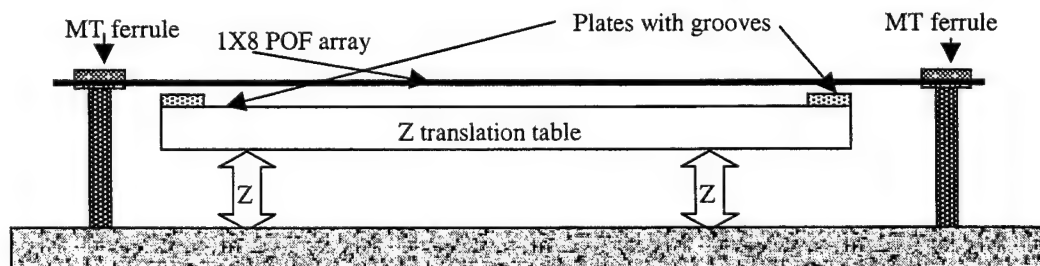


Fig 15: Setup for fixing the POF's in the grooves.

grooves, then the POF'S are fixed with UV-curing glue. Finally the POF's are cut with a hot knife (110°C) (fig 16). Critical points in the procedure are the actual pushing of the POF's in the grooves: the POF's need to be positioned at the bottom of the groove. Otherwise the precision of the ablation technology will be lost. Also the hot knife cutting needs to be done with great care in order not to destroy the ablated structure.

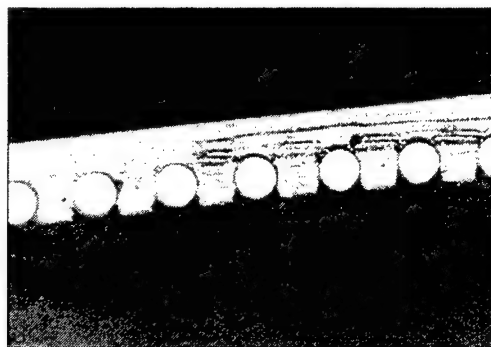


Fig 16: POF's glued in plate with grooves.

4.1.3. Experimental results.

Measurements were done on some plates with fixed POF's: the position of the fiber cores was determined with a scanning experiment. By scanning the POF'S with a RCLED and measuring the transmitted power through the fiber one can find the position of the fiber core. We found an average pitch of 248 μ m with a standard deviation of 6 μ m (fig 17). The average Y

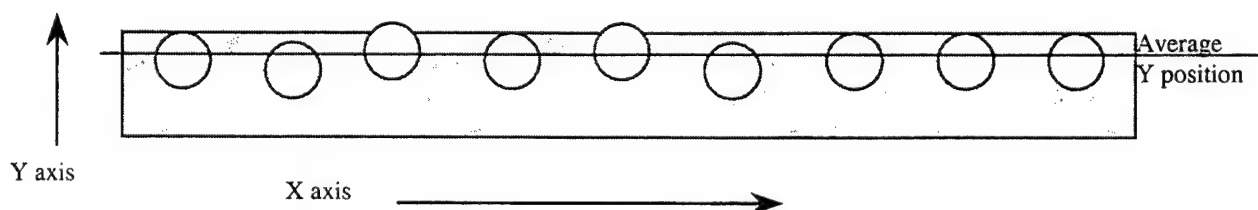


Fig 17: Position of POF cores in plate.

position was calculated. The average distance between the POF cores and this average Y position was 1.3 μ m with a standard deviation of 4.8 μ m. These deviations seem quite large but one should consider that the core-cladding non-concentricity and the variation on the core diameter contribute to this phenomenon to a considerable extent.

4.2. Creating 2D POF arrays.

4.2.1. "Virtual" alignment.

After fixing the POF's in the grooves the plates need to be stacked at a pitch of 250 μ m. A special setup has been built for this purpose. (fig 18) Essential are the precise translations of the object table and the use of two independently movable cameras. This allows us to avoid the use of master tools. The principle of "virtual" alignment is explained in figure 19. Important for a good functioning is a good adjustment of the setup before the actual alignment is done. E.g. the crosshairs of the cameras need to be parallel with the translations (x,y) of the objecttable. This has to be adjusted with high precision. After the plates are aligned they are fixed with UV-curing glue.

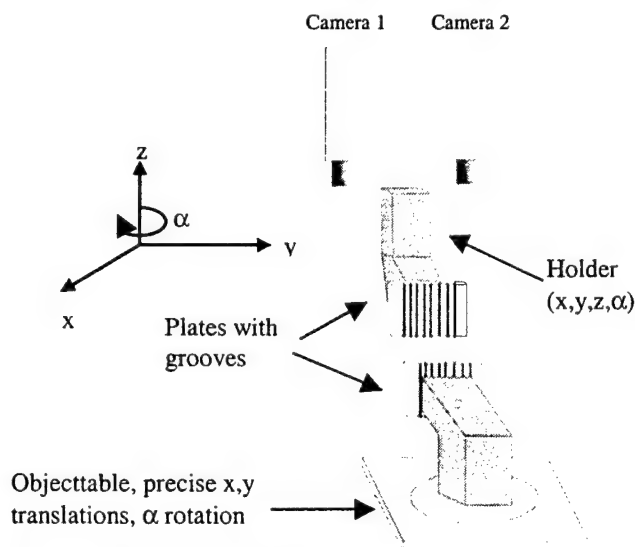


Fig 18: "Virtual" alignment setup.



Fig 19a: The plate positioned at the objecttable is looked at with the two cameras.



Fig 19b: The corners of the plate are positioned on the crosshairs.



Fig 19c: The plate is moved over an exact distance of $250\mu\text{m}$.



Fig 19d: The second plate (on the holder) is brought in the vicinity of the first plate.

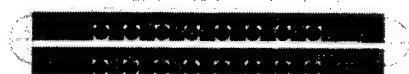


Fig 19e: The second plate is positioned on the crosshairs and hence it is at $250\mu\text{m}$ of the first plate. Afterwards the plates are glued.

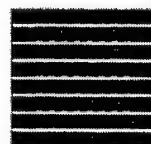


Fig 19f: By repeating the procedure an $m \times n$ array is obtained.

4.2.2. Experimental results.

Some plates were stacked and glued as can be seen in figure 20. Since the plates had a thickness of about $270\mu\text{m}$ we stacked them at $280\mu\text{m}$. Then the position of the POF cores was determined with the same scanning method as described above. Following results were found (fig 21): the distance between the average y positions of both rows of POF cores (y_{av}) was $279.5\mu\text{m}$. The angle between both POF rows was 0.15° . The offset between two adjacent POF's on the same vertical line (Δx) was $4\mu\text{m}$ with standard deviation $7\mu\text{m}$. Here again one should consider that the geometrical properties of the POF themselves contribute to the results of this experiment.

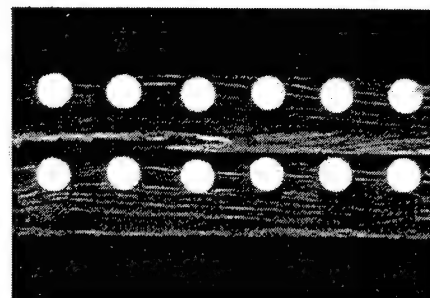


Fig 20: Stacked plates with POF's.

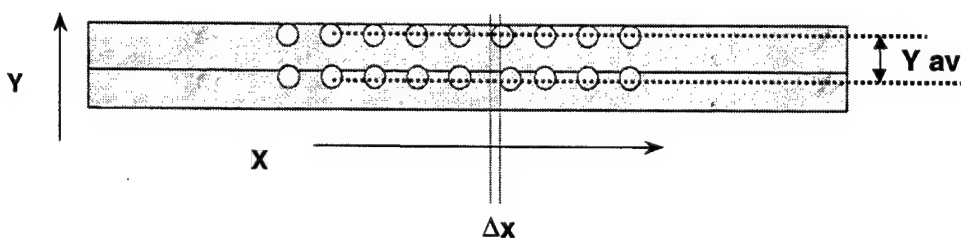


Fig 21: Distances between POF cores in 2 stacked plates.

5.CONCLUSIONS.

We developed RCLED's with promising characteristics for the use in POF based parallel optical links. However some improvement needs to be done on the substrate removal technique in order to obtain a better yield. We possess adequate techniques for the fabrication of parallel optical links, but the uniformity of the experimental results needs to be enhanced. 63/125µm Step index POF is a suitable candidate for the optical transmission medium although a more controlled geometry would certainly increase the precision and uniformity of the optical pathways. As an overall conclusion we can state that the combination of substrate removed 850nm RCLED and 63/125µm step index POF seems to be a promising option for the realization of chip-to-chip parallel optical datalinks.

ACKNOWLEDGMENTS.

The authors thank the Flemish IWT for partial support as well as the ESPRIT project OIIC and the Belgian IUAP IV-13 project

REFERENCES.

1. J.M. Van Campenhout: "Optics and the CMOS interconnection problem: a systems and circuit perspective." *International Journal of Optoelectronics* 1998, Vol 12, No 4, 145-154
2. M. Jöhnck, A. Neyer: "2D Optical interconnects using plastic optical fibers", *Electron. Lett.*, 1997, 33, pp.888-889
3. B. Wittman, Andreas Neyer: "Optical interconnect based on 62µm Core POF", POF Conf. 1999, Japan, proceedings pp. 140-143
4. B. Dhoedt: "Optically Interconnected Integrated Circuits to solve the CMOS interconnect bottleneck", ECTC Vol. (1998) pp.992-998
5. R. Bockstaele: "Realisation and characterisation of 8x8 Resonant Cavity LED arrays mounted onto CMOS drivers for POF based interchip interconnections", *JSTQE*, Vol 5 no 2, pp166-171.
6. Y. Koike: "Status of POF in Japan", POF Conf.1996 Paris, proceedings pp. 1-7
7. J. Mizusawa: "Advantages of POF WDM Design", POF Conf. 1999, Japan, proceedings pp. 6-8
8. Mario Tokoro: "Information technology & home-networking", POF Conf. 1999, Japan, proceedings pp. 31-35
9. E.Zeeb et al: "Optical Data Links for Mobile Systems", POF Conf. 1999, Japan, proceedings pp. 238-241
10. Van Hove A. et al: "Termination of small 12.Diameter (125 µm) plastic optical fiber for 1x12 datacommunication", Proc 48th Electronic Components and Technology Conf, Seattle", W, May 1998, pp. 783-789
11. E. F. Schubert, N. E. J. Hunt, R. J. Malik, M. Micovic and D. L. Miller: "Temperature and modulation characteristics of resonant-cavity light-emitting diodes", *J. Lightw. Techn.* Vol. 14-7 (1996) pp. 1721-1728
12. D.L. Huffaker, C. C. Lin, J. Shin and D. G. Deppe: "Resonant cavity light-emitting diode with an AlOx/GaAs reflector", *Appl. Phys. Lett.* Vol. 66-23 (1995) pp. 3096-3098
13. R. Bockstaele, C. Sys, J. Blondelle, H. De Neve, B. Dhoedt, I. Moerman, P. Van Daele and R. Baets : "microcavity LED's with an overall efficiency of 4 % into a numerical aperture of 0.5", LEOS Summer Topicals Vol. (1997) pp. 69-70
14. H. De Neve, J. Blondelle, P. Van Daele, P. Demeester, R. Baets and G. Borghs: "Recycling of guided mode light emission in planar microcavity light emitting diodes", *Appl. Phys. Lett.* Vol. 70-7 (1997) pp. 799-801
15. R. Windish, A. Knobloch, J. Potemans, B. Dutta, G. Dohler, G. Borghs and P. Heremans: Light-emitting diode with 17% external quantum efficiency at 622 Mb/s for high-bandwidth parallel short-distance optical interconnects ', *JSTQE*, Vol 5 no 2 pp 166-171

Correspondence: tel: +32 9 264 33 41, fax: +32 9 264 35 93, Email: tcoose@intec.rug.ac.be

Efficiency Optimization in Ionically Self-Assembled Thin Film Polymer Light-Emitting Diodes

D. Marciu, M. Miller, A.L. Ritter

Luna Innovations, Inc., P.O. Box 11704, Blacksburg, VA 24062-1704

M.A. Murray, P.J. Neyman, W. Graupner, J.R. Heflin

Department of Physics, Virginia Tech, Blacksburg, VA 24061-0435

H. Wang, H.W. Gibson

Department of Chemistry, Virginia Tech, Blacksburg, VA 24061-0212

R.M. Davis

Department of Chemical Engineering, Virginia Tech, Blacksburg, VA 24061-0211

ABSTRACT

We present detailed studies of polymer light emitting diodes fabricated from ionically self-assembled monolayer thin films. The ionically self-assembled monolayer (ISAM) films are created with a new thin film fabrication technique that allows detailed structural and thickness control at the molecular level. The ISAM fabrication method simply involves the dipping of a charged substrate alternately into polycationic and polyanionic aqueous solutions at room temperature. Importantly, the ISAM technique yields exceptionally homogeneous, large area films with excellent control of total film thickness. Our studies concentrate on improving the performance of ISAM light emitting diodes that include poly(para-phenylene vinylene) (PPV). The individual thickness of each monolayer and the interpenetration of adjacent layers can be precisely manipulated through the parameters of the electrolyte solutions. The effects of the pH and ionic strength of the immersion solutions, the total film thickness, and the PPV thermal conversion parameters on the photoluminescence and electroluminescence yields have been systematically studied. Through the ISAM process we can also deposit well-defined thicknesses of different polymers at the indium tin oxide and aluminum electrode interfaces. The interface layers are found to affect the electroluminescence efficiency.

Keywords: polyelectrolytes, ionically self-assembled monolayers, polymer light emitting diodes, poly(paraphenylene vinylene)

1. INTRODUCTION

The first demonstration of a light emitting diode fabricated from a conjugated polymer¹, has generated continued interest in developing new materials and improving the efficiency of the devices. Conjugated polymers are characterized by a delocalized π -electron system along the polymer backbone, which gives them the semiconducting properties. The advantages of using polymers for the fabrication of optoelectronic devices consist in their ease of fabrication, processability, and the possibility of designing new materials with various bandgaps and electron affinities. For display applications, the most heavily studied polymer has been poly(para-phenylene vinylene) (PPV)^{2,3} along with its derivatives^{4,5}. The typical process of forming thin films of these materials is the spin coating technique. Our approach is to fabricate homogeneous thin films through the ionically self-assembled monolayer (ISAM) technique, developed by Decher and coworkers^{6,7} and demonstrated for light emitting diodes (LED) applications by Rubner and coworkers^{8,9}. The technique allows for detailed structural control of materials at the molecular level combined with ease of fabrication and low cost. The ISAM method involves the alternate dipping of a charged substrate into an aqueous solution of a cation followed by dipping in an aqueous solution of an anion at room temperature. Since the adsorption is based on the electrostatic attraction of interlayer charges, each layer is self-limiting in thickness and uniform at the molecular level. This occurs because the film molecules are free to adjust their positions to improve the overall packing since they are not covalently bound to the substrate. Sequential layers are rapidly fixed by drying at room temperature and in air. The typical bilayer thickness is on the order of a nanometer and can be precisely controlled (0.5 to > 5.0 nm) by the parameters of the dipping solutions. Multilayer films several microns in thickness are easily

fabricated by repeating the dipping process with no practical limit to the number of layers that can be deposited. The resulting pliable films are mechanically very robust. The advantages afforded by molecular control on the subnanometer level provide opportunities for dramatically enhanced photonic¹⁰, electronic, and optoelectronic¹¹ devices.

2. EXPERIMENTAL DETAILS

The materials used for the fabrication of the emissive ISAM films were cationic precursor poly(para-phenylene vinylene) (PPVpc), prepared by the classic route^{8,12} and poly(methacrylic acid) (PMA) purchased from Polysciences. For the interface study we used several polymers. The polythiophene acetic acid (PTAA) was prepared according to Reference 13. Poly(allylamine hydrochloride) (PAH) was purchased from Aldrich, poly(sodium 4-styrenesulfonate) (PSS) was purchased from Polysciences, and the polymeric dyes poly S-119, and poly R-478 were purchased from Sigma. The pH and the ionic strength were adjusted accordingly for the different studies as described in the sections below. The films were prepared at room temperature and in air. After the deposition of the films on glass slides and indium tin oxide (ITO) coated glass slides, the films were thermally treated under dynamic vacuum at 300 °C for approximately 8 hours. Absorption spectra were taken with a Jasco spectrophotometer and fluorescence spectra were taken with a Perkin Elmer fluorescence spectrometer. For the electroluminescence spectra we used an Ocean Optics spectrometer. The I-V curves were obtained using a Keithley source unit, and the luminance values were read with a Minolta luminance meter. All measurements were carried in air at room temperature. Evaporated aluminum was used as the top electrode of the devices.

3. OPTIMIZATION OF THE ABSORPTION

In the initial study, we optimized the parameters of the dipping solutions for the absorbance of the films and thus, the thickness of the films. Two basic variables have been studied that control the amount of PPV precursor adsorbed into each monolayer: the presence of salt in the PPVpc solutions, and the pH of the PPVpc solution. The polyanion PMA dipping solution was adjusted to 10 mM concentration, pH=3.5 and salt concentration of 0.05 M. For the first series, the precursor PPV was 0.3 mM, 0.05 M salt, and the pH values were 3.5, 6.5, and 8.0. The films with the same number of bilayers were deposited on glass and we recorded the absorption spectra of the films for the three values of the pH, after the thermal conversion of the PPV. As seen in Figure 1 (left), the best (PPV/PMA)₂₀ (where the subscript indicates the number of bilayers deposited) film is obtained for pH=3.5. The high pH values of the PPVpc solution decreased the amount of PPVpc that adsorbed to the slides. In order to examine the light emission of the films, we also performed fluorescence measurements on the same films. The excitation wavelength was 360 nm. Figure 1 (right) shows the fluorescence spectra obtained for films made for the pH study, after the thermal conversion. The trends of the fluorescence spectra follow those of the absorption. The slide with the highest fluorescence intensity had the pH of 3.5, having the photoluminescence peak around 485 nm. These results indicate that the films fabricated from PPVpc solution with pH 3.5 had the largest amount of PPVpc adsorbed to the substrate.

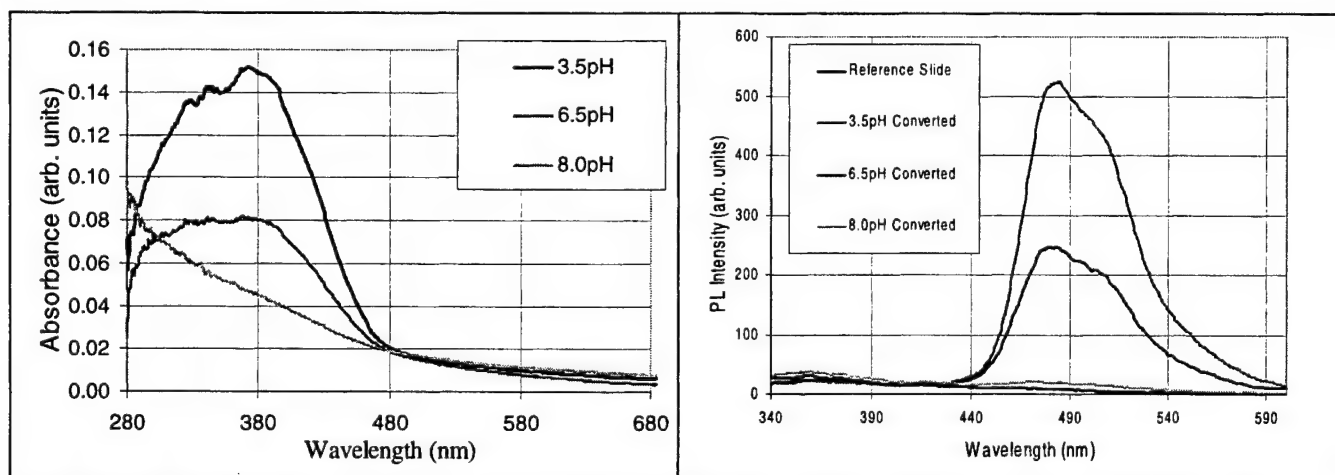


Figure 1. Results of the effects of pH on absorbance (left) and photoluminescence (right) of (PPV/PMA)₂₀ films on glass substrate. The absorption spectra (left) from bottom to top are for pH values of 8.0, 6.5, and 3.5. The post-conversion photoluminescence spectra (right) from bottom to top are for pH values of 8.0, 6.5, and 3.5.

The next study examined the adsorption of the (PPV/PMA)₂₀ films on glass as a function of the ionic strength of the PPVpc dipping solution. All solutions had pH adjusted to 3.5, and the salt content for the PPV varied as shown in Figure 2 where the absorption spectra were taken after the thermal conversion of the PPVpc. The absorbance of the films increases with increased ionic strength of the solution, up to 0.5 M, after which the absorbance decreases with increased ionic strength. However, the salt concentration does not seem to affect the position of the peaks, as all are at approximately 370 nm. This indicates that the conjugation length distribution of the PPV is unchanged. The fluorescence measurements (Figure 3) for this series also follow the trend observed in the absorption. The excitation wavelength was 360 nm. The spectra show increasing luminescence up to 0.5 M and decreasing luminescence beyond that point, similar with the absorbance results. The fixed position of the peak for all spectra confirms that the conjugation length distribution of the PPV is unchanged.

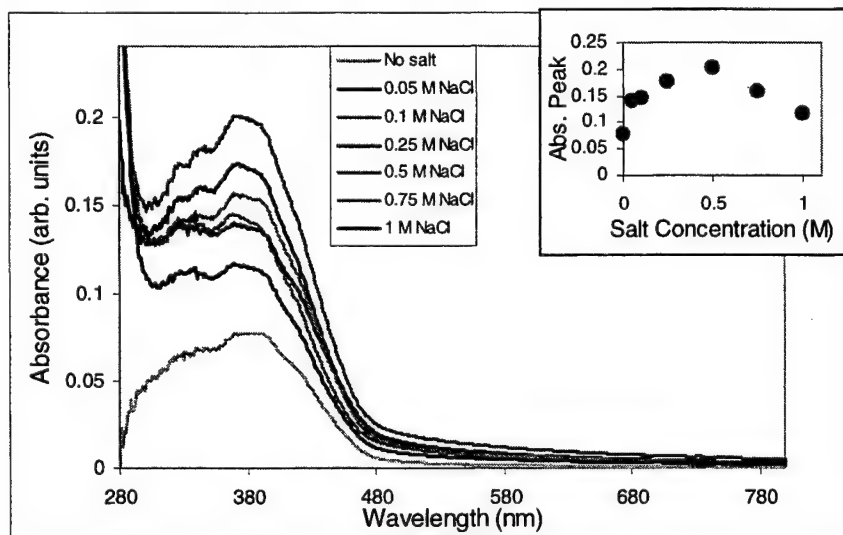


Figure 2. Absorption spectra of (PPV/PMA)₂₀ films with different salt content. The spectra from bottom to top are for salt concentrations of 0.0 M, 1.0 M, 0.05 M, 0.1 M, 0.75 M, 0.25 M, and 0.5 M. The curve with highest absorbance was obtained for 0.5 M salt. The inset shows the absorption peak (at 370 nm) vs. the salt content.

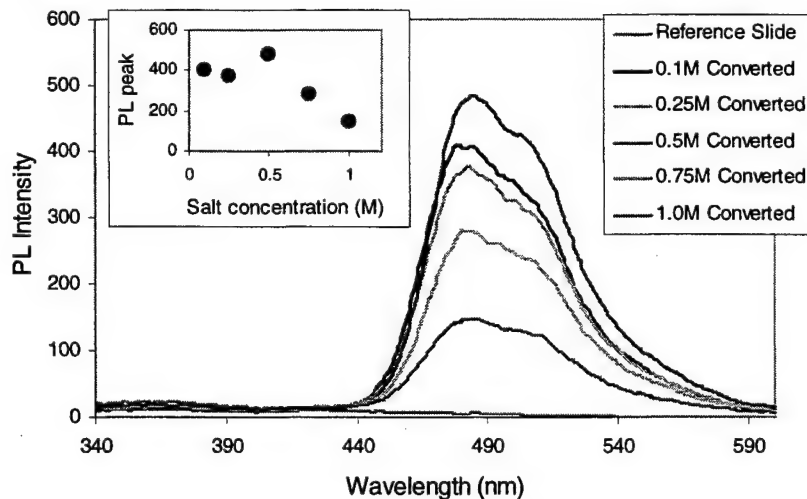


Figure 3. Photoluminescence spectra for post-conversion slides with a pH of 3.5 and varying salt molarity. The spectra from bottom to top are for salt concentrations of 1.0 M, 0.75 M, 0.25 M, 0.1 M, and 0.5 M. The highest intensity in the photoluminescence was obtained for 0.5 M salt. The inset shows the PL peak intensity at 485 nm vs. salt concentration.

4. PPV/PMA LED DEVICES

The device configuration is typical for a polymer LED device. On top of an indium tin oxide (ITO) coated glass slide we deposited the ISAM (PPV/PMA)_x film, where x denotes the number of bilayers, and on top of the film we deposited the aluminum electrodes by resistive evaporation. Figure 4 contains the absorbance, photoluminescence, and electroluminescence spectra for typical ISAM (PPV/PMA)_x device. The photoluminescence spectrum was obtained using the excitation wavelength of 440 nm, where the maximum for absorption occurs. The electroluminescence spectrum has the maximum at 506 nm and has similar features with the photoluminescence spectrum, as expected for a good thermal conversion of the PPVpc to the fully conjugated form. Typical current-voltage and light-voltage curves for the films are presented in Figure 5. The low luminance values are due to the fact that we used a low concentration for the PPVpc dipping solution and therefore obtained very thin films. More recent results from devices prepared with more concentrated solutions, yielding thicker films, showed an increased value for the luminance.

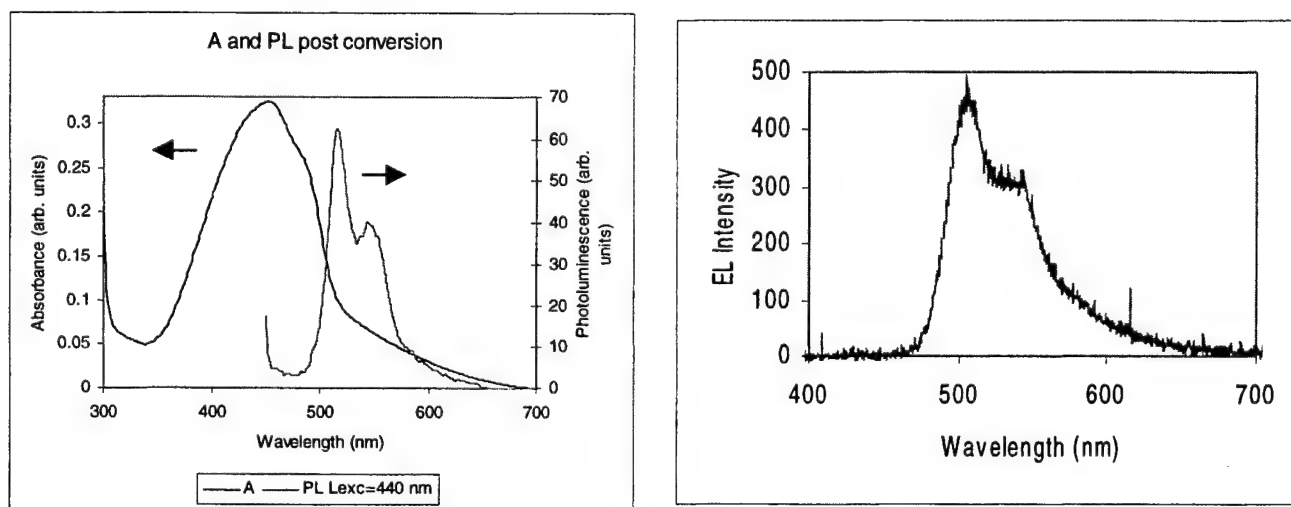


Figure 4. Absorbance, photoluminescence, and electroluminescence spectra for a typical ISAM (PPV/PMA)₂₀ LED device.

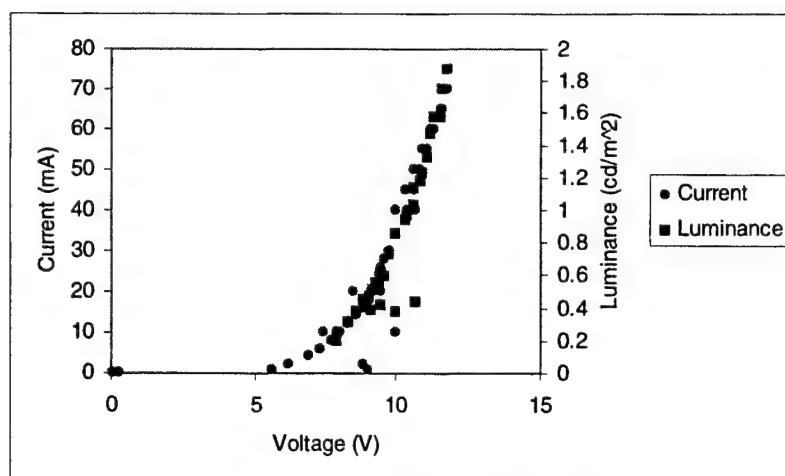


Figure 5. Current and luminescence vs. voltage for ITO/(SPS/PPV)₅/(PMA/PPV)₃₀/Al₂O₃/Al.

Interesting results were obtained from the measurements of small (0.6 cm x 0.3 cm) and large (0.6 cm x 0.7 cm) area devices, which were fabricated on the same ITO coated glass slide. The device size is determined by the size of the deposited Al electrodes. The films had 20 bilayers of (PPV/PMA). Figure 6 (left) shows that the small devices had a higher current density for the same applied voltage, and both types of devices had the threshold voltage at around 3.5 V. Figure 6 (right) shows that the luminance values of the devices are similar for current densities below 200 mA/cm². Beyond this value, the large area device failed during testing, while the small device sustained much higher current densities. The higher heat generation combined with the larger number of defects present in the large area devices may cause the device failure. Our smallest devices are still much larger than the typical devices described by other groups⁸, which used 0.2 cm x 0.2 cm polymer LEDs that yielded higher luminances.

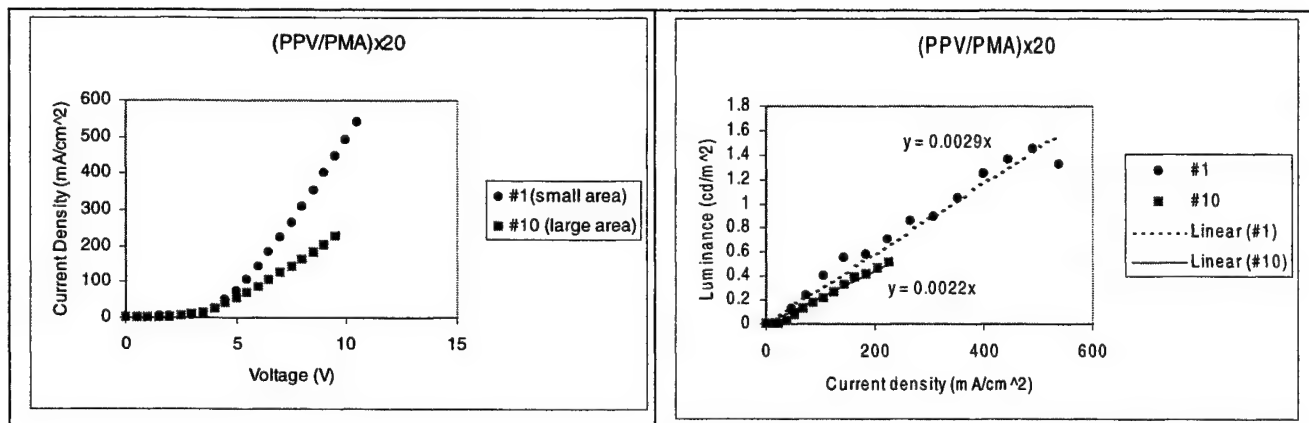


Figure 6. Current density vs. voltage (left) and luminance curves (right) for the small (#1) and large (#10) area devices made with (PPV/PMA)₂₀.

5. CONTROL OF POLYMER-ELECTRODE INTERFACES

The interface study was aimed at finding ways to improve the ISAM thin film (PPV/PMA)_x device performance by inserting different layers between the emissive ISAM film and the anode (ITO) or the cathode (aluminum). By manipulating the interface layers it is possible to modify the injection of the carriers at the electrodes, and ultimately to control the efficiency of the devices. It has been shown previously¹⁴ for MEH-PPV spin coated devices that the efficiency can be controlled by inserting conducting, semiconducting or insulating polymer self-assembled layers between the organic emissive layer and the anode. Onitsuka et al.¹⁵ also demonstrated that the efficiency of the self-assembled light emitting diodes could be influenced through manipulation of the thin film/electrode interface and through use of various polyanions in combination with the PPV.

The materials that we used for the interface study were polyallylamine hydrochloride (PAH) as the polycation, and for polyanions several polymers were employed: poly(sodium 4-styrenesulfonate) (PSS), polythiophene acetic acid (PT), poly S-119, and poly R-478. The two polymeric dyes, poly S-119 and poly R-478 are water soluble polymeric dyes and are compatible with the ISAM technique. All ISAM interface layers were made of three bilayers, using the same polycation, PAH. The parameters, (concentration, pH, and ionic strength) of the dipping solutions are listed in Table 1. The films were deposited on ITO coated glass slides, in the combinations shown in Table 2. Aluminum electrodes were then deposited on top of the ISAM layer.

Table 1 Polymers and the solutions parameters used the interface study of ISAM LEDs

	Concentration	pH	Salt
PPV	1.8 mM	4.5	0.3M
PMA	10 mM	2.5	0.1M
PAH	1 mM	3.0	0.1M
PSS	10 mM	3.0	0.1M
PT	6.6 mM	5.5	No NaCl
R478	1 mM	3.0	0.1M
PS119	1 mM	3.0	0.1 M

Table 2. ISAM films used for the LED interface measurements

$(\text{PAH/PT})_3(\text{PPV/PMA})_{20}$	$(\text{PPV/PMA})_{20}(\text{PAH/PT})_3$
$(\text{PAH/PSS})_3(\text{PPV/PMA})_{20}$	$(\text{PPV/PMA})_{20}(\text{PAH/PSS})_3$
$(\text{PAH/R478})_3(\text{PPV/PMA})_{20}$	$(\text{PPV/PMA})_{20}(\text{PAH/R478})_3$
$(\text{PAH/PS119})_3(\text{PPV/PMA})_{20}$	$(\text{PPV/PMA})_{20}(\text{PAH/PS119})_3$
$(\text{PPV/PMA})_{20}$	

In previous work, we have studied these polymeric dyes for nonlinear optical applications and demonstrated that they exhibit reasonably large second order nonlinear susceptibility values, comparable to that of quartz^{10,16}. The chromophore is attached to the polymer backbone and the resulting ISAM film has the dipole moments aligned perpendicular to the film substrate. Depending on the chromophore incorporated into the polymer, the dipole moments can point towards or away from the substrate. Using this property of the film, we investigated the possibility of modifying the work function of the ITO and/or of the top electrode, respectively, by inserting a thin ISAM layer between the PPV containing layer and one of the electrodes. Initially, we measured the work function of the two polymeric dyes using a Kelvin probe experiment¹⁷. The resulting value is reported with respect to a gold electrode. The ISAM polymeric dyes were deposited on a 200 nm vacuum-deposited aluminum layer. The results indicated that when bare aluminum was measured against the gold, the difference in the work functions was 0.8 eV, in agreement with the difference between the known work functions values for the Al (4.25 eV) and Au (5.10 eV). When the polymeric dyes were deposited on top of the aluminum, the Kelvin probe measurements yielded 0.67 eV for poly R-478 and 0.82 eV for poly S-119, indicating that the resulting “work function” of the aluminum/dye film was changed to 4.38 eV and 4.23 eV, respectively, from the initial value of 4.25 eV. We thus expected to be able to tailor the injection of either carrier from its respective electrode by using an appropriate material between the organic layer and the electrode. We present here preliminary results of the interface study, with the specification that there is work in progress in synthesizing new polymeric dyes specifically designed for the efficiency control of the devices.

For an accurate comparison of the data, the entire set of films for the interface study was prepared from the same batch of PPVpc solution, which was more concentrated than the films described in the previous sections. The pH of the PPVpc solution was adjusted to 4.5 and the ionic strength to 0.3 M. For the polyanion, we used PMA with 10 mM concentration, pH=2.5 and 0.1 M NaCl. The absorption spectra of the films are similar, indicating that the introduction of the interface layers did not modify the position of the absorption peak. In Figure 7 we present the absorption spectra of all slides, after the thermal conversion of the PPVpc. The peak of the absorption is around 450 nm, demonstrating a good conversion of the PPVpc to the conjugated form. As observed from these absorption spectra the absorption peak of the polymeric dyes does not show in these curves, since we only deposited 3 bilayers, compared to the 20 bilayers of (PPV/PMA) film. Poly S-119 has maximum absorption at wavelength 475 nm and poly R-478 has the maximum absorption at 519 nm.

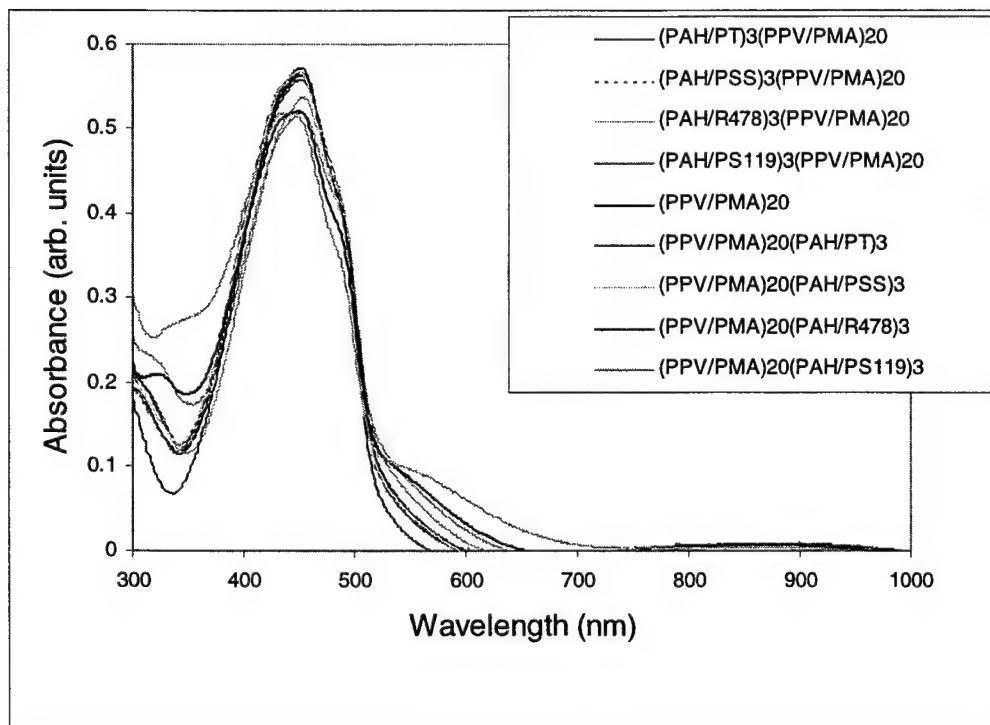


Figure 7. Absorption spectra for the films used in the interface study.

The current-voltage, luminance-current, and power conversion efficiency curves for the devices prepared for the interface study are presented in Figures 8-13. All devices have an active area of approximately 0.6 cm x 0.3 cm. As it can be seen from these graphs, when (PAH/PT)₃ is deposited between the ITO and the (PPV/PMA)₂₀ layer, the device has similar performance as the device with (PPV/PMA)₂₀ only. For the device configuration with the interface layer between (PPV/PMA)₂₀ and the aluminum electrode (Figure 9), the (PAH/PT)₃ layer appears as a wide band gap insulator, and we observe a much higher turn-on voltage of approximately 13 V. Figure 9 shows that all devices that had the interface layer between the organic and the aluminum electrode had the turn-on voltage at higher values (around 13 V) than the device with (PPV/PMA)₂₀ only (approximately 7 V). It should also be noted that the current observed at 2-4 V in the film with no interface layers is due to a short-circuit defect that burnt out at 4 V. The luminance-current plots for both cases are shown in Figure 10 and Figure 12. The device with the (PAH/PT)₃ layer between the ITO and (PPV/PMA)₂₀ indicates improvement in the efficiency of the LED, compared to the device where there is no interface layer towards the ITO. Similar improvement in the device efficiency can be noticed for the (PAH/PSS)₃ layer placed on the ITO side. The devices with the polymeric dyes incorporated in the ITO interface layer have poorer performance than (PPV/PMA)₂₀.

In the case when the interface layer was placed between (PPV/PMA)₂₀ and aluminum, the devices sustained larger current densities than in the case where the interface layer was between ITO and (PPV/PMA)₂₀, although the luminance values were significantly lower than the luminance values for the devices with the interface layer towards ITO. This indicates that the presence of the layer at the aluminum side increases even further the energy gap between aluminum and the (PPV/PMA)₂₀ layer, thus blocking the electron injection from the aluminum. This assumption is confirmed by the sharp rise in the current density for the devices with the interface layer at the aluminum. The improvement in the luminance for the devices with the (PAH/PT)₃ and (PAH/PSS)₃ layers at the ITO suggests that the presence of these layers improves the device efficiency, as can be seen from the slopes of the luminance-current curves.

The power conversion efficiency curves (Figure 11 and Figure 13) indicate that the efficiency of the devices reaches a maximum around 6 V when the interface layer is placed on the ITO, similar to the (PPV/PMA)₂₀ device with no interface layer (Figure 11). When the interface layer is placed towards the aluminum (Figure 13), the maximum power conversion efficiency varies from device to device, from 6 V for the (PPV/PMA)₂₀ to 15 V for (PPV/PMA)₂₀(PAH/PSS)₃, and 16 V for

(PPV/PMA)₂₀(PAH/PT)₃. The devices with the polymeric dyes included in the interface towards aluminum do not show the decrease in the power conversion efficiency, although the performance of these devices was not as good as of the other devices. In general, the power conversion efficiencies are larger when the interface layer is placed at the ITO rather than the aluminum electrode. Although the luminance values are relatively large at high values of the applied voltage, the power conversion efficiencies of many of these devices are already reduced in the high voltage regime.

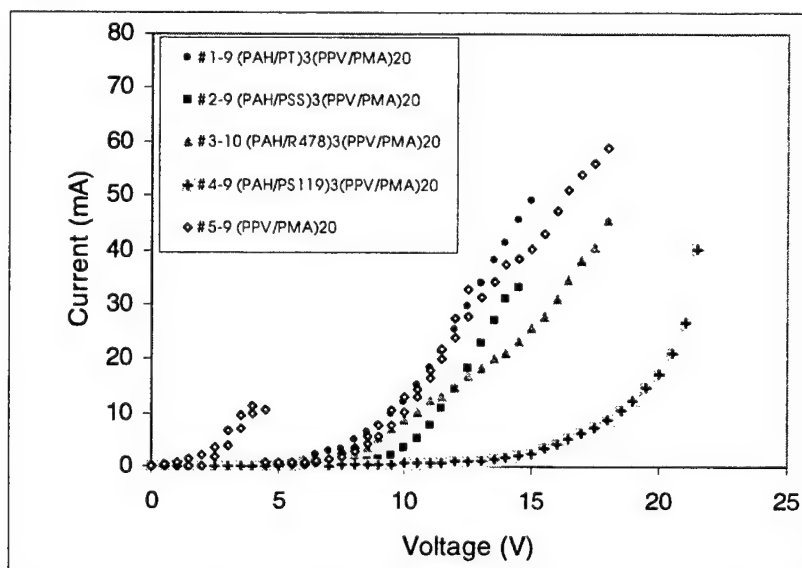


Figure 8. Current-voltage characteristics for the devices with the interface layer placed between the ITO and (PPV/PMA)₂₀.

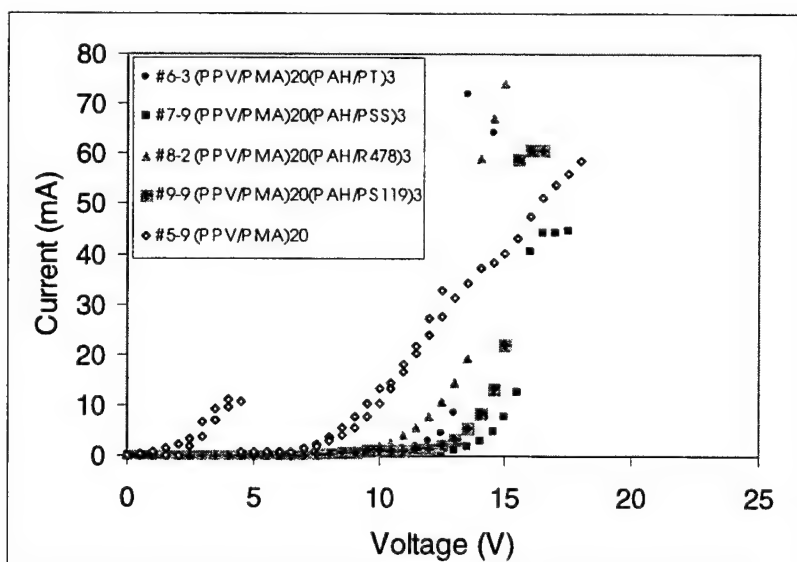


Figure 9. Current-voltage characteristics for the ISAM LED devices with the interface layer placed between (PPV/PMA)₂₀ and the aluminum electrode.

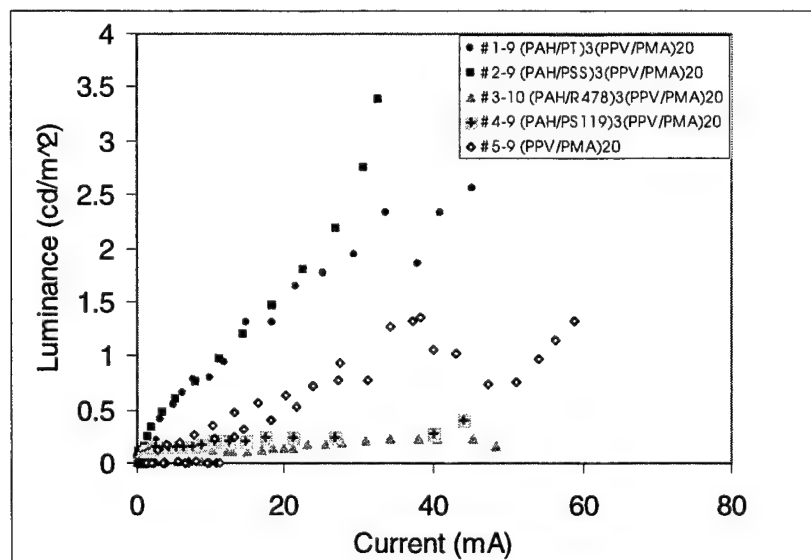


Figure 10. Device efficiencies for the interface placed between ITO and emissive (PPV/PMA)₂₀ layer.

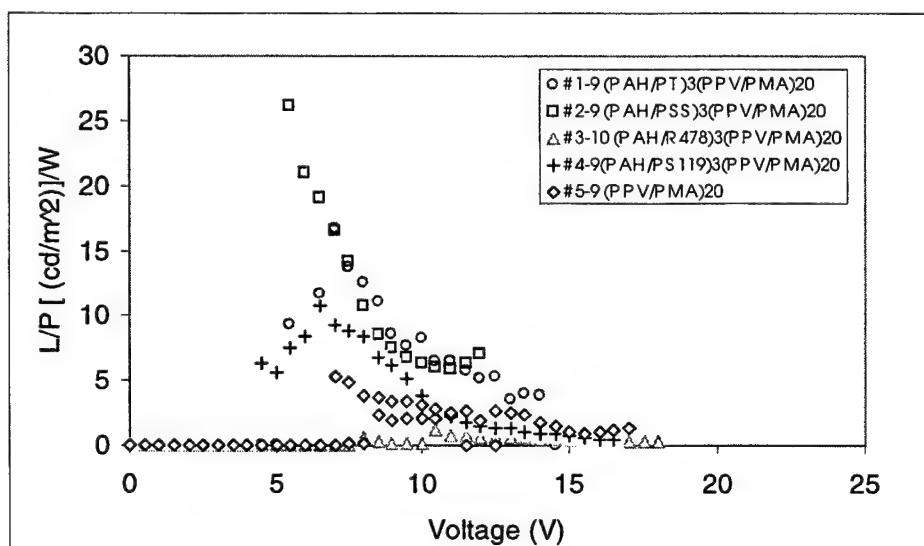


Figure 11. Power efficiency conversion for the devices with the interface placed between ITO and emissive (PPV/PMA)₂₀ layer.

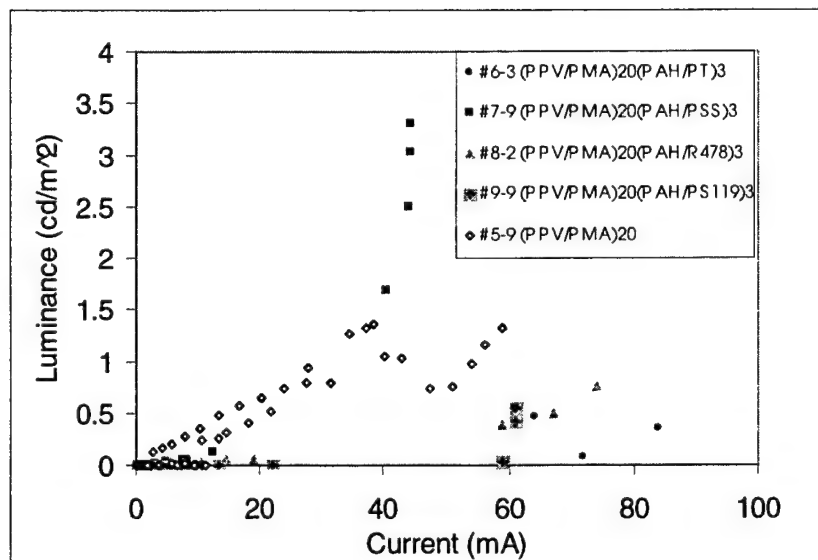


Figure 12. Device efficiencies for the interface placed between the emissive (PPV/PMA)₂₀ layer and aluminum electrode.

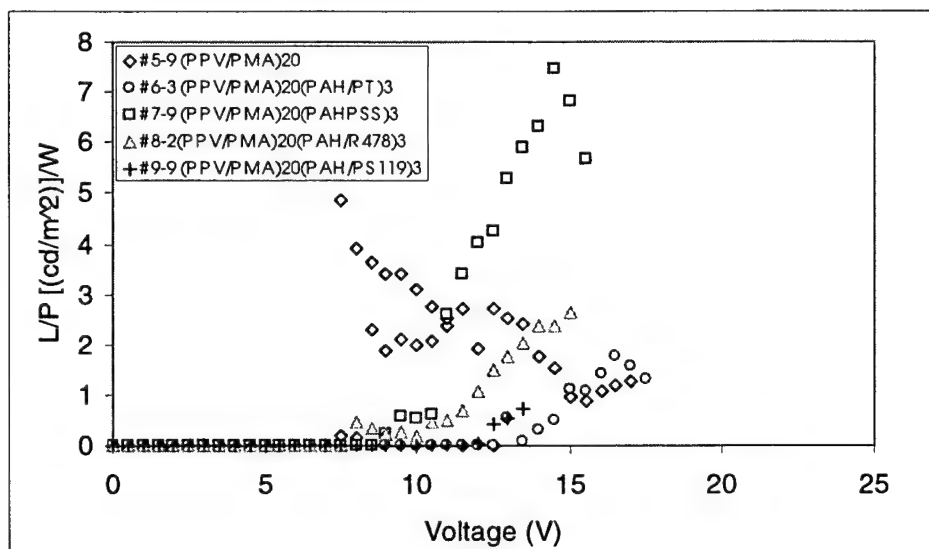


Figure 13. Power conversion efficiency for devices with the interface layer placed between the emissive (PPV/PMA)₂₀ layer and aluminum electrode.

CONCLUSIONS

The ionically self-assembled monolayer (ISAM) technique can successfully be used for the fabrication of polymer light emitting diodes, yielding homogeneous deposition and buildup of monolayers. The amount of deposited PPV can be controlled through pH and salt concentration. Lastly, the efficiency of the devices can be improved through manipulation of the interface layers. The ISAM technique is appropriate for this procedure, allowing for detailed structural and thickness control at the molecular level.

ACKNOWLEDGMENTS

The authors would like to thank Winston Matthews for the help in the preparation of the samples. This research was supported by the U. S. Navy under contract no. N00014-98-C-0161 and in part by the U. S. Department of Energy under contract No. DE-FG02-99ER86091, whose support does not constitute an endorsement by DOE of the views expressed in the article.

REFERENCES

1. J. H. Burroughes, D. D. C. Bradley, A. R. Brown, R. N. Marks, K. Mackay, R. H. Friend, P. L. Burns, and A. B. Holmes, *Nature*, **347**, 539 (1990).
2. P. L. Burns, A. B. Holmes, A. Kraft, D. D. C. Bradley, A. R. Brown, and R. H. Friend, *J. Chem. Soc., Chem. Commun.*, **32** (1992).
3. A. R. Brown, D. D. C. Bradley, J. H. Burroughes, R. H. Friend, N. C. Greenham, P. L. Burn, A. B. Holmes, and A. Kraft, *Appl. Phys. Lett.*, **61**, 2793 (1992).
4. D. Braun and A. J. Heeger, *Appl. Phys. Lett.*, **58**, 1982 (1991).
5. N. C. Greenham, S. C. Moratti, D. D. C. Bradley, R. H. Friend, and A. B. Holmes, *Nature*, **365**, 628 (1993).
6. G. Decher and J. D. Hong, *Makromol. Chem., Makromol. Chem. Symp.*, **46**, 321 (1991).
7. G. Decher, J. D. Hong, and J. Schimitt, *Thin Solid Films*, **210/211**, 831 (1992).
8. A. C. Fou, O. Onitsuka, M. Ferreira, M. F. Rubner, and B. R. Hsieh, *J. Appl. Phys.*, **79**, 7501 (1996).
9. J-K. Lee, D. Yoo, and M. F. Rubner, *Chem. of Materials*, **9**, 1710 (1997).
10. J. R. Heflin, Y. Liu, C. Figura, D. Marciu, R. O. Claus, *Proc. SPIE*, **3147**, 10 (1997).
11. S. L. Clark, E. S. Handy, M. F. Rubner, and P. T. Hammond, *Adv. Mater.*, **11**, 1031 (1999).
12. F. R. Denton III, P. M. Lahti, F. E. Karasz, *J. Polym. Sci. Part A: Polym. Chem.*, **30**, 2223 (1992).
13. A. T. Royappa, M. F. Rubner, *Langmuir* **1992**, **8**, 3169.
14. P. K. H. Ho, M. Granstrom, R. Friend, and N. Greenham, *Adv. Mater.* **10**, 769 (1998), and references within.
15. O. Onitsuka, A. C. Fou, M. Ferreira, B. R. Hsieh, and M. F. Rubner, *J. Appl. Phys.* **80**, 4067 (1996).
16. J. R. Heflin, C. Figura, D. Marciu, Y. Liu, R. O. Claus, *Appl. Phys. Lett.* **74**, 495 (1999).
17. Stephen D. Evans, Surface Potential, "Characterization of Organic Thin Films", editor Abraham Ulman, Materials Characterization Series, Butterworth-Heinemann (1994).

LED backlight: design, fabrication, and testing

Daniel M. Brown^a, Robert Dean^b, Jeremiah D. Brown^a

^aMEMS Optical, LLC, 205 Import Circle, Huntsville, AL 35806

^bCenter for Advanced Vehicle Electronics, 200 Broun Hall, Auburn University, AL 36849

ABSTRACT

This paper reports on work to determine the feasibility of fabricating a liquid crystal display (LCD) backlight using an array of LEDs. The purpose of this backlight is to overcome the efficiency loss of the absorptive color filters in the LCD. Two types of arrays were fabricated and tested. An array of white LEDs was designed for use with an interference color separation filter. An array of red, green, and blue LEDs was designed for use with a cylindrical lenslet array which focuses the three colors onto the appropriate color apertures of the LCD. Although promising results were achieved with standard off-the-shelf LEDs, significant improvements in surface radiance uniformity and efficiency could be obtained with special beam-shaping lenses on the LEDs.

1. INTRODUCTION

A typical color liquid crystal display (LCD) consists of an array of rectangular apertures, with each pixel containing three apertures overlaid with red, green, and blue color filters. A broadband diffuse light source is generally placed behind the LCD. Due to the color filtering and the opaque conductor areas surrounding the apertures, only a small fraction of the generated light is directed toward the observer. Gunn and Halstead^[1] estimate that less than 7% of the generated light is transmitted out of the LCD. Increasing the power efficiency of LCD displays is desirable for applications such as laptop computers and avionic systems.

One method currently under development for improving the power efficiency is to use an echelon grating^{[2] [3]} multiplexed with a focusing lens. Such an element is sometimes referred to as an interference color separation (ICS) filter. The ICS filter splits the incident white light into three color bands and focuses the bands onto the appropriate apertures at each pixel, thus eliminating the need for an absorptive color filter. However, the backlight source must be collimated, typically to within 2 to 3 degrees, to realize efficiency improvements with an ICS filter. This paper reports on an investigation of the feasibility of using white LEDs to form a compact, collimated backlight source suitable for use with an ICS filter.

A second proposed method to achieve color separation without absorptive color filters is to use arrays of red, green, and blue LEDs. The three colors can be sequentially pulsed in synchronization with their corresponding color apertures, as proposed by Hewlett Packard.^[4] Alternatively, lenslet arrays can be used to focus each color onto the appropriate apertures. Instead of an ICS filter, which tends to be difficult to fabricate, a simple cylindrical lenslet array

focuses red, green, and blue lines onto their corresponding apertures. We also report on the fabrication and testing of such a backlight.

Since the purpose of this project was to demonstrate feasibility of the concept at minimal expense, we chose to use off-the-shelf LED components. Ideally, bare LED die or specially fabricated LEDs would be used in a beamshapper configuration to obtain a uniform radiance over the backlight.

2. OPTICAL DESIGN

Standard off-the-shelf three millimeter diameter LEDs were selected as the light source. In order to obtain a beam divergence of 3 degrees or less, the effective focal length of the collimating lens needs to be at least 29 mm. However, since the radiance in exit pupil of the LED is not uniform it can be slightly less than this. Fig. 1 shows the layout of one LED and its fresnel collimating lenslet.

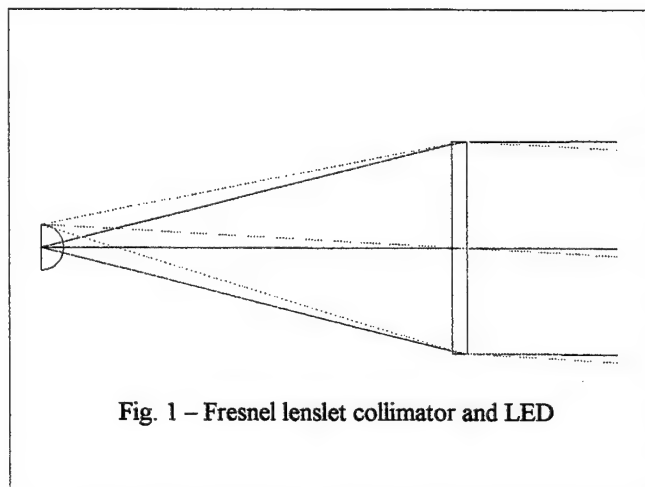


Fig. 2 shows the beam profile from a typical LED. To maximize efficiency the lenslet should capture all the light emitted by the LED, which from the figure would require that it have an NA of about 0.77. However, the radiance across the lenslet must also be relatively uniform to serve as an acceptable backlight. This means that the intensity of the LED should be constant over the entire surface area of the lenslet, which, as the figure shows, is not the case. Ideally, the lens on the LED would form a tophat beam profile. As a

compromise, we arbitrarily set the NA of the lens across the diagonal to be 0.34, which allows no more than a 30% rolloff in intensity from the LED. For lenslets in a square packing this then sets the lenslet array pitch to 14 mm center-to-center, and likewise for the LED array. The collection efficiency can then be determined by the ratio of the integrated irradiance over the surface of the lenslet to the total emitted flux;

$$E = \frac{\iint I(x,y) \cos^3 \theta \, dx \, dy}{f^2 2\pi \int I(\theta) \sin \theta \, d\theta} \quad (1)$$

where I = intensity, $\cos \theta = \frac{f}{\sqrt{x^2 + y^2 + f^2}}$, f = focal length.

Calculating these integrals for the above parameters indicates that only about 20% of the LED light is collimated by its corresponding fresnel lenslet. The remainder is captured by adjacent

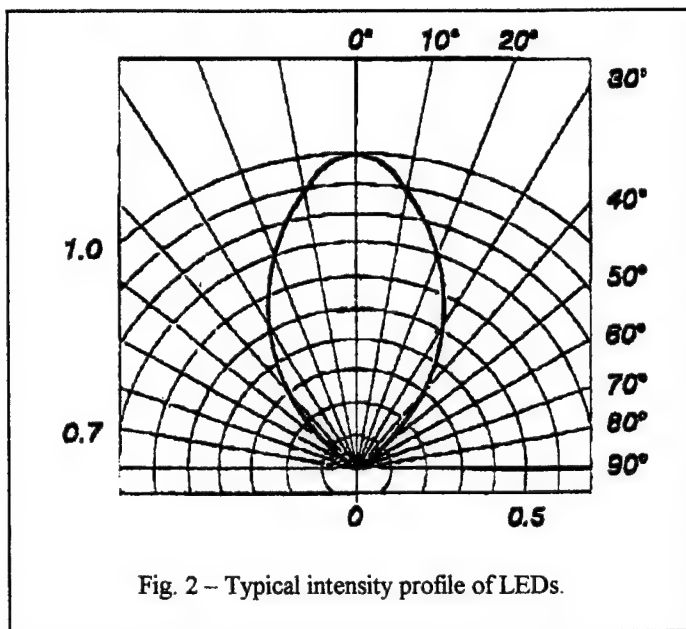


Fig. 2 -- Typical intensity profile of LEDs.

lenslets and scattered into eight distinct off-axis spots surrounding the main lobe. A special beam shaping lens on the LED would no doubt improve the efficiency.

The spatially separated three-color LED design is shown in Fig. 3. Each fresnel lenslet collimates the light from a triplet of red, green, and blue LEDs. The three colors are angularly separated in collimated space, which, when incident onto a secondary cylindrical lenslet array, are focused onto the appropriate color apertures of the LCD. The cylindrical lenslet array has the same pitch as the LCD.

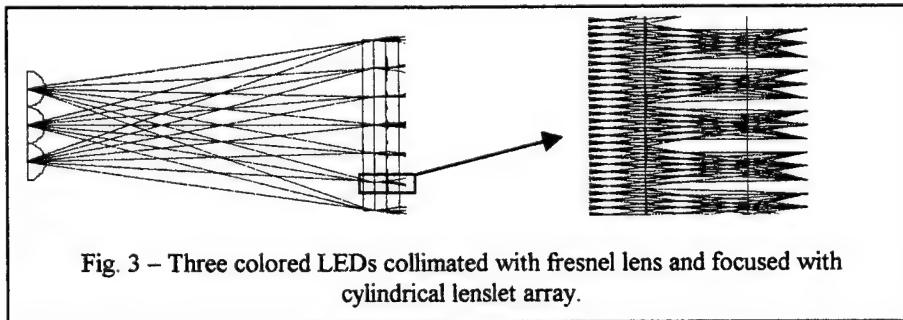


Fig. 3 -- Three colored LEDs collimated with fresnel lens and focused with cylindrical lenslet array.

3. LED BOARD DESIGN

The color LED board is a double layer printed circuit board with a 100 element, 10 by 10, array of RGB LED triads. Fig. 4 shows a photograph of the LED board. Each LED triad consists of a red LED (Sun LED LMR32DG), a green LED (Sun LED LMG32D) and a blue LED (Sun LED LUB32D). Each LED in a triad is spaced 3mm apart and each LED triad is spaced 14mm apart. The board requires +5V to bias the three power amplifiers, and +5V and -5V to power the amplifiers and LEDs.

Three power amplifiers provide power to the LEDs, one amplifier for all LEDs of the same color, which allows for color balancing. Also, the three LED types require different drive voltages. Each LED is connected in series with a current limiting resistor to limit the maximum possible current to 25mA and prevent damage to the device. Since the 3 types of LEDs required different drive voltages, different values of current limiting resistors are used for each type of LED: 127 Ohms for the red LEDs, 113 Ohms for the green LEDs, and 20 Ohms for the blue LEDs. Since it is desirable to have equal luminous intensity from all LEDs of the same color,

1% resistors are used for the current limiting resistors. The voltage output of each amplifier can be independently adjusted to balance the intensity between the three colors.

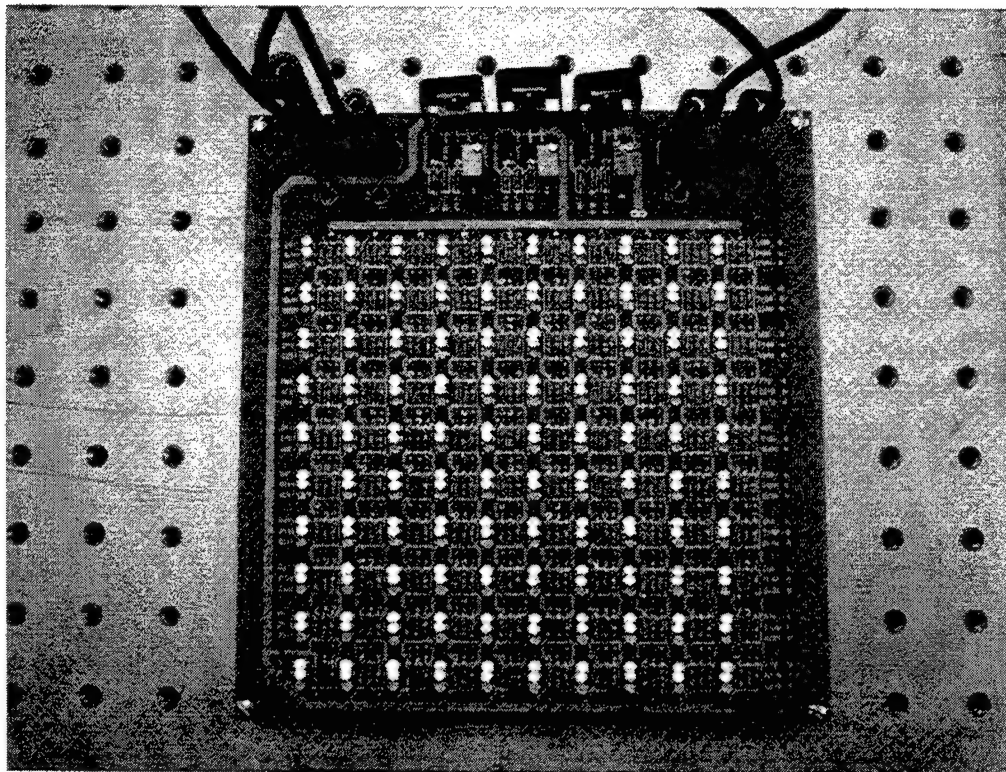


Fig. 4 - Photograph of the color LED board.

Experimental data suggests that the optimum drive voltages for the three types of LEDs are: 1.7V for the red LEDs, 2.3V for the green LEDs, and 3.3V for the blue LEDs. A schematic diagram of the power amplifier that powers the red LEDs is shown in Fig. 5. The value for resistance R2, 3010 Ohms, sets the reference voltage for the amplifier at 1.16V. This results in an output voltage range for VR of 0V to 2.32V. Pot R4 sets the gain of the amplifier from 0 to 2. Therefore the maximum output voltage is 2.32V. Each red LED has a 127 Ohm resistor in series with it, resulting in a drive current of approximately 4.8mA per LED, because the voltage across the LED is 1.7V. Similarly, the power amplifiers for the green and blue LEDs use 6340 Ohms and 5620 Ohms, respectively, for their equivalent of R2 to generate output voltages of 3.88V and 3.60V, respectively. This sets the maximum drive currents at approximately 14mA for the green LEDs and 15mA for the blue LEDs. Therefore, at maximum brightness, each RGB triad requires approximately 120mW of power. The entire array then requires approximately 12W of power, excluding the minimal power required to bias the 3 power amplifiers. However, experiments showed that the array could be driven at much lower power levels and still produce more than adequate intensity.

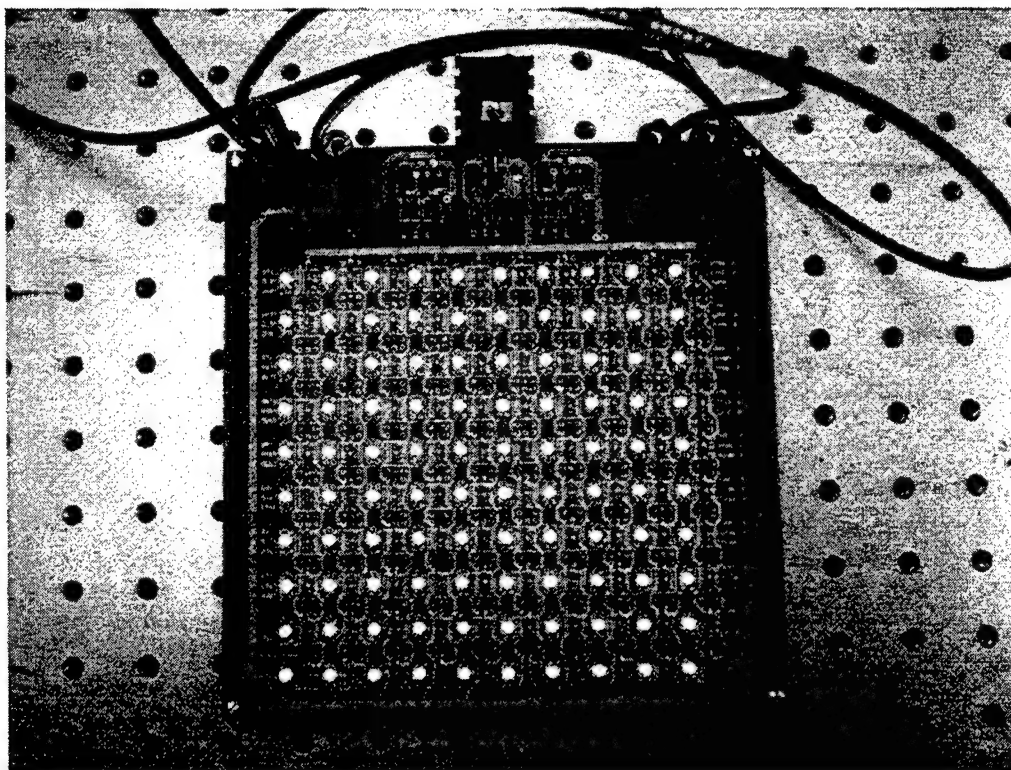
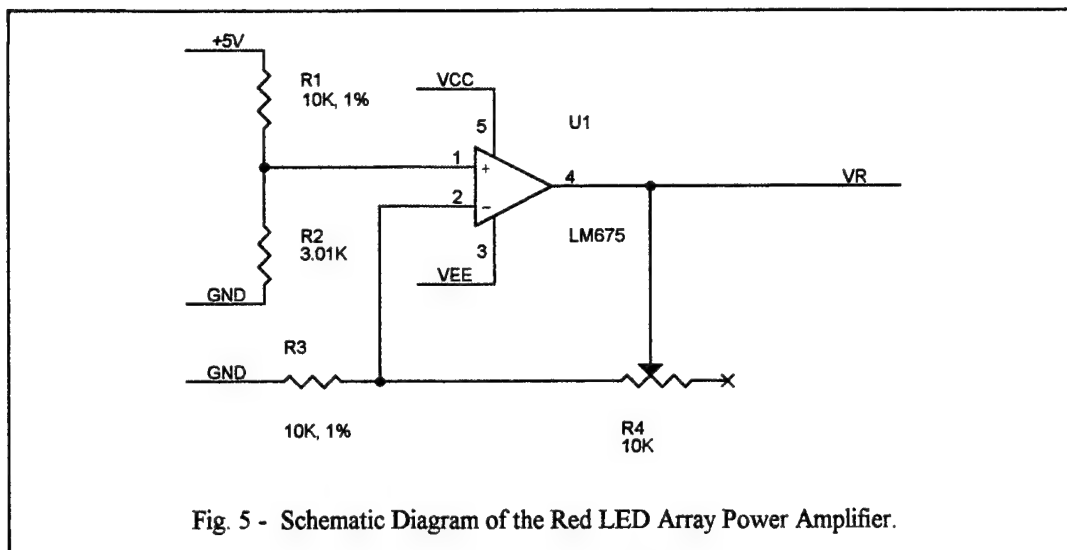


Fig. 6 - A Photograph of the White LED Board.

The white LED board, shown in Fig. 6, uses the same printed circuit board as the color LED board, except that each RGB LED triad is replaced by a single Kingbright L2310BSPW white LED. Only one power amplifier is used on this board. Experiments showed that this LED performs best with a drive current of no more than 30mA, which occurred at a drive voltage of

approximately 3.4V. Therefore a 20 Ohm resistor is used as the current limiting resistor and the power amplifier is biased to produce a maximum voltage of 4.0V. The array of 100 white LEDs then requires approximately 12W of power at full brightness, although experiments showed that it can be driven at much lower power levels and still produce adequate brightness.

4. FABRICATION

An 11-by-11 array of fresnel lenslets was fabricated onto a 6-inch fused silica plate using gray scale mask photolithography and reactive ion etching. The surface profile was measured using a Zygo New View 5000 optical profilometer. Fig. 7 shows the Zygo measurement of one of the lenslets. The smooth zone profiles are characteristic of the gray scale mask fabrication method. The deep etch depth required about 18 hours of etch time and is thus an unsuitable fabrication method for mass production. Plastic injection molding could provide a more cost-effective solution. Cylindrical lenslet arrays were also fabricated in photoresist but not etched. Fig. 8 shows a profilometer measurement of the cylindrical array.

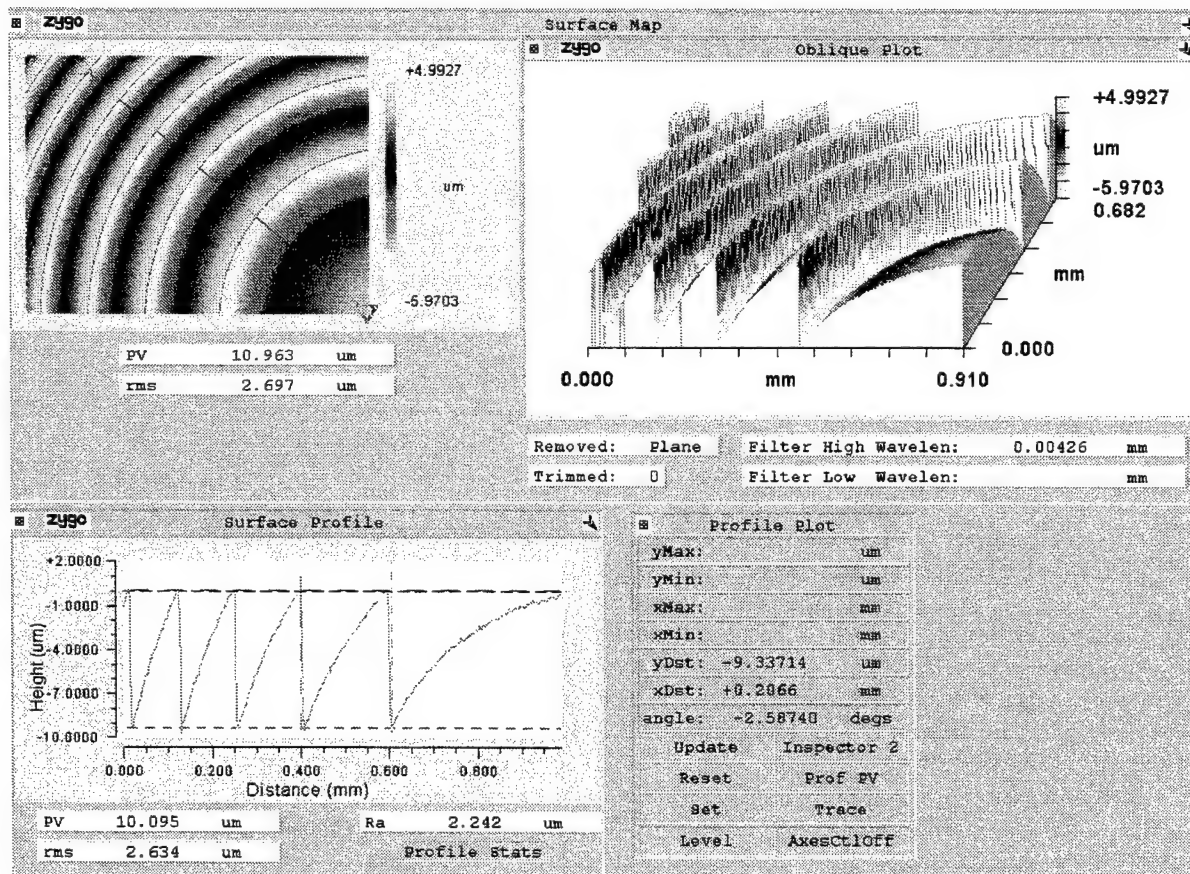


Fig. 7 – Surface profile measurement of fresnel lenslet array.

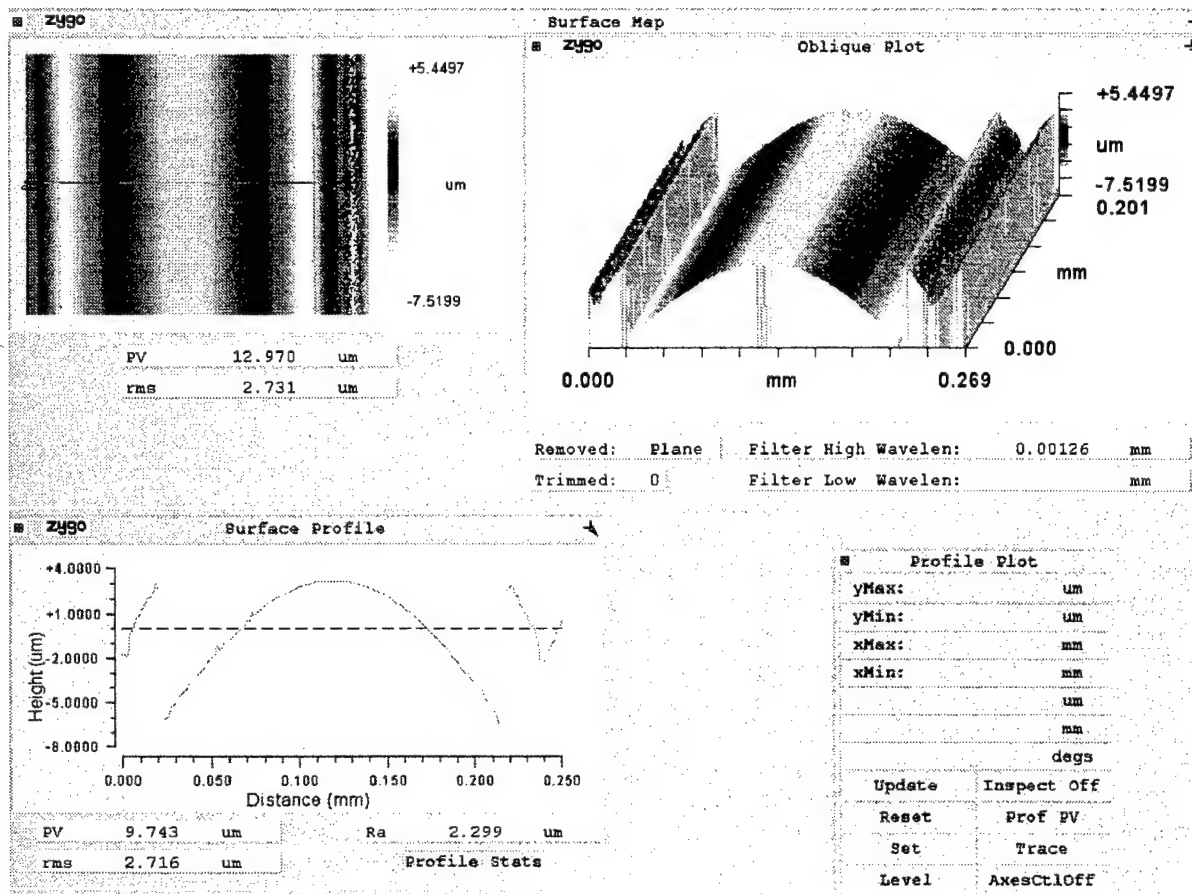


Fig. 8 – Surface profile measurement of cylindrical microlens array.

5. TESTING

Measurements showed the radiance of the white LED backlight to be 13 times brighter than a typical CRT computer screen and 24 times brighter than a typical laptop LCD screen, which is not unusual given the backlight's high degree of collimation. With the addition of the polarizers, lightvalves, and interference color separation filter we estimate the surface radiance would be reduced by a factor of 9, making it only about two to three times as bright as a laptop screen. The total area was 196 square centimeters and power consumption was 0.9 watts.

The three-color LED board was also tested with the fresnel lenslet array and cylindrical lenslet array. Inspection at the focal point of the cylindrical lens with a microscope showed clearly separated lines of the three colors. Power consumption was 2.8 watts for a total area of 196 square cm.

6. CONCLUSION

The main culprit for the loss of surface radiance in a color liquid crystal display is the absorptive color filters at each pixel. The many recent advancements made in LED technology provide reason to believe that LEDs will become the light source of choice for LCD backlights in overcoming this efficiency loss. However, it would be premature at this point to predict which LED method will prevail. Three potential methods of using LEDs to overcome the current LCD efficiency loss include; a) white LEDs with an ICS filter, b) spatially separated color LEDs focused into the appropriate apertures, and c) time multiplexed color LEDs. Our preliminary investigations into the feasibility of the first two methods indicate promising results, although more development is needed. Perhaps other methods of using LEDs as LCD backlight sources will also surface in the near future.

REFERENCES

- [1] Gunn, T. V., and Halstead, W. H., "Diffractive Color Separation Fabrication," SPIE Proceedings, 3363, pp.198-208, 1998.
- [2] M.W. Farn, R.E. Knowlden, M.B. Stern, W.B. Veldkamp, "Color separation gratings," NASA Conference Publication 3227, Conference on Binary Optics, 1993. Publications, 3227, pp. 409-421, 1993.
- [3] Damann, H., Color separation gratings," Applied Optics, vol. 17, no. 15, p. 2273-2279, 1978.
- [4] Full Color LCD Backlighting with LEDs, Hewlett Packard Application Brief I-011.

Multi-Spectral, Reflectance-Mode Fiber Optic Deposition Rate Monitor

James T. Daly^a, John A. Wollam^a, Fei Luo^b, Theodore F. Morse^b, Andreas Kussmaul^c, and Dan Pulver^c

^aIon Optics, Inc., Waltham, MA 02452

^bLaboratory for Lightwave Technology, ECE, Boston University, Boston, MA 02215

^cLasertron, Inc., Bedford, MA 01730

ABSTRACT

We have developed and demonstrated a reflection-mode optical fiber-based instrument for *in situ* monitoring and feedback control of thin film dielectric deposition processes. The instrument operates in single-wavelength or multi-wavelength mode. One end of the fiber is placed in the deposition zone, close to the samples being coated. Single or multi-wavelength light is sent down the fiber and the reflected light from the end being coated is analyzed for intensity vs. wavelength. The fiber end being coated features an easily replaced tip to prevent loss of resolution when the coating becomes too thick.

For processes in which the index of refraction or composition of the thin films is fixed, the less expensive single wavelength instrument is sufficient and measures thickness of the films by counting interference fringes. For processes in which film composition or index of refraction are variable, we use a white light source and compact spectrograph to measure reflectance vs. wavelength. For critical applications like diode laser facet coating where yield loss is significant cost driver, this monitor measures the thickness and index of refraction of single and multi-layer thin films as they are deposited. More importantly, it measures the critical parameter of interest: reflectance at the actual laser emission wavelength. This instrument replaces quartz crystal oscillators and other, more complex instruments.

Keywords: thin film deposition monitor, optical fiber sensor, laser facet coating

1. INTRODUCTION

Thin-film deposition is an important step in the fabrication of virtually every advanced optoelectronic or photonic device. This is true regardless whether the films are deposited by chemical vapor deposition (CVD), metalorganic CVD (MOCVD), or physical vapor deposition techniques (including molecular beam epitaxy, sputtering, and electron-beam or thermal evaporation). In each of these methods, at the research, development, or production level, the need for control over the growing film is great. Improved knowledge of a film's structure, defect density, and composition leads directly to lower cost, speedier development of new devices, and improved quality.

In the case of diode lasers for optical fiber communications, the reflectivity of the lasers' front and rear facets must be controlled using thin film coatings in order to achieve optimum device characteristics. The quality of the optical coatings and the precise thickness and index of refraction thus directly affects laser performance, manufacturing yield and cost. By the time a diode laser advances to the facet coating step, it is a high value-added item. Any yield loss at that point is expensive. Further, customers are demanding progressively more advanced devices which require increasingly stricter control over the properties of these coatings. This is therefore an important area for laser manufacturers. Any technology that can improve process control in existing facet coaters could have a potentially large financial impact for the company.

Methods now employed to make real-time, *in situ* measurements of thin film characteristics include reflection high-energy electron diffraction (RHEED), time-of-flight ion-beam surface analysis, quartz crystal monitors, and optical probe techniques including ellipsometry, spectral ellipsometry and interferometry. By far the most common technique in the semiconductor and optics industries, and the only one permitting wide-band thickness measurement, is the quartz crystal oscillator. This is a micro-mechanical "tuning fork" which changes its characteristic frequency in response to the addition of mass as material deposits on its surface. There are tens of thousands of these in use in labs throughout the world. They provide no information on film quality, refractive index, or surface roughness, but give only thickness, and then only when film thickness at the crystal location can be reliably related, through an empirically-determined "tooling factor," to film thickness deposited on the working substrate.

Thin film optical coatings are deposited at Lasertron using e-beam evaporation of various oxide materials. The deposition rate and final layer thickness are currently controlled by quartz crystal monitors, which measure the change in resonance

frequency of a piece of quartz due to the mass of depositing material. This conversion from frequency shift to mass to thickness is prone to numerous errors due to subtle changes in material properties (strain, density, age of crystal, temperature of sensor) and is completely insensitive to index changes. Furthermore, the quartz crystal monitors need to be placed a few inches away from the part to be coated to avoid shadowing effects. This results in a difference in deposition rate, which can fluctuate from run to run and lead to unpredictable changes in final thickness.

Optical probe techniques, like interferometry and ellipsometry, have been under development for many years and these techniques offer the promise of substantially more information on as-growing films. (Indeed, these techniques are probably the most common diagnostics for examining and evaluating as-deposited thin film coatings outside of the deposition chamber and after the fact.) One inescapable fact for optical techniques is that an optical probe beam must get into the deposition region and it must get back out of the deposition region. This means the use of optical windows: and in all real-life deposition systems, material is deposited not just on the desired substrate but on chamber walls, fixtures, liners, and windows. The optical probe beam samples both the window and the substrate so that incidental deposits on the window confound the optical signal from the substrate. This problem, colloquially "the window crud problem," has stymied many efforts to implement real time optical monitors.

Measurements must be made through windows located at positions which depend on the type of measurement, and for phase and polarization sensitive measurements, the apparatus must sometimes be reproducibly mounted to within a fraction of a wavelength of light. In addition, and this is no small detail, windows through which interferometric or ellipsometric measurements are made must be coating-free. Although this condition can be met in a (very expensive and very slow-growing) molecular beam epitaxy (MBE) system, even with shields and shutters it is virtually impossible to achieve in the relatively high-throughput CVD reactors and physical deposition systems characteristically employed in production situations. In these systems, where most thin-film semiconductor materials are grown, the environment is inherently "dirty" and it is extremely difficult to keep windows from becoming coated.

We have developed and demonstrated a reflection-mode optical fiber-based instrument for *in situ* monitoring and feedback control of thin film dielectric deposition processes. The method is called "fiber-optic reflectometry" and was conceived by one of the authors (T. Morse) and his research group while still at Brown University. The method resembles optical reflectance spectroscopy (ORS), though without the need for precise optical alignment. It consists of inserting an optical fiber into the region where material is being deposited on a substrate, and locating it so that the end of the fiber will be coated as well. In essence, this simple invention has turned the "window-crud problem" upside down – instead of confounding the optical measurement on the substrate, the material deposited on the optical fiber provides the measurement.

2. SENSOR DESIGN

When light is projected down the fiber, it reflects from both the fiber tip and the free surface of any film covering the tip. The film then becomes, in essence, a Fabry-Perot cavity, and the back-reflected interference pattern contains information on film thickness and composition. The technique's fundamental premise is that deposition on the end of the optical fiber correlates with deposition on neighboring surfaces. This has proven to be the case for *in situ* monitoring in reactors in research and production settings, where thickness projected by the monitor has, for a variety of materials, agreed well with post-deposition measurements obtained from ellipsometry and TEM.

A block diagram showing the components and characteristics of an elementary system designed to take advantage of this effect is given in Figure 1. The basic reflectometer consists of signal processing electronics and a readout, a light source, a fiber-optic probe, mounting and feedthrough hardware, signal detection and readout electronics, and software to interpret the signal and archive it. The light source can be either single wavelength, such as a diode laser, or multi-wavelength, such as a light bulb. The detector then is usually either a photodiode or a spectrograph with photodiode array, respectively. The fiber itself is multimode for maximum throughput and can be either a single fiber or multi-strand bundle. The fiber tip is designed to be easily replaced in a few seconds with one hand during sample loading/unloading between depositions. The tips can then be disposed of or cleaned *ex situ* and re-used.

We have built two prototype fiber reflectometers. The first is a single wavelength sensor that uses a diode laser and silicon photodiode with armored multi-strand, multimode fiber and is shown in Figure 2. The diode laser operates at 670 nm and can run pulsed or cw. The second prototype uses a tungsten (white) light bulb and an Ocean Optics (Dunedin, FL) miniature spectrograph with silicon photodiode array detector. It operates in the wavelength range 500-1100 nm and can monitor multiple wavelengths simultaneously.

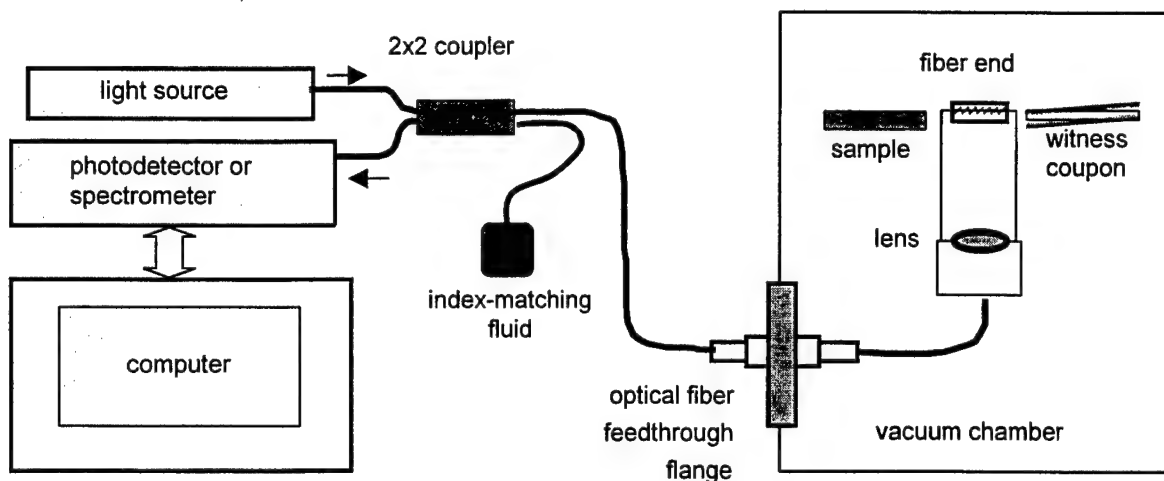


Figure 1 The fiber-optic reflectometer concept is shown schematically in this block diagram. Light from a single or multi-wavelength source is directed down the fiber to the tip which is next to the samples and is coated at the same time. The reflected signal is monitored by either a photodetector or spectrometer.

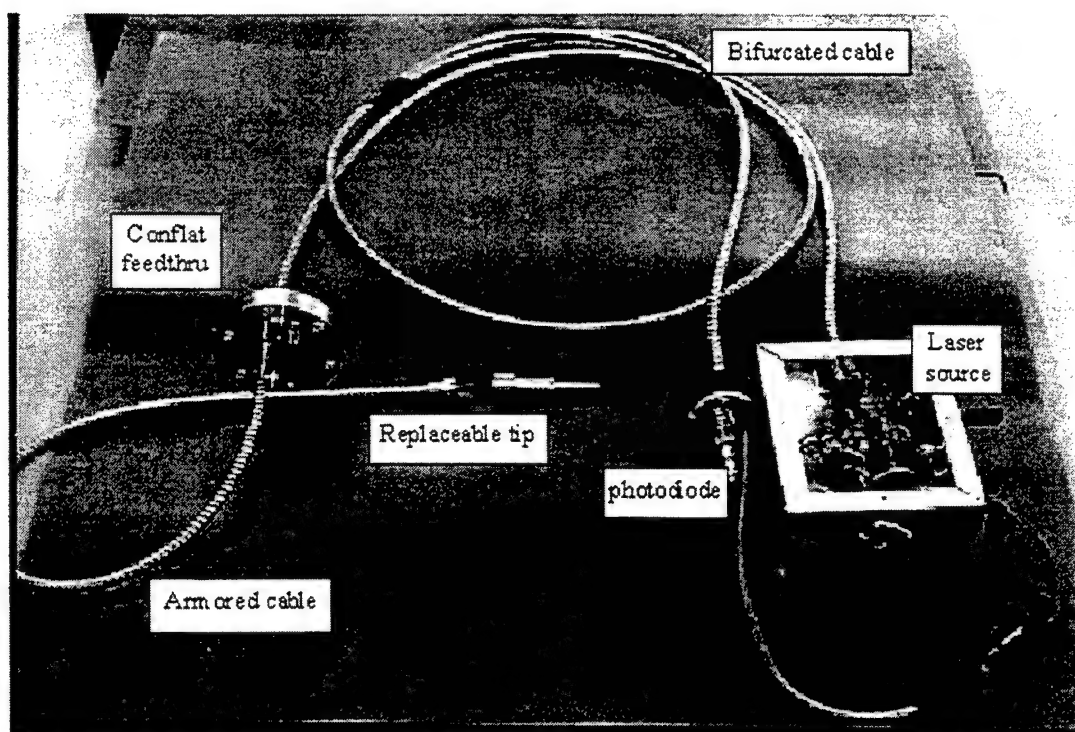


Figure 2 Single wavelength reflectometer features 670 nm diode laser; armored multi-fiber bundle, which enters the vacuum coater inside a flexible bellows thus allowing the fiber end to be located right next to the samples being coated; a replaceable fiber tip; and silicon photodiode detector. This design maximizes signal-to-noise by minimizing losses at intermediate connectors.

For the fiber-optic monitor to be of use in an industrial environment, it is necessary that a clean deposition surface be provided after every run, or after a number of runs which will be empirically determined. One way would be to deposit directly on the cleaved end of a fiber and provide a freshly cleaved surface between each run. However, obtaining a well-cleaved surface requires practice and skill and it would be difficult to inspect without removing the fiber to a microscope.

We therefore developed two designs for a replaceable fiber end which could be changed by one operator, on the production floor, with no tools and in a matter of seconds, as shown in Figure 3. One uses a short (~1.5 inch) clear fused silica light pipe (~0.2 inch diameter) in a stainless steel sheath. It is press-fit into a nut which threads on to the fiber end. It is rugged and the deposits can be removed by etching or re-polishing the light pipe's end. The second design uses a GRIN collimating lens (Oz Optics, Ontario, Canada) at the end of the fiber and a replaceable window/substrate. This window can be any material transparent to the measurement wavelength such as clear fused silica, sapphire, or calcium fluoride.

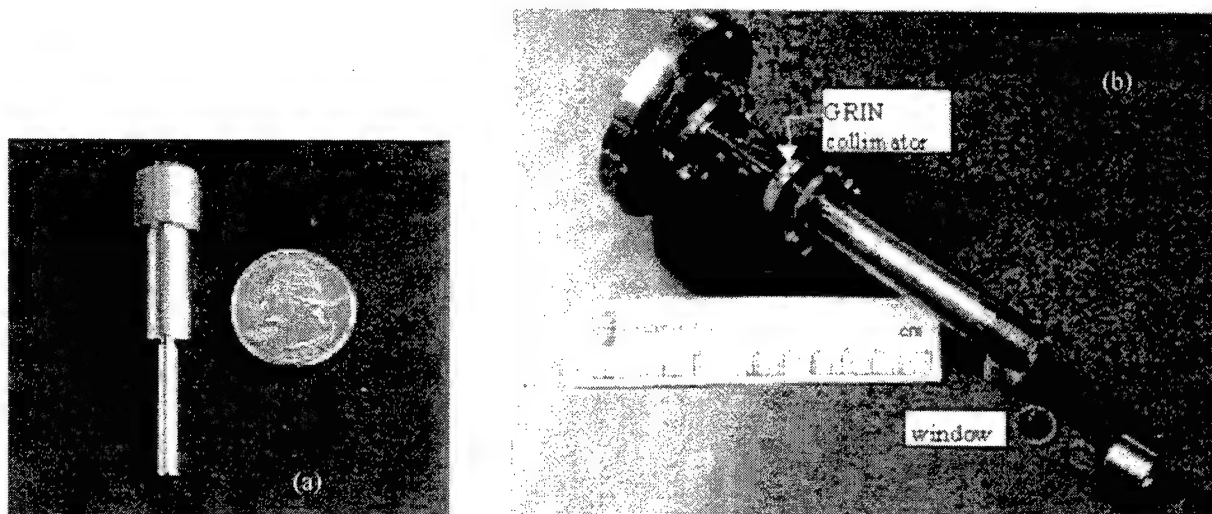


Figure 3 (a) Replaceable or refurbishable fiber tip is a stainless steel-clad silica light pipe. Both ends of the light pipe are polished. One end is threaded on to a common fiber bundle containing hundreds of fibers, and the other is placed in-plane with the target substrate. After a run the tip is easily replaced, and can be re-polished and re-used. (b) Fiber end using GRIN lens and replaceable window/substrate. The window can be easily replaced between batches.

3. THEORY OF OPERATION

Consider a fiber optic waveguide in which light propagates through the fiber by total internal reflection. When light reaches the fiber tip, the difference in index of refraction between the fiber core ($n=1.458$) and air or vacuum ($n=1$) causes about 4% to be reflected back into the fiber at the freshly cleaved tip, according to the formula for normal Fresnel reflection:

$$R = \frac{(n-1)^2}{(n+1)^2} \quad (1)$$

The index, n_f , of the fiber is generally a function of wavelength, λ , however, in the spectral region produced by a white light source (400 nm to 1050 nm), the wavelength dependence (dispersion) is quite small and can be neglected.

Suppose we now place one end of the fiber in the deposition zone of an evaporator or sputtering unit so that whatever films are being deposited also accumulates on the end of the fiber, as shown in figure 4. Then as the thin film of index n_1 accumulates onto the fiber tip, reflection from the fiber tip is modified by the interference of light from the fiber-film and film-vacuum interfaces. For a single layer of thickness d on a substrate (or fiber), the complete expression for the reflectance is given by:¹

$$R = \frac{(n_f^2 + n_1^2)(n_1^2 + n_0^2) - 4n_0n_1n_f + (n_f^2 - n_1^2)(n_1^2 - n_0^2)\cos(2\delta)}{(n_f^2 + n_1^2)(n_1^2 + n_0^2) + 4n_0n_1n_f + (n_f^2 - n_1^2)(n_1^2 - n_0^2)\cos(2\delta)} \quad (2)$$

where n_f , n_1 and n_0 are the fiber core (substrate), thin film, and air indices, respectively, and $\delta = 2\pi n_1 d / \lambda$. This expression is for the (artificially) simple case where all layers are transparent, of uniform refractive index, and ideally flat. For real-life

systems with multiple layers and interfaces which scatter, reflection and transmission are computed numerically in terms of a product of optical transfer matrices for each layer. These calculations are typically made with an optical thin-film software package such as FilmStar (by FTG Associates).

The reflectance R will reach a maximum or minimum when the film's optical thickness is a multiple of one-quarter of the light wavelength.²

$$n_i d = m \frac{\lambda}{4} \quad (3)$$

where m is a positive integer. If m is even, the coating is said to be neutral and the reflection equals that of the bare fiber/vacuum interface (at that one particular wavelength); if m is odd, the reflection will be either maximized (if the film index is higher than the substrate index) or minimized (if the film index is lower).

There are two ways to measure these interference effects. At a single fixed wavelength, the growing film will cause reflectance to go through periodic maxima and minima, between the value corresponding to the bare substrate and a second value, either greater or smaller, dependent on both indices. Alternatively, a complete spectrum can be taken at a given thickness, and peaks and valleys in the reflectance observed for those wavelengths where condition (3) is met. The multi-wavelength measurement has the advantage that it can determine index of refraction as well as film thickness. If two wavelengths λ_1 and λ_2 both achieve a maximum (or minimum) at the same thickness, one with a value m and the other with $m+1$, then from (2), the index n will be given by³:

$$n = \frac{1}{\left(\frac{1}{\lambda_2} - \frac{1}{\lambda_1}\right) d} \quad (4)$$

In the case of alumina films, which are commonly used for laser front facet coatings, the refractive index is very close to 1.6 at visible wavelengths. With an index value for the fiber core of 1.458, the following expression is obtained:

$$R = \frac{1.75 - 0.68 \cos(2\delta)}{31.43 - 0.70 \cos(2\delta)} \approx 0.0557 - 0.0216 \cos(2\delta) \quad (5)$$

Thus, reflectance has a sinusoidal dependence on wavelength. Notice that the modest difference in refractive index between the glass fiber and alumina films provides a very stringent test for our prototype because of the small reflection signal (~5%) which is expected. Figure 5 shows a FilmStar calculation of the time-dependence of reflection at two wavelengths, 670 nm and 1300 nm. More rapid interference cycles are observed at shorter wavelengths, where higher measurement precision is obtained.

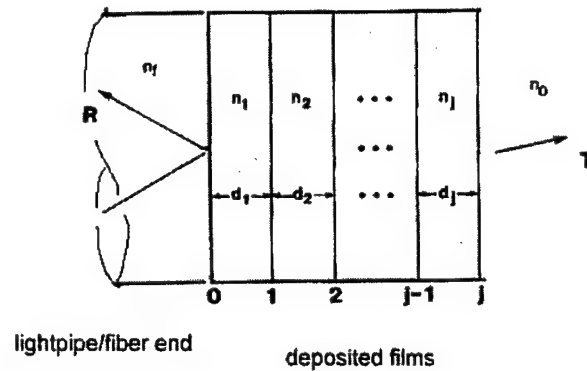


Figure 4 Multiple thin films deposited on the end of the fiber/lightpipe.

Discrete wavelength monitoring

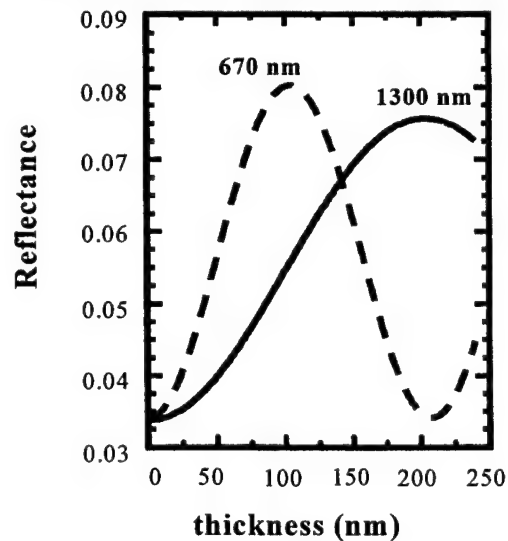


Figure 5 Films deposited on the end of the fiber/lightpipe give rise to interference fringes in the measured reflectance.

4. SENSOR EXPERIMENTS

Benchtop Tests

The (bifurcated) multiple fiber bundle to vacuum feedthrough to fiber to tip configuration (figure 2) was assembled and tested on the benchtop in Ion Optics' facilities. Reflection from the coating on the replaceable tip was simulated by placing the tip in intimate contact with a front-surface gold-coated mirror. We found that even in the absence of a reflection from the replaceable tip, we still were seeing a lot of reflected signal. We determined that the 4 glass-to-air interfaces at the vacuum feedthrough were giving unacceptably high reflection. In fact, in this configuration, the difference between no reflection and complete reflection from the replaceable tip was only 25-30% of the total reflected signal. We therefore decided to eliminate the windowed feedthrough and design a feedthrough that would allow us to use a continuous fiber bundle while maintaining ruggedness and leak tightness. The result is a continuous (armored) fiber bundle passes through the flange and is contained in a 3 ft long flexible bellows tube with a vacuum tight (Swagelok) fitting that seals to the end of the bundle at the point where the replaceable tip attaches. This greatly reduces unwanted reflected signal. Bench tests with this configuration showed that the difference in reflectance between a coated and uncoated tip was now 90% of the total measured signal.

We have also developed a single multimode fiber version of the probe. For this version we have demonstrated a simpler vacuum feedthrough using a Conax compression fitting. We have tested this arrangement using an optical fiber patchcord outside the chamber, and a polyimide coated fiber protected by a Teflon sleeve inside the vacuum. A low vapor pressure epoxy was used to glue the parts of the vacuum feed through, and no outgassing was detected. Both the multi-fiber bundle and single fiber versions have shown to be vacuum tight to at least 10^{-7} torr. The single fiber version is however slightly less expensive than the fiber bundle.

One area of concern was that since the fiber end was pointed toward the evaporator sources, short wavelength thermal radiation from these crucibles would be transmitted through the depositing film and add to the reflected signal thereby confounding the reflectance measurement. We tested this by shining a flood light onto the end of the fiber and indeed recorded a large increase in returned signal. To correct this, we made two changes to the probe's design. First, in the single wavelength version, we added a narrow band filter centered on the diode laser wavelength to the front of the photodiode. This ensured that the photodiode would only see the wavelength being reflected. Second, we decided not to operate the probe in a cw or dc mode, rather we modulated the light source, either with a vane chopper or by electrical pulsing of the diode current. We then incorporated a phase sensitive detection subroutine into the LabView .vi or "virtual instrument" that recorded the data. The result was that the reflected signal became immune to interference from external sources, even when pointed directly at a 150W flood lamp.

In Situ Deposition Measurements

We measured deposition of an alumina film designed to simulate a diode laser front surface mirror. The demonstration was performed *in situ* in a production vacuum coater in Lasertron's facilities using our single wavelength prototype. The end of the probe, *i.e.* the replaceable fiber tip, was located right next to the rotating sample stage. The results presented in figure 6

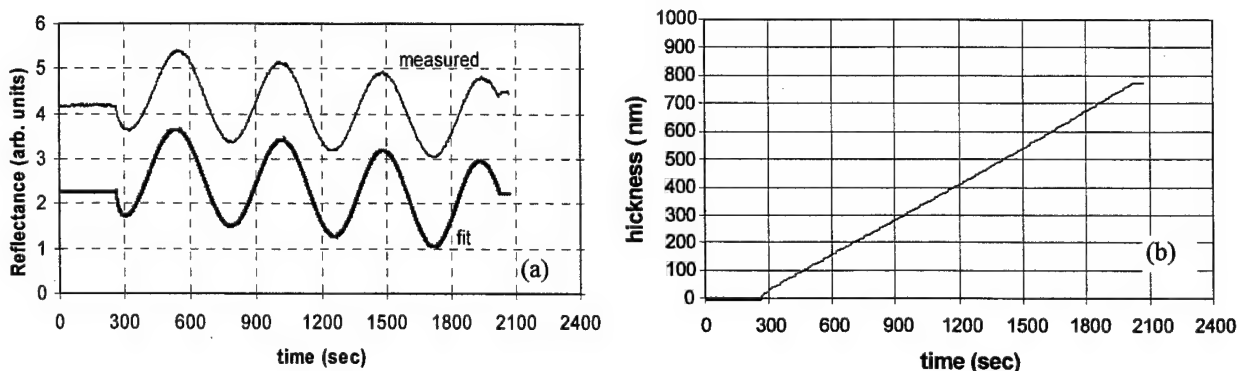


Figure 6 Single wavelength measured reflectance (a) and calculated fit (offset for clarity) for alumina film deposition measured *in situ* in a production vacuum coater used for diode laser facet coating. Resulting thickness calculated (b) at 774 nm and showing constant growth rate.

clearly show the sinusoidal oscillation in the reflectance intensity predicted above. We are also able to fit the measured data using the equation shown in (5) and to extract the thickness and growth rate vs. time, as shown in figure 6b. In this case, we can see that the facet coater used by Lasertron easily maintains a constant deposition rate from start to finish. Our fiber sensor measured film thickness as 774 nm; the nearby quartz oscillator measured thickness as 580 nm. This suggests that deposition inside the chamber is non-uniform and reinforces the importance of measuring film reflectance directly, possibly in multiple locations.

We performed similar measurements for alumina deposition using the multiwavelength, spectrometer-based unit. In this case, tests were performed in an e-beam evaporator at a university research facility. Rather than track all 2048 channels available with the spectrometer which makes for cluttered data, we chose to monitor only three individual pixels (pixels 200, 800 and 1600) as functions of time. Their corresponding wavelengths are 564.61 nm, 781.22 nm, and 1042.02 nm. During the deposition run, the deposition rate was increased after about 30 minutes. As seen in figure 7, the fiber sensor easily sees the change in growth rate as an increase in oscillation frequency. One other thing to note from the figure, the measured data at 1042 nm shows more oscillation than expected and more than a fit calculated from equation (5) with $\lambda = 1042$ nm would indicate. In fact, the measured curve vs. time is a superposition of two signals: one with $\lambda = 1042$ nm and one with a wavelength half that, i.e. 521 nm. This means that we must incorporate an order sorting filter into the final design.

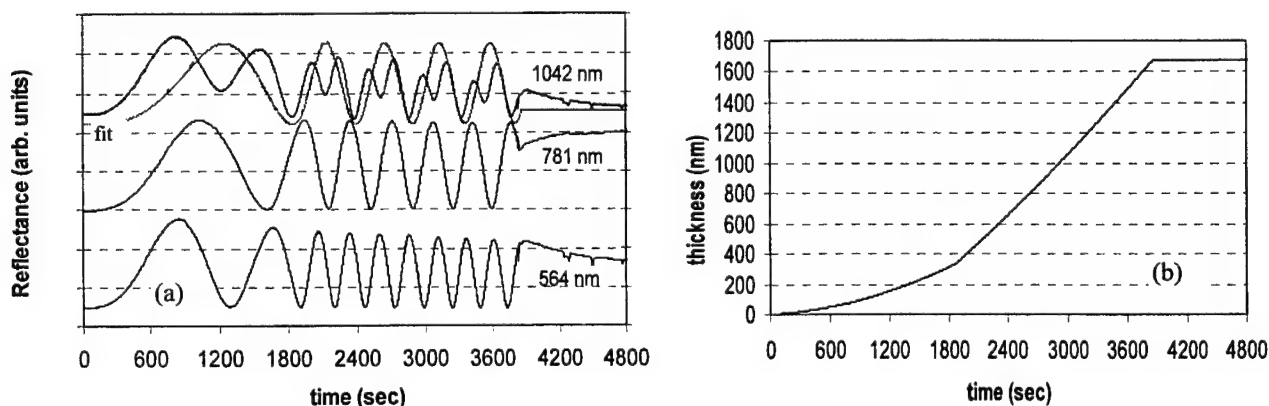


Figure 7 Multi-wavelength recording for reflectance (a) measured in situ during alumina film deposition. Resulting calculation (b) of thickness vs. growth time. Final layer thickness: 1672 nm.

We also used the multiwavelength deposition monitor to measure CVD growth of a Bragg reflector from alternating layers of silicon nitride and silicon-rich silicon nitride. The Bragg mirror consists of 60 pairs of $\lambda/4$ layers consisting of silicon nitride ($n = 1.8$, $d = 116$ nm) and silicon-rich silicon nitride ($n \approx 1.9$, $d = 110$ nm). The measured reflectance peak (figure 8) occurs as expected at 840.7 nm with FWHM = 17.8 nm.

5. DISCUSSION & CONCLUSIONS

We have developed and demonstrated a reflection-mode optical fiber-based instrument for *in situ* monitoring and feedback control of thin film dielectric deposition processes. We have incorporated a number of design features into the system in order to improve repeatability, eliminate interference from the system being measured, and improve usability. For example, for repeatability and ease of use by our customers, we have designed two different types of replaceable fiber tips which can be changed by an operator in seconds using only one hand. This ensures a repeatable starting point for each deposition run. We have also incorporated vacuum feedthrough techniques which reduce the number of fiber couplings and thereby eliminate reflectance from those couplings so that most of the reflected signal comes only from the fiber tip in the deposition zone.

The instrument operates in single-wavelength or multi-wavelength mode. In single wavelength version, a diode laser provides the light source and the reflected signal is measured with a photodiode. For the multiwavelength version, we use a white light source (tungsten lamp) and miniature spectrograph with 2048 pixel photodiode array covering the range from 500 to 1100 nm. The signal is recorded by computer running a custom LabView .vi. The single wavelength version is useful for processes in which the index of refraction or the composition of the deposited film is fixed. In this case, the reflected signal varies sinusoidally as layer thickness increases and it is relatively simple to convert reflectance value to thickness. The

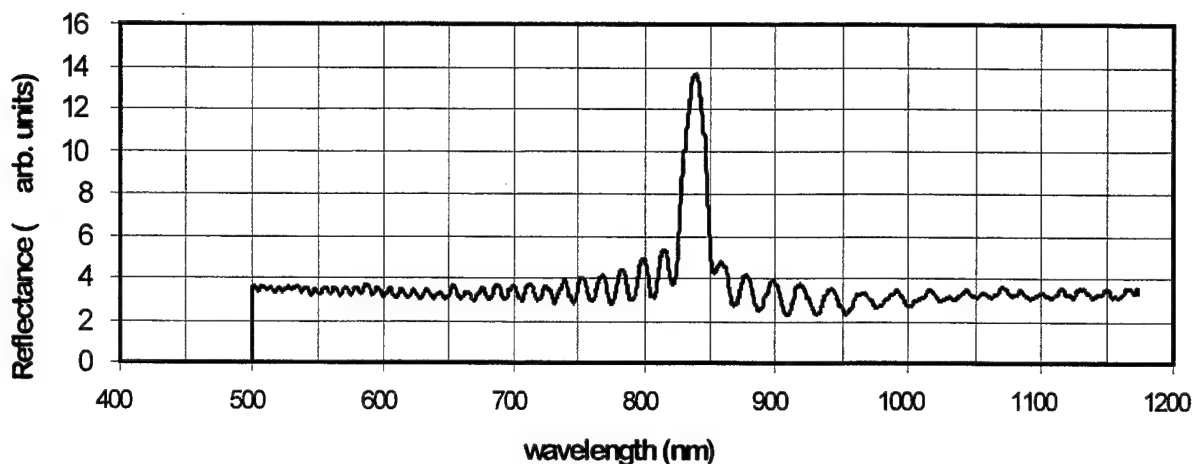


Figure 8 Multi-wavelength reflectance spectrum measured *in situ* for a Bragg reflector deposited on window in figure 3b. The Bragg mirror consists of 60 pairs of $\lambda/4$ layers consisting of silicon nitride ($n = 1.8$, $d = 116$ nm) and silicon-rich silicon nitride ($n \approx 1.9$, $d = 110$ nm). Reflectance peak occurs at 840.7 nm with FWHM = 17.8 nm

multiple wavelength version is useful for processes in which the index of refraction varies or is unknown. With only two different wavelengths, it is possible to calculate from the reflectance spectrum both thickness and index of refraction of the deposited film(s). When multiple wavelengths are used, resolution is enhanced at the shorter wavelengths where more interference fringes are seen, as long as the film is still transparent.

In order to reduce interference from light transmitted into the fiber from the coating chamber, we modulate the light source, either by chopping or in the case of the diode laser source by pulsing the diode current, and use phase sensitive detection. For the single wavelength version of the fiber probe, we also take the added step of employing a bandpass filter on the detector to ensure that it sees only the source wavelength.

The single wavelength version is especially useful for monitoring deposition of diode laser front facet coatings where yield loss is a significant cost driver. It has the advantage of being able to measure film reflectance directly which is the most important quality of the facet coating. Values of 5%-25% are typical at the diode emission wavelength.

The multiple wavelength version is particularly useful for monitoring the deposition of anti-reflection coatings, notch filters, and Bragg reflectors. As we can see in figures 7 and 8, not only can we monitor interference fringes from the deposited film in order to determine index and thickness, but we can also measure reflectance vs. wavelength to verify and perhaps control the center wavelength and peak reflectance (or transmittance) value.

In summary, we have demonstrated a reliable and accurate measurement instrument for monitoring the deposition of dielectric thin films *in situ*. The instrument is useful in a variety of applications including diode laser facet coating and the production of anti-reflection coatings, notch or bandpass interference filters, Bragg reflectors and even thermal control coatings on plate glass. This instrument replaces quartz crystal oscillators and other, more complex *in situ* monitoring instruments and has the advantage of measuring not just thickness but reflectance vs. wavelength directly.

ACKNOWLEDGEMENTS

The authors would like to thank Juan Hernandez-Cordero of Boston University for useful discussions, Walter Daly of Lasertron for assistance with *in situ* measurements, and Ward Weathers for his assistance with assembly and test. This work was supported by the National Science Foundation under STTR contract no.: DMI-9805281 and by Lasertron.

REFERENCES

- ¹ O.S. Heavens, *Optical Properties of Thin Solid Films*, p. 85, Dover, New York (1991).
- ² See for example, M. Born and E. Wolf, *Principles of Optics*, 5th ed., pp. 61-67, Pergamon, Oxford (1975).
- ³ J.I. Pankove, *Optical Processes in Semiconductors*, p. 95, Dover, New York (1971).

4mW micro cavity LED at 650nm on germanium substrates

Mark D'Hondt ^{a,b}, Prasanta Modak ^b, Danaé Delbeke ^b, Ingrid Moerman ^b,
Peter Van Daele ^b, Roel Baets ^b, Piet Demeester ^b, Paul Mijlemans ^a

a: Union Minière - Advanced Materials Business Group, Kasteelstraat 7, B-2250 Olen, Belgium

b: University of Gent/IMEC - INTEC, Sint-Pietersnieuwstraat 41, B-9000 Ghent, Belgium

ABSTRACT

We report on the realisation of red micro cavity LED's on germanium substrates, offering a significant cost advantage compared to GaAs wafers. The MCLED structure, grown by LP-MOVPE, consists of 3 GaInP quantum wells within a (detuned) 1- λ AlGaInP cavity, enclosed by Al_{0.5}GaAs/Al_{0.5}GaAs DBR's, with a current spreading layer on top. MCLED's with a 200 μ m aperture, exhibit a quantum efficiency up to 4.35% (at 10mA) and an optical power higher than 4mW (at 80mA), without any packaging. The optical spectrum was centered at 650nm, with a FWHM of ± 13 nm. Because of the detuning the opening angle of these structures was as much as 120°. Rudimentary packaging resulted in a luminous intensity of 2.5cd at 30mA, with an opening angle of $\pm 13^\circ$. Initially the electrical performance was not optimal, but additional tests and a new processing have indicated that forward biases as low as 2.0V (at 20mA) can be obtained for LED's on Ge-substrates. The new processing further resulted in an improved optical output with 5mW at 80mA. We feel there is room for further improvement, but already we have demonstrated the feasibility of germanium substrates for commercial red (to orange/yellow) LED applications.

Keywords: Ge, germanium, micro cavity, LED, light emitting diode, AlGaInP, GaInP

1. INTRODUCTION

The impact that germanium has on today's information society, is often underestimated. Although Ge was discovered more than 60 years later than silicon, the starting shot for the multi-billion dollar semiconductor industry, was the demonstration in 1947 of the very first transistor, which was made of germanium. Also nowadays germanium is used in large quantities in different branches of information technology. About 40% (on weight basis) is used for the fabrication of optical fibres, where the germanium is used as a dopant to form the fibre core [1]. In view of turn-over however, the most important application is substrates for GaAs-based solar cells, offering the most economical solution for a satellite's power supply. Also within the world of infrared optics, germanium finds applications in windows and lenses, but also as a photodetector material.

Germanium is the mostly used substrate in the world of MOVPE [2], due to the success of germanium wafers within the fabrication of solar cells. We investigate whether Ge can also replace GaAs wafers in other application domains. Germanium indeed offers some advantages which can make it a valuable alternative: first of all it is significantly cheaper (e.g. half of the price for a 100mm wafer). It is also mechanically stronger, allowing the substrates to be made thinner, which can be a weight advantage or a cost advantage (e.g. no thinning required for packaging). Next, germanium wafers are nowadays of splendid quality: epi-ready wafers up to 150mm, exhibiting zero EPD (etch pit density) have already been demonstrated. The lattice constant of germanium is very close to that of GaAs, making it not too difficult to apply the same epitaxial growth processes on the 'new' substrate. There are however some crystallographic differences between both materials, which require an adequate buffer layer in order to obtain decent material quality [3-7].

Previously we have already reported on successful implementations of AlGaAs-based 850nm and 980nm LED's and laser diodes on germanium, which were the first significant proofs of concept that Ge could be employed instead of GaAs wafers [8]. Also high performance Hall-sensors and magnetoresistive sensors on Ge-substrates have been realised [9-10].

Everybody agrees that the future of visible LED's looks very bright, mainly because of the fact LED's promise to be more cost-efficient compared to incandescent lamps in wide ranges of applications. Although the LED fabrication cost may still be higher, issues as lifetime and luminous efficiency can result in an overall cost reduction. More specific for high efficiency red LED's, applications include traffic lights, brake and tail lights for cars, indication panels and large screen displays. But also in the world of printers, scanners and fax machines, dense LED arrays have a great potential.

It is thus not surprising that industrial alliances have been formed, in order to acquire as much as possible market share. Of capital concern is the LED fabrication cost, to which wafercost contributes significantly, being the reason why one could choose for germanium substrates. We report on the realisation of red *micro cavity* LED's on germanium substrates, because MCLED's can offer some advantages compared to alternative structures.

In general MCLED's consist of an active region which is well positioned within an optical cavity, with dimensions in the order of the wavelength of the light [11]. This can result in enhanced spontaneous emission in certain directions, whereas in other directions it can be suppressed, resulting in an enhanced optical output in the direction of choice, or if desired in a narrow output beam. Although MCLED's do not promise record high efficiencies such as the 55% by HP (inverted truncated pyramid [12]) or the 40% by IMEC (surface roughening + bottom mirror [13]), they do offer one important advantage: they do not require a complicated processing in order to obtain their high efficiency, opening the way to low cost, high efficiency devices, especially when combined with germanium substrates.

2. FABRICATION

1. Growth of (Al)GaInP materials on Germanium

All device layers were grown by means of metal-organic vapour phase epitaxy (MOVPE) in a closely spaced vertical reactor. The 3-inch n-type germanium wafers (supplied by Union Minière) were in a central position on a single wafer susceptor. Pure AsH_3 and PH_3 were used as group-V sources, and TMI, TMG and TMA were the group-III precursors. All device layers were grown at a pressure of 76 Torr and mainly at a temperature of 730°C. The GaAs buffer layer, which accounts for the transition from the Ge to the GaAs-material, is grown at 700°C and is only a few 100nm thick. Prior to the growth of this buffer layer, the wafer is baked out at 700°C under an AsH_3 overpressure.

Compared to the (In)(Al)GaAs material system, which is quite 'easy' to grow, the (Al)GaInP material system requires some very specific growth conditions (growth temperature, V/III-ratio) in order to obtain the preferred 'disordered' material. Mainly the high growth temperature results in additional difficulties since the indium tends to desorb from the grown material with increasing temperature. This makes the process very dependent on growth temperature and its uniformity.

By tuning the temperature distribution inside the reactor it was possible to obtain very nice wavelength and intensity uniformity. In Figure 1 we show the PL-mapping of a quantum well calibration run on a 3-inch germanium wafer. The standard deviation on the wavelength is only 0.3nm.

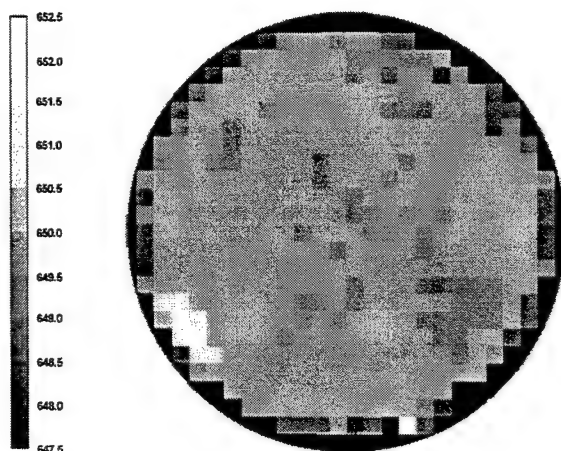


Figure 1: PL wavelength mapping of GaInP/AlGaInP quantum wells grown on a 3-inch Ge wafer.

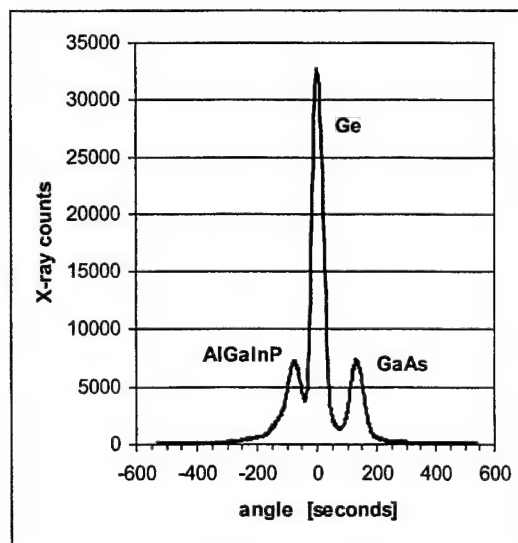


Figure 2: the AlGaInP material should be slightly compressively strained to the Ge substrate.

Finally, (Al)GaInP materials are quite sensitive to strain, therefore it is important that the In-fraction of the (Al)GaInP materials is slightly increased when growing on Ge-substrates, compared to growth on GaAs wafers. In Figure 2 we show an DCXRD rocking curve where one can observe the layer peaks from the Ge-substrate, the GaAs buffer and the AlGaInP layer, the latter being slightly compressively strained to the Ge.

2. Calibration prior to the actual device run

As already mentioned, the working principle of micro cavity LED's is based on cavity resonance. This implies that careful calibration is necessary in order to have DBR, cavity and quantum well emission tuned to each other. It further also implies that uniformity over the wafer should be fairly constant, in order to have acceptable yields.

If growth conditions are well controlled, the tuning of the DBR and the cavity can be obtained in a single growth run. It can be easily understood that an exact $1-\lambda$ cavity, applied on top of a DBR, taking into account the right changes in refractive indices, will show as a dip inside the DBR spectrum in a reflection measurement. This is illustrated in Figure 3. The side walls of the DBR peak can be used to extract the central DBR wavelength, while the dip in the spectrum, originating from the $1-\lambda$ cavity, can give the exact growth velocity of the spacer layer material.

Figure 4 shows the PL-measurement for the last quantum well calibration prior to the growth of the MCLED's.

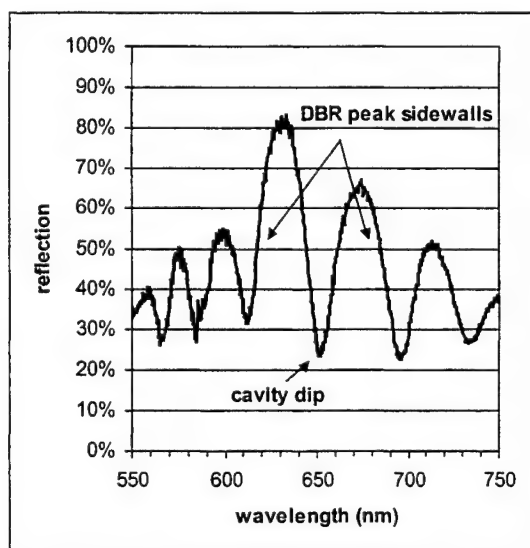


Figure 3: reflection measurement on structure with DBR + $1-\lambda$ cavity, for accurate tuning before the MCLED growth

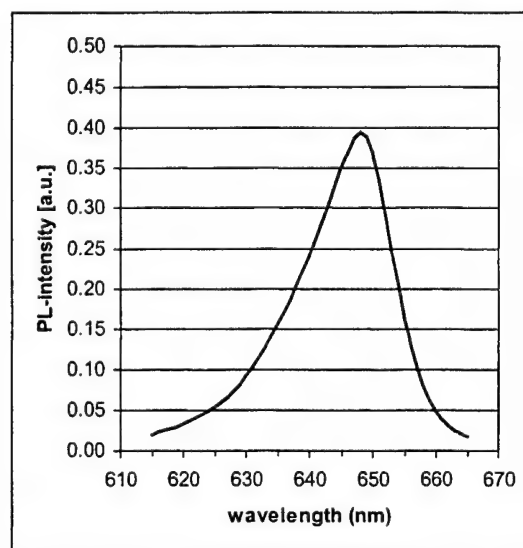


Figure 4: PL-measurement of the quantum well calibration prior to MCLED growth

3. Device growth and processing

Three different device structures were grown (Figure 5):

- I: a standard microcavity LED, with a 26.5period bottom DBR and a 5 period top DBR.
- II: a microcavity LED, identical to structure I, but including a $5\mu\text{m}$ $\text{Al}_{0.55}\text{GaAs}$ current spreading layer on top.
- III: a reference LED, without any mirrors, but including the same $5\mu\text{m}$ current spreading layer.

Both DBR's consisted of alternating $\text{Al}_{0.95}\text{GaAs}$ and $\text{Al}_{0.55}\text{GaAs}$ layers, with abrupt interfaces for the n-type part, and with graded interfaces (10nm) for the p-type part. To prevent oxidation of the top $\text{Al}_{0.55}\text{GaAs}$ layer the last DBR-layer (or the current spreading layer) was ended on 5nm $\text{p}^+\text{-GaAs}$, which was also believed to improve contact resistance (but as we will show later was not very successful in doing so).

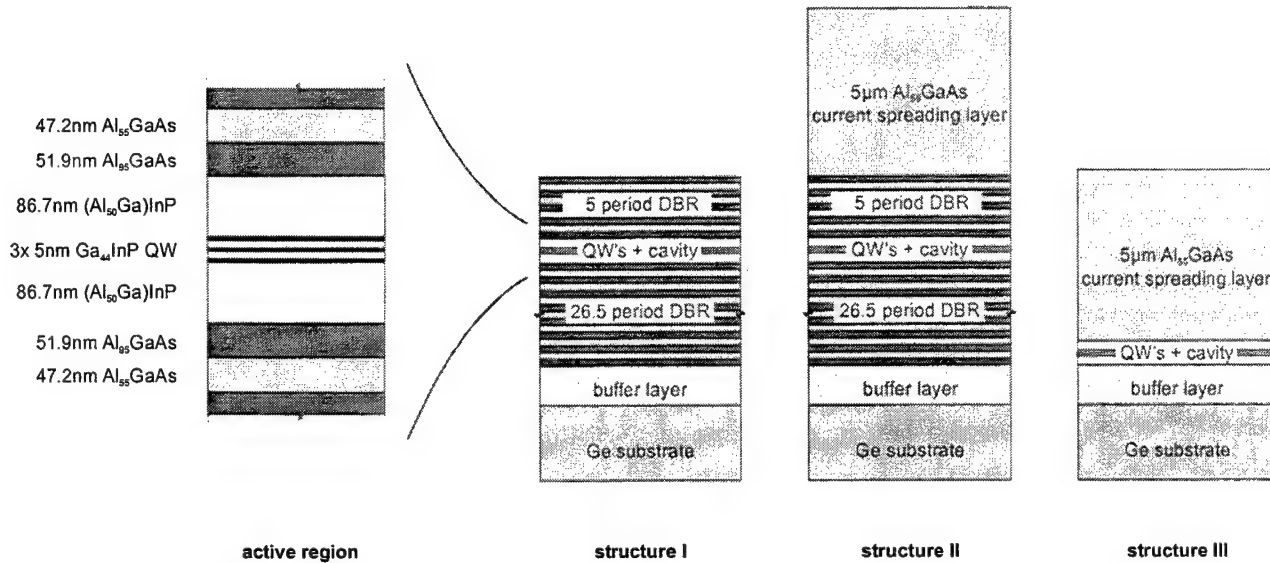


Figure 5: different (MC)LED structures used within this study

The active region consisted of 3 compressively strained $\text{Ga}_{0.44}\text{In}_{0.56}\text{P}$ quantum wells (5nm) embedded within 8nm $(\text{Al}_{0.50}\text{Ga})\text{InP}$ barriers. The spacer layers needed to define the $1-\lambda$ cavity consisted of the same material, and were intentionally detuned (in total the cavity was aimed to be $\pm 8\text{nm}$ thicker), in order to improve the optical power output. SiH_4 was used as dopant for both the n-DBR and the n-type spacer, while Cp_2Mg was used as dopant for the p-spacer and DEZ for the p-DBR and current spreading layer. A SEM picture of the type-II LED layer structure is shown in Figure 6.

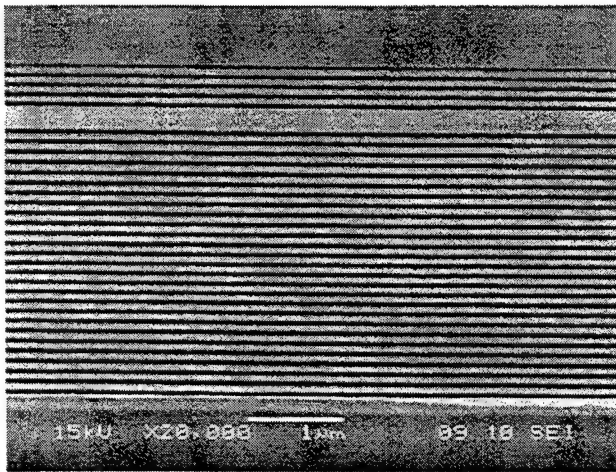


Figure 6: SEM-picture of cross section of structure II, showing both DBR's and the micro cavity in between

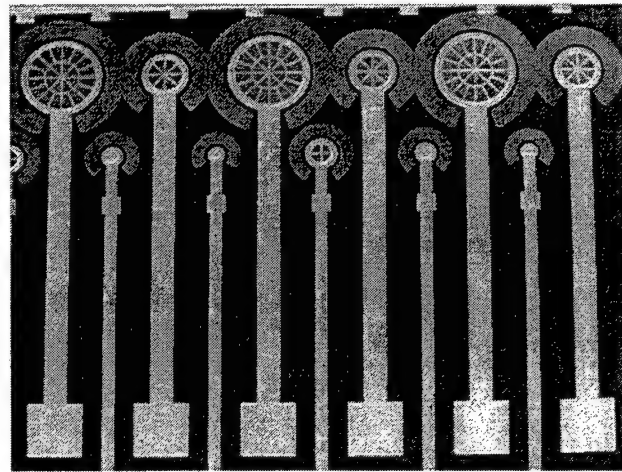


Figure 7: SEM-picture of processed MCLED's with different apertures (largest one is $200\mu\text{m}$)

The devices were processed to circular mesa-type LED's using H_2SO_4 -based chemical etching. This etching was for all three structures carried out completely through all top AlGaAs layers (current spreading and/or DBR) and was stopped on the AlGaInP spacer layer interface. Ti/Au was used as the p-type contact and AuGe/Ni as the back side contact. The top-contact was electroplated with Au to improve serial resistance and overall strength. The LED's had apertures of different sizes, up to $200\mu\text{m}$, with a mesh structure inside the window to improve the current spreading (Figure 7).

3. RESULTS AND DISCUSSION

1. Spectral measurements

In Figure 8a-c we show the optical spectra of the LED's made from the three different structures, all being 200 μ m aperture devices, measured at 20mA current. The spectrum from structure III (Figure 8c) is more or less the spontaneous emission we can expect from a non resonant device, except for some very slight resonance modes originating at the semiconductor/air interface. The measured FWHM is 18nm. For structure I the design was such that the top DBR and the semiconductor/air interface act together as 1 mirror, which explains the narrow spectrum (Figure 8a). The FWHM of the emission peak is only 7nm, a nice illustration of the micro cavity effect. The central wavelength is 652nm, which is very close to the expected 650nm. This illustrates that the calibration procedure prior to the MCLED growth was very accurate.

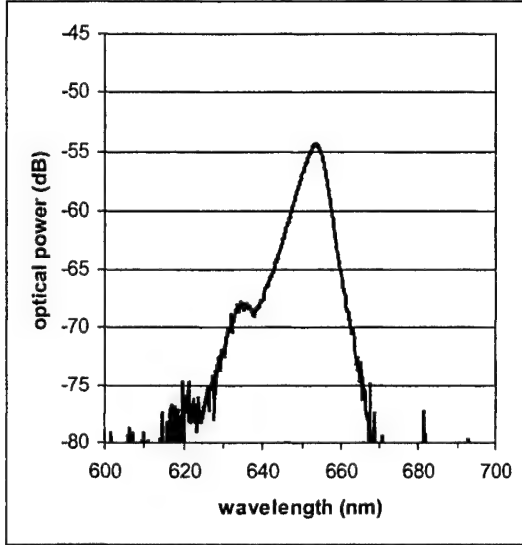


Figure 8a: optical spectrum originating from structure I (i.e. MCLED without current spreading layer)

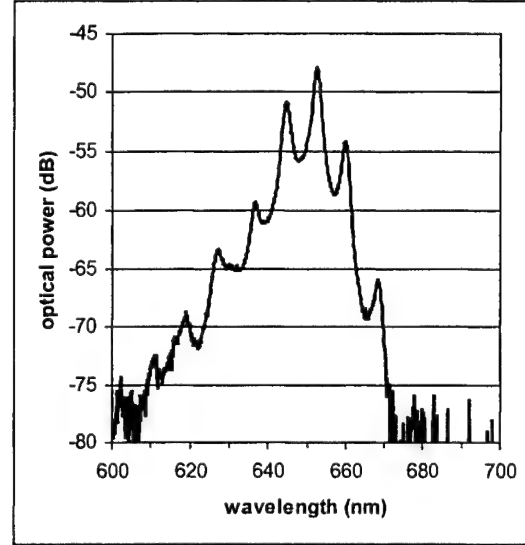


Figure 8b: optical spectrum originating from structure II (i.e. MCLED with current spreading layer)

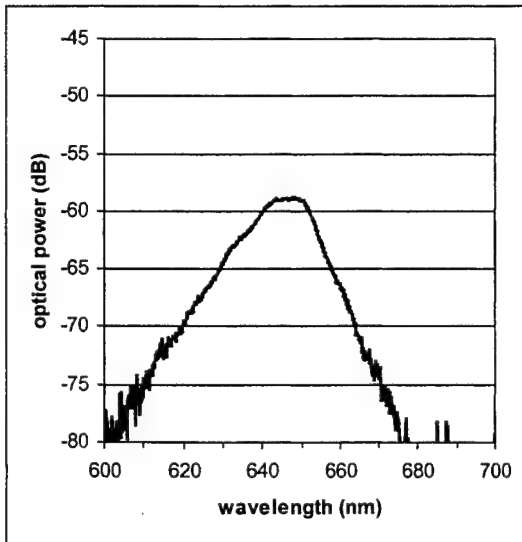


Figure 8c: optical spectrum originating from structure III (i.e. non resonant LED with current spreading layer)

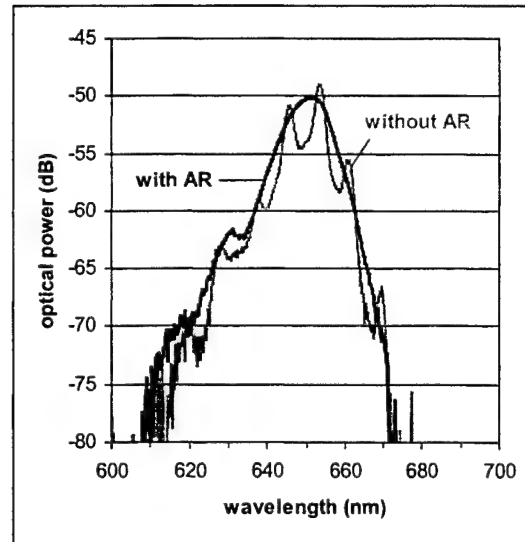


Figure 9: influence of anti reflection coating on optical spectrum of LED with structure II

The optical spectrum of the LED originating from structure II (Figure 8b) shows a lot of different peaks, originating from the parasitic reflection at the semiconductor/air interface (at the top of the current spreading layer). It is however possible to suppress these extra resonance modes, by applying a suitable anti-reflection coating. In Figure 9 we show the influence of a 95nm HfO₂ coating (hafnium oxide). The spectrum does not get as narrow as for structure I, but the 13nm is still narrower than the non resonant LED. There was also a slight improvement on the total optical output.

2. Optical power

All optical power measurements were performed by placing a large area Si-detector (of an optical power meter) as close as possible to the LED (which was contacted by probing needles). Since not all light is captured and a significant part of the light is incident under an angle (and hence reflected), the resulting figures are an underestimate.

In Figure 10 we show the optical power as a function of the current for 200µm aperture devices fabricated from structures I, II and III. In Figure 11 we give the according external quantum efficiencies. Although, from a purely optical point of view, the standard MCLED *without* current spreading layer (structure I) should have higher performance compared to the MCLED *with* current spreading (structure II), it appears to be significantly inferior. This is explained by the poor current spreading in the 5-period DBR, which is only p-doped to about $1 \times 10^{18}/\text{cm}^3$. The best optical output is clearly obtained by the MCLED with current spreading layer, which has an increase in output power of roughly 5 times compared to the reference non resonant LED. The external quantum efficiency reaches 4.35% at 10mA, and a total power of more than 4mW is obtained at 80mA. Please note that all these results are for unpackaged devices.

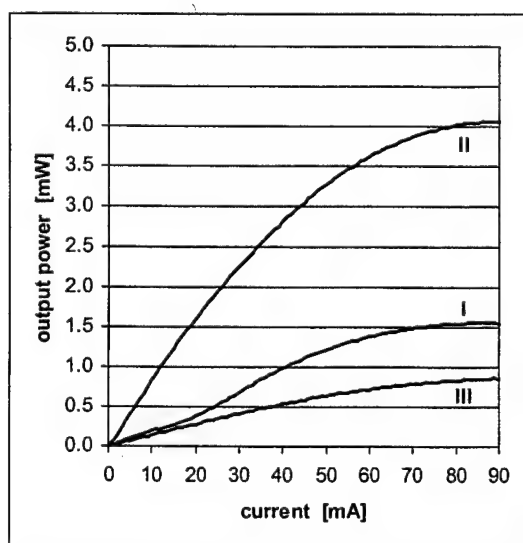


Figure 10: Optical power versus current for the three different LED structures

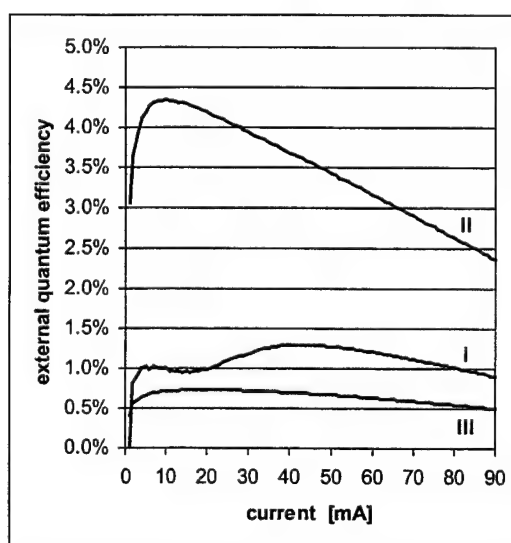


Figure 11: External quantum efficiency versus current for the three different LED structures

As we will indicate in section 4 (electrical behaviour), there is still quite some room for improvement of the devices. Both MCLED devices exhibit a strange behaviour in the low current regimes (mA and sub-mA range): initially the light is very localised at one or more spots within the LED window, which move around with increasing current. In a voltage driven mode the devices emit no light unless a certain (quite high) voltage is applied, which suddenly switches on the LED. This phenomenon is however not observed for the reference LED (structure III).

3. Far field radiation pattern

In Figure 12 we show the radiation pattern for a 200µm aperture LED, based on structure II (i.e. the MCLED structure with a current spreading layer). It is clear that this is a different pattern than what one would expect from a standard LED, but it is what one can expect from a detuned MCLED. The maximum intensity occurs at an angle 36° away from the normal angle and has a FWHM of $\pm 120^\circ$. The luminous intensity in the normal direction was $\pm 55 \text{ mcd}$ (30mA). It should be clear that these figures can be altered by a different tuning of the cavity thickness, which will of course also influence the total emitted power.

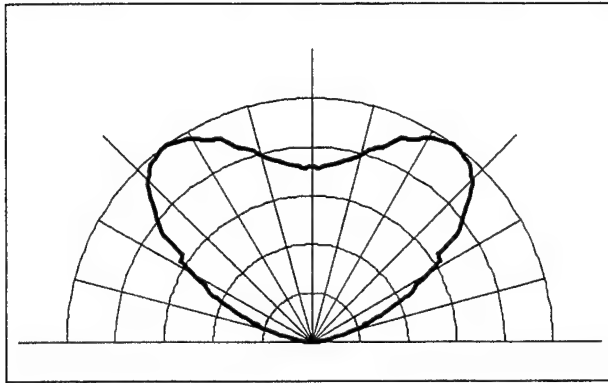


Figure 12: *farfield radiation pattern from unpackaged MCLED origination from structure II*

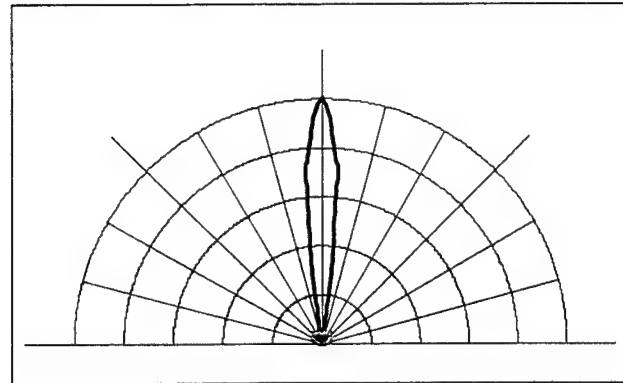


Figure 13: *farfield radiation pattern from 'packaged' MCLED, origination from structure II (hardly visible near the center, we have plotted in grey the pattern from the unpackaged LED in the same scale)*

So far we have concentrated on unpackaged devices. Packaging allows for a better focussing of the light, but more importantly it can give a better index matching (combined with the shaping of the top lens). We don't have any facilities to do professional packing, but we were anyhow able to do some rudimentary experiments. Some LED samples were mounted into a TO-can, and commercially available UV-hardening glue was applied into the can (and on top of the LED) until a certain lensed shape was obtained. The influence of this 'package' was quite remarkable. In Figure 13 we show the radiation pattern of a similar 200 μm aperture LED after this way of packaging. The resulting opening angle reduced to only 13° and the luminous intensity reached $\pm 2.5\text{cd}$ at 30mA. In the same picture also the pattern of the unpackaged LED is shown. It is clear that a well designed package should result in even better figures.

4. Electrical behaviour

Although optically we have some quite good LED's, electrically there appears to be room for improvement. The I-V curve for the optically well performing 200 μm aperture MCLED with current spreading layer, is shown in Figure 14 (a&b). The current was measured for both increasing and decreasing voltage. It appears that there is an important hysteresis effect, or perhaps the word 'thyristor effect' describes the phenomenon better. A certain voltage is necessary to switch the LED on (both current wise and optically), but then the voltage can drop again to lower values, without switching the LED off. Even in the 'best' part of the hysteresis curve the I-V curve is not quite good: more then 4V is necessary to sustain a current of 5mA.

We realise that this electrical behaviour is not acceptable for commercial applications, and we have been digging to find the origin of this phenomenon. Three different problems were identified.

In Figure 14 we also show the I-V for the reference non resonant cavity LED, which does not show the thyristor effect, indicating that a problem is present within the layer structure. It has been found that the interface between the top (Al_{50}Ga)InP layer and the first $\text{Al}_{95}\text{GaAs}$ DBR layer tends to behave as a barrier to the electrical carriers. Apparently the phenomenon can be prevented by changing the composition of one of both layers, e.g. $\text{Al}_{55}\text{GaAs}$ instead of $\text{Al}_{95}\text{GaAs}$ or (Al_{70}Ga)InP instead of (Al_{50}Ga)InP.

The I-V curve for the non resonant LED however indicates that the turn-on voltage, even for this simple structure, is too high (more than 3.5V required to obtain 5mA). Further tests have indicated that both metallic contacts could be improved.

The main problem of the forward voltage is related to the Ti/Au contact on top of our $\text{Al}_{55}\text{GaAs}$ material (covered with 5nm $\text{p}^+\text{-GaAs}$). It appears that this combination results in a schottky like behaviour, leading to high serial resistance and poor current spreading through the mesh. Preliminary tests have indicated that AuZn contacts do exhibit ohmic behaviour and that they would give us a significant reduction in forward bias.

A last, but minor problem is situated at the backside: the AuGe/Ni n-type contact on the germanium substrate was found to become less resistive by adapting the alloying time. Although the contact resistance decreased roughly 2 orders of magnitude to $1\sim 2 \times 10^{-4} \Omega \cdot \text{cm}^2$, it might only have a minor effect on the demonstration LED's, since the whole backside of the sample (few cm^2 area) is metallised.

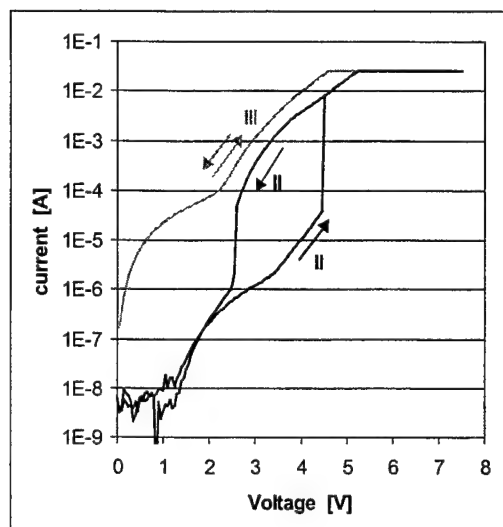


Figure 14a: Illustration of the thyristor like I-V behavior for the LED from structure II (black). In grey we show a more normal behavior for an LED from structure III.

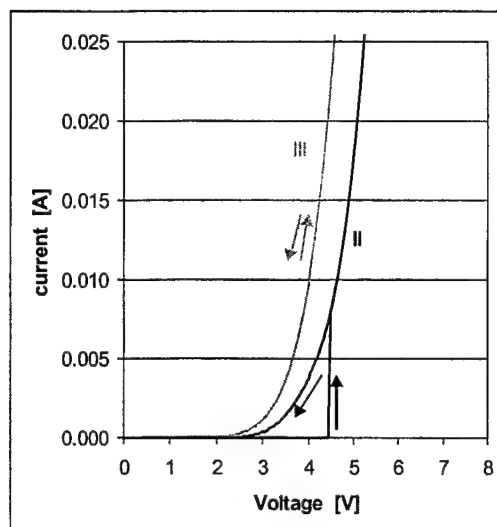


Figure 14b: Linear scale

Based on these findings, a new processing was performed with the improved metallisation scheme. In Figure 15 we show the I-V curves for LEDs processed from structure II (MCLED with current spreading) and III (reference LED). We only show the reverse path for structure II; of course the thyristor effect still exists since it is inherent to the layer structure. We do however notice that the forward voltages have reduced significantly: for a 20mA current we only need 2.7V for structure II and only 2.0V for structure III. This indicates that the growth on germanium as such, is not hindering in obtaining low bias voltages. A next observation is that the differential resistance for both structures is very similar (13.0Ω for III, 13.7Ω for II), indicating that the DBRs in the MCLED do not contribute significantly to the serial resistance. Or in other words this indicates that the difference in turn-on voltage is almost entirely caused by the problem at the layer interface.

As expected, the better electrical behaviour of the contacts also results in an improved optical output, as illustrated in Figure 16 for the MCLED with current spreading layer (II). The main influence of the new contacts is less saturation, resulting in output powers of 3mW at 40mA, and 5mW at 80mA, for unpackaged devices.

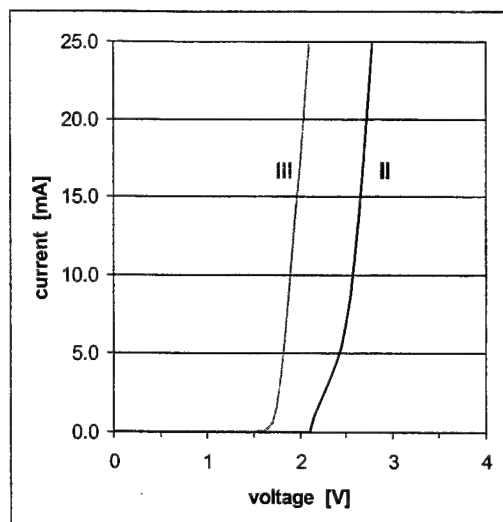


Figure 15: A processing with new contacts results in a much better serial resistance. The thyristor-like behaviour still exists, we only show the reverse curve for structure II.

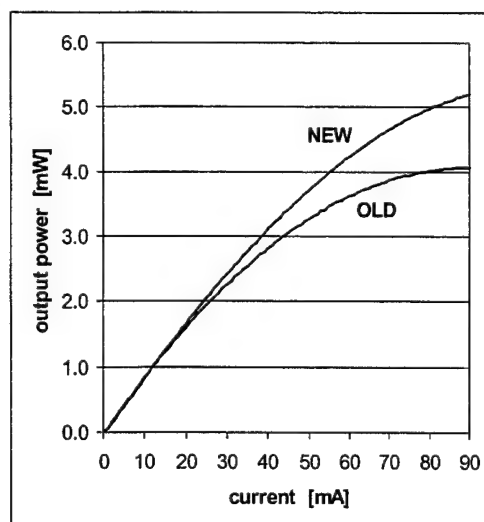


Figure 16: As expected, the new processing also resulted in increased optical power output, illustrated here for the MCLED with current spreading layer (str.II).

4. CONCLUSION

In this paper we have demonstrated that high efficiency red (MC)LED's on germanium substrates are feasible. Micro cavity LED's including a current spreading layer exhibited an external quantum efficiency of 4.35% (at 10mA) and an output power of 3mW at 40mA and 5mW at 80mA, for devices with a 200 μ m aperture. The optical spectrum indicated that the structure was indeed matching to the design specifications, thanks to an accurate calibration procedure prior to the device growth. Parasitic reflections on the semiconductor/air interface are visible in the optical spectrum, but can be eliminated by applying a suitable AR-coating. Also in the far field radiation pattern the micro cavity effect was prominent, with maximum intensity occurring at an angle of 36° from the main axis, and an opening angle of 120°. By applying a rudimentary packaging we could boost the LED performance to a luminous intensity of 2.5cd, with an opening angle of $\pm 13^\circ$. The electrical behaviour of the original devices was initially rather poor, but further tests and a new processing have indicating that LEDs could be fabricated on germanium with a turn-on voltage as low as 2.0V (20mA).

5. ACKNOWLEDGEMENTS

This work was performed with support from the IWT (= Institute for the Promotion of Innovation by Science and Technology in Flanders). We also wish to thank Steven Verstuyft, Kristien Caekebeke, Steven van Put and Luc Vanwassenhove for the device processing, and Charlie Viaene and Joachim Goeminne for assistance in the measurements. Ronny Bockstaele is acknowledged for offering his time in some interesting discussions.

6. REFERENCES

1. P. Mijlemans, I. de Ruijter, "Merits of Germanium as a multi-purpose substrate material", *Compound Semiconductor Outlook 99*, San Diego, 1999
2. F. Steranka, M. Peanasky, "III-V Epitaxial Growth Processes", *Pre-Conference Workshop I of Compound Semiconductor Outlook*, San Diego, March 1, 1999
3. H. Kroemer, "Polar-on-nonpolar epitaxy", *J. Cryst. Growth* v.81, pp.193-204, 1987
4. G. Timo *et al.*, "The effect of the growth rate on the low pressure metalorganic vapour phase epitaxy of GaAs/Ge heterostructures", *J. Cryst. Growth* v.125, pp.440-448, 1992
5. L. Lazzarini *et al.*, "Structural properties of GaAs/Ge heterostructures as a function of growth conditions", *Mat. Sci. & Eng. B28*, pp.502-506, 1994
6. Y. Li *et al.*, "On the formation of antiphase domains in the system of GaAs on Ge", *J. Cryst. Growth* v.163, pp.195-202, 1996
7. Y. Li, L. Giling, "A Closer study on the self-annihilation of antiphase boundaries in GaAs epilayers", *J. Cryst. Growth* v.163, pp.203-211, 1996
8. M. D'Hondt, Z.-Q. Yu, B. Depreter, C. Sys, I. Moerman, P. Demeester and P. Mijlemans, "High quality InGaAs/AlGaAs lasers grown on Ge substrates", *J. Cryst. Growth* v.195, pp. 655-659, 1998
9. M. Behet, J. De Boeck, G. Borghs, P. Mijlemans, "High-performance InAs quantum well Hall sensors on germanium substrates", *Electr. Lett.* v.34, p.2273-2274, 1998
10. M. Behet, J. De Boeck, P. Mijlemans, G. Borghs, "High Performance InAs quantum well based Corbino magneto-resistive sensors on germanium substrates", *Jap. J. Appl. Phys. Part 1.* v.38, pp.1310-1013, 1999
11. H. Benisty, H. De Neve, C. Weisbuch, "Impact of planar microcavity effects on light extraction: I. Basic concepts and analytical trends", *IEEE J. Quantum Electron.* v.34, pp. 1612-1631, 1998
12. M.R. Krames *et al.*, "High-power truncated-inverted-pyramid (Al_xGa_{1-x})_{0.5}In_{0.5}P/GaP light-emitting diodes exhibiting >50% external quantum efficiency", *Appl. Phys. Lett.* v.75, pp.2365-2367, 1999
13. R. Windisch *et al.*, "Non-resonant cavity light-emitting diodes", *SPIE-Photonics West*, paper N° 3938-03, January 22-28, 2000

Long-wavelength shift of ZnSSe metal-semiconductor-metal light emitting diodes with high injection currents

Y. K. Su^a, W. R. Chen¹, S. J. Chang^a, F. S. Juang^b,
W. H. Lan^c, A. C. H. Lin^c, and H. Chang^c

^aDepartment of Electrical Engineering, National Cheng Kung University,
Tainan, Taiwan 70101, R.O.C.

TEL: 0886-2757575 ext 62382, E-mail: yksu@mail.ncku.edu.tw

^bDepartment of Electro-Optics Engineering, National Huwei Institute of
Technology, Huwei, Yunlin 63208, Taiwan, R.O.C.

^cChung Shan Institute of Science and Technology Lung-Tan, Taiwan 325, R.O.C.

ABSTRACT

The reliable n^+ -ZnSSe metal-semiconductor-metal (MSM) blue-green light emitting diodes (LEDs) have been fabricated. The contact metal was CuGe/Pt/Au. The current transport mechanisms agree very well with the back-to-back tunneling diodes. The kink phenomena were observed in the MSM current-voltage curves. In the metal-semiconductor interface, the element Zn in ZnSSe can be replaced by Cu results in some acceptor levels as radiative recombination centers in the MS interface. The peak wavelength in the LED electroluminescent (EL) spectra was strongly dependent on the injection currents from 5 to 40 mA. The peak wavelength and full width at half maximum are 510 and 10 nm, respectively, at 10 mA injection current. When the injection current increases to 15 mA, the peak wavelength shifted to 530nm due to different recombination centers. Further increasing the injection currents, the peak wavelength shifted slightly to the long wavelength side.

Keywords: II-VI, ZnSSe, MSM light emitting diodes.

The wide bandgap ZnSSe compound semiconductor is a promising material for optoelectronic devices. Due to a large bandgap with 2.7eV at room temperature, ZnSSe can emit at blue-green spectrum. Since the first blue-green laser diode has been made in 1991 by 3M Haase et al. [1]. The most difficult problem is the lack of low resistance ohmic contact to p-ZnSe. Over the past years, the optimized contact structure is the ZnSe: N/ZnTe: N superlattice (SL) which is developed by Sony groups [2][3]; this contact was used in a ZnCdSe/ZnSSe/ZnMgSSe single quantum well (SQW) separated confinement heterostructure laser diode (SCH LD) whose lifetime was over 400h [4].

We found the CuGe/Pt/Au contact onto p-ZnSe and p-ZnMgSSe which showed good ohmic contact characteristics, and the specific contact resistance is as low as the order of $10^{-5} \Omega\text{-cm}^2$. In this part we will apply this contact mechanism to n^+ -ZnSSe and attempt to fabricate the metal-semiconductor-metal (MSM) blue-green light-emitting diodes (LEDs). The HP-4156A semiconductor parameter analyzer was used to identify the electrical characteristics, and electroluminescence spectra revealed the optical properties.

The n^+ -ZnSSe with layer thickness about $1\mu\text{m}$ was grown on GaAs (100) substrate by molecular beam epitaxy (MBE) and doped by the ZnCl_2 with donor concentration about 10^{19}cm^{-3} . The schematic diagram of the MSM LEDs is shown in Fig.1. After the surface cleaning, the $200\mu\text{m} \times 80\mu\text{m}$ metal mesa was first defined, and the CuGe/Pt/Au was deposited onto the sample with total thickness about 200nm. Then the pattern with dimension of $220\mu\text{m} \times 120\mu\text{m}$ for etching was transferred into the ZnSSe sample. After etching processes of 60nm depth, the active region appeared. Figure 2 shows the energy band diagram of MSM light emitting diodes at (a) thermal equilibrium, (b) low electric field condition and (c) high electric field condition.

When the CuGe/Pt/Au was deposited onto the n^+ -ZnSSe, the back-to-back metal-semiconductor (MS) tunneling diodes were formed in the semiconductor surface. The element Zn can be replaced by Cu that result in some p-type acceptor levels, i.e. E_{A1} and E_{A2} . This in turn will increase the hole concentration at the MS surface as indicated in Fig.2. It will be noticed that highly doped n^+ -ZnSSe have a degenerated Fermi level near the conduction band. At cathode side with reverse biased condition, the MS contact behaves as a tunneling diode. The electrons that transit from the cathode metal tunnel through the interface (See Fig. 2(c)), so the MS tunneling diode at cathode side behaves linear current-voltage curve that the dominant mechanisms are electrons tunneling. At anode side with forward biased condition, the result is very different. When the applied voltage was small, the electrons will transit from the n^+ -ZnSSe layer to the acceptor vacancy in the anode MS interface. The larger the bias, the higher the conduction band in the n^+ -ZnSSe. When the lowest conduction band in n^+ -ZnSSe layer becomes higher than the energy levels of the acceptor vacancies in the interface, at this time, no acceptor vacancies exist for electrons to reach, so the current decreases. The current-voltage (I-V) characteristic is shown in Fig.3. Since there are multi-acceptor levels in the MS interface, the I-V curve shows several kink phenomena. The tunneling current increases when the Fermi level on the n^+ -ZnSSe can match with the acceptor levels in the MS interface by increasing forward biases. Otherwise, the current will decrease. But at high electric field conditions, the currents increase rapidly. Because the transition mechanisms changed to the thermionic emission process at anode side, and at the same time the reverse bias of the MS contact at cathode side gives rise to large amount of tunneling currents as shown in Fig.2(c). The electrons on the conduction band and the holes on the valence band (or in the acceptor level) will recombine and emit the light at anode side as shown in Fig.2(c).

In order to reduce the threshold current of the MSM light emitting diodes, an extra procedure was added to improve the MSM structure as shown in Fig.1(a). After the mesa etching, the CuGe/Pt/Au was deposited as passivation onto the large area beyond the previously deposited metal region in the MSM structure. The etched mesa structure with the threshold current density less than one order compared to the un-etched sample. The light efficiency will thus increase. Also, the confinement walls were formed between the large area CuGe/Pt/Au and the original metal contacts, as shown in Fig.1(b). In order to identify the I-V characteristic of MS tunnel diode, we replaced the CuGe/Pt/Au on the large area by Ti/Pt/Au, because Ti can form really good ohmic contacts. The I-V curve is shown in the Fig.4. The standard I-V characteristics of tunneling diodes were observed as expected.

When the applied voltage increased over 1.5V, the light emits from the forward-biased junction near anode side. The room temperature continuous-wave electroluminescence (EL) spectra are shown in Fig.5. When 10mA injection current for MSM LED was applied, the peak emission wavelength was 510nm whose corresponding energy is 2.43eV (conduction band to E_{A1}), and the full width at half maximum (FWHM) is 10nm. When the injection current increased to 15mA, the wavelength red shifted to 530nm (i.e. 2.34eV, conduction band to E_{A2}), and when the injection current further increases to be larger than 15mA, the emission spectra further shift to the long wavelength side due to the increasing thermal energy. Also, the FWHM broadened with increasing injection current. These phenomena agree with the prediction of multi-acceptor levels existing in the MS interface as shown in the band diagram of Fig.2 and also agree well with the results from the I-V measurements. At low injection currents (0-10mA), only low acceptor level (E_{A1}) was filled with holes, and the electron-hole recombination with 510nm green light occurred between conduction band and E_{A1} level. At high injection currents (15-40mA), all acceptor

levels, E_{A1} , E_{A2} were filled with holes, and the dominant recombination changed from E_{A1} to E_{A2} or higher levels, then 530-534nm light were emitted.

In this paper, the reliable n^+ -ZnSSe metal-semiconductor-metal blue-green light emitting diodes have been fabricated with very easy techniques and simple structures. Low cost, simple processes and high brightness are possible. The contact metal was CuGe/Pt/Au. The current transport mechanisms agree well with the back-to-back tunneling diodes. Several kink phenomena were observed in the MSM I-V curves. After passivation onto the large area beyond the metal contact region, the threshold current can be reduced. In the metal-semiconductor interface, the element Zn in ZnSSe can be replaced by Cu that results in some acceptor levels as recombination centers, which were studied in detail. One is 2.43eV and the others are 2.32-2.34eV measured from the conduction band to the acceptor levels. The electroluminescent spectra were studied in detail. When the injection current increases from 10 to 15 mA, the peak of the EL spectrum shifted from 510 to 530nm due to different recombination centers, E_{A1} and E_{A2} respectively. Further increasing the injection currents, the peak wavelength showed slightly red-shift phenomena.

Acknowledgement: This work is supported by the National Science Council of ROC under contract number: NSC-88-2215-E-006-005

References

- [1]. M. A. Hasse, J. Qin, J. M. DePuydt, and H. Chang: "Blue-Green Laser-Diodes", Appl. Phys. Lett. 59, 1272 (1991)
- [2]. A. Ishibashi. Y. Mori, J.: "Advances in Blue Laser-Diodes", Crystal Growth 138, pp. 677 (1994)
- [3]. Y. Fan, J. Han, L. He, J. Saraie, R. L. Gunshor, M. Hagerott, H. Jeon, V. Nurmikko, G. C. Hua, N. Otsuka: "Graded band gap ohmic contact to p-ZnSe", Appl. Phys.Lett. 61, pp. 3160 (1992)
- [4]. E. Kato, H. Noguchi, M. Hagai, H. Okuyama, S. Kijima, and A. Ishibashi, "Significant progress in II-VI blue-green laser diode lifetime", Electron. Lett. 34, 282(1998)

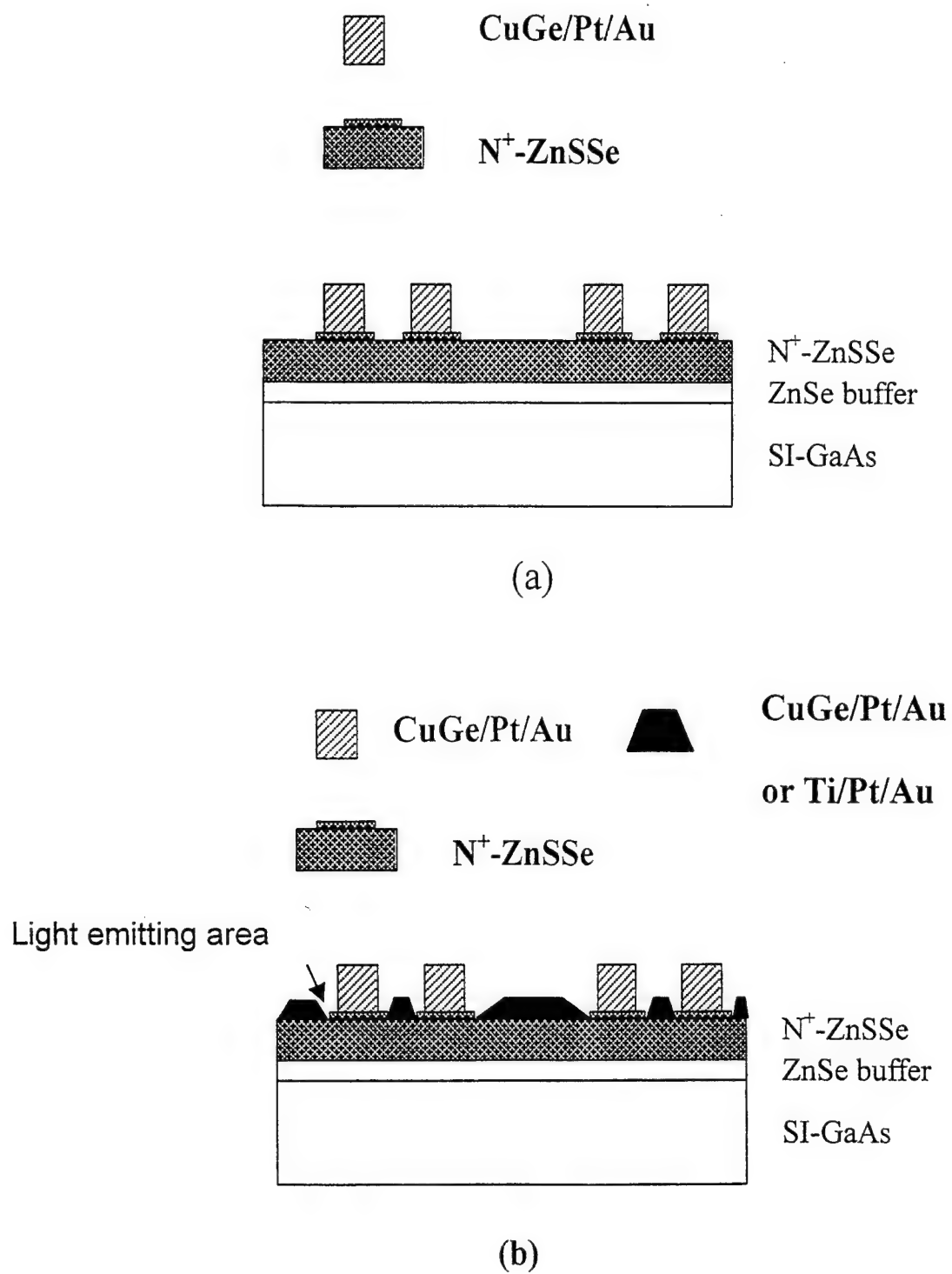
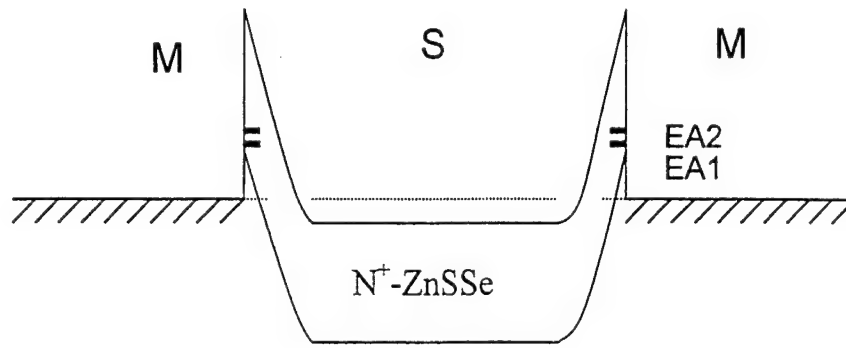
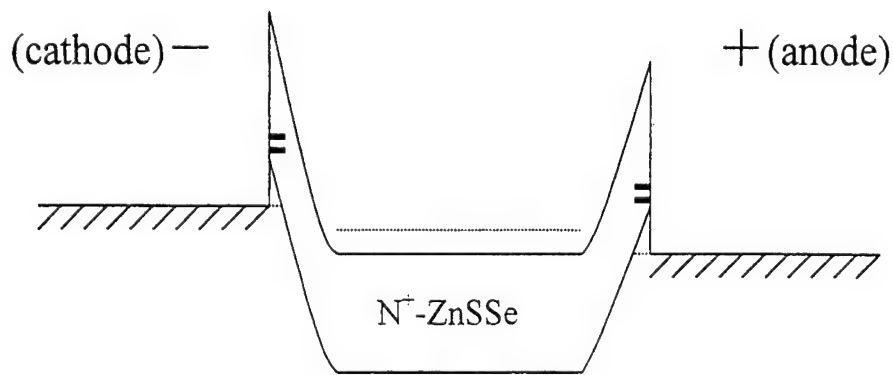


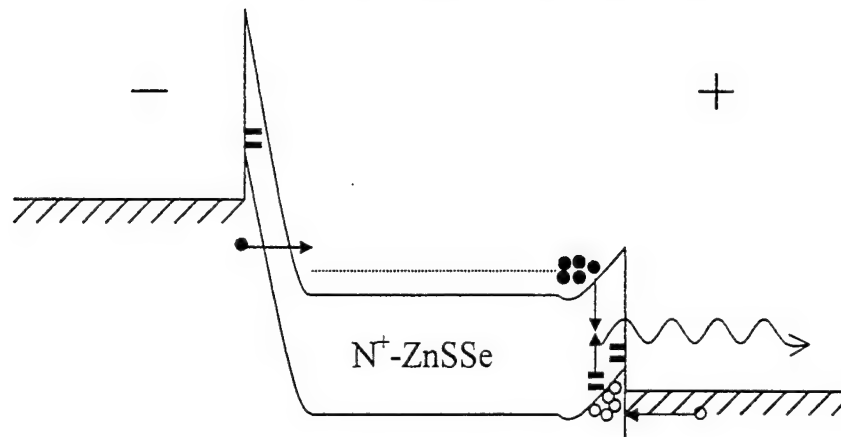
Fig.1 (a) The schematic of the MSM light emitting diode, (b) the structure of the high efficiency MSM LED.



(a) Thermal equilibrium



(b) Low electric field condition



(c) High electric field condition

Fig.2 The energy band diagram of MSM light emitting diode at (a) thermal equilibrium (b) low field (c) high field.

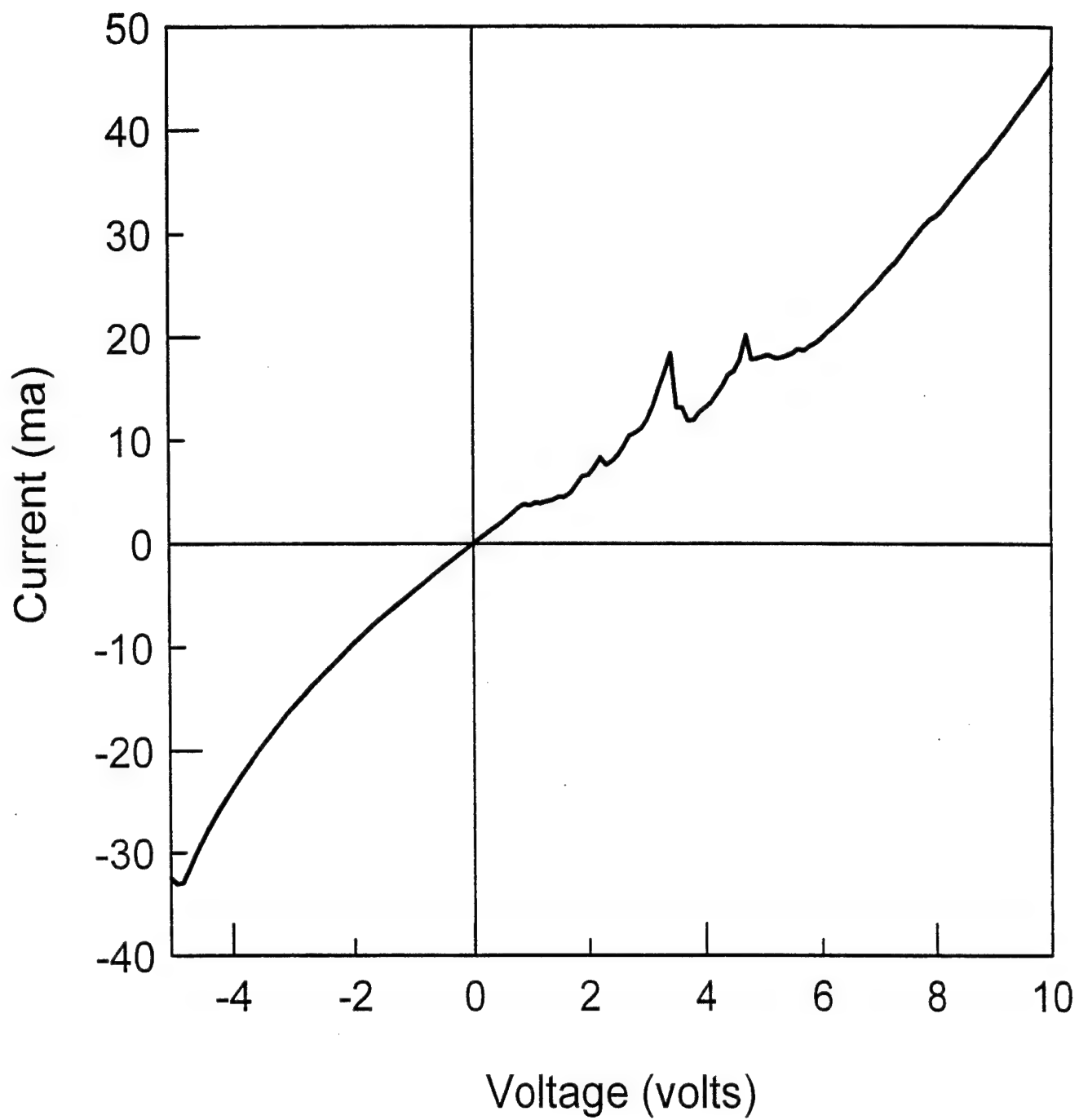


Fig.3 The I-V curve of the MSM light emitting diode.

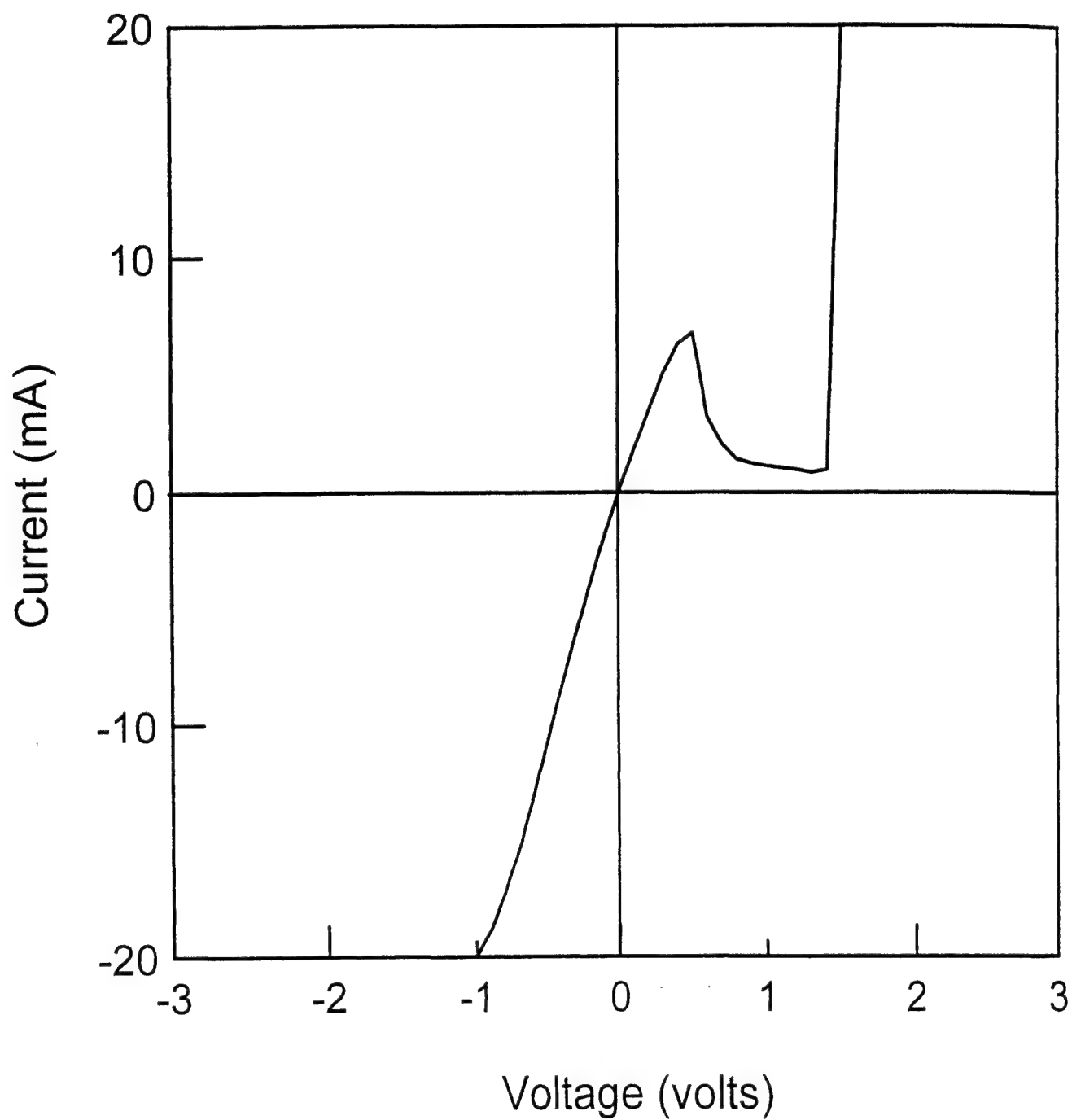


Fig.4 The I-V curve of the CuGe/Pt/Au-ZnSSe-Ti/Pt/Au MS tunneling diode.

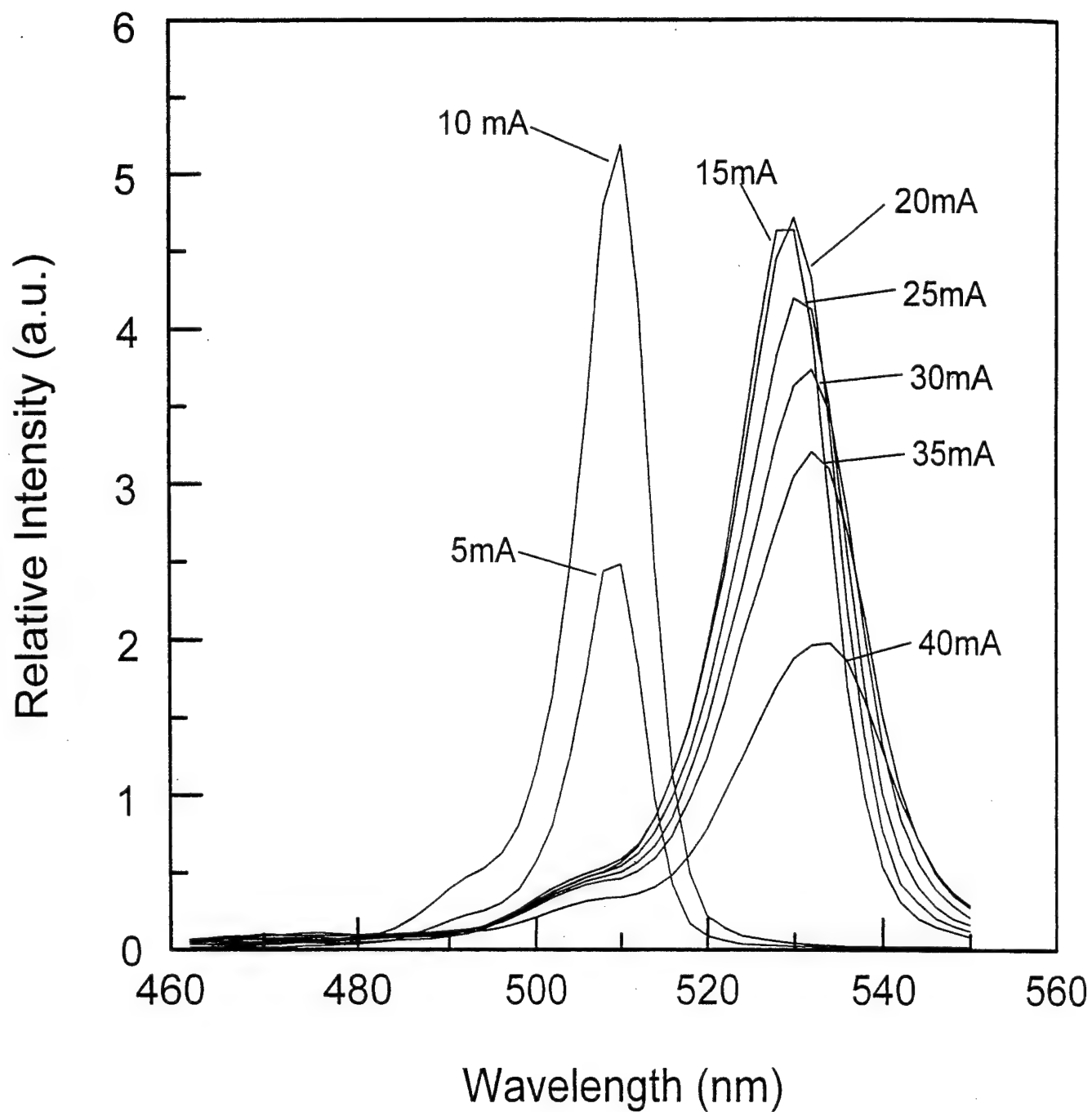


Fig.5 The EL spectra of the MSM light emitting diode under different injection current.

Poster Session

Effects of buffer layer growth conditions on GaN epilayer quality by MOCVD

Fuh-Shyang Juang^{*a}, Yan-Kuin Su^b, Shouu-Jinn Chang^b, T. K. Chu^b, C. S. Chen^b, L. W. Chi^c, K. T. Lam^c

^aDepartment of Electro-Optics Engineering, National Huwei Institute of Technology,
Huwei, Yunlin 632, Taiwan

^bDepartment of Electrical Engineering, National Cheng Kung University,
Tainan 70101, Taiwan

^cDepartment of Automation Engineering, Kao Yuan Institute of Technology and Commercialism,
Lu-Chu Hsiang, Kaohsiung, Taiwan

ABSTRACT

We have found that the electrical and optical properties of GaN epilayers strongly depend on buffer TMGa flow rates and NH₃ flow rates. At low flow rate of 4 sccm, the buffer layer quality was good so the concentrations of undoped GaN epilayers decreased and a stronger band-edge emission of 362 nm can be observed in photoluminescence spectra. The carrier density of the films can be reduced from 10¹⁸ to 10¹⁷ cm⁻³ by increasing the NH₃ flow rate from 0.5 up to 1 SLM and comparatively increased the near-band-edge emission. So, with a NH₃ flow rate as high as 1 SLM, the GaN epilayers with good optical quality can be obtained. The excitation power density of He-Cd laser influences the photoluminescence property of GaN epilayers. At high excitation power density of 637 W/cm², the near-band-edge luminescence (362 nm) is dominant and the deep level luminescence (near 550 nm) appears very weak. But at low excitation power density, the luminescence from defect yellow band levels is stronger than the near-band-edge transitions.

1. INTRODUCTION

Gallium nitride (GaN), a III-V compound semiconductor with direct energy gap near 3.4 eV has attracted a great deal of attention due to its application as a light-emitting device in the blue to violet region [1]. For the fabrication of these optical devices, high quality GaN films are required. It has been difficult to obtain high-quality GaN epilayers on sapphires because of the large lattice mismatch and the large difference in the thermal expansion coefficients between GaN and substrates. Since Akasaki [2] and Nakamura [3] adopted the low-temperature buffer layer technique for growth on mismatched substrates like sapphire, the device quality of GaN grown at a higher temperature has improved tremendously. As a result, high-brightness light emitting diodes [4] and continuous-wave laser diodes [5] have been demonstrated. So, the quality of the buffer layer plays a very important role in growing a good epitaxial GaN film [6]. In present time, GaN and AlN or their combination are mainly used serving as buffer layers [7-9].

2. EXPERIMENTS

GaN films were grown by metalorganic chemical vapor deposition on 1x1 cm² sapphire (0001) substrates with a H₂ carrier gas. Ammonia (NH₃) and trimethylgallium (TMGa) were used as source materials. The growth was conducted in a vertical rotating disk reactor. The group III and group V elements are injected separately into the reactor through a water cooled showerhead to avoid undesired upstream pre-reactions. A tungsten resistance heater is used to raise the temperature of a graphite susceptor up to 1200°C. The rotation speed of the susceptor was 100 rpm. Deposition was performed under low pressure of 100 Torr.

The substrates were degreased in organic solvents (acetone, methanol) and etched in HCl. Before growth the substrates were baked out at 1060°C in a hydrogen atmosphere. After the bake-out the substrate is flushed with NH₃ to nitride the surface. The growth of GaN is performed as a two step process. In the first step a nucleation layer is grown at a low temperature 560 °C. Then the temperature of the substrate is raised to 1100°C with a increasing rate of 150 °C/min. During the raising period the nucleation layer recrystallizes and on this improved nucleation surface the GaN epilayer is deposited. For GaN epilayers the standard flow rates that were applied for carrier, NH₃ and TMGa are 0.5 L/min, 1 L/min and 16 cc/min, respectively. For GaN buffer layers all the flow rates are the same as epilayer, except for those of TMGa varying from 4 to 6 cc/min to obtain good quality GaN epitaxy.

*Correspondence: E-mail: fsjuang@ksmail.seed.net.tw

Several growth conditions were varied to optimize the growth process. GaN films were characterized by Hall measurements to examine the electrical properties. Optical characterization was performed by photoluminescence (PL) measurement, where the 325 nm line of He-Cd laser with 20 mW powers was used to excite the samples. A focus lens with 10 mm focus length was used to adjust the excitation power density of W/cm^2 unit.

3. RESULTS AND DISCUSSIONS

Figure 1 shows the effects of buffer layer TMGa flow rates on the mobility and concentration. At high flow rate of 6 sccm, the buffer layer quality was poor so the concentrations of undoped GaN epilayers increased. The room temperature PL spectra from GaN films grown with different TMGa flow rates for buffer layer growths are shown in Fig.2. At the low flow rate of 4 sccm, a stronger band-edge emission of 362 nm can be observed. These phenomena agree with the results obtained from the concentration measurements.

We examined carrier transport properties of undoped GaN films under different NH_3 flow rates of 0.5 and 1 SLM, respectively. Figure 3 shows the influence of NH_3 flow rates on the epilayer carrier density and mobility. The results indicate that the carrier density of the films can be reduced from 10^{18} to 10^{17}cm^{-3} by increasing the NH_3 flow rate from 0.5 up to 1 SLM. The comparison of room temperature photoluminescence (PL) spectra for GaN films grown with different NH_3 flow rates is shown in Fig.4. For the sample grown with higher NH_3 flow rate of 1 SLM, the near-band-edge emission (362 nm) appears in the PL spectra but comparatively very weak emission for 362 nm bands was obtained in the low NH_3 flow rate of 0.5 SLM. A near band edge emission is clearly observed in the sample with 1 SLM NH_3 flow rate. So, with a NH_3 flow rate as high as 1 SLM, the GaN epilayers with good optical quality can be obtained.

In the range of 5000-6000Å, it shows a yellowish emission peak attributed to the defects such as N vacancies or carbon contamination [10]. The origin of yellow band is believed to be associated with crystal defects. For NH_3 flow rate of 0.5 SLM, yellow band becomes dominant, suggesting the presence of a large amount of crystal defects. There appears a shoulder at around 3690 Å that may be due to the localized defect levels like the N vacancies [11].

Figure 5 shows typical PL spectra of the GaN epilayers excited by He-Cd laser with different power density from 1 to 637 W/cm^2 . It is clearly seen that the near-band-edge luminescence (362 nm) is dominant and deep level luminescence (near 550 nm) very weak at high excitation power density of 637 W/cm^2 . As the excitation power density was decreased, the excitation energy was absorbed more easily by the defect levels than the near-band-edge transitions. As shown in Fig.5, the yellow band luminescence in the range of 5000-6000Å becomes the dominant feature in the PL spectrum at excitation power density as low as 1 W/cm^2 .

Figure 6 shows the excitation power density dependence of the 362 and 550 nm peak intensity of the photoluminescence peaks. The 362 nm peak intensity increases but the 550 nm decreases with increase of the excitation power density. Increasing the excitation power increases the near-band-edge emission and decreases the yellow-band emission. The increase of the 362 nm peak indicates that at high excitation power density the near-band edge transitions are easier to occur. Contrastly, at low excitation power density, it is difficult to excite the near-band edge transitions but the large amount of defect levels are easily photo-excited to emit the luminescence.

4. COCLUSIONS

We have found that the electrical and optical properties of GaN epilayers strongly depend on buffer TMGa flow rates and NH_3 flow rates. At low flow rate of 4 sccm, the buffer layer quality was good so the concentrations of undoped GaN epilayers decreased and a stronger band-edge emission of 362 nm can be observed in photoluminescence spectra. The carrier density of the films can be reduced from 10^{18} to 10^{17}cm^{-3} by increasing the NH_3 flow rate from 0.5 up to 1 SLM. With a NH_3 flow rate as high as 1 SLM, the GaN epilayers with good optical quality can be obtained. It was also found that the excitation power density of He-Cd laser influenced the photoluminescence property of GaN epilayers apparently. Increasing the excitation power increases the near-band-edge emission and decreases the yellow-band emission. Contrast, at low excitation power density it is difficult to excite the near-band edge transitions but the large amount of defect levels are easily photo-excited to emit the luminescence.

ACKNOWLEDGEMENTS

The authors wish to thank Dr. J. K. Sheu for his helpful discussions and Dr. Way Lin for carrying out Hall measurements. This work is supported by National Science Council, Republic of China, under Contract No. NSC89-2215-E-150-002.

REFERENCES

1. B. Shou, X. Li, T. L. Tansley, K. S. A. Butcher, M. R. Phillips, "Growth of GaN films by combined laser and microwave plasma enhanced chemical vapor deposition", *J. Cryst. Growth*, 151, pp.249-253(1995).
2. H. Amano, N. Sawaki, I. Akasaki, *Appl. Phys. Lett.* 48, 353(1986).
3. S. Nakamura, *Jpn. J. Appl. Phys.* 30, L1705(1991).
4. S. Nakamura, M. Senoh, N. Iwasa, S. Nagahama, *Appl. Phys. Lett.* 67, 1868(1995).
5. S. Nakamura, M. Senoh, S. Nagahama, N. Iwasa, T. Yamada, T. Matsushita, Y. Sugimoto, H. Kiyoku, *Appl. Phys. Lett.* 69, 4056(1996).
6. K. G. Fertitta, A. L. Homes, J. G. Neff, F. J. Ciuba, and R. D. Dupuis, *Appl. Phys. Lett.* 65, 1823(1994).
7. M. A. Khan, D. T. Olson, J. M. Van Hove, and J. N. Kuznia, *Appl. Phys. Lett.* 56, 1515(1991).
8. H. Amano, N. Sawaki, I. Akasaki, and Y. Toyada, *Appl. Phys. Lett.* 48, 353(1986).
9. X. Li, D. V. Forbes, S. Q. Gu, D. A. Turnbull, S. G. Bishop, and J. J. Coleman, *J. Electron. Mater.*, 24, 1711(1995).
10. R. Niebuhr, K. Bachem, K. Dombrowski, M. Maier, W. Pletschen, U. Kaufmann, *J. Electron. Mater.* 23(1995)1531.
11. C. Wetzel, S. Fischer, J. Kruger, E. E. Haller, *Appl. Phys. Lett.* 68(1996)2556.

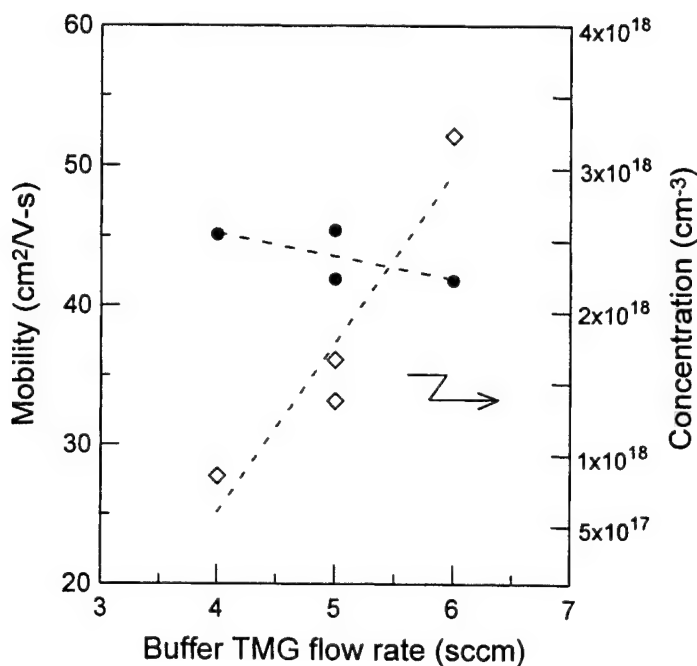


Fig.1 Room temperature mobility and concentration as a function of TMGa flow rates for buffer layer growths.

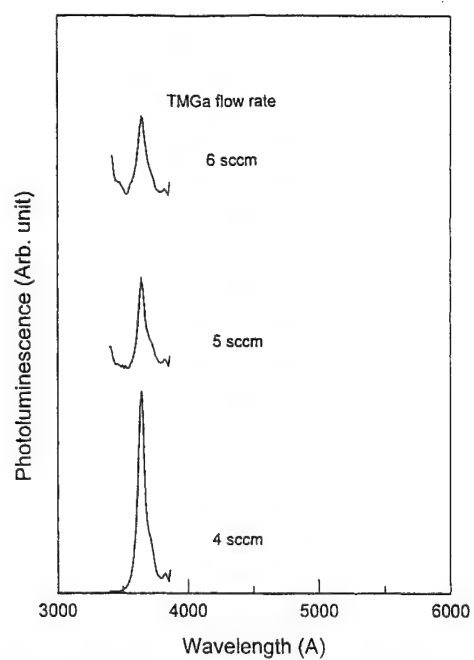


Fig.2 Room temperature photoluminescence spectra for GaN epilayers grown on buffer layers with different TMGa flow rates.

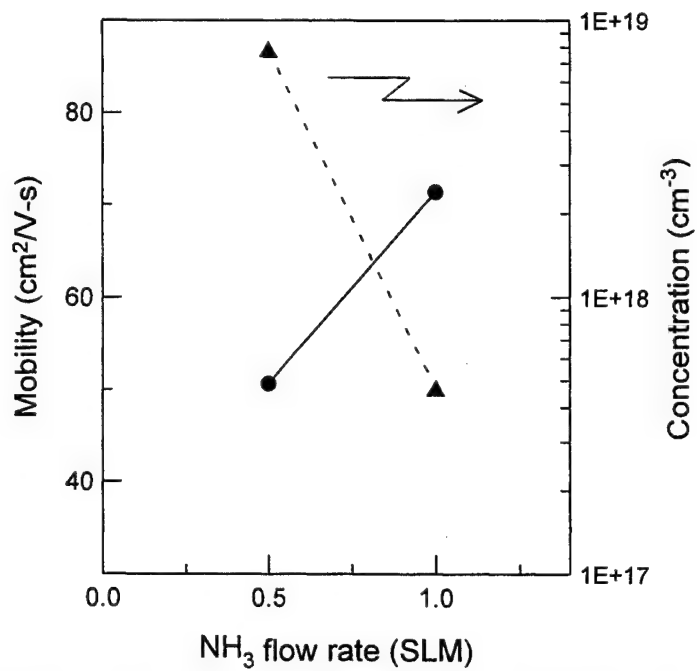


Fig.3 Room temperature mobility and concentration of GaN epilayers as a function of the NH_3 flow rates.

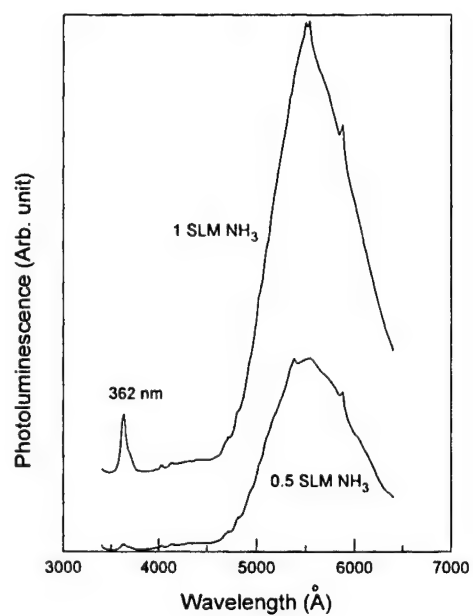


Fig.4 Room temperature photoluminescence spectra for GaN epilayers grown with different NH₃ flow rates.

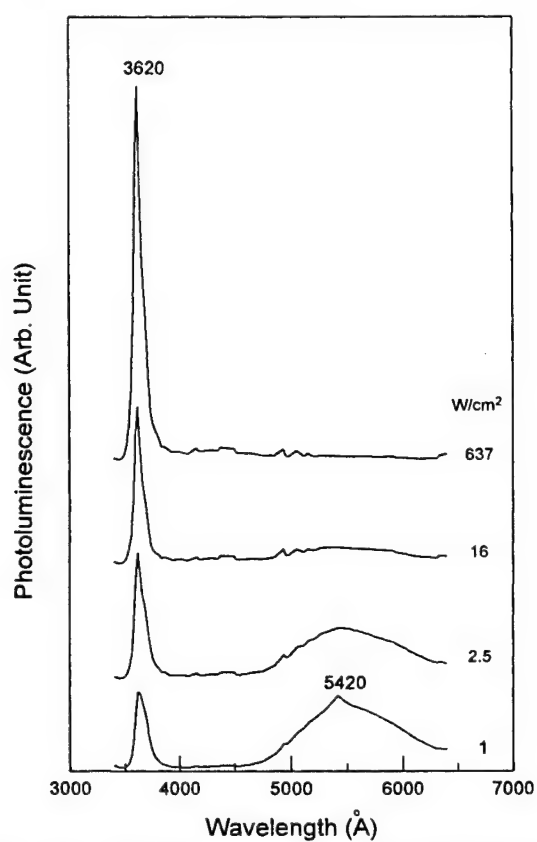


Fig.5 The near-band edge and yellow band photoluminescence spectra of GaN epilayers excited at various power density (W/cm²).

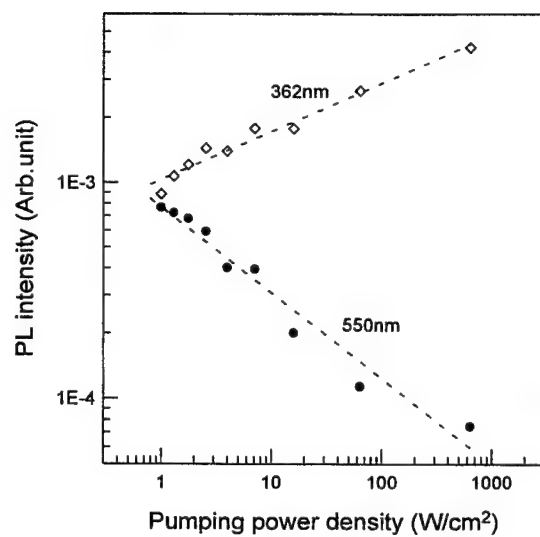


Fig.6 Peak intensity of the near-band edge and yellow band spectra as a function of the excitation power density.

Ohmic Contacts to GaN with Rapid Thermal Annealing

L. W. Chi^a, K. T. Lam^a, Y. K. Kao^a,
F. S. Juang^b, Y. S. Tsai^b,
Y. K. Su^c, S. J. Chang^c, C. C. Chen^c, J. K. Sheu^c

^aDepartment of Automation Engineering, Kao Yuan Institute of Technology

^bDepartment of Electro-optics Engineering, National Huwei Institute of Technology

^cDepartment of Electrical Engineering, National Cheng Kung University/Taiwan

ABSTRACT

This research attempted to use metals with lower work functions, such as Ti, Al, to form ohmic contacts to n-GaN. Then we used metals with higher work functions, such as Ni, Pd, Pt, and Au to form ohmic contacts to p-GaN. The work functions of these metals indeed influence the performance of ohmic contacts, indicating that the Fermi level of GaN is unpinned. The specific contact resistance measured and calculated by TCL model, was $2.35 \times 10^{-3} \Omega \text{cm}^2$ for as-deposited Ti/Al on GaN. After RTA processes at different temperatures in the range of 400~900°C, the minimum ρ_c of $7.4 \times 10^{-5} \Omega \text{cm}^2$ can be obtained for RTA temperature of 600°C. The oxidized Ni/Au contact exhibited the lowest contact resistance of $1.02 \times 10^{-2} \Omega \text{cm}^2$, among Ni/Au, Pd/Au, Pt/Au contact schemes on p-GaN. It was also observed that the I-V curves of the triple-layer contact, Pt/Ni/Au, was near-linear while the others were rectifying even after annealing.

Keyword: Ohmic Contact, GaN, TCL, RTA

1. INTRODUCTION

1.1. Properties and applications of GaN

Gallium nitride (GaN) is a wide bandgap semiconductor in the III-V nitride family with a wurtzite structure being the stable phase at room temperature and pressure, and a zincblende structure which is metastable. The bandgap of the wurtzite form is reported to be 3.4 eV at room temperature, while the bandgap for the zincblende structure has been reported to be 3.2 eV.^[1] Both the wurtzitic and zincblende phases demonstrate direct gap transitions, which is a prime reason that GaN is an excellent candidate for optoelectronic applications.^[2]

GaN also forms a continuous range of alloys with AlN (6.2eV) and InN (1.9eV). Thus, optoelectronic devices with energy bandgap from visible to deep ultraviolet regions are theoretically possible by using group III-nitrides. The wide bandgap of group III-nitrides and their strong atomic bonding force make them possible for the application of high-power and high-temperature devices.

Consequently, a great deal of effort is being expended on synthesis and characterization of these materials, and processes necessary to develop devices based on them.^[3-5] Digital storage may especially benefit from short wavelength coherent sources, lasers, based on III-V nitrides, because the diffraction limited optical storage density can be increased quadratically as the probe laser wavelength is reduced.

GaN has been used to fabricate a number of devices. For example, Khan et al. reported the first GaN based metal semiconductor field effect transistor (MESFET) in 1991.^[6] Because of its large bandgap, GaN has the potential to operate at temperatures above 850K, as compared to the maximum operating temperature for a GaAs device of 350K.^[7] In addition, nitride-based devices may be able to operate in caustic environments.^[7]

GaN-based light emitting diodes (LEDs) are now being produced commercially^[8] with efficiencies and brightness greater than competing SiC and ZnSe based devices. In addition, Nakamura et al.^[9] have announced the successful fabrication of an electrically injected diode laser from a GaN-based structure. These diode lasers are expected to have longer lifetimes than ZnSe-based diode lasers because of the higher resistance to defect degeneration.^[10] LEDs and diode lasers are possible in the GaN-based system since GaN forms a continuous direct gap alloy with AlN and InN, allowing the use of bandgap engineering to create quantum well and other heterostructures which are critical for high performance diode lasers.^[11]

*Correspondence: Email: lwji@ms41.hinet.net; Telephone: 886-939 746 692

1.2. Ohmic Contacts to GaN

The wide-bandgap GaN and related materials have been extensively investigated in recent years, due to their exciting applications in visible and ultraviolet (UV) lasers and light-emitting diodes (LEDs) for display and data storage, field-effect transistors (FETs) for high-temperature and high-power electronics, and solar-blind UV detectors.^[13] These exciting applications present numerous challenges in making high-performance metal contacts to GaN-based materials, which is crucial for device performances. In general, making low-resistance ohmic contact is difficult for wide bandgap semiconductors, especially for p-type GaN due to the difficulty in doping. This difficulty has been one of the major obstacles in fabricating efficient nitride lasers and LEDs, and it is yet to be overcome completely. Furthermore, conventional metallization schemes may not have the adequate thermal stability when devices operate at high power and high temperatures.

It is often said that due to the substantial ionic component of the bonds in III-V nitrides the Fermi level at the nitride surface and at the metal-nitride interface should be unpinned; the barrier height should consequently depend on the work function or the electronegativity of the contacting metal.^[13] Schottky barrier heights of a variety of elemental metals including Au, Ti, Pt, Pd, Ni and Cr have been reported.^[14-16] We note that the Schottky barrier height, ϕ_B (on n-GaN), indeed varies with the metal work function within experimental scattering. The strategy to form ohmic contacts on n-GaN is to use a metal with a small work function such as Ti; and to use a metal with a large work function such as Pt to form Schottky barriers on n-GaN. In the following we will discuss several aspects of the metal-GaN contact technology.

2. Theory and Measurement of Ohmic Contact

2.1. Schottky Barrier Formation

The work function Φ_m of a metal is the amount of energy required to raise an electron from the Fermi level to a state of rest outside the surface of the metal (the so-called vacuum level). Any modification in the surface electron charge distribution, for example by absorption of gas atoms on a clean metal surface, will lead to a change in the dipole layer and hence in Φ_m .

The height of the barrier Φ_b measured relative to the Fermi level is given by $\Phi_b = \Phi_m - \chi_s$. In most practical metal-semiconductor contacts, the ideal situation is never reached because there is usually a thin insulating layer of oxide, about 10–20Å thick, on the surface of the semiconductor. But this equation is still a very good approximation. In obtaining it, a number of important assumptions have been made, namely that the surface dipole contributions to Φ_m and χ_s do not change when the metal and semiconductor are brought into contact (or, at least, that the difference between them does not change), that there are no localized states on the surface of the semiconductor, and that there is perfect contact between the semiconductor and metal, i.e., no intervening layer.

According to Schottky-Mott theory, an ohmic contact can be produced between a metal and a semiconductor if the work function of the metal is less than that of the semiconductor.^[17] However, Fermi level pinning at the semiconductor surface can lead to a contact barrier height which is insensitive to the metal work function as described by Bardeen.^[17] For a large number of important semiconductor, Si and GaAs included, the dependence of barrier height on work function difference has not been observed, a result attributed to the existence of surface states which pin the Fermi level at the interface.^[18]

To predict the barrier of metal-semiconductor contacts, Kurtin et al.^[19] have related the contact properties of different metals on semiconductor surface to a basis on the type of bonding in the semiconductor. The former were reported to be susceptible to surface Fermi level pinning and insensitive to work function difference between the metal and the semiconductor; however, the latter did not suffer from this Fermi level pinning phenomenon.

The electronegativity difference for GaN is 1.87eV.^[20] This puts GaN above the knee of the curve implying that the properties of metal-GaN contact can be predicted base on Schottky-Mott theory. The work function of GaN has been measured to be 4.1eV.^[21] Therefore, any metal with a work function equal to or lower than that of GaN should form essentially ohmic contacts to n-type GaN and any metal with a work function higher should form rectifying contacts to n-type GaN.

One could expect that metals with small work function such as Al, Ti, In, Ta, and Cr are the good choices for the formation of ohmic contacts to n-GaN, and metals with large work function for example: Pt, Au, Pd and Ni are suitable for high Schottky barrier formation to n-GaN.

2.2. Transmission Line Model (TLM)

For the determination of specific contact resistance of ohmic contact systems in semiconductor devices, test patterns of either rectangular or circular geometry are commonly used. By forcing a constant current through the adjacent pairs of

rectangular contact pads, with different spacings, d , the voltage drop ΔV across the same pads can be plotted versus d , and this would result in a straight line with slope proportional to the semiconductor sheet resistance (R_s) and an intercept $2L_T$ to the negative d -axis, where L_T is the transfer length. The potential distribution $V(x)$ under the pad, for the rectangular geometry, obtained from the transmission line model (TLM) can be expressed in the manner, ^[22]

$$V(x) = \frac{i_0 R_s L_T}{Z} \left[\frac{\cosh(X/L_T)}{\sinh(W/L_T)} \right] \quad (1)$$

Where L_T is the transfer length or inverse of attenuation constant given by

$$L_T = \sqrt{\frac{R_c}{R_s}} \quad (2)$$

When $W \gg L_T$, the voltage drop under one of the contact pads becomes,

$$V(W) = \frac{i_0 R_s L_T}{Z} \quad (3)$$

As the voltage ΔV drop is measured across both pads it can be written as,

$$\Delta V = i_0 R_s \left[\frac{d}{Z} + \frac{2L_T}{Z} \right] \quad (4)$$

In the rectangular contacts, the current flow at the contact edge can significantly affect the results of contact resistance measurement unless mesa structures are fabricated in order to eliminate the unwanted current flow patterns. In circular test patterns this complication can be totally avoided without making mesa structures. However, errors can occur due to finite radius of the contact patterns as may be seen from the following equation^[23] for the voltage drop across the separation d :

$$\Delta V = \frac{i_0 R_s}{2\pi} \left[\ln\left(\frac{r_1}{r_0}\right) + \frac{L_T}{r_0} \frac{I_0(r_0/L_T)}{I_1(r_0/L_T)} + \frac{L_T}{r_1} \frac{K_0(r_1/L_T)}{K_1(r_1/L_T)} \right] \quad (5)$$

where I_0 , I_1 and K_0 and K_1 are the modified Bessel Functions and r_0 and r_1 are the radius that define the separation d . when r_0 and r_1 are greater than L_T at least by a factor of 4, then both I_0/I_1 and K_0/K_1 approximate to unity. ^[24] Thus, equation (5) becomes

$$\Delta V = \frac{i_0 R_s}{2\pi} \left[\ln\left(\frac{r_1}{r_1 - d}\right) + L_T \left(\frac{1}{r_1} + \frac{1}{r_1 - d} \right) \right] \quad (6)$$

Note that if $r_1 \gg d$ the above reduces to equation (4) with $2\pi r_1 = Z$.

3.Results and Discussion

As for ohmic contacts to n-GaN, Ti- or Al-based metallization schemes (e.g., Al, Ti, Ti/Al, Ti/Au, Ti/Al/Ni/Au, and Pd/Al) have been widely investigated. In such metallization schemes, low contact resistances ranging from $\sim 10^{-5}$ to $\sim 10^{-8} \Omega\text{cm}^2$ have been reported, and these resistance values are good enough for the operation of the optical and electronic devices.^[25-27] For the ohmic contacts to p-GaN, however, there are two main obstacles making it difficult to develop devices with good quality ohmic contacts on p-type GaN. The first arises from a difficulty in growing a heavily doped p-GaN ($>10^{18}\text{cm}^{-3}$). The second results from the absence of appropriate metals having work functions larger than that of p-type GaN ($\sim 7.5\text{eV}$). These problems have led to contact resistances of $\geq 10^{-2} \Omega\text{cm}^2$. Trexler et al.^[28] investigated Ni/Au, Cr/Au, and Pd/Au metallization schemes for P-GaN ($9.8 \times 10^{16}\text{cm}^{-3}$) ohmic contacts and showed that only the Cr/Au contact was ohmic with a specific contact resistance of $4.1 \times 10^{-1} \Omega\text{cm}^2$, when the sample was annealed at 900°C for 15s. Jang et al.^[29] investigated ohmic contacts on p-GaN by using a Ni/Pt/Au metallization scheme and the results showed that the metal contact was ohmic with a contact resistance of $2.1 \times 10^{-2} \Omega\text{cm}^2$, when the sample was annealed at 500°C for 30s in a flowing Ar atmosphere. Mori et al.^[30] investigated electrical properties of ohmic contacts on p-GaN using Pt, Ni, Au, and Ti single layers, and they reported a specific contact resistance of $1.3 \times 10^{-2} \Omega\text{cm}^2$ for the as-deposited Pt/p-GaN contacts. Formation of low resistance ohmic contacts to p-GaN is complicated due to the nature of the semiconductor. In general there are two methods of forming an ohmic contact to a p-type semiconductor. The semiconductor can be degenerately doped to decrease the depletion distance and allow tunneling to occur or a large work function metal can be used to decrease the potential offset at the metal/semiconductor interface. In GaN the Fermi level is believed to be unpinned leading to the potential barrier being work function dependent. However, in p-GaN neither of these methods is presently viable. GaN tends to auto-dope n-type and has only been reliably doped to the mid 10^{18}cm^{-3} p-type with Mg. This is due to the problems with activation of the deep Mg acceptor and the formation of H-Mg complexes which decrease the number of active carriers.

Concerning the second approach, GaN, with a band gap of $E_g = 3.4$ eV and an electron affinity of $\chi = 4.1$ eV, requires a metal with a work function of ~ 7.5 eV to provide zero offset at the interface. Unfortunately, metal work functions are never much larger than $5\text{ eV}^{[31]}$ so there will still be a noticeable energy barrier to conduction.

The contact schemes investigated here were chosen on the basis of their large work functions and their ability to react with GaN to provide the opportunity for doping of the near surface region which would increase the probability for tunneling to occur. The work functions are Au:5.1eV, Ni:5.15eV, Pd:5.12eV, and Pt:5.65eV. All metals were deposited on MOCVD grown GaN doped p-type with Mg acceptors to a carrier concentration of $2 \times 10^{17} \text{ cm}^{-3}$. The thin film metallizations were deposited in an electron beam evaporator with a base pressure under 3×10^{-6} Torr for all depositions. Before insertion into the vacuum chamber, the samples were degreased in HCl: DI water (1:1) solution for 3 minutes to remove possible native oxide. After metal deposition, the circular transmission line model (c-TLM) patterns were defined by metal wet etching. It is due to the difficulty to define these patterns by conventional lift-off process. Auger electron spectroscopy (AES) depth profiles were used to study the interfacial reactions between the contact metals and the p-GaN. The electrical properties were studied on as-deposited and annealed samples using room temperature current-voltage (I-V) measurements by HP4156 semiconductor parameter analyzer.

3.1. Ti/Al Ohmic Contact to N-type GaN

In this study, the GaN film was grown on c-face sapphire substrate by metalorganic vapor phase epitaxy (MOVPE). Trimethylgallium (TMGa) and ammonia (NH_3) were used as the sources for Ga and N, respectively. Si_2H_6 was employed as the n-dopant. The GaN films were grown at 1050°C . The Si-doped GaN epitaxial layer was $2.5\mu\text{m}$ thick. Hall measurement revealed that the film has a bulk carrier concentration of around $7 \times 10^{17} \text{ cm}^{-3}$ and a mobility of about $250 \text{ cm}^2/\text{V}\cdot\text{s}$.

Before loading the GaN samples into the evaporation chamber, they were treated in TCA, acetone (ACE) and methanol (CH_3OH) by ultrasonic vibration for 5 minutes, respectively. Then they were dipped in HCl : H_2O (1 : 1) solution for 30 seconds, rinsed in de-ionized water, blown dry with nitrogen, and immediately transferred into the evaporator for metallization. The Ti/Al (250Å/1000Å) metal layer were deposited sequentially by electron beam evaporation under a base pressure of $\sim 3 \times 10^{-6}$ Torr.

A lift-off process was employed to define circular structures for measuring specific contact resistance by the transmission line model (TLM) method. Circular contacts with a ring-shaped gap between them were formed using contact lithography. The circular contact design avoids the need to isolate the metallization structures by implantation or etching. This contact method is especially useful for GaN because it is relatively difficult to use pattern-requiring plasma processing to achieve significant etch rates. The outer circular contact had a constant radius of $200\mu\text{m}$ and gaps between inner and outer contacts are 5, 10, 15, 25, 35, $45\mu\text{m}$, respectively. After lift-off, the samples were annealed by rapid thermal annealing (RTA) in nitrogen atmosphere.

The current-voltage characteristics of as-deposited Ti/Al contacts on n-GaN are shown in Figure 1. Samples annealed at 600°C and 900°C for 30 seconds were also compared as shown. The as-deposited Ti/Al was observed to be slightly rectifying, while the annealed samples exhibits ohmic behavior. Besides, we found the contact resistance of 600°C -annealed sample was smaller than that of 900°C -annealed sample. It might be attributed to oxidation of Ti/Al contact at this higher temperature. The similar results were observed at different annealing temperatures.

Figure 2 shows the specific contact resistances of Ti/Al contact scheme as a function of rapid thermal annealing temperature. The annealing time was 30 seconds. The specific contact resistances were $2.35 \times 10^{-3} \Omega\text{cm}^2$ for as-deposited Ti/Al, and found to decrease as annealing temperature increased until a minimum ρ_c , $7.4 \times 10^{-5} \Omega\text{cm}^2$, was obtained at 600°C . Further increases in the annealing temperature degraded Ti/Al metallization as shown.

The low specific contact resistance of Ti/Al bilayer metallization was believed due to the formation of a highly n-type doped GaN layer and a thin TiN interfacial layer from the reactions between Ti and GaN. It was estimated that only two monolayers of TiN are needed to form in order to generate a 100\AA layer of GaN with an electron density of 10^{20} cm^{-3} .^[32] This highly doped GaN interfacial layer shall facilitate current tunneling through the barrier, and the TiN interfacial layer may also lower the effective barrier height, facilitating current conduction through the junction.

Figure 3 shows the current-voltage-temperature characteristics of Ti/Al (250Å/1000Å) contact annealed at 600°C for 30 seconds. It is clear to find that the I-V characteristics were almost the same as temperature varied from 150K to 450K. Thus, the current conducting mechanism in this study is assumed to be dominated by tunneling due to highly doped surface at metal-GaN interface as mentioned above.

3.2. Ohmic Contact to P-type GaN

Ni/Au

Figure 4 shows the I-V characteristics of Ni/Au (400Å/500Å) contact scheme annealed at different atmosphere, nitrogen and air. It can be observed that the as-deposited Ni/Au contact exhibits very rectifying behavior in the -10V~10V range while the annealed samples exhibit more ohmic. It is also observed that the Ni/Au contact annealed in air behaved more linearly than that annealed in nitrogen. The same results were obtained when air is replaced by pure oxygen. The lowest specific contact resistance is $1.02 \times 10^{-2} \Omega \text{cm}^2$ when the contact was annealed in air for 10 minutes.

To observe the AES depth profile of as-deposited and annealed Ni/Au (300Å/200Å) contact, we found, before the annealing, no inter-diffusion was observed and clear interfaces between Au, Ni, and GaN could be seen. However, for the sample annealed at 500 °C in air, there is a large scale diffusion of Ni through the Au capping layer to the surface of the contact where it was oxidized. Jin-Kuo Ho and co-workers^[33] speculated the improvement of oxidized Ni/Au contact is related to the formation of NiO. NiO was reported to behave as a p-type semiconductor with nickel vacancies and/or oxygen interstitials, and possibly with the incorporation of monovalent atoms, e.g. lithium.^[34] Sato et al.^[35] found that the hole concentration of NiO films prepared by sputtering deposition can be as high as $1.3 \times 10^{19} \text{cm}^{-3}$ which is about one to two orders higher than that of common p-type GaN films. The high carrier concentration of NiO makes a metal easy to achieve an ohmic contact on it. Ho assumed the actual contact of oxidized Ni/Au contact may regard as a Au/p-NiO/p-GaN conjunction. However, in our study it can be seen that the NiO film was almost formed at the top of Au film, which was close to p-GaN. Only a few amounts of Ni and oxygen can be observed at the Au-GaN interface. Some further studies, such as the analysis of high resolution transmission electron microscopy (TEM) and high resolution and high power x-ray diffraction in grazing incident angle configuration, will be conducted to understand the interfacial reaction. These interfacial chemical products can substantially influence the electrical properties of the contacts.

Although, Foresi and Moustakas^[36] observed that metal contacts on GaN should have barrier heights which depend directly on the difference of the work function between the metal and GaN. However, as generally known, chemical reactions between the metal and the semiconductor can substantially influence the electrical properties of metal-semiconductor contact. In a practical metal/semiconductor system with Fermi level pinning, the Schottky barrier height is empirically expressed as $\phi_{bn} = S\phi_m + C$, where S is a slope parameter and C is a constant. In other words, the formation of the interfacial compounds near the metal/GaN interface during thermal alloying can possibly lead to a decrease of the S parameter, and thereby influence the barrier height.

Temperature dependent I-V measurement was performed on a Ni/Au sample annealed at 700°C for 10 minutes in air. As shown in Figure 5, the current increased substantially with an increase in measurement temperature. As a result, the conducting mechanism should be dominated by thermionic emission.

Pd/Au

Figure 6 shows the I-V curves of Pd/Au (500Å/1000Å) on p-GaN. As-deposited sample exhibited very rectifying character while the sample which was annealed at 800°C for 3 minutes by rapid thermal annealing (RTA) in nitrogen was significantly improved but still remained slightly rectifying. As compared to Ni/Au contact scheme, it could be observed that Ni/Au still behaved more linearly than Pd/Au.

According to the AES depth profiles of as-deposited and annealed Pd/Au samples, the reactions were very different than those of Ni/Au contact. For as-deposited sample, no inter-diffusion was observed. However, when Pd/Au contact annealed at 600 °C for 30 minutes, Pd diffused into the Au capping layer, but not through it like Ni. The amount of Pd also found to be consumed significantly after annealing. As the annealing temperature went up to 800°C, there was evidence of dissociation of GaN. Nitrogen out-diffusion leaving the surface N vacancies which act as shallow donors could explain the increase of contact resistance.

Pt/Au and Pt/Ni/Au

It was expected that the Pt/Au showed the lowest contact resistance since the work function of Pt (5.65 eV) is higher than those of Ni (5.15 eV) and Pd (5.12 eV). Contrary to the expectation, the Pd/Au contacts exhibited the lowest resistance among the three kinds of as-deposited contact schemes, as shown in Figure 7. We attribute the lowest contact resistance of the Pd/Au to the fact that the Pd could act as an acceptor in GaN and this phenomenon causes the near interface region to be highly doped.^[37]

The I-V curve of triple layers Pt/Ni/Au contact is also shown in Figure 7. From previous studies, we found the oxidized Ni/Au contacts exhibited the lowest contact resistance comparing to others. Rectifying behavior was also observed near the origin of the I-V curve, indicating that noticeable barrier height existed between metal-GaN interface, so we use the higher work function metal, Pt, as the interlayer between Ni/Au and GaN. The reduction of barrier height was indeed obtained by using Pt/Ni/Au triple-layer contact. Figure 8 shows the I-V curves of as-deposited and annealed Pt/Ni/Au contacts. After RTA annealing at 900°C for 3 minutes, the I-V characteristics were significantly improved and exhibited near-linear behavior, indicating the reduction of barrier height comparing to Ni/Au. However, it should be noted that the

oxidized Pt/Ni/Au became very poor while the oxidized Ni/Au improved its characteristics.

Figure 9 shows the best results of the Ni/Au, Pd/Au, Pt/Au, Pt/Ni/Au contacts studied in this thesis. It could be found that only Pt/Ni/Au contact was near-linear while the others were still rectifying.

4. Conclusion

This study used metals with lower work function, Ti/Al, to form ohmic contact to n-GaN. The specific contact resistance was $2.35 \times 10^{-3} \Omega \text{cm}^2$ for as-deposited Ti/Al, and found to decrease as annealing temperature increased until a minimum ρ_c , $7.4 \times 10^{-5} \Omega \text{cm}^2$, was obtained at 600°C for 30 seconds in RTA. Then we used metals with higher work function, such as Ni, Pd, Pt, and Au to form ohmic contacts to p-GaN, and found that the oxidized Ni/Au contact exhibited the lowest contact resistance, $1.02 \times 10^{-2} \Omega \text{cm}^2$, among Ni/Au, Pd/Au, Pt/Au contact schemes studied here. We also observed that the I-V curves of the triple-layer contact, Pt/Ni/Au, was near-linear while the others were rectifying even after annealing.

References

1. R.F. Davis, *Proc. IEEE* **5**, p.702, New York, 1991.
2. T. Lei, K.F. Ludwig and T.D. Moustakis, *J. Appl. Phys.* **74**, p.4430, 1993.
3. H. Morkoc, S. Strite, G.B. Gao, M.E. Lin, B. Sverdlov and M. Burns, *J. Appl. Phys. Rev.* **76**, p.1363, 1994.
4. S.N. Mohammad, A. Salvador and H. Morkoc, *Proc. IEEE* **83**, p.1306, 1995.
5. S.N. Mohammad and H. Morkoc, *Prog. Quantum Electron.*, in press.
6. M. Asif Khan, J.N. Kuznia, A.R. Bhattarai and K.T. Olson, *Appl. Phys. Lett.* **62**, p.1786, 1993.
7. E.D. Jungbluth, *Laser Focus* **5**, p.33, 1993.
8. S. Nakamura, T. Morkia and M. Senoh, *Appl. Phys. Lett.* **64**, p.1689, 1994.
9. S. Nakamura, M. Senoh, S. Nagahama, and Y. Sugimoto, *Jpn. J. Appl. Phys.* **35**, L74, 1996.
10. H. Morkoc, S. Strite, G.B. Gao, M.E. Lin, B. Sverdlov and M. Burns, *J. Appl. Phys. Rev.* **76**, p.1363, 1994.
11. J.I. Pankove, E.A. Miller and J.E. Berkeyheiser, *RCA Rev.* **32**, p.383, 1971.
12. Chen, Q., Yang, J. W., Osinsky, A., Gangopadhyay, S., Lim, B., Anwar, M. Z., Khan, M. A., Kuksenkov, D. and Temkin, H., *Appl. Phys. Lett.* **70**, p.2277, 1997.
13. Kurtin, S., McGill, and Mead, C. A., *Phys. Rev. Lett.* **22**, p.1433, 1969.
14. Hacke, P., Detchprohm, T., Hiramatsu, K. and Sawaki, N., *Appl. Phys. Lett.* **63**, p.2676, 1995.
15. Binari, S. C., Dietrich, H.B., Kelner, G., Rowland, L.B., and Gaskill, D. K., *Electron. Lett.* **30**, p.909, 1994.
16. Guo, J. D., Feng, M. S., Guo, R. J., Pan, F.M. and Chang, C.Y., *Appl. Phys. Lett.* **67**, p.2657, 1995.
17. E.H. Rhoderick, and R.H. Williams, in *Metal-Semiconductor Contacts*, 2nd ed., p.15.
18. J. Bardeen, *Phys. Rev.* **71**, p.717, 1947.
19. S. Kurtin, T.C. McGill, and C.A. Mead, *Phys. Rev. Lett.*, **22**, p.1433, 1969.
20. C.M. Wolfe, N. Holonyak, Jr., and G.E. Stillman, *Physcal Properties of Semiconductors*, Prentice Hall, Englewood Cliffs, 1989.
21. J.I. Pankove and H.E.P. Schade, *Appl. Phys. Lett.* **25**, p.53, 1974.
22. R.K. Willardson and A.C. Beer, *Semiconductors and Semimetals*, Vol. 7, pp. 175-183, Academic Press, New York, 1971.
23. V. Ya. Niskov and G.A. Kubetskii, "Resistance of ohmic contacts between metal and semiconductor films," *Sov. Phys. Semicond.* **4**, p.1553, 1971.
24. W.G. Bickley, *Bessel Functions*, pp. 220-255. University Press, Cambridge, 1960.
25. J.S. Foresi and T.D. Moustakas, *Appl. Phys. Lett.* **62**, p.2859, 1993.
26. M.E. Lin, Z. Ma, F.Y. Huang, Z.F. Fan, L.H. Allen, and H. Morkoc, *Appl. Phys. Lett.* **64**, p.1003, 1994.
27. Z. Fan, S. Mohammad, and W. Kim, *Appl. Phys. Lett.* **69**, p.1556, 1996.
28. J.T. Trexler, S.J. Pearton, P.H. Holloway, and R.F. Karlicek, *Mater. Res. Soc. Symp. Proc.* **449**, p.1091, 1997.
29. J.S. Jang, K.H. Park, H. K. Jang, and S.J. Park, *J. Vac. Sci. Technol.* **B**(to be published).
30. T. Mori, t. Kozawa, T. Ohwaki, and M. Koite, *Appl. Phys. Lett.* **69**, p.3537, 1996.
31. S.M. Sze, *Physics of Semiconductor Devices*, 2nd ed., p.251, John Wiley & Sons Inc. Publishers, New York, 1981.
32. S. Ruvimov, Z. Liliental-Weber, and J. Washburn, *Appl. Phys. Lett.* **69**, p.1556, 1996.
33. Jin-Kuo Ho, Chang-Shyang Jong, Chien C. Chiu, Chao-Nien Huang, Chin-Yuen Chen, and Kwang-Kuo Shih, *Appl. Phys. Lett.* **74**, p.1275, 1999.

34. J.H. de Boer and E.J.W. Verwey, *Proc. Phys. Soc.* **49**, p.59, London, 1937.
35. H. Sato, T. Minami, S. Takata, and T. Yamada, *Thin Solid Films* **27**, p.236, 1993.
36. J.S. Foresi and T.D. Moustakas, *Appl. Phys. Lett.* **63**, p.1859, 1993.
37. J.T. Trexler, S.J. Pearton, P.H. Holloway, M.G. Mier, K.R. Evans, and R.F. Kalicek, "III-V Nitrides", *MRS Fall Meeting*, 1996

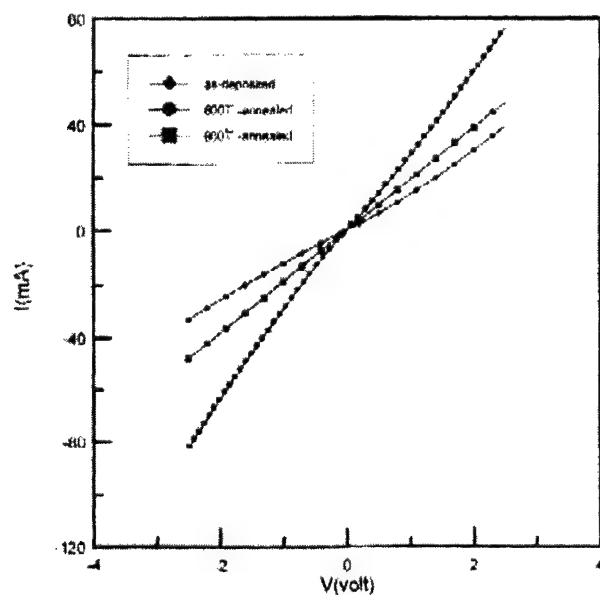


Figure 1 I-V characteristics of as-deposited and annealed Ti/Al contacts on n-GaN.

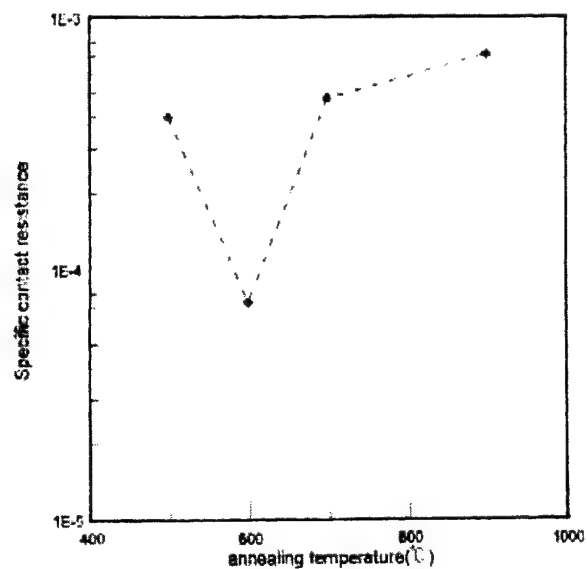


Figure 2 The specific contact resistance of Ti/Al contact as a function of rapid thermal annealing temperature.

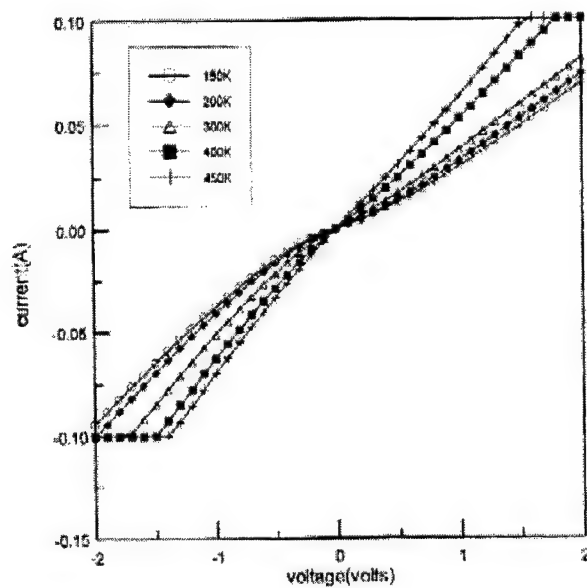


Figure 3 Temperature dependent I-V curves of Ti/Al contact annealed at 600°C for 30 seconds.

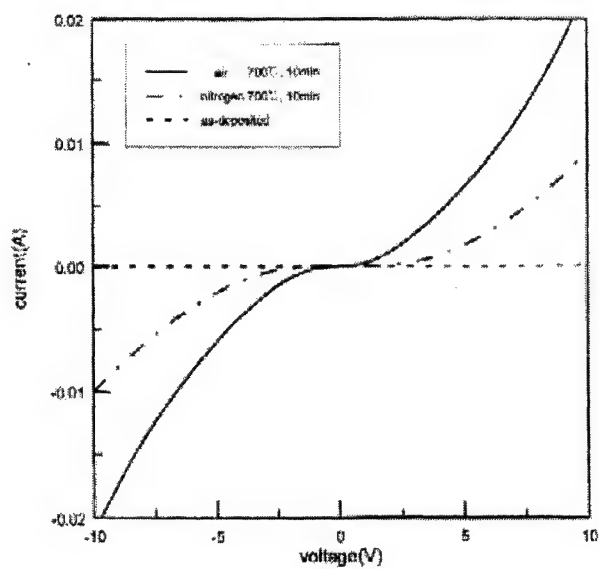


Figure 4 The I-V characteristics of Ni/Au conatcts annealed at different atmosphere.

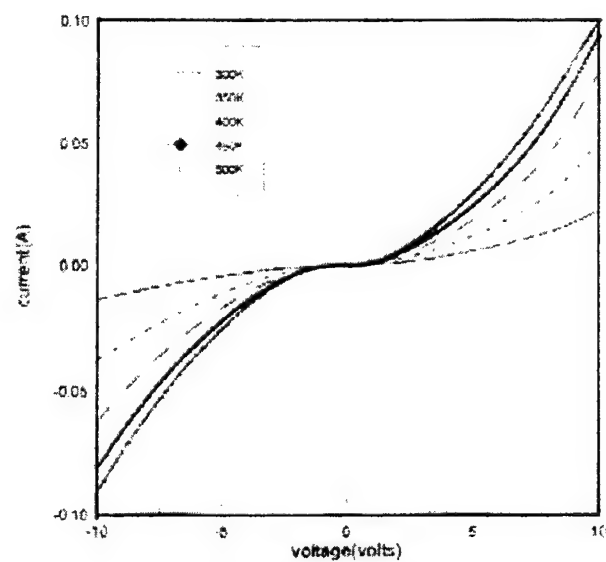


Figure 5 Temperature dependent I-V curves of Ni/Au contact.

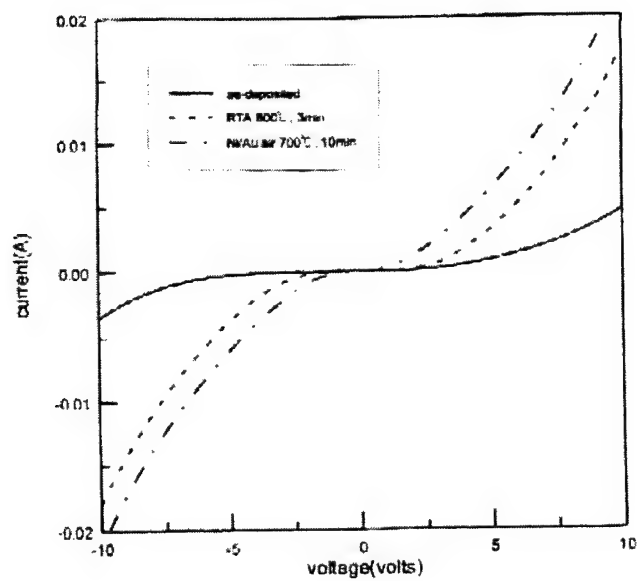


Figure 6 The I-V curves of Pd/Au.

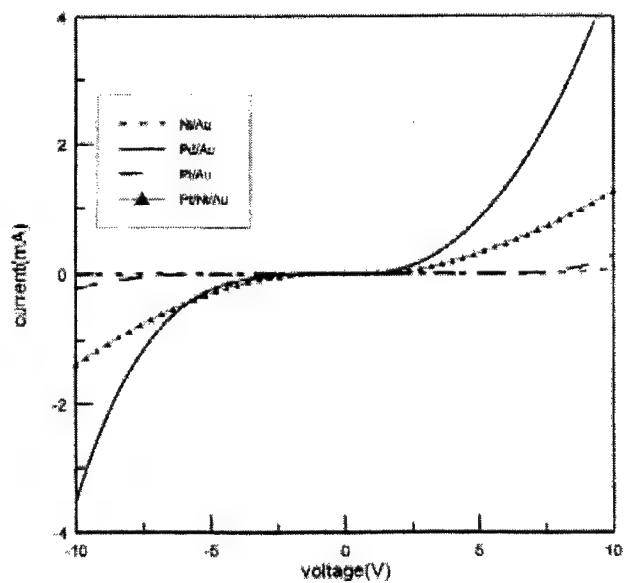


Figure 7 The I-V curves of as-deposited metal contact schemes.

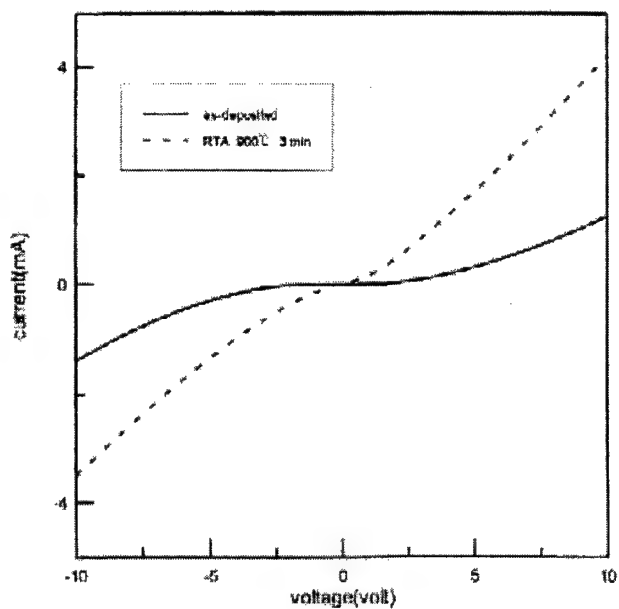


Figure 8 The I-V curves of Pt/Ni/Au contacts.

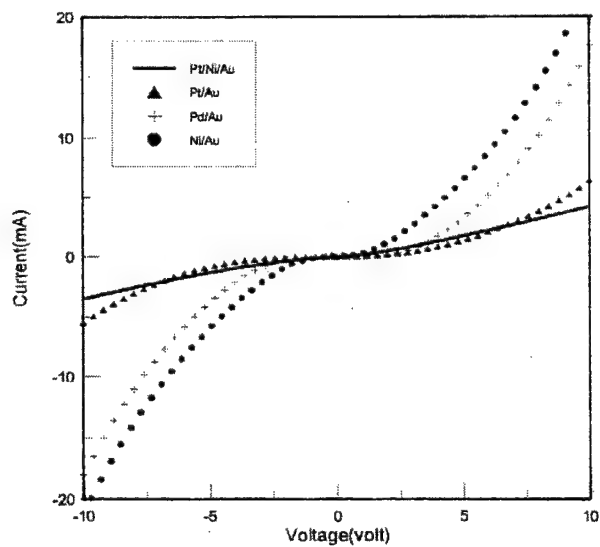


Figure 9 The best results of various kinds of metal contacts.

Study of optical properties of $\text{Fe}_{(1-x)}\text{Co}_x\text{Si}_2$ thin films

Y. J. Zhang, Y. X. Zheng, R. J. Zhang and L. Y. Chen*

Physics Department, Fudan University, Shanghai 200433, China

Abstract

A series of $\text{Fe}_{(1-x)}\text{Co}_x\text{Si}_2$ thin films with variation of x was prepared by reactive deposition epitaxy (RDE) method. The optical properties of the samples are reported in this paper. The dielectric function of the samples was measured by spectroscopic ellipsometer in the photon energy range of 0.26-4.8 eV at room temperature. It's interesting to find that the dielectric function of $\text{Fe}_{(1-x)}\text{Co}_x\text{Si}_2$ films is strongly dependent on the phase of the films: (a) The dielectric function spectra show interference peaks in the low photon energy range for the beta phase $\text{Fe}_{(1-x)}\text{Co}_x\text{Si}_2$ samples. (b) The dielectric function spectra show a feature between the semiconductor and metal feature for the samples containing both beta and sigma phase $\text{Fe}_{(1-x)}\text{Co}_x\text{Si}_2$. (c) The dielectric function spectra show metal feature for the sigma phase $\text{Fe}_{(1-x)}\text{Co}_x\text{Si}_2$ samples. According to the x-ray diffraction results, the variation of the dielectric spectra is arisen from the change of the Fe-Si phase in the samples, rather than that from the variation of x .

Key words: optical properties, dielectric function, metallic silicide

1. Introduction

Recently, the metallic silicide have been studied extensively and demonstrated to have interesting potential application in silicon-based optoelectronic industry¹⁻⁴. This is for the following reasons: a). Such materials have a wide gap range from 0.12 to 0.90eV. b). Such materials can be prepared by MBE on silicon wafers. C). The cost of the device's made by this kind of materials is relatively low. There are many optical and electric properties studies carried out on the pure metallic silicide. Eppenga et al.⁵, Leong et al.⁶ and Arushanov et al.⁷ reported the electronic structure, the optical properties and the electric properties of pure metallic silicide, respectively. Meanwhile, doping plays an important role in the metallic silicide materials. But so far few works on the optical properties of the doped metallic silicide have been reported.

In this work we present the study of optical properties of the doped metallic silicide. We've prepared a series of

* Email: lychen@fudan.ac.cn (Prof. Liang-Yao Chen)

Fe_(1-x)Co_xSi₂ thin films with variation of x and measured the dielectric function spectra of the sample in a wide photo energy region.

2. Experiments

A series of Fe_(1-x)Co_xSi₂ thin films was fabricated on the n-type Si(111) wafers in UMS500P ultrahigh vacuum chamber using reactive deposition-solid phase epitaxy (RDE) method, the pressure of the chamber during the deposition process was 10-8mbar. The substrate temperature was 600°C and the depositing rate was about 0.1nm/s. The thickness of the films was controlled by quartz-resonator. The evaporator source was the high purity Fe(99.99%) or fusing Fe-Co alloy, in which the original content of Co was 10±0.001at%. X-ray diffraction(XRD) method was used to examine the quality and structure of the films. The composition of the films was deduced from the Rutherford backscattering spectroscopy(RBS) after the deposition. The complex dielectric function spectra were measured by a rotating-analyser-polarizer(RAP) type of spectroscopic ellipsometer⁸. For an ideal two-phase situation, the dielectric function ε can be determined by⁹:

$$\varepsilon = \varepsilon_a \left\{ \sin^2 \phi + \sin^2 \phi \tan^2 \phi \left[\frac{(1-\rho)}{(1+\rho)} \right]^2 \right\} \quad (1)$$

where $\rho = \rho_0 \exp(i\Delta) = \tan \psi \exp(i\Delta)$, ε_a and ϕ is the dielectric constant of the ambient and the incident angle of the light coming to the sample, respectively. The measurements were made in the 0.26-1.25eV photon energy range in the near IR region and 1.5eV-4.8eV photon energy range in the visible region. All measurements were taken at room temperature.

3. Results and discussions

The measured complex dielectric function $\varepsilon = \varepsilon_1 + i\varepsilon_2$, of the β - Fe_(1-x)Co_xSi₂ thin films with x=0, 0.05, 0.06 and 0.09, are shown in Fig.1. It can clearly be seen that there are a few interference peaks in the 0.26-1.25eV photon energy ranges for all the samples, but the peaks disappear in visible region. This shows that the films are transparent in the IR region and become opaque in the visible region, since the higher optical absorption occurs in the visible region. This is the character of the semiconductor phase of Fe-Si. In Fig.1 the numbers of the peaks changes for the samples that have different film thickness.

The energy gap(E_g) of the films can be derive from the experimental data as shown above. For the β - Fe_(1-x)Co_xSi₂ thin films, E_g is about 0.804eV, 0.862eV, 0.873eV and 0.888eV for x=0.00, 0.05, 0.06 and 0.09, respectively. As the photon

energy equals to the energy gap E_g in the 0.8-0.9 eV range, the direct and strong optical transition occurs for the samples mentioned above. This is consistent with the results reported by M.C.Bost¹⁰.

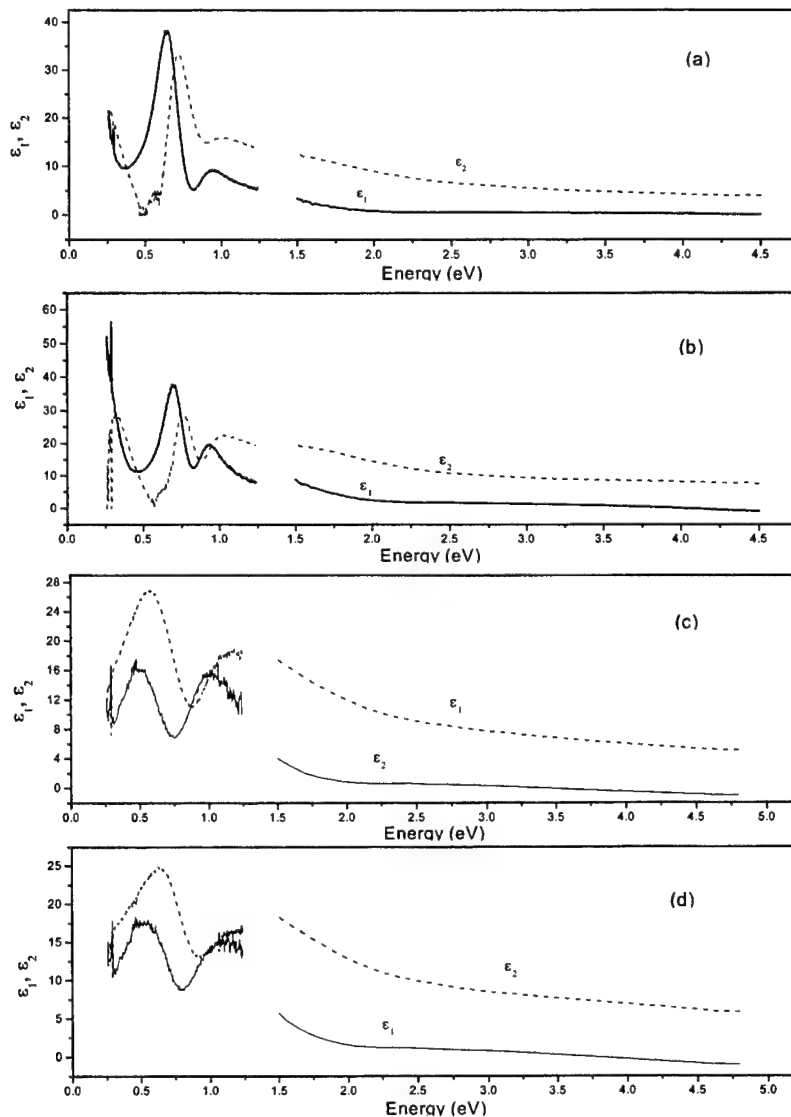


Fig. 1 The measured complex dielectric function spectra of β - $\text{Fe}_{(1-x)}\text{Co}_x\text{Si}_2$ thin films: (a). β - FeSi_2 ; (b). β - $\text{Fe}_{0.95}\text{Co}_{0.05}\text{Si}_2$; (c). β - $\text{Fe}_{0.94}\text{Co}_{0.06}\text{Si}_2$ and (d). β - $\text{Fe}_{0.91}\text{Co}_{0.09}\text{Si}_2$.

It's interesting to see that there are no peaks appeared in the spectra of dielectric function in the $\text{Fe}_{(1-x)}\text{Co}_x\text{Si}_2$ films that are not the β phase. The spectra of the dielectric function have a different feature from that shown for the β - $\text{Fe}_{(1-x)}\text{Co}_x\text{Si}_2$ samples. There are three kinds of features for those spectra with three different phases: a.) the semiconductor-like spectra, in which the interference peaks occurs in the low photon energy range and disappears in the higher photon absorption region;

b.) the metal-and-semiconductor-mixed spectra, in which the spectra of dielectric function show a feature for the sample that has a mixed the semiconductor and metal phase; c.) the metal-like spectra, in which the spectra of dielectric function show the spectral feature like the metal. Fig. 2 shows the three kinds of features of complex dielectric function of $\text{Fe}_{0.9}\text{Co}_{0.1}\text{Si}_2$ films in three phases. Fig. 2(a) shows the semiconductor-like spectra, in which the energy gap E_g is at about 0.832eV for this sample. Fig. 2(b) and (c) shows the metal-and-semiconductor-mixed and metal-like spectra, respectively.

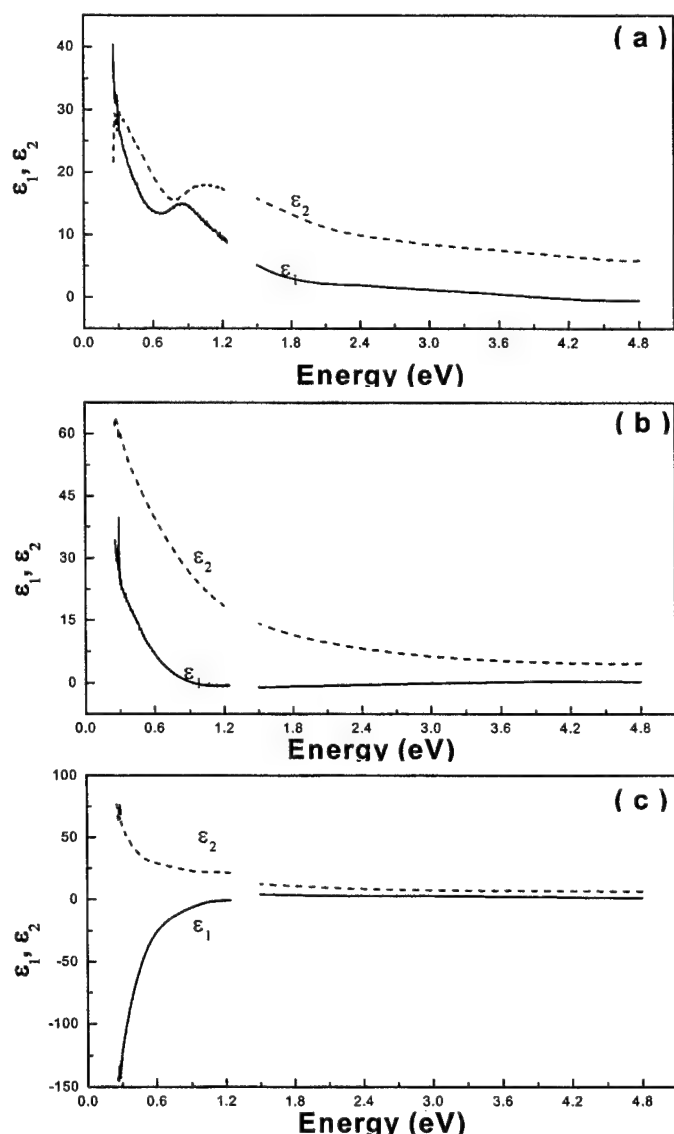


Fig. 2 The three kinds of features of complex dielectric function of $\text{Fe}_{0.9}\text{Co}_{0.1}\text{Si}_2$ thin films with three different phases: (a). in the semiconductor phase; (b) in the mixed phase, and (c). in the metal phase.

The XRD results indicate that the $\text{Fe}_{(1-x)}\text{Co}_x\text{Si}_2$ films with the same x value may have three different Fe-Si phases, as showed in Fig. 3. The XRD pattern is for the $\text{Fe}_{0.9}\text{Co}_{0.1}\text{Si}_2$ samples. The pattern shown for a semiconductor phase is given in Fig. 3(a), in which the diffraction peaks occurred at (101), (200) and (021) etc. indicate a polycrystal structure with a beta Fe-Si phase. This is consistent with the feature of the dielectric function as shown in Fig. 2(a). For the phase-mixed sample as the pattern shown in Fig. 3(b), majority of XRD peaks is in the sigma phase and minority is the beta phase, resulting in the spectral feature as shown in Fig. 2(b). As the pattern shown in Fig. 3(c), the XRD peaks indicate that sample is in the sigma Fe-Si phase, resulting in a metal-like spectra as shown in Fig. 2(c).

4. Conclusion

In this paper, a series of $\text{Fe}_{(1-x)}\text{Co}_x\text{Si}_2$ thin films with variation of x was prepared by RDE method. The optical properties of the samples are reported. The dielectric function spectra of the samples were measured by the spectroscopic ellipsometer in the photon energy range of 0.26-4.8 eV at room temperature. There are three kinds of features for these spectra. According to the x-ray diffraction results, different features shown in the spectra of the dielectric

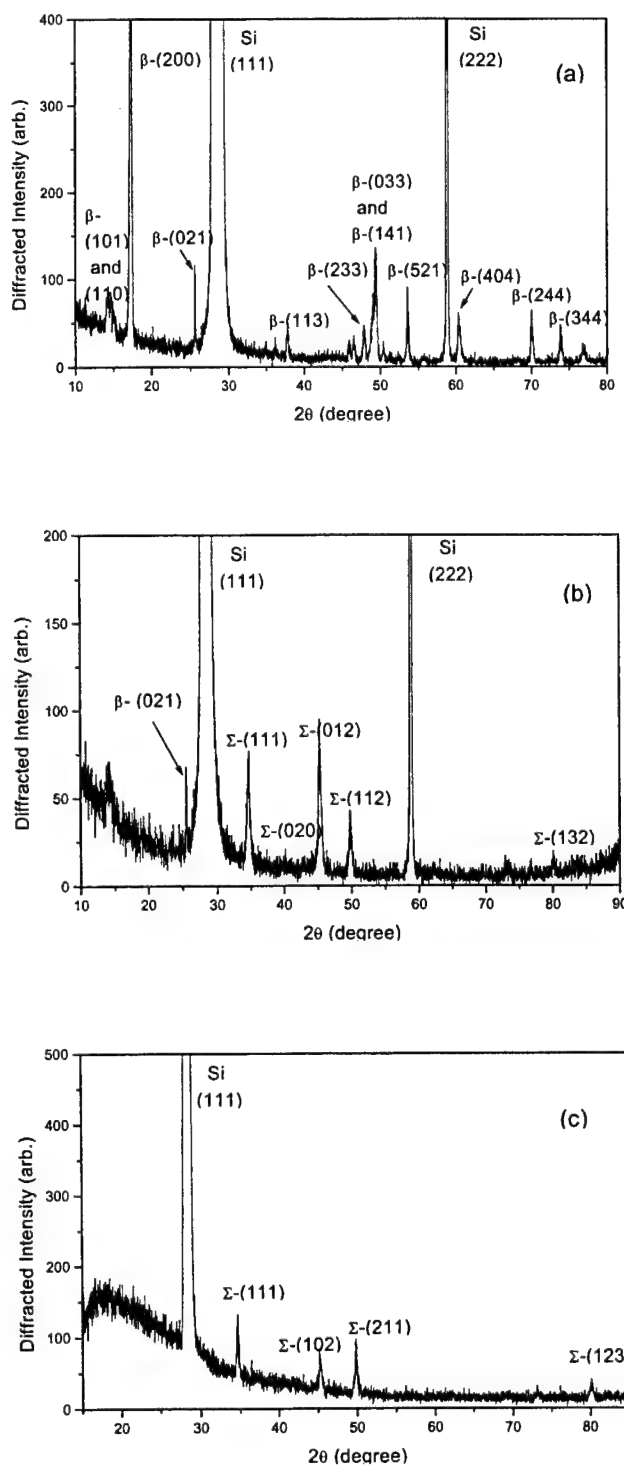


Fig. 3 The XRD spectra of three kinds of $\text{Fe}_{0.9}\text{Co}_{0.1}\text{Si}_2$ thin films show that: (a). the semiconductor phase; (b) the mixed phase, and (c). the metal phase.

function is arisen from the change of the Fe-Si phase in the samples, not from the variation of x . The three phases observed in XRD and spectra of the dielectric functions are: (a). The sample with the dielectric function spectra in which the interference peaks occurs in the low photon energy range is in the beta Fe-Si phase. (b). The metal-and-semiconductor-mixed phase. (c). The sample with a metal-like spectra of the dielectric function is in the sigma Fe-Si phase.

5. Acknowledgements

The authors would like to thank Dr. L. W. Wang of Shanghai Institute of Metathrurgy for preparing the samples. This work was supported by the NSF and SRCAP of China.

6. References

1. J. Y. Natoli et al., "Growth of β - FeSi₂ on Si(111) by chemical beam epitaxy," Appl. Phys. Lett., **65**, pp. 1439-1441 (1994).
2. G. Guizzetti et al., "Measurement and simulation of anisotropy in the infrared and Raman spectra of β - FeSi₂ single crystals," Phys. Rev., **B55**, pp. 14290-14297 (1997).
3. A. B. Filonov et al., "Theoretical and experimental study of interband optical transitions in semiconducting iron disilicide," J. Appl. Phys., **83**, pp. 4410-4414 (1998).
4. L. Miglio et al., "Origin and nature of the band gap in β - FeSi₂," Phys. Rev., **B52**, pp. 1448-1451 (1995).
5. R. Eppenga, "*Ab initio* band-structure calculation of the semiconductor β - FeSi₂," J. Appl. Phys., **68**, pp. 3027-3029 (1990).
6. D. N. Leong et al., "On the origin of the 1.5 μ m luminescence in ion beam synthesized β - FeSi₂," Appl. Phys. Lett., **68**, pp. 1649-1650 (1996).
7. E. Arushanov et al., "Photoconductivity in n -type β - FeSi₂," Phys. Rev., **B52**, pp. 20-23 (1995).
8. L. Y. Chen, X. W. Feng et al., "Improved rotating analyser-polarizer type of scanning ellipsometer," Opt. Appl. **33**, pp. 1299-1304 (1994).
9. D. E. Aspnes, Optical Properties of Solids. Ed. By Abeles F., North Holland, Amsterdam, p. 808 (1976).
10. M. C. Bost and J. E. Mahan, "Optical properties of semiconducting iron disilicide thin films," J. Appl. Phys., **58**, pp. 2696-2703 (1985).

Characterizing White LEDs for General Illumination Applications

Nadarajah Narendran*, Nishantha Maliyagoda, Andrew Bierman,
Richard Pysar, and Martin Overington
Lighting Research Center, Rensselaer Polytechnic Institute, Troy, NY 12180

ABSTRACT

During the past few years several manufacturers have introduced white Light Emitting Diodes (LEDs). At the present time these LEDs do not provide sufficient luminous flux for general lighting applications. Many manufacturers are studying the possibility of grouping several LEDs and overdriving them to produce more luminous flux. The impact of higher drive current on long-term performance of LEDs is not well known within the lighting community. Therefore, an experimental study was conducted to investigate the photometric characteristics of white LEDs as a function of time for different drive currents. The LEDs investigated in this study were the 5-millimeter type that uses GaN-based blue LEDs and $\text{Y}_3\text{Al}_5\text{O}_{12}$ (yttrium aluminum garnet) phosphors (YAG phosphors). These LEDs produced 65 percent more light output at 55 mA compared to the light output at 20 mA. Groups of ten LEDs were driven continuously at constant current 20, 30, 50, 70, 90, and 110 mA and their relative light output were monitored at regular intervals for over 4000 hours. The light output degradation rate increased with increasing drive currents. Typically, LED manufacturers do not recommend driving these LEDs above 20 mA. However, it was noticed that the light output of these LEDs degraded to 65% of its initial value around 4000 hours even for those LEDs driven at 20 mA, which is the manufacturer recommended value for drive current. Considering the amount of flux produced by these 5mm type white LEDs and their light output degradation rate, they are not yet suitable for general lighting applications.

Keywords: White light, LED, general lighting, degradation

1.0 INTRODUCTION

In 1993 Gallium Nitride (GaN) based blue Light Emitting Diodes (LEDs) were introduced into the marketplace by Nichia Chemical Company of Japan [1, 2]. Since then the development of GaN-based LEDs has progressed rapidly, and several manufacturers have introduced white LEDs. Architectural lighting is one of the potential applications for this new technology. Although at present, white LEDs do not provide sufficient luminous flux for general lighting applications, experts in the field are optimistic that within the next few years these devices will provide higher luminous flux to make them attractive for architectural lighting applications [3]. Furthermore, researchers around the world are aggressively working on developing LEDs that produce ultra-violet (UV) radiation. These UV LEDs in combination with phosphors may ultimately produce the white light that is needed for architectural lighting applications. In anticipation of this promising application, several third-party manufacturers have introduced white light sources, using the 5-millimeter white LEDs, in a cluster form with screw bases for general lighting applications. Long life and potential for energy savings are two main factors that have captured the attention of the architectural lighting industry. Long life, 50,000 to 100,000 hours, is an advantage that is commonly claimed for LED devices. However, the term life as used in the LED industry may need revision for use in the lighting industry since the "useful life" of LEDs for the target application may be shorter, and will be discussed in this manuscript at a later section.

White LEDs produce higher light output with higher drive current. Some manufacturers exploit this feature to increase light output from the LED. However, the impact of higher drive current on long-term performance of LEDs is not well known within the lighting community. The goal of this study is to understand how the photometric parameters of white LEDs change with different drive currents and with time. A literature survey was conducted to identify what information is available in the public domain. The literature survey showed that during the past few years there have been an enormous number of publications related to GaN technology and devices and there were several publications attempting to identify the degradation mechanisms of GaN devices [3-5]. There were other papers including manufacturers' data sheets, that showed data for light output variation with time for GaN based blue LEDs [6-9]. However, there was no published information available on how the light output of GaN-based white LEDs depreciates over time. Therefore, an experimental study was conducted to

understand the photometric characteristics of a sample of white LEDs at different drive currents and how these parameters change over time.

2.0 EXPERIMENT

The white LEDs used in this study were the 5-mm GaN-based blue LEDs with YAG phosphors. A short pilot study was conducted to gain better understanding of the behavior of white LEDs with different drive currents. The goals of this pilot study were to help design the apparatus needed for photometric testing of white LEDs, to help select the appropriate drive currents that would allow us to achieve the desired results, and to develop the necessary testing protocols.

In the first experiment of the pilot study, the white LEDs were driven at various constant currents, 20 mA to 120 mA dc, and the corresponding light output were recorded using an illuminance meter at a fixed distance. The light output data was gathered for 600 seconds at regular intervals and the results are illustrated in Figure 1. It can be seen from Figure 1 that initially it takes about 180 seconds for the LED light output reach stability. The same data are plotted differently in Figure 2, which shows relative light output as function of drive current at different time intervals. Both figures show that light output degradation rate increases with increasing drive current.

In a second experiment of the pilot study, the spectral power distributions of the LED light output were measured using an integrating sphere and a spectrometer. The LEDs were driven at constant currents, 10 mA to 120 mA dc at 10 mA intervals. Prior to collecting spectral data the LEDs were allowed to stabilize for 180 seconds after changing the drive current. Figure 3 illustrates the relative spectral power distributions (spd) of these white LEDs at 20, 40, 60, 80, 100 and 120 mA. Figure 3 shows partial data to avoid too many data in a single graph and to make it readable. The spectrum plots in Figure 3 are on a relative scale. It is interesting to see that the peak wavelength of the blue LED at 465 nm initially shifts towards shorter wavelength when the current is increased from 20 mA to about 60 mA. After that, the peak wavelength shifts towards longer wavelengths and at the same time the peak starts to broaden. This is different to what P. Schlotter and others have shown for their GaN-type white LED. In their study, the peak wavelength of the blue LED emission remains unchanged approximately at 420 nm for three-drive currents 2 mA, 10 mA, and 40 mA [10]. Similar to what we observed in our study, S. Nakamura, in one of his recent papers, showed blue shift of the emission spectra of a blue InGaN LED at various drive currents from 0.1 mA to 20 mA and mentions that blue LED on sapphire also showed similar behavior [8]. However, Nakamura's paper does not mention what happens when the drive current is increased further. It can be observed from Figure 3 that when the peak wavelength at 465 nm shifts towards higher wavelength and broadens the phosphor conversion efficiency decreases. As an example, comparing two spectral power distributions, at 20 mA and 120 mA, it is evident that the re-emitted portion of the light from the phosphor is higher at 20 mA than at 120 mA, even though the heights of the blue peaks are very similar. Figure 4 illustrates the measured color values plotted on the 1931 CIE chromaticity diagram for the different drive currents. The CIE x,y value of the light output at 10mA is on the blackbody locus. With increasing drive current the chromaticity value shifts towards blue and at 120 mA, LED light output appears distinctly blue. This is mainly due to decrease of phosphor conversion efficiency when the emission peak of the blue LED shifts towards longer wavelength. It was observed during this experiment that the LED returns to its original chromaticity value and appears white when the drive current was reduced back to 10 mA. This was only true for the short term testing.

Figure 5 illustrates how the relative luminous flux changes with different drive currents and the associated changes in relative efficacy. All the values were normalized to the 20 mA value since it is the manufacturer-recommended drive current value for these LEDs. As seen in Figure 5, the relative flux of the LED increases with drive current up to about 55 mA but decreases beyond that value. However, from the beginning, the efficacy of the LED decreases steadily with increasing drive current from 10 to 120 mA. From figure 5, it appears that the maximum light output gain is approximately 65 %, which occurs around 55 mA. At this point the efficacy is below 50 percent of the 20-mA value. From Figure 4 it can be seen that at 55 mA the chromaticity value is very close to the black-body locus and indicates that the color of the light is still white. These data are valid only for the plastic-encapsulated, 5 mm LEDs without additional heat sinks. The next question is what happens to the life of the LED when the drive current is increased to produce more flux. Based on the knowledge gained in the pilot study an experiment was designed to understand the affect of higher drive currents on LED life.

2.1 Life Test Experiment

Six drive currents, 20, 30, 50, 70, 90 and 110 mA, were selected for the life test experiment. All LEDs used in this investigation came from a single batch and from a single manufacturer. The LEDs were mounted on printed circuit boards with their current regulating circuits mounted behind the boards. An image of a single printed circuit board is shown in Figure 6, and the schematic of the current regulator circuit is shown in Figure 7. The wire traces on the circuit boards

adjacent to the LEDs were 12 mils wide, and all circuit boards had identical dimensions. To study the affect of wire trace dimension, an additional circuit board was made with 50 mil wire traces, and the LEDs in this group were driven at 110 mA. The current in each individual LED is controlled by the LED's own circuit. Altogether, there were seven circuit boards (denoted as bay#1, bay#2, etc. in Figure 9) and each board carried ten LEDs, all driven at the same current.

During this experiment it was noticed that the light output of LEDs is very sensitive to the ambient temperature. Therefore, an imaging type setup as shown in Figure 8 was developed to ensure that the surrounding environment of the LEDs was not disturbed while gathering light output information. All seven circuit boards were mounted on a common mounting plate, and the system was driven by a regulated power supply at 12 Volts dc. The mounting plate with the LED circuit boards was placed vertically in front of an optically diffusive glass plate, and a CCD camera was placed on the opposite side as shown in Figure 8 to capture the luminance images of the LEDs. A sample camera image of the LEDs is shown in Figure 9. A software program associated with the CCD camera system was utilized to obtain the relative luminance of each individual LED. This was accomplished by drawing regions of interest, circular segments of the same diameter, around the LEDs, as shown in Figure 9. The software package automatically determines the total light output within these circular segments. Luminance images were captured at regular intervals with the same exposure time, and the software estimated the relative luminance of each individual LED. This procedure significantly simplified the data collection process. Two thermocouples, one at the middle of the top row and the other at the middle of the bottom row, were mounted to monitor the ambient temperature near the LEDs. The temperature at the bottom row where the 20 mA LEDs were situated remained around 25°C throughout the experiment. The temperature at the top row was initially around 55°C and after the 110 mA LEDs ceased to operate the temperature dropped to around 45°C. Although the test room had a temperature controller, it was not sufficient to maintain the operating temperature of the LEDs to within 0.5°C. There was an overall random temperature swing of about 5°C during the experimental period.

Figure 10 illustrates the mean light output value of the ten LEDs on each board for all seven boards. At the time this manuscript was prepared, the LEDs have continuously operated for over 4000 hours. As expected the light output depreciation increased with increasing drive current. The ambient temperature fluctuation directly impacts light output and is seen in each light output depreciation curve as small oscillation about the average trend.

Of the two boards operated at 110 mA, the one that had thinner wire traces had slightly faster light output depreciation compared to the one that had thicker wire traces. The thinner wired circuit LEDs show slightly higher light output compared to the thicker wired circuit LEDs towards the end when the light output remains unchanged. It appears that with more heat sink the light output depreciation rate can be reduced. More experimentation is needed to confirm this effect and to explain why the LEDs with thinner wires end up at higher light level than the one with thicker wires.

It is interesting to see from Figure 10 that the light output reached 65% of its initial value around 4000 hours for those LEDs driven at 20 mA, which is the manufacturer-recommended drive current. This light output degradation rate seems excessive compared to data published in literature for GaN-based blue LEDs [7]. The authors suspect the increased degradation rate is due to either degrading phosphor [11] or change in transmittance of the encapsulating plastic [9]. However, this cannot be confirmed without additional testing. Currently, the LED industry rates LED life at 50 percent light output. Typically, this is done by gathering data for a limited time and extrapolating it to the necessary light output value. A logarithmic curve fit is commonly used for this extrapolation. Although, this may work for GaN and AlGaP LEDs the same extrapolation may not be valid for white LEDs since they have an additional component, namely the phosphor, which degrades along with the semiconductor device. From the data gathered so far, the life of the LED at 50% light output can be obtained directly for drive currents 110, 90, 70 and 50 mA. However, for drive currents 30 mA and 20 mA, the data points have to be extrapolated. It appears that these white LEDs would reach 50% light output around 5000 to 6000 hours at these two drive current, which is much shorter than commonly assumed 50,000 to 100,000 hours life.

The graphs shown in Figure 10 raises an interesting question regarding the definition of life for these LEDs, especially if they are to be used for general illumination applications. Unlike other light sources used in the illumination industry that fail to produce light after a period of time due to failed electrodes or filaments, LEDs in general do not fail catastrophically. However, the light output slowly depreciates over time. Therefore, the key question is what is the useful life of a white LED for general illumination applications? Some of the characteristics of LEDs resemble the characteristics of certain metal halide lamps used in general illumination applications. Similar to these types of metal halide lamps, the 5-mm white LEDs also have significant color variation between similar LEDs. Also, the light output depreciation curves for these LEDs look very similar to those for some metal halide lamps. Although, the term life for metal halide lamps denote the time at which 50 percent of lamps survive and 50 percent have ceased to operate, their useful life is about 60 to 70 percent of their rated life. This is

mainly due to the fact that metal halide lamps have high lumen depreciation rates and undergo color shift. As an example, a metal halide lamp rated at 10,000 hours has about 6000 hours of useful life. At this point the metal halide lamp produces about 70 percent of its initial light output. Usually, manufacturers recommend the useful life as the time for group relamping of metal halide lamps in certain applications [12]. The LED light sources intended for use in the illumination industry also need a similar useful life definition based on light output and color shift.

3.0 SUMMARY

An experimental study was conducted to investigate the photometric characteristics of white LEDs over time for different drive currents. The LEDs were characterized for light output and color shift when they were driven at constant currents, ranging from 10 mA to 120mA. With increasing current, light output increased; however, the rate of light output degradation also increased. The color of the light output shifted towards blue with increased current and at 120mA it appeared distinctly blue.

To understand how drive currents affect the light output of LEDs over time, groups of ten LEDs were driven continuously at constant current, 20, 30, 50, 70, 90, and 110mA, and their relative light output were monitored at regular intervals for over 4000 hours. As expected, the light output degradation rate increased with increasing drive currents. It was noticed from the experimental results that the light output reached 65% of its initial value around 4000 hours even for those LEDs driven at 20 mA, which is the manufacturer-recommended drive current value. It appears from the data that these white LEDs would reach 50% light output around 5000 to 6000 hours which is much shorter than commonly claimed 50,000 to 100,000 hours life. This light output degradation rate seems excessive. Therefore, the authors suspect the increased degradation rate is due to either degradation of phosphor and/or change in transmittance of the encapsulating plastic. All LEDs used in the initial investigation came from a single batch and from a single manufacturer. A second group of LEDs, bought from two different manufacturers at a later time, was subjected to similar testing. These LEDs have, to date, lasted 2000 hours, and the light output degradation curves look very similar to the ones observed from the first test. The results of the second test will be published elsewhere once sufficient data are collected to confirm their performance. An important lesson learned in this study is that the LED sources intended for use in the illumination industry need a useful life definition based on light output and color shift to better represent the life time of LED light sources.

The authors of this paper wish to point out that the progress of white LEDs has been rapid over the past year, and therefore the absolute values for light output degradation and color shift may be different for some of the newer products. In addition, the usefulness of the source will depend very much on how the LEDs are packaged to form the light source. Although, at the present time original equipment manufacturers (OEMs) are using these 5-mm white LEDs to form white light sources, they are not yet suitable for general illumination applications, since they produce very little light and they have short useful life. LED device manufacturers are working on devices that produce more light from a single LED and are in the process of improving their overall performance by providing improved heat sinks to meet the needs of the target applications.

4.0 ACKNOWLEDGMENTS

The authors gratefully acknowledge the support of the Lighting Research Center. The authors are grateful to Dr. Mark Rea, Russ Leslie, Conan O'Rourke of the Lighting Research Center and Dr. S.H.A. Begemann of HP/LumiLeds Lighting for their valuable discussions.

5.0 REFERENCES

1. S. Nakamura, T. Mukai, M. Senoh, "Candela-class high brightness InGaN/AlGaIn double-heterostructure blue-light-emitting diodes," *Appl. Phys. Lett.* 64, 1994.
2. S. Nakamura and G. Fasol, "*The Blue Laser Diode*," Springer-Verlag Berlin Heidelberg New York, 1997.
3. D. Houghton, "Getting the LED out," *Architectural Lighting*, Aug./Sept. 1999.
4. S. Nakamura, "Progress with GaN-Based Blue/Green LEDs and Bluish-Purple Semiconductor LDs," *Photonics and Communications in Japan*, Part 2, Vol 81, No 5, 1998.
5. A.E. Yunovich, A. N. Kovalev, V.E. Kudryashov, F. I. Manyakhin, and A.N. Turkin, "Aging of InGaN/AlGaIn/GaN Light-Emitting Diodes," *Material Res. Soc. Symp. Proc.* Vol 482, (1998).
6. F. Manyakhin, A. Kovalev, and A.E. Yunovich, "Aging mechanisms of InGaN/AlGaIn/GaN Light-Emitting Diodes Operating at High Currents," *MRS Internet Journal of Nitride Semiconductor Research*, Volume 3, Article 53, 1999.
7. D. Evans, "High Luminance LEDs Replace Incandescent Lamps in New Applications," *SPIE Vol.* 3002, 1997.
8. S. Nakamura, "InGaIn-based blue light-emitting diodes and laser diodes," *Journal of Crystal Growth*, 201/202: 1999.

9. D. L. Barton, M. Osinski, P. Perlin, C. J. Helms, and N. H. Berg, "Life tests and failure mechanisms of GaN/AlGaIn/InGaIn Light emitting Diodes", SPIE Vol.3279, 1998.
10. P.Schlottter, J.Baur, Ch.Hielscher, M.Kunzer, H.Obloh, R. Schmidt, J.Schneider, "Fabrication and characterization of GaN/InGaIn/AlGaIn double heterostructure LEDs and their application in luminescence conversion LEDs," Material Science and Engineering B59, 1999.
11. Illumination Society of North America 1993, *Lighting Handbook: Reference and application*, 8th Edition (Mark S. Rea, Editor), New York: Illumination Society of North America.
12. *The Metal Halide Specification Book*, Venture Lighting, 1995.

Correspondence: Email: narenn2@rpi.edu; WWW: lrc.rpi.edu; Telephone: 518 276 4803; Fax 518 276 4835.

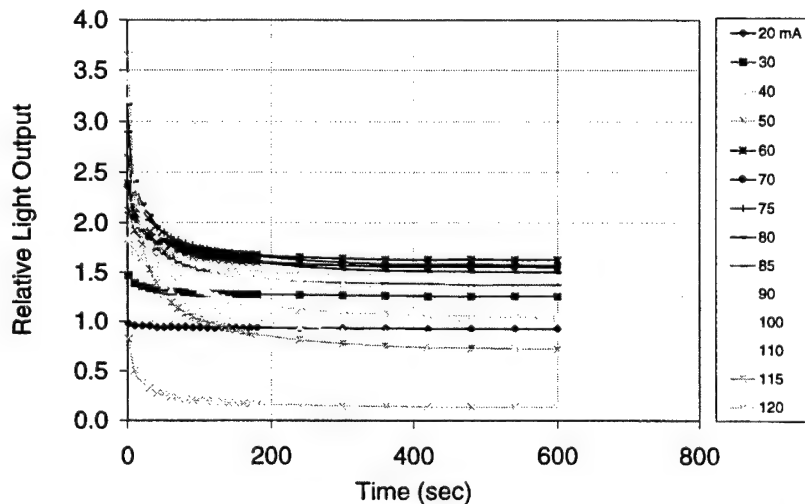


Figure 1: Relative light output as a function of time for different drive currents

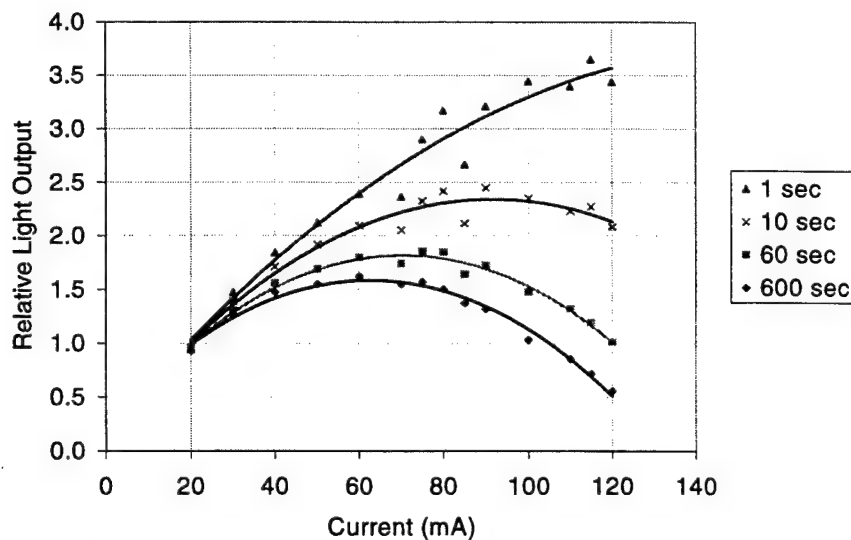


Figure 2: Light output variation as a function of drive currents at different time intervals

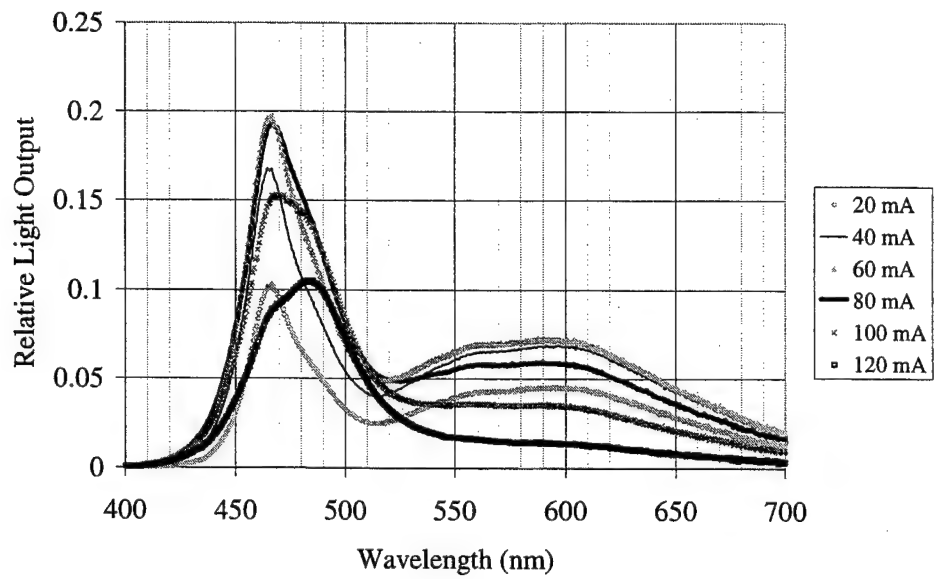


Figure 3: The measured spectral power distribution at various drive currents

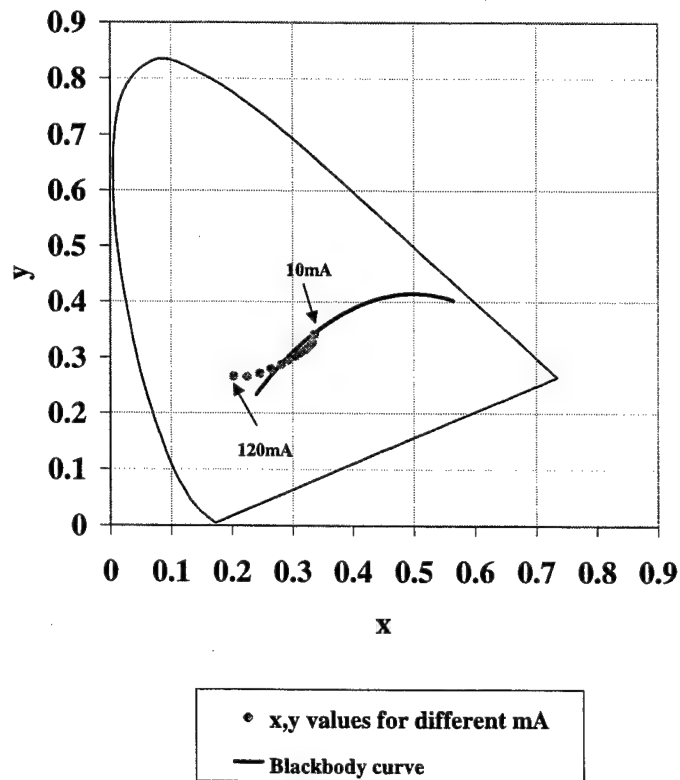


Figure 4: The measured CIE x, y values for different drive currents

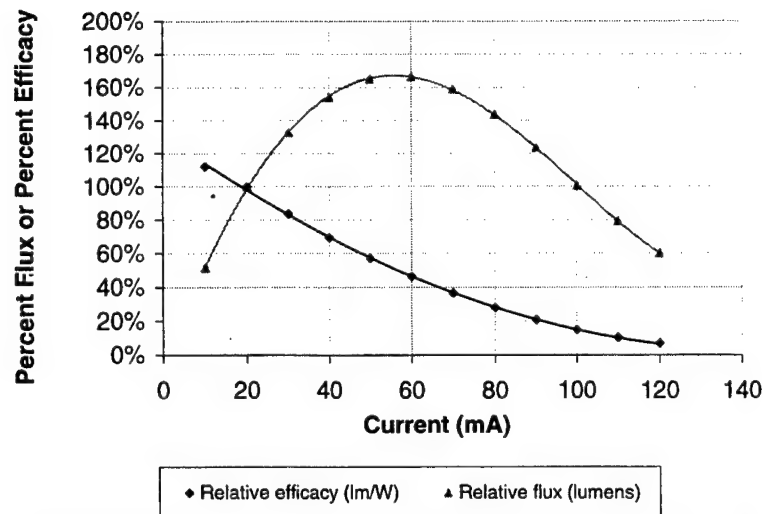


Figure 5: Plot of relative flux output of a white LED as a function of drive current and the corresponding relative efficacy values.

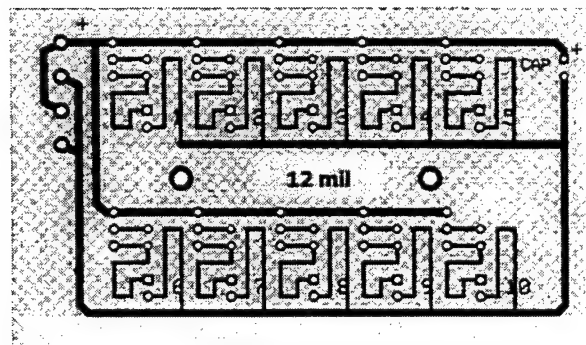


Figure 6: Layout of the printed circuit board.

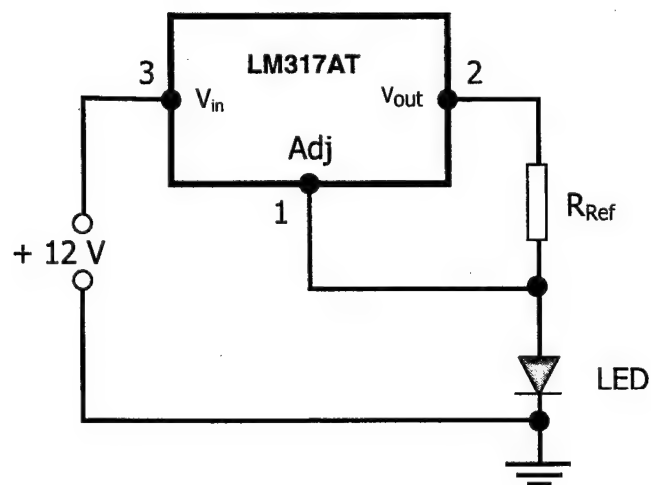


Figure 7. The regulator circuit used for controlling the current through the LED.

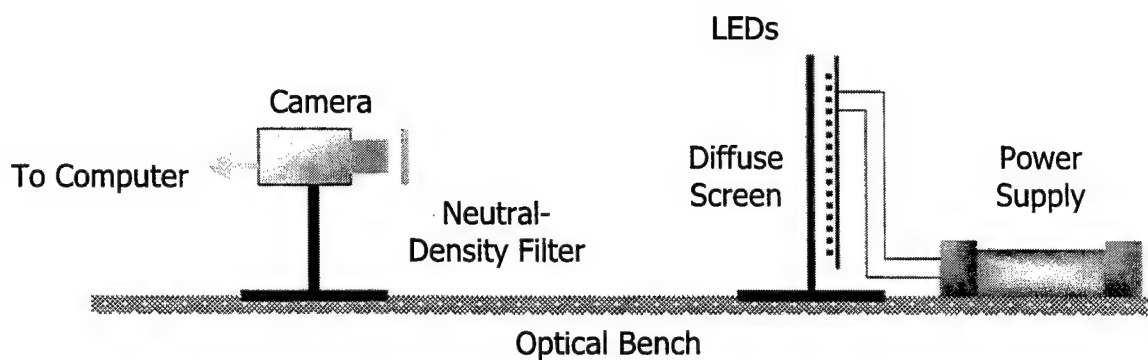


Figure 8. Life test experimental setup.

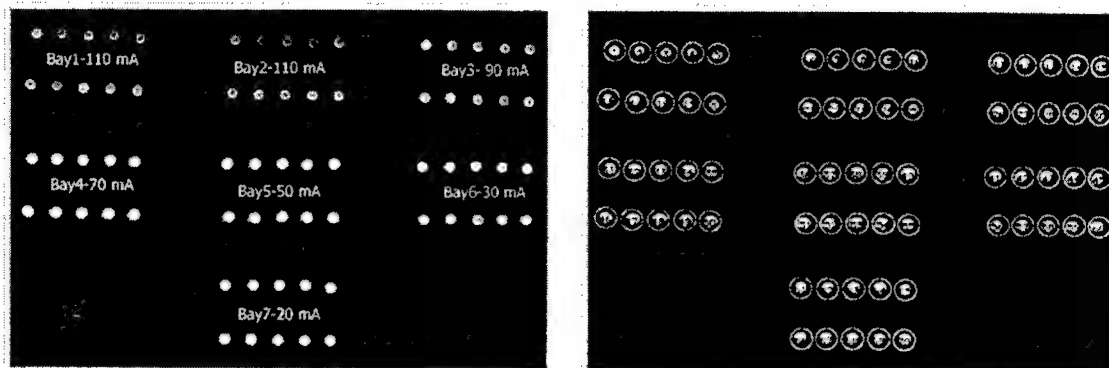


Figure 9. Sample intensity images captured using the digital camera. (a) Image of the board layout with corresponding drive-current for each bay. (b) The same image with circular segments drawn around each LED.

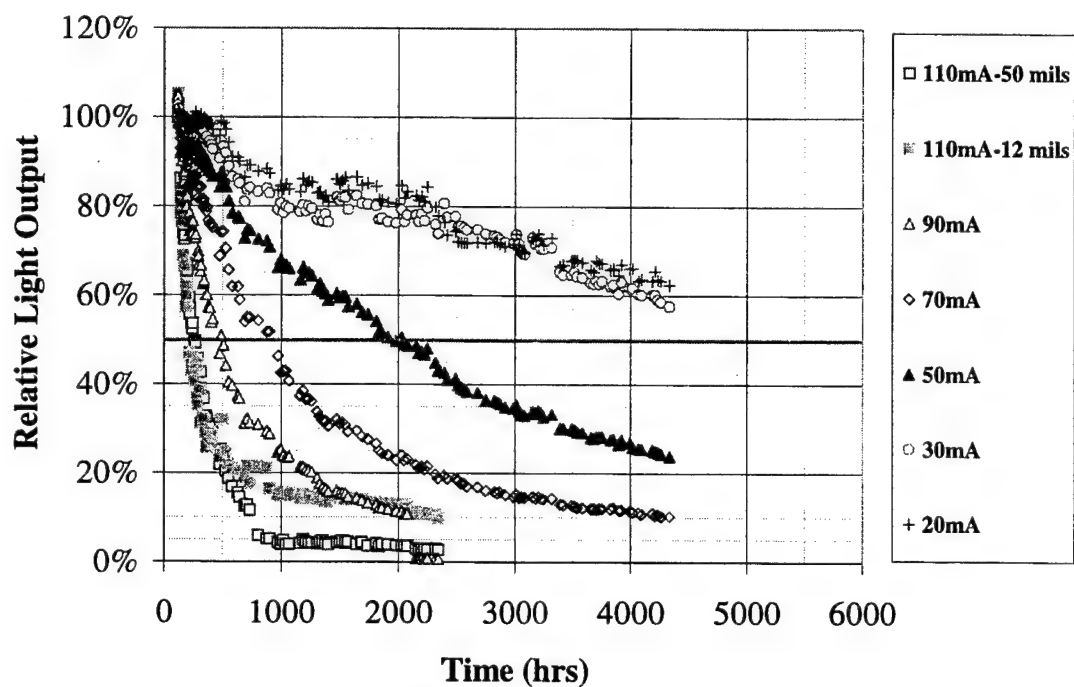


Figure 10: Relative light output as a function of time and drive current.

Georg Bogner¹, Alexandra Debray¹, Dr. Klaus Höhn²

¹OSRAM Opto Semiconductor GmbH, Germany, ²Siemens AG Corporate Technology ZT MF3, Germany

High Performance Epoxy Casting Resins for SMD-LED Packaging

Abstract

In order to come up with high volume SMD-LED production encompassing 1.9 billion devices for current fiscal year we did basic exploratory work to establish structure-processing-property relations for robust epoxy casting resin packages with identical ppm level of one.

Bisphenol A-based epoxy casting resins (DGEBA) with acidic ester modified Hexahydrophthalic anhydride (HHPA) hardeners using strictly controlled high-grade raw materials were formulated and thermally transferred to highly transparent polyester networks. For 1 mm thick samples transparency in the 400 to 800 nm region is above 90 %. Thermal aging tests for 6 weeks at 120 °C reveal only slight discoloration with a color distance of 2. To avoid significant light losses within the LED operating life of 100,000 hrs stress on mechanically sensitive light-emitting chips was reduced by matching glass transition temperature T_g and E-modulus to 115 °C and 2,800 MPa, respectively. Total chloride content below 1,000 ppm imply low corrosion potential.

Further, resin composition, epoxy-hardener mixing ratio as well as curing profile were adapted to materialize fast curing for demand quantities while introducing effective low stress moieties in the final structure. Low internal stress, superior thermal shock and crack resistance were derived from supreme fracture toughness: K_{IC} and G_{IC} values were 1.350 MPam^{1/2} and 560 J/m². With favourable water absorption behaviour LED-packages withstand all soldering processes including TTW(through the wave) soldering. Thus, SMD-LEDs fulfill electronic industry standard JEDEC LEVEL 2.

Keywords: *SMD-Light-Emitting Diodes, Packaging, Epoxy Casting Resins, Moisture Uptake, Fracture Toughness*

1. Introduction

In the field of (opto-)electronics there is a general trend towards expanding functionality and performance including higher reliability in more adverse environments with increasing service temperatures and decreasing package size for demanding applications in automotive industries. Due to cost, processing, performance and reliability considerations, polymeric materials are of growing significance at a rapid pace for (opto-)electronic packaging.

Epoxy resin thermosets are currently the material of choice for optoelectronic packaging, because of their chemical resistance, mechanical and electrical strength associated with excellent thermal stability. Liquid state epoxy casting resins insure optical clarity and product uniformity. In addition to their unique processing and fabrication capabilities, epoxy resins are polymeric materials by design to suit desired applications by molecular engineering.

Besides high light transmission in the visible region, excellent colour stability upon long-term temperature exposure up to 120°C the whole package has to reach 100,000 hrs operation life time for light-emitting diodes (LED). Attachment of surface mount (SMD-)LEDs to a circuit board involves thermal soldering stress that mostly affects reliability regarding package cracking and delamination. Crack- and void-free epoxy thermosets comprising well-balanced mechanical properties, strong adhesion, especially, to the light-emitting chip as well as a robust design pave the way for reliable SMD-LEDs.

Reliability of the package depends mainly on two factors, namely, moisture uptake and mechanical stress developed during processing and operation attributed to the cure stress and cooling stress from the CTE (coefficient of thermal expansion) mismatch. Of major importance for SMD-packages is to withstand thermal stress profiles during soldering, particularly in TTW(through the wave)-processing. To this end the focus of our investigations was to improve fracture toughness features to render epoxy resin thermosets, which are inherently brittle owing to their high crosslink density suitable for SMD-LED packages. Noteworthy, from a polymeric materials view, it is not possible to change one property of the thermoset without altering another. For example glass transition T_g vs. E-modulus, CTE as well as network density and brittleness. Material science have to find out the optimum level of properties to accommodate all facets for the specific application.

This contribution reports the development of a two-component epoxy casting resin that possess outstanding properties for optoelectronic packaging. Thermal crosslinking of conventional-type Diglycidyl ether of bisphenol A (DGEBA) epoxy resin formulations are accomplished by acidic ester modified anhydride hardeners using specific accelerators. Another goal was to exclude HSE (health, safety, environmental) concerns for suitable formulations by the right choice of raw materials. Casting technology in conjunction with optimized reactivity for short curing cycles at reasonable temperatures allow successful high volume production for SMD-LEDs.

2. SMD-LED Assembly

In diagram 1 the flow chart for the SMD-LED manufacture is pictured. A stable automatic reel-to-reel process enables an efficient mass production for currently 1.9 billion units with a high output. Before

mounting the chip the aromatic Polyphthalamide (PPA) housing is injection molded. Within the casting line the premixed epoxy casting resin is precisely brought upon the LED reflector using a multiple dosing system. After curing the resin, the galvanic bath treatment, splitting and testing, the LEDs are dry packed for transportation. The LEDs are suitable for automatic pick-and-place equipment in the field of SMT-technology.

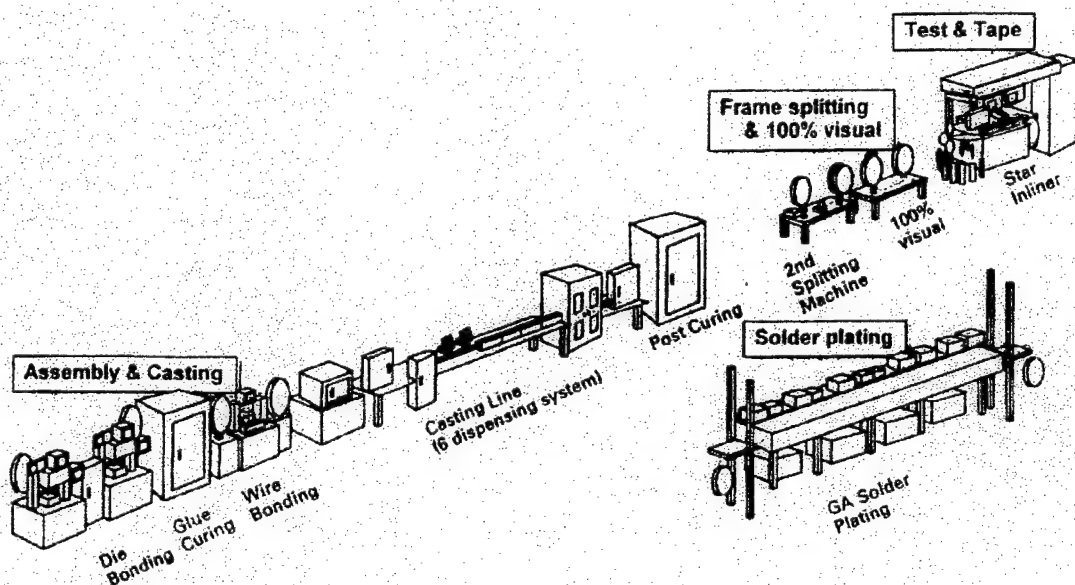


Diagram 1. Schematic set-up for SMD-LED manufacture.

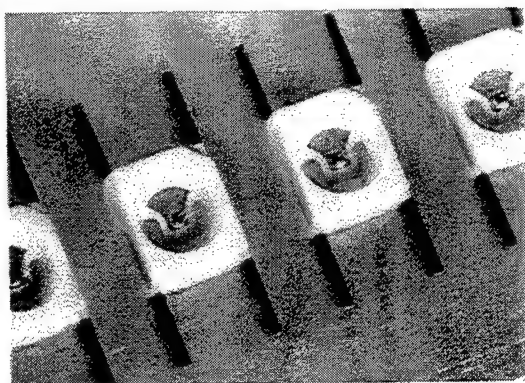


Figure 1. Premoulded SMD-LED upon reel after wire bonding.

3. Chemistry

Epoxy resin chemistry and technology for a wide range of applications are outlined in the literature [1]. The specific requirements for transparent epoxy resins in safe mass production processes for optoelectronics comprise:

- a low viscosity of the bubble-free, homogeneous casting resin along with a pot life of at least four hours for trouble-free dosing
- and a specific cure chemistry to realize fast curing cycles at medium temperatures to overcome internal package stress caused by volatiles and thermal shrinkage.

Other desired criteria are a broad formulation potential with an appropriate mixing ratio, shelf life of the components of at least 6 months as well as low cost. Additionally, the readily cured epoxy package has to protect the LED-device from mechanically and chemically extreme environments during the galvanic bath process and the entire service life.

The most widely utilized class of epoxy casting resins represent Bisphenol-A-based bifunctional prepolymers. Diglycidyl ether of bisphenol A (DGEBA) is the main constituent for the epoxy opto formulation with the chemical structure shown in diagram 2. The physical properties of the epoxy formulation are listed in table 1.

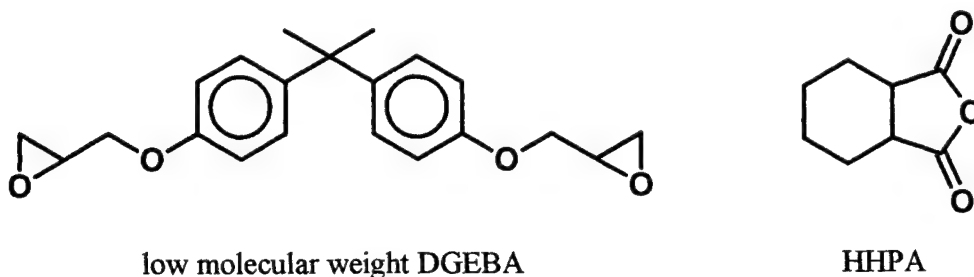


Diagram 2. Chemical structure for the Diglycidyl ether of bisphenol A (DGEBA) and the Hexahydrophthalic anhydride (HHPA) hardener.

Table 1. Physical properties of the actual epoxy opto formulation.

Appearance	transparent, slightly blue
Viscosity (25 °C)	2,200 mPas
Epoxy value	0.56 mole epoxy/100 g resin
Specific gravity (20 °C)	1.20 g/ml
Refractive index n_D^{20}	1.569
Color number (gardner)	≤ 1
Shelf life (max. 30 °C)	15 months

In order to achieve high heat and chemical resistance along with low color drift during service life thermal curing is accomplished by a Hexahydrophthalic anhydride (HHPA) hardener (diagram 2.) formulation mediated by a specific accelerator agent. Besides a low viscosity of the hardener some Acidic ester modifications are introduced to match the reactivity and the mechanical features for the final Polyester-structured thermoset. The network formation is via an addition reaction mechanism without evolution of low molecular weight by-products accompanied by a small shrinkage of below 3 %. The key features for opto casting resins are exemplified in table 2.

Table 2. Key features of the LED casting resins.

Viscosity (25 °C)	600 – 800 mPas
A:B mixing ratio	100:(80-95)
Pot life	> 4 hrs
Chloride content:	
Total (DIN 53474)	800 ppm
Hydrolyseable (DIN 53188)	250 ppm
Free (DIN 53188)	< 5 ppm
Volume shrinkage	< 3 %

4. Reactivity

In DSC (differential scanning calorimetry) experiments changes of the heat capacity with temperature or with time in the isothermal mode are detected very precisely in the mg scale for versatile materials. Thus, DSC is ideally suited to study the reactivity and the extent of cure for epoxy thermosets. In a conventional DSC run the reactive formulation is subjected to a heat ramp of 10 K/min. The exothermic enthalpy for the chemical reaction of the crosslink process is indicated by the area under the curve. Further valuable features are the onset and the peak temperature. In addition to the reaction heat these data is vital to the process engineer to work out the curing profile in the assembly to accomodate short curing times on the one hand and to avoid too much overheating for stable packages on the other hand. Figure 2 shows the dsc line shape for epoxy anhydride opto formulations with increasing accelerator amounts. The lower the accelerator content the lower the reactivity and the higher the onset and peak temperatures. Obviously, network formation is more selective at higher accelerator amounts as the cure exotherm spans a smaller temperature range. For a given epoxy-hardener ratio (A:B) the cure exotherm was adjusted to an onset temperature of 140 °C that reveals a reasonable thermal budget necessary to compensate internal stress during network formation without posing time constraints in the production line.

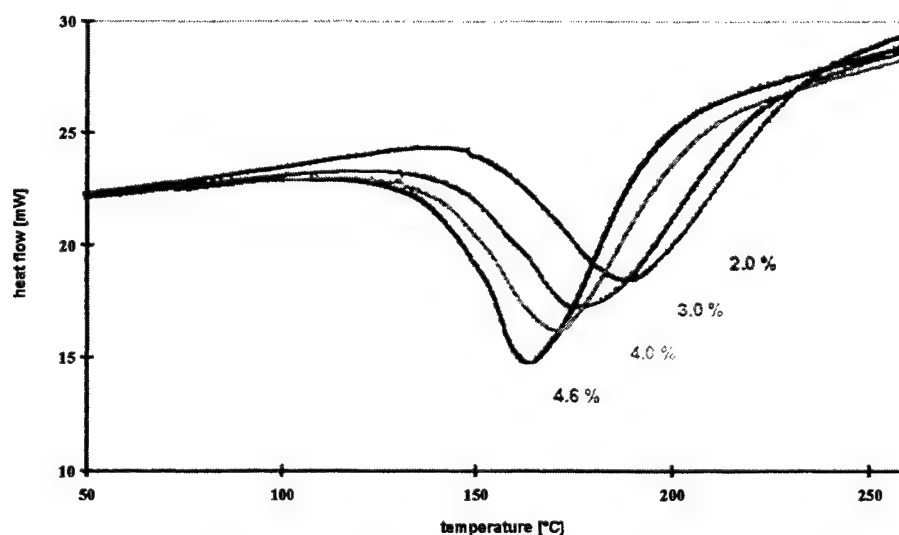


Figure 2. DSC cure exotherms for an epoxy opto resins with variable accelerator amounts (ramp: 10 K/min).

Another exploratory tool necessary to fine-tune the reactivity of the casting resin for specific line conditions is the gel time to transfer the liquid resin to a semi-solid state at the gel point. Gel times for an optimized A:B mixing ratio at a fixed accelerator content on a hot plate are summarized in table 3. Gel time vs. $1/T$ are pictured in diagram 3. The graph reveals a change of the reaction mechanism at around 140 °C with fast network formation at above this temperature. To come up with high volume demands precuring has to be performed at temperatures above 150 °C.

Table 3. Gel times for the actual epoxy opto resin (0.4 g).

T [°C]	$1/T \cdot 10^{-3}$ [1/K]	Gel time [s]
100	2.68	2,000
120	2.54	1,200
130	2.48	750
140	2.42	360
150	2.36	240
160	2.31	160
170	2.26	100
180	2.21	60

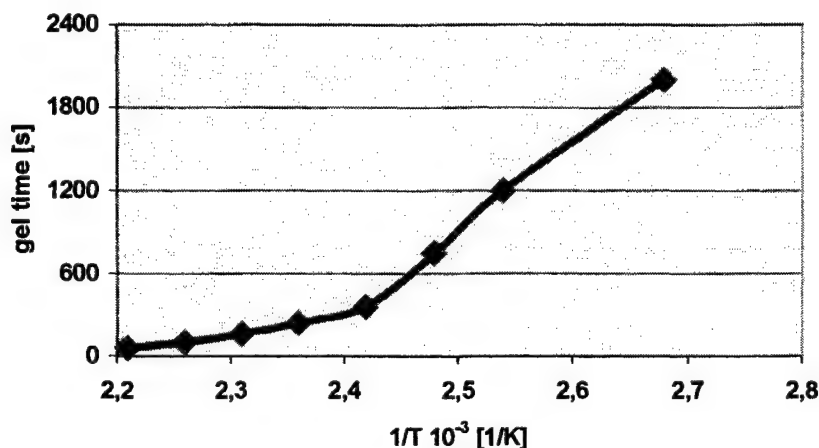


Diagram 3. Gel time vs. $1/T$ in Kelvin for the actual epoxy opto resin.

5. Transmission and cure stage properties

A strong performance feature of these LED epoxy resins is their clarity, their high light transmission in the visible range and their outstanding thermal stability. The transmission of a machined and polished 1 mm specimen is nearly 90 % in the visible range (diagram 4). Considering reflectance losses on the surface a total material transmission of roughly 98 % is reached. After 6 weeks thermal aging at 120 °C a color shift of 2.2 was observed. The high optical stability of the opto resin is further proved by a climate weathering test using Xe-radiation according to DIN 53387. After 1,000 hrs a color shift of 2.5 was found. Practically, there is no reduction of transmission after moisture saturation at 23 °C. Favourable LED light output is ensured by a reasonable refractive index n_D^{20} of 1.53. Further material characteristics are completed in table 4.

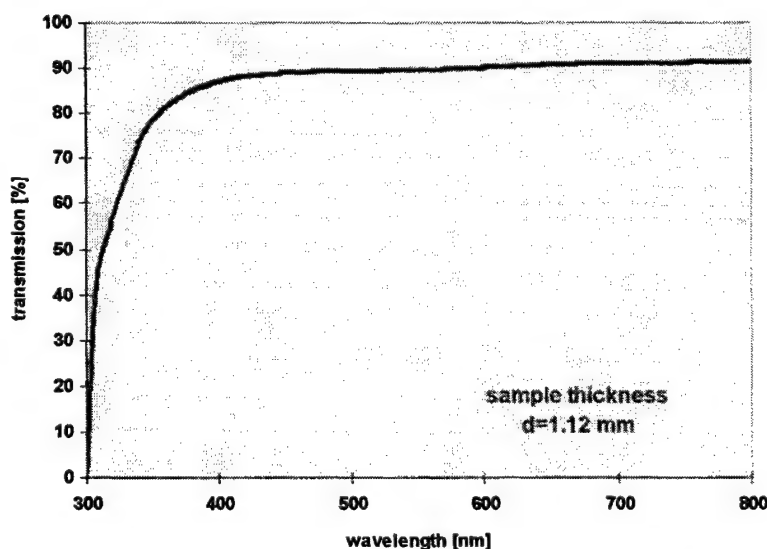


Diagram 4. Transmission characteristic for the actual epoxy opto resin.

Table 4. Complementary material characteristics for the actual epoxy opto thermoset.

Glass transition T _g (DSC: 10 K/min)	115 °C
Shore D hardness	87
CTE	
-50 to + 50 °C	65 ppm/K
> T _g	185 ppm/K
E-modulus (tensile, 1 Hz, 3 K/min)	
at 20 °C	3,100 MPa
at 100 °C	1,900 MPa
Bending modulus (DIN53452)	2,900 MPa
Flexural strength (DIN53452)	130 MPa
Tensile shear strength (DIN53283)	18.3 MPa

6. Moisture

The effect of environmental moisture absorption from the surrounding is critical as mechanical and electrical properties as well as functionality of moisture sensitive devices suffer. Under elevated temperatures in the presence of high humidity loadings, the package quality deteriorates and corrosion as well as chip degradation are likely. Potential humidity-related concerns imply formation of crazes, voids, microcracks along with moisture induced interfacial delamination and popcorning during reflow soldering. In order to understand the factors that control water absorption and to improve the hydrolytical durability in moist environments, investigations on moisture uptake behaviour for epoxy thermosets are an important technical objective.

Theoretical approaches on the sorption issue and moisture diffusion in glassy thermosets were cited in [2, 3]. Empirical thermodynamic models for accelerated humidity testing correlate sorption data at different temperatures successfully [4]. Water uptake in epoxy thermosets upon versatile temperature-humidity profiles were studied in detail [5]. General findings comprise:

- moisture saturation w_{∞} is proportional to relative humidity (r. h.)
- $\log w_{\infty}$ is proportional to the reverse temperature $1/T$ in Kelvin units
- kinetically water absorption happens in two stages
- at low levels water absorption is diffusion controlled according to the Fickian model
- the diffusion coefficient D for polymers is in the order of $10^{-8} \text{ cm}^2/\text{s}$ at ambient T
- Arrhenius approximation describes the T dependence for the diffusion coefficient D
- equilibrium data at higher water amounts support the hypothesis of penetrant water clustering

Extensive experimental reports point out the individual parameters for water absorption associated with the epoxy resin chemistry employed such as the type of the cure chemistry and the extent of cure for a given epoxy-hardener stoichiometry at specific temperature-time regimes [6, 7].

Voids and structural imperfections, free volume, polarity of the epoxy network and the nature of the polymer-water affinity involving the capability of H-bond formation control the amount of water absorbed. Besides optical grounds properly cured anhydride epoxy resins outperform amine curing systems by far in terms of moisture uptake behaviour and hydrolytical stability in wet conditions [8].

Material screenings on anhydride cured epoxy resins using accelerated water absorption tests at 85 °C/85 % r. h. reveal a considerable lower water uptake for an aromatic DGEBA-based formulation compared to a cycloaliphatic epoxy resin based on ERL4221 (3,4-Epoxy-cyclo-hexylmethyl-3',4'-epoxy-cyclo-hexanecarboxylate) (table 5). In line with an increasing free volume and the evolution of volatiles during high temperature cure the equilibrium water absorption for the cycloaliphatic epoxy resin with a Tg of 155 °C also increases.

Table 5. Gravimetrical water gain for fully anhydride cured epoxy casting resins at 85 °C/85 % r. h. (specimen: 50x6x4 mm).

Resin Base	Time [hrs]	Water gain [%]
DGEBA	4	0.21
	168	1.00
	336	1.09
ERL4221	4	0.49
	168	2.72
	336	3.22

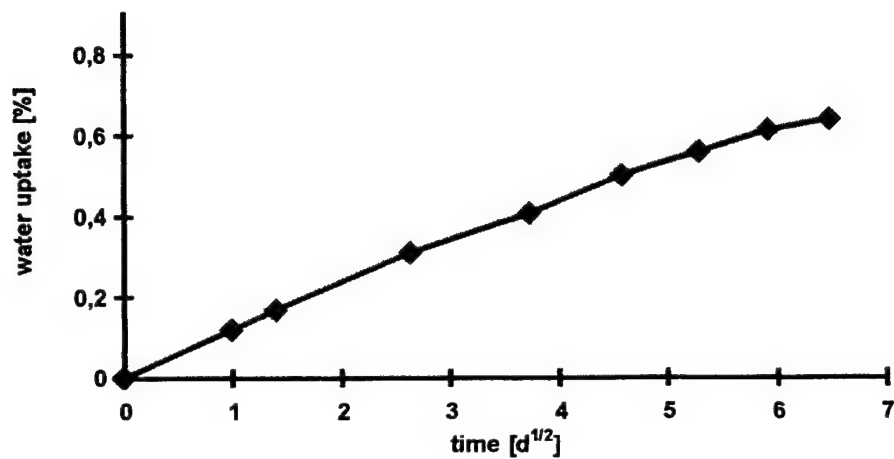
Comparative water immersion experiments at 23 °C on DGEBA-samples cured with HHPA-type and MHHPA-type opto hardeners yielding 0.64 % and 0.77 % ultimate water absorption after 1,000 hrs , respectively, show that the HHPA-type opto hardener system is more reasonable. As a result the actual epoxy casting resin is made up of a formulated DGEBA epoxy resin with a HHPA-based hardener.

The water absorption isotherm at 23 °C for the actual epoxy packaging material complies also with a two stage absorption mechanism including a diffusion controlled pickup within the first 7 days and penetrant clustering in the equilibrium region starting after 3 weeks immersion (table 6, diagram 5). Saturated water content w_{∞} is extrapolated to 0.70 % with a mean diffusion coefficient $D_{\infty}(23\text{ °C})$ in the order of $10^{-10}\text{ cm}^2/\text{s}$. The mean water absorption rate k_w at 23 °C is decreasing linearly with the square root of time (diagram 6). Unfortunately, from this graph no two-stage water absorption mechanism is evident.

Table 6. Moisture absorption characteristics for water immersion at 23 °C (DIN 53 495) for the actual LED epoxy resin (specimen: 50x6x4 mm).

Immersion time [d]	Immersion time [\sqrt{d}]	Uptake [%]	Rate k_w [%/ \sqrt{d}]
1	1.00	0.12	0.120
2	1.41	0.17	0.121
7	2.65	0.31	0.117
14	3.74	0.41	0.110
21	4.58	0.50	0.109
28	5.29	0.56	0.106
35	5.92	0.61	0.103
42	6.48	0.64	0.099

Diagram 5. Water uptake for the actual opto resin with immersion time \sqrt{d} at 23 °C.



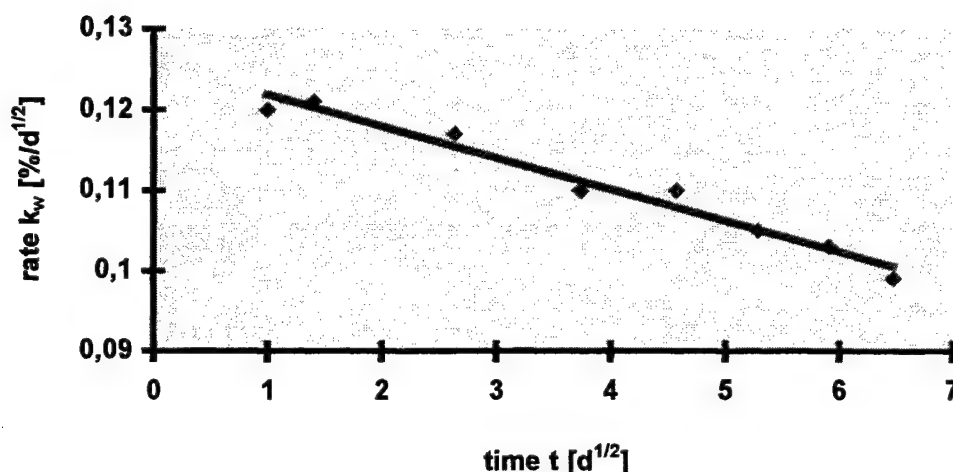


Diagram 6. Water absorption rate $k_w(23\text{ }^{\circ}\text{C})$ for the actual opto resin with immersion time \sqrt{d} .

Moisture-related T_g drops due to matrix plasticization were largely reversible even after pc-testing (pressure cooker: $121\text{ }^{\circ}\text{C}$, 100% r.h., 2.08 atm , 24 hrs). No acid was set free via hydrolytical decomposition nor a T_g decrease of the fully desiccated samples were observed after soaking in water for 3 d at $65\text{ }^{\circ}\text{C}$. In addition, sorbed water have not induced any further crosslinking of the anhydride cured epoxy thermoset. In this connection, it should only be stated here, that moisture concentration gradients will generate compressive and tensile force distributions within the epoxy package. For an E-modulus of $3,000\text{ MPa}$ the mean internal stress at $23\text{ }^{\circ}\text{C}$ created by a 0.8% load of water is calculated to 5 MPa .

7. Fracture toughness

Brittleness in epoxy thermosets arises from their highly crosslinked chemical architecture. Reliability of epoxy packages in a wide range of severe environments for different commercial applications encountering diverse mechanical stress situations depends mostly on the ability of the epoxy polymer to relieve stress peaks to overcome package cracking. Over the years a manifold of papers addresses the toughening issue for epoxies [9]. Improvement of the fracture strength is brought about by the incorporation of elastomer, rubber and core-shell particles. Intense studies on the size, size distribution, dispersability and hardness of the particles as well as on the nature of the particle-epoxy interaction along with demanding morphological investigations brought out controversial standpoints on toughening mechanisms [10]. Apart from that it is generally accepted, that fracture resistance is attributed to a series of energy-consuming events to take place in the stressed region of the resin, namely, shear yielding and crack propagation.

Because of restricted transparency of particle-modified epoxy resins attention was paid here on the question of how to toughen the neat epoxy matrix. Fracture resistance progressively decreases with increasing crosslink density and T_g . As for too low a T_g the fracture energy to dissipate stress also decreases, fracture toughness performs best at medium crosslink density. In order to build the ideal

molecular lattice for ductile epoxy casting resins, selective raw material screenings for composing the optimum epoxy-hardener components were carried out. Further fine-tuning efforts were made to optimize the A:B mixing ratio and the cure process.

Fracture toughness experiments were performed at room temperature on single-edge-notched specimens in the three-point-bending mode (SENB) according to ASTM E399 D790 guidelines. Acidic ester modified acid anhydride-cured DGEBA-thermosets indicate unique fracture toughness characteristics. Applying linear elastic fracture mechanics the critical stress intensity factor K_{IC} and the fracture energy G_{IC} for the actual epoxy opto thermoset are 1.350 MPa \sqrt{m} and 560 J/m², respectively. For the epoxy thermoset matrix usually K_{IC} 0.55 to 0.65 MPa \sqrt{m} and G_{IC} 80 to 150 J/m² were reported. Actually, measurements on HHPA-cured DGEBA-resins without acidic ester modification show K_{IC} and G_{IC} 0.59 MPa \sqrt{m} and 110 J/m², respectively. To our knowledge the presented LED epoxy resin exhibit the highest fracture values for neat epoxy thermosets reported so far.

Specific acid ester modification of the HHPA-hardener for DGEBA-based thermosets allows outstanding fracture strength for crack-resistant, reliable SMD-LED packages. The hydrolytically resistant LED epoxy thermoset exhibit reasonable moisture absorption characteristics indicative for low deficiencies for SMD-LEDs during galvanic bath treatment and after reflow shock testing. Thus, LEDs are approved for all kinds of IR reflow soldering and TTW solderability for JEDEC level 2.

8. Conclusion

In packaging technology based on epoxy thermosets there is a strong structure-processing-property interdependence. In conclusion, the reliability of an epoxy package is strongly dependent on the chemical composition of the formulation and the time-temperature profile of the curing process. Systematical molecular engineering using the appropriate chemistry of epoxy resins and hardeners along with suitable accelerators cover the overall requirements for the fabrication of reliable SMD-LEDs in optimized mass production assemblies. Reliability has been verified in actual devices and systems by routine qualification tests that no critical failure is likely to occur during manufacturing, testing, transportation and operation. The robust LED design opens the door for widespread applications. Huge SMD-LED volumes for backlighting of dashboards and indicator panels are the stars in the automotive sector. Due to the low moisture uptake and attractive stress-relieving nature of the epoxy package encompassing superior fracture toughness characteristics humidity level JEDEC 2 was adopted. A low stress, high temperature epoxy casting resin for high power SMD-LEDs with a T_g of 135 °C is already in the channel and will supersede this standard opto resin in the very near future.

Acknowledgements:

The principal author would like to thank Siemens AG, Corporate Technology, for financial support to attend the symposium and colleagues from Osram OS for an open discussion and provision of test results from diverse qualification modes.

9. References

- [1] C. A. May, in *Epoxy Resins Chemistry and Technology*, 2nd Edition, Marcel Dekker, Inc., New York, Basel, 1988
- [2] J. S. Vrentas, C. M. Vrentas, *J. Appl. Polym. Sci.*, 71, (1999) 1431
- [3] M. R. Vanlandingham, R. F. Eduljee, J. W. Gillespie Jr., *J. Appl. Polym. Sci.*, 71, (1999) 787
- [4] J. E. Gunn, R. E. Camenga, S. K. Malik, *Rapid Assessment of the Humidity Dependence of IC Failure Modes*, Proc. Rel. Physics, 1983
- [5] D. J. Belton, M. J. Molter, E. A. Sullivan, *Coat. Appl. Polym. Sci. Proc.*, 59, (1988) 629
- [6] M. T. Aronhime, X. Peng, and J. K. Gillham, *J. Appl. Polym. Sci.*, 32, (1986) 3589
- [7] J. B. Enns, and J. K. Gillham, *J. Appl. Polym. Sci.*, 28, (1983) 2831
- [8] B. H. Eckstein, *Org. Coat. Plast. Chem.*, 38, (1978) 503
- [9] G. Levita, S. De Petris, A. Marchetti, A. Lazzeri, *J. Mat. Sci.*, 26, (1991) 2348
- [10] J. Karger-Kocsis, and K. Friedrich, *Colloid Polym. Sci.*, 270 (6), (1992) 549

Addendum

The following papers were announced for publication in this proceedings but have been withdrawn or are unavailable.

- [3938-01] **Present status of InGaN-based LEDs**
S. Nakamura, Nichia Chemical Industries, Ltd. (Japan)
- [3938-04] **Effect of lateral epitaxial overgrowth on GaN LEDs and laser diodes**
S. P. DenBaars, M. A. Hansen, H. Marchand, G. Parish, P. Fini, T. Katona, M. Craven, U. K. Mishra, Univ. of California/Santa Barbara
- [3938-11] **Growth and characterization of InGaN/GaN multiquantum well blue light-emitting diodes**
G.-C. Chi, J. K. Shen, National Central Univ. (Taiwan)
- [3938-15] **High-efficiency InGaN light-emitting diodes**
M. Boroditsky, I. Gontijo, R. Coccioli, E. Yablonovitch, Univ. of California/Los Angeles
- [3938-24] **Strained multiquantum wells AlGaInP light-emitting diodes**
Y. Li, G. Wang, X. Ma, Y. Zhang, H. Peng, S. Wang, L. Chen, Institute of Semiconductors (China)
- [3938-27] **Way out of the dilemma of pyro- and piezoelectric fields in (Al, Ga, In)N heterostructures: growth of wurtzite M-plane GaN(100) on g-LiAlO₂(100) substrate**
K. H. Ploog, P. Waltereit, O. Brandt, M. Ramsteiner, Paul-Drude-Institut für Festkörperelektronik (Germany)
- [3938-28] **Speed limit of 1.3 μm multiquantum well microcavity light-emitting diodes**
P. Landais, B. J. Roycroft, A. Shaw, Trinity College Dublin (Ireland); B. Depreter, I. Moerman, Univ. Gent (Belgium); J. Hegarty, Trinity College Dublin (Ireland)
- [3938-29] **Some key problems of superhigh-density storage**
W. Wu, X. Pei, Huazhong Univ. of Science and Technology (China)
- [3938-32] **Design and analysis of superbrightness light-emitting diode chip array lamps**
S. J. Lee, B. G. Song, S. I. Ahn, Chungnam National Univ. (Korea)
- [3938-36] **Improvement for organic electroluminescence via ITO modification**
C.-I. Chao, E.-C. Chang, R. Y. Tsai, Industrial Technology Research Institute (Taiwan)
- [3938-37] **N₂ plasma discharge versus NH₃ cracking in (Al, Ga, In)N MBE growth**
K. H. Ploog, O. Brandt, P. Waltereit, A. Thamm, R. Muralidharan, Paul-Drude-Institut für Festkörperelektronik (Germany)

Author Index

- Abare, Amber C., 113
 Ahn, Seung Ik, Addendum
 Akasaki, Isamu, 52
 Amano, Hiroshi, 52
 Baets, Roel G., 160, 196
 Banas, Michael A., 13
 Basile, David, 2
 Bierman, Andrew, 240
 Bockstaele, Ronny, 160
 Bogner, Georg, 249
 Borghs, Gustaaf, 70
 Boroditsky, Misha, Addendum
 Brandt, Oliver, Addendum
 Bremser, Michael D., 100
 Brown, Daniel M., 180
 Brown, Jeremiah D., 180
 Carter-Coman, Carrie, 77
 Chang, En-Chung, Addendum
 Chang, Horng, 205
 Chang, Shouu-Jinn, 205, 218, 224
 Chang, Ying-Lan, 2
 Chao, Ching-lan, Addendum
 Chen, C. S., 218
 Chen, C. C., 224
 Chen, Eugene I., 77
 Chen, Liang-Yao, 234
 Chen, Lianghui, Addendum, 154
 Chen, Wen Rui, 205
 Chen, Yang Fang, 137
 Chi, Gou-Chung, Addendum
 Chi, L. W., 218, 224
 Chow, Peter P., 113
 Chow, Weng W., 13
 Christenson, G., 2
 Chu, T. K., 218
 Coccioli, Roberto, Addendum
 Collins, D., 2
 Collins, David, 77
 Cook, L. W., 2
 Coosemans, Thierry, 160
 Craford, M. George, 2, 77
 Craven, M., Addendum
 Crawford, Mary H., 13
 D'Hondt, Mark, 196
 Daly, James T., 188
 Davis, Rick M., 169
 Dean, Robert N., 180
 Debray, Alexandra, 249
 Debray, Jean-Philippe M., 44
 Delbeke, Danaé, 196
 Demeester, Piet M., 196
 DenBaars, Steven P., Addendum, 113
 Depreter, B., Addendum
 Derluyn, Joff, 160
 Döhler, Gottfried H., 70
 Dumitrescu, Mihail M., 82
 Dutta, Barundeb, 70
 Ebeling, Karl J., 90
 Eberhard, Franz, 90
 Edwards, A., 2
 Eliashevich, Ivan, 44
 Ferguson, Ian T., 105
 Figiel, Jeffrey J., 13
 Fini, P., Addendum
 Fletcher, Robert M., 2
 Gardner, Nathan F., 2, 77
 Gervaux, David, 144
 Gibson, Harry W., 169
 Goetz, Werner K., 2
 Gontijo, Ivair, Addendum
 Graff, John W., 60
 Graupner, Wilhelm, 169
 Grillot, Patrick N., 77
 Guo, Xiaoyun, 60
 Han, Jung, 13
 Hansen, Monica A., Addendum
 Hasnain, Ghulam, 2, 52
 Heber, Jörg, 144
 Heflin, James R., 169
 Hegarty, John, Addendum
 Heremans, Paul L., 70
 Heuken, Michael, 100
 Heuschen, M., 2
 Hirano, Atsuo, 24
 Hofer, Gloria E., 77
 Höhn, Klaus, 249
 Holcomb, Mari O., 77
 Hsieh, Kuang Yeu, 124
 Huang, H. S., 124
 Huang, Jen-Wu, 77
 Hueschen, Mark, 77
 Hwang, C. H., 124
 Imler, William R., 2
 Iwayama, Sho, 24
 Jäger, Roland, 90
 Johnson, E., 2
 Joos, J., 90
 Juang, Fuh-Shyang, 205, 218, 224
 Kaneko, Y., 52
 Kao, Y. K., 224
 Karlícek, Robert F., Jr., 44, 60
 Kato, Hisaki, 24
 Katona, T., Addendum
 Kern, R. Scott, 2

Khare, Reena, 2
 Khrushchev, Igor Y., 52
 Kiesel, Peter, 70
 Killeen, K., 2
 King, Roger, 90
 Kish, Frederick A., 2, 77
 Klaassen, Jody J., 113
 Knobloch, Alexander, 70
 Kocot, Christophe P., 2, 77
 Koike, Masayoshi, 24
 Kojima, Akira, 24
 Krames, Michael R., 2, 77
 Kuijk, M., 70
 Kussmaul, Andreas, 188
 Lam, K. T., 218, 224
 Lan, W. H., 205
 Landais, Pascal, Addendum
 Lee, Song Jae, Addendum
 Lester, Steven, 2
 Li, Xiaobing, 144
 Li, Yuzhang, Addendum, 154
 Lin, Alpha C. H., 205
 Lin, Tai Yuan, 137
 Long, Frederick H., 105
 Lowery, C., 2
 Ludowise, Mike J., 2
 Luenenbuerger, Markus, 100
 Lukacs, Stephan J., 105
 Luo, Fei, 188
 Ma, Xiaoyu, Addendum, 154
 Malakhov, Vladislav Ya., 131
 Maliyagoda, Nishantha, 240
 Mann, R., 2
 Maranowski, M., 2
 Maranowski, Steven A., 2
 Marchand, Hugues, Addendum
 Marciu, Daniela, 169
 Marinelli, Claudio, 52
 Martin, Paul S., 2
 Melanen, Petri, 82
 Mijlemans, Paul, 196
 Miller, Jeffrey N., 2
 Miller, M., 169
 Miller, Michael, 90
 Mishra, Umesh K., Addendum
 Modak, Prasanta, 196
 Moerman, Ingrid, Addendum, 160, 196
 Morse, Theodore F., 188
 Mueller, Gerd O., 2, 30
 Mueller-Mach, Regina, 2, 30
 Muralidharan, R., Addendum
 Murray, M. A., 169
 Naessens, Kris, 160
 Nagai, Seiji, 24
 Nakamura, Shuji, Addendum
 Narendran, Nadarajah, 240
 Neyman, Pat J., 169
 O'Shea, J., 2
 Orsila, Seppo, 82
 Overington, Martin, 240
 Parish, Giacinta, Addendum
 Park, Kwang, 77
 Pei, Xiandeng, Addendum
 Peng, Huode, Addendum
 Penty, Richard V., 52
 Pessa, Markus, 82
 Phillips, Christopher C., 144
 Ploog, Klaus H., Addendum
 Pophristic, Milan, 105
 Posselt, Jason, 77
 Protzmann, Harry, 100
 Pullin, Mark J., 144
 Pulver, Dan, 188
 Pysar, Richard M., 240
 Ramsteiner, M., Addendum
 Ritter, A. L., 169
 Rorison, Judy M., 52
 Rosamond, M. F., 113
 Rosner, S. Jeffrey, 2
 Roycroft, Brendan J., Addendum
 Rudaz, S. L., 2
 Saarinen, Mika J., 82
 Savolainen, Pekka, 82
 Schmid, Wolfgang, 90
 Schneider, Richard P., 2, 52
 Schubert, E. Fred, 60
 Shaw, A., Addendum
 Shen, J. K., Addendum
 Sheu, J. K., 224
 Shul, Randy J., 13
 Sipilä, Pekko, 82
 Song, Bung Gi, Addendum
 Steigerwald, Dan A., 2
 Stockman, Steve A., 77
 Su, Yan Kuin, 205, 218, 224
 Takeuchi, T., 52
 Takeuchi, Tetsuya, 2
 Tan, I. H., 77
 Tan, Michael R. T., 52
 Tan, T. S., 2, 77
 Tasi, Y. S., 224
 Tezen, Yuta, 24
 Thamm, A., Addendum
 Thompson, J., 2
 Toivonen, Mika, 82
 Tran, Chuong A., 44, 105
 Tsai, Rung Y., Addendum
 Tu, Li Wei, 124
 Uemura, Toshiya, 24
 Van Daele, Peter, 160, 196
 Van Hove, An, 160
 Vanwassenhove, Luc, 160
 Venugopalan, Hari, 44
 Vilokinen, Ville, 82
 Waltereit, P., Addendum
 Wan, Wu, Addendum

Wang, Guohong, Addendum, 154
Wang, Hong, 169
Wang, Shih Yuan, 52
Wang, Shutang, Addendum, 154
Watanabe, S. W., 52
White, Ian H., 52
Wierer, Jonathan J., 2
Windisch, Reiner, 70
Wollam, John A., 188
Yablonovitch, Eli, Addendum
Yamada, N., 52
Yamasaki, Shiro, 24
Yan, Chun Hui, 113
Yang, H. C., 137
Yao, H. Walter, 113
Yu, J. G., 2
Zavada, John M., 113
Zhang, Lei, 13
Zhang, Rong Jun, 234
Zhang, Ying-Jun, 234
Zhang, Yufang, Addendum, 154
Zheng, Yu-Xiang, 234